The Simulation, Composition and Shielding of Radiation-Induced X-ray-like Background in Space-Based X-ray Astronomy Missions

Thesis

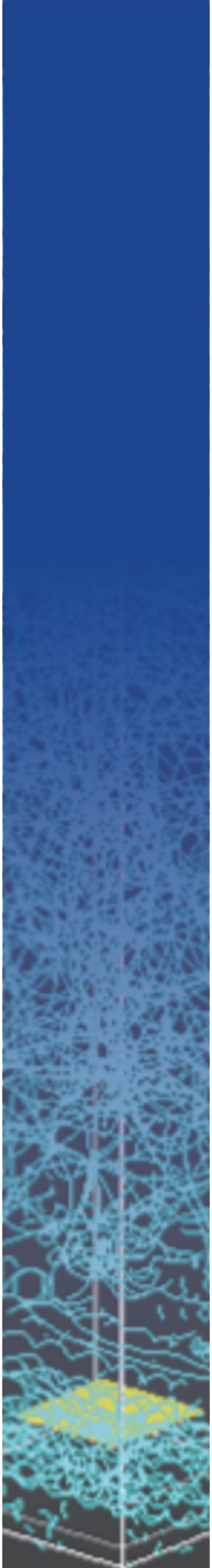

The Simulation, Composition and Shielding of Radiation-Induced X-ray-like Background in Space-Based X-ray Astronomy Missions

Christopher S. W. Davis

March 2021

Thesis submitted for the degree of Doctor of Philosophy

Supervised by Dr David J. Hall at the Center for Electronic Imaging, School of Physical Sciences, The Open University

Co-supervised by Dr Jonathan J. Keelan and Professor Andrew D. Holland

Research funded by STFC and Teledyne-e2v

Abstract

X-ray-like background has the ability to introduce significant systematic and statistical errors to astronomical measurements from space-based X-ray observatories. Statistical errors from radiation-induced X-ray-like background can dominate the noise in images produced by space-based X-ray telescopes and can severely reduce scientific output. However, the composition and quantity of radiation-induced X-ray-like background events that will be present in a space-based X-ray observatory is not well understood.

The work presented in this thesis has investigated several key research areas. The results of two experimental campaigns are presented, which are used to assess the accuracy of Geant4 at simulating low energy radiation to mimic the space-based environment. Geant4 simulations are then used to predict the particle composition of radiation-induced background in the environment of space.

The composition of background for a detector in a spherical shell spacecraft model is characterised through Geant4 simulations, and it is found that on-chip filters could significantly reduce the background due to electrons and low energy photons. It is also found that for the purposes of maximising signal-to-noise ratio in an ideal detector, there exists an optimal detector thickness for a given particle composition of background.

Finally, key results for investigations into shielding methods include the creation of a mathematical model for the determination of optimal graded-Z shielding locations, and the demonstration that a Helmholtz coil magnetic field structure could be used to significantly reduce the background induced by both low energy fully absorbed electrons, and backscattering electrons.

Much of the simulation work in this thesis was performed on geometries similar to the expected geometry of the Wide Field Imager (WFI) in the European Space Agency's ATHENA mission as an example of a general X-ray astronomy mission, and to predict the background that will be present in images from the WFI when ATHENA launches in the 2030s.

Declaration

I hereby declare that no part of this thesis has been previously submitted to this or any other university as part of the requirement for a higher degree. The work described herein was conducted solely by the undersigned except for those colleagues and other workers acknowledged in the text.

Chris Davis

02 June 2021

Dedication

To Amy, and my mum, dad and Connor.

Acknowledgements

I would like to genuinely thank every person who has helped me through this PhD process. It is no exaggeration to say that the last four years have been an extremely difficult time of my life and while it's somewhat cliché to say, it is absolutely true that there is no way I would have been able to complete this thesis without the huge number of friends, colleagues and loved ones who have been supported me.

I would firstly like to thank my supervisor, David Hall. I am extremely glad to have had a supervisor who has been so supportive of me throughout this PhD, and accommodating whenever I've had difficulties. I can confidently say that without David's guidance and advice I would not have evolved into the scientist I am today.

I would like to thank all my friends and colleagues on the ATHENA team at the CEI, who I worked with extensively throughout the four years of this PhD, including Oliver Hetherington, Michael Hubbard, Neil Hollyhoke, Jonathan Keelan, Mark Leese, Timothy Arnold and Andrew Holland.

I would also like to thank all of my great friends I have met at the CEI, including Anton Lindley-DeCaire, Alice Dunford, Matt Lewis, Daniel-Dee Lofthouse-Smith, Tom Buggey, James Ivory, Harry Fox, Lawrence Jones, Saad Ahmed, Zoe Lee-Payne, Domenic Ward, Daniel Evan, Chiaki Crews, George Randall, Michael Holland, Nathan Bush, Matt Soman, Jesper Skottfeld, Edgar Allenwood, Xiao Meng, David Gopinath, David Burt, Konstantin Stefanov and more. I will really miss all the great chats and banter we had in the office, and I will definitely be keeping up with you through D&D, gaming sessions and other social events.

I would also like to thank every one of my friends and family who have supported me over the last few years. I would not have been able to complete this thesis without the help of my best friends including Lela Palin, Max Swann and Cheryl McMaster to name a few. My mum, dad and brother have also been immensely supportive of me throughout all of this, and I am so thankful of all the love and support they have given me throughout all of this.

Most importantly I would like to thank my life partner, Amy Rogers. She has helped me through so much over the past few years, sacrificed so much to help me progress through this stage in my life, and made me the person I am today. I am incredibly lucky to have her, and her support for me every single day made me able to keep pushing through to the end.

I would like to use the final paragraph of this Acknowledgements section to express something that is very important to me, as a message to anyone reading this who is going through mental health difficulties. Most of my friends and work colleagues know that I have suffered from severe anxiety

and also depression throughout this PhD, and I want to let anyone reading this who also might be going through mental health issues, that you are not alone. Anxiety and depression are very common but debilitating diseases and so many good, decent people are struggling with them, particularly in academia. It is very important for everyone to know that if you are currently afflicted by these horrible diseases, it is not in any way, shape, or form your fault, and that there are so many loving, caring people out there who may be able to help you.

Despite all of the challenges I have had to go through over the last few years, I am immensely proud of both how much I have grown as a person, and the work I have done during this PhD. I hope that the research I have done provides value to whoever is reading through this.

Table of Contents

Chapter 9 188

The Effect of Spacecraft Geometry and Detector Design on Instrument Background

Chapter 10 221

Shielding Mechanisms

List of Acronyms

ADU	Analog-to-Digital Units
AGN	Active Galactic Nucleus
AREMBES	Athena Radiation Environment Models and x-ray Background Effects Simulator
ATHENA	Advanced Telescope for High ENergy Astrophysics
BCB	BenzoCycloButene
CAD	Computer Aided Design
CCD	Charge-Coupled Device
CCE	Charge Collection Efficiency
CME	Coronal Mass Ejection
CREME96	Cosmic Ray Effects on Micro-Electronics (1996 Revision)
CSDA	Continuous Slowing Down Approximation
CXB	Cosmic X-ray Background
DEPFET	DEPleted Field Effect Transistor
EMCCD	Electron Multiplying Charge-Coupled Device
EPIC	European Photon Imaging Camera
ESA	European Space Agency
FWHM	Full Width at Half Maximum
GCR	Galactic Cosmic Ray
GDML	Geometry Description Markup Language
GEANT4/Geant4	GEometry ANd Tracking version 4
HEO	High Earth Orbit
LEO	Low Earth Orbit
LIS	Local Interstellar Spectrum
MEO	Medium Earth Orbit
MHD	MagnetoHydroDynamics
MIP	Minimally Ionising Particle
MOS	Metal–Oxide–Silicon
MOSFET	Metal–Oxide–Semiconductor Field-Effect Transistor
NIST	National Institute of Standards and Technology
PIXE	Particle-Induced X-ray Emission
PN	Positive-channel, Negative-channel
PNCCD	Positive-channel, Negative-channel Charge-Coupled Device
QE	Quantum Efficiency
SAA	South Atlantic Anomaly
SAC	Self-AntiCoincidence
SEP	Solar Energetic Particle
SPENVIS	SPace ENVironment Information System
TDI	Time Delay and Integration
TRL	Technology Readiness Level
WFI	Wide Field Imager
XIFU	X-ray Integral Field Unit
XMM-Newton	X-ray Multi-Mirror Newton/X-ray Multi-Mirror mission

Chapter 1

Introduction

The experimental background, the presence of signal in an experiment when no scientific measurements are being taken, is an essential consideration in scientific experiments across almost every scientific field. The presence of background is capable of both creating systematic errors in experimental results and increasing experimental statistical noise. In many scientific experiments, noise generated by background can be the dominant source of statistical errors, and can significantly reduce the signal-to-noise ratio. As the signal-to-noise ratio is frequently used as a measure for the quality of measurements in X-ray astronomy, the presence of background has the potential to limit the success of an X-ray observatory.

In space-based X-ray astronomy, background can be a crucial limiting factor for the success of a mission. A large background can obscure faint but potentially scientifically interesting sources and can reduce signal-to-noise ratios. As astronomical X-ray missions attempt to observe fainter sources deeper and deeper into the universe, the signal from sources becomes weaker and less intense relative to sources of background. This background is composed of both 'sky' background such as foreground and background sources of X-rays in images, or by non-sky components such as straylight and the primary focus of this thesis, particles generated by the interaction of external radiation with internal spacecraft structures. In order to maintain a sufficiently large signal-to-noise ratio when viewing distant sources, mitigation strategies for the removal of radiation-induced background will need to be developed for future generations of space-based X-ray observatories.

This thesis will use Geant4 (Agostinelli et al. 2003) simulations to characterise the background generated by radiation impacting spacecraft so that mitigation strategies can be designed to remove this background. This characterisation will be performed for simplified spherical shell models in order to characterise how background changes with spacecraft and detector design, and it will also be performed on the full mass model for the ATHENA Wide Field Imager (Barcons et al. 2015). The effectiveness of graded-Z shielding and magnetic shielding mechanisms at background mitigation will also be investigated both theoretically and through Geant4 simulations.

As part of the work performed in this PhD project, two major experiments were also performed to verify Geant4's use in simulations of background in the space-based environment, and these will be reported on in Chapters 6 and 7.

1.1 The acquisition of signal in X-ray astronomy

To assess the effect of background on the signal-to-noise ratio, it is necessary to discuss the basics of image taking in space-based X-ray observatories. X-ray observatories are typically designed such that single photons are detected by individual pixels in an image. X-rays are significantly more energetic than the bandgap energy of silicon, such that when they are absorbed into a pixel photoelectrically, they typically generate many electrons rather than a single electron. The mean number of electrons produced is proportional to the energy of the initial photon, meaning that spectroscopy can be performed on outputted images by converting the total charge in activated pixels into initial photon energies.

As the statistics for taking an astronomical image is simply the statistics for photon counting, the signal-to-noise ratio for observations where no background is present can be expressed using background noise, where the standard error in observations N_S is equal to the square root of the number of signal photons within the energy range of interest $\sqrt{n_S}$. This means that the signal to noise ratio can be expressed as

$$\frac{S}{N_S} = \frac{n_S}{\sqrt{n_S}} = \sqrt{n_S} \tag{1.1}$$

Equation 1.1 can be expressed in terms of the actual mean flux from a scientific source F_S in units of cts / cm^2 / s using the relation that $n_S = F_S \times t_d \times A_d$, giving

$$\frac{S}{N_S} = \sqrt{t_d A_d F_S} \tag{1.2}$$

where t_d is the total time that source was observed for, and A_d is the area of the region of the detector in which photons were counted for the observation. Equation 1.2 indicates that for an observation with no background present, doubling the signal-to-noise ratio requires quadrupling the observation time. Equivalently it means that dividing the intensity of a source by four causes the signal-to-noise ratio to be halved.

An increase in observation time to gain better statistics is problematic in general as it limits the time an observatory can spend performing other scientific activities. In addition to a lowered flux causing drops in signal-to-noise ratio, the presence of background is also capable of reducing the signal-to-noise ratio. This means that either the statistical quality of observations will be lowered or that the observation time will need to be increased.

1.2 X-ray-like background

As background acts to reduce the signal-to-noise ratio, Equation 1.2 will need to be adapted to include the effect of background. First, however, it is necessary to discuss the basics of particle-induced background in astronomical X-ray images.

Because an X-ray mission is only interested in viewing photons, any particle track that can be identified as not from a photon can be removed algorithmically from images. Many X-ray observatories use on-board event detection algorithms to remove features such as particle tracks from images, which are generated by high energy electrons or ions penetrating multiple pixels in the detector. It is also possible to use methods such as self-anticoincidence (Ding 2018) to identify single-pixel events associated with background if those events are sufficiently near to a particle track.

However, it is often not possible to algorithmically separate events created by background particles that only deposit energy in a single-pixel from X-rays created by an astronomical source. Such types of background are the 'X-ray-like' background that the title of this thesis refers to and will be the key component of background in images that the work presented in this thesis will seek to reduce.

The physics behind X-ray-like background generation from the interaction between cosmic radiation and spacecraft structures will be discussed in further detail in Chapter 2 and Chapter 3.

1.2.1 Statistical errors and noise

As stated previously, the presence of background adds random statistical errors to measurements and reduces the signal-to-noise ratio of scientific observations. This is because the noise N on the total number of counts received is no longer just the square root of the number of signal counts, it is the square root of the total number of accepted events, $N = \sqrt{n_S + n_B}$, where n_B is the total number of X-ray-like background counts. The signal S remains unchanged under the assumption that background can be perfectly subtracted using dark frames. Therefore the signal-to-noise ratio becomes

$$\frac{S}{N} = \frac{n_S}{\sqrt{n_S + n_B}} \tag{1.3}$$

$$= \frac{tA_dF_S}{\sqrt{tA_dF_S + tA_dF_B}} \tag{1.4}$$

$$= \sqrt{tA_d}\frac{F_S}{\sqrt{F_S + F_B}} \tag{1.5}$$

Where F_B is the mean background flux over the same energy range as F_S, in units of cts / cm^2 / s. From Equation 1.5 it can be seen that signal-to-noise ratio is still proportional to the square root of the observation time t, however for values of F_B that are comparable or significant compared to F_S in intensity, the signal-to-noise ratio is no longer proportional to the square root of F_S. A 'quality factor',

QF, can be defined to reflect the quality of an observation as only a function of F_S and F_B (here defined similarly to the definition for 'quality figure' given by David J. Hall and Holland (2010)):

$$QF = \frac{1}{\sqrt{tA_d}} \times \frac{S}{N} = \frac{F_S}{\sqrt{F_S + F_B}} \tag{1.6}$$

The effect of F_B on the signal-to-noise ratio can be seen when F_B is set to be a fraction of F_S, $F_B = rF_S$. This means that the signal-to-noise ratio becomes

$$\frac{S}{N} = \sqrt{tA_d}\frac{F_S}{\sqrt{F_S + rF_S}} = \sqrt{\left(\frac{t}{1+r}\right)A_d F_S} \tag{1.7}$$

By comparing Equation 1.7 to Equation 1.2, it can be seen that an increase in X-ray-like background flux can be expressed as decreasing the effective observation time. Substituting $r = 1$ corresponding to the case where the mean background flux is equal to the mean signal flux gives an effective observation time that is half the observation time for the case where no background is present.

Therefore if the background could be removed in such cases, the required observation time for such measurements could be reduced by a factor of 2. Likewise, for the case where X-ray-like background flux is twice the signal flux, $r = 2$, the required observation time can be cut by a factor of 3. This indicates that shielding a detector from radiation-induced background could allow observation times to be reduced dramatically for situations where the signal flux is comparable to the radiation-induced background flux.

While this thesis will primarily use equations 1.5 to 1.7 in discussions of the effect of X-ray-like background on the signal-to-noise ratio, it should be noted that extra noise σ_D is also introduced by the subtraction of background using dark frames. The extra noise introduced is equal to the square root of the total number of dark frame background counts received, divided by the dark frame observation time t_D and the detector area used for dark image measurements A_D and then multiplied by the signal observation time and detector area used for the scientific observation. σ_D must then be added to the noise in the observation in quadrature. When this is done the signal-to-noise ratio becomes

$$\frac{S}{N} = \frac{n_S}{\sqrt{n_S + n_B + \sigma_D^2}} \tag{1.8}$$

$$= \frac{tA_d F_S}{\sqrt{tA_d F_S + tA_d F_B + \frac{t^2 A_d^2 F_B}{t_D A_D}}} \tag{1.9}$$

while this may contribute to noise in scientific measurements, noise originating from dark images can be reduced by using longer dark image observation times. However, the necessity of using dark frames to remove background can introduce serious systematic errors.

1.2.2 Systematic errors

In addition to introducing statistical errors, X-ray-like background can introduce large systematic errors. This is primarily because the spectrum of incoming radiation varies over time, both on short timescales and on long timescales, something that will be discussed in further detail in Chapter 2 and Chapter 4. This means that the X-ray-like background found using dark frames may not necessarily be representative of the X-ray-like background present in actual scientific images, particularly if there is a large time gap between dark image taking and scientific image taking. Therefore background subtraction using dark frames will not perfectly remove background from spectra, and systematic errors will be introduced to data.

Systematic errors due to time differences between dark frames and scientific images can be reduced by the taking of more dark frames closer to the time of a scientific observation, however, this reduces the available observation time for scientific measurements.

The presence of such systematic errors can significantly reduce scientific quality and is another reason why shielding detectors from radiation background could significantly improve scientific output.

1.2.3 Background fluorescence lines

As well as the X-ray-like background continuum causing statistical and systematic errors, fluorescence lines present in background can also interfere with scientific goals. Fluorescence lines in background are created by high energy particles passing through materials in spacecraft and causing them to fluoresce. For the X-ray observatories that will be discussed in this thesis, the relevant energy range of detection is between 0.1 keV to 15 keV, and X-rays within this energy range are typically only able to penetrate several millimeters of shielding. Therefore fluorescence X-ray background typically originates from materials within line-of-sight of the detector.

Fluorescence lines in background can reduce scientific quality by making it more difficult to identify spectral lines from scientific spectral sources, making it more challenging to identify the composition of astronomical objects. Additionally, if the energy resolution of a detector is imprecise, a fluorescence line may appear as a relatively broad Gaussian on spectra produced from images. If this Gaussian is sufficiently broad, it could effectively form a pseudo-continuum (Silvano Molendi, private presentation to the ATHENA Background Working Group, 2019), and add both statistical and systematic errors to a wide energy range in spectra. This effect is especially prominent if several background fluorescence lines are located near to each other in energy, potentially affecting a wide area of the spectrum, such as that observed in the pn-CCD in XMM-Newton (as will be discussed in Section 4.1).

Graded-Z shielding is a type of shielding mechanism that is capable of shielding a detector from X-ray fluorescence lines, and the effectiveness of several graded-Z shielding configurations will be investigated in Chapter 9.

1.3 Research goals

As discussed above, X-ray-like background can significantly reduce the scientific output of X-ray observatories. However, while research has been performed on the mechanisms behind background generation and detection, there are still many questions about the particle composition of background and the physics behind its creation and effect on images. Additionally, it is unknown how well Geant4, the primary program that is used to simulate radiation in the space environment, simulates the particles and processes that are expected to induce X-ray-like background in detectors at the appropriate energies. Therefore this thesis will investigate three main research goals:

- The accuracy of Geant4 at simulating X-ray-like background in the space-based environment will be assessed. This will be done through two major experiments that were performed at 6 MeV and 200 MeV proton beamlines, where the experimental results will be compared to simulation results.

- Geant4 simulations will be used to determine the expected composition of X-ray-like background that will be present in future X-ray astronomy missions, and how the X-ray-like background will vary with detector design and spacecraft structure. While some research has been performed attempting to investigate the composition of background in X-ray astronomy missions, many of the simulations involved in previous research have been performed on specific and complex spacecraft geometries. This can make it challenging to investigate background from a more theoretical perspective. Therefore in this thesis, Geant4 simulations will be performed on simplified spherical shell spacecraft models, which will be used to analyse the composition of background from a theoretical perspective, and for different geometric configurations and detector designs. This removes the individual characteristics of background that might be specific to a spacecraft design.

- Finally, mechanisms for shielding a space-based detector from X-ray-like background will be investigated. In particular, the effect of two different shielding mechanisms, graded-Z shielding and magnetic shielding, will be investigated. Potential shielding designs for each of these mechanisms will be discussed, and Geant4 simulations will be performed to assess the effectiveness of each mechanism at reducing X-ray-like background.

1.4 Thesis organisation

Chapter 2 discusses the radiation environment present in the solar system near Earth, and how the composition of incoming radiation varies with location and time. While the simulations in this thesis will use static spectra, the actual composition of space-based radiation is highly variable and unknown for many locations. Therefore the variability of radiation in space will be a key caveat that must be considered in relation to simulations that will be presented in this thesis.

Chapter 3 describes some of the X-ray-like background inducing particle components that are expected to be prominent in the X-ray observatories that will be discussed in this thesis, some of the mechanisms by which these particles generate background in a detector and how they can be generated by incoming radiation.

Chapter 4 describes the X-ray-like background that was present in the X-ray astronomy mission XMM-Newton and the design of its successor mission ATHENA. A significant proportion of the work performed in this thesis was performed as part of the ATHENA WFI team at the Center for Electronic Imaging, so many of the simulations presented in this thesis were designed as a direct analogy to the ATHENA WFI instrument.

Chapter 5 describes the simulation toolkit Geant4. Geant4 will be used extensively throughout this thesis, and this chapter will describe both the general considerations that need to be included in Geant4 simulations and analysis when it is used for simulations of the space-based environment. This chapter will also discuss current research on Geant4 and its validity for simulations of X-ray-like background.

Chapters 6 and 7 begin the presentation of new work performed for this PhD thesis, giving the results of the two major experiments and corresponding simulations that were performed to verify the use of Geant4 in the space-based environment. These were performed at a 6 MeV beamline and a 200 MeV beamline and were able to verify Geant4's ability to simulate several expected particle components of X-ray-like background while raising potential issues with Geant4's ability to simulate certain regions of the electron spectrum in some cases.

Chapter 8 will present the results of simulations performed on a spherical shell model. The data produced by these simulations will be analysed in a significant level of detail, to characterise the composition of X-ray-like background fully and to determine the locations from which particles producing X-ray-like background originate.

Chapter 9 will investigate how background should be expected to vary with spacecraft geometry and detector design through mathematics and Geant4 simulations. The Geant4 simulations presented will utilise variations on the spherical shell model presented in Chapter 8 in order to assess theoretically

how X-ray-like background should be expected to change with changes in spacecraft structure and detector design.

Chapter 10 will investigate the ability of graded-Z shielding and magnetic shielding to remove X-ray-like background. Mathematical methods and Geant4 simulations will show that both graded-Z shielding and magnetic shielding are likely to be effective methods of removing background associated with cosmic X-rays, and knock-on electrons, respectively.

Finally, Chapter 11 will present results from simulations performed on the full mass model for the ATHENA WFI. This will partly be done to compare the results of spherical shell model simulations performed previously to results from a model that is closer to an actual model of a spacecraft geometry but will also be used to further investigate the effectiveness of graded-Z shielding. Several graded-Z shielding configurations will be tested in these simulations, which are candidate configurations for the actual shielding that will be present on the ATHENA WFI.

1.5 Publications

The results from work presented in this thesis are partly contained within the following publications:

1. "Mitigation strategies against radiation-induced background for space astronomy missions"

   Chris Davis, David Hall, Jonathan Keelan, Andrew Holland, James O'Farrell, Mark Leese

   Journal of Instrumentation 13.01 (January 2018): C01015.

2. "Predicting the particle-induced background for future x-ray astronomy missions: the importance of experimental validation for GEANT4 simulations"

   David Hall, Jonathan Keelan, **Chris Davis**, Oliver Hetherington, Mark Leese

   High Energy, Optical, and Infrared Detectors for Astronomy VIII. Vol. 10709 (July 2018)

   International Society for Optics and Photonics

3. "Enhanced Simulations on the Athena/WFI instrumental background"

   Tanja Eraerds, Valeria Antonelli, **Chris Davis**, David Hall, Oliver Hetherington, Andrew Holland, Jonathan Keelan, Norbert Meidinger, Eric Miller, Silvano Molendi and Emmanuelle Perinati,

   Space Telescopes and Instrumentation 2020: Ultraviolet to Gamma Ray, Vol. 11444, p. 114443Y, (December 2020)

   International Society for Optics and Photonics.

Chapter 2

The Radiation Environment in the Solar System

In order to either design mitigation strategies aimed at reducing radiation-induced background, or to attempt to predict the background a detector will receive, it is first necessary to understand the structure and spectrum of radiation throughout the solar system.

The radiation environment of the solar system is complex, and an active field of research (e.g. Gombosi et al. 2018; Koldobskiy, Kovaltsov, and Usoskin 2018; Aguilar et al. 2015). The solar system radiation environment is highly variable depending upon solar activity and the presence of magnetic fields around the solar system. Predictions of cosmic radiation and solar flux over a given time period therefore rely on detailed modelling and MagnetoHydroDynamic (MHD) simulations (e.g. Odstrcil 2003; Washimi et al. 2015; Schwadron et al. 2010), and much of the plasma physics underpinning the radiation structure within regions of the solar system is still unknown. Solar physics and the physics of the interactions between the Earth's magnetic field and solar particles for instance are currently being studied experimentally and theoretically.

A factor to consider when assessing the accuracy and capabilities of Monte Carlo simulations of radiation-induced instrument background is the accuracy of software used to model the effect of radiation on a detector. The primary toolkit used in background simulation for X-ray detectors currently is Geant4 (Agostinelli et al. 2003). However, Geant4 is known to exhibit systematic errors when simulating low energy particles, depending on the settings and models used in simulations (e.g. David J. Hall et al. 2018; Pandola, Andenna, and Caccia 2015; Basaglia et al. 2015; Bolst et al. 2017).

The complexity of simulating both the radiation environment for a spacecraft, and the actual effect of incident radiation on a spacecraft and detector means that quantitative simulation-based approaches cannot currently be solely relied upon. Simulation results must, therefore, be combined with an understanding of the qualitative theory underpinning the variation of radiation particle components across the solar system, and the effect radiation has on a detector in the solar system.

Chapter 3 will describe some of the theory underpinning the effect of different radiation components on the radiation-induced background. In contrast, this Chapter will focus on describing the radiation environment throughout the solar system and its spatial and temporal variation.

2.1 The particle component composition of the solar system radiation environment

The radiation environment of the solar system is composed of many ion species and low mass particles, such as photons and electrons. It is not feasible or necessarily useful to simulate the effect of every single particle component on background, as only a few of the particle components in the radiation environment will contribute significantly to background in a detector. Therefore, before performing simulations to determine the detector background, it is first necessary to identify the particle components with non-negligible contributions to the detector background.

There are two primary factors to be taken into consideration when determining if a particle component contributes significantly to the background; the energy of the particle, and the particle count rate impacting the spacecraft. The effect of the particle count rate on background is straightforward: background increases in proportion to count rate. The effect of particle energy on background, however, is more complicated.

If a particle does not have enough energy to penetrate the body of a spacecraft, it can be ignored. However, the dependence of the actual number of background counts generated in an image on primary particle energy depends on spacecraft design, detector design and particle type. The physics of this will be discussed in further detail in Chapter 3.

The dependence of background on both particle count rate and particle energy means that the significance of a particle component of the radiation environment is dependent upon its entire kinetic energy spectrum. Therefore, before discussing the physical processes through which a particle may induce background, it is necessary first to examine the different particle flux components in the solar system that are capable of producing significant quantities of background in X-ray detectors and their spectra.

2.1.1 Galactic Cosmic Rays (GCRs)

Galactic Cosmic Rays (GCRs) (Ackermann et al. 2013), are present and significant at every location in the solar system. GCRs are the radiation component that is predicted to be the most significant source of background in the ATHENA mission (von Kienlin et al. 2018) that this thesis will use as a baseline example of a space mission. Generally, the term cosmic ray is used to refer to any charged particle with an intrinsic mass that originates from outside the solar system (usually from extragalactic sources), although the GCR spectrum is primarily composed of protons. Due to the fact that a higher

atomic number corresponds to a decrease in penetration depth through a material, protons are also typically more penetrative than heavier ions with the same kinetic energy.

For instance, according to NIST's PSTAR database (Shen et al. 2018) the Continuous Slowing Down Approximation (CSDA) range of a proton with 100 MeV of kinetic energy is approximately 3.7 cm. This means that a proton needs a kinetic energy of at least 100 MeV to penetrate 3.7 cm of aluminium such as the walls of a spacecraft. In contrast, to penetrate 3.7 cm an alpha particle requires approximately 400 MeV.

Figure 2.1 displays the kinetic energy spectra of several GCR components at solar minimum, as given by the CREME96 model (Tylka et al. 1997) at a distance from the Sun of 1 astronomical unit. As can be seen in this figure, a significant quantity of GCR protons are capable of penetrating virtually all practical shielding configurations for any space mission with negligible energy loss, as much of the spectrum is greater than several hundred MeV in energy. For example, according to PSTAR a proton of 1 GeV in energy is capable of penetrating approximately 150 cm of aluminium, and many GCR are sufficiently energetic such that they are capable of penetrating Earth's atmosphere and being detected by surface-based detectors (Hess 1912).

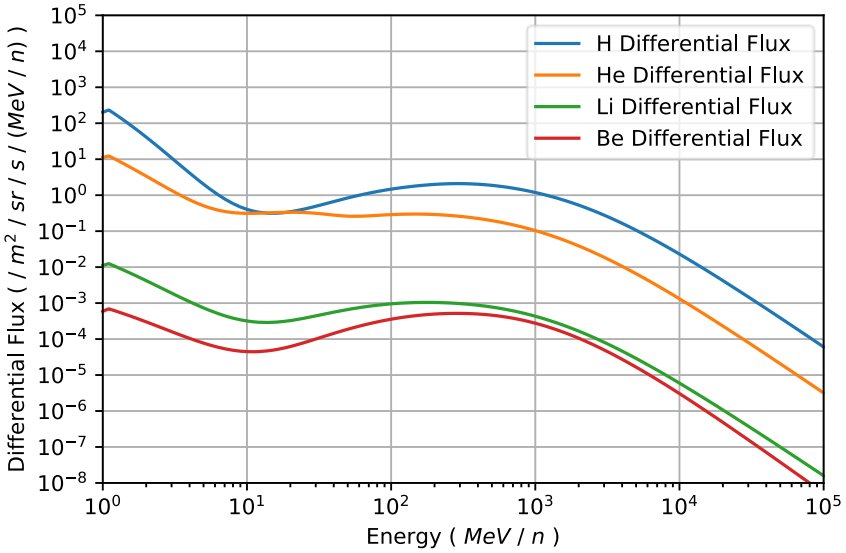

Figure 2.1 The Galactic Cosmic Ray (GCR) spectra for H ions (protons), He ions, Li ions and Be ions. The proton flux is significantly greater than the flux for elements with atomic number greater than 2 across the 1 MeV/n to 105 MeV/n spectra spectrum by several orders of magnitude. The data is from the CREME96 model (Tylka et al. 1997).

Despite the extrasolar origins of GCR, the variation of GCR flux across the solar system is complex and dependent upon GCR kinetic energy and solar cycle (Perko and Fisk 1983; Cane et al. 1999).

To qualitatively understand the mechanism by which GCR are affected by objects in the solar system, it is first necessary to understand the physics dominating the solar system at large scales and how it differs from physics at the scale of a spacecraft.

At the scale of a single spacecraft, charged energetic particles that are capable of penetrating spacecraft shielding can be treated as independent rays incident upon the spacecraft. The density of charged particles in a given volume of space across the solar system is too low for a significant quantity of particles to interact with each other. The velocity of each particle is also large enough that deviations in velocity due to the concentration of charged nearby particles will have a negligible impact upon the cosmic ray's trajectory.

In contrast, at the scale of planets and at the scale of the solar system itself, distance scales become large enough that the small deviations in velocity due to other charged particles in a volume of space become significant enough to add up to major variations in astronomical trajectory. This change in scale means a different approach must be taken towards predicting the motion of cosmic rays across the solar system; the solar system must be modelled as a low-density plasma. Under this physics regime, the trajectory of cosmic rays through the solar system can be understood as becoming impeded by the presence of ions originating from the Sun, and this leads to GCR flux throughout the solar system varying periodically and inversely with solar activity. This modulation of the cosmic ray flux can be described through concepts like the 'force field approximation' (Corti et al. 2016) to predict the spectrum of cosmic rays in the Local Interstellar Spectrum (LIS) over time.

To complicate matters further, at planetary scales and larger, the magnetic fields of objects in the solar system now also have to be taken into account, particularly the magnetic field of the sun (Cane et al. 1999). For detectors positioned near Earth or at the L2 Lagrangian point, the magnetic field of Earth must also be taken into account for missions which are expected to receive a large background due to soft protons (Rothwell and Quenby 1958; Lepping et al. 1991).

Therefore, calculating the cosmic ray flux a mission will receive requires a good knowledge of solar physics along with good predictions of solar activity throughout the mission and accurate MagnetoHydroDynamic (MHD) simulations of both the magnetic fields of the sun and Earth. Both solar physics and the magnetic field structures of the Earth and Sun are active fields of research. Although models do exist which are capable of producing representative fluxes for a mission (Tóth et al. 2012), they may not be capable of precisely reproducing the flux a mission will receive. The GCR flux has also been measured experimentally at several positions around the solar system (Aguilar et al. 2015; Koldobskiy, Kovaltsov, and Usoskin 2018), although many potential spacecraft orbit locations may be unaccounted for experimentally.

One simplification that can be made to simulate GCR flux in detectors situated in the Earth's magnetic field system is that the Earth's magnetic field is too weak to significantly impact the trajectory of soft protons with kinetic energies greater than several MeV (Minow, Blackwell, and Diekmann 2004). As protons with energies less than several MeV in kinetic energy are not energetic enough to pass through several centimetres of aluminium shielding, protons of these energies can be

neglected from some simulations of off-axis radiation-induced background. Particles such as these will therefore be ignored for the simulations performed in this thesis, as this thesis will focus exclusively on investigating off-axis background. However, particles of such energies are still capable of travelling through open telescope apertures. Soft protons must therefore be included in simulations for spacecraft which have no magnetic diverter to prevent them from travelling into the spacecraft through openings.

2.1.1.1 'Soft' Protons vs 'Hard' Protons

The proton spectra can be split into two different categories. For this thesis, protons with energies less than several hundred keV are labelled 'soft protons' (Fioretti et al. 2018), while protons with energies greater than several MeV are known as 'hard protons'. Soft protons and hard protons are both affected differently by conditions in the solar system, and generally induce background in detectors through different mechanisms, which is why it can be useful to distinguish these two parts of the proton spectra as different components.

Soft protons generally cause background through absorption in a detector through the same mechanisms as a photon, i.e. through ionisation, and despite being blocked by a few centimetres of shielding they have been capable of passing through the mirror systems of some past X-ray observatory missions (Diebold et al. 2015; Turner et al. 2001).

In contrast, hard protons are generally capable of penetrating several centimetres of shielding and therefore can arrive at a detector from all directions. Through the use of image processing techniques (David James Hall 2010), hard protons can be distinguished from X-rays due to the tracks they leave in images. However, it is not necessarily possible to distinguish the secondary particles generated by incoming protons as they travel through the spacecraft from scientific signal X-rays. These X-ray-like secondary particles produced by cosmic protons are expected to form the majority of induced background from hard protons in ATHENA (von Kienlin et al. 2018). The mechanisms by which secondary particles can create background in a detector will be discussed in Chapter 3.

Another key difference between hard protons and soft protons is the fact that hard protons are significantly less affected by magnetic fields than soft protons (Minow, Blackwell, and Diekmann 2004). The mathematics behind this will be expanded upon in Section 2.3, and some of the effects this has on the radiation environment of the solar system around Earth will be discussed.

In general, the main differences between soft protons and hard protons from the context of instrument background could be described as that soft protons are highly variable and hard to predict, but possible to shield. In contrast, hard protons are unaffected by the magnetic fields of the solar system but are difficult to shield. However, there are still methods available for removing background from hard GCR protons, and these will be discussed in Chapter 10.

2.1.2 Cosmic X-ray Background (CXB)

In contrast to the complexity of the galactic cosmic ray spectrum, the Cosmic X-ray Background (CXB) (Fabian and Barcons 1992) component of incident radiation is relatively straightforward but still forms the second most significant predicted source of background for the ATHENA WFI (von Kienlin et al. 2018). Later simulations in Chapters 10 and 11 of this thesis will reveal that CXB-induced background would likely contribute about half of the X-ray-like background in the ATHENA WFI if graded-Z shielding were not planned to be present.

The CXB is the general constant X-ray radiation background in the solar system that originates from sources outside the solar system. In other words, the CXB is the accumulation of X-rays from each X-ray source in the universe outside the solar system (Moretti et al. 2009) and can be expressed as a mean constant flux. As X-rays are unaffected by magnetic fields, the CXB does not vary with solar cycle or the position of objects in the solar system like the GCR radiation environment and thus is relatively constant at all locations throughout the solar system. However, it does have some angular dependence as the CXB originates primarily from areas of the sky which contain larger densities of X-ray sources (Fabian and Barcons 1992; K Nandra et al. 2014).

Two models of the CXB spectrum (Gruber et al. 1999; Moretti et al. 2012) are displayed in Figure 2.2, and the attenuation coefficient for photons in silicon is displayed in Figure 2.3.

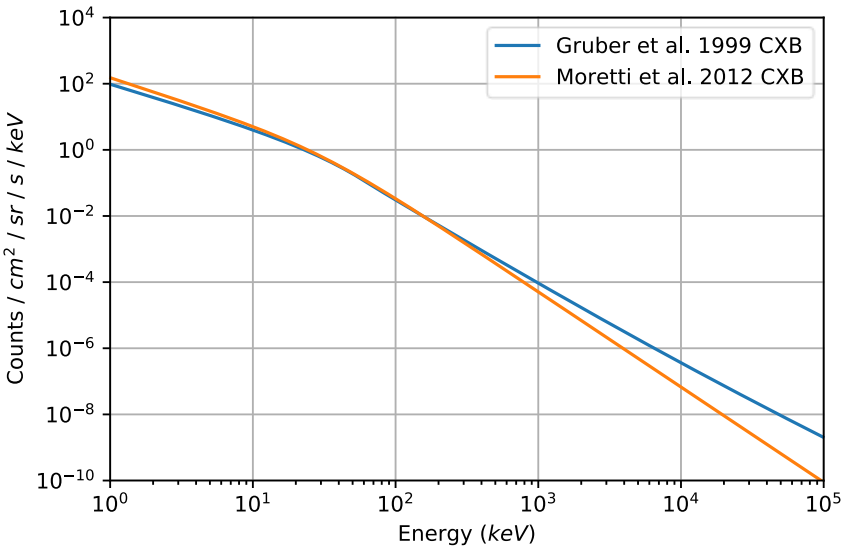

Figure 2.2 Two different versions of Cosmic X-ray Background (CXB) spectra, taken from the results of Gruber et al. (1999) and Moretti et al. (2012).

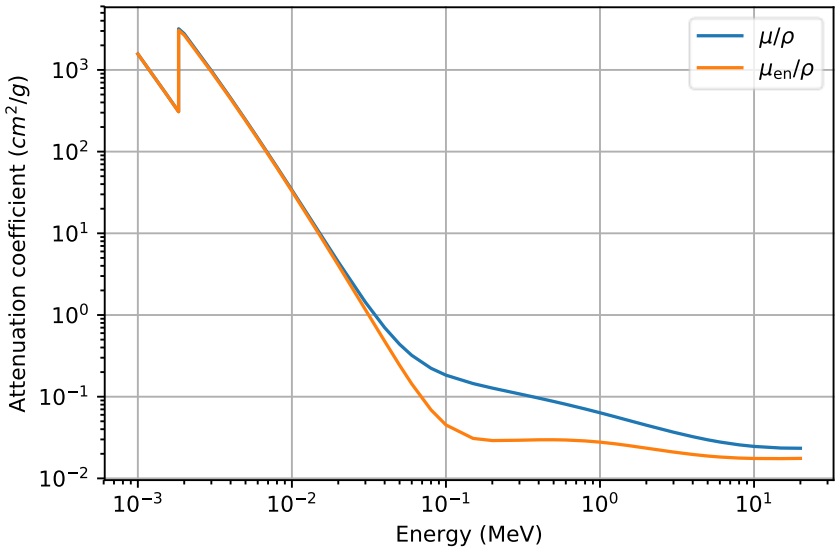

Figure 2.3 The attenuation coefficients of silicon as a function of photon energy (Xcom 2010). *μ/ρ is the mass attenuation coefficient, while μ_{en}/ρ is the energy absorption coefficient.*

While the CXB spectrum is more predictable than the GCR spectrum with regards to orbit location and solar cycle, a key factor limiting the precision of CXB flux models is instead the difficulty obtaining accurate experimental data on the CXB spectrum. While the GCR spectrum can be obtained experimentally with relative ease through the counting of particle tracks in detectors, it is difficult to separate the CXB from the other radiation components such as those of secondary particles experimentally. This means that measurements of the CXB to date differ significantly (Moretti et al. 2009) depending on the flux of other background components and spacecraft structure.

CXB photons with energies corresponding to the energy detection range of the detectors that will be considered in this thesis are unlikely to be able to penetrate spacecraft shielding. The maximum detection energy for a detector that will be considered is 15 keV, in accordance with the energy range of the ATHENA WFI, and a photon of this energy has a half-value layer of 323 µm in aluminium (Xcom 2010). This is small relative to the expected thickness of aluminium shielding on the ATHENA WFI of approximately 4 cm. However, high energy photons are capable of penetrating shielding and depositing energy in a detector via Compton scattering or by creating secondary particles within the detector energy range. For example, 300 keV photons have a half-value layer of 2.46 cm in aluminium, meaning that such a photon could penetrate several centimeters of shielding and reach a detector. A half-value layer is the distance at which the intensity of a group of photons travelling through a material is halved, and can be calculated be dividing $\ln(2)$ by the attenuation coefficient for the photons in the material.

2.1.3 Solar Energetic Particles (SEPs)

Solar Energetic Particles (SEPs) (Reames 2013) are the label given to highly energetic, charged particles that originate specifically from the Sun (as opposed to GCRs which originate from extrasolar sources). The mean flux of SEPs is variable on both on a day to day basis and on the timescale of years, due to the existence of the solar cycle, which has a period of approximately 11 years (Hathaway 2015). The variation of SEP flux on both these time scales means that it is challenging to predict the SEP-induced instrument background a mission will experience both before it is launched and on a day-to-day basis while it is in orbit. Predicting the solar weather is much like predicting the weather on Earth where general trends can be identified on a year-to-year basis, but predictions on a day-to-day basis have a high degree of error.

As will be discussed in Section 2.3, the solar system radiation environment acts as a plasma within a magnetic field. Therefore simulations of SEP flux must take into account not only the solar internal plasma physics and particle output influencing the particle output of the Sun but also the MagnetoHydroDynamics (MHD) of the solar wind travelling through the solar system. For any missions located near Earth this means that simulations quickly become complex, especially because the magnetohydrodynamics of the Sun and Earth's magnetosphere are still active areas of research with many unknowns. Simulations of SEP flux are therefore subject to not only high statistical noise, but they may be subject to large systematic errors too.

While general solar activity contributes to SEP instrument background over the whole lifetime of a mission, there is also the possibility that major solar events can occur during a mission lifetime such as a Coronal Mass Ejection (CME) (Antiochos, DeVore, and Klimchuk 1999) or solar flare (Svestka 1976). These can increase the SEP flux by several orders of magnitude. In fact, despite the infrequency of these events, in some missions, the majority of radiation damage induced in a device originates from SEPs produced during several solar events (Boscherini et al. 2003). Such events typically occur over the time scale of days and occur only several times during a mission's lifetime (Kurczynski et al. 1999; Boscherini et al. 2003). While these events do increase radiation-induced X-ray-like background for a short length of time, in general, the actual reduction in observing time this causes for a mission is small relative to a mission length.

However, the more problematic consequence of solar events is the sizeable non-ionising radiation dose, comparable to the entire dose received from other sources during the rest of a mission lifetime, which causes radiation damage to a detector. Radiation damage typically occurs through the creation of traps in the silicon of a detector, which can cause a loss of effective area in a detector.

2.1.4 Cosmic electrons

Much like cosmic rays, cosmic electrons originate from extrasolar sources and represent a small but not insignificant part of the predicted background for the ATHENA WFI (von Kienlin et al. 2018).

The predicted mean background flux of cosmic electrons is displayed in Figure 2.4. As is the case for the cosmic ray spectrum, the cosmic electron spectrum decreases with energy, except for the case of a local maximum at approximately several hundred MeV. However, electrons have a larger Continuous Slowing Down Approximation (CSDA) range in aluminium than protons at kinetic energies lower than several hundred MeV (Shen et al. 2018), meaning that lower kinetic energies of electrons must be considered when assessing which areas of the spectrum have an effect on background. Figure 2.5 shows the CSDA ranges in aluminium of protons and electrons versus kinetic energy (Perinati et al. 2012; Adriani et al. 2017). Here it can be seen that the threshold kinetic energy for electrons penetrating 4 cm of aluminium is approximately 20 MeV, in contrast to a threshold of approximately 100 MeV for protons.

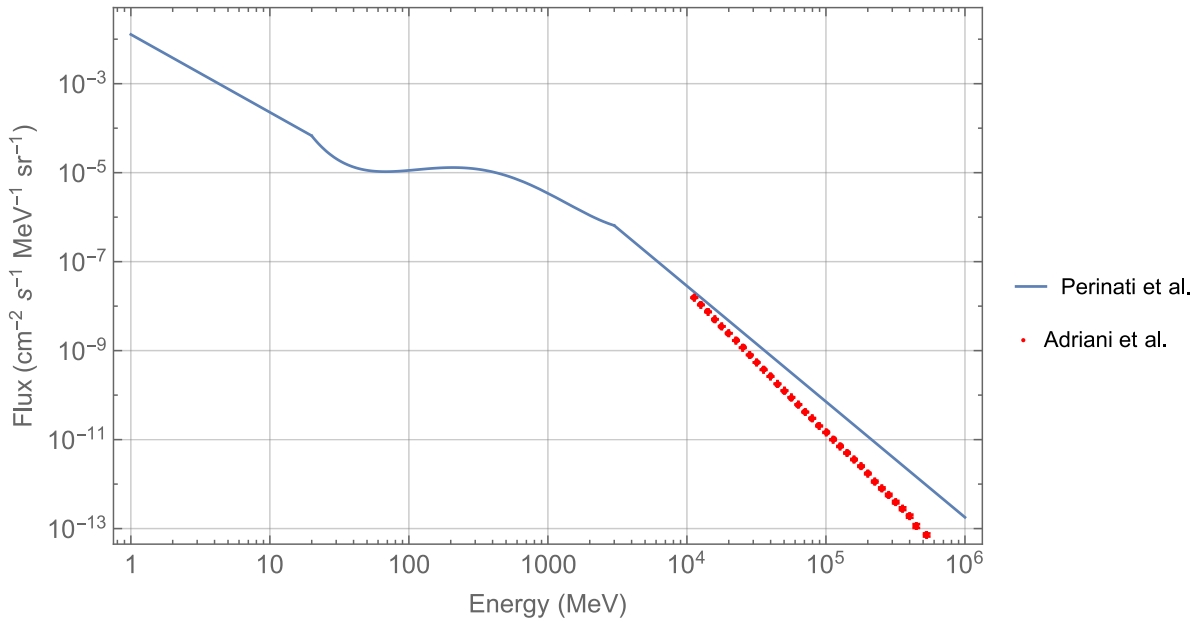

Figure 2.4 The expected mean flux of electrons at L2 and at low Earth orbit as extracted from Perinati et al. (2012) and Adriani et al. (2017) respectively. Data for energies lower than 20 MeV were reproduced using figure 3 in Perinati et al. It should be noted that the data points taken from Adriani et al. were taken from a detector mounted on the International Space Station, in low Earth orbit rather than in L2 , which may contribute to explaining why the experimental data deviates significantly from the data in Perinati et al.

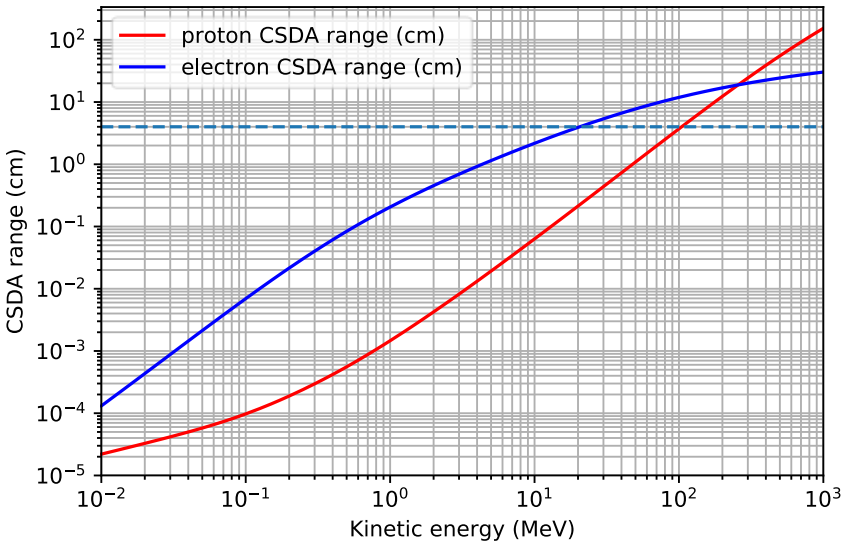

Figure 2.5 A comparison of the Continuous Slowing Down Approximation (CSDA) ranges of protons and electrons through aluminium (Shen et al. 2018)*. The dashed blue line represents a CSDA range of 4 cm in aluminium, the range at which an ion may be able to penetrate the ATHENA WFI proton shield.*

However, above several tens of MeV, the cosmic electron spectrum becomes smaller than the cosmic proton spectrum by an order of magnitude (Figure 2.6), and this leads to a significantly reduced background relative to the galactic proton spectrum.

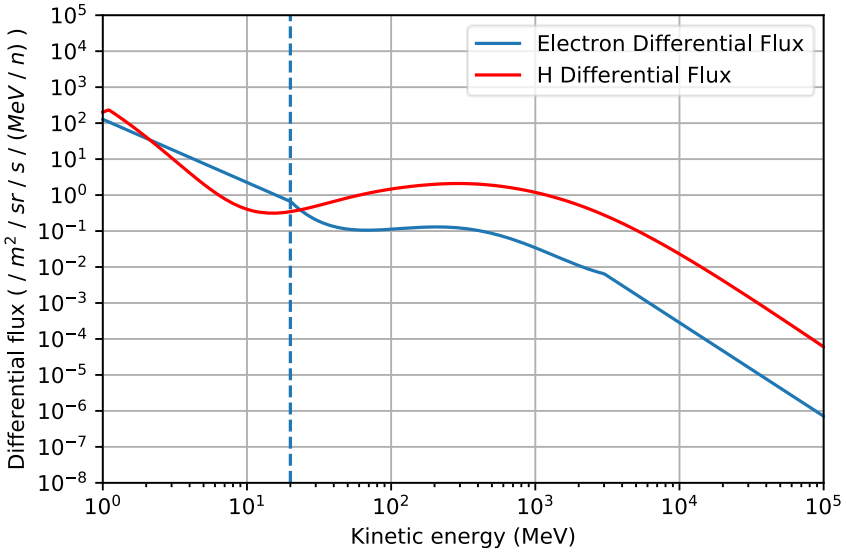

Figure 2.6 A comparison of the differential flux spectra from electrons and protons. The dashed blue line represents 20 MeV, the energy above which the CSDA range of electrons allows for electrons penetrating through 4 cm of aluminium. Proton data is from the CREME96 model (Tylka et al. 1997)*, and electron data is taken from Perinati et al. (2012).*

It is important to note that the electron spectra shown in Figure 2.4, Figure 2.5 and Figure 2.6 are subject to significant statistical and systematic errors due to variations in the solar wind and the magnetic fields of the solar system. Electrons are affected significantly more than protons by magnetic fields due to their lower mass, which means that the Earth's magnetosphere could lead to

high systematic errors in simulations of the cosmic electron flux at the low kinetic energy side of the spectrum.

As has been described throughout this section, all the charged components of the radiation environment of the solar system are strongly impacted by the presence of magnetic fields in the solar system. Therefore, before discussing the radiation environment surrounding potential locations for X-ray detectors, the next section will elaborate upon some of the physics of magnetic fields and the mechanisms by which they can impact the trajectories of charged particles in the solar system. The physics of magnetic fields will also be necessary for later discussions on magnetic shielding in spacecraft, in Chapter 10.

2.2 The trajectory of a particle in a magnetic field

It has been established in Section 2.1 that the flux of many of the particle components in the radiation environment of the solar system are significantly altered by magnetic fields, particularly the magnetic field around the Earth and the Sun. Different particle components of the radiation environment will also be affected differently by internal spacecraft magnetic diversion mechanisms, which will be investigated in detail in Chapter 10, depending on their energy, charge and mass. Appendix A gives derivations of some commonly used features of motion in a magnetic field that will be used in this thesis, including in particular the concept of a gyroradius or Larmor radius (Chen 1984), which can be described by

$$r_g = \frac{|\boldsymbol{p}_\perp|}{|q||\boldsymbol{B}|} \tag{2.10}$$

Where r_g is the particle gyroradius, q is the charge of the particle, $\boldsymbol{B}$ is the magnetic field the particle is travelling through, and $\boldsymbol{p}_\perp$ is the component of the particle's momentum that is perpendicular to the magnetic field. The gyroradius r_g is particularly useful as a length scale comparison; as a measure of showing how effectively a magnetic field will divert a charged particle from its original path. In fact, the mathematical measure of curvature for a trajectory in any magnetic field is actually defined as $\kappa = \frac{1}{r_g}$. A smaller r_g represents a more tightly confined motion around the particle's guiding centre, and therefore can be viewed as a measure of the effectiveness of a magnetic field at confining a particle to motion along its magnetic field lines.

Equation 2.10 can also be expressed as a function of the kinetic energy perpendicular to the magnetic field, as

$$r_g = \frac{1}{|q||\boldsymbol{B}|c}\sqrt{(E_k + m_0c^2)^2 - (m_0c^2)^2} \tag{2.11}$$

Here, c is the speed of light, E_k is the particle kinetic energy associated with momentum components perpendicular to the magnetic field, and m_0 is the particle rest mass. For non-relativistic particles, the simpler classical mechanics approximation may be used:

$$r_g = \frac{\sqrt{2mE_k}}{|q||\boldsymbol{B}|} \tag{2.12}$$

From equations 2.11 and 2.12 it can be seen that an increase in particle mass or kinetic energy causes an increase in gyroradius. This means that electron motion is affected significantly more than proton motion by magnetic fields for a given kinetic energy, which will be important for discussions on magnetic shielding in Chapter 10. This concept is sometimes quantified by defining the 'rigidity' of a particle, which is equal to the momentum of a particle divided by its charge (Herbst, Kopp, and Heber 2013), typically in units of gigavolts. Particles with the same rigidity take identical trajectories in a magnetic field, and a higher rigidity means the trajectory of a particle will be less influenced by magnetic fields acting upon it.

Using the properties of magnetic fields above, as well as the equations given in Appendix A, a general qualitative picture of the mechanisms by which a slowly varying magnetic field affects the motion of a charged particle can be described.

A magnetic field redirects particles while conserving particle kinetic energy, such that they travel along its field lines in a helical motion, with the confinement to the field line increasing with magnetic field strength, and decreasing with the magnitude of momentum perpendicular to the field line. If the momentum of the particle perpendicular to the field lines is sufficiently small, then the particle could be approximated to be entirely travelling along the magnetic field lines. However, if r_g is sufficiently large relative to the system size, or significantly larger than the area over which a magnetic field operates, then the particle could be assumed not to be affected by the magnetic field at all.

Due to r_g increasing with kinetic energy in directions perpendicular to field lines, this means that kinetic energies corresponding to gyroradii that are significantly greater than the length over which a magnetic field operates can be assumed to be unaffected by magnetic fields at all.

To give an idea of the change in gyroradii as the kinetic energy of a particle increases, Figure 2.7 and Figure 2.8 display gyroradii as a function of kinetic energy for several different particles at two

different magnetic field strengths, corresponding to specific positions in Earth's magnetosphere under a bar magnet approximation. At energies where the gyroradius becomes greater than several times the Earth's radius, R_E, it becomes likely that the particle will be approximately unaffected by Earth's magnetosphere. For example, from Figure 2.8 it appears that protons with energies above approximately 100 MeV passing through areas of Earth's magnetosphere that have a magnetic field of 0.00312 μT may be unaffected by the presence of the magnetosphere.

However, it is important in this case to bear in mind the caveat that the gyroradii plotted in figures 1.3 and 1.4 represent the gyroradii if a particle's motion is entirely perpendicular to the magnetic field, and therefore the maximum gyroradius. Therefore, the actual gyroradius a particle will have will be less than this.

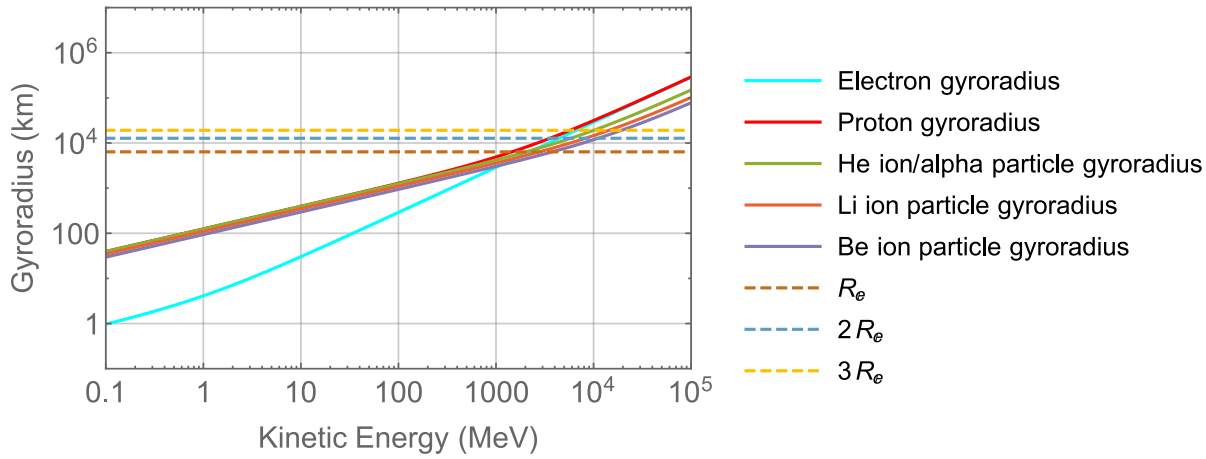

Figure 2.7 The gyroradius of different ions in a magnetic field of 1.156 μT, the equatorial magnetic field strength at a distance of 3 R_E *from Earth's centre, based on the approximation that Earth is a perfect dipole* (Mauk 1996)*. Due to the rest mass of the electron being significantly smaller than the rest mass of the proton, the electron gyroradius is significantly smaller than the proton gyroradius until approximately 1 GeV. This means that electrons are more strongly confined to magnetic field lines than protons of equivalent energies.*

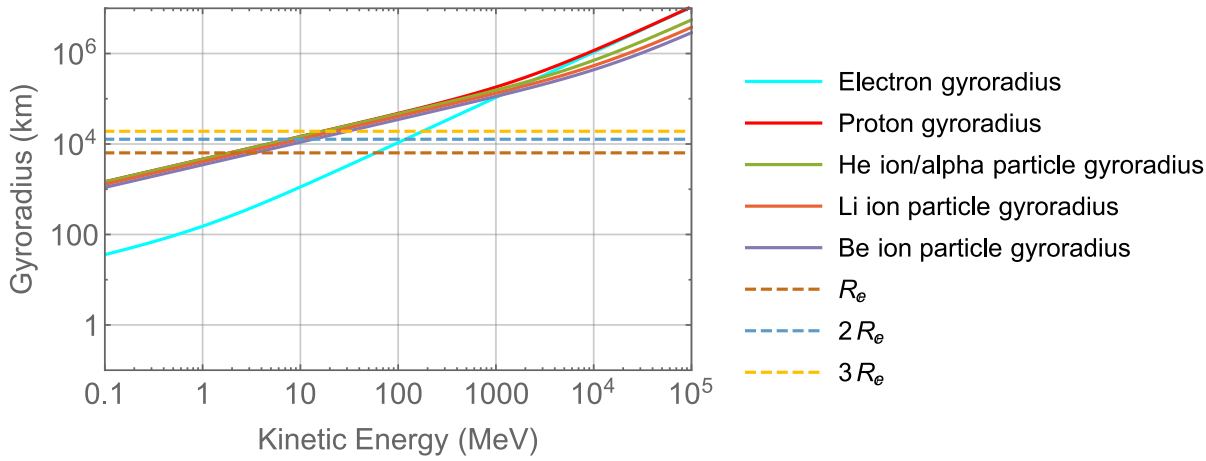

Figure 2.8 An equivalent plot to Figure 2.7, but for a magnetic field of 0.00312 μT, approximately the equatorial magnetic field strength at 10 R_E *from the centre of Earth* (Mauk 1996)*. The equivalent kinetic energy required to reach a gyroradius of* 1 R_E *decreases by more than a factor of 1000. This shows that the effect Earth's magnetosphere will have on the trajectory of a charged particle depends strongly on how closely a particle passes to Earth's centre.*

The concepts described in the above equations derived in this section will be used throughout this thesis. Chapters 6 and 7 will present experiments which contained magnetic diversion mechanisms, and Chapter 10 will investigate the possibility of using magnetic shielding to remove knock-on electron-induced background on spacecraft.

As has been shown above, magnetic fields impact the different particle components of the solar system very differently depending on both particle species and particle kinetic energy. This means that real, non-uniform, magnetic systems in the solar system are often complex and difficult to predict even through simulation.

2.3 The effect of orbit location on radiation environment

The primary magnetic fields affecting the radiation flux impacting the spacecraft structures surrounding X-ray detectors are the magnetic fields of the Sun and the Earth. As was described in Section 2.1, changes in the Sun's magnetic field are the cause of many of the physical processes that generate SEPs and cause variations in cosmic ray flux. The Earth's magnetic field also interacts with SEPs and GCRs to create a structured but highly variable radiation environment surrounding Earth. Solar radiation is often referred to as the 'solar wind', alluding to the idea that the radiation environment is often as unpredictable and variable as the atmospheric weather on Earth.

Not only is the radiation environment challenging to predict due to its variability with time, but it is also difficult to simulate due to the complexity of the physics affecting the trajectory of the solar wind. At planetary scales, the approximation that particles comprising radiation in the solar system do not interact with each other can no longer be applied, and the radiation environment now has to be treated as a plasma. Not only does this mean that simulations now have to include the complex physics of magnetohydrodynamics, but it also means that the radiation environment has a feedback effect on the Earth's magnetic field. This is due to several physical processes such as currents forming in the plasmas surrounding the Earth's magnetosphere, for instance (Fedder and Lyon 1995). Simulations including the physics of all these processes are challenging to perform, especially because much of the physics involving these processes are still active areas of research.

Due to the complex and difficult to predict dependency of the charged radiation spectrum on spacecraft orbit location, simulations of the effect of the radiation environment on a detector must be designed with individual orbit locations in mind.

2.3.1 The radiation environment at Earth

The interaction between Earth's magnetic field and the solar wind leads to a structured environment where particles comprising the solar wind become divided and trapped in different regions of the

Earth's magnetosphere depending on their mass, energy, and initial trajectory (Ratcliffe and Holzer 1973; Moore 1991). Some of the key features of Earth's magnetosphere are displayed in Figure 2.9.

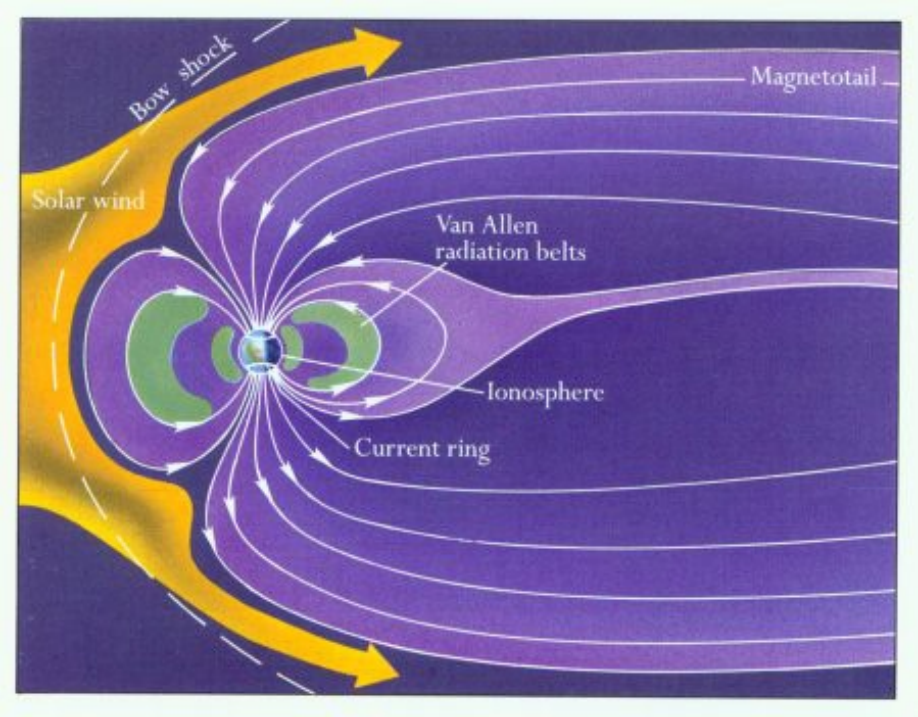

Figure 2.9 A diagram displaying some of the general features of Earth's magnetosphere (credit: NASA).

The furthest feature from the Earth on the dawn side (i.e. facing the Sun) is the 'bow shock' (Kivelson, Kivelson, and Russell 1995). In Section 2.2 it was shown that charged particles attempt to follow a helical motion along magnetic fields; with particles following the magnetic field line while simultaneously gyrating around it. The bow shock represents the location where Earth's magnetic field becomes strong enough that particles in the solar wind travelling towards Earth begin to gyrate faster around the magnetic field lines than the bulk speed at which they were ejected towards the Earth. This effect causes the solar wind to rapidly transition from travelling in the direction of Earth to confinement in Earth's magnetic field and spread along the Earth's magnetic field lines towards the north and south.

In Figure 2.10, the bow shock of Earth can be seen approximately 10 R_E to the dawn side of Earth, where pressure increases dramatically during a period of increased solar activity. The variability of the features of the Earth's magnetosphere with time can also be observed in Figure 2.10, as the three heatmaps only span one hour in total.

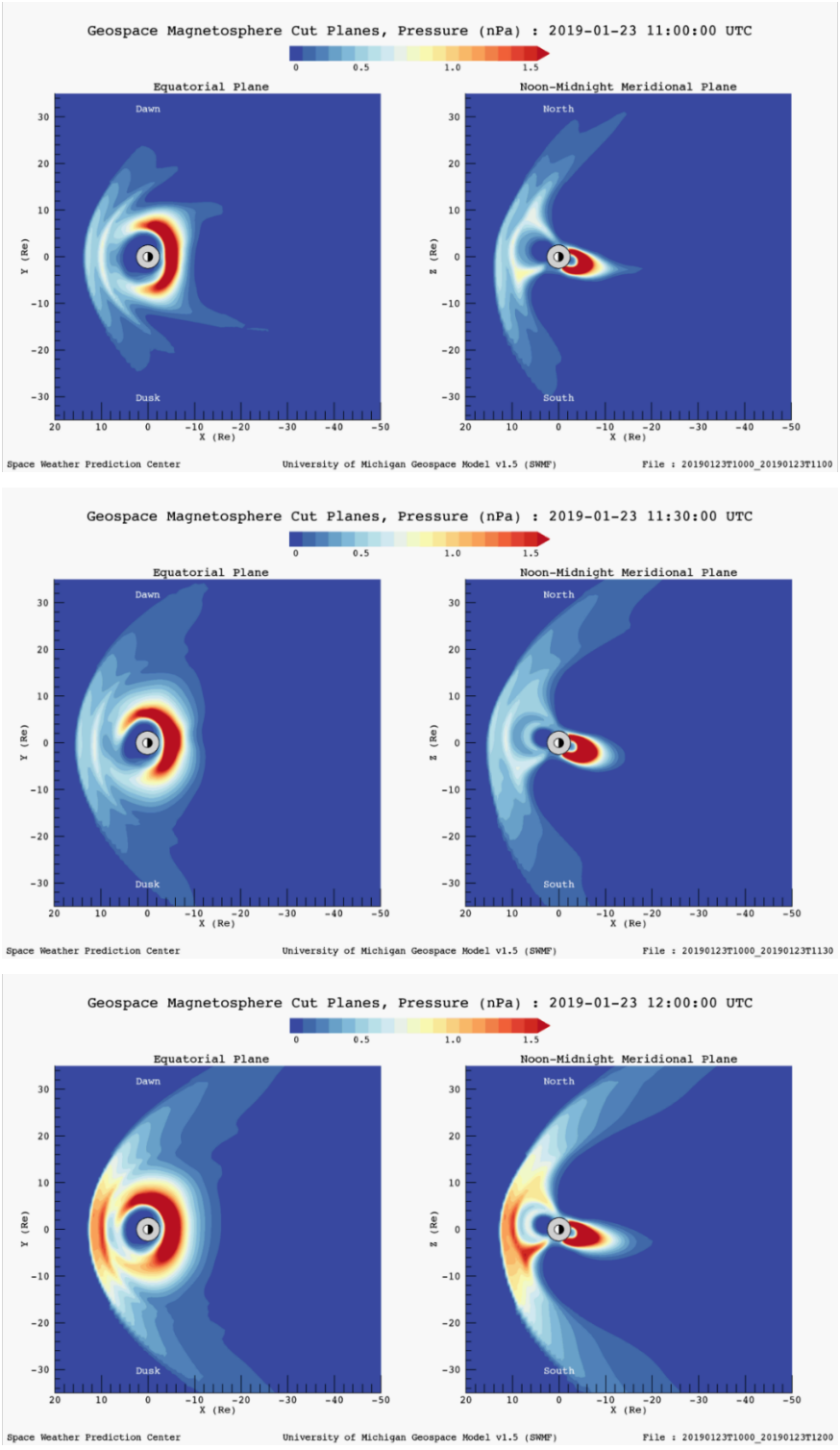

Figure 2.10 Simulations of pressure throughout the Earth's magnetosphere at three different times on 2019-01-23, at half an hour intervals. Features of Earth's radiation environment can be observed such as the Van Allen radiation belts. The images also show the capability of Earth's radiation environment to vary on the scale of tens of minutes. These images were extracted from animations created by the Space Weather Prediction Center, which were carried out using the SWMF/BATSRUS tools developed at The University of Michigan Center for Space Environment Modeling (CSEM) and made available through the NASA Community Coordinated Modeling Center (CCMC) ("Https://Www.Swpc.Noaa.Gov/Products/Geospace-Magnetosphere-Movies," n.d.).

Closer to Earth than the bow shock, on the dawn and dusk sides of Earth, are the two Van Allen radiation belts (Mauk 1996; Reeves et al. 2013; Horne et al. 2005), which can also be observed in Figure 2.10. These two belts surround the Earth in almost toroidal shapes and consist of energetic

charged particles which are trapped along the field lines of Earth's magnetic field. These particles are trapped because the Earth's magnetic field at these locations effectively forms a magnetic mirror, causing the particles to oscillate back and forth along the field lines. Second-order effects also cause an eastward drift of electrons along the radiation belts and a westward drift of positively charged particles.

Particles in the outer Van Allen belt have been theorised to originate from particles in the solar wind undergoing what is known as 'radial cross L-shell diffusion' (Elkington et al. 2001), a magnetic effect where particles can diffuse radially inward in a magnetic field.

The inner Van Allen belt, on the other hand, is believed to be created by the production of ions from Earth's upper atmosphere by the interaction of cosmic rays, and these ions then become trapped in Earth's magnetosphere. The inner Van Allen belt is slightly offset relative to Earth's geometric centre, with the closest point to Earth's surface positioned approximately over Brazil and the South Atlantic. This results in a feature of Earth's magnetosphere known as the South Atlantic Anomaly, a region that has been an important consideration for several space missions in Earth orbit.

As a part of the inner Van Allen belt, the South Atlantic Anomaly (Pavón-Carrasco and De Santis 2016) causes a relatively large radiation dose in spacecraft travelling through it. An image of proton track frequency across Earth, created using data from the most proton intensive image frames taken in NASA's Terra mission is displayed in Figure 2.11. Figure 2.11 provides an indication of how much extra radiation a mission might experience as it orbits through the South Atlantic Anomaly.

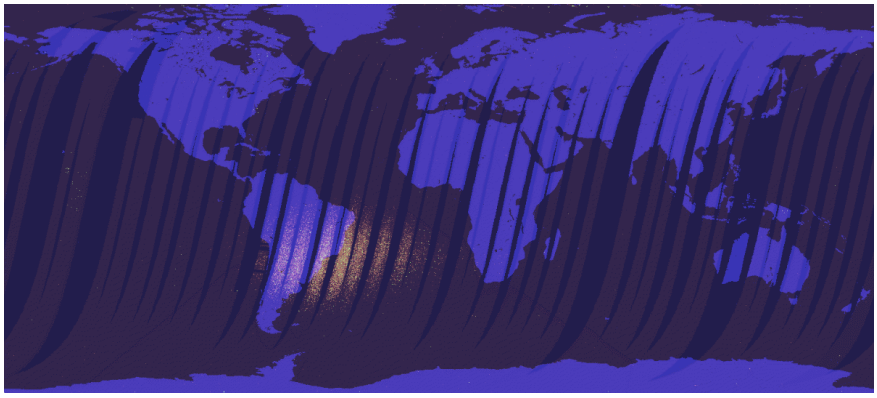

Figure 2.11 A map created by NASA using proton tracks in dark frames from the Multi-angle Imaging SpectroRadiometer (MISR) instrument on the Terra mission ("Https://Eosweb.Larc.Nasa.Gov/Project/Misr/Gallery/South_atlantic_anomaly," n.d.). *The frequency of proton tracks dramatically increases while the spacecraft is passing over the South Atlantic Anomaly (SAA). Only dark frames containing the largest number of proton tracks in a region were included in data used here, accentuating the contrast between the South Atlantic Anomaly (SAA) and other regions. Image taken from the NASA Atmospheric Data Center website, with saturation and contrast modified for visibility.*

In addition to the two Van Allen belts, there has also been evidence discovered recently that during a Coronal Mass Ejection, a third Van Allen belt can briefly form (Mann et al. 2016).

Moving away from Earth-based orbit locations, the feature of the Earth's magnetosphere stretching the furthest to the dusk side of Earth is the Earth's magnetotail (Russell 1993). The Earth's magnetotail consists of a stream of charged particles which have been redirected around the Earth, rather than trapped by Earth's magnetic field, during their passage from the Sun. The magnetotail varies significantly in direction and size depending on solar activity but can cause an excess of radiation flux for spacecraft orbiting around the Earth's L2 point (Minow, Blackwell, and Diekmann 2004).

All of the features of Earth's magnetosphere described above are complex and involve accurate simulation to predict in detail. As the flux of radiation a spacecraft will receive depends heavily upon the orbit location of the spacecraft within the Earth's magnetosphere, to be able to determine the flux a spacecraft will receive accurately, it is necessary to understand the regions of the Earth's magnetosphere a spacecraft will travel through during its orbit.

2.3.2 Types of Earth orbit

Geocentric orbits vary significantly depending on both altitude and eccentricity, with different types of orbit having advantages and disadvantages depending on the mission requirements involved. Such mission requirements do have to take into account the radiation environment surrounding the spacecraft. However, the chosen orbit location is also dependent on engineering considerations such as the mass of the spacecraft, and the apparatus required to position the spacecraft in orbit (Swinerd 2009).

A Low Earth Orbit (LEO) is typically defined as an orbit with an altitude of approximately a third the radius of Earth (2000 km) or less. LEO orbits typically have a low eccentricity (i.e. they are approximately circular rather than elliptical), although some highly elliptical orbits can pass through the LEO region.

Some of the advantages of a LEO orbit are that it is easier and cheaper to launch a spacecraft into an LEO orbit and that communication with Earth requires a lower bandwidth, which can translate into a spacecraft requiring less complicated and less massive communications devices. However, LEO orbits do have disadvantages, such as the fact that for space telescopes Earth will obstruct a large portion of the sky at any one time, and the fact that it may be challenging to position a spacecraft pointing at one location for an extended period of time, due to having a maximum orbital period of approximately 128 minutes. Additionally, while LEO orbits are positioned below the inner Van Allen belt, they can still be affected by the South Atlantic Anomaly, should they pass through it.

While orbits at greater altitudes than LEO may be preferable for a space telescope, they will also start to encroach upon the Van Allen belts, and experience larger fluxes of radiation. This is the case for

Medium Earth Orbits (MEO), which are orbits situated between LEO orbits and geostationary orbits (between 10000 km and 35786 km in altitude, although definitions of MEO orbits vary (Rossi 2008)).

The upper limit of MEO orbits of 35786 km is approximately the altitude of geostationary orbits. Geostationary orbits have the advantage of orbiting the Earth with the same angular velocity as the rotation of Earth, meaning that a satellite at a geostationary orbit will maintain the same position above Earth for the full duration of its orbit.

In contrast, orbits at higher altitudes than geostationary orbits are referred to as high Earth orbits and orbit Earth at slower angular velocities than Earth's rotation.

In addition to orbiting at a particular altitude, spacecraft are often given Highly Elliptical Orbits (HEO, not to be confused with high Earth orbits) (Fortescue, Swinerd, and Stark 2011) around Earth, which may pass through a broad range of altitudes during its orbit. This makes HEO radiation flux particularly challenging to predict due to multiple radiation zones it may pass through over a short period of time. The precursor mission to ATHENA, XMM-Newton, had a highly elliptical orbit, and some of the background features this caused will be discussed in Chapter 4.

While geocentric orbits are often used for space telescopes, they can be unfavourable for many missions for multiple reasons, including the fact that the radiation environment can be unpredictable and complex. For this reason, another set of points in the solar system is often used for the location of space missions: the Earth-Sun Lagrangian points.

2.3.3 The Earth-Sun Lagrangian points

Lagrangian points (also known as libration points) are locations within a gravitationally bound two-body system where a third body with negligible mass will always maintain a constant location relative to the other two massive bodies (Koon et al. 2000; Farquhar and Dunham 1990).

In mathematical terms, Lagrangian points of a gravitationally bound system are the stationary points of the gravitational effective potential (gravitational potential energy plus the gravitational centripetal force) in a reference frame that rotates with the orbital speed of the bodies.

There are exactly 5 Lagrangian points in a two-body gravitationally bound system, and due to symmetry, each of these points orbits around the centre of mass of the system at the same rate as the two massive bodies. Any small body stationed or orbiting around a Lagrangian point, will therefore always maintain its general location relative to the main two massive bodies.

The Lagrangian points in the Earth-Sun system can be seen in Figure 2.12. It should be noted that in the Earth-Sun system, the Earth and Moon can be treated as a single gravitational body due to their proximity to each other relative to their distances to the sun.

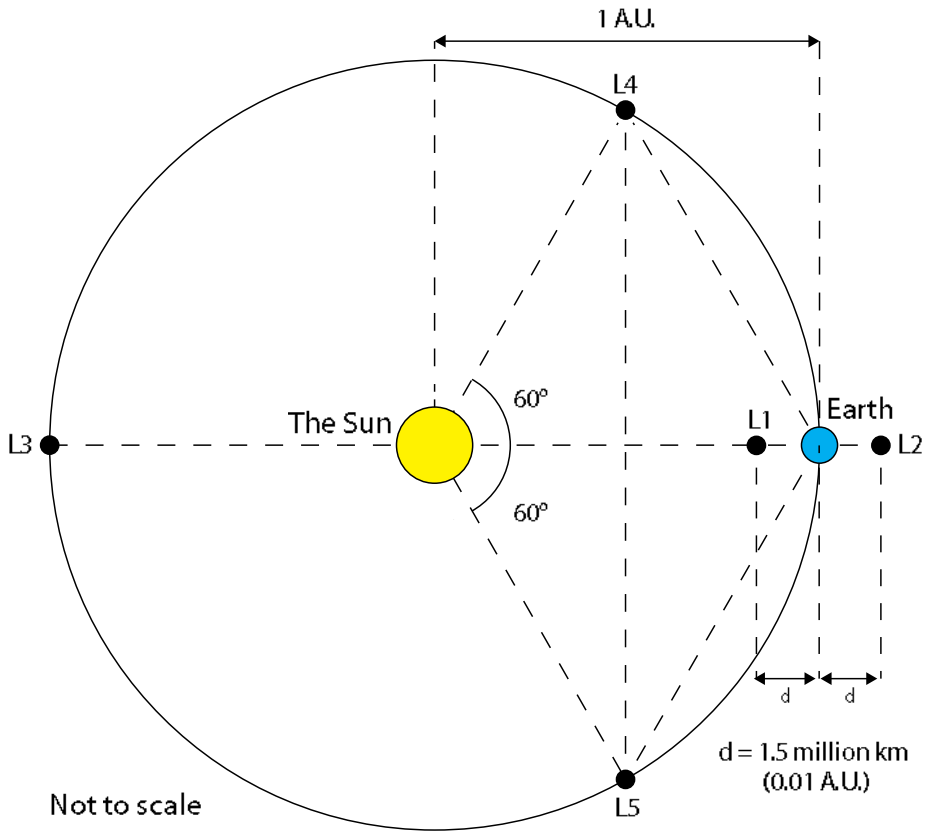

Figure 2.12 A diagram displaying the Lagrangian points for the Earth-Moon-Sun system.

Due to their relative proximity to Earth of $1.51 \pm 0.03 \times 10^6$ km ($236\ R_E \pm 4\ R_E$), the L1 and L2 points, in particular, are frequently chosen as candidate orbit locations for space telescopes.

Some examples of observatories which have been positioned at L1 include the Advanced Composition Explorer (ACE) (Stone et al. 1998), Deep Space Climate Observatory (DSCOVR) (Burt and Smith 2012) and LISA PathFinder (LPF) (McNamara 2006).

Some examples of observatories which have been positioned at L2 include the Wilkinson Microwave Anisotropy Probe (WMAP) (Weiland et al. 2011), the Herschel Space Telescope (Pilbratt 2003), and the Planck Space Observatory (Doyle, Pilbratt, and Tauber 2009). The ATHENA mission, the mission that this thesis will focus on, is currently planned to orbit at L2.

An observatory positioned at L2, in particular, has a geometric advantage over a spacecraft positioned at L1 in that it can always be positioned facing away from both the sun and Earth in such a way as to get a clear and unobstructed view of the sky (Farquhar and Dunham 1990). However, the radiation environment at L1 is more predictable as it is less affected by the interaction between Earth's magnetic field and solar wind.

The radiation environments of extrasolar particles at both L1 and L2 are similar due to their proximities to Earth relative to the Sun, but due to the Earth's magnetosphere experience different SEP fluxes. A spacecraft at L1 is exposed to the normal solar system radiation environment without influence from Earth's magnetosphere because the Earth's bow shock, the feature of Earth's magnetosphere most distant from Earth on the Earth's dawn side, does not reach Earth's L1 point.

A spacecraft at L2, on the other hand, is within the magnetotail of Earth. This means that the SEP flux, as well as other charged particle components of the solar system radiation environment travelling toward the spacecraft approximately from the direction of Earth will be modified by the Earth's magnetic field.

The radius of Earth's magnetotail at L2 has been studied by several authors using data from GEOTAIL (Kokubun et al. 1994). Christon et al. (1998) defined the radius of Earth's magnetotail as $\sim 25\ R_E$ at L2 based on a greater than 50% probability of encountering the Earth's magnetosheath at this radius. Other authors have found similar values, such as Maezawa and Hori (Maezawa and Hori 1998) who obtained a radius between 25 R_E and 27 R_E for a distance from Earth along the Earth-Sun axis between 150 R_E and 220 R_E, and Fairfield (Fairfield 1992) used data from the ISEE 3 mission to find a magnetotail radius between 20 R_E to 30 R_E.

The magnetotail also has many non-cylindrical features, and varies in both radius and position (Evans 2003). Crucially, missions often orbit the L2 point with large radii, for instance GEOTAIL orbited L2 between 0 R_E and approximately $50\ R_E$ (Eastman et al. 1998), which means it was capable of passing through all possible structures within Earth's magnetotail.

As the exact radiation environment at L2 is still relatively unknown, simulation results displayed later in the thesis will be assumed to have a large degree of potential error. Because this thesis will focus on the general physics behind the impact of radiation on detector background, as opposed to attempting to give precise numerical predictions of background in particular missions, representative radiation fluxes will be used to establish and investigate the most significant causes of background in X-ray detectors. Unless otherwise stated, simulations of GCR protons incident upon a spacecraft will use the spectrum generated by the CREME96 model (Tylka et al. 1997), and simulations of CXB incident upon a spacecraft will use the spectrum as described by Moretti et al. (2012).

2.4 Summary

The radiation environment of space contains numerous components that vary in time and space. This chapter has given a very general overview of some of key background-inducing particle species in the space-based environment, and the ways in which they vary with spacecraft location and over time.

Due to the complexity of the space-based environment, this thesis will use fixed spectra that are representative of the flux a spacecraft might experience at an L2 orbit, the expected orbit of the ATHENA mission. Simplifying the incident spectra meant that the work performed in this thesis could focus on the physics of background generation from incident particles hitting a spacecraft, a topic that is also complex, and which will be the subject of the next chapter.

Chapter 3

Components of X-ray-like Background

As discussed in Chapter 2, the radiation environment varies significantly across the solar system. Therefore, to predict the background for a particular mission, bespoke simulations must be performed with spectra specific to the radiation environment that will be present. However, understanding the particle environment surrounding a spacecraft only represents the first step in calculating the level of background a mission will experience.

The definition of X-ray-like background and the general ways in which particles might induce background were introduced previously in Chapter 1. Here it was discussed that background-inducing particles might not necessarily have the same kinetic energy as the energy they deposit in a detector (which defines the background spectrum produced from an image).

Particles that induce X-ray-like background in this thesis will therefore be split into two categories, particles that have a kinetic energy greater than the detector energy range, which will be described as ‘hard’, and particles that have a kinetic energy within the detector energy range, which will be described as ‘soft’. This differs from the definitions used in Chapter 2, where soft protons were described as protons that are not capable of penetrating spacecraft shielding which could be up to hundreds of MeV in energy. However as protons that are unable to penetrate proton shielding do not affect the X-ray-like background, ‘soft’ will be defined in the rest of this thesis as having a kinetic energy between 0.1 keV and 15 keV, the energy range of the ATHENA WFI.

As will be described in this chapter, there are numerous methods by which a particle may induce background in a device, each of which are influenced by spacecraft structure and detector design. This leads to a large variation in background depending on the design of a mission. Bespoke simulations must therefore not only be designed specifically for the radiation environment of the spacecraft, but must also be tailored for the spacecraft structure of the mission, and the detectors used in the mission.

Silicon-based detectors for X-ray observations typically operate on the principle that a photon interacting with the detector will deposit its energy into a photoelectron, which will then in turn generate a number of further electrons in proportion to its kinetic energy that can be counted through measuring the charge present in the pixel. However, this principle means that any particle or

mechanism that generates an electron in the detector within the energy range could be registered as X-ray-like background.

Background can either be induced in a detector through a primary particle or a secondary particle. A primary particle in this context means a particle that originated from outside the spacecraft. In contrast, a secondary particle is a particle created by the interactions between a primary particle and the materials composing the spacecraft.

The number of mechanisms by which a particle can induce background make simulations complex, and there is no single way to remove all types of background induced by radiation. This means that multiple mitigation strategies must be employed to significantly reduce background, something which may be difficult depending on the engineering constraints imposed by other requirements on the spacecraft structure.

For example, reducing the thickness of the detector may reduce the number of X-ray-like Compton events observed in the detector. However, it may also reduce the signal the detector receives coming through the optics through a reduction in quantum efficiency. As is the case with many engineering decisions in a space mission, making a decision on whether or not to use a background mitigation strategy or deciding how a detector might be modified to reduce background is about compromise. Many mitigation strategies must be enacted at the cost of another aspect of the mission, whether it is reducing some signal, using up more of the mass budget, or simply taking up too much space. This means that it is important to assess the precise effectiveness of a particular mitigation strategy so that compromises can be made should a mitigation strategy infringe upon other aspects of a mission.

However, before it is possible to determine how much a mitigation strategy will reduce background, or even what mitigation strategies are necessary, it is first necessary to understand the types of particle events that can cause background. This chapter will therefore give a brief overview of each particle component that is believed to be significant to X-ray-like background, including some of the mechanisms by which they induce background, and some of the factors that can influence their generation and detection.

It should be noted that this thesis will treat all materials discussed as amorphous. This is partly because Geant4 simulations, which will be used extensively in this thesis, treat all materials as amorphous, but also because there is currently little research into how the crystalline structure of the silicon detectors used in space might affect background components. There are some experiments being planned to investigate this at the Center for Electronic Imaging, and the caveat should be considered throughout this thesis that components such as electron backscattering and hard photon Compton scattering may be influenced in unknown ways by the detector silicon structure.

3.1 Background induced by soft protons

Soft protons, described earlier in Chapter 2, are usually primary protons that have a kinetic energy that is comparable to the energy range of the detector that can travel through the optics and baffle of a space telescope, hitting the detector and causing an X-ray-like event.

Chapter 2 described how soft protons vary in flux significantly across the solar system due to magnetic fields in the heliosphere, meaning their impact on background depends where in the solar system the mission is placed. However, for missions placed in areas with a high soft proton flux, a proton shield can be used to block protons from hitting detectors. Typically several centimetres of a material such as aluminium is capable of blocking protons of up to approximately 100 MeV in kinetic energy. Such a proton shield is currently being developed for the WFI in the ATHENA mission to prevent soft protons from both causing significant radiation damage, and from causing X-ray-like background.

While a proton shield can be used to stop soft protons from entering the telescope from the sides or back, a proton shield cannot be used to block soft protons from entering the telescope through the optics. Therefore, many space missions employ the use of a magnetic diverter in the telescope baffle to divert soft protons and electrons away from the detector. In ATHENA, simulations of the magnetic diverter have shown the diverter to be nearly 100% effective (Fioretti et al. 2018).

Magnetic diverters and proton shields are effective against soft protons specifically because soft protons have low enough energies that they are significantly affected by both of these mitigation strategies. However, as was discussed in Chapter 2, there is a significant flux of high energy cosmic rays throughout the solar system, and these are less easy to mitigate. Typically these particles are high energy enough to pass through shielding while losing minimal kinetic energy. Such particles are also high energy enough to fully penetrate detectors, and will be referred to in this thesis as ‘fully-penetrating particles’.

3.2 Background induced by fully-penetrating particles

A fully-penetrating particle will be used in this thesis to refer to any massive, charged particle that has sufficient kinetic energy to penetrate the full thickness of a detector. Such particles can originate from either outside a spacecraft or can be secondary particles produced from surfaces within a spacecraft. However, fully-penetrating particles that induce X-ray-like background are most commonly comprised of cosmic protons and secondary knock-on electrons (D. Hall, Holland, and Turner 2008).

Fully-penetrating particles are often ‘minimally ionising’, and because of this, fully-penetrating particles are sometimes also referred to as Minimally Ionising Particles (MIPs). A MIP is defined by its stopping power curve with respect to energy. A feature of massive particles is that the stopping

power of the particle (the rate of decrease of energy with respect to distance in a material) decreases as particle kinetic energy increases.

However, at around several GeV in kinetic energy stopping power hits a broad minimum before beginning to steadily increase, as shown in Figure 3.1.

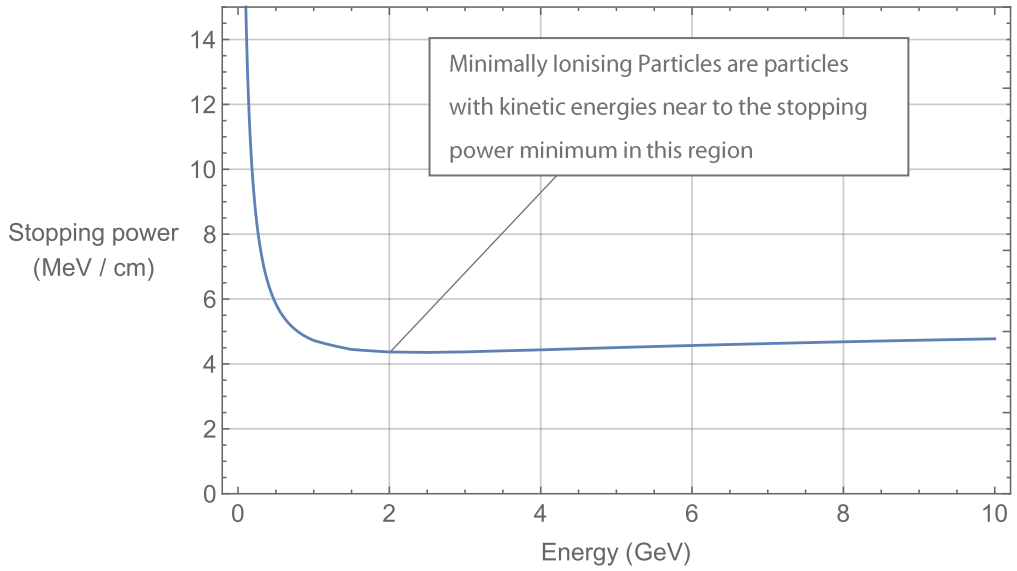

Figure 3.1 The stopping power of a proton travelling through aluminium, as a function of particle kinetic energy (M. J. Berger et al. 2017).

Particles approximately at energies which correspond to the minimum stopping power or more are described as minimally ionising and are typically too energetic for any shielding material in a spacecraft to reduce the kinetic energy of a minimally ionising particle significantly. For example, the CSDA range of a 2 GeV energy proton in aluminium is 3.76 m (M. J. Berger et al. 2017), significantly larger in scale than the 3 cm – 4 cm thickness of proton shielding that the ATHENA WFI will contain. The CSDA ranges of protons and electrons are displayed in Figure 3.2.

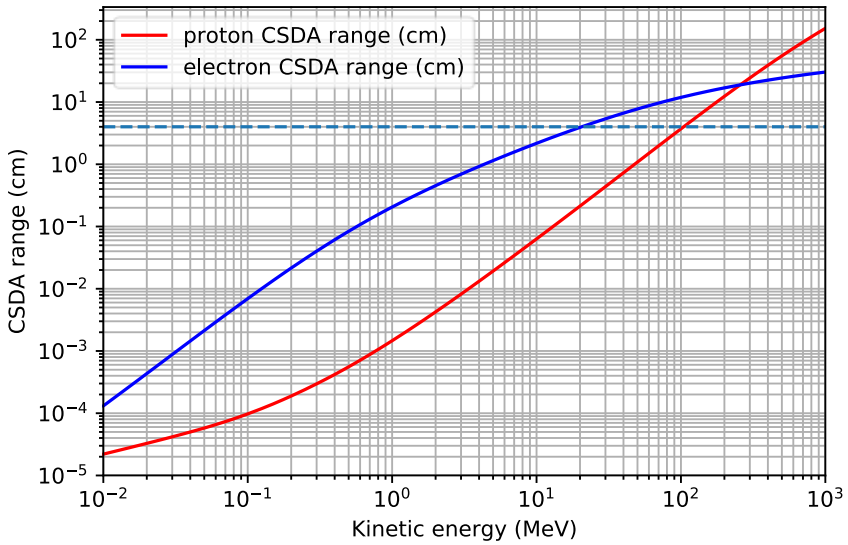

Figure 3.2 CSDA ranges for protons and electrons in aluminium as a function of kinetic energy (M. J. Berger et al. 2017). *The dashed blue line represents a CSDA range of 4 cm in aluminium, the range at which an ion may be able to penetrate the ATHENA WFI proton shield.*

While the kinetic energy of a fully-penetrating particle is significantly larger than the detection energy range of a soft X-ray detector, a fully-penetrating particle passing through a detector only deposits a fraction of its energy into electrons in the detector. Depending on the fully-penetrating particle kinetic energy as well as the angle of entry into the detector, this energy may fall within the detector energy range.

As illustrated in Figure 3.3 and Figure 3.4, which show the initial stopping power × density × material thickness of silicon for high energy protons and electrons travelling through silicon, it is not possible for a fully-penetrating proton or electron to deposit within the energy range of 0.1 keV to 15 keV for silicon detector thicknesses above several tens of microns. This will also be shown in later simulations in Chapter 9, where the wide spectral peak associated with MIPs disappears from the background as detector thickness is increased.

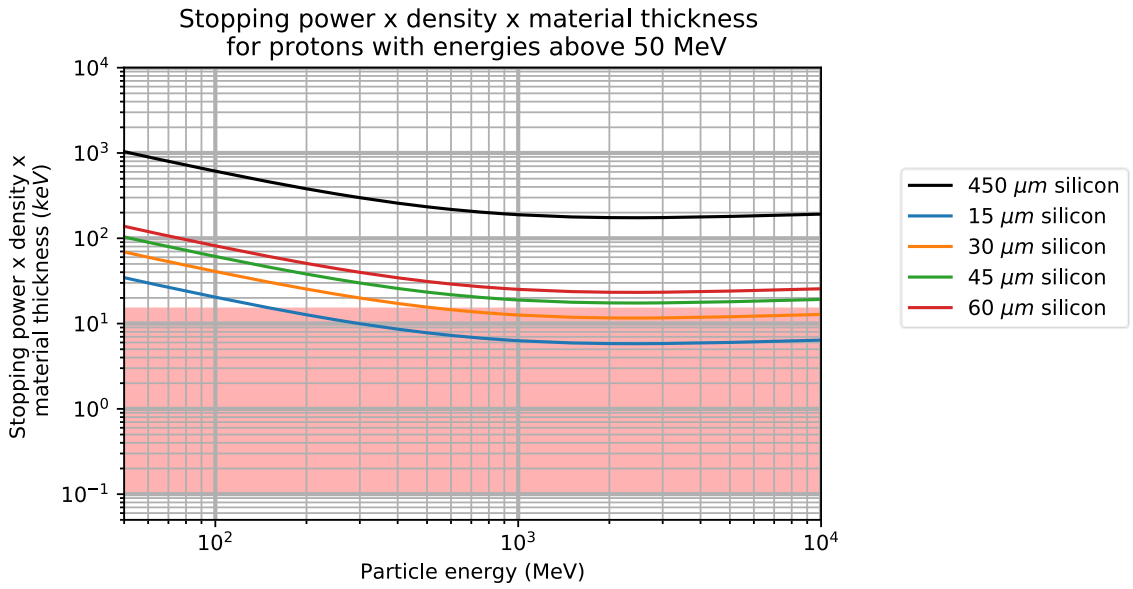

Figure 3.3 The initial stopping power × density × material thickness of silicon for varying kinetic energies of protons. If the proton were to impact the silicon perpendicularly, and if the proton is approximated to having a large energy relative to its stopping power, this would be equivalent to the deposited energy in a silicon device. The pink band represents deposited energies between 0.1 keV and 15 keV, the energy range of the ATHENA WFI. At 450 μm of silicon thickness, a high energy proton in this energy range is unable to deposit energy within the energy band for any kinetic energy. The CSDA range of a 50 MeV proton in silicon is 12.24 mm, which is significantly greater than 450 μm of silicon.

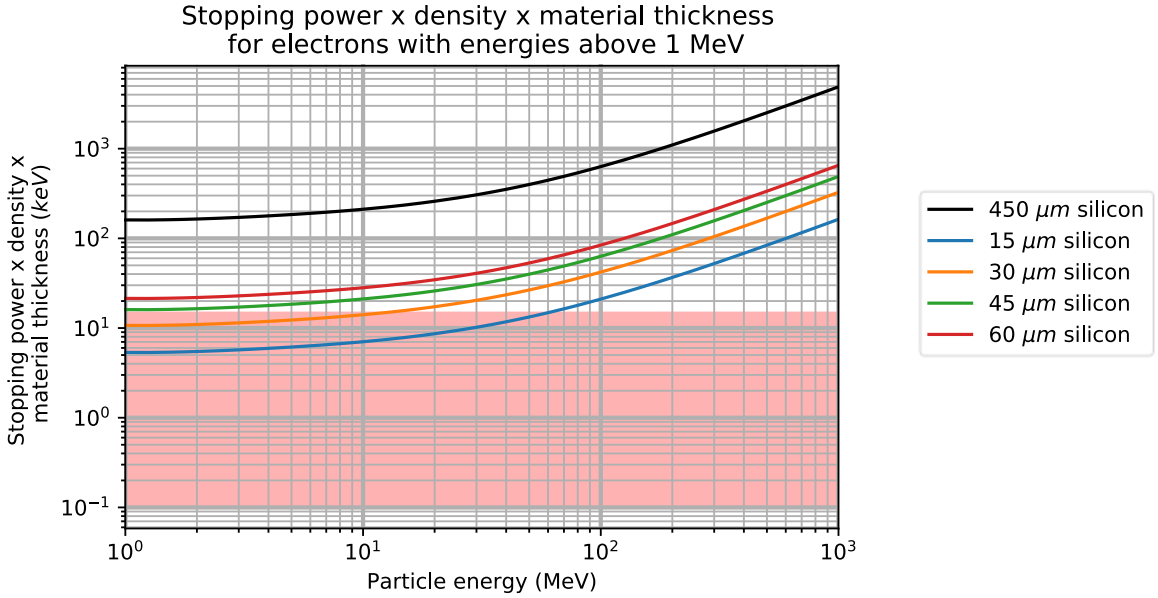

Figure 3.4 The stopping power × density × material thickness of silicon for varying kinetic energies of electrons. The CSDA range of a 1 MeV electron in silicon is 2.312 mm, which is significantly greater than 450 μm of silicon.

The fact that fully-penetrating particles cannot deposit energy within the detector energy range if the detector is sufficiently thick means that fully-penetrating particles are only an issue for X-ray-like background in detectors which are several tens of microns or less in thickness.

There are several methods of mitigating the background induced by fully-penetrating particles in detectors that are within several tens of microns in thickness. In a detector with a high thickness to

pixel side length ratio, there is a large probability that a fully-penetrating particle will pass through multiple pixels, unlike X-rays, which are absorbed in a single pixel. A fully-penetrating particle passing through multiple pixels will therefore create a charge track along the detector that can be seen in images. The paths a fully-penetrating particle might take through a detector are displayed in Figure 3.5.

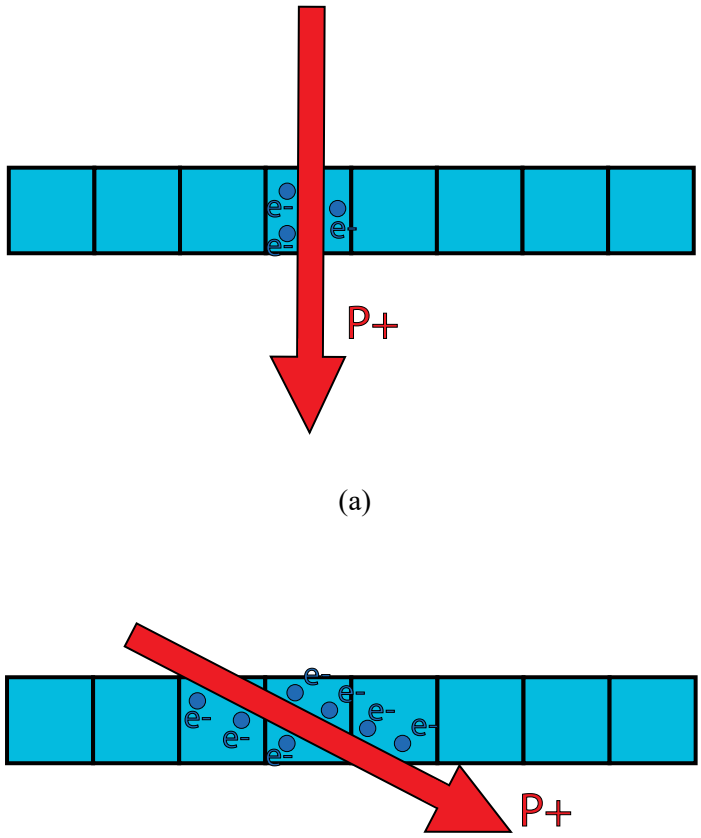

(a)

(b)

Figure 3.5 The possible paths a fully-penetrating proton might take through a thin detector. If a fully-penetrating particle only deposits energy/creates charge in a single pixel, such as in Figure 3.5(a), it will not be able to be removed through image processing. However, if it penetrates several pixels, as shown in Figure 3.5(b), charge will be deposited as a track, and image processing algorithms will be able to remove the track from images.

Image processing techniques are used in all X-ray astronomy missions to remove charge tracks associated with cosmic rays from images, and these can therefore be designed to additionally remove tracks associated with fully-penetrating background-inducing events in general while retaining single-pixel or Gaussian events. A method known as 'Self-Anti-Coincidence' (SAC) (Burrows et al. 2019; Bulbul et al. 2020) can also be combined with this to also remove secondary particles associated with other X-ray-like background events that are generated by the initial fully-penetrating particle.

Another mitigation method which is sometimes used is to use a separate anticoincidence detector for detectors with a low thickness and with high frame rates. This involves the use of a second detector

surrounding or near to the main detector, which can detect a particle passing through. When a particle travels through the second detector, the associated image frames in the primary detector are removed, so that only frames that don't contain cosmic rays are used. While the ATHENA XIFU instrument is expected to use anticoincidence detectors, the ATHENA WFI will not, so anticoincidence detectors will not be discussed at length in this thesis.

As this thesis will primarily focus on detectors that are similar to the ATHENA WFI, which will have a sensitive region that is approximately 450 μm in thickness, fully-penetrating particles will deposit too much energy in the ATHENA WFI to generate X-ray-like background, and will therefore not be present in most of the simulations or analysis performed. Fully-penetrating particle X-ray-like background will, however, be present in simulations and analysis discussed in Chapter 9, where changes in background with respect to detector thickness will be examined.

3.3 Background induced by soft photons and fluorescence

Soft photons are simply X-rays within the detector energy range that are generated by GCRs interacting with materials in the spacecraft within line-of-sight of the detector. Soft photons are identical to signal photons and generate charge in a detector through exactly the same mechanisms. Although there are many mechanisms by which incident radiation could theoretically generate a soft photon continuum from spacecraft materials, simulations performed in Chapter 8 will indicate that only X-ray fluorescence lines from materials contribute significantly to the soft photon background.

X-ray fluorescence lines are produced by the de-excitation of electrons in an atom after excitation by an incoming particle, as electrons drop from one energy level to another within the energy band structure of an atom. When a particle impacts an atom, there is a certain probability that the particle will 'excite' the atom by depositing some energy. Usually, this involves moving one or more electrons from their ground states to a higher energy level. Eventually, the electrons drop down to lower energy states, releasing the energy difference between the two states in a fluorescence photon, as shown in Figure 3.6.

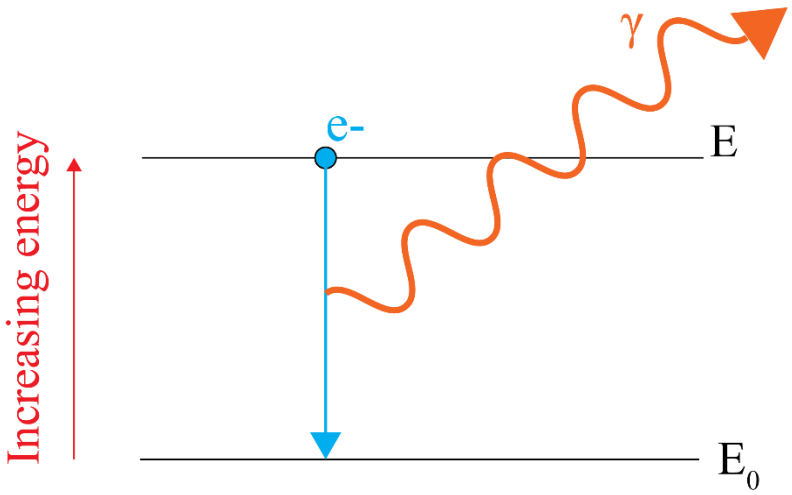

Figure 3.6 An energy level diagram showing the emission of a photon from an electron dropping an energy level.

Fluorescence lines appear in high energy resolution detectors as approximately discrete vertical lines. In a theoretical universe, where each atom could be modelled by solving the Schrodinger Equation for a hydrogen-like system, each atom would have mathematically discrete well-defined energy levels. In the physical universe, however, there are several effects that cause energy levels to have an intrinsic variance such as the well-known uncertainty principle and effects like broadening of energy levels due to atomic lattices or thermal effects.

However, these effects only typically cause the energy of a band to vary on the order of several electronvolts, which is small relative to the energy range of many detectors, and small relative to the energy of the fluorescence line.

In a perfect detector, these lines could be removed from spectra with relative ease, as the lines would be well defined enough that minimal signal would be lost by simply removing areas of spectra corresponding to such lines. However, in real detectors, a degree of variation is introduced due to low energy resolutions caused by effects such as Fano noise (James Henry Tutt 2012) and read noise (J. R. Janesick 2001).

This noise often causes a fluorescence line to appear as a Gaussian distribution in spectra, with a width large enough to reduce signal over a wide region of the spectrum. While these fluorescence lines can be removed through subtracting with dark frames, and potentially Gaussian fitting, these methods are unable to account for systematic errors introduced by the variation of external radiation over time, as described in Chapter 1.

Additional problems are introduced if multiple fluorescence lines are present near each other on spectra. If the fluorescence lines are near enough that their distributions can overlap, this creates a fluorescence line ‘pseudo-continuum’, which can lead to a broad region of the spectrum having a

reduced scientific quality (Silvano Molendi, private presentation to the ATHENA Background Working Group, 2019).

Additionally, the presence of background fluorescence lines can interfere with scientific observations by acting as false scientific fluorescence lines within a spectrum. If they appear sufficiently close to scientific spectral lines, background fluorescence lines may also cause difficulties in analysing the intensity of those lines and potentially obscure them.

Not only do fluorescence lines cause problems for specific spectral regions, but fluorescence lines may exhibit a spatial distribution across a detector as well. As fluorescence lines are generated from materials on the spacecraft, an object placed close to a particular region of the detector may cause a large fluorescence background within that region of pixels. Chapter 4 will show an example of where this happened in the XMM-Newton mission, where spectral lines from a circuit board placed behind the EPIC-PN detector could be seen in images, exhibiting the same shape as components on the circuit board itself.

The fact that fluorescence lines are created by materials surrounding detectors means that to mitigate this background, it is important to carefully consider which materials are within line-of-sight of a detector when designing the surrounding spacecraft. Fluorescence lines are typically emitted from within several microns of surrounding spacecraft materials. For instance, a photon of 5 keV in energy has a half-value layer of 13.3 μm in aluminium (Xcom 2010). This means that care should also be taken to cover or coat any materials that could produce high fluorescence with a material that absorbs the fluorescence line, but does not itself emit significant fluorescence.

Selecting a material that can do this requires compromising between the ability of a material to emit low fluorescence and engineering considerations. The quantity of fluorescence lines in an element, the fluorescence energy of each line and the fluorescence yield increase with the atomic number Z, as shown in Figure 3.7 and Figure 3.8. This means that to minimise the number and intensity of fluorescence lines, it is necessary to minimise the quantity of high atomic number materials (also referred to as high-Z materials) within direct line-of-sight of a detector.

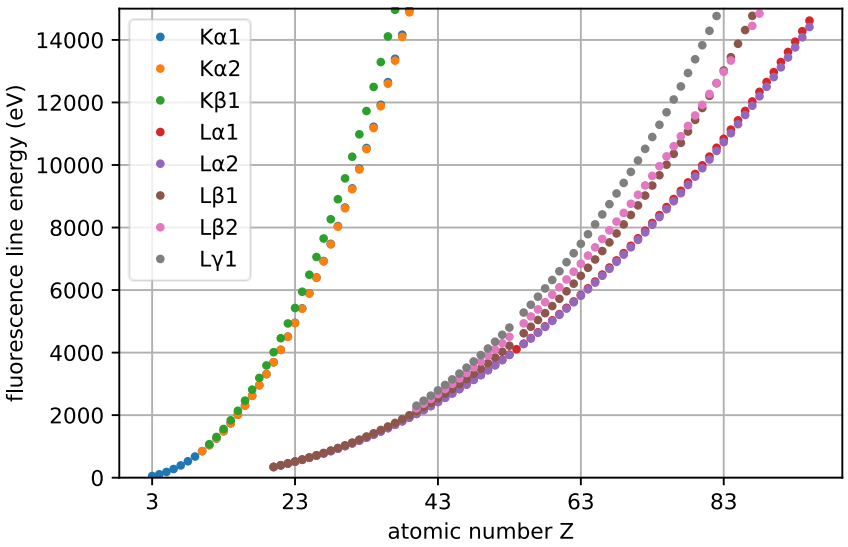

Figure 3.7 The energy of fluorescence lines for different materials as a function of atomic number, labelled using Siegbahn notation (Ralchenko et al., n.d.).

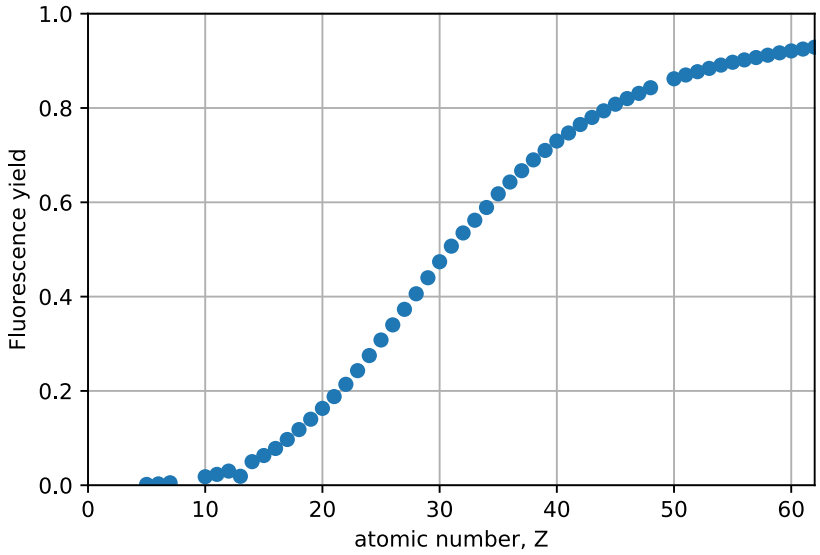

Figure 3.8 The fluorescence yield for the Kα1 fluorescence line as a function of atomic number (Ralchenko et al., n.d.).

This is not always possible or optimal due to other considerations such as engineering considerations.

In these cases, it may be useful to place shielding between the detector and these materials. One such shielding design that is capable of shielding detectors from fluorescence lines is graded-Z shielding, which will be investigated in Chapter 10 and Chapter 11.

3.4 Background induced by hard photons

Low energy X-rays such as fluorescence photons can be shielded using thin shielding layers as they have small half-value layers relative to common spacecraft material thicknesses. Photons of 15 keV or less, for example, have small half-value layers of 0.323 mm in aluminium (Xcom 2010).

Unfortunately, high energy photons are also capable of depositing energies within the energy range of a detector. Instead of being absorbed by the photoelectric effect, high energy X-rays typically deposit energy through Compton scattering. These photons will be described as 'hard photons' in this thesis.

Compton scattering occurs when a high energy photon interacts with a charged particle and scatters from it, rather than being fully absorbed such as in the photoelectric effect. If a photon Compton scatters from an electron in a detector, the photon will scatter and distribute some of its energy to the electron. The scattered electron will then disperse its energy throughout the pixel through the same mechanisms by which an electron produced through the photoelectric effect from a soft photon disperses its energy. As this process occurs due to a single interaction, Compton scattering events unfortunately do not produce tracks in detectors as fully penetrating particles do, and are not removeable through image processing.

The two primary sources of hard photons in a detector like the ATHENA WFI are expected to be the CXB and secondary photons produced internally by cosmic protons. To develop strategies to mitigate against these sources of background it is necessary to understand the factors that can affect the probability of a Compton scattering event occurring. The probability of a Compton scattering event occurring is governed by the Klein-Nishina Equation (Weinberg 1995), which if the incoming photon is unpolarised is:

$$\frac{d\sigma}{d\Omega} = \frac{1}{2}\alpha^2 r_c^2 P(E_\gamma, \theta)^2 \left[P(E_\gamma, \theta) + P(E_\gamma, \theta)^{-1} - \sin^2(\theta)\right] \tag{3.1}$$

where

$$P(E_\gamma, \theta) = \frac{1}{1 + (E_\gamma / m_e c^2)(1 - \cos(\theta))} = \frac{\lambda}{\lambda'} \tag{3.2}$$

Here, E_γ is the photon energy, m_e is the mass of an electron, θ is the scattering angle, λ is the initial photon wavelength, λ' is the final photon wavelength, c is the speed of light, α is the fine structure constant, r_c is the reduced Compton wavelength of an electron and $\frac{d\sigma}{d\Omega}$ is the differential cross-section.

The mass attenuation coefficient for an 80 keV photon Compton scattering through silicon is 0.1483 cm^2/g (Xcom 2010) meaning that the half-value layer for an 80 keV photon travelling through silicon that is restricted to only Compton scatter is 2.006 cm. As this is significantly larger than the size of a typical space-based silicon detector, which are between tens and hundreds of microns in thickness, the probability of a given photon Compton scattering in a detector is low.

As will be examined in Chapter 9, the fact that the probability of a particular photon Compton scattering through a detector is low means that the number of background-inducing Compton interactions in the detector is approximately proportional to the detector volume. This is because the

flux of photons passing through the detector is large relative to the flux of photons absorbed or scattered through the detector, and therefore the mean quantity of photons capable of Compton scattering in the detector at any given point in the detector volume is approximately constant.

Therefore one method of reducing the background is to minimise the detector thickness, although as with all aspects of background reduction, this requires considerations of other aspects beyond background, and a reduction in detector thickness may actually cause other background components to increase. Chapter 9 will investigate the effect of varying detector thickness on overall background and will use both simulations and mathematics to identify the optimal detector thickness.

In addition to varying detector thickness, there are other mitigation strategies available for reducing Compton background. In addition to attenuating fluorescence lines, the high-Z layer in graded Z shielding is designed to attenuate high energy photons. The ability of graded-Z shielding to do this will be examined in Chapter 10 and Chapter 11.

3.5 Background induced by soft electrons

Soft electrons will be used in this thesis to describe electrons that have a kinetic energy within the detector energy range that interact with the detector and deposit their full kinetic energy into a pixel. Electrons directly produced by incident ions are also sometimes referred to as ‘secondary electrons’, ‘delta rays’ or ‘knock-on electrons’, and these terms will also occasionally be used throughout this thesis where appropriate.

Soft electrons interact with a detector through the same mechanisms that a photoelectron generated by a signal photon might, and therefore register as X-ray-like background.

It should however be noted that the X-ray-like background spectrum produced by soft electrons will not be the same as the kinetic energy spectrum of soft electrons incident upon the detector surface. This is because electrons can backscatter off the detector surface, or be absorbed in surface materials, rather than being absorbed within the sensitive regions of the detector. In addition, backscattered electrons might still deposit some but not all of their energy within the detector, further altering the spectrum.

Secondary electrons are created by both Galactic Cosmic Ray MIPs and by X-rays from the Cosmic X-ray Background as they pass through materials surrounding a detector. In the energy range of 0.1 keV to 15 keV, electrons only have a maximum CSDA range of 2.63 μm (M. J. Berger et al. 2017), meaning that as with fluorescence photons, soft secondary electrons detected by the WFI should originate from within several microns of surfaces within line of sight of the detector.

Mitigating the electron-induced background is difficult using materials, because any material used as shielding will emit electrons of its own when GCR pass through it. Furthermore, there is evidence

from theory and simulation that there is little variation in proton-induced electron yield with respect to material, including Sternglass' theory of secondary electron production for instance, which suggests that electron yield is constant with respect to material atomic number (Sternglass 1957). Simulations of the ATHENA WFI presented by von Kienlin et al. (2018) also indicate that the presence of inner shielding layers made out of different materials makes no difference to overall X-ray-like background, despite the fact that electrons comprise a significant proportion of background.

However several methods for reducing X-ray-like background due to electrons will be examined in this thesis, including both material based methods and magnetic shielding methods in Chapter 8, Chapter 9 and Chapter 10. Here it will be found using mathematics and simulations that the use of on-chip filters, passivation layers and magnetic shielding methods may be effective mechanisms for mitigating electron-induced background.

3.6 Background induced by hard electrons

While the backscattering of electrons can reduce the background due to soft electrons, it also allows electrons of higher energies than the detector energy range to create X-ray like background, here referred to as 'hard electrons'.

Even though an incident electron is not absorbed into a detector when it is backscattered, it is often able to deposit some of its energy into the detector within the detector energy range, generating an X-ray-like background event. Additionally, as backscattering electrons only travel about a third of the maximum range (Assa'd and El-Gomati 1998) into a material, they often do not penetrate far enough into a material to generate tracks and are therefore not removable from spectra using image processing like proton or electron MIPs.

As the majority of X-ray-like events created by backscattering are generated by charged particles with energies higher than the detector energy range, they may be more difficult to shield than particles depositing all their energy into a pixel, due to being both more penetrative and less affected by magnetic shielding.

However, as stated previously in Section 3.5, the effectiveness of both material shielding methods and magnetic shielding at removing electron-induced background will be investigated in Chapters 8, 9 and 10. Here simulations will indicate that on-chip filters, passivation layers and magnetic shielding methods could also be effective at removing hard electron in addition to the soft electron induced background.

3.7 Other X-ray-like background Sources

While the particles types described in this chapter represent the known particle types that are expected to cause significant X-ray-like background, as this is an active area of research and based primarily on

examination of simulation results, it is possible that there may be other particle components within the X-ray-like background spectrum.

For instance some results presented in Chapter 9 will indicate that secondary neutrons created by GCR passing through the spacecraft may generate further secondary particles that can generate a non-insignificant background flux for cases where a significant mass of material is present in simulations. This means that it is also possible that cosmic neutrons may be able to induce background in detectors. Neutrons only interact with materials through nuclear interactions because they have no charge, and would therefore be expected to have a low cross-section for inducing charged electrons in a detector within the detector energy range. Therefore the neutron-induced background would be expected to have similarities to hard photon-induced background, which also has a low cross-section of being created per photon. This means that a large quantity of neutrons would have to be present to generate X-ray-like background in significant quantities.

It should also be noted that the mechanisms for background generation by incident charged particles described in this chapter could also be caused by any incident charged particle of the correct energy. This might include for instance secondary protons or other baryons or mesons generated by incident GCR inducing nuclear interactions in spacecraft materials. However, as simulations performed to date have not indicated that these components are significant relative to other components, these will not be investigated in this thesis.

3.8 Summary

This chapter has discussed each of the background components that are currently known to cause X-ray-like background in detectors, and for the purposes of this thesis, each of the particle species that can cause background have been split into ‘soft’ and ‘hard’ components. These components each induce background through different mechanisms, and this thesis will attempt to investigate and characterise the contribution of each component to X-ray-like background in X-ray astronomy missions.

Each of the X-ray-like background components presented in this chapter have a complex relationship with the materials in a spacecraft and detector design and are likely to vary significantly in strength with the design of a mission. Therefore, it is necessary to discuss the design of the particular mission and detector this thesis will use as a baseline design: the Wide Field Imager for the Advanced Telescope for High ENergy Astrophysics.

Chapter 4

The Advanced Telescope for High Energy Astrophysics (ATHENA)

Background induced by the radiation environment of space affects images produced by every space-based astronomical imaging mission, simply due to the nature of the response of an imaging device to radiation and the quantity of high energy radiation present in the space-based environment. However, work in this thesis will focus on the Wide Field Imager (WFI) for the European Space Agency's upcoming Advanced Telescope for High Energy Astrophysics (ATHENA) mission in particular, due to the Center for Electronic Imaging's involvement with the mission, and so that simulations can be tailored to the ATHENA WFI as a specific example of an instrument where removing radiation-induced background is an important factor in maximising the quality of scientific output of the mission.

Before discussing ATHENA however, it is first instructive to discuss the precursor mission to ATHENA, XMM-Newton, to examine why background reduction plays an important role in current X-ray astronomy missions and how background can vary spatially, temporally, and with detector design.

4.1 XMM-Newton

The X-ray Multi-Mirror mission (XMM-Newton) (Jansen et al. 2001) launched in 1999 as part of ESA's Horizon 2000 program, and is often regarded as the precursor mission to ATHENA. An artist's rendition of XMM-Newton is displayed in Figure 4.1.

Figure 4.1 An artist's impression of XMM-Newton from https://www.esa.int/Enabling_Support/Operations/XMM-Newton_operations

XMM-Newton was launched in December 1999 as part of ESA's Horizon 2000 program with the aim to observe many astronomical sources of X-rays, including both sources within the solar system and extragalactic sources. Some achievements that were made possible using data from XMM-Newton include (Schartel et al. 2010):

- The discovery of the mechanism underpinning the emission of X-rays from comets, which was found to be caused by the interaction between charged solar wind and neutral atoms in comet gases.
- The mapping of X-ray emission from pulsars, which led to the discovery of pulsar surface hotspots.
- The discovery of intermediate-mass black holes, which can merge to create supermassive black holes.
- The first large scale 3D mapping of both dark matter and ordinary matter throughout the universe, in combination with data from the Hubble Space Telescope.

According to Ness, Parmar, and Valencic (2014), between 2005 and 2012 approximately 300 papers directly using XMM-Newton data were published every year, illustrating the large level of scientific productivity generated by XMM-Newton.

XMM-Newton contains three primary instruments, of which the key instrument of relevance to the investigations in this thesis is the European Photon Imaging Camera (EPIC) ("XMM-Newton Users Handbook" 2019), which is composed of the two EPIC-MOS cameras and the EPIC-PN camera. XMM-Newton also has a highly elliptical Earth based orbit, which is quite different to the L2 orbit expected to be used for ATHENA, but would still be expected to be similar from a GCR or CXB induced background perspective.

4.1.1 EPIC-MOS

The EPIC-MOS (Turner et al. 2001) consists of two cameras, each comprised of seven front-illuminated MOS CCDs. Each CCD has a depletion region between 30 – 40 µm in thickness and contains an approximately 80 µm thick epitaxial layer in front of the device. The MOS devices are primarily used for detection of photons of several keV, with an energy resolution of approximately 75 eV for 2 keV photons ("XMM-Newton Users Handbook" 2019). An image of one of the MOS cameras is displayed in Figure 4.2.

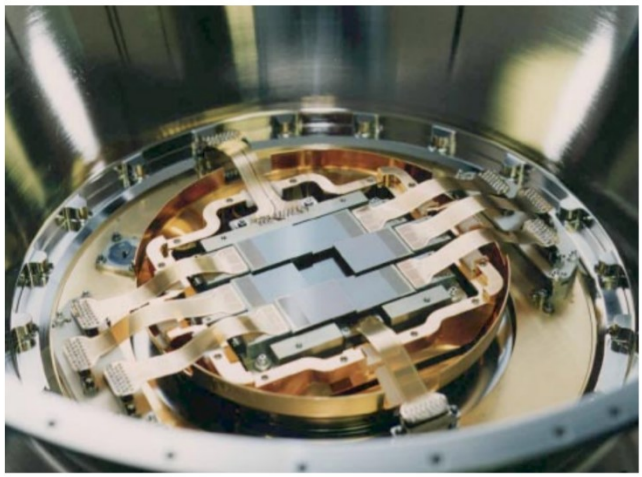

Figure 4.2 One of the EPIC MOS cameras (Turner et al. 2001)

4.1.2 EPIC-PN

The EPIC-PN (Strüder et al. 2001) consists of 12, 3 x 1 cm, back-illuminated PN CCDs with sensitive regions of 280 µm in thickness. This thicker depletion region and back illumination mean that the EPIC-PN has a significantly higher quantum efficiency than the EPIC-MOS for the detection of photons with energies below 1 keV and above 4 keV. This means that the EPIC-PN is used for the detection of high energy photons. A picture of EPIC-PN is displayed in Figure 4.3.

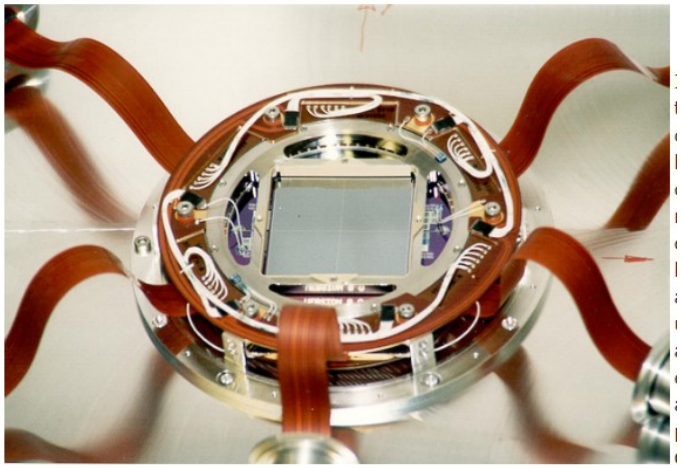

Figure 4.3 A picture of the EPIC PN from https://www.cosmos.esa.int/web/xmm-newton/technical-details-epic

4.1.3 The background in XMM-Newton

The mean background received by the EPIC-MOS and EPIC-PN are displayed in Figure 4.4 and Figure 4.5, respectively.

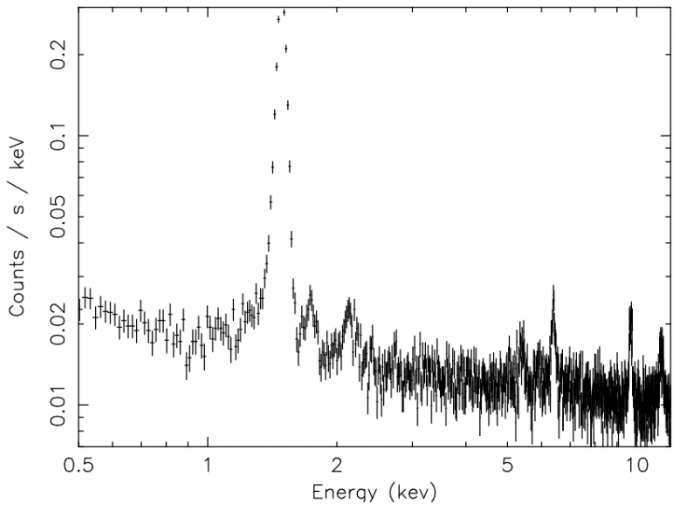

Figure 4.4 The X-ray-like background exhibited by the EPIC-MOS device in XMM-Newton (Lumb et al. 2002).

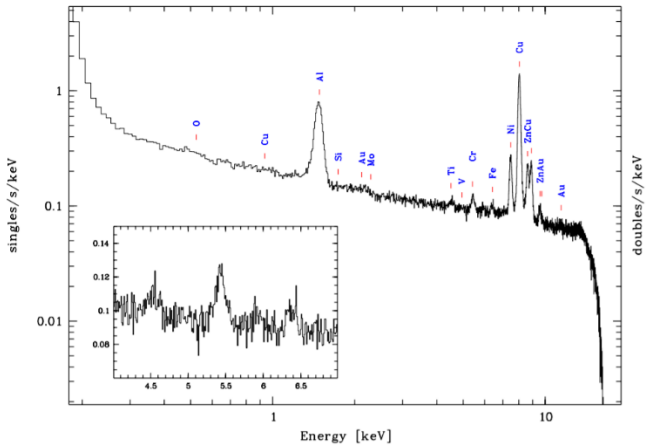

Figure 4.5 The X-ray-like background exhibited by the EPIC-PN device in XMM-Newton (Freyberg et al. 2004)

In both spectra, fluorescence lines for multiple materials can be seen, which reflect the materials present near the detector. It can be seen that many of the fluorescence lines are capable of significantly reducing the signal-to-background in some areas of the spectrum. In particular, it can be seen that around approximately 8 keV in Figure 4.5, several fluorescence lines appear near the same region of the spectrum, causing the signal-to-background to be significantly reduced over a broad region. This is particularly impactful at the 8 keV region as opposed to other regions, as the quantum efficiency for the EPIC PN at 8 keV is significantly lower than the quantum efficiency at lower energies, and therefore the intensity of photons is already low in this region.

The impact of fluorescence lines in the background can therefore be significant in reducing signal-to-background, in addition to acting as a false X-ray emission line which might obscure fluorescence lines from scientific sources. One mechanism of reducing background due to fluorescence lines is to utilise graded-Z shielding, which will be utilised on the ATHENA mission. The ability of graded-Z shielding to remove background will be investigated in Chapter 10.

While background fluorescence can reduce the scientific quality of a mission in specific regions of a spectrum, the background continuum is capable of reducing signal-to-background across the whole spectrum and is therefore of high importance to all scientific observations at low signals. D. Hall, Holland, and Turner (2008) produced the plot shown in Figure 4.6 comparing the X-ray-like instrument background from both the EPIC-PN and EPIC-MOS as well as for several other instruments from Suzaku and Swift.

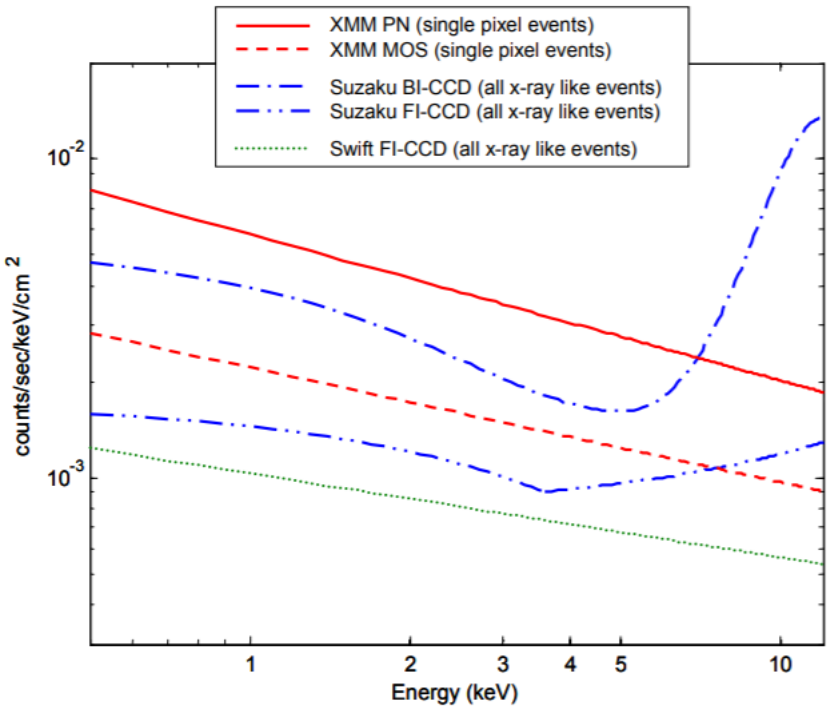

Figure 4.6 A comparison of the background from both the XMM-Newton EPIC PN and MOS, as well as several detectors on Suzaku and Swift, by Hall et al (D. Hall, Holland, and Turner 2008).

The continuum background exhibited by the EPIC PN is significantly larger than the background exhibited by the EPIC MOS. This would normally be as expected, as the extra thickness of the depletion region means that the EPIC PN is more susceptible to both incident photons that are fully absorbed within the detector, and to high energy photons that pass through the detector and Compton scatter. However, according to the paper by Hall et al., ~97% of the X-ray-like background in each simulated detector is due to knock-on electrons, indicating that other factors related to differences in geometry may be causing the differences in background.

One major difference between the detectors that the paper discussed is the fact that the PN-CCD is back-illuminated, whereas the MOS CCD is front-illuminated, meaning that the electrons hitting the MOS CCDs have to pass through an on-chip electrode structure first, and Hall et al. suggest that this difference is the main cause of the difference in background levels. The variation of X-ray-like background with the presence and thickness of on-chip layers will be investigated in Chapter 9, where it will be found from simulations that on-chip layers are indeed capable of significantly altering the X-ray-like background.

4.1.3.1 The variation of background over time

While the variation of background across the energy spectrum influences the signal-to-background ratio as a function of energy, as discussed in Chapter 2 the variation of background over time influences the systematic errors that are introduced by the presence of background. Figure 4.7 shows

the background experienced by XMM-Newton as a function of time, which shows that there is both a short-term day-to-day variation in background and long-term seasonal and solar cycle related variations in background.

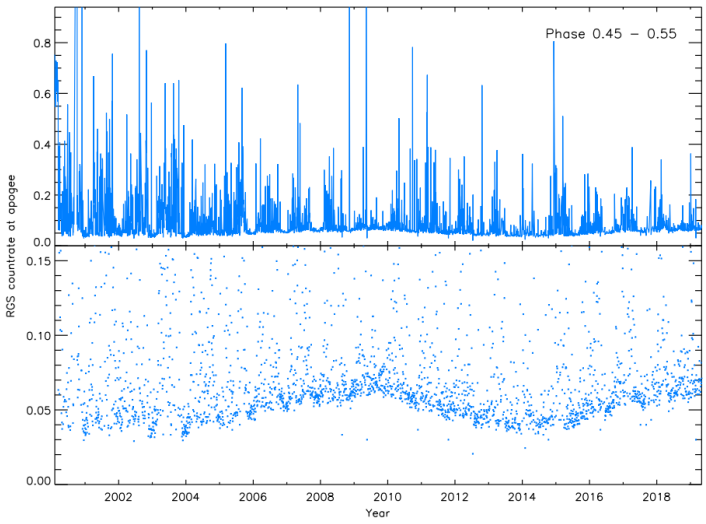

Figure 4.7 The variation of XMM-Newton background over time (Gonzalez-Riestra and Rodriguez-Pascual 2014).

The presence of both short-term and long-term components of background variation makes it challenging to produce dark frames in an X-ray observatory that will be representative of the actual X-ray-like background in a scientific observation, as such dark frames must be taken at a different time to when the observations are taken. While it is possible to use non-illuminated regions of detectors to estimate the X-ray-like background, there are problems associated with this too, due to non-uniformity of the background across an image.

4.1.3.2 The variation of background across detector images

A uniform background across a detector is preferable as it means that it is possible to estimate the background across a whole device and at the same time as observations were taken. However, a uniform background is not guaranteed, and in the case of both EPIC detectors, the background was non-uniform at the energies of several fluorescence lines, as shown in Figure 4.8 and Figure 4.9.

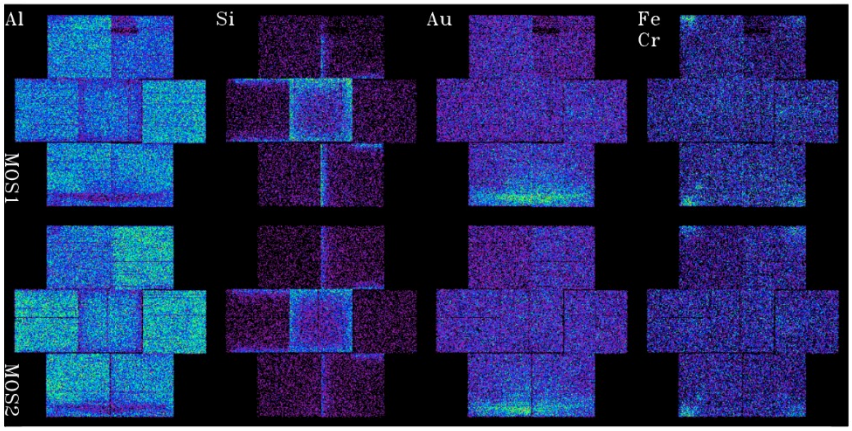

Figure 4.8 The variation of several fluorescence line intensities across the EPIC MOS (Kuntz and Snowden 2008)

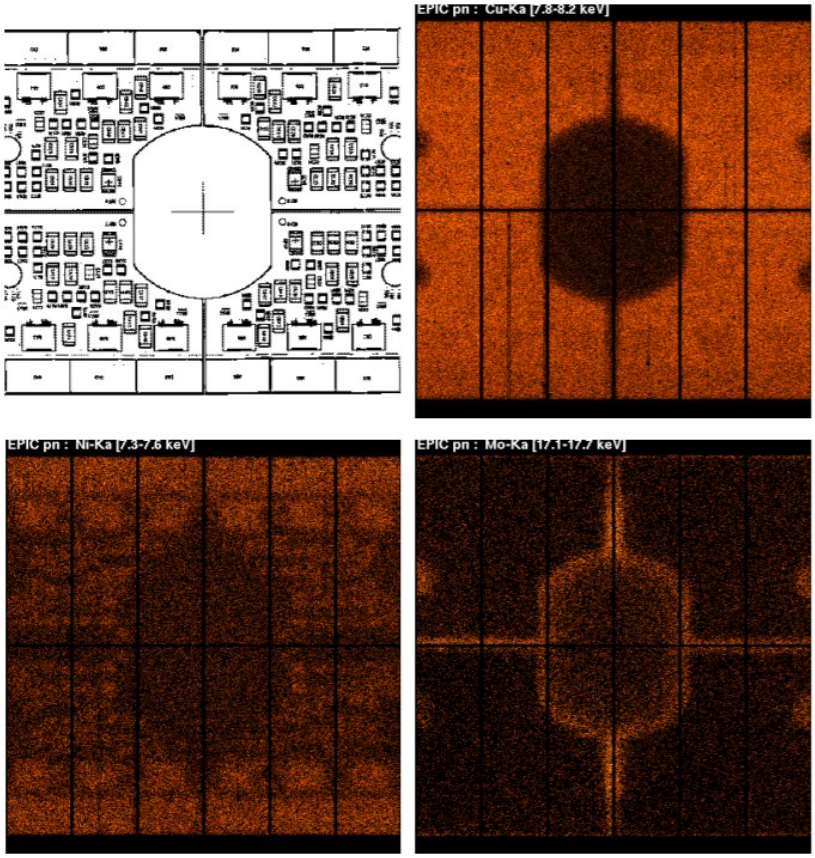

Figure 4.9 Images showing background fluorescence from EPIC PN (Freyberg et al. 2004)

In Figure 4.9 it can be seen that in the case of the EPIC PN in particular, there is a very non-uniform spatial distribution of background at fluorescence energies due to the presence of a circuit board placed on the non-illuminated side of the detector, highlighting the importance of keeping objects with high atomic number distant to the detector.

A high degree of non-uniformity means that the X-ray-like background impacting a region of the image cannot be estimated for the device as a whole but instead must be estimated for the region of scientific interest itself, which also corresponds to a smaller sample size for the background and an increased noise on background-subtracted spectra. A larger dark frame region can be chosen, but increasing the size of the region may correspond to an increase in systematic errors at the expense of lowered statistical errors.

In addition to fluorescence lines causing non-uniformity in background, it may also be possible for the continuum background to vary across a device. The possibility of this occurring in a device will be investigated in Chapter 8.

In summary, the case of XMM-Newton indicates that the background flux in an X-ray observatory can vary significantly for devices with both a thin and thick sensitive region with energy, time and spatial position. Each of these factors must therefore be taken into account when attempting to minimise background in X-ray observatories, including in the ATHENA WFI.

4.2 The ATHENA mission

ATHENA (Kirpal Nandra 2012; Barcons et al. 2015; K Nandra et al. 2014) is ESA's next major X-ray telescope, one of ESA's three 'L-class' missions, with an expected launch date to be in the early 2030s. As part of ESA's 'Hot and Energetic Universe' science theme, ATHENA will be used to achieve a large number of science goals related to observations of X-rays in the distant universe. These goals range from performing observations of black holes and the methods by which they influence the structure of galaxies, to investigating the evolution and distribution of baryonic matter in the universe. An artist's impression of the ATHENA mission is displayed in Figure 4.10.

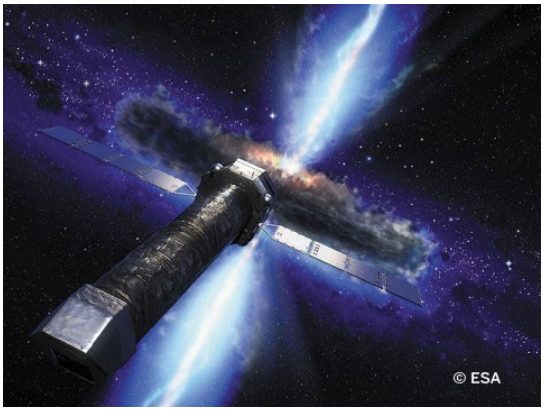

Figure 4.10 An artist's impression of the ATHENA mission from https://www.esa.int/ESA_Multimedia/Images/2012/11/Athena_X-ray_Observatory

Some of ATHENA's science goals can be found in the mission proposal for ATHENA (K Nandra et al. 2014), and include:

- Testing models for galaxy evolution, necessary for constraining possible ideas on the nature of dark matter (Aird et al. 2013).
- Determining non-gravitational heating processes and their effect on clusters at different epochs in the universe's evolution.
- Determining how Active Galactic Nuclei (AGN) can affect clusters.
- Assessing the chemical makeup and density of filaments of large gas clouds and determining as precisely as possible the local cosmological baryon density, in an attempt to test models which suggest there are baryons hidden from current observations.
- Obtaining experimental observations of the chemical makeup of the first stars, from gases surrounding AGN.
- Measuring how accretion changes throughout cosmic time.
- Determining the full mechanisms behind how accretion works.

To achieve these science goals, ATHENA will contain two instruments: the Wide Field Imager (WFI) for imaging across a wide spectral band and the X-ray Integral Field Unit (X-IFU) for imaging at higher spectral resolutions. The work performed in this PhD project focused on reducing the noise component from off-axis background radiation in the ATHENA WFI as a representative X-ray detector in the space-based environment; however, the mitigation strategies presented in this thesis can be applied to future space-based X-ray observatories in general. As will be shown in Chapter 9, the background noise that X-ray observatories experience, as well as the mitigation strategies that might be employed to reduce it, must be tailored specifically towards the design of an instrument, as the particle composition of background is dependent on both the instrument design and the design of the surrounding spacecraft.

4.2.1 The ATHENA Wide Field Imager (WFI)

The Wide Field Imager (WFI) (Meidinger et al. 2016; Rau et al. 2013), of which a draft design is displayed in Figure 4.11, is a combination of two independently operated detector systems, a small detector designed for high time-resolution images of particularly bright objects, and a large detector system (composed of four separate identical detectors, or quadrants) for imaging across a larger spectral area. Both detector systems will use DEpleted P-channel Field Effect Transistor (DEPFET) detectors. The DEPFETs within both WFI detector systems will be relatively thick, where each pixel's thickness is currently planned to be a thickness of approximately 450 μm with a sensitive area covering 130 μm × 130 μm. Each quadrant in the large area detector as currently designed will contain 512 × 512 pixels, and the high count rate detector as currently designed will contain 64 × 64 pixels, with the orientation of the filter wheel above the WFI to control which detectors are illuminated. The image of a draft design of the ATHENA WFI is displayed in Figure 4.11.

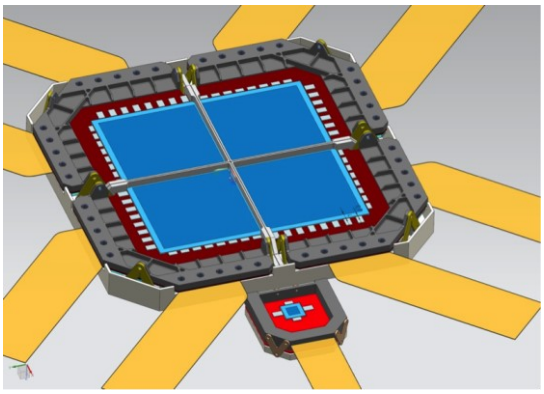

Figure 4.11 An image of a draft design of the WFI from https://www.mpe.mpg.de/ATHENA-WFI/instrument.html.

The WFI is designed to be one of the most sensitive space-based X-ray detectors developed to date, as shown by Figure 4.12 and Figure 4.13, which display the expected effectiveness of ATHENA and the WFI against other X-ray missions.

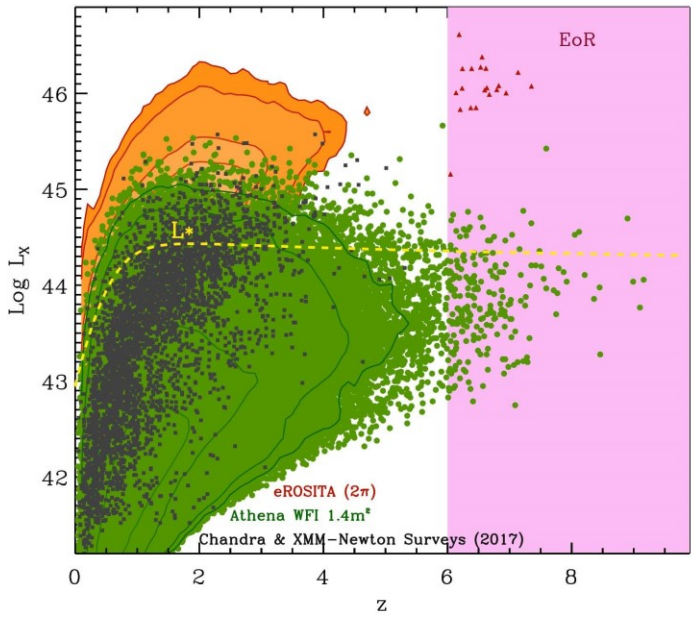

Figure 4.12 A simulated distribution of the sources ATHENA will detect, as compared to the distribution that other missions have detected. Here LX is luminosity and z is redshift. The area in pink represents the Era of Reionisation (EoR), which occurred from redshifts 6<z <20. Figure by A. Merloni and J. Aird. Figure presented at the 6th WFI Proto-Consortium in Warsaw by Arne Rau (10-12th October 2017).

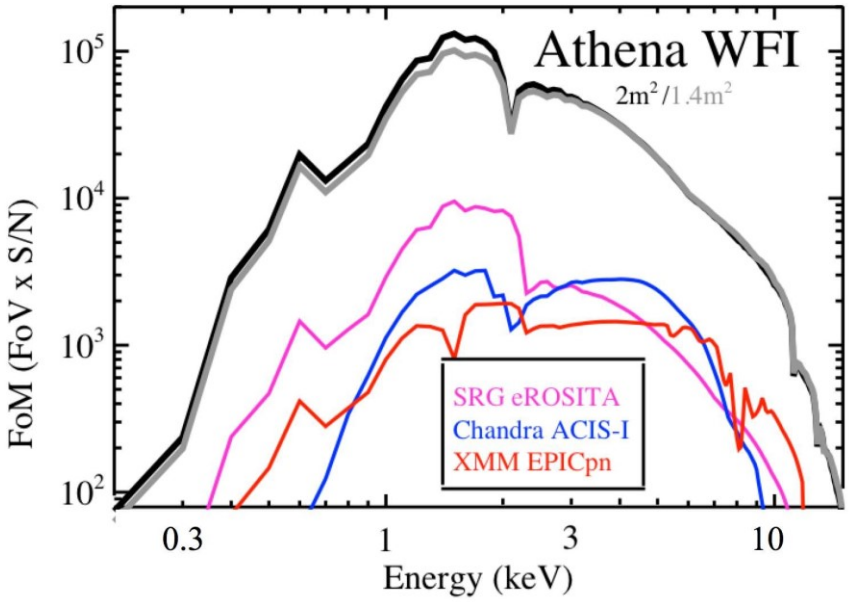

Figure 4.13 The Figure of Merit (FoM) for the WFI plotted against energy. Figure by D. Wik and A. Hornschemeier. Figure presented at the 6th WFI Proto-Consortium in Warsaw by Arne Rau (10-12th October 2017).

Figure 4.12 displays a simulated distribution of sources the WFI might observe at given redshifts and luminosities, plotted against sources observed by Chandra, XMM-Newton and eRosita. Here it can be seen that the WFI is expected to be able to observe a significantly larger number of sources than each of these missions, particularly sources in the era of reionisation, allowing for the history of the universe, particularly during the era of reionisation, to be mapped in greater detail than ever before.

Maximising the signal-to-noise ratio will be necessary for this role, as if the background count rate is too great, fainter X-ray sources will be obscured, and the ability of the WFI detectors to observe distant, faint sources will be diminished.

Additionally, Figure 4.13 displays the Figure of Merit (FoM) for several space missions, which has been chosen by Wik and Hornschemeier to be Field of View multiplied by the Signal-to-noise ratio (FoV × S/N), versus energy. In this case, the FoM of ATHENA greatly exceeds that of other missions across the 0.1 keV - 15 keV energy range. The FoM is also proportional to the signal-to-noise ratio in this case, again displaying the effectiveness of mitigating background noise at increasing the science capabilities of ATHENA.

4.2.2 The ATHENA WFI DEPFETs

The design of the DEPFETs comprising the WFI will be a significant influence on the effectiveness of the WFI. Some of the characteristics of the WFI, as well as necessary instrument performance targets, are summarised in Table 4.1. These include the maximum non-X-ray background noise count

rate for the WFI to be capable of achieving its primary science goals, as well as other factors that will affect its science capabilities, such as the time resolution and spectral resolution.

WFI Characteristics	
Large Area Detector Field Of View	40 arcmin × 40 arcmin
Energy Detection Range	0.1 keV - 15 keV
Spectral Resolution	<150 eV at 6 keV
Time Resolution	~8 μs full window mode, ~1.3 ms full frame
Count-Rate Capacity	~1 Crab
Non-X-ray Background (L2 orbit)	$< 5 \times 10^{-3}$ cts cm^{-2} s^{-1} keV^{-1}
Quantum Efficiency	>20% for 277 eV >80% for 1 keV >90% for 10 keV

Table 4.1 Some characteristics of the ATHENA Wide Field Imager (WFI) (Barret et al. 2016).

The overall instrument background in any space mission is expected to depend significantly upon the type of detector system used and its surrounding structure, as will be discussed in detail in Chapter 9. The WFI DEPFETs and surrounding material will therefore need to be carefully designed in such a way as to minimise incident background noise. The currently planned WFI sensitive region thickness of 450 μm means that in terms of X-ray-like background the WFI will likely be similar to the XMM-Newton EPIC PN, which had a sensitive region of 280 μm in thickness.

Because the design of the DEPFETs will be necessary for discussions of the nature of the incident background, it is instructive to consider planned DEPFET structures and mechanisms for WFI. The DEPFET arrays themselves are complex devices with several different configurations. Each pixel is effectively a single DEPFET device and is capable of performing both sensing and amplifying. An example of one possible DEPFET design for the WFI detectors is displayed in Figure 4.14 (Meidinger et al. 2015). DEPFETs use the electronics of Metal Oxide Semiconductor Field Effect Transistors (MOSFETs) to achieve these capabilities. A detector may either be frontside or backside illuminated, where the frontside of a MOS device refers to the side of the device which contains the gates of the device. DEPFETs are capable of being backside illuminated, which means there are fewer components that can attenuate X-rays than in frontside illumination before they reach the silicon bulk and that the quantum efficiency of the system is high. DEPFETs can also be fully depleted to maximise the quantum efficiency by applying a sufficiently large negative bias voltage (Bähr et al. 2014).

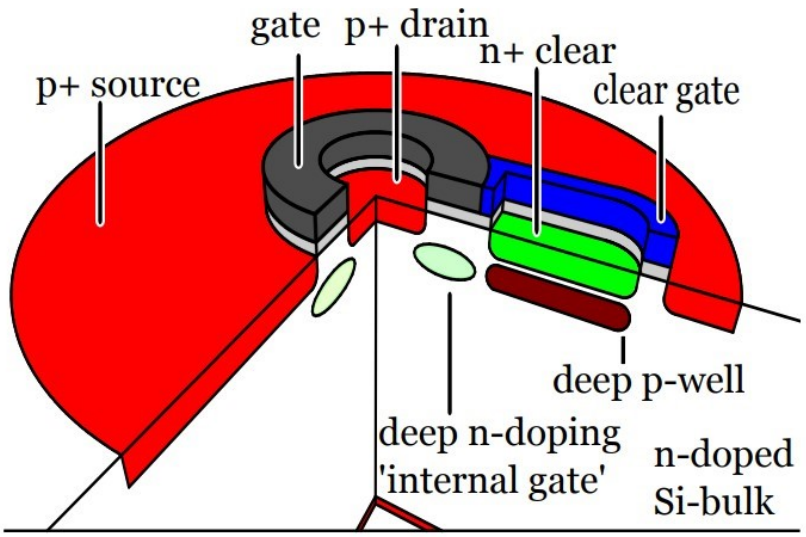

Figure 4.14 A possible structure for the DEPFET devices which will compose pixels in the WFI. Design sourced from (Bähr et al. 2014).

During the integration phase of an observation, electron-hole pairs will be generated in the silicon bulk by incident photons. The internal gate represents a potential minimum within the silicon of the bulk, and thus charges generated within the bulk are drawn to this location. During readout, a voltage can be applied across the source and the drain. The presence of free charges within the internal gate means that the conductivity of the silicon bulk between the p+ source and p+ drain will be increased, depending on the number of free charges that exist in the internal gate. Measuring this conductivity in the readout phase, by applying a voltage across the source and the drain, allows for the number of electrons, and therefore the number of photons absorbed within the material, to be measured. After the readout phase, a voltage can be applied to the clear gate and n+ clear, which causes charge to be removed from the internal gate, and acts as a reset for the system.

Multiple possible DEPFET designs are being researched as options for use in the WFI design. In the design displayed in Figure 4.14, the DEPFET continues to absorb photons during readout, which can cause a form of instrument background known as misfit events. One modification to the basic DEPFET design that can alleviate the issue of misfits is the addition of ‘blank’ gates, which attract charges before they can reach the internal gate. This means that when a voltage is applied to the blank gates, the DEPFET will not record any events, and should receive no misfits. A DEPFET which includes blank gates is known as ‘gateable’ DEPFET and shall be the DEPFET design that will be utilised in the high count rate detector design (Lutz, Richter, and Strüder 2001), whereas non-gateable DEPFETs are planned to be used in the large area detector system (Ott et al. 2016).

One problem with gateable DEPFET designs is that they cause ‘dead time’ during readout: time when a pixel is not taking readings, and this reduces the effective area of the device. To reduce the dead time, a pixel design exists called an infinipix DEPFET, a DEPFET composed of two sub-pixels which

alternate out of phase with each other between integration and readout phases. This design has been investigated as a possible design for use in the high count detector (Meidinger et al. 2015).

4.2.3 Surrounding material structures

Along with the design of the WFI detector itself, the design of structures and materials surrounding the detector are expected to have a large impact on the X-ray-like background, as discussed in Chapter 3. The WFI will be surrounded by two main features that can affect background, the proton shield, and graded-Z shielding.

4.2.3.1 The proton shield

A proton shield is material shielding designed to block soft protons and reduce the flux of ionising radiation reaching the detector, therefore reducing the radiation damage that the detector will receive. For the ATHENA WFI, the proton shield is designed to be made of aluminium and is planned to be between 3 cm and 4 cm in thickness. The proton shield should therefore be capable of blocking protons of up to approximately 30 MeV in kinetic energy (M. J. Berger et al. 2017).

In addition to aluminium there will also be significant quantities of molybdenum in the WFI camera head. Both aluminium and molybdenum are capable of producing fluorescence lines at the energies in the detection range which can cause X-ray-like background. Therefore graded-Z shielding is planned to be used in the WFI shielding design in order to both reduce the intensity of fluorescence lines and reduce the X-ray-like background induced by the cosmic X-ray background.

4.2.3.2 Graded-Z shielding

Graded-Z shielding (Fan et al. 1996) is designed to remove off-axis X-rays from the instrument background by attenuating high energy photons primarily from the CXB while only emitting X-rays at energies lower than detector energies. An example of such a design is shown in Figure 4.15, where CXB photons, as well as aluminium and molybdenum fluorescence photons, are both absorbed in the graded-Z shielding layers before reaching the detector.

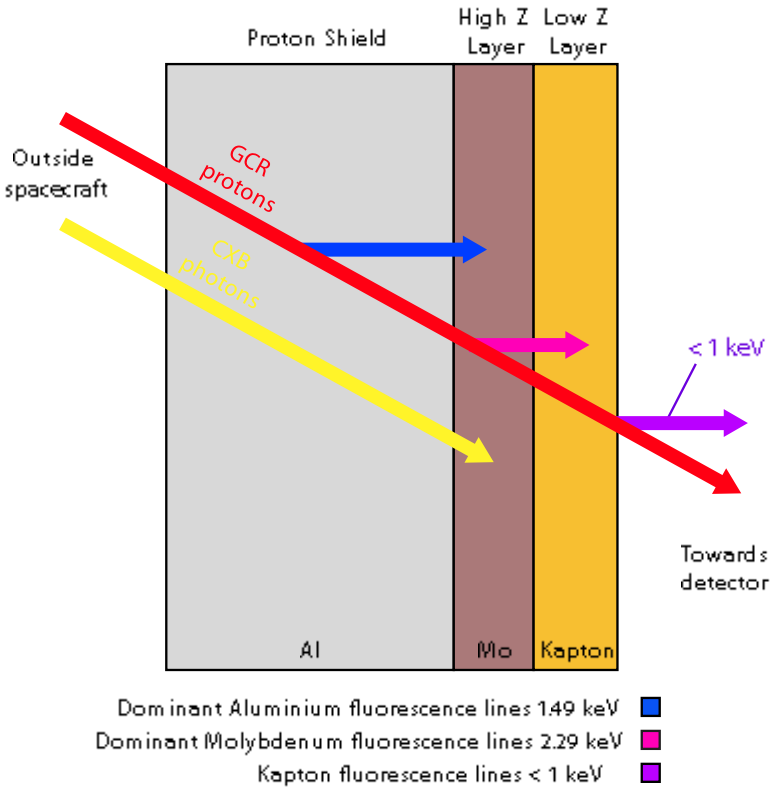

Figure 4.15 A diagram displaying the mechanism by which graded-Z shielding works. The Al-Mo-kapton combination shown here is only one example of how a graded-Z shield might be designed. Other materials with different thicknesses can be used, providing the high-Z layer is capable of attenuating hard X-rays significantly, and the low Z layer has few or no fluorescence lines within the detector energy range. The blue, pink and purple arrows represent X-rays at the K energies of Al, Mo and kapton respectively.

The design relies on Moseley's Law (Moseley 1913); that the energy and fluorescence yield of $K\alpha$ and $K\beta$ fluorescence lines decreases as atomic number decreases, in accordance with $E \propto Z^2$. The design shown in Figure 4.15 therefore utilises molybdenum's high atomic number to attenuate the high energy photons from the CXB, while the kapton placed on the inner surface of the materials absorbs the lower energy fluorescence lines from the molybdenum. The presence of both layers also means that the aluminium fluorescence line is attenuated.

4.3 Summary

This chapter has discussed some of the key features of X-ray-like background in XMM-Newton, as well as some of the features of the ATHENA WFI that are likely to influence the X-ray-like background it will experience.

The spatial, temporal and spectral variation of background in XMM-Newton were discussed and how variations like these can lead to systematic errors in astronomical data if the background flux is too high. The EPIC PN and EPIC MOS detectors in XMM-Newton were also discussed from an X-ray-like background perspective, and how their designs impacted the background they experienced. The

expected design for the ATHENA WFI detectors as well as structures surrounding the WFI detectors were also discussed in relation to X-ray-like background.

The impact of detector geometry and proton shield design on X-ray-like background will be investigated through simulations in Chapter 9 and Chapter 10. The impact of graded-Z shielding in the ATHENA WFI will be investigated in Chapter 10 and Chapter 11, where the ability of graded-Z shielding to remove both fluorescence and CXB-induced background will be examined. These simulations, like almost all of the simulations presented in this thesis, will be performed using Geant4. As Geant4 will be used extensively in this thesis, and because a significant amount of the work presented in this thesis relates to validating Geant4 for simulations of the space-based environment, it is necessary to discuss the use and accuracy of Geant4 in space-based simulations.

Chapter 5

Simulating the Environment of Space using Monte Carlo Methods and Geant4

To design mitigation strategies aimed at reducing the radiation-induced X-ray-like background, it is first necessary to investigate the structure and physics that generate background in space astronomy missions through simulations. In this thesis, this will be primarily done using the particle physics software Geant4 (Agostinelli et al. 2003), which is the toolkit used in all simulation research described in this thesis.

Geant4 was designed by CERN and KEK in 1993 ("Introduction to Geant4" 2010) as detector simulation software based on the object-oriented capabilities of C++. Geant4 was initially designed to perform simulations relating to subatomic particle physics but has since been updated and modified such that it is now used in many fields, such as medical physics, nuclear physics and space physics. While a significant amount of work has been performed to adapt Geant4 and its physics from its original particle physics regimes, to the energy ranges, particles and materials present in the space-based environment, there are still questions over its accuracy.

As Geant4 will be used in all the simulations presented within this thesis, it is necessary to discuss how Geant4 simulates particles, particularly some of the shortcomings and limitations that can occur within Geant4. The mechanisms underpinning Geant4 simulations will also be necessary for the research performed in Chapters 6, and 7 where experiments designed to test Geant's ability to simulate the space-based environment are analysed. Previous work on this subject will be discussed in Section 5.7.

As Geant4 is complex software, this chapter will not describe in general how to create a Geant4 simulation, for which several online resources exist ("Geant4 User Documentation" n.d.). This chapter will, however, discuss some of the general considerations to be taken when designing a Geant4 simulation specifically for the space-based environment as well as some aspects of the general structure of a Geant4 simulation.

5.1 The structure of a Geant4 simulation

In order to understand some of the abilities and challenges inherent in Geant4 simulations, it is necessary first to discuss the steps taken by a Geant4 simulation upon running. Figure 5.1 shows a generalised diagram broadly outlining these steps.

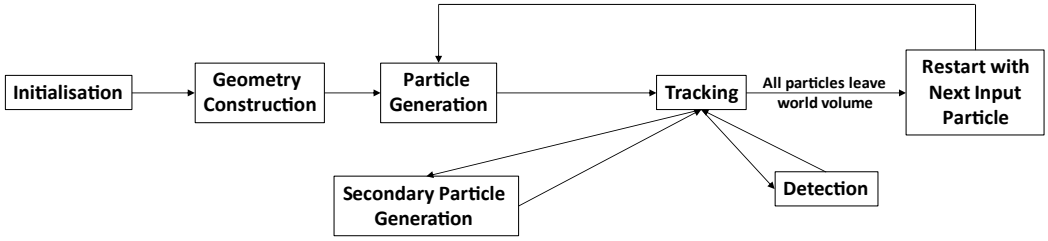

Figure 5.1 The general structure of a Geant4 simulation.

The simulation is first initialised, and the user-defined geometry is constructed. The program then begins looping over all primary particles the user has set to be simulated, where each loop is referred to as an 'event' and assigned a unique event ID.

Within each loop, the full physics of a primary particle travelling through the simulation geometry is simulated. Once the primary particle has left the world volume, secondary particles that were created during the tracking of the primary particle are tracked in order of creation, as well as further particles that are created by secondary particles. Once all particles have been tracked and left the world volume, Geant4 then moves to the next event.

Within the simulation geometry, the user must define some volumes as detectors, as are described in Section 5.5. As Geant4 is a toolkit rather than a standalone program, the user must define a lot of the mechanisms by which Geant4 will perform certain operations, including how detectors output simulation data. A 'hit' is registered in a detector for each step a particle takes within a detector, and the user can write functions that tell Geant4 what actions to perform when a hit is registered. A user can therefore choose to either print hits to a file as hits are registered, or to save hits for printing at a later time in the simulation.

5.2 Input parameters and settings for a Geant4 Simulation

Geant4 contains a large number of parameters that can be used to control simulations and to optimise simulations for accuracy or speed. While there are too many parameters and settings available to be easily described here, some of the most important parameters to simulations of the space-based environment will be discussed. Experiments to assess the accuracy of Geant4 simulations as a function of various input parameters and settings are described later in this thesis in Chapters 6 and 7.

One particularly important setting is the choice of physics list, an object in Geant4 that contains each of the physics processes to be accessed during a Geant4 simulation.

5.2.1 Physics lists

Each physics list contains different physics approximations and equations that are suited to different physics simulations, and offer compromises between accuracy and speed depending on the science being performed.

Physics lists can also be modified within simulation code, and processes can be turned on or off to either improve simulation accuracy or improve the speed of a simulation, depending on whether or not the process is expected to be important to the simulation results. Geant4 includes several flags in the `G4EmProcessOptions` object that can do this for common processes, such as `setauger()` and `setfluo()`, which can be used to turn on or off Auger electron creation or fluorescence respectively.

Table 5.1 displays some of the physics lists that are commonly used in the simulation of the space-based radiation environment. These physics lists are designed to be able to simulate the interactions of particles at lower energies than are typically used in the high energy particle physics experiments for which Geant4 was initially designed.

Physics List	Description
G4EmStandardPhysics_option4	A variant of the default Geant4 'option 0' electromagnetic physics list but specifically designed for use with low energy particles, with some physics processes adapted for use below several MeV and in some cases below several tens of keV.
G4EmLivermorePhysics	A variant of the above option 4 electromagnetic physics list, with some changes made to several physics processes including electron bremsstrahlung.
G4EmPenelopePhysics	Another variant of the above option 4 electromagnetic physics list, with some changes made to several physics processes involving bremsstrahlung, photon scattering and ionisation.
QBBC + Space Users Physics List	QBBC is a separate physics list to the standard electromagnetic physics lists that was explicitly designed for use with low energy particles for space and medical applications. The Space Users Physics List is a separate set of physics that is currently being developed as part of the AREMBES project, and can be used on top of QBBC using the `replacephysics` method within a `G4VModularPhysicsList` object.

Table 5.1 Some of the common physics lists used in the simulation of X-ray-like background in space-based X-ray detectors.

This thesis will primarily use the PENELOPE physics list and the Space Users Physics List. Both of these physics lists are capable of reasonably simulating the interactions of particles at energies corresponding to that of the space-based radiation environment reasonably well, as will be shown from experimental results described in Chapters 6 and 7.

5.2.2 Production cut length

While the choice of physics list describes specific physics approximations that will be made for interactions within the system, production cut length is a continuous quantity that can be used to control the precision of the simulation as a whole. Production cut length is the key parameter that can be used to set the minimum energy of particles that will be simulated within a simulation. Lowering the production cut length increases the accuracy of simulations, but can cause simulations to take significantly longer to run. It is therefore important to determine the maximum cut length that will achieve the required simulation accuracy before running a simulation.

The production cut length is defined as the minimum distance a particle must be able to travel on average upon particle creation within its volume of generation for Geant4 to define the particle as 'generated'. If the energy of the particle is such that the particle is not able to travel this threshold distance, the particle is instead not created, and the energy it would have been given is instead defined as deposited within its volume of creation. The required production cut length can therefore be found by calculating the minimum mean penetration distance of particles which are within the relevant energy ranges to the simulation results.

The production cut length can either be set for the entire simulation, or it can be set for individual volumes within a Geant4 simulation. The advantage of setting production cuts for individual volumes is that volumes which are only expected to produce a small number of relevant particles at low energies can be given a higher production cut length, which will, therefore, reduce the total simulation time. For example, in simulations of the space-based environment, particles with energies within the detector energy range are predominantly expected to originate from within several microns into surfaces within line of sight of the detector. This means that volumes that are not within line-of-sight of a detector can be assigned a larger production cut length than volumes within line-of-sight. However, for simplicity, the simulations discussed in this thesis have been given a single default production cut length, rather than differing production cut lengths for different volumes.

5.3 Simulating incoming radiation with Geant4

In order to simulate the radiation environment of space using Geant4, the distribution of incoming radiation must first be specified. This must be done for each particle type present in the space-based environment that has a significant impact on the X-ray-like background, where both the momentum direction distribution and spectral distribution must be specified. A spatial direction distribution can also be specified, which might be necessary for simulations where significant radiation sources originate from the Sun. However, in the simulations presented within this thesis where X-ray-like background from the cosmic X-ray background and cosmic protons dominates, the space-based radiation environment will be approximated as isotropic. In order to discuss how to model this environment, it is first necessary to describe the mathematical methods that will be utilised.

5.3.1 Probability Density Functions (PDFs)

While a discrete random variable such as the roll of a die is typically modelled by the probability of achieving a particular value, all possible values of a continuous random variable each have an infinitesimal probability of occurring. Therefore continuous random variables must be instead modelled using probability density (Kalos and Whitlock 1986; Devore and Berk 2012). Several of the properties of probability density functions will be described in this section, but a full list of properties that will be used in this thesis is given in Appendix B.1.

In this thesis, the normalised probability density function of a single variable will be denoted as $PDF_x(x)$ where x is the continuous random variable, while multi-variable functions will be described using $PDF_{x,y}(x,y) = PDF_x(x) \times PDF_y(y)$ where x and y are continuous random variables.

The total probability of $a < x < b$ can be described by

$$P(a < x < b) = \int_a^b PDF_x(x)\, dx \tag{5.1}$$

And the total probability of $a < x < b$ and $c < y < d$ is

$$\begin{aligned} P\big((a < x < b) \wedge (c < y < d)\big) &= \int_a^b \int_c^d PDF_x(x) \times PDF_y(y)\, dy\, dx \\ &= \int_a^b \int_c^d PDF_{x,y}(x,y)\, dy\, dx \end{aligned} \tag{5.2}$$

Essentially the probability of achieving a particular value of x can be described by the infinitesimal $PDF_x(x)dx$. All of the usual probabilistic rules of addition and multiplication for discrete random variables apply to probability density functions, with the caveat that at the end of calculations all infinitesimals need to be summed over/integrated over a range of output values. In this thesis probability density functions will sometimes be shortened such that $PDF_x(x) \rightarrow PDF_x$ for the sake of brevity.

Another important technique that will be used in this thesis is the determining of probability density functions of variables that are themselves functions of random variables. These can be calculated by utilising the fact that probability is conserved for both variables, which can be expressed as

$$\begin{aligned} &P\big((a < x < b) \wedge (c < y < d)\big) = \\ &\int_a^b \int_c^d PDF_{x,y}(x,y)\, dy\, dx = \int_\alpha^\beta \int_\gamma^\epsilon PDF_{u,v}(u,v)\, dv\, du \end{aligned} \tag{5.3}$$

Where u and v are functions of x and y, and α, β, γ and ϵ are the maximum limits of u and v given the constraints that a, b, c and d are the limits of x and y. Using Equation 5.3, it is possible to determine that

$$PDF_{u,v}(u,v) = PDF_{x,y}(x,y) \times |J| \tag{5.4}$$

where $|J|$ is the Jacobian for x, y and u, v where $|J| = \begin{vmatrix} \frac{\partial x}{\partial u} & \frac{\partial x}{\partial v} \\ \frac{\partial y}{\partial u} & \frac{\partial y}{\partial v} \end{vmatrix}$.

For the single dependent variable case, for example where $u = u(x)$, $PDF_u(u) = PDF_x(x) \times |J|$, the Jacobian is just the magnitude of the derivative $|J| = \left|\frac{dx}{du}\right|$.

These rules will be applied extensively in Chapter 9 and Chapter 10 in order to determine the probability of a particle inducing an event as a function of detector thickness in Chapter 9, and the statistical trajectory of electrons in a magnetic field in Chapter 10 in order to determine the effectiveness of magnetic field configurations.

5.3.2 Generation of particles in a probability distribution

Probability density functions are also necessary for understanding the initial generation of particles in a Monte Carlo simulation, where there are many methods used for distributing particles. Two general methods will be used in this thesis to distribute particles according to a given probability density function (Kalos and Whitlock 1986, Chapter 3), 'sampling' and 'rejection'.

In the sampling method, a list of uniform random numbers between 0 and 1 is generated using a standard random number generator in code. A function is then mapped across the list which will cause the new random number list to be distributed according to the necessary probability density function. The necessary function can be determined by first performing a general integral across a uniform distribution u and the probability density function, where $PDF_u(u) = 1$,

$$\int_{x_0}^{x} PDF_x(x)\, dx = \int_0^u du \tag{5.5}$$

Here x_0 is the minimum value of the domain of x. By solving these integrals and then solving the resulting equation for x, the generating equation can be found to be

$$x = CDF_x^{-1}(u) \tag{5.6}$$

Where $CDF_x(x) = \int_{x_0}^{x} PDF_x(x)dx$. One of the main difficulties with this method is if $PDF_x(x)$ is non-integrable, which means that $CDF_x(x)$ cannot be found, in which case the rejection method must be used.

Rejection utilises algorithmic methods rather than analytic methods. In this method, the entire probability density function must be multiplied by a factor such that across the domain, it is always less than 1. Then a random value from the domain must be generated as well as a random value between 0 and 1. The random value from the domain is then inserted into the modified probability density function, and if the outputted value is less than the random value between 0 and 1 the value is accepted as part of the outputted distribution and rejected if it isn't. This algorithm can be continuously be run until enough coordinates, and other parameters have been generated for the simulation.

This method has the advantage that it can be used for any probability density function regardless of whether it is integrable. However, the disadvantage of this method is that for some functions, it may take significantly longer than the analytic methods to run.

5.3.3 Distributing incoming radiation energy according to a spectrum

As with position distributions and other parameter distributions, a spectrum of particle energies can be generated both analytically and through interpolation.

Geant4 has several methods for distributing particle energies, both analytic and interpolation-based. In this thesis, particle energies in Geant4 will be distributed using interpolation, where particle spectra have been taken from SPENVIS (Heynderickx et al. 2005). While the spectra that will be used are representative of the space-based environment, numerous sources do give different spectra for different locations in space and in different time periods as was discussed in Chapter 2. Chapter 2 also discussed some of the considerations that must be taken into account when choosing the minimum and maximum kinetic energy to use for the input spectrum.

When choosing a spectrum, it is crucial that the tabulated spectrum can be accurately integrated such that the total flux in cts / cm^2 / s can be found. The total flux is necessary for calculating the overall spectral normalisation and finding the total background in the correct units at the end of data analysis, so an incorrect total flux factor could dramatically alter the final results.

Importantly, as will be discussed in Section 5.6.2 where the normalisation process will be described, an incorrect normalisation does not change the spectral shape of data and only multiplies the data by a factor, meaning that an incorrect normalisation is very difficult to find by exclusively looking at background spectra, and care must be taken to ensure integration of the initial spectrum is consistent with Geant4's generation of particles.

Spectra for interpolation must be either specified directly into a macro file using `/gps/hist/point`, or specified in a csv file, which is specified in the macro file using `/gps/hist/file` followed by the file name.

To indicate to Geant4 that interpolation is to be used, and that the interpolation should be applied to energy in particular, the lines `/gps/ene/type Arb` and `/gps/hist/type arb` must be used.

When choosing an interpolation mechanism, a choice also needs to be made about whether to interpolate linearly or logarithmically, depending on the nature of the inputted dataset. While both options will successfully perform an interpolation, if a dataset samples something that can be approximated as a power law, and which is sampled logarithmically, a logarithmic interpolation will produce a more accurate sampling. Choice of interpolation may also affect the data normalisation, and

care must be taken to ensure that Geant4's production of primary particles matches the expected flux of particles within the energy range that was expected.

An example of a spectrum specification in a macro file of an energy spectrum is shown below.

```
/gps/ene/type Arb
/gps/hist/type arb
/gps/hist/point 1.000e+01 1234e-01
/gps/hist/point 1.010e+01 1248e-01
/gps/hist/point 1.020e+01 1257e-01
/gps/hist/point 1.030e+01 1289e-01
…
/gps/hist/inter Log
```

While distribution of a particle energy spectrum must typically be done through interpolation of tabulated data, distribution of momentum direction can typically be performed mathematically.

5.3.4 Distributing radiation according to momentum direction

In addition to distributing radiation according to energy, it is also necessary to distribute particle momentum direction. Momentum direction must typically be distributed such that radiation is treated as originating approximately equivalently in flux from all locations in space, also known as originating from a diffuse source. This type of distribution can be modelled mathematically by distributing particles on a theoretical volume surrounding a spacecraft using Lambert's cosine law (Lambert 1760).

Lambert's cosine law gives the probability density function for an isotropically emitted particle impacting a surface with a momentum at a given angle to the normal θ and an azimuthal angle about the normal ϕ as

$$PDF_{\theta,\phi}(\theta,\phi)d\theta d\phi = \frac{1}{2\pi}\cos(\theta)\, d\Omega \tag{5.7}$$

or equivalently directly in terms of θ and ϕ as

$$PDF_{\theta,\phi}(\theta,\phi)d\theta d\phi = \frac{1}{2\pi}\sin(2\theta)\, d\theta d\phi \tag{5.8}$$

A derivation for this expression is given in Appendix B.2, and a method for computationally distributing particle positions and momenta on a spherical generation surface is given in Appendix B.3. In Geant4, Lambert's cosine law is a built-in option for particle generation using General Particle Sources and can be turned on using input macro commands or files.

5.3.4.1 Distributing incoming positions and momenta using macro files

To specify how particles should be generated in Geant4, several features must be specified. Firstly, the surface where particles will be generated needs to be specified. Geant4 contains many default surfaces that can be used for this purpose, including spheres and boxes. If the surface is to reflect the isotropic environment of space, this surface must be placed surrounding all relevant volumes in the simulation.

Several default surfaces are given as general particle source macro commands, and to construct a sphere as will be used in all simulations in this thesis, the following commands can be used

```
/gps/pos/type Surface
/gps/pos/shape Sphere
/gps/pos/centre 0.0 0.0 0.0 mm
/gps/pos/radius 9 cm
```

To specify that a cosine distribution must be used in a simulation, the line `/gps/ang/type cos` must be added to the input macro file for the simulation, as well as a maximum and minimum value of θ must also be specified using `/gps/ang/mintheta` and `/gps/ang/maxtheta`.

This provides constraints on the minimum and maximum angles between the particle's momentum and the normal to the internal surface. While a value of `maxtheta` greater than 90 degrees will not alter the distribution of particles incident upon volumes in the simulation, it will mean that some of the particles generated in the simulation will be ejected outwards from the surface rather than inwards. This would therefore change the normalisation as well as unnecessarily increase simulation time.

`mintheta` and `maxtheta` can also be used to restrict the values of θ and reduce simulation time. In many situations, some values of θ will cause particles to travel in directions where they will not affect the background, while still taking up simulation time by travelling through spacecraft materials. Therefore it can sometimes be useful to restrict the values of θ to only relevant values. However, simulation normalisation must be modified to take into account these new values, as will be described in Section 5.6.2.

With each of the commands described above are put together, a macro file may look as shown below.

```
/gps/ang/type cos
/gps/ang/mintheta 0.0 deg
/gps/ang/maxtheta 90.0 deg

/gps/pos/type Surface
/gps/pos/shape Sphere
/gps/pos/centre 0.0 0.0 0.0 mm
/gps/pos/radius 9 cm
```

In addition to using Geant4 macros like this, it is also possible to write particle generation through a

cosine distribution directly into source code for either a G4ParticleGun or a G4GeneralParticleSource. However, care must be taken to ensure that the program mathematically produces the correct spectrum as small errors in code may cause momentum direction to be distributed incorrectly.

5.4 Construction of geometries in Geant4

Simulations in the space-based environment are set up the same way as in other Geant4 simulations. Volumes are given dimensions, are assigned to a logical volume with a material and then are placed at a location within the simulation geometry.

The volumes within a simulation can either be hardcoded into the simulation source code, or they can be imported through the use of Geometry Description Markup Language (GDML) files. GDML files are frequently used for simulations when the geometry being simulated is too complex to feasibly code by hand, and are often created through the use of external programs. One such program is Fastrad (Pourrouquet et al. 2011), which allows both for the creation of GDML geometries, and the conversion of existing CAD file types into GDML files. Simulations that will be discussed in Chapter 7 and Chapter 10 utilise GDML geometries of the ATHENA WFI mass model that were created using Fastrad as part of work to assess the background that the ATHENA WFI will experience in orbit.

GDML files do not provide information to Geant4 regarding how particle hits should be processed. Therefore detector volumes need to be described for both hard-coded and GDML based geometries. As Geant4 does not provide default mechanisms for simulating detectors beyond reporting energy depositions in materials, this needs to be explicitly designed by the user depending on the detector being simulated, and differently depending on what analysis the user wishes to perform.

5.5 Simulating detectors in Geant4

While a detector has a volume within the geometry of a Geant4 simulation, a detector requires additional descriptions to register particles.

A detector must first be set up as a volume within the geometry, in the same way as any other volume and set to be made of silicon for a silicon-based detector. Despite the range of doping levels and types of silicon-based detectors that are available for space-based astronomy, it is often sufficient to model the sensitive region of X-ray detectors as simply a volume of solid silicon.

This is because, for X-rays, the quantum efficiency of a detector does not significantly vary with respect to the doping concentration, as the concentration of dopants is typically not significant compared to the concentration of silicon atoms. Additionally, the probability of a high energy particle generating a photoelectron is not dependent on the bandgap energy, due to the bandgap energy being

significantly lower than typical X-ray energies in the range of several keV (*McEvoy's Handbook of Photovoltaics* 2018).

However, this does not mean that the entire device should be necessarily entirely modelled as a single block of silicon. Non-sensitive features of a detector, such as electronics, filters or other features placed on or around the device in the path of X-rays or other particles moving toward the device may attenuate particles, block them completely or fluoresce. These features should be included in the simulation as separate volumes attached to the detection volume. Some of these features may include optical blocking filters and passivation layers, and Chapter 8 will examine the effects of both of these structures on X-ray-like background.

As well as setting a detector as silicon it can also be useful to set a detector volume to be a vacuum, which is done in Geant4 by setting the material to "G4_Galactic". This means that instead of registering a hit when a particle makes an energy deposition, hits will only be registered when a particle passes through the boundaries of the detector volume. This can speed up simulation time and simplify analysis at the expense of losing information relating the actual amount of energy a particle deposits in a detector. This is therefore ideally used when only the particles impacting the detector are of interest and not the image they might create in a detector.

After the detector volume is defined, the detector logical volume must be assigned a G4VSensitiveDetector. A G4VSensitiveDetector is an abstract class and must, therefore, be designed by the user in such a way as to write particle hit information to a file. By modifying this class, the user may decide which variables should be printed as well as perform any analysis within Geant4 on the variables and particle hits within an event.

Some of the parameters that can be outputted as part of a hit by a Geant4 detector are:

- Current particle attributes at the time of the particle hit, including the particle name, charge, mass etc, and dynamic particle information such as particle kinetic energy, particle location.
- Particle energy deposition information such as the total ionising energy and non-ionising energy deposited in a particle hit in the detector material.
- Information relating to the particle origin including the location where the particle was created (known as the creation vertex) as well as the physics process that generated the particle. Some information is also retained by default about the parent particles that caused the generation of a particle, including the parent particle name and kinetic energy.
- Information about the current Geant4 event, including information about the primary particle for the event, as well as event metadata such as the event id.

Geant4 is also capable of saving custom user-designed information in a user-defined class called G4UserTrackInformation. As each particle has access to the G4UserTrackInformation of its parent particle, it is possible to transfer information from parent particle to daughter particle to retain information about the chain of interactions that led to a particle hit. This mechanism will be utilised in Chapter 8 to analyse the generation of high energy photons in aluminium by incoming protons.

5.6 Post-simulation processing of simulation data

As was described earlier, Geant4 is only capable of producing particle information and energy deposits as outputs by default. Separate processing and analysis must be performed by the user to replicate effects introduced by both a real device and to determine which events are classified as X-ray-like background. Geant4 does not perform calculations by default to produce X-ray-like background spectra, so these calculations must be either coded into simulation source code by the user or performed on hit data output files. For the work presented in this thesis, analysis was performed on data after all relevant simulation output had been printed to a file.

5.6.1 Event detection

As Geant4 only reports particle energy depositions within a Geant4 step by default, hits must be processed to convert them into a list of X-ray-like background particle hits.

The ultimate goal is to generate a list of valid X-ray-like events that would be recognised as valid X-rays in an actual X-ray astronomy mission. This will be performed in two ways within this thesis, either through conversion to a detector-like image and then applying an event detection algorithm, or by grouping particle energy depositions according to the particle that generated them upon impact with the detector.

Conversion to a detector image can be performed by converting particle energy deposition locations to pixel coordinates and then summing all the energy depositions in each pixel over the integration time of the real detector. This creates an image that looks similar to an actual dark frame from a real space-based detector. Algorithms can be applied to this image to simulate some of the features that can be added by a detector to an image. Section 5.6.3 will describe some of the ways in which charge spreading and Fano noise can be added to simulations so they better model real devices, and algorithms to do this were used in simulations described in Chapters 6 and 7. After this is done, an event detection algorithm must be applied to the image to extract valid X-ray-like events and remove features such as particle tracks such as would be used on actual X-ray astronomy images.

A commonly used algorithm in background simulations (Steffen Hauf 2009) is to surround each local maximum in the image with an ‘exclusion radius’. For each local maximum, the event detection algorithm checks each pixel directly adjacent to the cluster of pixels encompassed by the exclusion

radius. If any pixels have an energy greater than a set threshold, the local maximum is rejected, as displayed in Figure 5.2.

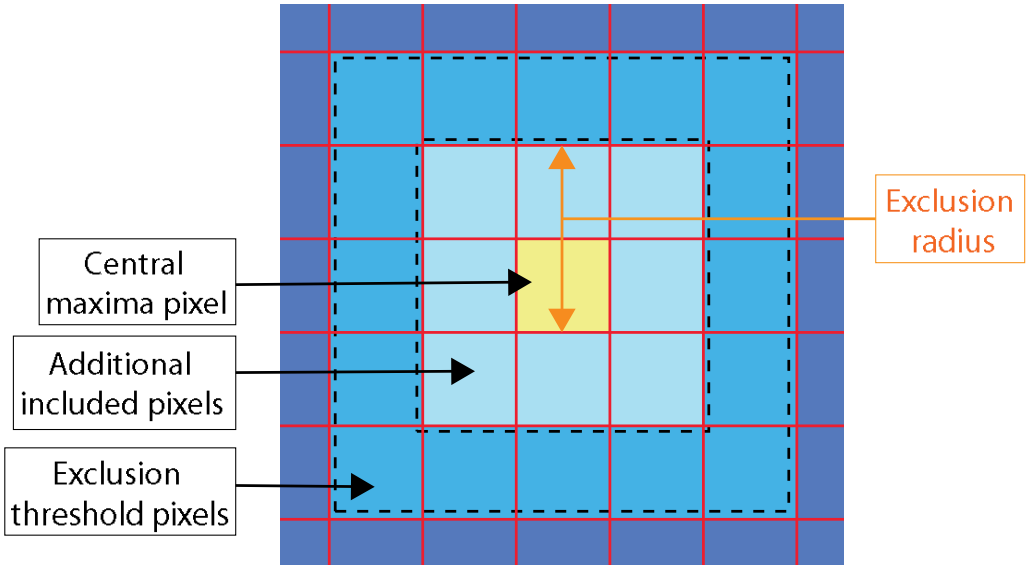

Figure 5.2 A diagram showing one of the methods that can be used in event detection. All the pixels within the exclusion radius are summed to give the total signal produced by a particle hit, and if any of the exclusion threshold pixels are above the set signal threshold, the entire hit is rejected as a probable particle track.

This algorithm removes tracks and is also capable of removing some X-ray-like events that fall near tracks on a detector image. This can reduce the total background as X-ray-like events frequently hit detectors near to the track of the proton that generated them (von Kienlin et al. 2018). In Chapters 6 and 7, algorithms similar to this algorithm will be employed in the event detection of images generated during experiments at a 6 MeV proton beamline and a 200 MeV beamline.

The main difficulties with this algorithm are that it can take a long time to run in some situations, particularly if images the algorithm are applied to are large, or if it needs to be run on a large number of images. As the algorithm is only applied to a total energy deposition image, it may also be complex to retain metadata about each accepted particle hit after event detection.

For this reason, much of the work presented in this thesis, particularly in Chapter 8 and onwards, utilises a different approach where energy depositions are summed for each particle impacting the detector, and all particle hits are recorded as depositing energy only at the position where the particle first contacted the detector. While it might be expected that this could cause particle tracks in an image to be registered erroneously as X-ray-like events, due to stopping power considerations, it is not possible for a fully penetrating proton or electron to deposit less than the maximum detection energy of the WFI of 15 keV of energy in detectors of thickness greater than approximately 100 μm, as discussed in Chapter 3, and therefore these tracks can be ignored.

In both methods, it is also necessary to remove hits which hit near to the edges of the detector. While high energy particles are not capable of depositing within the detector energy range when passing completely through the bulk of the detector, they are capable of passing through the edges of the detector and depositing within the energy range while not leaving a track. Even though few high energy particles do this relative to the number that hit the detector, the flux of background events within the energy range relative to the total number of high energy particles hitting the detector is often small. Therefore, high energy particles hitting detector edges can erroneously generate a large increase in background.

With each of these methods, a list of X-ray-like background hits will be produced. An energy deposition spectrum can be generated by histogramming the total energy deposition of each of these hits and then dividing each bin count by the corresponding bin width. This histogram must then be normalised using the initial primary particle spectrum, the total number of events run in Geant4, and the size of the initial Lambertian surface.

5.6.2 Normalisation of data

Particle hits can be converted into a spectrum by histogramming the deposited energies and then dividing by the histogram bin widths. To convert particle hits into the units that are applicable to the space-based environment, an expansion of the general mathematics described in Appendix B can be used to determine the integration time for a spherical Lambertian surface that a simulation run is equivalent to (Lotti et al. 2018)

$$T = \frac{4\pi N_p}{\Phi \times S_{ext}} \tag{5.9}$$

Where T is the total integration time, N is the total number of primary particles that were simulated, Φ is the total integrated flux from the spectrum in $cts\ /\ cm^2\ /\ s$, and S_{ext} is the total surface area of the Lambertian sphere. Equation 5.9 can be inserted into Equation 5.10 to give the total background which is given in Equation 5.11:

$$F_B = \frac{N_B}{A_d \times T} \tag{5.10}$$

$$= \frac{N_B \Phi S_{ext}}{4\pi A_d N_p} \tag{5.11}$$

Where F_B is the total background spectrum in units of $cts\ /\ keV\ /\ cm^2 /\ s$, A_d is the total area of the detector surface facing the sky, and N_B is the number of X-ray-like background counts per unit energy, as calculated by histogramming accepted X-ray-like background count energy depositions and dividing by the bin width.

Von Kienlin et al. (2018) also suggest including a further normalisation factor in some cases relating to the possibility that the removal of some pixels through event detection may also inadvertently remove other background counts if integration time is long.

While the above analysis is sufficient to analyse the background under the assumption that a detector is an ideal energy deposition counter, there are many different features a detector might add to the background spectrum depending on its design. Some of these features are capable of significantly altering parts of the received background spectrum as compared to the ideal detectors in Geant4, and Chapters 6 and 7 will attempt to model some features of the experimental detector used in experiments at a 6 MeV and 200 MeV proton source.

5.6.3 Inclusion of physical device characteristics

While Geant4 is capable of simulating detector characteristics relating to the energy deposition of particles within a detector, Geant4 is not able to simulate the effects of device physics beyond the basic radiation physics of silicon. Therefore, to obtain a complete simulation of the expected images that a detector might generate, the results of Geant4 simulations may have to be processed further to include features such as readout noise, charge spreading and charge collection efficiency.

For the context of X-ray detectors, a fluorescence line can be approximated as occurring at a discrete energy level as effects such as line broadening only induce spectral widths on the order of several eV, which is small compared to typical X-ray energies of several keV. However, as all silicon devices are fundamentally electron counters, and the quantity of electrons generated by an incoming particle is a stochastic process with a statistical error associated with it, the quantity of electrons-hole pairs generated has an error associated with it, leading to delta functions of fluorescence becoming Gaussian distributions with a finite energy width. For a CCD this energy width is characterised by the ‘Fano factor’, or by the ‘modified Fano factor’ (James H Tutt et al. 2012) in the case of EMCCDs.

To convert a spectrum of particle energies to an image more representative of an actual image it is, therefore, necessary to either add random Gaussian noise to each particle hit or convolve the spectrum with a Gaussian, where the standard deviation of the Gaussian is dependent on deposited energy.

Charge cloud spreading (Soman 2014) is another feature that must be added to simulated images to make them representative of a real image in some devices. In a simulated image, particles impact a pixel and then deposit energy at a particular location. However, many real devices are not fully depleted, and any electrons created by energy deposition within the field-free region may diffuse somewhat before being collected. This means that in many devices, should a particle deposit energy in the device’s field-free region, charge may spread across multiple pixels and create a blooming effect on images. To account for this, real astronomical images use event detection software to identify the

total charge and centroid of a charge cloud, but charge cloud spreading does still increase the effects of pile up.

Another effect that can cause experimental deviations from simulated spectra generated using idealised simulated detector images is Charge Collection Efficiency (CCE) (J. R. Janesick et al. 1987), which refers to effects in devices where charge is lost from output images due to internal device physics. This frequently occurs in CCDs during readout when charge is being transferred along columns of the detector and causes some loss of charge with each row passed. While this is usually a small effect for X-ray energies, it can cause significant quantities of charge to be lost from hits in which a particle is absorbed close to the surface of a detector, such as low energy X-rays, or soft electrons.

5.7 The accuracy of Geant4 at simulating the space-based environment

Many experiments have been performed examining the accuracy of Geant4 at simulating different situations; however, for space-based X-ray astronomy missions, only particles that deposit energies of several keV are of interest. Therefore, only studies investigating the ability of Geant4 to simulate particles that deposit several keV in a detector, or the production of such particles, are relevant to X-ray-like background and these studies are much rarer.

Kim et al. (2015) and Basaglia et al. (2015) investigated the ability of Geant4 to simulate electron backscattering for carbon, silicon, copper and gold. They found a reasonable agreement for backscattering from copper and gold between experiment and simulation, however for electrons of lower energies than 4 keV in both the carbon and silicon cases they found a significant deviation in electron backscattering yield. Below 4 keV in carbon and silicon, the experimental electron backscattering yield increased significantly, while the simulated electron backscattering yield decreased. This means that at low energies in low Z materials, background could be overestimated by Geant4, as Geant4 may overestimate the number of electrons below 4 keV that are absorbed in a detector instead of backscattered.

Basaglia et al. also found issues with Geant4's geometry detection mechanisms, and found that small changes in the distance between volumes when the volumes were adjacent to each other could cause large changes in backscattering fraction. This indicates that care must be taken in Geant4 in ensuring that volumes are indeed separated and that Geant4 may not necessarily correctly find overlaps between volumes and warn the user of them.

Batič et al. (2013) investigated the ability of Geant4 to correctly simulate energy deposition from electrons in the 0.3 - 1.0 MeV energy range in several materials, finding a reasonable accuracy with some deviation appearing in beryllium at lower energies in the energy range. While it is useful that

Geant4 is indeed capable of accurately determining the energy deposition for electrons in the 0.3 MeV - 1.0 MeV range, this energy range is significantly higher energy than the ATHENA WFI energy range of 0.1 keV – 15 keV. This does not therefore necessarily mean that Geant4 will be accurate at energies of several keV.

Fioretti et al. (2017) tested Geant4's treatment of soft protons (< 300 keV) passing through X-ray optics, intending to replicate the experimental results given by Diebold et al. (2015). The simulations were designed to approximate the scattering of protons in the eRosita mission (Predehl et al. 2014) and involved irradiating gold-coated nickel with protons from a multitude of angles and measuring the flux with respect to scattering angle. Several physics lists were being developed as part of this work in order to simulate the scattering of protons, and the accuracy of each list was compared. It was found that models based on Firsov scattering were relatively inaccurate, while models based on Remisovich scattering and the default Geant4 scattering models exhibited a reasonable accuracy for calculating the scattering efficiency of protons of scattering angles greater than 1.5 radians.

On the other hand calculations of the energy deposition due to single scattering deviated significantly from experimental results for protons of 250 keV. Both Geant4 multiple scattering and single scattering models exhibited similar results above 1.5 radians. While the protons used here are unlikely to significantly impact the background in an instrument like the ATHENA WFI, it is promising that Geant4 appears to be reasonably accurate for calculating the scattering efficiency of charged particles between tens to hundreds of keV. In Chapter 8, analysing the results of spherical shell models will reveal that much of the background in a thick detector originates specifically from backscattering electrons with kinetic energies on the order of magnitude of 100 keV.

Dondero et al. (2018) performed detailed simulations as part of the AREMBES project of electrons backscattering from different materials and comparing the simulation backscattering coefficients to experimental backscattering coefficients. This was performed between energies of 0.1 keV to 1 MeV, for numerous physics lists, and found that single scattering was accurate for the whole energy range. There was found to be a large variation in backscattering coefficient with respect to physics list overall; however, it was noted that below 100 keV in electron kinetic energy there was also a large variation in experimental results due to differences in experimental set-ups. Additionally, there was a large variation in accuracy for all the models with respect to incident electron angle, energy and material, and different scattering models exhibited different accuracies in different situations.

Bakr et al. (2018) also performed research on the Particle Induced X-ray Emission (PIXE) cross-sections that Geant4 uses as part of research into the development of new physics lists for more accurate simulation of X-ray emission. It was found that the new Geant4 cross-sections were able to

simulate proton and alpha-particle induced fluorescence from K and L shells very well while producing differing results for M shell X-ray emission.

5.8 Summary

This chapter has given an overview of how Geant4 can be used to simulate radiation impacting a spacecraft, and how to determine the X-ray-like background a detector will experience from these simulations. An overview of the statistics that can be used in the space-based environment for theoretical analysis has also be given, which was used extensively in this PhD project to derive some of the key results which will be described in Chapters 9 and 10.

The ability of Geant4 to accurately simulate the space-based environment was also discussed. Some aspects of Geant4 for the space-based environment have been examined in the literature, including electron backscattering and the ability of Geant4 to replicate fluorescence produced by PIXE processes. However, there remains a lot of physics in the simulated space-based environment that has yet to be examined including the production of low energy electrons from incoming protons, and the ability of simulated space-based X-ray detectors in Geant4 to accurately register particle energy depositions such as electron backscattering in the same way as real detectors. This motivated two experiments to further expand knowledge of Geant4's ability to replicate the space-based environment, one at a 6 MeV proton beamline, and one at a 200 MeV beamline, the former which will be described in Chapter 6, and the latter in Chapter 7.

Chapter 6

Experimental Verification of Geant4's Treatment of Secondary Particle Production and Detection using 6 MeV Protons

As described in Chapter 5, there is currently insufficient verification for fully validated use of Geant4 in the space environment. Therefore, as part of work on the ATHENA project at the Center for Electronic Imaging and as part of this PhD project, two experiments were set up to verify Geant4 for use in simulating X-ray-like background. The first experiment was performed at the 5 MV tandem accelerator at the STERIS ion beam facility in Harwell, Oxfordshire, with a proton beam kinetic energy of 6 MeV, which will be described in this chapter. The second experiment was performed at the Paul Scherrer Institut (PSI) Proton Irradiation Facility (PIF) beamline at a beam kinetic energy of 200 MeV, which will be described in Chapter 7. Some of the preparatory work that was performed before these experiments is described in David J. Hall et al. (2018), while some of the key results that were found from the 200 MeV experiments are summarised in Eraerds et al. (2020).

6.1 Motivation for experiments

The 6 MeV proton beam experiment was performed in June 2018 at the STERIS ion beam facility. A primary aim of this experiment was to verify the accuracy of Geant4's treatment of low energy physics processes in the space-based environment, in particular Geant4's treatment of secondary particles that are produced from surfaces surrounding the detector when a proton passes through them.

As it is not possible to replicate the space-based environment in an Earth-based experiment, it was necessary to verify the simulation of individual particle species and physics processes within Geant4. As was discussed in Chapter 5, the accuracy of different physics processes and the simulation of different particle species in Geant4 is expected to vary with particle energy. For example, Geant4

could simulate electrons at energies of several keV to a high degree of accuracy; however, it might be possible that Geant4 incorrectly simulates the physics of the creation of X-rays with energies on the order of several keV. In that situation, Geant4 would be an accurate toolkit for simulating the background in space-based X-ray missions where the electron component dominates the background spectrum but would produce incorrect results in a mission where soft X-rays dominate the background. Therefore the purpose of this experiment was to attempt to verify whether Geant4 is capable of accurately simulating X-ray-like background across the whole energy spectrum and determine which particle interactions it is capable of accurately simulating.

6.2 Experimental design

A picture of the beamline at STERIS used in this experiment is displayed in Figure 6.1. The 5 MV tandem accelerator at STERIS is capable of supplying protons of approximately 6 MeV to a chamber connected to the end of the beamline.

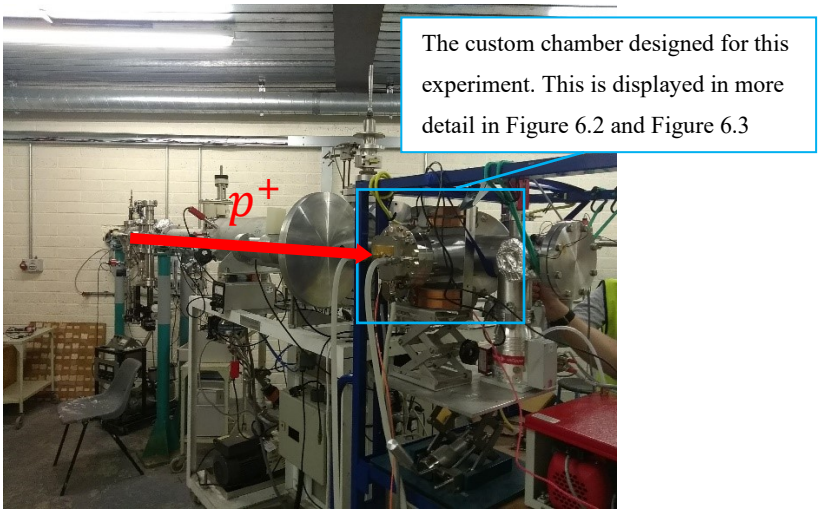

Figure 6.1 The 5 MV tandem accelerator at STERIS, with the custom experimental apparatus.

The chamber for the experiment was designed as an aluminium T-shaped structure, displayed in Figure 6.2 and Figure 6.3. This design was intended to replicate the situation where a cosmic ray produces background-inducing secondaries from shielding while not passing through the detector itself. Instead of passing directly through the detector, the beamline passed through a target plate made of aluminium, carbon or tungsten at a 45-degree angle. Protons would interact with the target producing secondary particles, many of which were produced in a direction perpendicular to the beamline toward a CCD97 detector, and causing an X-ray-like event.

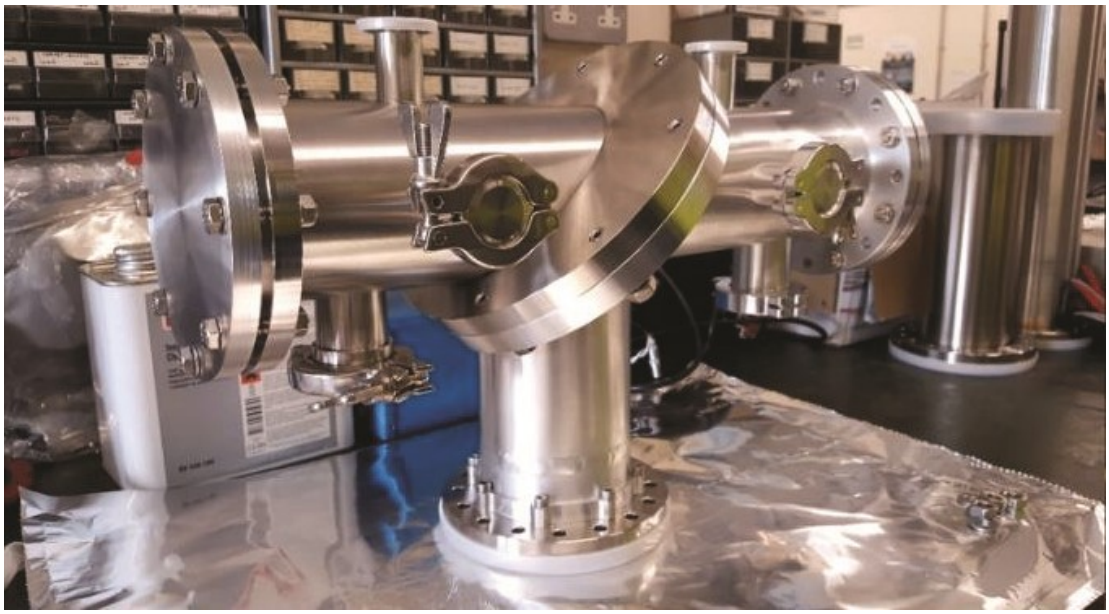

Figure 6.2 The custom chamber used in this experiment, not including the magnetic field generating Helmholtz coils.

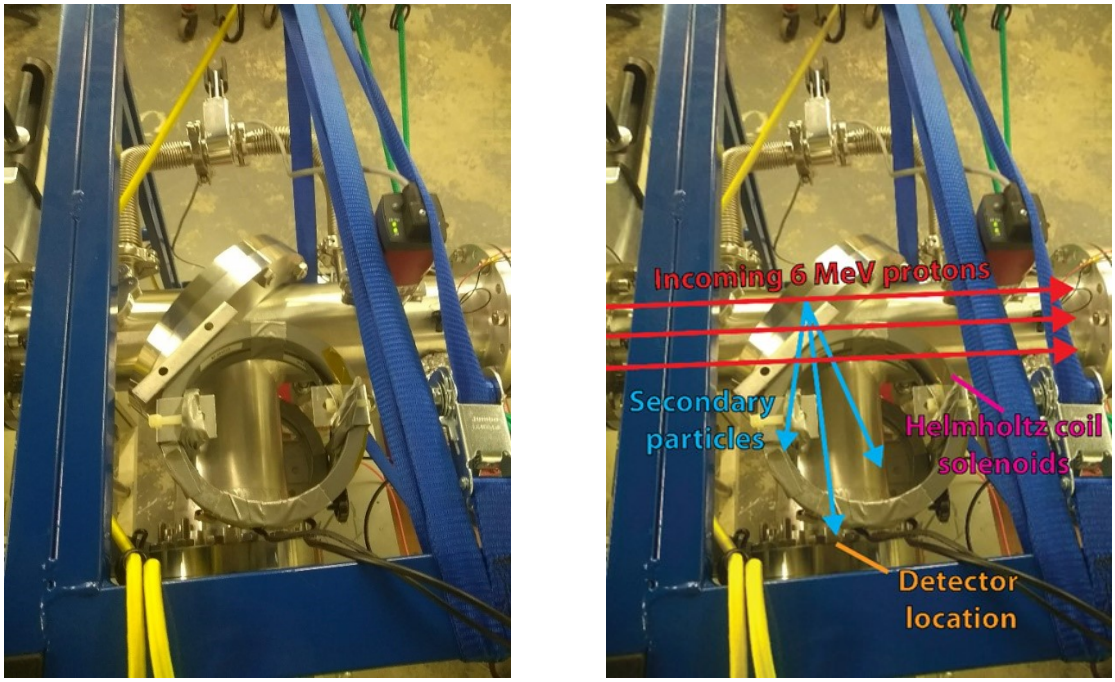

Figure 6.3 The custom chamber used in this experiment, as shown in Figure 6.2, as it was placed in the STERIS beamline. The image on the left is identical to the right, but with text and particle directions removed for clarity. Particles enter the chamber from the left and impact a thin target film, producing secondary electrons and photons. Some of these secondary particles are produced in a direction such that they hit the CCD97 and generate an X-ray-like hit.

To perform photon counting of secondary particles, a Teledyne-e2v CCD97 EMCCD was chosen as the detector in this experiment. Using an EMCCD allows for the gain to be optimised to the relevant secondary particle kinetic energies during the experiment. Additionally, the CCD97 is capable of being operated in a time integration mode which allows for the capture of particles over an interval of several seconds in a single image, minimising the ratio of readout time to integration time.

The CCD97 has a pixel length of 16 μm ("CCD97-00 Back Illuminated 2-Phase IMO Series Electron Multiplying CCD Sensor Datasheet," n.d.), and has a field-free region of 11 μm (James H Tutt et al. 2012), as well as a fully depleted region of 3 μm, giving a total depletion region thickness of 14 μm. A depletion region of this thickness means that the CCD97 is primarily sensitive to photons below several keV in energy, as the quantum efficiency of silicon absorption for a sensitive region of 14 μm drops to 0.55 for photons of 5 keV in energy (Xcom 2010). Additionally, this thickness falls within the range of thicknesses where fully penetrating protons and electrons are capable of acting as X-ray-like events (as previously described in Chapter 3), a fact that would become important in experiments performed at PSI, described in Chapter 7.

The three target materials used in this experiment were 100 μm of aluminium, 60 μm of carbon and 25 μm of tungsten. Each are candidate materials for graded-Z shielding in X-ray space telescopes. Unfortunately, due to hardware failure, most of the data acquired during the tungsten irradiations were lost, and therefore only the results from aluminium and carbon irradiations will be reported in this chapter.

As protons of 6 MeV in kinetic energy have a CSDA range of ~45 cm in air (M. J. Berger et al. 2017), small enough to be comparable to distance scales within this experiment, all elements internal to the beamline and chamber were pumped to vacuum pressure. Ensuring that the chamber was under vacuum was also necessary to ensure that secondary particles generated by incident protons were unobstructed, further replicating the environment under which secondary particles would be generated in space.

While it was necessary for this experiment to replicate the space-based environment it was not possible for the CCD97 used in the experiment to distinguish between different background components on its own. Distinguishing between different background components would allow for further examination into which components and interactions Geant4 was successfully simulating. Therefore, two solenoids (composed of two pairs of separate solenoids connected in series) were added to the experimental design in a Helmholtz coil configuration.

When a direct current was applied through the solenoids, the magnetic field produced acted to redirect soft electrons with kinetic energies in the range of up to 10s of keV away from the CCD97 and into the chamber walls. This meant that the magnetic field could effectively be used to separate background induced by soft electrons from background induced by photons or hard electrons. The design and inclusion of the solenoids and their magnetic field will be discussed in further detail in Section 6.5.

Each electron or photon impacting the detector generates a hit event depending on its energy using the mechanisms described in Chapter 3. However, to determine which events could be described as X-ray-like, an image processing pipeline had to be designed to convert images to lists of X-ray-like hits.

6.2.1 Image format

To discuss the algorithms used in the image processing pipeline, it is important to describe the format in which images were taken. The experimental images were taken using the CCD97's Time Delay and Integration (TDI) mode, which influenced the spectral normalisation. TDI mode allows for the creation of single images with a large integration time, but with a lower pile-up than an equivalent image created by a simple increase in integration time. During normal image acquisition modes, a CCD is usually given a set integration time, after which charge is read out row by row. In contrast, in TDI modes, integration and readout coincide, so that charge induced in a row is quickly transferred between rows and readout. In TDI modes, the effective integration time per image pixel is the total time per row transfer multiplied by the number of rows in the device, reflecting the fact that this quantity expresses the total length of time that an image pixel (as opposed to the physical device pixel, which does not actually move) is exposed and integrating.

As a device can be run in TDI mode for any user-defined length of time, the total number of rows integrated and read out can be selected by the user and is not limited to the physical device geometry. In this experiment, the number of rows to be read out was set to 8000, meaning that output images had dimensions of 512 x 8000. A sample image taken during the experiment is displayed in Figure 6.4.

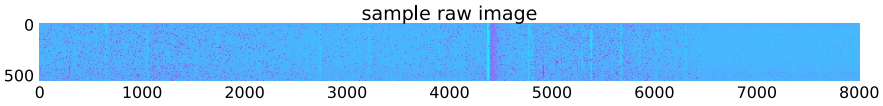

Figure 6.4 An example of an image taken by the CCD97 while the experiment was running.

One caveat of TDI mode is that the first full set of pixels on an image corresponding to the number of physical device rows experiences a different integration time to other rows in outputted images. This occurs because charge contained in these rows has not been integrated across the full device dimensions, only for an integration time corresponding to its row number multiplied by integration time per row. Therefore the first 1200 image rows were excluded from data.

6.3 Image processing pipeline design

Designing the image processing pipeline to convert both experimental images and simulation output files into spectra was non-trivial, as an incorrect treatment of the data could result in an incorrect output spectrum produced. The overall aim of the image processing software created for the

experiments described here was to convert experimental and simulated images into single-particle events corresponding to the energy deposited within the detector. The same event detection algorithm was applied to both experimental and simulated images to allow comparison between Geant4 simulations and experimental results without differing event detection methods introducing significant discrepancies.

The general image processing pipeline for both simulation and experimental data is displayed in Figure 6.5. The experimental data is first passed through a background removal script, followed by an event detection script, which produces a final image that is then converted into spectra. Simulation data, on the other hand, is first converted into an experimental data-like image, before being passed through the same event detection script as experimental data. Spectra are then produced from the image outputted from both sets of event detected images. Each stage of this process is capable of adding systematic errors to the output spectrum, so it is necessary to discuss the workings of each stage of the pipeline, and how they could influence the produced spectra.

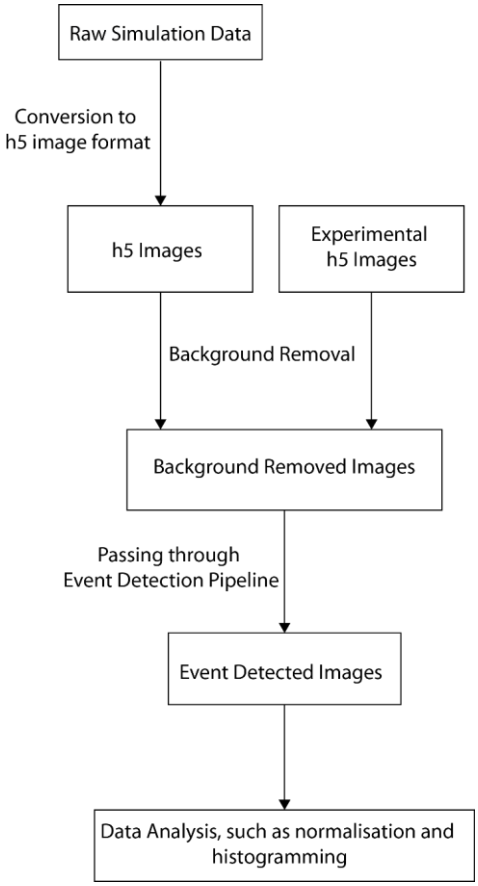

Figure 6.5 The data analysis structure utilised for the analysis of both experimental and simulation data for this experiment. The h5 image format used is a standard scientific image format that can contain groups of images and associated metadata. Simulated particle hits were converted into h5 images so that direct comparisons with experimental images could be made.

6.3.1 Converting simulation data files into experiment-like images

Simulation data files were first run through an algorithm designed to convert the data files to h5 images, similar to the experimental images generated during the experiment. The simulation equivalent of the CCD97 was a 4 cm by 4 cm by 14 μm block of silicon, which the h5 conversion algorithm binned into pixels based on the reported positions of energy depositions within the silicon, before summing all energy depositions within a pixel. The number of pixels was deliberately chosen to give a similar pixel density to the experimental pixel density so that any errors caused by pile-up could be compared to the actual spectrum incident on the simulated detector from the raw simulation data files. The h5 conversion algorithm then looped through each energy deposition location, adding device induced effects.

Firstly, Fano noise was added to images. Fano noise (James H Tutt et al. 2012; J. Janesick et al. 1988) causes a variation in the signal induced in a pixel due to the Fano statistics of energy distributing across numerous electrons in a pixel from the original impact electron or generated electron. Fano noise manifests as a Gaussian distribution in the spectrum and causes features in the spectrum to become smoothed. In particular, it is a primary reason why fluorescence lines often appear Gaussian-like rather than as delta functions in spectra.

For an EMCCD like the CCD97, the 'modified' Fano factor must be used instead of the usual Fano factor (James H. Tutt et al. 2012) to take into account the gain an EMCCD applies to the charge collected in a pixel. Even though the gain in this experiment could not be directly determined, it was still possible to utilise the Fano factor to calculate the standard deviation of charge clouds by using the experimentally determined standard deviation at the 1.48 keV Al fluorescence line and then utilising the fact that the standard deviation approximately scales with $A\sqrt{E}$ when Fano noise is dominant. Here A is approximately equal to $\sqrt{\frac{f}{\omega}}$ where f is the modified Fano factor, E is the energy deposited in a pixel and ω is the energy required to generate an electron-hole pair in silicon.

After including the effects of Fano noise, the algorithm then loops across all pixels again and spreads simulated charge from pixels around the sites of particle interactions in a circle of radius 3 pixels surrounding the original pixel. While this charge distribution process gives slightly different charge cloud shapes to the actual charge clouds inside a device, it would give a sufficiently representative shape such that event detection would process them similarly.

Images produced by this process are then outputted as h5 files and processed through the same event detection algorithm as experimental images. In addition to producing these output images, the bespoke h5 conversion program designed here also generates several image files containing metadata

associated with each particle interaction pixel. Some of these attributes include, for example, the name of the particle which interacted with the pixel, the maximum depth the particle reached within the pixel, and the particle's creation physics process. These attributes are used in Section 6.7 to analyse the data in more depth and to determine which aspects of Geant4 secondary particle production physics the experiment successfully probed.

6.3.2 Background determination and removal

The first stage of the image processing pipeline was to remove the device-induced background from images. Internal device background originates from many effects caused by device electronics. Detector background in an EMCCD is capable of varying from pixel to pixel both randomly and systematically across the device and varies in each experiment depending on different experimental factors, such as the device gain.

In general, the device background can be determined from dark frames taken immediately before an experiment, by taking the median signal in an image. This median background can then be subtracted from pixels to give the actual detected signal. The median signal must be used as opposed to the mean signal, as the mean signal can be skewed by anomalous energetic events such as cosmic ray impacts.

It was found during this experiment that while the median row in the CCD97 images contained an approximately constant background signal across the device, there was a non-insignificant variation in device background with respect to the column number. Therefore device background removal was applied to each column individually, rather than for the whole image.

The background subtraction algorithm was run independently across each image taken, and for each image column, to produce an outputted background-subtracted image. Firstly, the median background signal, and the standard deviation of the median background signal in each column were calculated from dark frames taken from immediately before the experiment. The program would then begin looping through all images taken from a particular experimental run and would subtract the median background signal from each corresponding column in the image.

6.3.3 Event detection

The next step in the image processing pipeline for this experiment was to apply an event detection algorithm to the background-subtracted image. The reason why an event detection algorithm was needed in this experiment, as opposed to binning the signal in each pixel, is because the design of the CCD97 means that for many detected particle interactions charge is capable of diffusing across multiple pixels. This charge spreading means that for a given cluster of pixels containing signal, an

algorithm must be used to both determine the pixel in which the original particle interaction occurred, and to sum the signal in each affected pixel to calculate the total energy deposition.

Charge clouds occur if a particle interaction occurs within the field-free region of a detector (Soman 2014). Charge clouds typically spread across a device spatially as a Gaussian distribution with a standard deviation that is dependent upon the distance of the original particle interaction into the detector, although as the signal present in a particular pixel is the sum of all charge within that pixel, the observed signal in a pixel is the integral of a Gaussian across the pixel dimensions, an 'error function'. The full Equation for the charge in a particular pixel, Q, is given in Equation 5.1 (Soman 2014),

$$Q = \frac{Q_0}{4}\left(\mathrm{erf}\left(\frac{x_1 - x_0}{\sqrt{2}\sigma}\right) - \mathrm{erf}\left(\frac{x_2 - x_0}{\sqrt{2}\sigma}\right)\right) \times \left(\mathrm{erf}\left(\frac{y_1 - y_0}{\sqrt{2}\sigma}\right) - \mathrm{erf}\left(\frac{y_2 - y_0}{\sqrt{2}\sigma}\right)\right) \quad (5.1)$$

where the total charge is denoted by Q_0, σ is the standard deviation of the charge cloud, x_0 and y_0 are the coordinates where the charge cloud initially began (the location of particle impact), and x_1, x_2 and y_1, y_2 are the coordinates of the pixel sides corresponding to the pixel where the charge is being counted. $\mathrm{erf}(z)$ is the 'error function', which is defined as $\frac{2}{\sqrt{\pi}}\int_0^z e^{-t^2} dt$.

That charge clouds spread as a Gaussian means that the pixel where the original particle interaction occurred should be expected to be the pixel with the largest signal, and should also be the only pixel within the cluster where there is a local signal maximum. Therefore, one method of identifying the locations and energy depositions of particle interactions within a detector is to identify the locations of local maxima in an image and then sum the signal in pixels surrounding it.

One potential issue with this algorithm in this experiment is that the background image inputted into the algorithm contains local maxima associated with device noise as well as the local maxima associated with events. Therefore a threshold signal needed to be set to exclude local maxima of small signals so that device noise is not included in the spectrum. In this experiment, the threshold was set to 700 ADU (Analog-to-Digital Units), equal to 5 times the standard deviation of the median device background.

6.3.3.1 Pile-up

One important consideration that can cause that algorithm to break down is 'pile-up'. Pile-up occurs when the event density is too high, such that two particles impact the detector close enough for their respective charge clouds to merge. This effect may modify spectra in complex ways, depending on the structure of incident particle spectra. There are several ways to experimentally limit the effects of this, including decreasing integration time or using a lower flux of incident particles.

Experiments at Harwell were however significantly influenced by pile-up, and it was therefore necessary to build pile-up reduction into the event detection algorithm used. The event detection algorithm used was similar to the algorithm described in Chapter 5, albeit with some key differences, including a different pile-up rejection mechanism. The method used here first generated a list of the positions from all local maxima within images above the threshold as described previously but then removed positions from the list which were too spatially close to other local maxima, in this case within 5 pixels. The algorithm would then loop through each local maxima position still in the list, and sum the signal from all pixels within a radius of 3 pixels.

One concern with this algorithm might be that summing pixels outside this radius might also sum from pixels which aren't a part of the charge cloud. However, the background reduction algorithm described in Section 6.3.2 causes pixels not associated with particle interactions to have a median of 0 ADU. This means that errors introduced by the addition of such pixels such cancel out on average.

The event detection algorithm is not able to entirely remove pile-up, as two particles landing in the same pixel or adjacent pixels may only create a single local maximum rather than two local maxima that are close together. However, it is still able to remove the majority of overlapping charge clouds, and significantly improved the quality of outputted spectra.

A potential problem created by removal of pile-up is that there can be a significant loss of signal in cases where there is a high density of events and a significant number of overlapping charge clouds. This was the case in the 6 MeV proton experiments, where the algorithm described above removed approximately 50% of local event maxima. To correct for the change in normalisation due to this loss of signal, the event detection program calculated and saved the ratio between the total number of local maxima above threshold in an image and the number of accepted non-pile-up local maxima to the output file. When spectra are then generated later, they are re-normalised by multiplying the output spectrum by this ratio.

After identifying the positions of events as well as the sum of their charge clouds, the algorithm produces an image of the same dimensions as the original image, but with charge clouds replaced with the summed ADU across the charge cloud placed in the pixel corresponding to the charge cloud local maxima.

Figure 6.6 compares a section of a raw image taken during this experiment with its corresponding event detected equivalent.

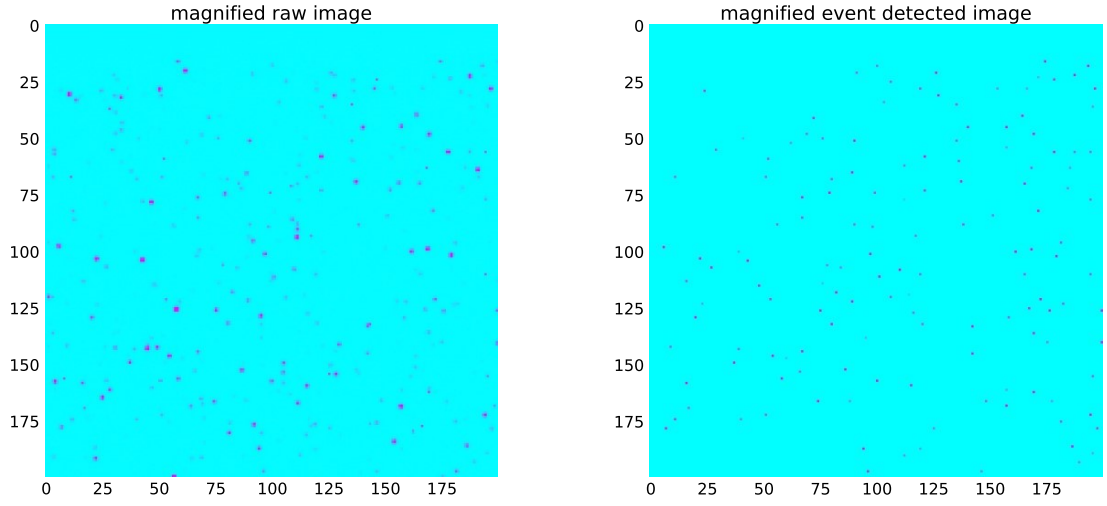

Figure 6.6 A comparison between a raw image and an event detected image. The event detection algorithm used successfully converts charge clouds into single-pixel events, and ignore possible events that are positioned too close to other possible events.

It can be seen that the event detection algorithm successfully sums charge clouds in Figure 6.6(a) from the raw images into single pixels in Figure 6.6(b).

6.3.4 Determination of ADU to keV conversion factors

It was not possible in this experiment to reliably determine the conversion factor between the reported signal in ADU and the actual deposited energy in keV using device parameters alone due to the use of EM gain. Instead, the CCD97 was calibrated here using fluorescence lines of known energies.

In this experiment, the ADU to keV conversion factors could be calculated using the aluminium fluorescence line in the aluminium experiment when the magnetic field was turned on and the current in the solenoids was set to 2 amperes. The magnetic field removed the majority of electrons influencing the spectrum leaving only the shape of the aluminium fluorescence peak, optimising the effectiveness of fitting. The aluminium fluorescence peak was fitted to a Gaussian plus a linear component, where the peak of the Gaussian corresponded with the aluminium fluorescence energy in ADU.

6.3.5 Conversion of event detected data into a spectrum

Once the above algorithms had been used to convert raw images comprised of charge clouds in ADU to event detected images comprised of single pixels in units of keV, the event detected images are then be binned into a spectrum. First, all non-zero pixels in event detected images were imported into analysis software and binned into a histogram. This histogram was then normalised to the number of protons that were initially incident upon the sample plates in the experiment.

For event detected simulation data, the number of protons simulated was already present within the generated hit data files. However, the area of the simulation beam profile was greater than the area of the target plate along the beamline axis. This meant that the number of protons had to be multiplied by the ratio of the target plate area along the beam axis to the beamline area to calculate the mean number of particles that hit the target plate.

For event detected experimental data, on the other hand, the STERIS beamline reports the spatially uniform beamline flux over time. However, this showed the flux as highly variable, and there were periods where flux cut out altogether in images. It is unclear whether these periods where flux cuts out are accounted for within Harwell's reporting of flux. During analysis that will be presented in Section 6.7, there is evidence from systematic deviations between experimental and simulation spectra that the dosimetry used by the beamline was inaccurate, and formed part of the motivation for performing the experiment at the PSI PIF in Chapter 7.

The total number of protons incident upon the sample plate could be calculated using the reported dosimetry data by taking the difference in integrated counts / cm^2 between the start and end times of image taking and multiplying by sample plate area. This total proton count then had to be multiplied by the ratio of integration time to total image taking time, to get the total number of protons hitting the sample plate during the full integration time.

Once total particle number was calculated, images were then imported into a spectrum production python script and then binned. To plot a spectrum logarithmically on both the x and y-axis, it was necessary to perform logarithmic binning, with bin widths increasing with x-value. Then the number of counts in each bin had to be divided by bin width to obtain the differential spectrum. This spectrum was then normalised by dividing by the detector area and the number of protons hitting the sample plate within the integration time.

Errors in each bin were calculated simultaneously, by taking the square root of the number of counts in each bin, then multiplying and dividing by the same normalisation factors by which each bin was multiplied.

6.4 Simulation design

As this experiment was explicitly designed to test Geant4's simulation ability, there was a priority to ensure that simulations were sufficiently accurate to the experiment within the constraints of Geant4. It was considered important to design the experiment such that the probability of a slightly incorrect geometry, approximated beam profile, or incorrect hit counting method adding systematic errors to the spectrum was minimised. If too many systematic errors were introduced through approximations

within the simulation set-up, it would make differences in the spectrum caused by such errors indistinguishable from errors induced by inaccurate physics within the Geant4 toolkit itself.

The simulation geometry is displayed in Figure 6.7. Some elements, such as flanges present in the experimental chamber were not necessary for the simulations, as their presence would not cause any variation in detected spectra.

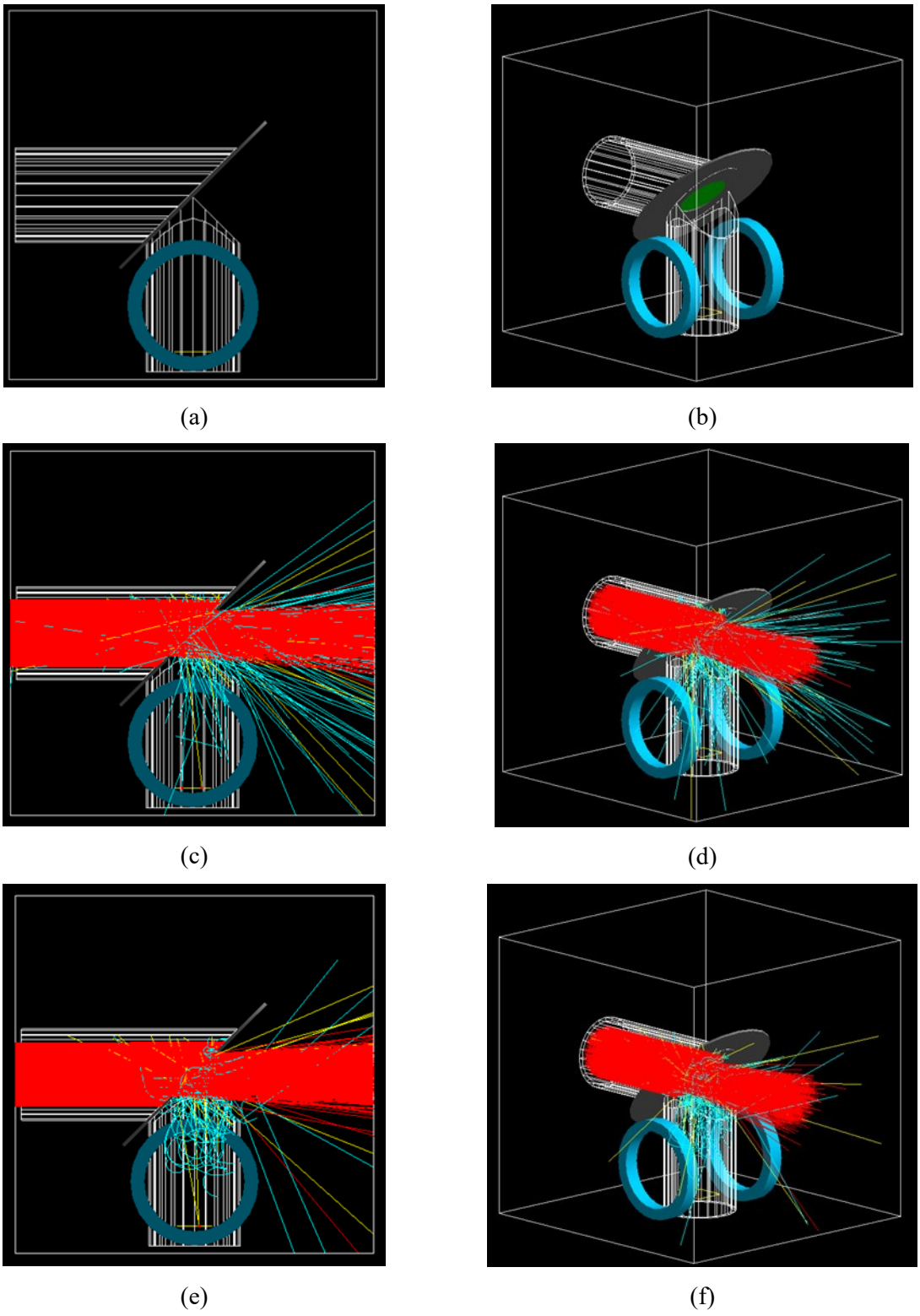

Figure 6.7 The Geant4 simulation geometry used in simulations for this experiment. (a) and (b) show the geometry with no protons passing through, (c) and (d) show the geometry with 1000 incident protons and no magnetic field, while (e) and (f) show the geometry with 1000 incident protons and a magnetic field corresponding to the magnetic field of the Helmholtz coils used in this experiment with a current of 2 A passing through them.

The effectiveness of the applied magnetic field can be seen in Figure 6.7(e), and Figure 6.7(f), where electrons take curved paths through the geometry and many electrons that would otherwise have impacted the detector are prohibited from reaching it.

The Harwell proton beam is designed to give a spatially uniform flux across its opening aperture, and so the Geant4 simulation for this experiment was also designed to generate a uniform flux incident upon the sample plates. As the beam width was unknown, however, it was not possible to directly simulate the full beamline incident upon the sample plate. Fortunately, the knowledge that the CSDA range of a 6 MeV proton in aluminium is only 0.26 mm (M. Berger et al. 2005) means that any proton incident upon the 3.3 mm thick aluminium vacuum seal will not affect the signal in the detector, and only protons hitting the sample plate will create a signal in the detector. This means that instead of normalising the detector signal to the total number of protons passing through the beamline, the detector signal can be normalised to the total number of protons hitting the sample plate. The number of protons hitting the sample plate can be calculated by multiplying the proton flux by the area of the sample plate projected along the initial momentum direction of incident protons.

As described in Chapter 5, while Geant4 simulates the passage of radiation through matter, it is not intrinsically designed to simulate the effect of detector physics on the received signal. Therefore in this experiment, the CCD97 was modelled as a single block of silicon, of thickness 14 μm. The simulation software was then written such that as a particle passes through this detector volume particle attributes such as the particle name, energy deposition, position and momentum would be written to a "hit data" file. This hit data file was then run through the scripts described in Section 6.3, which applied the effects of various detector physics to the energy depositions recorded in the output file.

6.5 Testing the magnetic field design and inclusion in Geant4

As mentioned previously, an important feature of this experiment was the ability to separate components of the spectrum so that Geant4 may be validated for simulations of the space-based environment in detail. In particular, it would be useful to validate Geant4's treatment of physics surrounding both secondary photon production, and secondary electron production. However, it is not possible to easily distinguish between secondary electron events and photon events in the CCD97, and the only reported experimental quantity is the total number of counts in the CCD.

Therefore, to distinguish between the electron spectrum and photon spectrum, four Teltron Helmholtz coil D solenoids ("Helmholtz Pair of Coils D 1000644 Instruction Sheet" 2015) were placed on either side of the chamber in the configuration displayed in Figure 6.8. Each pair of solenoids effectively formed a single solenoid, collectively forming a single Helmholtz coil magnetic system surrounding

the chamber. Increasing the current through the Helmholtz coil would increase the magnetic field strength and would allow the secondary electron spectrum to be reduced or even removed entirely while not influencing the photon spectrum.

Figure 6.8 The position of the Helmholtz solenoids above and below the chamber, when the chamber was connected to STERIS.

Even if the magnetic field were unable to remove the electron component of the spectrum entirely, it would still be possible to use the information gained by the difference between spectra at different magnetic fields to extract information about the particle components of the magnetic field. The reason for this is because the photon component of the spectrum is unaffected by the addition of a magnetic field, and so the difference between spectra at different magnetic fields exclusively probes the difference in the electron spectra at different magnetic fields.

Therefore, if Geant4 can successfully produce the correct difference between spectra at different magnetic field strengths, the electron spectral component can be validated. Validation of the photon component of the spectrum then follows if both the electron spectral component and the total spectrum are both successfully reproduced by Geant4. On the other hand, if the total spectrum were incorrect, but the electron spectrum was shown to be correct, then that would indicate that the photon component of the spectrum is being simulated incorrectly. This method of testing components using spectral differences will be used several times throughout analysis in this chapter and Chapter 7.

Including the Helmholtz coils also gave a secondary advantage of allowing the verification of Geant4's treatment of magnetic fields in space. This is useful as space missions often include

magnetic diverters for deflecting soft protons, and as will be discussed in Chapter 10, there also exists the prospect of using a magnetic diversion system to shield detectors from secondary electrons. To perform this verification, and to show that the magnetic fields in this chapter were constructed correctly, simulations were performed tracking the location and momentum of an electron as it travelled through a Helmholtz coil magnetic field. To discuss these simulations, it is necessary to discuss the theoretical magnetic field produced by a Helmholtz coil.

6.5.1 The theoretical magnetic field of a Helmholtz coil

The magnetic field for a single, thin solenoid positioned at $(0,0,0)$ can be described by the expressions given in equations 5.2 through 5.9 (Simpson et al. 2001), for a cylindrical coordinate system with coordinates (ρ, θ, z'), where z' is aligned along the solenoid axis:

$$I_{tot} = N \times I \tag{5.2}$$

$$c = \frac{\mu_0 I_{tot}}{\pi} \tag{5.3}$$

$$\alpha = \sqrt{R^2 - 2R\rho + \rho^2 + z'^2} \tag{5.4}$$

$$\beta = \sqrt{R^2 + 2R\rho + \rho^2 + z'^2} \tag{5.5}$$

$$k = \sqrt{1 - \frac{\alpha^2}{\beta^2}} \tag{5.6}$$

$$B_\rho = \frac{cz'}{2\alpha^2\beta\rho}((R^2 + \rho^2 + z'^2)E(k^2) - \alpha^2 K(k^2)) \tag{5.7}$$

$$B_\theta = 0 \tag{5.8}$$

$$B_z = \frac{c}{2\alpha^2\beta}((R^2 - \rho^2 - z'^2)E(k^2) + \alpha^2 K(k^2)) \tag{5.9}$$

Here, R is the radius of the Helmholtz coils, I is the current passing through the solenoid where N is the number of coils per solenoid, μ_0 is the permeability of free space, ρ is the distance to the central solenoid axis, and z is the distance to the central coordinate of the solenoid. $K(k^2)$ and $E(k^2)$ are known as the elliptic integrals of the first and second kind, respectively. B_ρ, B_θ and B_z are the radial, angular and z components of the magnetic field, respectively. An important point to note is that due to the cylindrical symmetry of the system, the magnetic field is not dependent on θ.

The total magnetic field can be found by summing individual magnetic fields, which means that it is possible to construct the total Helmholtz magnetic field by positioning the two solenoids and adding their magnetic fields. Therefore the total magnetic field can be given by translating two solenoids along the z-axis and adding their magnetic fields, as given in Equation 5.10 where $\boldsymbol{B} = (B_\rho, B_\theta, B_z)$,

$$\boldsymbol{B_H}(z) = \boldsymbol{B}\left(z' \to z - \frac{S}{2}\right) + \boldsymbol{B}\left(z' \to z + \frac{S}{2}\right) \tag{5.10}$$

Where S is the separation between the two coils.

While the full Helmholtz coil magnetic field is needed for simulations of the experiment in Geant4, it is useful to characterise the magnetic field in terms of the magnetic field strength at the centre of the Helmholtz coil structure. The magnetic field at the centre of the Helmholtz coil structure can be calculated by setting ρ and z' equal to 0, reducing Equation 5.10 to

$$B_{H,\rho} = 0 \tag{5.11}$$

$$B_{H,\theta} = 0 \tag{5.12}$$

$$B_{H,z} = \frac{8R^2 I \mu_0}{(4R^2 + S^2)^{\frac{3}{2}}} \tag{5.13}$$

Using a value of the separation S of 16 cm, the Teltron Helmholtz coil radius R of 6.8 cm, and 640 wire turns, the central magnetic field as a function of the current through the coils can be calculated as described in Table 6.1.

Current	Magnetic field strength at central coil position
0 A	0 mT
1 A	3.22 mT
2 A	6.43 mT

Table 6.1 Values for the central magnetic field strength at different currents through the Helmholtz coils

6.5.2 Experimentally measuring the magnetic field of the Helmholtz coils, and comparisons to theory

While the mathematics regarding Helmholtz coils is well-known and understood, it is still worthwhile to test that these equations successfully represent the magnetic field that will be produced by the

particular solenoids that were used in this experiment. Testing the magnetic field produced by the coils would, for instance, ensure that the solenoids did follow the specifications provided in the instruction manual provided with them and that they were not damaged in any way.

It was also necessary to test the strength of the field induced by the coils within the chamber itself. While aluminium is paramagnetic, it has a low volume magnetic susceptibility of 2.2×10^{-5} (Young 1992), which means that it should not significantly alter the magnetic field structure generated by the Helmholtz coils. Therefore, the magnetic field as a function of the position should be approximately unaffected by the presence of the aluminium chamber. However, it was still necessary to test this experimentally, in case there happened to be any materials within the chamber present in small quantities such as steel, which may have been able to have a significant influence on the magnetic field strength.

Therefore a system was set up as displayed in Figure 6.9 to measure the magnetic field produced by the Helmholtz coil system. The chamber was propped up and the solenoids to be used in the full beamline experiment were placed either side of the chamber. A Hall probe was then attached to a stand, aligned such that the probe would measure the z component of the magnetic field, and inserted into the chamber such that the end of the probe was positioned between the two Helmholtz coils.

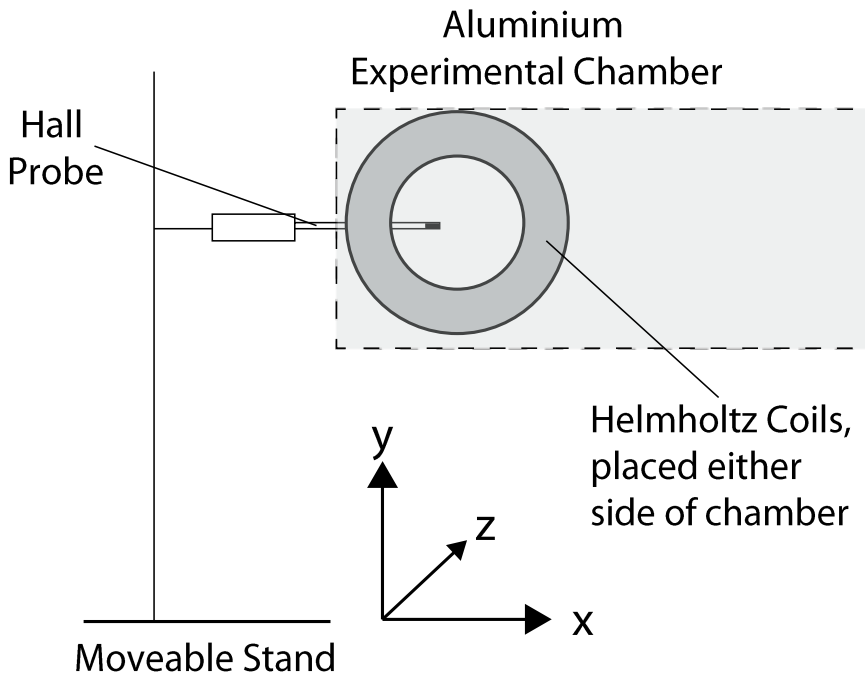

Figure 6.9 The experimental set-up for tests of the magnetic field structure generated by the Teltron Helmholtz coils within the experimental chamber.

The Helmholtz coil system was switched on at a current of 1A, and the position of the moveable stand along the x-z axis was varied, while the position of the Hall probe relative to the stand and orientation of the probe in the x-direction was held constant. The z component of the magnetic field was measured at various points along the x-z axis. Some fluctuation in magnetic field strength was recorded over time, so for each position, three magnetic field strength readings were taken. The magnetic field strength recorded was then the mean of the three readings.

Figure 6.10 and Figure 6.11 show the results of the verification, compared to the theoretical values given by Equation 5.10. In each figure, the predicted magnetic field component appears to agree with experimental values. Therefore it was concluded that the chamber does not significantly affect the magnetic field and that the coils do indeed accurately produce the predicted Helmholtz magnetic field.

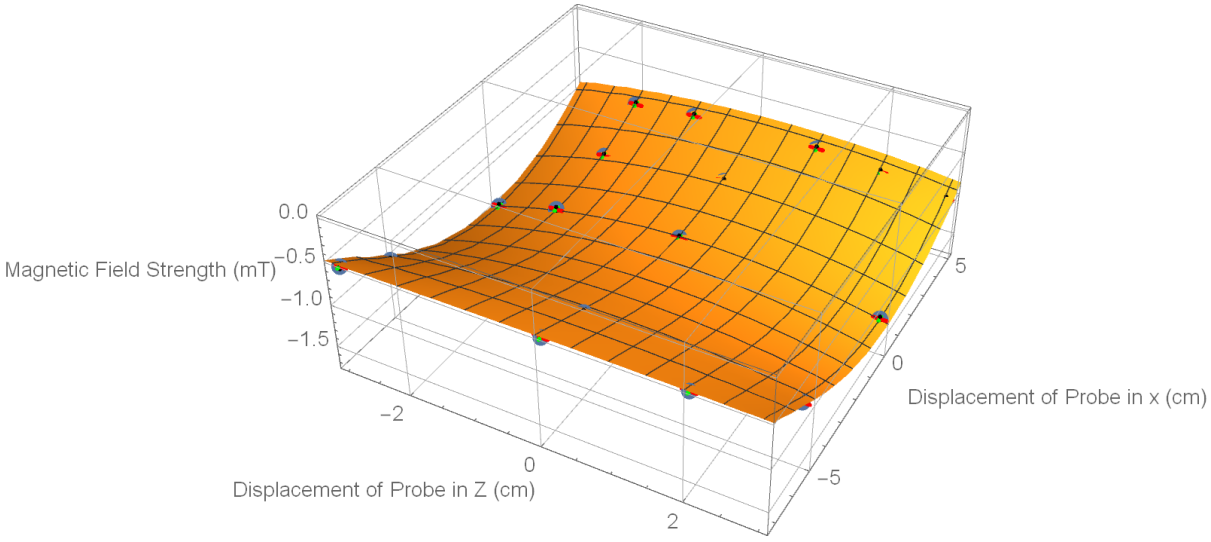

Figure 6.10 A 3D plot of the magnetic field strength versus x displacement and z displacement of the Hall probe. A good agreement is found between theoretical values and experimental values, indicating that Equation 5.10 describes the magnetic field within the experimental chamber well.

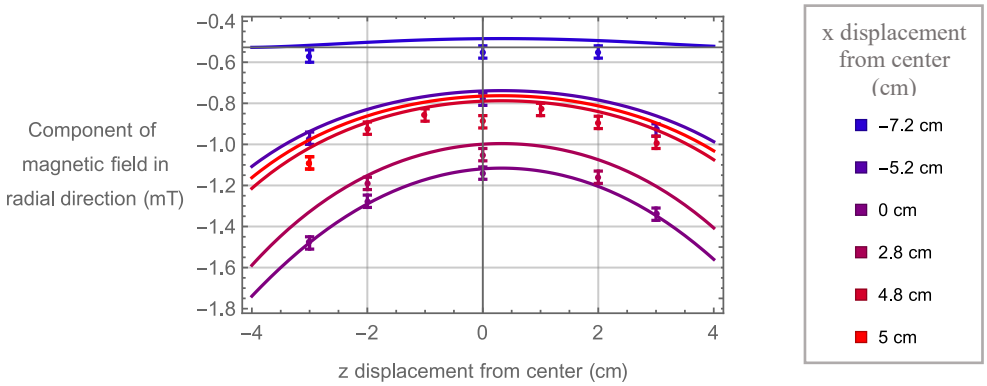

Figure 6.11 The same data displayed in Figure 6.10, plotted in 2D. The experimental data points show good agreement with the theoretical curves.

6.5.3 Verification of Geant4's simulation of particle trajectories in a non-uniform magnetic field

Before performing the actual simulations, it was necessary to test the accuracy of Geant4 in simulating the path of a particle in a magnetic field. Testing the accuracy of Geant4's ability to simulate magnetic fields would serve several purposes.

Firstly it would confirm that Geant4 is indeed capable of simulating complex magnetic field structures such as the Helmholtz coil magnetic field, and inform what parameters should be input into the Runge-Kutta numerical methods (Apostolakis n.d.). Secondly, it would verify that the magnetic field was correctly written into simulation code, a non-trivial consideration, due to the relative complexity of the magnetic field structure.

To verify Geant4's ability to simulate particle trajectories in a Helmholtz coil magnetic field, it was necessary to produce an analytic expression representing the actual particle trajectory produced by the magnetic field in Equation 5.10 so that comparisons could be made to simulated data from Geant4. Unfortunately, it was not possible to derive a general analytic expression for the trajectory of a particle in a Helmholtz coil magnetic field. However, using the cylindrical symmetry of the Helmholtz coil system, it is possible to derive another expression which can be used to verify the system.

The Lagrangian for a classical magnetostatic system (Brown 2007) for a single particle can be expressed as

$$\mathcal{L} = \frac{1}{2} m|\boldsymbol{v}|^2 + q\boldsymbol{v} \cdot \boldsymbol{A} \tag{5.14}$$

where $\boldsymbol{v}$ is the particle velocity, m is the particle mass, and where $\boldsymbol{A}$ is the magnetic vector potential corresponding to Equation 5.10, where $\boldsymbol{B} = \nabla \times \boldsymbol{A}$, where $\boldsymbol{A}$ can be given by $(0, A_\theta, 0)$ in cylindrical coordinates, and

$$A_\theta = \frac{C}{4\rho}\left(\left(\gamma_+ K(k_{H+}^2) + \gamma_- K(k_{H-}^2)\right) - \left(\gamma_+ E(k_{H+}^2) + \gamma_- E(k_{H-}^2)\right) - 8a\rho\left(\frac{K(k_{H+}^2)}{\gamma_+} + \frac{K(k_{H-}^2)}{\gamma_-}\right)\right) \tag{5.15}$$

Where $C = \frac{\mu_0 I}{\pi}$, $\gamma_\pm = \sqrt{4(a+\rho)^2 + (S \pm z)^2}$ and $k_{H\pm} = \frac{4\sqrt{a\rho}}{\gamma_\pm}$. Equation 5.15 was calculated using the expression given in spherical coordinates for the magnetic vector potential of a wire loop as given by Simpson et al. (2001), by adding the vector potentials of two solenoids positioned at $z = \pm\frac{S}{2}$.

Equation 5.14 is a classical mechanical equation; however, as was discussed in Chapter 2, electrons in the energy range of the detector are relativistic. While it would be possible to solve the relativistic Lagrangian instead of the classical Lagrangian for magnetostatics, the classical Lagrangian is correct as long as the 'relativistic mass' γm_0 is used as m.

This is because in special relativity the Lorentz force is identical to the Lorentz force in classical mechanics, of $\boldsymbol{F} = \frac{d\boldsymbol{p}}{dt} = q(\boldsymbol{E} + \boldsymbol{v} \times \boldsymbol{B})$. Combining this with the facts that $\boldsymbol{p} = \gamma m_0 \boldsymbol{v}$ (where γ is the Lorentz factor, and m_0 is the particle rest mass), and that magnetostatics are incapable of changing particle energies, and therefore that γ is a constant of the motion, means that $\gamma m_0 \dot{\boldsymbol{v}} = q(\boldsymbol{E} + \boldsymbol{v} \times \boldsymbol{B})$. This expression is identical to the equation of motion in the classical case but where m is set to γm_0. Therefore all physical properties of the relativistic trajectory should be able to be described by the classical Lagrangian, but with m set to γm_0.

For the Helmholtz coil system, this equation must now be written in terms of cylindrical coordinates, as displayed in Equation 5.16, with the simplification that $\boldsymbol{A} = (0, A_\theta, 0)$,

$$\mathcal{L} = \frac{1}{2}m\left(\dot{r}^2 + r^2\dot{\theta}^2 + \dot{z}^2\right) + qr\dot{\theta}A_\theta \tag{5.16}$$

The well-known Euler-Lagrange equations, which are given by

$$\frac{\partial \mathcal{L}}{\partial q_i} - \frac{d}{dt}\left(\frac{\partial \mathcal{L}}{\partial \dot{q}_\iota}\right) = 0$$

where q_i is any coordinate variable in the system and t is time, can then be used to construct three equations based on ρ, θ and z, by applying them to the Lagrangian in Equation 5.16. Of interest here, in particular, is the Euler-Lagrange equation for $q_i = \theta$ which evaluates to

$$\frac{d}{dt}\left(mr^2\dot{\theta}^2 + qrA_\theta\right) = 0 \tag{5.17}$$

Equation 5.17 provides the important relation that $mr^2\dot{\theta} + qrA_\theta$ is a conserved quantity throughout time for this system. Additionally, $mr^2\dot{\theta}$ can be recognised as the angular momentum L of the system about the line $r = 0$. Therefore,

$$mr^2\dot{\theta} + qrA_\theta = mr_0^2\dot{\theta}_0 + qr_0A_\theta^0 \tag{5.18}$$

or

$$L + qrA_\theta = L_0 + qr_0A_\theta^0 \tag{5.19}$$

where r_0 is the initial radial position, L_0 is the initial angular momentum, $\dot{\theta}_0$ is the initial angular speed, and A_θ^0 is the θ-component of the initial vector potential of the system. Rearranging Equation 5.19 means that the equation for the angular momentum of the system can then be described by the equation

$$L = L_0 + q(r_0A_\theta^0 - rA_\theta) \tag{5.20}$$

Equation 5.20 implies that the angular momentum of the system about the $r = 0$ axis is entirely dependent only on r, z, r_0, z_0 and the initial angular momentum of the system about the $r = 0$ axis L_0. Therefore even though the trajectory of the particle cannot be determined directly in the Helmholtz coil magnetic field system, the angular momentum can be analytically determined directly as a function of particle position. This provides a mechanism for verifying Geant4's treatment of particles in the Helmholtz coil magnetic field, as Geant4 is capable of outputting both the particle's position and velocity as a particle passes through a detector object. Therefore the analytical angular momentum as calculated from the Geant4 outputted particle position can be compared to Geant4's calculation of the angular momentum based on its numerical methods and the theoretically calculated angular momentum.

Should particle angular momenta match the analytically calculated angular momenta, this would represent good evidence that the magnetic field is being simulated correctly. If the numerical methods in Geant4 were to inaccurately predict the particle's trajectory, plotting the angular momentum with respect to radial position should indicate that the angular momentum curve

outputted by Geant4 begins to deviate from the analytic curve as the particle moves along its trajectory.

While it may be theoretically possible for a particle's trajectory to deviate from its correct trajectory while maintaining the same angular momentum, this is unlikely, as any movement of the particle from its correct trajectory would mean that the particle should act as if it were initially given a different angular momentum and position to the one it was given. As the initial position and angular momentum are only added to $-qrA_\theta$, this means that a deviation in particle trajectory should involve a translation of the angular momentum along the particle's trajectory.

To test that the simulated angular momentum matches the theoretical angular momentum as a function of radial position, a simulation was set up, as shown in Figure 6.12.

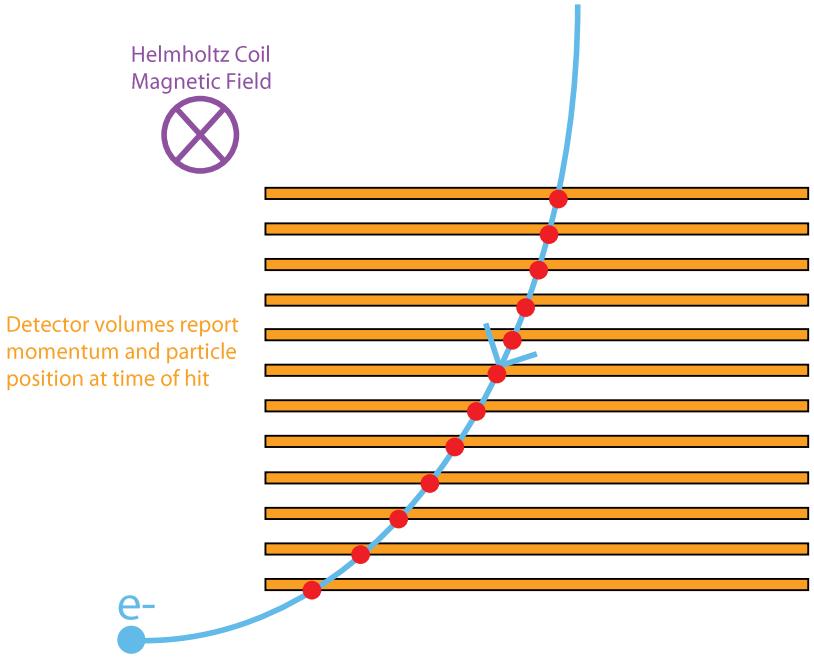

Figure 6.12 The design for the simulation to verify Geant4's treatment of particles in a Helmholtz coil magnetic field. An electron travels through the Helmholtz coil magnetic field, through a series of many detectors, which report the location and momentum of the electron at the time of each particle hit.

Parameter	Setting
fMinStep	0.01 mm
fDeltaChord	0.002 mm
fDeltaOneStep	0.01 mm
fDeltaInterSection	0.1 mm
fEpsMin	0.25 nm
fEpsMax	0.005 mm

Table 6.2 The Geant4 magnetic field trajectory calculation parameters that were used in simulations.

A Taylor expansion approximated version of the Helmholtz magnetic field to be used in the experimental simulations was applied across the system. Two electrons were then generated in two separate runs, with parameters as given in Table 6.3. As the electrons travelled through the detectors simulation geometry, their positions and momenta were recorded and output to a hit data file.

Run Number	Kinetic energy	Helmholtz coil current	Initial position relative to coil centre	Initial momentum direction
1	7 keV	1 A	(0,0,10 cm)	(0,0,-1)
2	7 keV	1 A	(7 mm, -1 cm, 11 cm)	(-0.29, -0.05, -0.96)

Table 6.3 The parameters used for Helmholtz magnetic field validation runs in Geant4.

The r positions and angular momenta about the Helmholtz coil axis could then be calculated from the particle velocities and radial positions. The results of each of these simulations can be seen in Figure 6.13. It should be noted that in the actual simulations of the experiments in this chapter and Chapter 7, the full analytical Helmholtz magnetic field was used and not the Taylor expanded version used for simulations in this section.

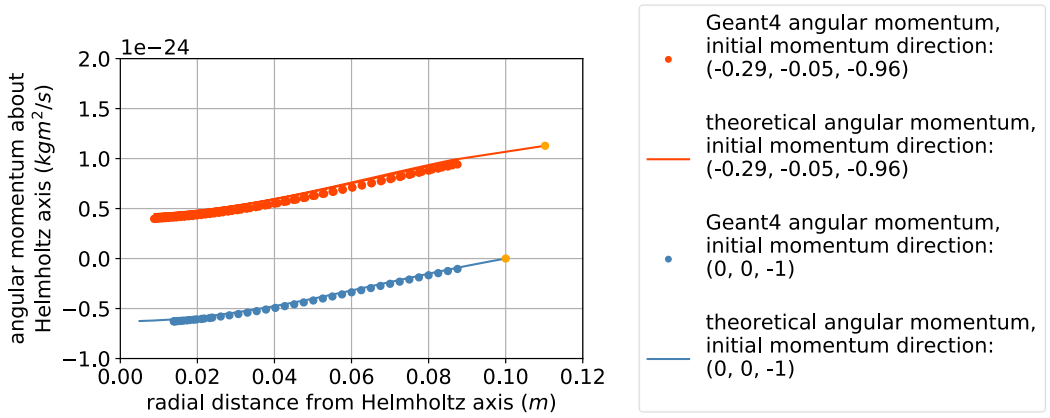

Figure 6.13 The angular momentum phase diagram for two particles initially placed at (0,0,0) in a Helmholtz coil magnetic field and initially travelling in different directions. The phase diagrams show good agreement with their theoretically derived phase diagram curves, indicating that Geant4's simulation of particles in a Helmholtz coil magnetic field is accurate. The slight deviation between simulated results and theoretical results was found in future simulations to be due to the Taylor expansion of the Helmholtz coil magnetic field in these simulations.

The results shown in Figure 6.13 indicate that for the numerical parameters given in Table 6.3, the ability of Geant4 to simulate particle trajectories in a Helmholtz coil magnetic field is indeed accurate. This also has the effect of validating the code to generate the magnetic field within Geant4, which could be directly copied into the full simulation of the STERIS beamline simulation.

Now that the magnetic field structure accuracy has been verified for both the experimental apparatus and simulation geometry, it is now possible to discuss the results of the experiment.

6.6 The experimental secondary particle spectra produced from carbon and aluminium

6.6.1 Experimental spectra

The event detected experimental energy deposition spectra for the carbon and aluminium samples at different magnetic fields are displayed in Figure 6.14 and Figure 6.15, while Figure 6.16 displays the spectra for aluminium and carbon at Helmholtz coil currents of 0 A and 2 A overlayed.

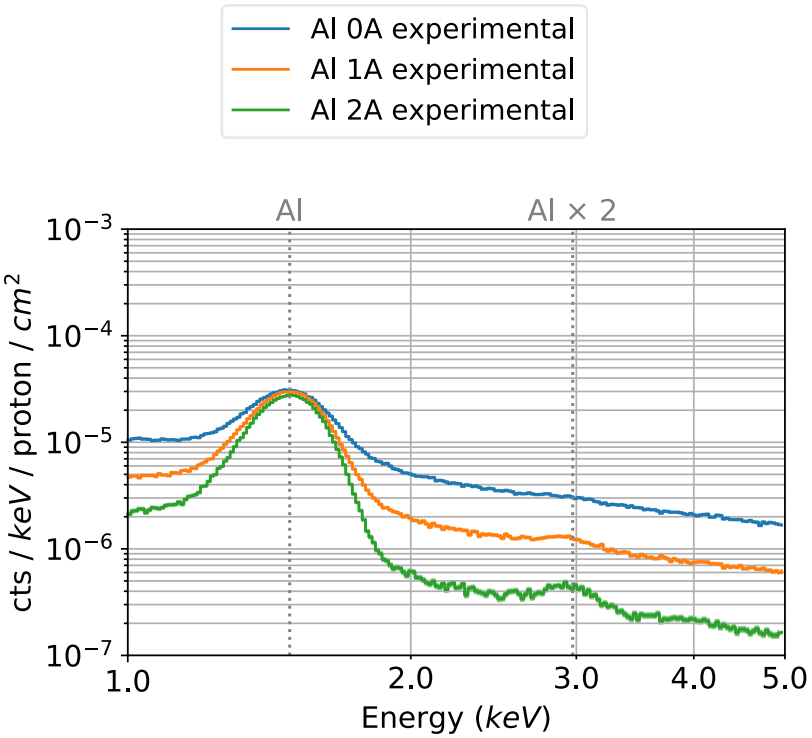

Figure 6.14 The total experimental spectra observed after event detection for the aluminium target and all three magnetic field strengths. Both the Al fluorescence line energy and twice the Al fluorescence line energy are labelled here, which match the positions of the two peaks in the experimental data. The higher energy peak is therefore likely to be caused by pile-up.

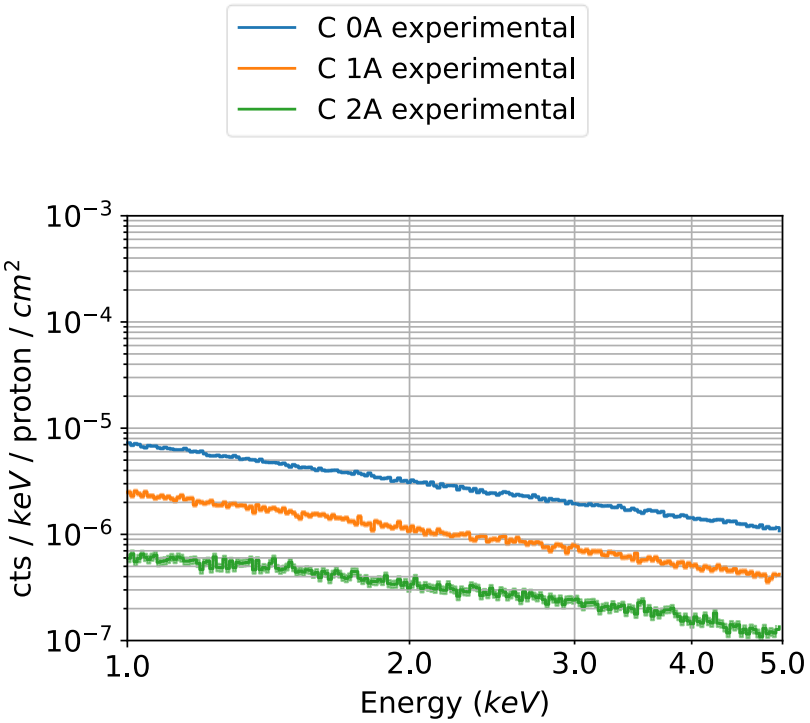

Figure 6.15 The total experimental spectra observed after event detection for the carbon target and all three magnetic field strengths.

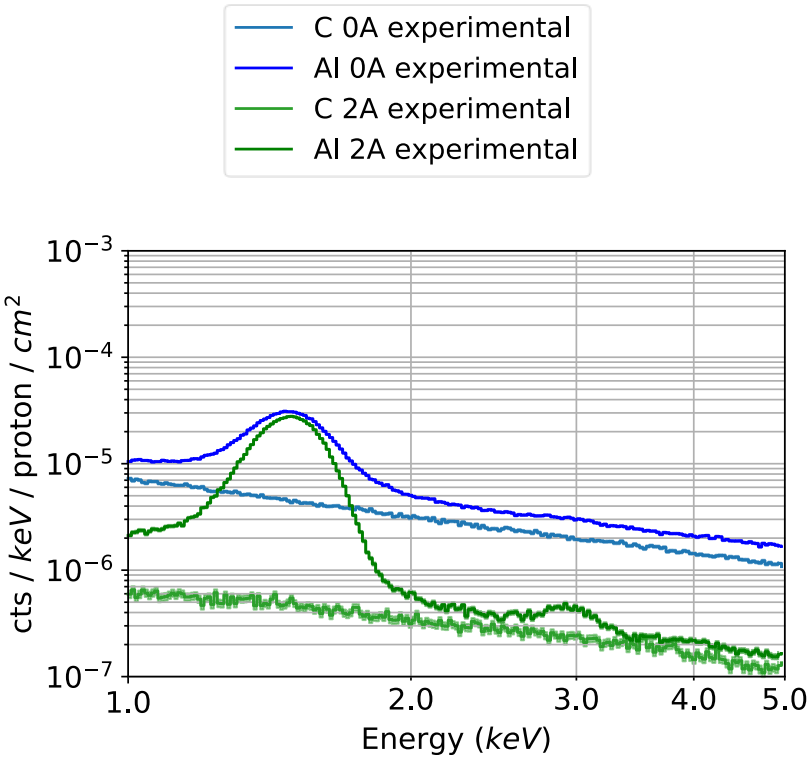

Figure 6.16 A comparison between the aluminium and carbon target spectra at a 0A Helmholtz current magnetic field, and 2A Helmholtz current magnetic field.

Each of these figures shows that the magnetic field successfully reduces the continuum regions of the spectrum by up to approximately a factor of 10 for a Helmholtz coil current of 2 A. Despite the complexity of the Helmholtz coil magnetic field structure, the effect of the magnetic field, in this case, appears to be approximately the same as multiplying the spectrum by a factor.

According to Figure 6.16, which compares the spectra of aluminium and carbon, the continuum regions of the spectrum, which will be shown in Section 6.7.2 to be dominated by secondary electrons, is not significantly affected by the change in materials. This agrees with the theory discussed earlier in Chapter 2, which suggested that the knock-on electron spectrum is not dependent on the atomic number. This interpretation is also implied by the fact that the continuum spectra still match after the application of the magnetic field, which implies that not only do the continuum spectra have the same energy distribution, but they also exhibit the same angular distribution.

In each of the figures, two spectral peaks appear at approximately 1.48 keV and at nearly 3 keV. The peak at 1.48 keV represents the fluorescence peak for aluminium. The second peak, at just below 3 keV is only exposed when the Helmholtz current is set to 1 A or 2 A. The second peak is likely caused by unremovable pile-up created by the existence of the aluminium fluorescence peak, as the peak is at approximately twice the energy of the aluminium fluorescence peak, and because the peak only seems to exist in the aluminium target images and is not present in the carbon target images.

6.7 Validating Geant4's treatment of secondary particle production against experiment

While comparing the total spectra of simulation and experimental data can provide insights into the physical processes occurring during the experiment, to fully understand the physics present it is necessary to analyse the Geant4 simulations in high detail.

As discussed in Section 6.4, the simulation analysis software was designed in such a way that metadata associated with each pixel was saved to separate files. This was done so that pixels could be categorised by the particle and its characteristics that induced an event in a given pixel, allowing the spectrum to be split into components associated with different impacting particle characteristics, a feature that will be examined throughout this section.

6.7.1 Comparing Geant4's energy deposition spectrum to experiment

Figure 6.17 and Figure 6.18 display the experimental and simulation energy deposition spectra for each experimental run for the aluminium target and carbon target, respectively. Figure 6.17(a) displays the actual comparison between simulated and experimental data. In contrast Figure 6.17(b) displays the same data but with the simulation spectra divided by 5.5 in order to better illustrate the

similarities and differences between the spectral shapes. On each of these plots there can be seen to be a significant discrepancy between experimental and simulation spectra, however in Figure 6.17(b) it can be seen that when the simulation spectra are divided by about 5.5, the continuum spectra for all three magnetic field intensities appear to match up. Therefore it appears the spectra may have been normalised incorrectly. There does also appear to be some difference in the gradient of the continuums with respect to increasing energy, for both the carbon and aluminium data, however this may be explained by pile-up causing some relative decrease in flux at lower energies.

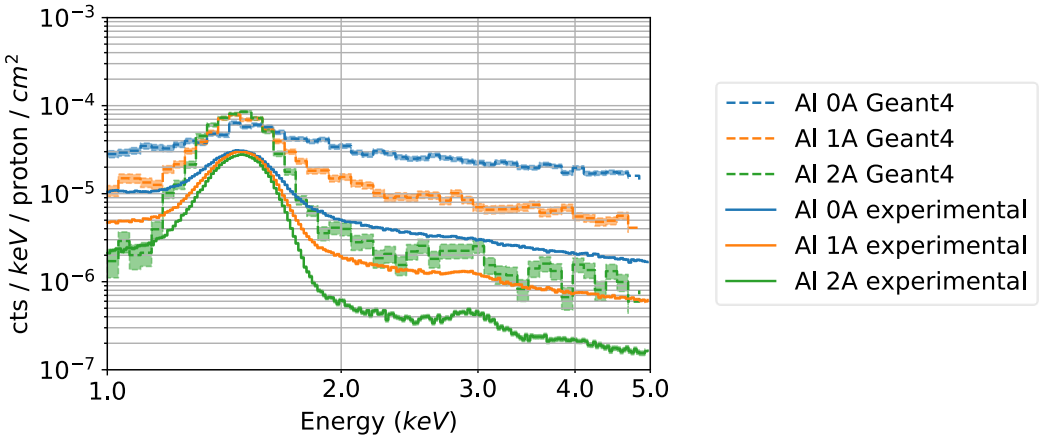

(a)

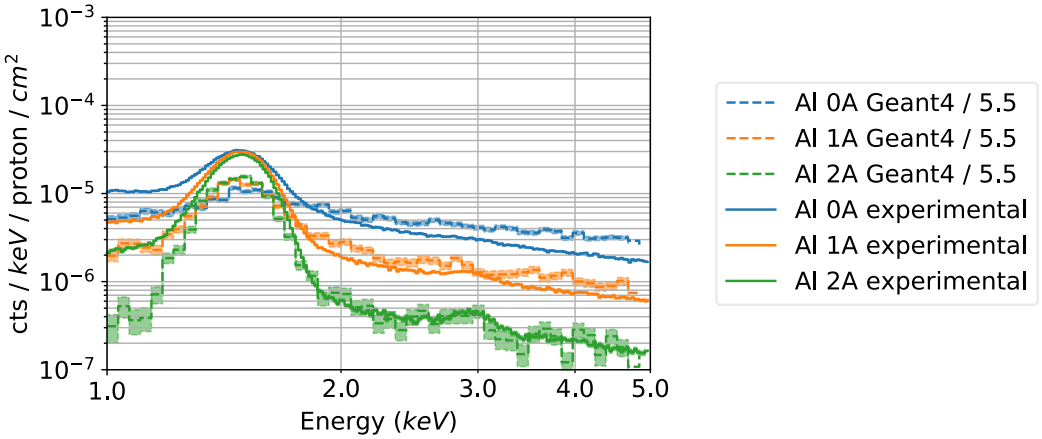

(b)

Figure 6.17 A comparison between the simulation spectra and experimental energy deposition spectra for the aluminium target, for each magnetic field strength. Figure 6.17 and Figure 6.18 display the experimental and simulation energy deposition spectra for each experimental run for the aluminium target and carbon target, respectively. Figure 6.17a displays the actual comparison between simulated and experimental data. In contrast, Figure 6.17b displays the same data but with the simulation spectra divided by 5.5 in order to better illustrate the similarities and differences between the spectral shapes.

Aluminium Spectra Fit Parameters

Spectrum type	Helmholtz current	Fluorescence fit $Ae^{-\frac{1}{2}\left(\frac{x-\mu}{\sigma}\right)^2}$ (A in units of cts / proton / keV / cm², σ in units of keV)	Power law continuum fit Ax^b (A in units of cts / proton / keV / cm², b unitless)
Geant4	0A	$A = (8.4 \pm 0.2) \times 10^{-5}$	$A = (4.9 \pm 0.3) \times 10^{-5}$, $b = -0.70 \pm 0.06$
	1A		$A = (2.4 \pm 0.3) \times 10^{-5}$, $b = -1.0 \pm 0.1$
	2A		$A = (0.7 \pm 0.9) \times 10^{-5}$, $b = -2 \pm 1$
Experimental	0A	$A = (2.614 \pm 0.008) \times 10^{-5}$ $\sigma = (0.1167 \pm 0.0004)$	$A = (1.07 \pm 0.01) \times 10^{-5}$, $b = -1.19 \pm 0.01$
	1A		$A = (0.4 \pm 0.2) \times 10^{-5}$, $b = -1.3 \pm 0.5$
	2A		$A = (0.12 \pm 0.07) \times 10^{-5}$, $b = -1.3 \pm 0.5$

Table 6.4 Fits to the Geant4 and experimental data for aluminium given in Figure 6.17. As the standard deviation of the aluminium fluorescence line was defined by the Fano noise applied during analysis of the Geant4 simulation data, which was calculated from the experimental fluorescence line standard deviation, σ was identical for both the simulation and experimental fluorescence line.

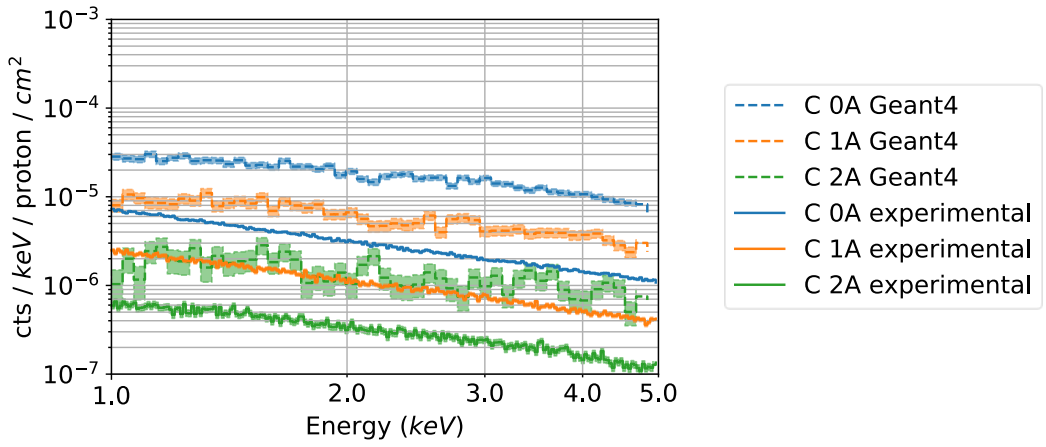

Figure 6.18 A comparison between the simulation spectra and experimental spectra for the carbon target for each magnetic field strength.

Carbon Spectra Fit Parameters

Spectrum type	Helmholtz current	Power law continuum fit Ax^b (A in units of cts / proton / keV / cm^2, b unitless)
Geant4	0A	$A = (3.0 \pm 0.3) \times 10^{-5}$, $b = -0.73 \pm 0.08$
	1A	$A = (0.8 \pm 0.1) \times 10^{-5}$, $b = -0.6 \pm 0.1$
	2A	$A = (0.22 \pm 0.07) \times 10^{-5}$, $b = -0.7 \pm 0.3$
experimental	0A	$A = (0.67 \pm 0.01) \times 10^{-5}$, $b = -1.12 \pm 0.01$
	1A	$A = (0.251 \pm 0.006) \times 10^{-5}$, $b = -1.16 \pm 0.02$
	2A	$A = (0.070 \pm 0.003) \times 10^{-5}$, $b = -1.03 \pm 0.04$

Table 6.5 Fits to the Geant4 and experimental data for carbon given in Figure 6.18.

There are several possible reasons for the differing spectra shown in Figure 6.17 and Figure 6.18. One possible issue may have been caused by inaccuracies in the dosimetry at the STERIS beamline. There were periods during image taking, for instance, where the beamline turned off randomly, and it is unknown whether the dosimetry successfully accounted for this. Other experiments performed by members of the Center for Electronic Imaging have also on occasion indicated that the reported flux at the STERIS beamline can differ significantly from the actual received flux (private communication).

While an erroneous normalisation due to an incorrectly reported flux might explain the discrepancy between the simulation continuum and experimental continuum, dividing the simulation spectra by a factor of 5.5 as shown in Figure 6.17(b) does not cause the fluorescence line shape to match despite causing the continuums matching. This would indicate that even if there is a normalisation error, it is possible that Geant4 could potentially be incorrectly simulating either the intensity of the continuum or the aluminium fluorescence line. While this would be an important finding, it is not possible to discount the possibility that this may be caused by other unaccounted for differences between experimental data and simulation data. This might include for instance the possibility that the CCD97 used in the experiment might have had a low charge collection efficiency near the surface of the device causing some electron flux to be lost. This possible effect was not accounted for in simulations, and will also be discussed in Chapter 7 with regards to the 200 MeV proton experiment.

Either way, the fact that the simulation spectra in Figure 6.17(b) match up reasonably well qualitatively to experimental data when renormalised gives evidence that Geant4 may indeed be simulating the aluminium continuum spectra correctly. Additionally, Chapter 7 will show that Geant4 gave approximately the correct fluorescence line intensity for the aluminium line under the 200 MeV proton irradiations and for fully penetrating electrons. This indicates that if Geant4 were to be simulating aluminium fluorescence incorrectly in this experiment, it would only be the case for 6 MeV proton irradiations, which are significantly lower energy than the background-inducing protons in the space-based environment. It is anticipated overall that despite the drawbacks that were present in this experiment, this experiment does provide evidence that Geant4 is successfully predicting the background continuum spectra, and that combining this data with data from future experiments with a plurality of several different set-ups and devices should be able to fully clarify how accurately Geant4 can simulate the space-based environment.

In addition to plotting the total spectrum the device receives, it is also instructive to plot the difference between spectra at different magnetic fields. Plotting this spectral difference as a function of deposited energy is useful because taking the difference between the spectra at different magnetic field strengths should cause components that do not vary with magnetic field strength to cancel out, such as the component of the spectrum associated with photons. These difference spectra can then be said to be explicitly probing the spectral components associated with charged low energy particles, which in this case refers to electrons.

The difference spectra are plotted in Figure 6.19 and Figure 6.20. In both plots, the spectra exhibit similar discrepancies as the total spectra in Figure 6.17 and Figure 6.18 in that there appears to be a normalisation error between simulation data and experimental data, and that the gradient of the continuums appears to exhibit only a small discrepancy in logarithmic space.

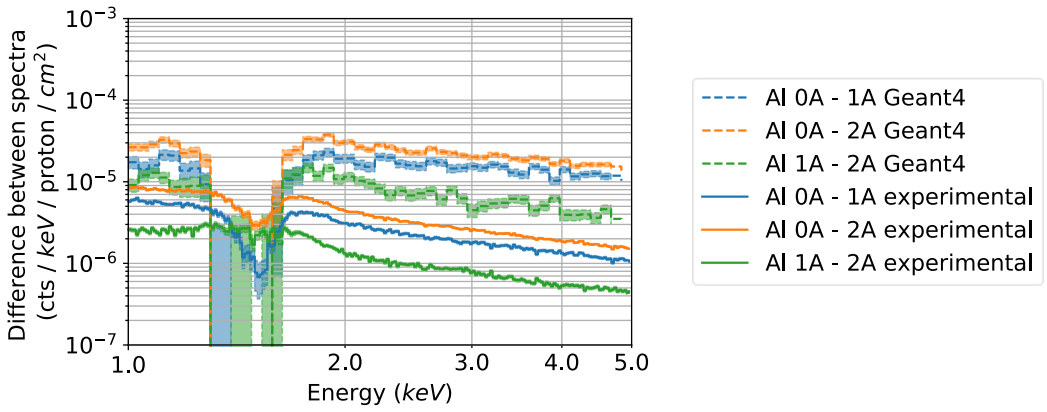

Figure 6.19 The difference in spectra at different Helmholtz coil currents, corresponding to different magnetic field strengths for the aluminium target runs.

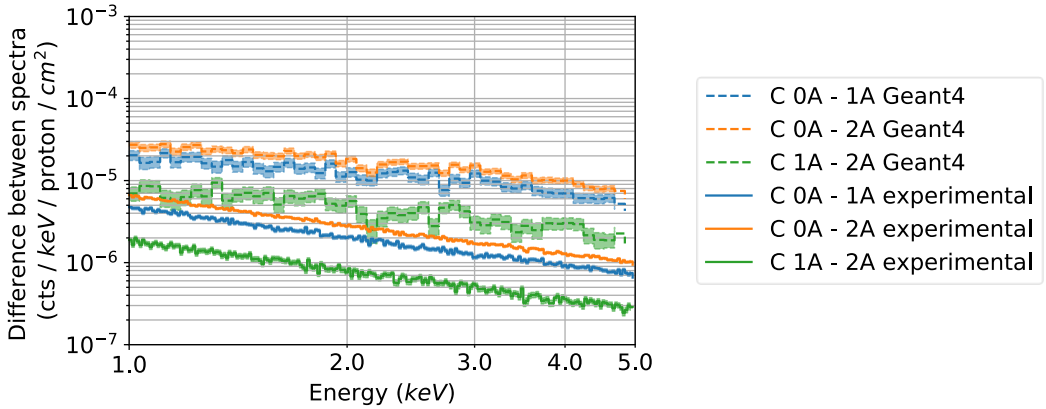

Figure 6.20 The difference in spectra at different Helmholtz coil currents, corresponding to different magnetic field strengths for the carbon target runs.

In Figure 6.19, a large trough in the experimental and simulation difference data can also be observed at the fluorescence peak. This trough is likely caused by the existence of small differences in the normalisation and ADU to keV conversion factors for different experimental and simulation runs, which specifically impact the difference spectra at fluorescence energies due to the large fluxes in these areas of spectra. At higher energies, this is not a significant effect, as can be seen in Figure 6.19, where despite the fluorescence line difference creating a trough, there is no corresponding trough for the peak generated by pile-up.

While the experimental spectra and simulation spectra do appear to diverge, the fact that continuum regions of spectra and difference spectra for experimental and simulation data are similar in shape adds weight to the hypothesis that the divergence is caused by erroneous normalisation rather than incorrect functioning of Geant4. To investigate further whether this is the case, it is necessary to analyse the simulation and experimental data in more detail.

6.7.1.1 Investigating discrepancies between simulation and experimental data

Figure 6.21 and Figure 6.22 display the ratio between simulation and experimental data for both aluminium and carbon. If the spectra match between different magnetic field runs except for an erroneous normalisation factor, then it should be expected that the ratio between them should be a constant value, and this does seem to be the case for both the aluminium and carbon spectra given the reasonable degree of standard error in the spectral bins (discounting areas near or below the aluminium fluorescence line, and taking into account the fact that the spectrum at lower energies might erroneously be decreased somewhat due to the pile-up reduction methods). The erroneous normalisation factor here would appear to be approximately 7.5.

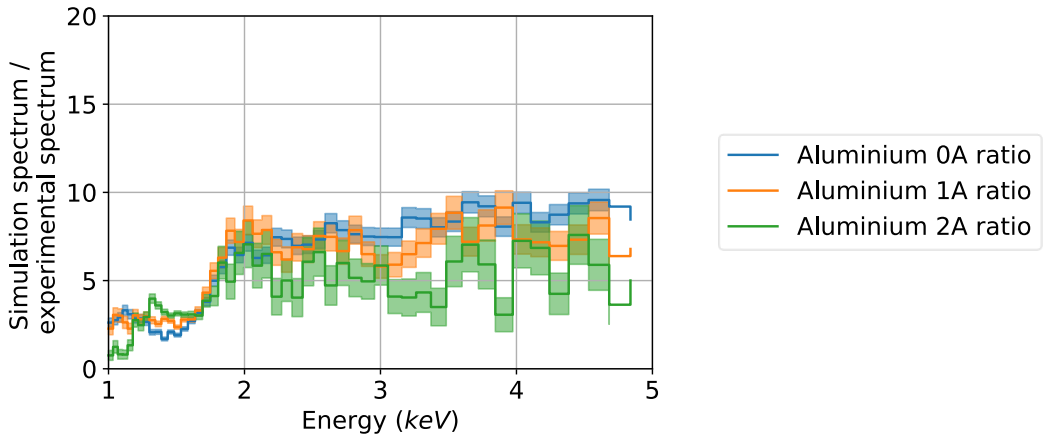

Figure 6.21 The ratio between spectra at different magnetic fields for the aluminium target runs.

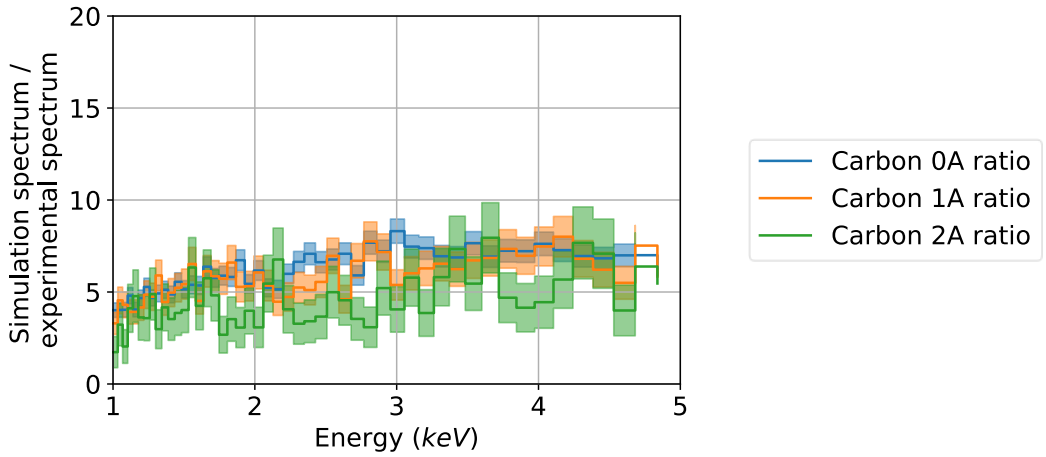

Figure 6.22 The ratio between spectra at different magnetic fields for the carbon target runs.

Instead of showing the simulation / experimental spectral ratio for total spectrum, Figure 6.23 and Figure 6.24 display the ratio of the differences in spectra for simulation and experimental data. In each case, the data displayed here also appear to be approximately constant between 2.5 keV and 4 keV.

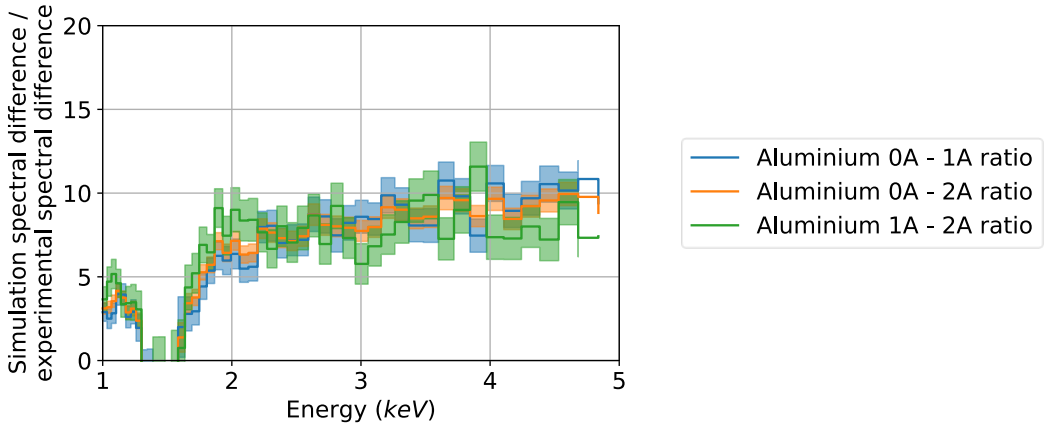

Figure 6.23 The ratio between magnetic difference spectra for aluminium.

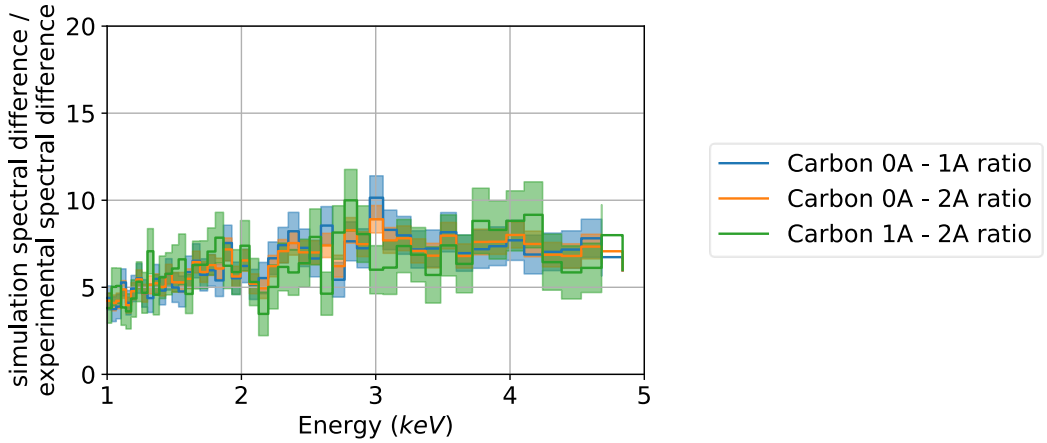

Figure 6.24 The ratio between magnetic difference spectra for carbon.

Each of the runs again appear to match an erroneous normalisation of approximately 7.5 in Figure 6.24.

6.7.2 Comparing Geant4's treatment of low energy electrons to experiment

One way to divide the spectrum is into events induced by different particle species, as is shown in Figure 6.25, which was generated by attaching saved particle characteristics to corresponding valid hits in event detected images.

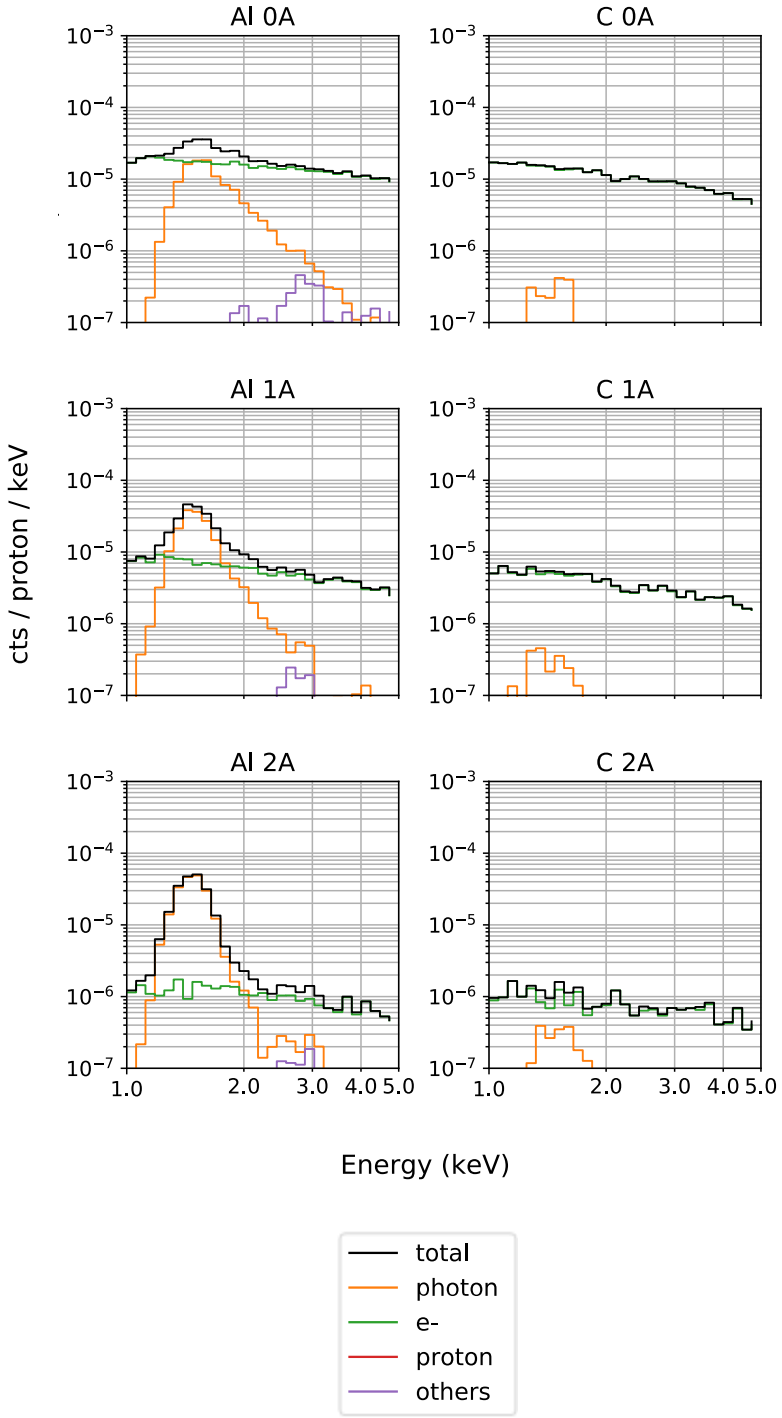

Figure 6.25 The total energy deposition spectrum for the different magnetic fields and target materials split by particle species.

In all cases, the fluorescence lines can be observed to be created by photons, as expected. The continuum sections of the spectra, however, appear to be dominated by electron-induced spectra. As

the Helmholtz current is increased, the electron spectrum decreases significantly, and in the 2A case, it can be seen that the photon spectrum for aluminium becomes significantly more exposed.

In addition to splitting the spectrum by particle type, another useful way to divide the spectrum is to plot the spectral components generated by particles of greater kinetic energy than the energy they deposit, versus particles which deposit the entirety of their kinetic energy. Figure 6.26 displays both the material configurations split into these components. In the majority of the material and magnetic field configurations, the continuum spectrum is composed primarily of particles which deposit the entirety of their energy upon interacting with the detector. In the case of the carbon runs, the spectrum appears to become less dominated by fully absorbed particles as the Helmholtz current is increased. This was expected because magnetic fields have less effect on higher energy particles than lower energy particles, as has been previously described in Chapter 2.

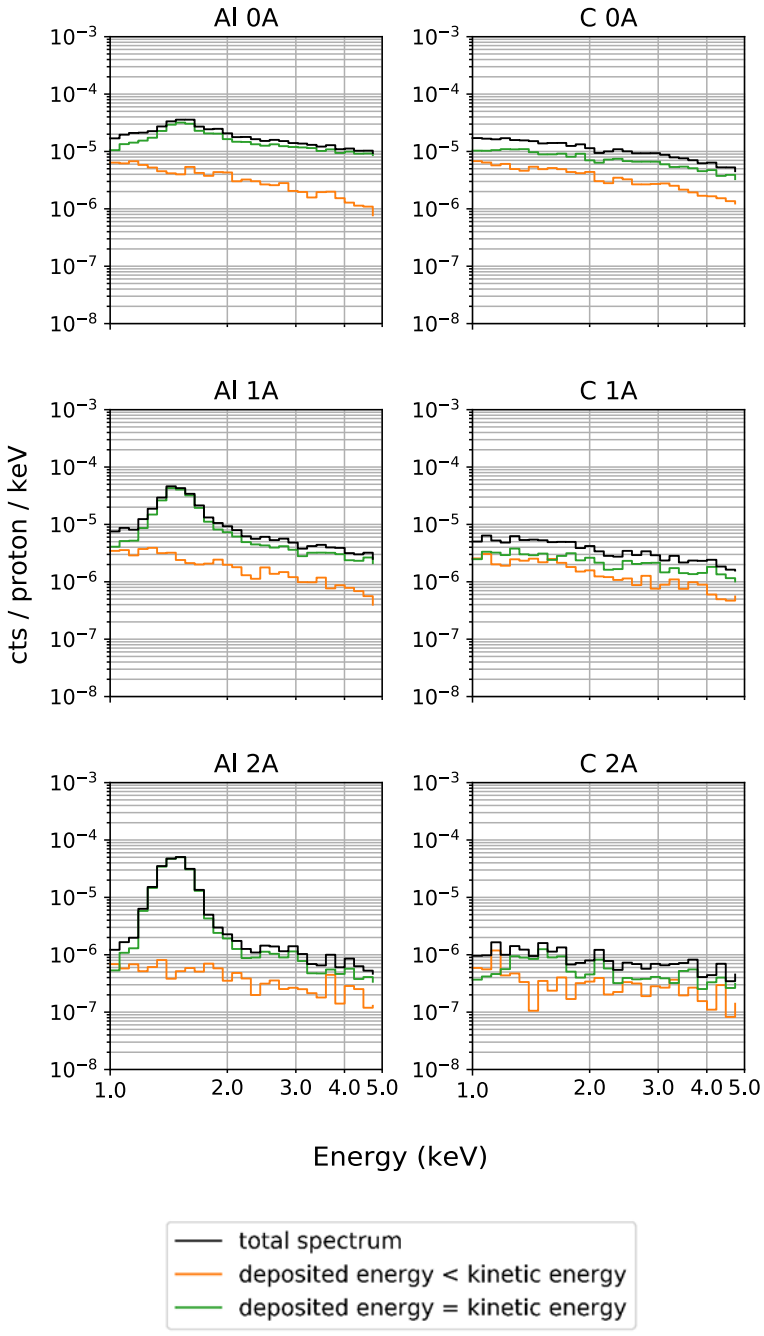

Figure 6.26 The total energy deposition spectrum for the different magnetic fields and target materials split by incoming particle energy.

One unusual aspect displayed in Figure 6.26 is that there appears to be a difference in kinetic energy components of the continuum spectra between the aluminium and carbon for the same Helmholtz current. This is something that potentially contradicts the interpretation that the knock-on electron spectrum is unchanged with respect to a change in material. This interpretation was initially motivated by the Sternglass theory of secondary electron production mentioned in Chapter 3, which previously indicated that the continuum spectra should be identical for carbon and aluminium.

6.7.3 Comparing Geant4's hadron ionisation process to experiment

To be able to verify Geant4 in higher detail, it is also necessary to investigate the physics that are being simulated in the situations that are being investigated here. Investigating the particle production physics is important because even though the experiments performed here are designed to be representative of the space-based environment, it is difficult or impossible for any Earth-based experiment to replicate the space-based environment. Therefore it is necessary to attempt to verify specific Geant4 physics lists rather than exclusively looking at Geant4's ability to simulate this experiment correctly.

Figure 6.27 shows the simulation spectra split by physics creation process. Creation processes in Geant4 refer to the physical process that caused a particle to be created, such as bremsstrahlung or the photoelectric effect. The cross-sections associated with different physics processes within Geant4 vary with different Geant4 parameters, as well as the physics lists that are used in a particular simulation.

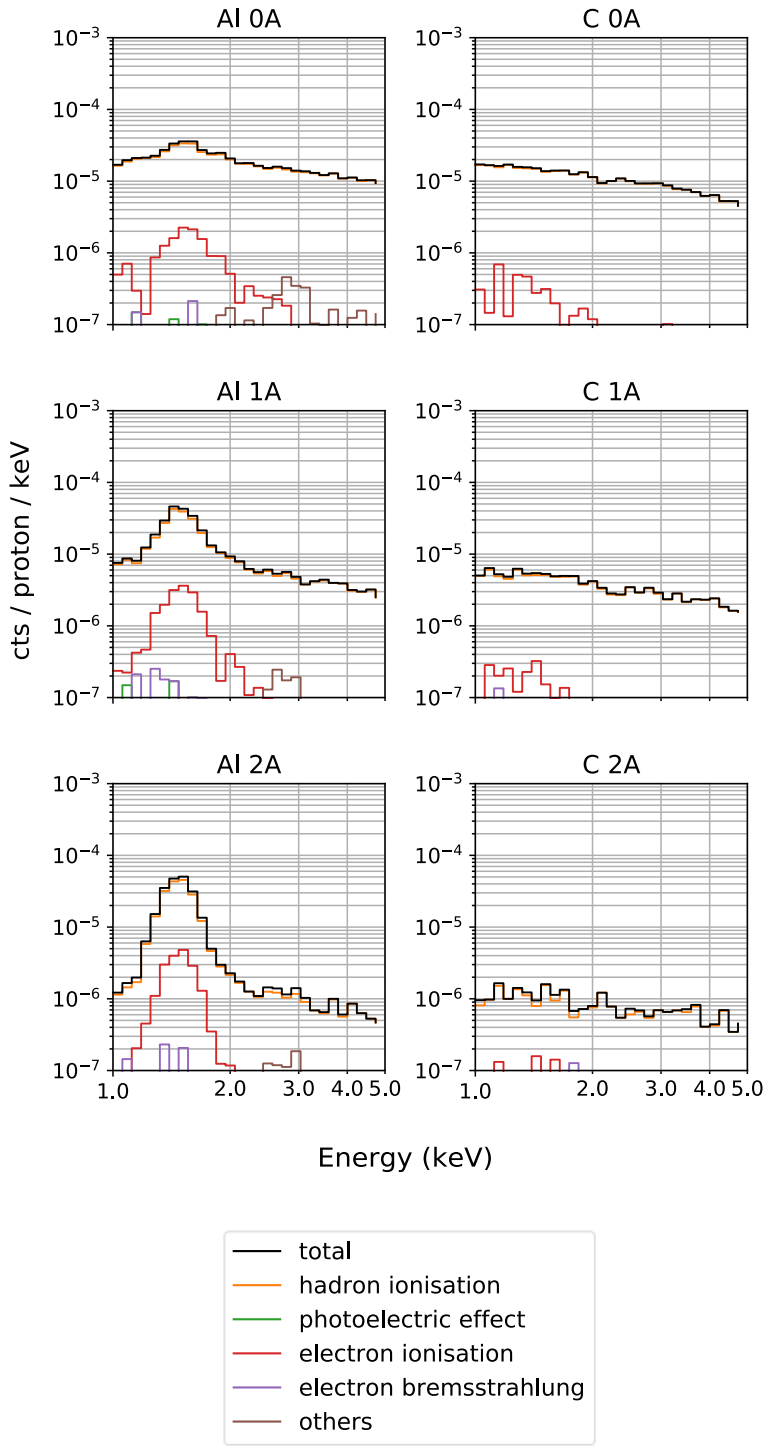

Figure 6.27 The total energy deposition spectrum for the different magnetic fields and target materials split by particle creation process.

In Figure 6.27, it can be seen that the hadron ionisation creation process dominates the entire spectrum in both the aluminium and carbon simulations. Therefore, the results of this experiment could be said to be explicitly probing the hadron ionisation process of Geant4. While it is useful to verify the hadron ionisation physics list, further experiments may also need to be performed in the

future to verify the other physics processes that contribute to the X-ray-like background. Hadron ionisation is present in significant quantities in simulations of the space-based environment, however as will be shown in Chapter 8, many particle creation processes contribute to the background.

6.7.4 Comparisons between the Space User's physics list and PENELOPE

As has been stated previously, each of the simulations performed in this chapter were performed using the Geant4 Space Users physics list (Dondero and Mantero 2017), however many simulations, such as those performed in Chapters 8 and 9 used the PENELOPE physics list. As there are several differences between the Space Users physics list and PENELOPE, including the use of single scattering as opposed to multiple scattering at low energies, it is instructive to investigate if PENELOPE and the Space Users physics list produce the same results for this experiment.

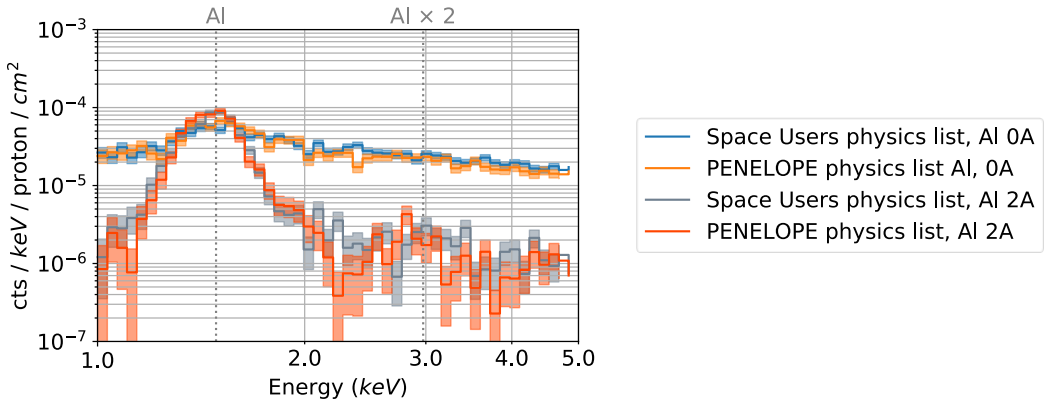

Figure 6.28 The spectra produced by both the Space Users physics list and PENELOPE physics list for 0A and 2A Helmholtz currents. The spectra here are based on slightly older simulations than the other simulations described in this chapter, and used an approximated magnetic field rather than the exact magnetic field, however this was found to make only minimal differences to the spectra. The spectra are consistent between physics lists.

Figure 6.28 displays the total spectrum produced by both the PENELOPE and Space Users physics lists for the aluminium target material runs. Both simulation runs appear to exhibit no significant differences, which indicates that both PENELOPE and the Space Users physics list exhibit no significant differences when simulating particles of the energies present in this experiment. Therefore it is likely they will also not produce significantly different X-ray-like background spectra when simulating particles with kinetic energies corresponding to the space-based environment, as was previously indicated for spherical shell models in Chapter 5.

This implies that the inclusion of single scattering among other differences between the physics lists does not appear to be significant in altering the physics of the detection of both photons and electrons by the CCD97 in this experiment. This fact that PENELOPE and the Space Users physics list appear not to exhibit significant differences may also mean that PENELOPE is a preferable physics list to use for simulations of X-ray-like background in the space-based environment instead of the Space User's

physics list, and may be faster to run while achieving the same accuracy as the Space User's physics list.

6.7.5 Comparison of simulation accuracy between simulation production cut lengths

In addition to confirming that the PENELOPE physics list produces the same spectra as the Space Users physics list, it is also useful to verify that the 1 µm production cut length used throughout this thesis is indeed valid. Therefore several additional simulations were performed of this experiment using cut lengths of 10 µm and 0.1 µm, where the spectra for the 0A and 1A Helmholtz current cases are plotted in Figure 6.29 along with the corresponding 1 µm spectra.

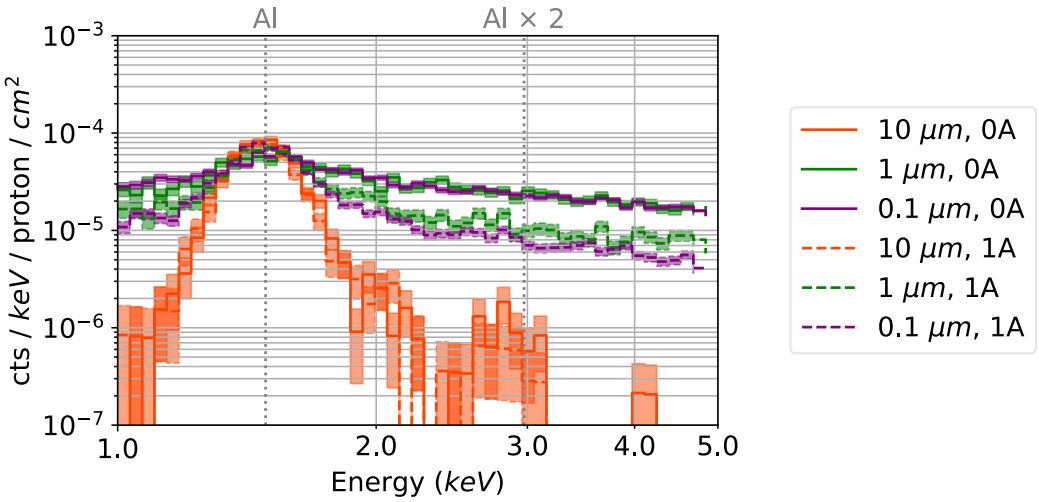

Figure 6.29 A comparison of the spectra produced in the 0A and 1A Helmholtz current cases for production cut lengths of 10 µm, 1 µm and 0.1 µm. The 0.1 µm spectra are consistent with the 1 µm spectra, while the 10 µm spectra erroneously predict that no electrons deposit energy within the energy range. As with the results shown in Figure 6.28, the spectra here are based on slightly older simulations than the other simulations described in this chapter, and used an approximated magnetic field rather than the exact magnetic field, however this was found to make only minimal differences to the spectra.

Figure 6.29 indicates that the 1 µm spectra and 0.1 µm spectra are very consistent while the 10 µm case erroneously predicts that no electrons deposit energy within the energy range. This implies that a production cut length of 1 µm is indeed optimal for simulations of the space-based environment for the physics lists used in this thesis above 1 keV, as the spectra produced are not significantly altered by the increased accuracy provided by the decreased cut length of 0.1 µm.

6.8 Conclusions

While this experiment has found what appears to be a normalisation discrepancy between the simulation data and experimental data, which may be the result of inaccuracies in dosimetry at the STERIS beamline or unsimulated aspects of the CCD97 used, it was found that the power-law shape of the simulation spectra was overall similar to that of the experimental spectra. This was true both when no magnetic field was applied across the chamber, and when the magnetic field was turned on,

and the ratio of simulation data to experimental data was found to be largely consistent for different magnetic field strengths. This provides evidence that Geant4 was correctly simulating the production and detection of electrons through hadron ionisation.

The experimental and simulation spectra also implied that the secondary spectrum produced by the aluminium and carbon foils both had a similar structure. This was previously implied theoretically from Sternglass' theory of secondary electron production mentioned in Chapter 3 (Sternglass 1957).

Additionally, the Geant4 simulation results for this experiment provided useful results in the verification of the use of different settings of Geant4 for the space-based environment. Comparisons of the simulation results for the PENELOPE and Space User's physics lists, as well as for several different production cut lengths in Sections 6.7.4 and 6.7.5 indicated that simulations performed during this thesis using PENELOPE with a production cut length of 1 μm are likely optimal accuracy, and simulations of the trajectory of a particle through a Helmholtz coil magnetic field in Section 6.5 showed that the Runge-Kutte methods within Geant4 to simulate a Helmholtz coil magnetic field are accurate.

While the results presented within this Chapter are useful for verifying the usage of Geant4 in the space-based environment, the inability to trust the dosimetry at the STERIS beamline did cause significant limitations and are likely the cause of the normalisation issues. Correcting for this normalisation also did not cause the aluminium fluorescence line region of simulation spectra to match with experimental spectra. Therefore the possibility cannot be ruled out that Geant4 may not have been correctly simulating the aluminium fluorescence line yields for these incoming proton kinetics energies.

The proton kinetic energy of 6 MeV used in this experiment is significantly lower energy than typical background-inducing protons in the space-based environment, as will be discussed in Chapter 8. Therefore the decision was made to perform additional experiments at the PSI Proton Irradiation Facility (PIF), which utilises more reliable dosimetry and is capable of providing protons of energies of 200 MeV, closer to the actual energies present in the space-based environment.

Chapter 7

Experimental Results for 200 MeV Proton Irradiation

7.1 Experimental setup

As discussed previously, issues with dosimetry at the STERIS beamline and the ability to use protons of 200 MeV rather than 6 MeV motivated the second round of irradiations to be performed at the Paul Scherrer Institut Proton Irradiation Facility (PSI PIF). This experiment was designed to be closer to the actual space-based environment, with the energy of protons being closer to those that cause X-ray-like background in X-ray detectors and material configurations and thicknesses that are more comparable to spacecraft structures surrounding detectors. Some of the key results from this work as well as some additional results are given in Section 4 of Eraerds et al. (2020).

This experiment was set up similarly to the STERIS beamline experiment described in the previous chapter, with the irradiated materials comprising a target representing graded-Z shielding candidate materials lying directly in the path of the beamline, and the detector placed at the end of a cylinder oriented 90 degrees away from the beamline direction, as shown in Figure 7.1. Figure 7.1 also displays the end of the PSI PIF beamline as well as the modified chamber for this experiment.

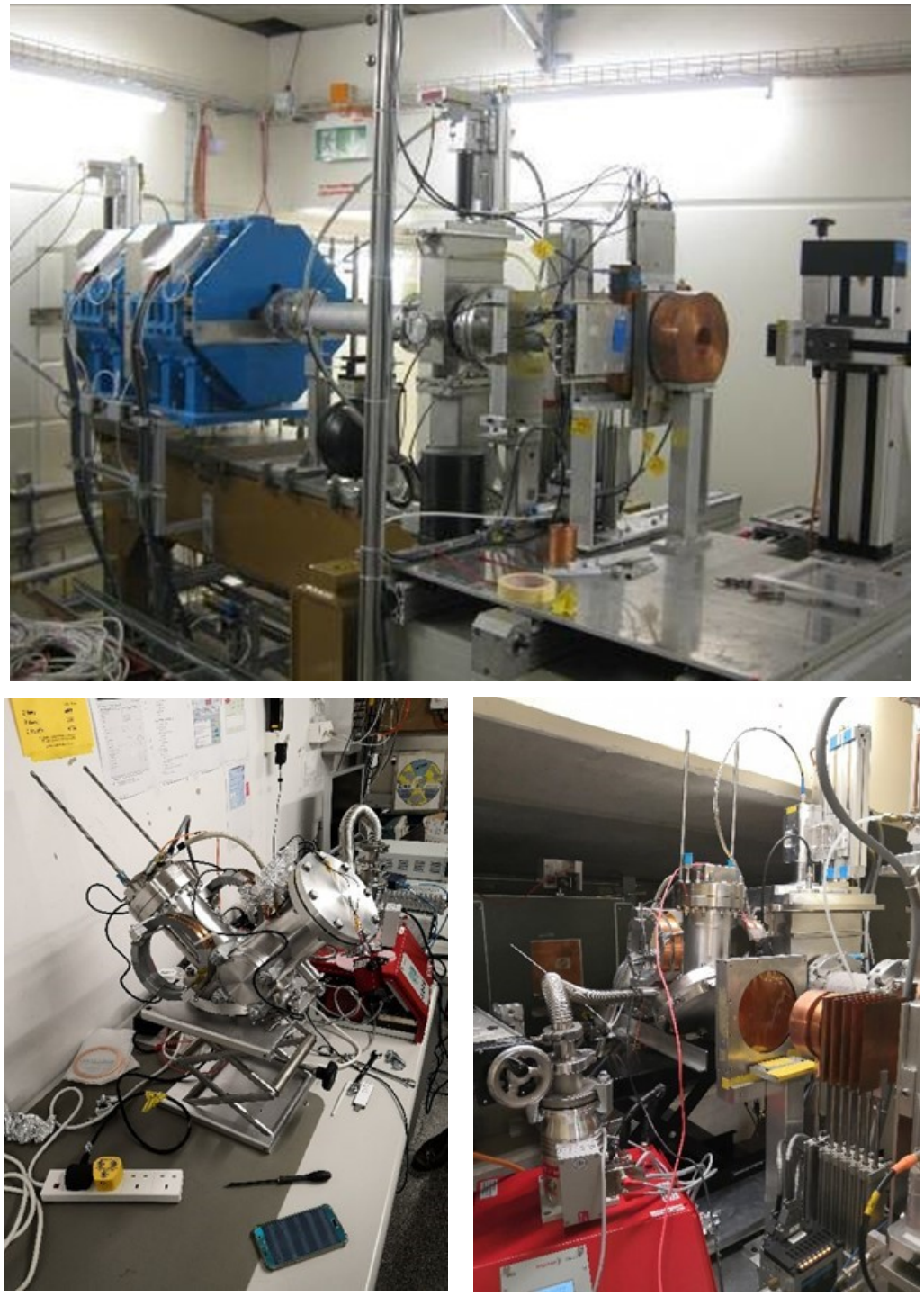

Figure 7.1 Images of the experimental chamber used at the Proton Irradiation Facility (PIF) at PSI. The top image is taken from the PSI PIF website ("Paul Scherrer Institut (PSI)," n.d.) *and shows the beamline on its own with no detector apparatus or chamber. The other images were taken at the beamline during experimental setup, where the experimental chamber on its own is shown in the bottom left image, while the bottom right image shows the experimental chamber in its position in the path of the beamline.*

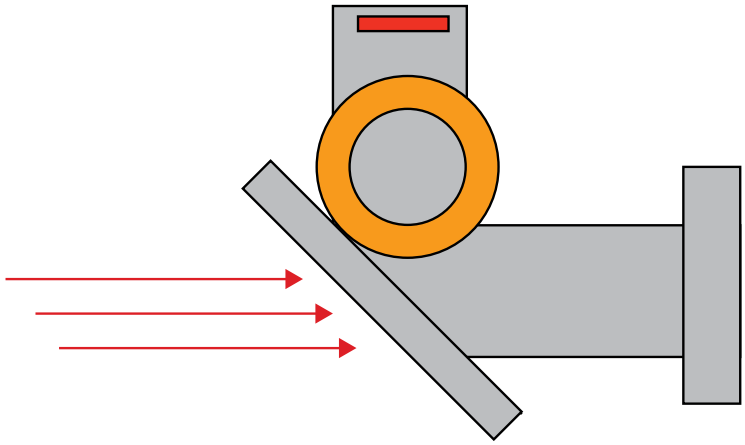

Figure 7.2 A diagram of the design for the experiments performed at the Proton Irradiation Facility (PIF) at the Paul Scherrer Institut (PSI).

While the STERIS beamline experiment and PSI PIF experiment were intentionally designed to have many similarities, there were a few key design differences. The most important difference, as discussed previously, was that the beamline was set to irradiate using 200 MeV protons as opposed to 6 MeV protons. Not only did this mean that the experiment would better reflect the actual radiation environment of space, but it also meant that the aluminium thickness could be increased to 2.828 cm, and added between the target and beamline to model the effect of a 4 cm proton shield on X-ray-like background. As the aluminium plate was oriented at 45 degrees to the beamline, the thickness of 2.828 cm would represent protons travelling through 4 cm of aluminium.

Another difference between this experiment and the STERIS beamline 6 MeV proton irradiation was the existence of an air gap between the beamline and the chamber to be irradiated. An air gap is the norm for experiments at PSI, as air does not significantly modify the energy or direction of 200 MeV protons. However, as this meant there were no flanges to lock the chamber onto, the chamber had to be manually aligned such that the beamline was pointed at the chamber. As the difficulty in determining the exact angle and position of the beamline relative to the chamber could lead to systematic errors in the spectra received by the CCD, stability analysis also had to be performed to determine the significance of these potential errors. Fortunately, errors introduced by this were found to be small.

While the error introduced by uncertainties in the beamline angle were small, a non-insignificant source of error was introduced by the non-uniformity of the PIF beamline. While Harwell uses a uniform beamline, the PIF uses an approximately Gaussian-shaped beamline with a Full-Width Half Maximum (FWHM) of ≈10 cm (“Paul Scherrer Institut (PSI),” n.d.). Fortunately, the PIF gives

dosimetry on the beamline structure, and the beamline count rates across the x and y planes of the beam are given in Figure 7.3.

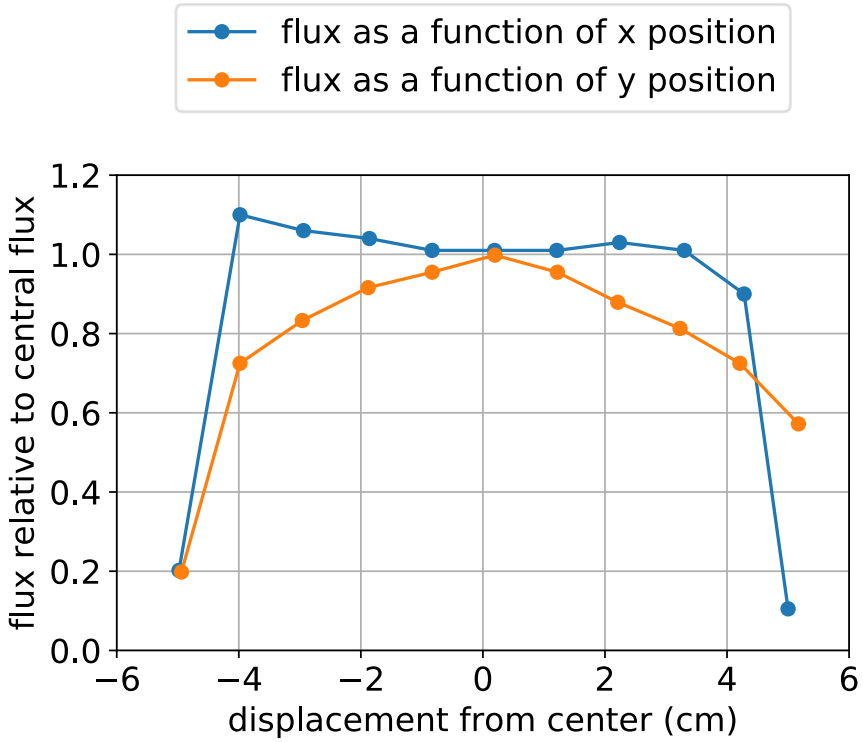

Figure 7.3 The spatial distribution of flux as a function of the x and y positions that are given at PSI. The total flux as a function of both x and y is given by these distributions multiplied together. No error bars were given in the provided dataset. As the spatial distribution of flux was non-uniform, an extra normalisation factor had to be introduced and included in spectra.

Although this distribution deviates significantly from a uniform distribution at the beamline edges, it is possible to approximate the distribution as uniform in simulations by using the effective area of a uniform distribution that when integrated over would produce the same number of particles as the distribution in Figure 7.3.

As was the case in the 6 MeV proton experiment, there was also an error introduced by an imprecise knowledge of the position of the Helmholtz coils. A key difference in this experiment was that the coils were positioned with greater separation between them due to geometric constraints around the chamber, with a separation of 25 cm instead of 16 cm due to geometric constraints at the beamline.

7.2 Simulation setup

Just as the experiment was designed to be similar to the Harwell experiment, much of the code used for Harwell simulations was reused for PSI simulations. The most significant difference was the use of a Geometry Description Markup Language (GDML) chamber geometry, designed using FASTRAD (“FASTRAD Software for Space Radiation Analysis” n.d.; Beutier et al. 2003) by Oliver Hetherington as opposed to a hardcoded geometry. This simulation, therefore, represents the geometry

of the PSI simulation more precisely than the simulations of the STERIS beamline experiment at the expense of some simulation speed. The GDML model describing the simulation geometry is displayed in Figure 7.4.

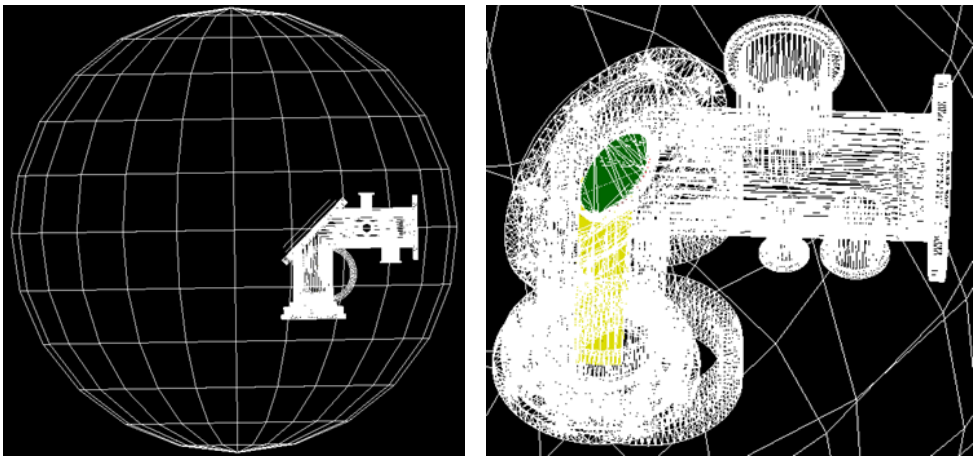

Figure 7.4 The geometry used for simulations of experiments at the PSI Proton Irradiation Facility. This geometry was designed by Oliver Hetherington.

In addition to the changes made to the materials present in the simulations, the magnetic field had to be altered to reflect both the increased separation between coils from 16 cm to 25 cm and an ambient magnetic field within the room discovered during the experiment. This ambient magnetic field was likely generated by the large quadrupole magnets that are placed around the beamline. The ambient magnetic field produced a mean magnetic field across the experimental chamber of (-162 μT, 95 μT, -113 μT), as measured using a Hall probe. As this magnetic field is not insignificant compared to the magnetic fields on the order of several mT generated by the Helmholtz coil structure, this ambient background magnetic field was approximated as a uniform field in Geant4 simulations and added to the magnetic field produced by the Helmholtz solenoids.

Input particles were set to be protons with a uniform circular spatial distribution as was the case in Harwell simulations, approximating the distribution of particles that were expected to be produced at the PSI PIF, once the beam non-uniformity normalisation correction described above was applied.

7.3 Raw image processing techniques

The PSI PIF experiments used almost entirely the same analysis techniques as were used in the Harwell proton source experiment in Chapter 6. The primary difference in image processing in this experiment was that there was a significantly lower density of events in PSI experiments, and that meant that event detection rejected significantly fewer events. This improvement in pile-up meant that there was a lower risk of errors being introduced through the event detection algorithm. However it was found that for electron induced events below approximately 2 keV in energy, event detection did introduce some systematic errors in spectral shape, so the electron continuum below 2 keV will not be

considered in detail here. The Al fluorescence lines also exhibited small deviations in spectral position due to the event detection algorithm.

7.4 Experimental results

The 6 MeV proton beam experiment at Harwell indicated that there is some evidence that Geant4 is simulating the physics of soft electrons correctly, albeit with several caveats, particularly the possibility that the data were likely incorrectly normalised due to errors in beamline dosimetry. The experiments performed at PSI, in contrast, had fewer issues, due to the improved beamline dosimetry and stability and the lesser impact of pile-up.

As was described in Chapter 5, the PSI experiment was not solely designed to test Geant4 and was also designed to examine the impact of different graded-Z shield configurations on the overall background in a space-based environment. This experiment was able to do this because 200 MeV protons are more representative of typical proton energies impacting inner surfaces within a spacecraft structure than the 6 MeV protons used in the Harwell experiment.

The total energy deposition spectra for the irradiation of each material configuration with no magnetic field applied are displayed in Figure 7.5.

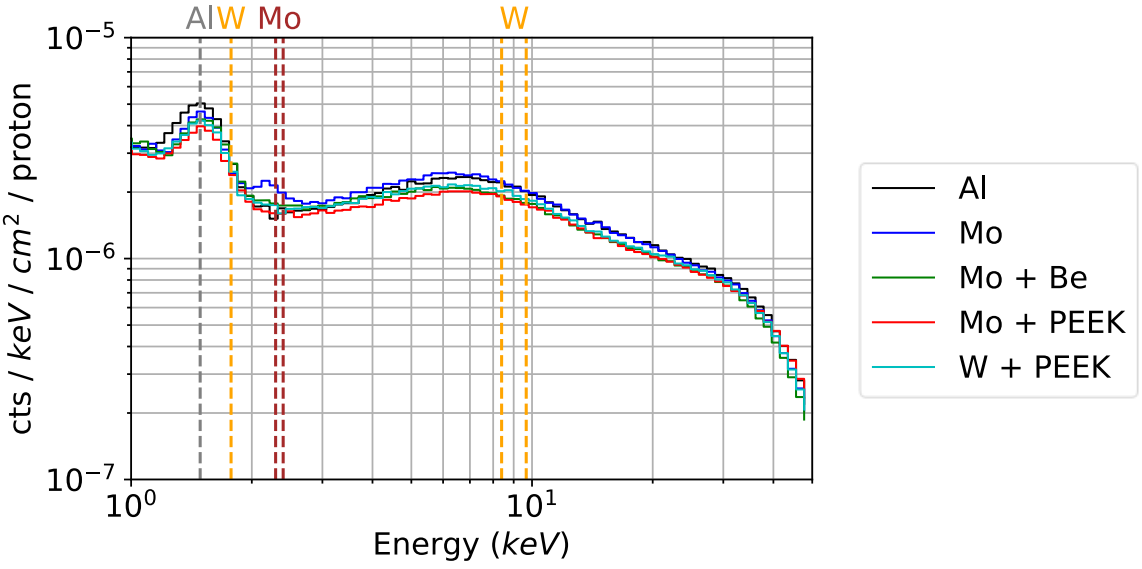

Figure 7.5 The total energy spectrum received for the irradiation of each material configuration of the experimental chamber, the design of which is described in Chapter 5. Errors are not shown as they are reasonably small compared to the count rate. As expected there appears to be a Gaussian peak corresponding to the Al fluorescence line, but there is also a broad high energy peak-like structure between 3 keV and above.

As expected, the aluminium fluorescence line is present in all material configurations at 1.48 keV, as for each configuration there is a significant solid angle of exposed irradiated aluminium within line-of-sight of the detector. For energies between the fluorescence line energy and approximately 6 keV,

the spectrum decreases in size before increasing again, forming a broad peak, and then decreasing again as approximately a power law between approximately 8 keV and 30 keV.

The continuum spectra for each configuration in Figure 7.5 are similar in both structure and total flux. A lack of variation in continuum spectra with respect to material configuration was also observed in Harwell experiments, where electron spectra dominated the continuum. As shall be discussed in Section 7.6.2, simulations indicate that electrons also dominate the PSI spectra for all material configurations.

A particular point of interest is the fact that the PEEK spectrum appears to have an identical continuum to that of the other material configurations despite having a very different chemical structure to the other materials tested, being a plastic rather than a metal, indicating that in addition to not being dependent upon atomic number, the knock-on electron spectrum is also not dependent upon chemical structure.

To analyse this data in full detail, the same techniques were utilised as used in the Harwell experiment, such as comparisons to simulation data and the results of this analysis are described in Sections 7.6 and 7.7. Before comparisons to simulation data were made, however, the experimental data alone could be used to answer some of the main questions this experiment was designed to answer. Of particular importance was the question of whether or not the continuum spectrum changes with material configuration, and whether or not the low-Z materials are capable of removing the Mo fluorescence line.

7.5 The effect of Mo, PEEK, Be and W graded-Z configurations on the spectrum

As was discussed in Chapter 3, any spacecraft structure will contain a complex design made up of numerous materials which means that determining the influence of different materials on the background spectrum is highly important. Therefore one of the goals of this experiment was to experimentally investigate both how the continuum varies with material, and whether or not the low Z materials tested in this experiment act as an effective graded-Z shield. The previous experiment at the STERIS beamline showed no change in continuum spectrum with respect to the material within line-of-sight of the detector, which was concluded to be possibly related to Sternglass' theory of secondary electron emission (Sternglass 1957), and this lack of variation was also discovered in this experiment.

7.5.1 The effect of Mo, PEEK, Be and W on the energy deposition spectrum continuum

The total spectra for Al only, Mo, PEEK, Be and W with the magnetic field applied with a current of 2 A are displayed in Figure 7.6. As was the case in the 6 MeV irradiation in Chapter 5, the fluorescence lines here have become more exposed due to the reduction in electron continuum spectra due to the presence of the magnetic field.

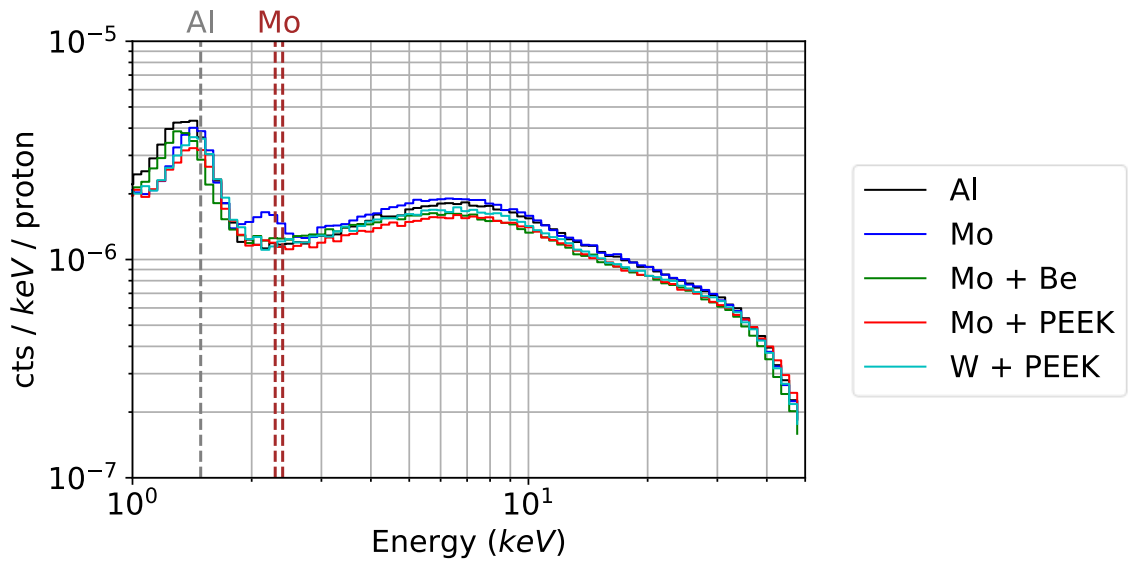

Figure 7.6 The total energy deposition spectrum for the 2 A magnetic field case. The Mo fluorescence lines between 2 keV and 2.5 keV are significantly more visible in this instance due to the reduction of the electron continuum.

The most major differences between the spectra due to the material configuration in Figure 7.6 again appear to be the prevalence and energy of X-ray fluorescence lines, in this case, the Al and Mo fluorescence lines. For each configuration, the Al fluorescence line is present despite the presence of the extra covering materials because in all material configurations the irradiated chamber plate is only partially covered by the sample materials. In contrast, the Mo and W fluorescence lines were found to be completely removed by the presence of the Be and PEEK.

7.5.2 The effectiveness of Be and PEEK at removing Mo and W fluorescence lines

To fully illustrate the effectiveness of Be and PEEK at removing the Mo fluorescence lines, Figure 7.7 displays the same data as Figure 7.6, but only plotted between the energies 1.5 keV to 3 keV.

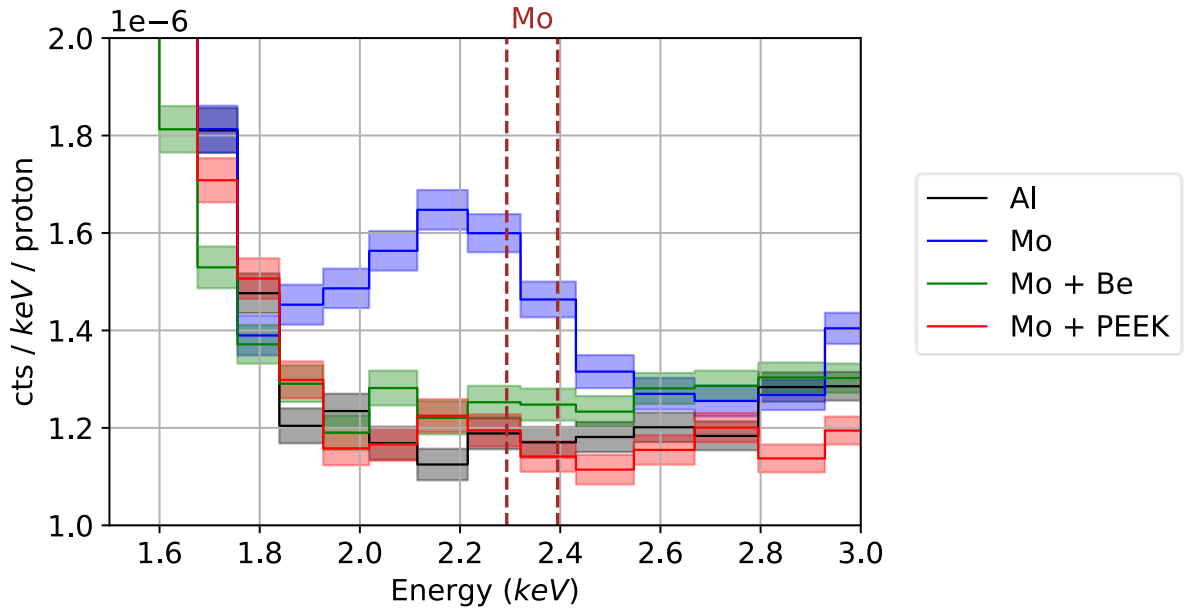

Figure 7.7 The total energy deposition spectrum generated by the Al, Mo, Mo + Be and Mo + PEEK material configurations, plotted between 1.5 keV and 3.0 keV. The Mo fluorescence line can be seen between 2.0 keV and 2.5 keV in the Mo configuration, although it is not present in either the Mo + Be or Mo + PEEK configuration. This indicates that the Be and PEEK are both thick enough to fully attenuate the Mo fluorescence line, as expected.

In Figure 7.7 it can be seen that both Be and PEEK are fully attenuating the Mo fluorescence line, as the spectrum appears to have reduced to the same electron-only spectrum that is present in this energy range for aluminium. Figure 7.8 displays the same plot but for W with PEEK compared to aluminium for the 1.775 keV and 8.398 keV X-ray fluorescence lines, where the spectrum again matches with the Al only configuration, with some deviation in the Al line location. This deviation is likely due to a slight offset in the gain, and the similar height of the Gaussian distributions indicates that they are indeed the same fluorescence line. Therefore it is likely that the PEEK is successfully attenuating the 1.775 keV line, and may be successfully attenuating the 8.398 keV fluorescence line, although this is less clear as it is also possible that the detector quantum efficiency is not sufficient at this energy to detect significant quantities of the 8.398 keV fluorescence line even when the PEEK is not present.

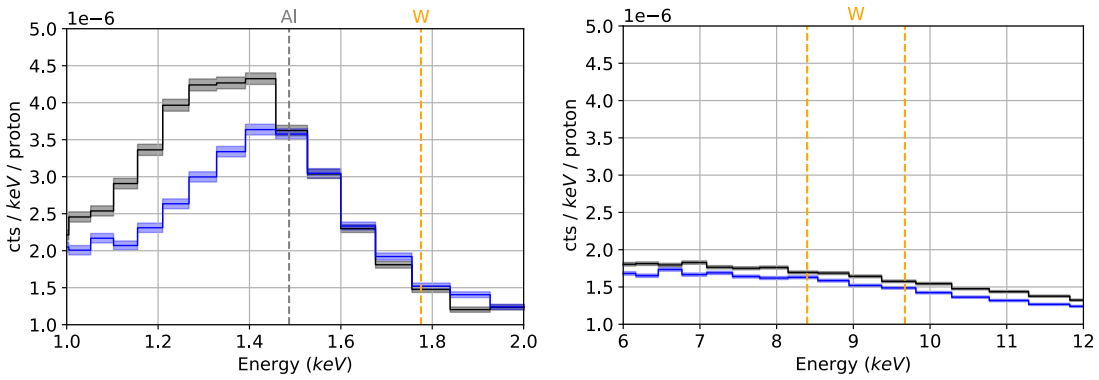

(a) (b)

Al only
W + PEEK

Figure 7.8 The total energy deposition spectrum plotted between 1.0 keV and 2 keV, and 8 keV and 9 keV. In each case, tungsten fluorescence lines do not seem to be present in significant quantities.

Both of these sets of experiments indicate that as expected, 1 mm of Be or PEEK is capable of fully attenuating the *Kα* Mo and W fluorescence lines without negatively impacting the continuum and that both materials would, therefore, be suitable for use in a graded-Z shield from a physics perspective.

7.6 Validating Geant4's treatment of secondary particle production from 200 MeV protons

The experimental spectra in the previous section indicate that the background continuum spectrum does not vary significantly with the material configuration in this experiment and that each graded-Z material in this case successfully attenuates the Mo fluorescence line fully. However, comparisons with simulations were necessary to answer further questions, including whether or not the experiment is indeed representative of the space-based background and how accurately Geant4 can simulate the physics of high energy protons generating secondary background in detectors.

In the 6 MeV experiments at the Harwell proton source it was found that while Geant4 successfully predicted the power law that the spectra followed for both the Al and C configurations, the experimental spectrum was found to be approximately a factor of ~7.5 greater than the simulation data. This discrepancy was believed to have been either caused by normalisation errors relating to uncertainties in the flux of the STERIS beamline or by Geant4 incorrectly simulating the physics of the situation. In this experiment, however, there appears to be relatively little difference in between simulation and experiment in terms of overall normalisation, and the Geant4 simulations appear to follow the experimental energy deposition spectra relatively accurately for much of the energy range.

7.6.1 Comparing the Geant4 energy deposition spectrum with experiment

As with the simulation data from the STERIS beamline experiments, it is worthwhile to examine the simulation data in detail and investigate features such as the physics invoked by Geant4 in these simulations.

The total experimental energy deposition spectra for each configuration are displayed in Figure 7.9, compared to the Geant4 simulated energy deposition spectra. In each configuration, for energy depositions higher than approximately 5 keV, the Geant4 spectra appear to be in good agreement with experimental spectra. The height of the aluminium fluorescence line is also in good agreement with the Geant4-produced aluminium fluorescence line, within the constraints of the systematic errors introduced by the event detection algorithm.

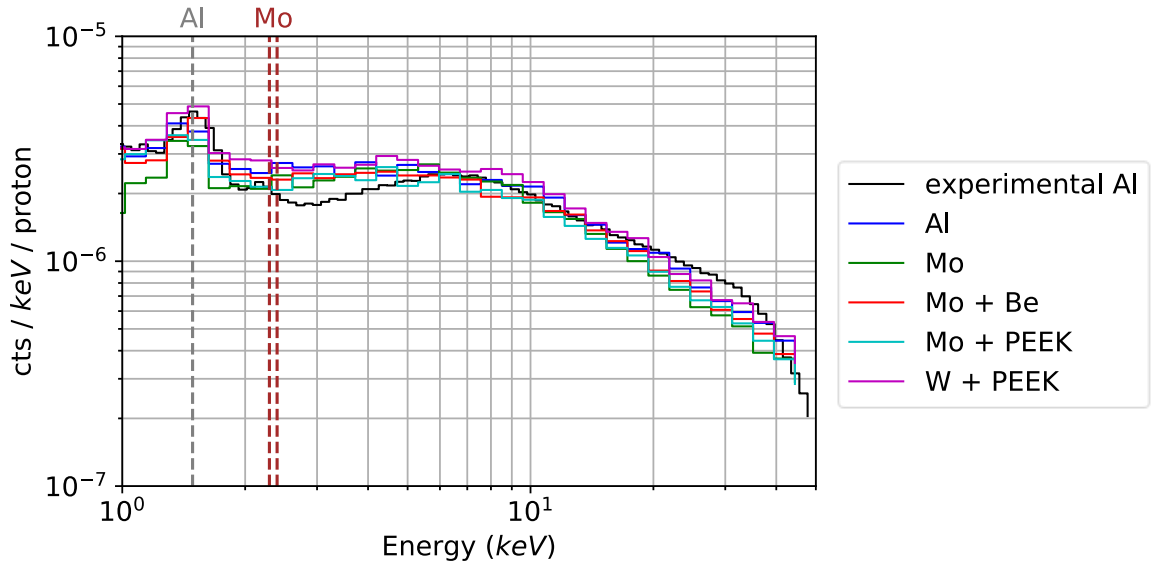

Figure 7.9 The total energy deposition spectra for each simulated material configuration, and the experimental Al only configuration. All the simulation configurations appear to follow the experimental spectral shape at energies above approximately 5 keV.

Between 2 keV and 5 keV there is significant spectral deviation between Geant4 and the experiment, where Geant4 simulations appear to overpredict the spectrum by up to approximately a factor of 2. There are several possible explanations for this.

One possible explanation is that the real detector is less sensitive to low energy electrons than the simulated detector, as low energy electrons have significantly lower CSDA ranges than the attenuation lengths of photons of equivalent energies (Xcom 2010). This is an effect that has been observed in previous experiments using the CCD97 with regards to low energy photon absorption by Moody et al. (2017).

In the experiments performed by Moody et al., the CCD97 detectors used were found to have a significantly lower quantum efficiency for photons with energies of approximately several hundred eV than were predicted by theoretical models. One explanation that has been proposed is that this is due to surface layers of the device exhibiting a low Charge Collection Efficiency (CCE) due to the internal shape of charge potentials. This means that energy deposited within the first tens or hundreds of nanometers of the device surface might not be registered in images. As electrons of several keV in kinetic energy have a CSDA range than is comparable to the attenuation length of photons with

several hundred eV in energy (for instance a 2.043 keV electron in silicon has a CSDA range of 100.9 nm (Pianetta 1986), while a 100 eV photon in silicon has an attenuation length of 134 nm (Xcom 2010)), it is possible that deposited energy from electrons specifically in the 2 keV to 5 keV kinetic energy range is being lost. Energy deposited by backscattering electrons may also be being lost too, as backscattering electrons often deposit energy within the surface layers of a device. This illustrates the importance of future experiments to validate Geant4 using a variety of devices in order to control for possible un-simulated aspects of a particular device as much as possible.

Some preliminary work was also performed to apply a correction method developed by Jonathan Keelan to the simulated data to account for this CCE issue. As this work only represents the first steps to developing a valid model for correcting the CCE, and because the correction method contains several unverified and sizeable assumptions, the corrected spectra are not shown here however they are displayed in Section 4 of Eraerds et al. (2020), which was written during this PhD project. While the spectra with the CCE correction method applied do not match the experimental data within statistical errors, the corrections do significantly reduce the size of the discrepancy between the simulation and experimental data. Therefore, it is certainly possible that a full model of the device CCE may be able to account for the discrepancy between the experimental data and simulated data.

While the experimental evidence from Moody et al. and CCE corrections displayed in Eraerds et al. indicates that charge collection efficiency will likely be having at least some effect on the generated experimental spectra, the possibility cannot yet be ruled out that Geant4 could be overestimating the intensity of secondary particles with energies in the 2 keV to 5 keV region of the spectrum. Should this interpretation be correct, this would mean that Geant4 is erroneous for the particles depositing energy at this particular region of the spectrum, meaning that simulations of the space-based environment using Geant4 may generate erroneous spectra between 2 keV and 5 keV. The possibility of this being true will be investigated further in Section 7.7 using the Helmholtz coil magnetic field.

7.6.2 Validation of Geant4's treatment of high energy knock-on electrons

One method of splitting the energy deposition spectra into components is to split by particle species incident upon the detector. The spectrum for the Al only material configuration split into different particle species is shown in Figure 7.10 and in Figure C.1 in Appendix C, where it can be seen that for all material combinations, the continuum spectra are dominated by electrons and that the only photon contribution to the spectra are fluorescence lines. The fact that the continuum spectra appear to be primarily composed of an electron continuum and photon fluorescence lines means that a validation of the total spectrum is only able to verify Geant4's treatment of the electron and fluorescence induced spectral components. Unfortunately, this means it was not possible to verify other components such as the Compton photon continuum which is known to also be present in space-based detectors.

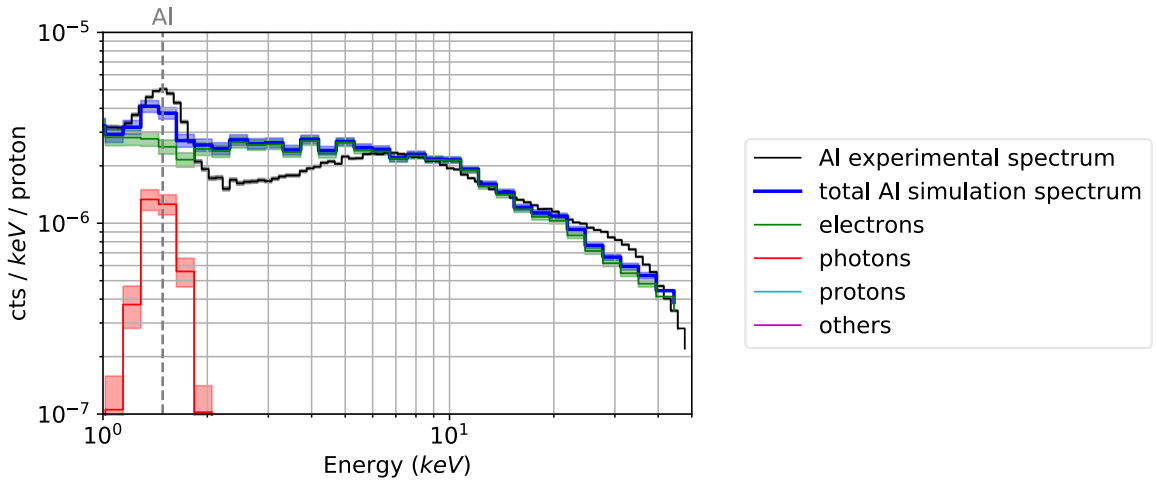

Figure 7.10 The simulated energy deposition spectrum, split by particle type. The continuum spectrum appears to be dominated by electrons, and the only significant non-electron energy deposition source appears to be the fluorescence line at 1.48 keV.

As has been discussed previously in Chapter 3, there are many cases where the energy registered in a detector by a particle event is not equal to the kinetic energy of the particle that created the event. Particle impacts such as Minimally Ionising Particles (MIPs) passing through a detector, or particles backscattering from a detector surface are both capable of creating particle events in detectors of lower energies than their kinetic energy.

To characterise the kinetic energies of electrons present in the PSI experimental spectra, it is useful to separate parts of the spectrum dominated by MIPs from parts of the spectrum dominated by fully absorbed low energy electrons. Separating the spectra like this is necessary for assessing the accuracy of Geant4 with respect to particle kinetic energy, as Geant4 is known to exhibit different accuracies at different particle energies, as discussed in Chapter 5.

Separating the spectra into particles that deposit the entirety of their energy and a fraction of their energy is straightforward as the kinetic energy of particles is directly printed in output files along with the deposited energy. However, separating fully-penetrating particles from backscattering particles is more complex, and requires splitting the spectrum by maximum penetration depth.

Figure 7.11 displays the maximum penetration depth into the detector for simulated particle hits in the 1 keV to 15 keV energy deposition range for particles that deposit less energy than their kinetic energy.

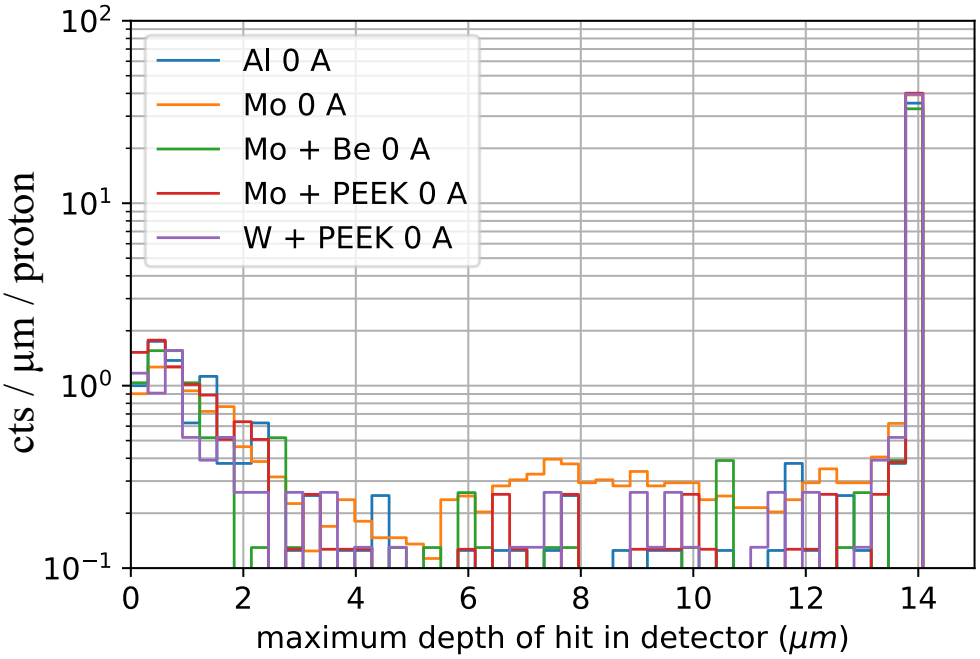

Figure 7.11 A normalised histogram of maximum penetration depth for particle hits between 1 keV and 15 keV. There appear to be two distinct peaks, a peak between 0 µm and 2 µm, and a peak at 14 µm. These peaks likely correspond to a backscattering peak, and a fully-penetrating peak, respectively. The data displayed here has less statistics than data displayed earlier in this chapter as these plots were generated from earlier datasets which were run over a shorter period of time.

Two significant peaks can be observed in Figure 7.11, the first between 0 µm and approximately 2 µm, and a second at 14 µm, representing the two sides of the detector. These peaks correspond to the backscattering and fully-penetrating peaks respectively, where the 14 µm peak is significantly larger than the 0 µm to 2 µm peak, indicating that the majority of the high kinetic energy spectrum is composed of fully-penetrating particles.

The maximum penetration depth can be combined with particle kinetic energies to generate the kinetic energy spectra displayed in Figure 7.12(a) and Figure 7.12(b).

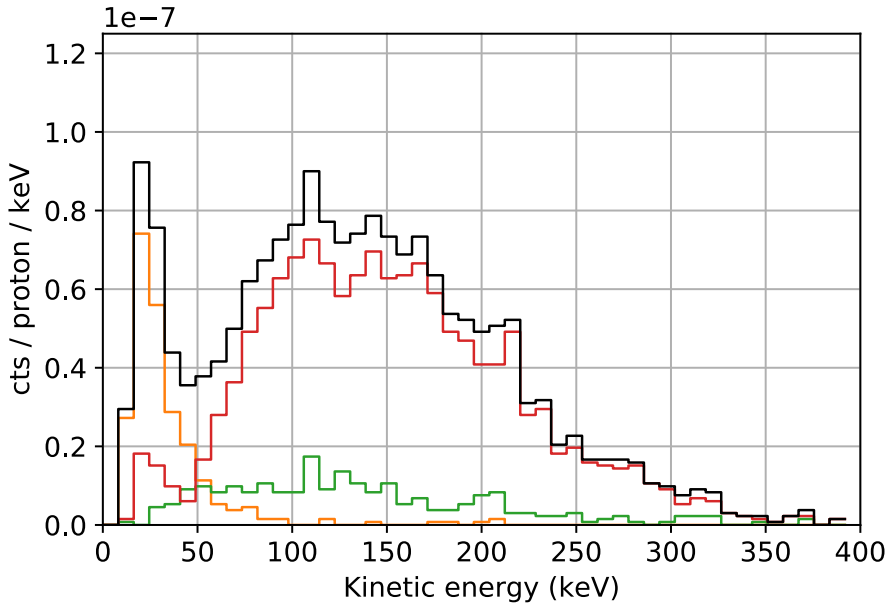

(a)

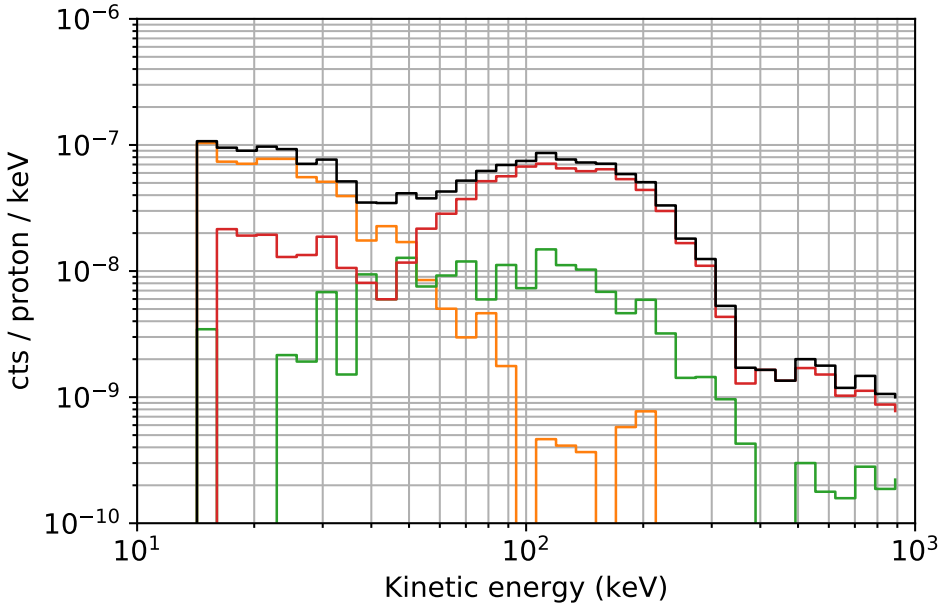

(b)

Figure 7.12 Histograms displaying the kinetic energies of particle hits that have kinetic energies greater than 15 keV (in linear space for Figure 7.12(a), and logarithmic space for Figure 7.12(b)). The kinetic energy of particles corresponding to a final depth of less than 2 μm, likely corresponding to backscattering particles, appears to be between 15 keV and 50 keV, whereas the spectrum of particles that fully penetrate the detector appears to peak between 50 keV and 200 keV.

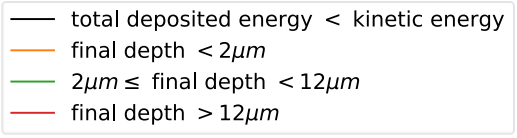

Figure 7.12 indicates that the kinetic energy spectrum for backscattered events peak at approximately 20 keV while the kinetic energy spectrum for fully-penetrating events have a higher energy peak corresponding to between 50 keV and 200 keV.

A similar figure can also be plotted, splitting the energy deposition spectra into components instead of the kinetic energy spectra. Figure 7.13 and Figure 7.14 display the spectra for the Al and Mo material combinations, separated by kinetic energy, while Figure 7.15 displays the same data as Figure 7.14 but with high kinetic energy components split even further into components that were either backscattered or fully-penetrating.

Figure 7.13, Figure 7.14 and Figure 7.15 indicate that the large peak observed above 5 keV specifically represents a fully-penetrating particle peak, whereas backscattering and fully absorbed particles appear to dominate at lower energies. The full range of spectra split by particle kinetic energy for all material and solenoid current configurations can be found in Figure C.1 in Appendix C. The results given in Figure 7.13, Figure 7.14 and Figure 7.15 indicate that Geant4's treatment of electron MIPs and the creation of electron MIPs by incoming protons is somewhat validated and that to validate Geant4's treatment of backscattered electrons and knock-on electrons it is necessary to investigate the spectrum of particles in this situation at lower energies than the MIP peak. One method for doing this using the Helmholtz coils present in the experiment is examined in further detail in Section 7.7.

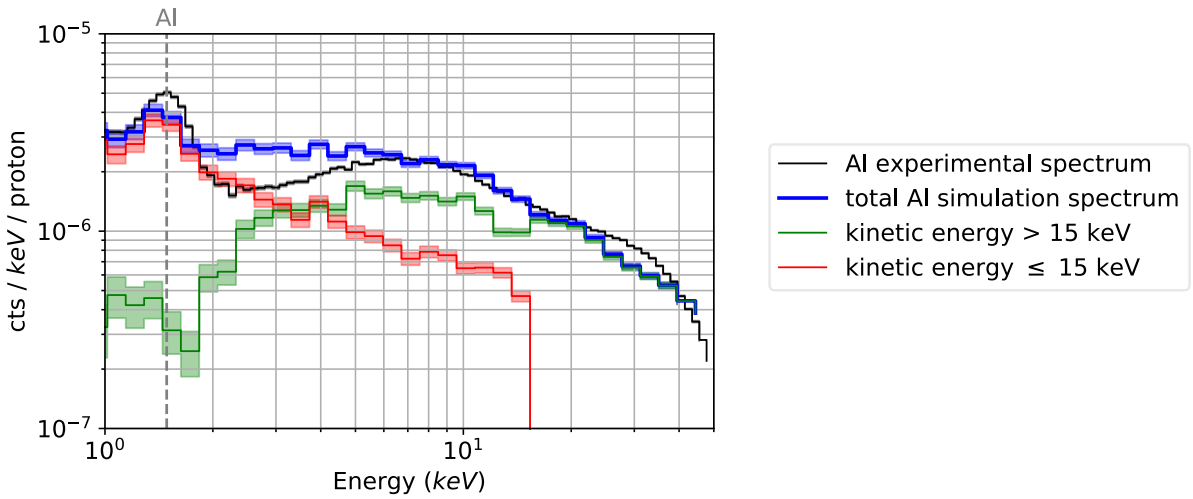

Figure 7.13 The total energy deposition spectrum for the Al only material combination split into components generated by particles with kinetic energy less than 15 keV and particles with kinetic energies more than 15 keV. The energy deposition spectrum above 5 keV appears to be dominated by particles with kinetic energies greater than 15 keV.

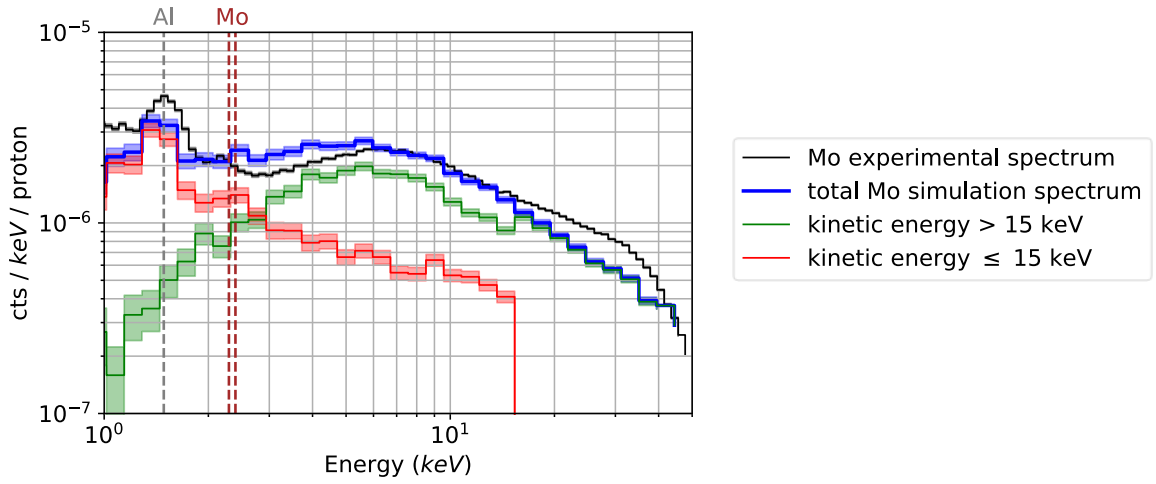

Figure 7.14 The total energy deposition spectrum for the Mo material combination split into components with kinetic energies greater than 15 and less than 15. It appears that, as in the Al only configuration, the wide peak between 3 keV and above is dominated by particles of greater than 15 keV in energy.

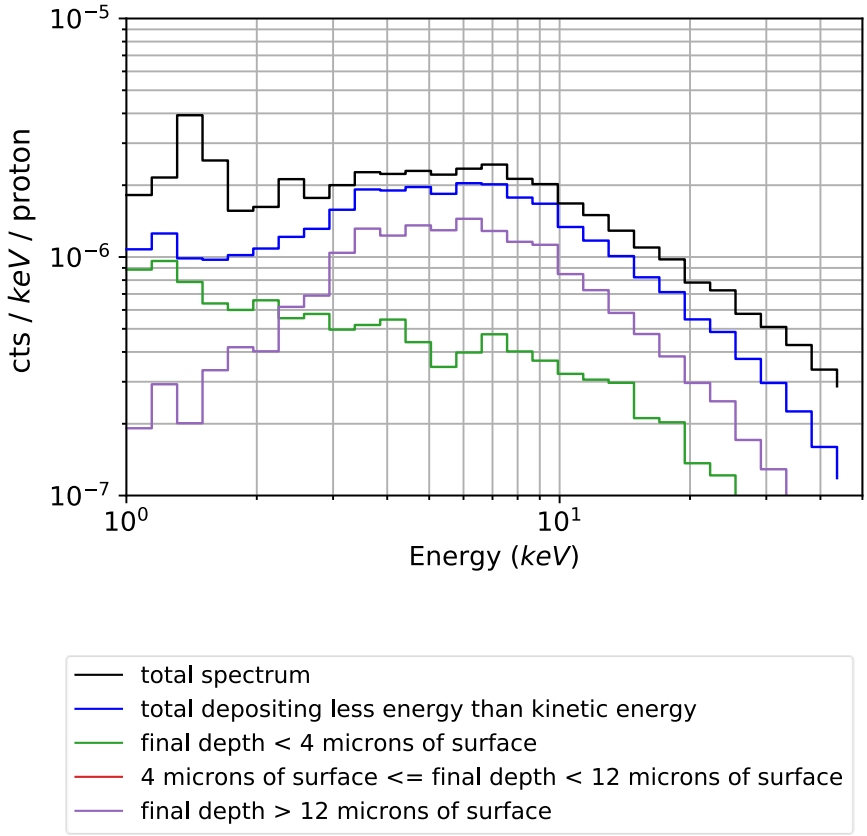

Figure 7.15 The total simulated energy deposition spectrum for the Mo material configuration split by penetration depth. It appears that the wide peak above 5 keV is primarily dominated by fully-penetrating electrons, plus an additional backscattering component. Note that this plot has smaller bin widths than Figure 7.13 and Figure 7.14, so more detail can be seen. This plot is somewhat different to the other plots in this chapter as it used earlier data from the same simulations but with statsitics and without Fano noise applied, which is why the Al fluorescence line is not a Gaussian in this plot.

The spectra displayed in each of these figures indicate that the soft electron (less than 15 keV in kinetic energy) continuum only appears to become significant below approximately 5 keV. This

indicates that the excess hits described earlier in the 2 keV to 5 keV range in the Al only case may be caused by Geant4 treating low energy electrons differently to the higher energy fully-penetrating particles, or that unsimulated aspects of the detector may be causing some low energy electrons to be lost from images. The analysis of spectra using the Helmholtz coils in Section 7.7 will also provide some evidence that this may be the case, where taking the difference between spectra at different magnetic field strengths also shows an excess of low energy electrons in specifically the Al case.

7.6.3 Validation of physics processes

In addition to looking at the particle type and energy, it is also possible using Geant4 to probe the physics underpinning the creation of a particle. As discussed in Chapter 5 and in the analysis of the 6 MeV experiments at Harwell proton source in Chapter 6, Geant4 contains separate physics processes that define the probabilities of events and interactions occurring. Therefore, if Geant4 simulations do not match with experiment, then this implies that one or more physics processes are producing incorrect interaction cross-sections for the particular energy range and particle species being simulated. Therefore by examining the physics processes involved in the creation of events in the detector, and determining which physics processes are generating particles detected within different regions of the spectrum, it is possible to assess the accuracy of individual physics processes.

Each particle in Geant4 is labelled with the physics process that was invoked for the particle's creation. Even though there will sometimes be multiple processes that were involved in the chain of interactions from the impact of a primary particle to the creation of a particle that impacts the detector, it is difficult within Geant4 to determine what these processes were, although verifying Geant4's treatment of the final particle creation process may also indicate that the chain of processes leading up to the final creation process were simulated accurately.

Figure 7.16 and Figure 7.17 show the particle spectra for the Al only and Mo material configurations split into particle creation process components respectively. In all material combinations, hadron ionisation appears to dominate as a physics process across the spectra, with the only other physics processes responsible for significant additional flux at specific parts of the spectra being Compton scattered electrons between 2 keV and 5 keV, and electron ionisation at the fluorescence line energies.

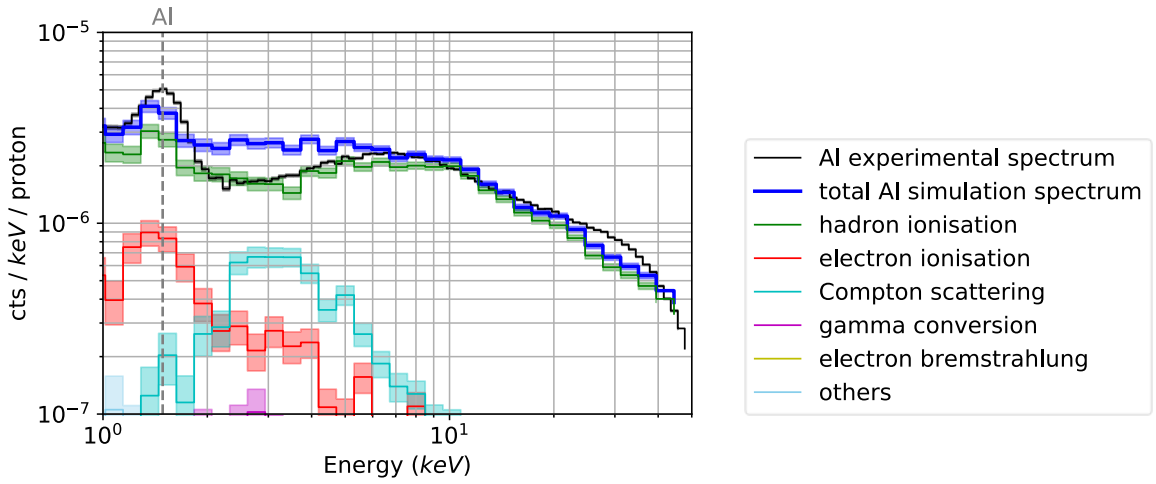

Figure 7.16 The energy deposition spectrum for the Al only material configuration, split by particle creation process. Particles created by hadron ionisation appear to constitute the majority of the spectrum, although there is some contribution from the electron ionisation and from Compton scattering.

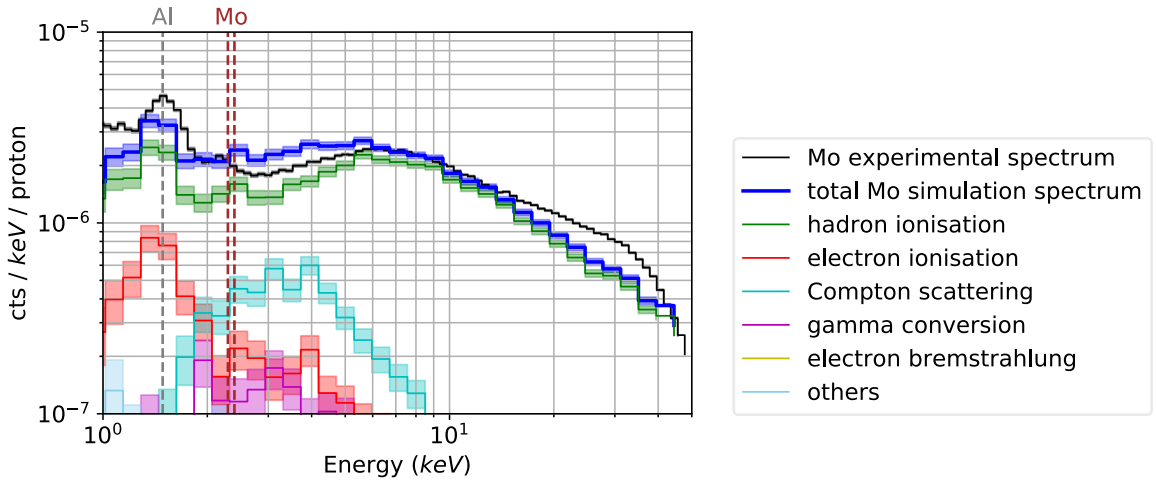

Figure 7.17 The total energy deposition spectrum for the Mo configuration split by creation process. The majority of the spectra in both the Al and Mo cases appears to be composed of particles generated by hadron ionisation, although there is some contribution from electron ionisation and Compton scattering.

The fact that Compton scattered electrons appear to only be significant between 2 keV and 5 keV, and that the hadron ionisation component in Figure 7.16 matches the experimental spectrum well implies that the presence of the Compton scattering component here could be causing the discrepancy between the simulation spectra and experimental spectra here. While this is a plausible explanation, as the Compton scattering component appears at approximately the same location for each spectrum, results described at different magnetic field strengths in Section 7.7 will cast some doubt on this hypothesis.

As shall be seen in Chapter 8, the dominant physics processes present in Figure 7.16 and Figure 7.17 do represent several of the physics processes expected to be involved in the actual radiation environment of space, but there are several processes present in the space radiation environment that are unfortunately unrepresented in the creation processes shown here. Therefore, even though this

experiment represents a partial verification of Geant4 in a space-based environment, there remains some physics unaccounted for in this particular experiment which may need to be separately verified in follow-up experiments.

Despite this limitation it can be concluded that the generation of high energy knock-on electrons through hadron ionisation, and potentially the generation of fully depositing soft electrons by hadron ionisation in Geant4 appears to exhibit reasonable accuracy within this experiment should the Compton scattering physics process by erroneous in these simulations.

7.6.4 Comparisons between physics lists and Geant4 versions

All of the simulations described in this chapter so far were performed using version 10.4.p01 of Geant4 and with the Space User's Physics List. However, as described in Chapter 5, Geant4 is known to produce different results with different physics lists and different versions.

As has been shown previously in the 6 MeV irradiation performed at the STERIS beamline, the choice of production cut length and the choice of physics list used can also significantly alter the spectrum produced in a Geant4 simulation. Therefore to validate Geant4 it is necessary to compare Geant4 simulations with a variety of physics lists to the results in this experiment, to assess the accuracy of each physics list for the simulation of the space-based environment, and to determine which physics list is most accurate in this scenario.

The Al only configuration total energy deposition spectrum for the Space Users Physics list for both Geant4 10.04.p01 and 10.03.p03, PENELOPE physics list and the LIVERMORE physics list are displayed in Figure 7.18, where PENELOPE and LIVERMORE were also used with Geant4 10.04.p01. The spectra for each of the physics lists for Geant4 version 10.04.p01 appear to be in good agreement with both each other and with the experiment. However, the Space Users physics list for Geant4 version 10.03.p03 appears to diverge significantly with the experimental spectrum at all energies.

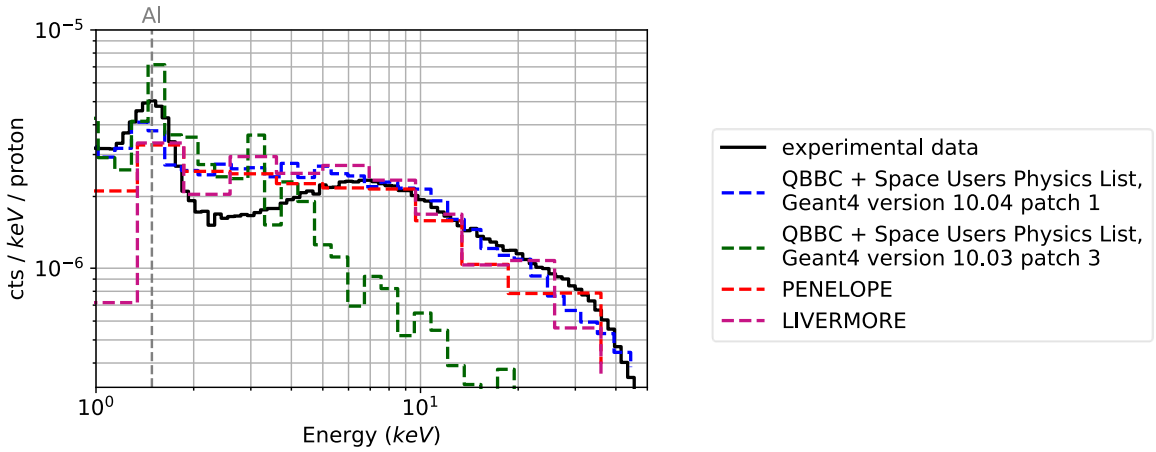

Figure 7.18 A comparison between the total energy deposition spectrum for each tested physics list. There appear to be few differences between each physics list that are more significant than the simulation statistical errors. There also appears to be a normalisation difference between the spectra, although this could be related to the event detection acting differently upon each spectrum.

The divergence of the 10.03.p03 spectrum from the other spectra at energies greater than approximately 5 keV is likely due to the fact that the Space Users physics list version used was 10.04.p01, which is designed to be used with the corresponding version of Geant4.

The spectra for each of the physics lists and versions are also displayed in Figure 7.19(a), Figure 7.19(b), Figure 7.19(c) and Figure 7.19(d), split by particle creation process.

QBBC + Space Users Physics List, Geant4 version 10.04 patch 1

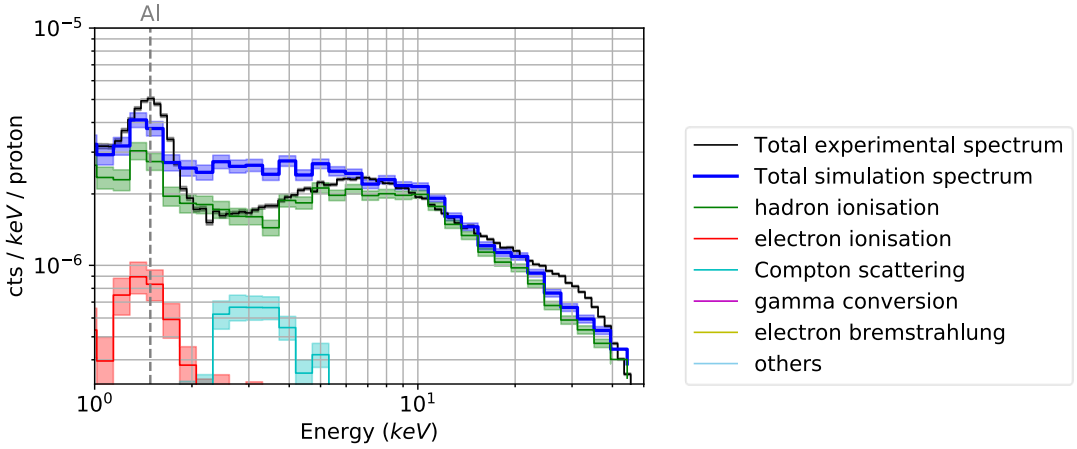

(a)

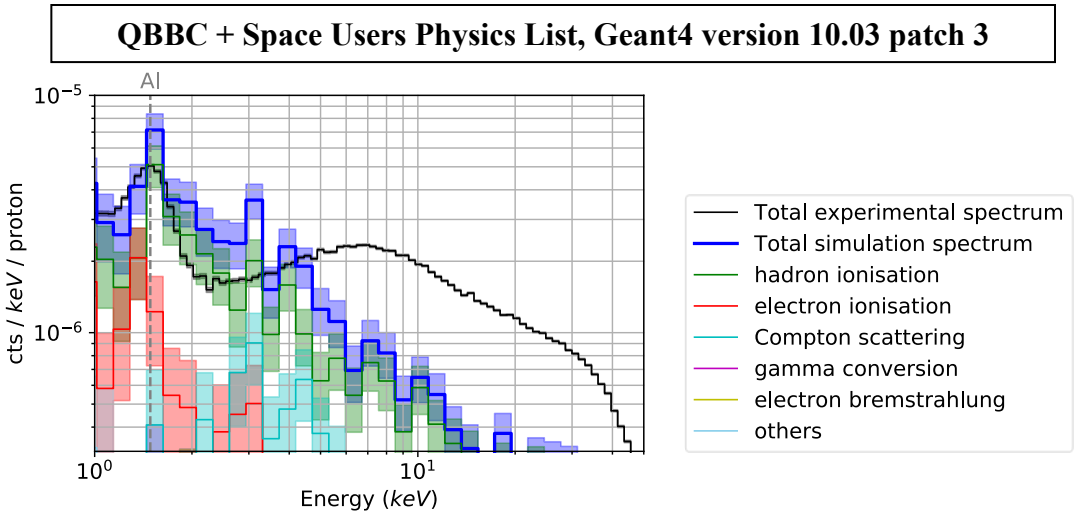
QBBC + Space Users Physics List, Geant4 version 10.03 patch 3
Al
10^{-5}
10^{-6}
cts / keV / proton
10^{0}
10^{1}
Energy (keV)
Total experimental spectrum
Total simulation spectrum
hadron ionisation
electron ionisation
Compton scattering
gamma conversion
electron bremstrahlung
others

(b)

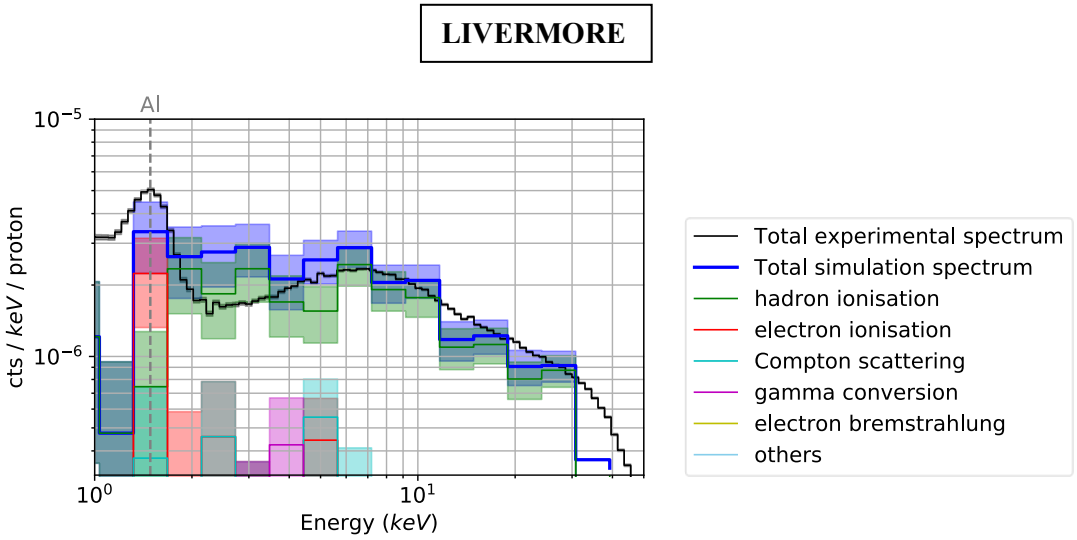
LIVERMORE
Al
10^{-5}
10^{-6}
cts / keV / proton
10^{0}
10^{1}
Energy (keV)
Total experimental spectrum
Total simulation spectrum
hadron ionisation
electron ionisation
Compton scattering
gamma conversion
electron bremstrahlung
others

(c)

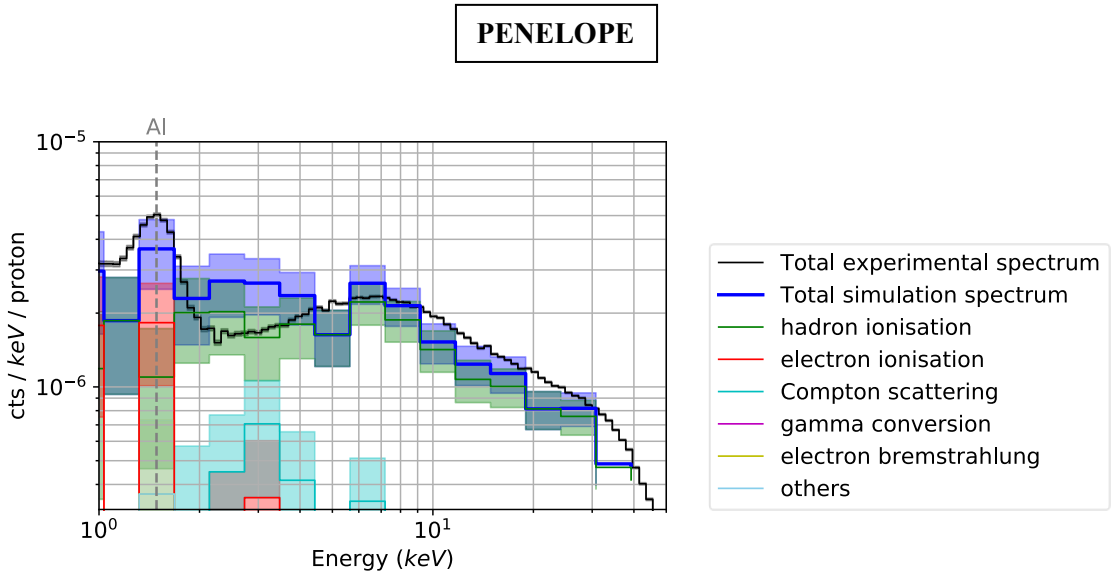

(d)

Figure 7.19 The spectra for the Al only case, split by particle creation process for each physics list. There appear to be few differences in the creation processes contributing to the spectrum that are not within statistical errors in the simulations, with the exception of the spectrum in the Geant4 v10.03.p03 simulation.

Each of the spectra aside from the 10.03.p03 spectrum exhibit similar characteristics, and appear to approximately agree with each other. As the deviation between physics lists is small each of the three physics lists will be assumed to be acceptable for space-based simulations within the limitations of this experiment. In Chapter 8, some test simulations will also be presented using different physics list configurations in order to verify that different Geant4 physics lists produce the same results.

7.7 Further validation of Geant4 using the Helmholtz coil magnetic field, and partial verification of Geant4's treatment of soft electrons

As was discussed earlier in this chapter, a Helmholtz coil was used in this experiment and in the 6 MeV STERIS beamline experiment described in Chapter 6 to remove secondary electrons from the spectrum. In Section 7.5 this was used to expose the 2.293 keV and 2.395 keV molybdenum fluorescence lines, and allow for better comparisons of graded-Z shielding configurations. However, it is also possible to use the removal of low energy secondary electrons to verify if Geant4 is successfully producing the correct low energy electron spectrum, as was used in the 6 MeV proton experiments.

Additionally, as the trajectory of a particle in a magnetic field is not only dependent on particle energy but also particle direction, a verification of Geant4's correct simulation of the energy deposition spectrum under a magnetic field would provide strong evidence that Geant4 is correctly modelling the angular differential cross-sections for physics processes.

7.7.1 The effect of a magnetic field on the total energy deposition spectrum

The total energy deposition spectra at different magnetic field strengths for both the simulations and the experiment are displayed in Figure 7.20 and Figure 7.21, for each material and Helmholtz coil current configuration. The total energy deposition spectra split into particle kinetic energy categories for each configuration are also plotted in Figure C.1 in Appendix C. Between a current of 0 A and 2 A, the spectrum decreases by a factor of approximately 25%, which is significantly less than would be expected if the spectrum were mostly composed of low energy electrons. As the gyroradius of an electron of energy 7 keV is 14 cm, which is less than the distance to the detector of ~17 cm, it would be expected that an electron initially travelling toward the detector should be almost entirely prohibited from reaching the detector, something that was found to be true in the experiments at Harwell described in Chapter 6.

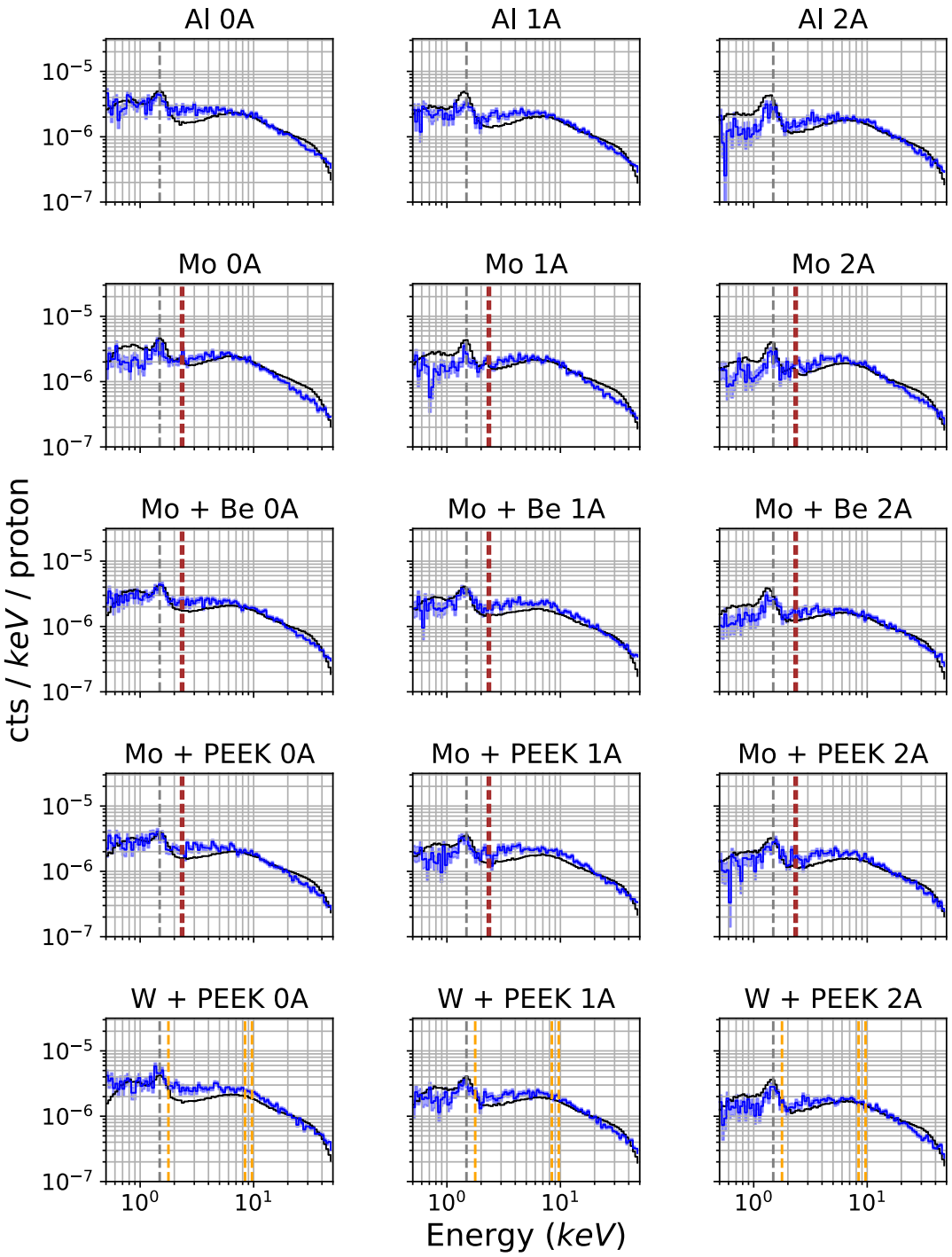

Figure 7.20 The total experimental and simulation energy deposition spectra plotted for each material and magnetic field current combination. Each simulation configuration appears to fit the experimental spectrum within statistical errors for energies above 5 keV, although for all material configurations apart from the Mo configuration, there appears to be a significant excess of simulation particle hits between 2 keV and 5 keV. This excess appears to decrease with increasing magnetic field strength, indicating that the excess may be caused by low energy fully absorbed particle components.

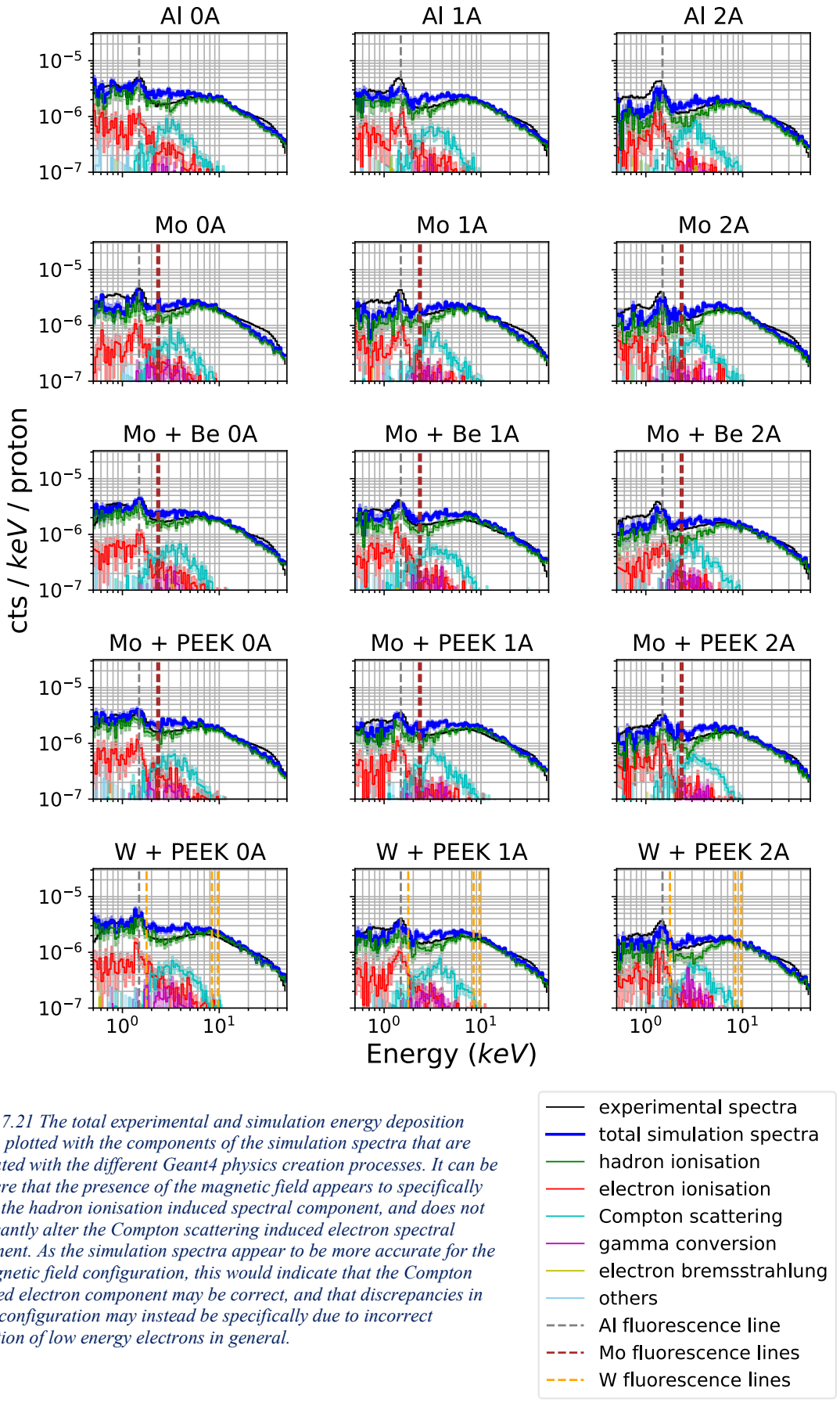

Figure 7.21 The total experimental and simulation energy deposition spectra plotted with the components of the simulation spectra that are associated with the different Geant4 physics creation processes. It can be seen here that the presence of the magnetic field appears to specifically reduce the hadron ionisation induced spectral component, and does not significantly alter the Compton scattering induced electron spectral component. As the simulation spectra appear to be more accurate for the 2A magnetic field configuration, this would indicate that the Compton scattered electron component may be correct, and that discrepancies in the 0A configuration may instead be specifically due to incorrect simulation of low energy electrons in general.

Figure 7.20 indicates that Geant4 appears to be producing an approximately accurate continuum spectrum for each Helmholtz coil current for energy depositions above approximately 5 keV. In all cases, Geant4 and the event detection algorithm also appear to be producing an approximately correct fluorescence line height. While some of the material configurations appear to deviate in both fluorescence line shape and continuum shape below approximately 2 keV, such as for the molybdenum simulations, analysis found that this is caused by systematic errors introduced by the event detection and not Geant4. As discussed previously, these systematic errors only affected the spectra in some configurations, and below 2 keV, and did not dramatically alter the height of fluorescence lines.

The fact that the continuum is not significantly altered by the presence of the magnetic field further verifies the suggestion from Geant4 simulations that this spectrum is composed of electrons with higher energies than 15 keV, as indicated in Section 7.6.2 by splitting the spectrum by particle composition. This is because, as was discussed in Chapter 2, magnetic fields cause greater deviations in trajectories of particles with lower kinetic energies, and it was therefore expected that the magnetic field should be capable of entirely deflecting almost all electrons with kinetic energies up to 15 keV. In contrast, fully-penetrating particles in these simulations were found in Section 7.6 to typically have kinetic energies between 50 keV and 200 keV, which are significantly less deflected than particles with kinetic energies of 15 keV.

A particular point of interest in Figure 7.20 is that the discrepancy between the simulation and experimental data between energy depositions of 2 keV and 5 keV decreases significantly with magnetic field strength, and almost completely disappears when the solenoid current is set to 2A. This implies that Geant4 could be overestimating the number of soft electrons the detector is receiving, or that unsimulated aspects of the detector such as Charge Collection Efficiency (CCE) could specifically be causing energy depositions by soft electrons to not be registered in images. Soft electrons however do not appear however to have been generated by the Compton scattering physics process, as the Compton scattering component does not significantly vary with magnetic field strength for any material configuration.

Another explanation for why the number of soft electrons detected is less than that predicted by Geant4 might be that Geant4 is underestimating the backscattering coefficient of soft electrons in silicon, which Geant4 was found to do in some cases for electrons of less than 4 keV in kinetic energy by Kim et al. (2015) and Basaglia et al. (2015).

Even though significant regions of the spectrum are composed of high energy MIPs that are not present in spectra produced by X-ray detectors that are thicker than ~50 μm, it is still possible to verify the ability of Geant4 to simulate low energy fully absorbed particles and backscattering particles by plotting the difference between spectra with respect to energy, which will be described

here as the ‘difference spectrum’. Taking the difference between spectra at different magnetic field strengths means that the spectral components belonging to particles which are unaffected by magnetic field strengths should cancel out, leaving only spectral components belonging to fully depositing soft electrons and some backscattering electron components. As the only spectral components that should significantly contribute to this ‘difference spectrum’ are low energy fully depositing electrons and backscattering electrons, the difference spectrum can be used to verify Geant4’s treatment of the soft electron background component, where the total energy deposition spectra were only able to verify Geant4’s treatment of high energy fully-penetrating components.

7.7.2 Comparing Geant4’s treatment of low energy electrons and backscattered electrons to experimental data using magnetic fields

The difference spectra for the Mo and Al only configurations between currents of 0 A and 2 A are plotted in Figure 7.22, where similarly to the total spectra, the difference spectra corresponding to continuum regions appear to be identical apart from features near the fluorescence line, caused by the slight variations in the gain for each experimental run. The invariance of the continuum difference spectra with respect to changing material indicates that the fully depositing soft electron spectrum does not depend on the material configuration, as has been indicated in the comparisons between spectra for different material configurations throughout this chapter, and Chapter 6. The evidence in this case, however, is particularly strong, as trajectories in a magnetic field are dependent on initial particle angle, indicating that not only is the kinetic energy constant, but the angular distribution of secondary particles ejected from the irradiated materials is also constant.

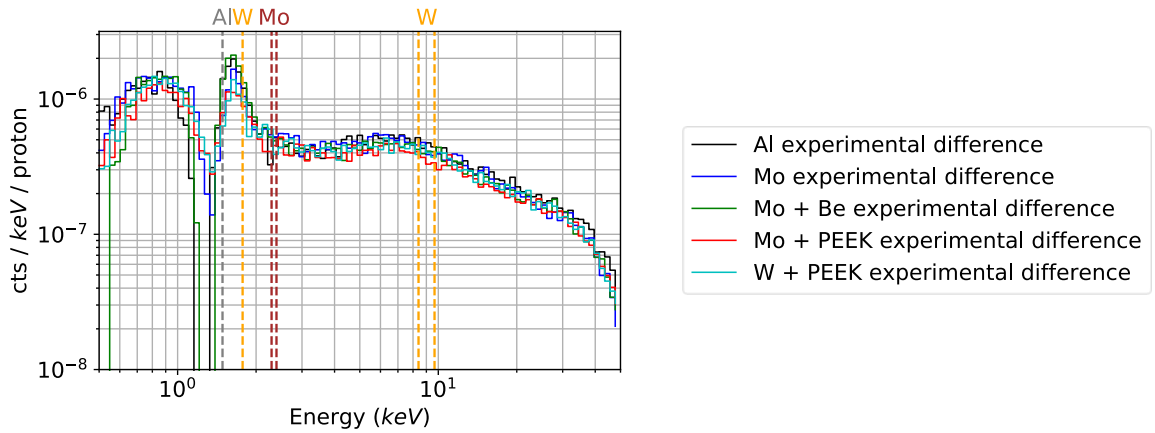

Figure 7.22 The difference spectrum for each experimental configuration between Helmholtz currents of 0 A and 2 A. Aside from features related to the Al and Mo fluorescence lines there appear to be few differences between the spectra, providing further evidence that the electron spectrum is identical for each material configuration. Unlike in the case where no magnetic field was applied, the magnetic field probes the angular distribution of electrons as well as the electrons produced in the direction of the detector.

The difference between 0 A and 2 A spectra for the Al only and Mo configurations are displayed in Figure 7.23 for Al and Figure 7.24 for Mo, and indicate that for the molybdenum case, the soft

electron spectral component does appear to exhibit the same spectral structure to the experimental spectrum. A range of additional magnetic difference spectra corresponding to each material configuration are also given in Figure C.2 in Appendix C for completeness, where spectra are split by particle species, creation physics process and kinetic energy.

The fact that the simulated difference spectra and experimental difference spectra for the Al configuration in Figure 7.23 agree above approximately 5 keV provides evidence that the hadronic ionisation physics list's simulation of the soft electron and backscattered electron spectrum from Al is accurate at these energies. However, the simulated spectral difference between 2 keV and 5 keV is significantly greater than the experimental spectral difference. This deviation in the Al only spectrum appears to occur at a similar energy range of 2 keV to 5 keV to the divergences in the Al simulation spectra that were present in the total energy deposition case.

Most of the other material configurations, shown in Figure C.2 in Appendix C, appear to have similar or better agreement to the experimental configuration albeit with systematic normalisation errors in some cases, which were a result of parts of the event detection process. The molybdenum configuration, shown in Figure 7.24, if renormalised to make the difference spectrum above 5 keV match the experimental difference spectrum, also exhibits the spectral excess between approximately 2 keV to 5 keV. However in this case the systematic uncertainty in normalisation makes it harder to definitively assert that this is the case.

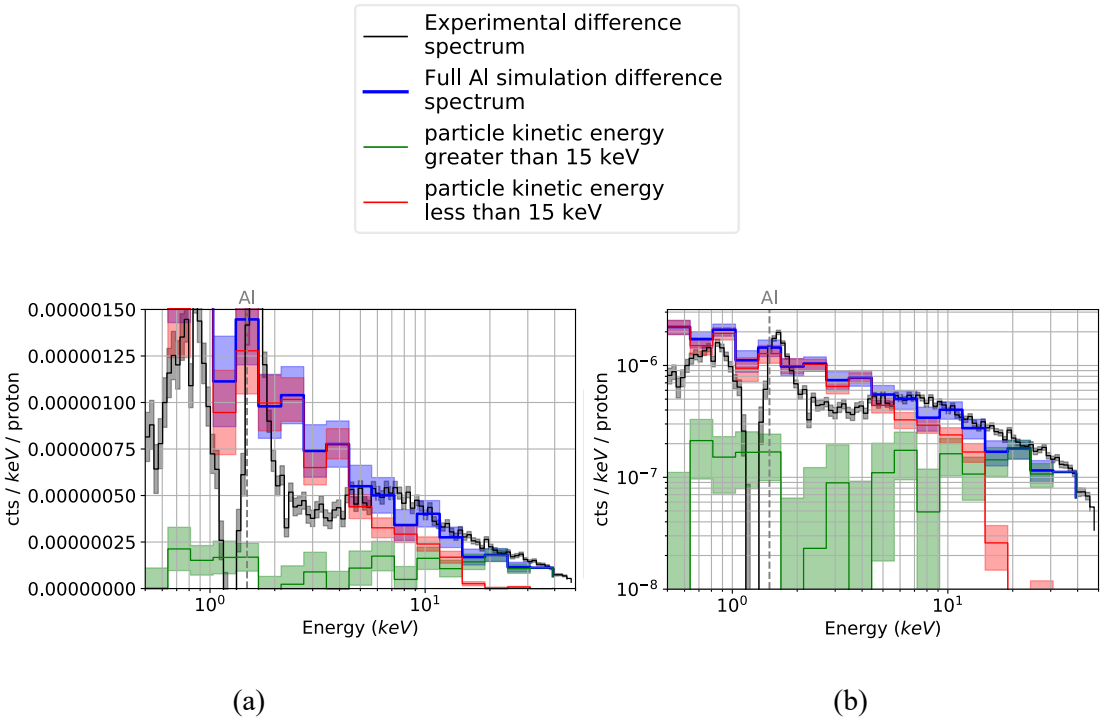

(a) (b)

Figure 7.23 The difference spectrum for the Al configuration as a function of energy. (a) and (b) show the same spectra, but with different y scales. In contrast to the Mo case in Figure 7.24, the difference spectrum appears to follow a very different spectrum. It displays a significantly higher difference in flux at energies below 3 keV, as well as a lower difference at energies above 3 keV.

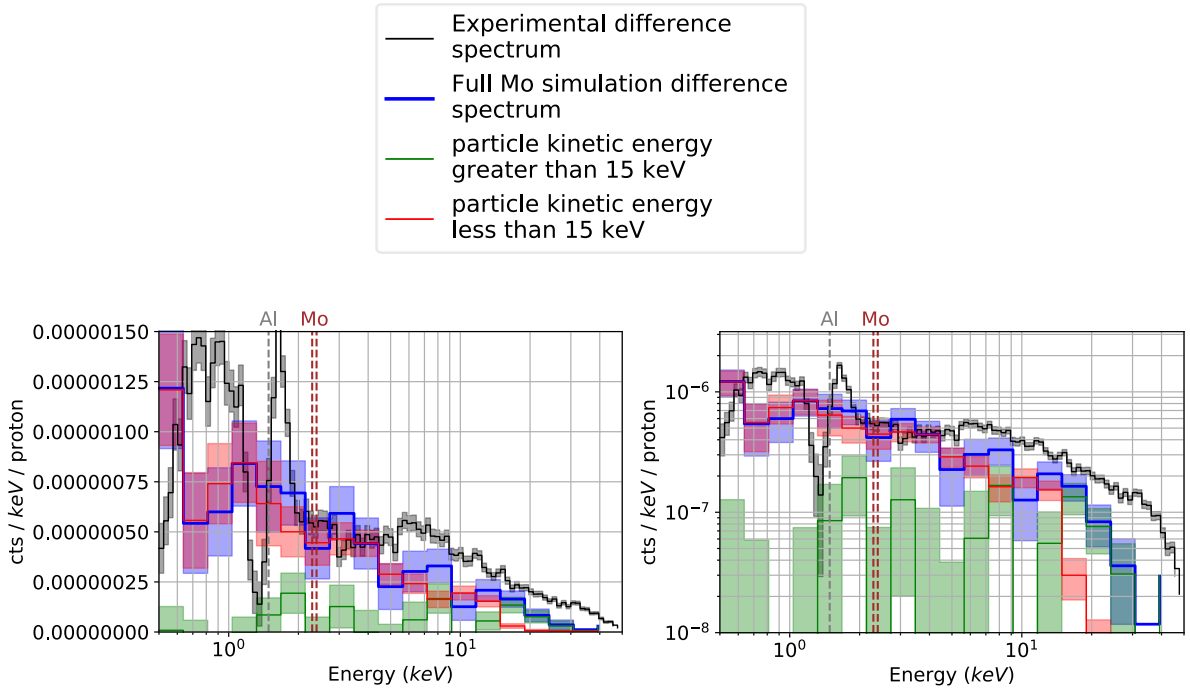

Figure 7.24 The difference between simulation spectra as a function of energy for the Mo configuration. (a) and (b) show the same spectra, but with different y scales. The difference spectrum appears to be within the error of the experimental difference spectra for energies above approximately 2 keV. Below 2 keV, the Al and Mo fluorescence lines dominate the spectrum and are not possible to remove from the experimental data without using a higher level of accuracy than was achievable in this case.

Previously, three possibilities have been discussed for why the simulations may be overestimating the spectral flux between 2 keV and 5 keV: that Geant4 is overestimating the number of low energy electrons in general, that Geant4 is overestimating the quantity of low energy electrons produced specifically by Compton scattering, or that this is the result of the simulations not accounting for CCD97 charge collection efficiency issues with detecting low energy electrons.

Figure 7.25 provides further evidence that the issue might be related to fully absorbed low energy electron production or detection in the simulations, rather than to production or detection of higher energy backscattering electrons or Compton scattering photons. Figure 7.25(a) and Figure 7.25(b) indicate that components generated by Compton scattering appear to form very little of the magnetic field difference spectrum. Additionally, Figure 7.20 indicated previously that the spectrum from the aluminium configuration with the 2 A magnetic field applied fits the experimental data more accurately within the 2 keV to 5 keV energy range than the spectrum with no magnetic field applied, implying that once fully absorbed low energy electrons are removed from the spectrum, the spectrum has a more accurate fit to the experimental data.

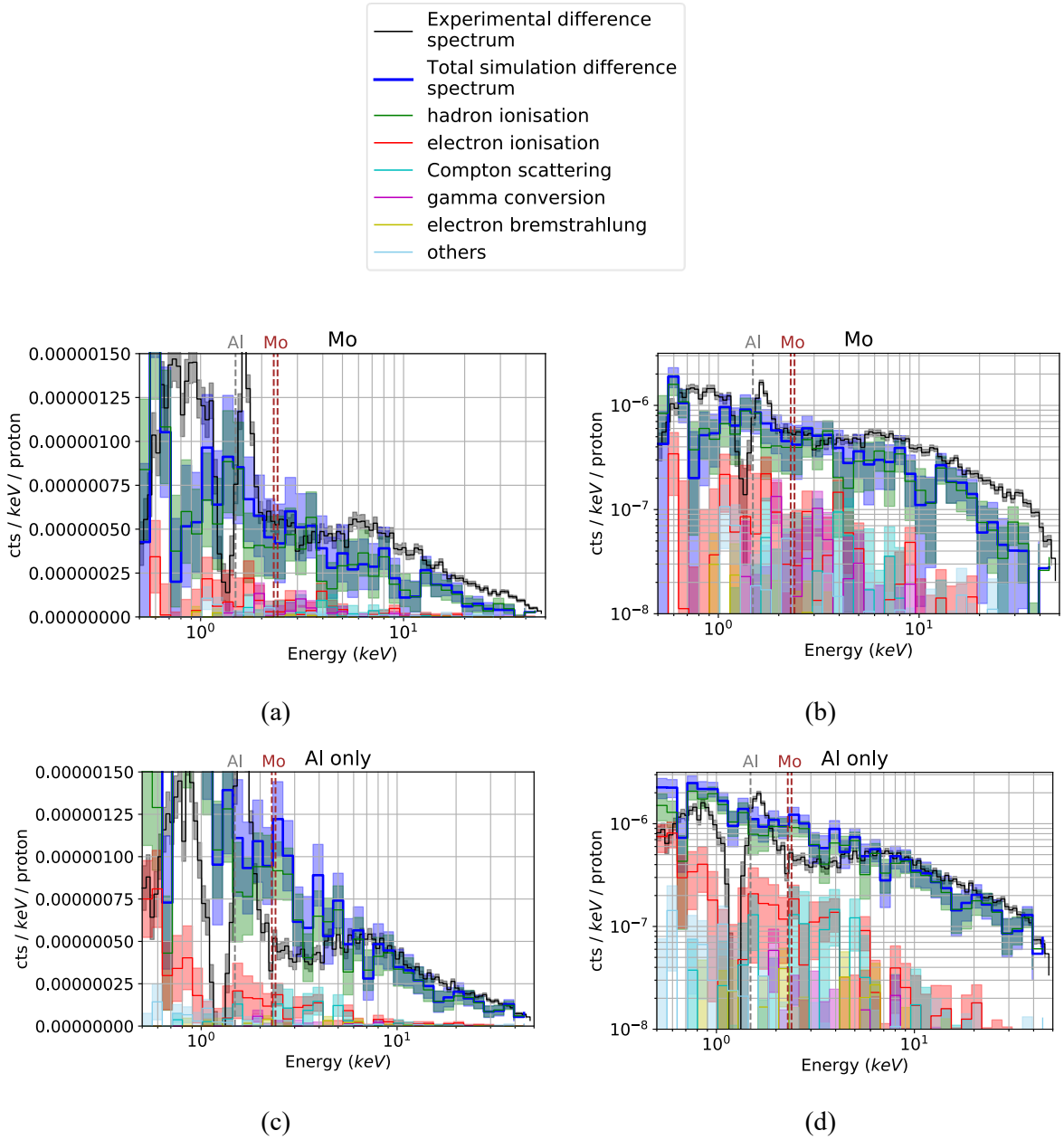

Figure 7.25 The magnetic difference spectrum for the Mo and Al configurations, split into creation physics process components. The data displayed in (b) and (d) are identical to (a) and (c) respectively but are plotted on a logarithmic y-axis. In both cases it appears that hadron ionisation dominates the difference spectrum, indicating that the majority of fully depositing electrons were generated by hadron ionisation.

While the discrepancies may be caused by an incomplete simulation geometry or incomplete detector simulation, it is possible that the simulations in this case are incorrectly simulating the production of electrons in the 2 keV to 5 keV energy range. As Geant4's simulation of low energy electrons produced by molybdenum appeared to be slightly more accurate in Figure 7.20, if this issue is a general issue with Geant4's simulation of low energy electrons in general, Geant4 may become less accurate for materials with lower atomic numbers. It is important for more experiments to be performed in the future assessing the accuracy of Geant4 at simulating the spectrum of electrons

depositing within the 2 keV to 5 keV energy range produced by both higher atomic number and lower atomic number materials.

7.8 Conclusions

For the physics processes that have been tested in this experiment, the total energy deposition spectra from the experiments at PSI indicate that Geant4 appears to exhibit a good accuracy at predicting the energy deposition spectra of high energy, fully penetrating electrons for all tested configurations.

The accuracy of Geant4 at simulating the production of low energy fully depositing electrons and backscattering electrons was also tested through varying the magnetic field across the system. Varying the magnetic field in the aluminium only configuration indicated that the simulations made good predictions for the difference spectra produced by backscattering electrons and soft electrons above 5 keV, indicating that Geant4 is correctly simulating particles that deposit in this energy range.

However, the simulations overpredicted the electron energy deposition spectra detected in the 2 keV to 5 keV energy range by a factor of up to approximately 2. This discrepancy appeared in all material configurations, albeit to varying extents, and may have been caused by several possible discrepancies between simulations and the experiment. Some possible explanations are that the experimental detector may have contained on-chip layers that could have blocked some electrons, the surface of the CCD97 used in the experiment may have had a low charge collection efficiency (internal device characteristics were not simulated), or Geant4 might have been inaccurate at simulating electrons at this energy deposition range.

The accuracy of several physics lists were also examined, and it was shown that the Space Users Physics List, PENELOPE and LIVERMORE physics lists all produce approximately the same spectrum and are in agreement with the experimental data for most of each spectra outside of the 2 keV – 5 keV range. However, it has also been shown that the Space Users physics list for Geant4 version 10.4.p01 combined with Geant4 version 10.3.p03 produces a substantial divergence between experimental data and simulation data.

Additionally, the ability of 1 mm layers Be and PEEK to attenuate the fluorescence lines from molybdenum was tested and as expected, successfully fully attenuated the 2.293 keV and 2.395 keV Mo fluorescence lines.

While this experiment has investigated and verified Geant4's treatment of several important components of space-based X-ray-like background, the experiment does leave some questions open such as how accurate is Geant4 at simulating the secondary photon contribution to the spectrum, as well as how accurate is Geant4 at simulating physics processes beyond just hadron ionisation. To determine Geant4's accuracy at simulating other components of the spectrum, future experiments will

need to be performed with a thicker detector to remove the MIP electron component from the spectrum. They may also require a stronger magnetic field to remove the electron backscattering component, to ensure Geant4's treatment of the secondary photon component is to be verified.

Now that Geant4's treatment of fluorescence, backscattering and fully-penetrating electrons has been verified and Geant4's treatment of fully depositing electrons has been partially verified, simulations can now be performed using some of the parameters such as a cut length of 1 μm that were used in simulations here.

Chapter 8

Characterising the X-ray-like Background in a Simplified Spherical Shell Model

Although some minor doubts still remain, the experiments described in Chapters 6 and 7 have verified the ability of Geant4 to correctly predict many of the aspects of secondary particle spectra depositing energy in the range of several keV. It is now possible to run simulations of the space-based environment using similar parameters to those used in Chapter 7.

This chapter will simulate a baseline spherical shell spacecraft geometry to characterise the X-ray-like background a generic ATHENA WFI-like X-ray astronomy mission might experience and to characterise the general physics behind X-ray-like background generation. This baseline geometry will then be modified in Chapter 9 to examine how X-ray-like background varies with changes to spacecraft geometry and detector design.

As described in Chapters 3 and 4, the X-ray-like background generated by the space-based radiation environment is expected to vary significantly with spacecraft design. However, the exact ways in which changes to spacecraft design affect the different components of X-ray-like background is not well known, making designing shielding to attenuate X-ray-like background difficult. Advancing knowledge of the significance of the various particle background components and their energies is necessary for the design of shielding, as shielding mechanisms are only capable of blocking or attenuating particles within specific energy ranges.

An understanding of the effect of spacecraft design on X-ray-like background may also mean that spacecraft design can be modified to lower background without the need for additional shielding in some circumstances. While reducing background may in many circumstances be a lower priority than achieving other technical requirements, there may be some instances where a small change can significantly reduce the background at a minimal cost to other technical specifications. Even if for a particular design choice the technical considerations do have precedence above X-ray-like background requirements, it can still be useful to know how such a choice will impact the background as a consideration. One example of this might, for instance, be the choice between placing an optical blocking filter on-chip, or in a filter wheel raised above the device, two possible configurations which

may have differing effects upon background. The impact of these configurations on the background will be examined in Chapter 9.

Ultimately, even if the technical requirements of a space mission can be fulfilled, the goal of any space astronomy mission is to perform high-quality science, and the presence of a significant background component is detrimental to this goal.

The X-ray-like background that will be present in a given space mission can be determined through the use of bespoke simulations, using accurate models of a spacecraft design. However, in this research, the goal was to examine the physics behind background generation in a manner that will inform the development of future X-ray astronomy missions as well. Moreover, complex geometries in Geant4 can take significantly longer to simulate than geometries containing simple shapes. Therefore, the simulations described in this chapter were based on spherical shell model geometries.

8.1 Simulation design

The location of materials surrounding detectors in X-ray astronomy missions is typically significantly more complicated than a spherical shell model. However, these simulations are still able to provide an understanding of the general physics processes that induce background, as well as order-of-magnitude estimations for the levels of X-ray-like background that should be expected to be present in a general mission.

Similar simulations have been performed previously on simplified spacecraft structure models in Geant4. For instance, simulations were performed on spherical shell and cuboidal shell models by Perinati et al (Perinati et al. 2017) for a device based on the ATHENA WFI. Here the effectiveness of a BCB passivation layer, and several graded-Z shielding combinations for background mitigation were investigated using a box model and spherical shell model respectively.

Some research was also presented by Meidinger et al (Meidinger et al. 2016) which compared the background spectrum produced from several ATHENA WFI configurations. It was found that the secondary electron background spectrum significantly reduces across the whole spectrum when a 3 μm BCB passivation layer and 90 nm optical blocking filter is added to the detector, particularly at lower energies. The effectiveness of a BCB passivation layer at reducing X-ray-like background will be further evidenced in simulations presented in Section 8.3.3.2, and the effectiveness of graded-Z shielding combinations will be analysed in Chapter 10.

Each simulation described in this chapter used the same detector design displayed in Figure 8.1.

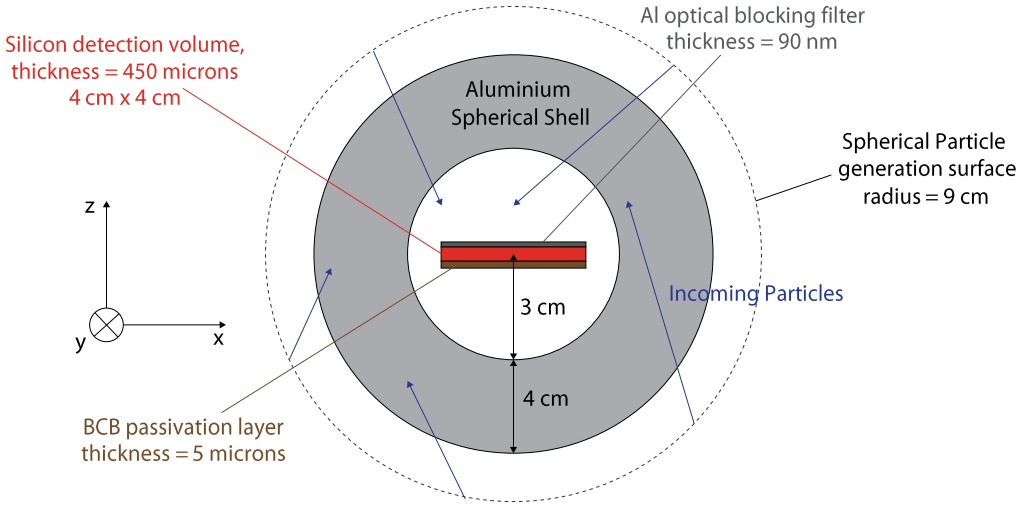

Figure 8.1 A diagram of the spherical shell model simulations. The detector was a 450 µm thick cuboid of silicon, with a 90 nm layer of on-chip aluminium placed on top, and a 5 µm thick layer of BCB placed on-chip below the detector. A 4 cm shell of aluminium was chosen to surround the detector to represent a similar thickness of aluminium to that of a spacecraft proton shield.

The detector in these simulations was represented by a simple cuboidal volume of silicon of 450 µm in thickness, and 4 cm in width and length. As described in Chapter 5, Geant4 reports energy deposition within volumes that are designated as detector volumes, and other detector features such as charge collection efficiency or pixelation, for instance, must be included in simulated images by post-processing of the raw Geant4 simulation results.

Two surface features were added above and below the detector volume, a 90 nm thick layer of aluminium on top of the detector, representing an optical blocking filter and a 5 µm thick layer of BenzoCycloButane (BCB) on the bottom of the detector. These layers were included to match the simulations to approximately the general structure of the ATHENA WFI, which is expected to have a thickness of 450 µm, with an optical blocking filter and a BCB passivation layer. A passivation layer is a layer deposited onto a semiconductor device, often to protect it from the environment or provide additional structural stability to the device. In the case of the ATHENA WFI, BCB is a good candidate material as a passivation layer from a background perspective, as it has no fluorescence lines within the WFI energy range.

For initial simulations, a spherical shell of aluminium with a thickness of 4 cm was used, to represent the proton shield which will be present around the WFI. The proton shield is designed to be sufficiently thick such that it can block low energy ions. For instance, an aluminium thickness of 4 cm is capable of blocking protons of less than 28.6 MeV under continuous slowing down approximations (M. J. Berger et al. 2017). However, it is unable to shield the detector from protons with energies of the order of several GeV.

The primary particle spectra used in spherical shell geometry simulations were the Galactic Cosmic Ray (GCR) and Cosmic X-ray Background (CXB). While helium ions and electrons are expected to have a non-insignificant impact upon the X-ray-like background (von Kienlin et al. 2018), they are expected to represent a significantly smaller component than that generated by the CXB and GCR spectra, and so were therefore not considered here. These spectra were generated from a spherical Lambertian surface of radius 9 cm surrounding the spacecraft geometry, with a cosine momentum direction distribution as described in Chapter 5. The CREME96 spectrum was used to generate protons from the GCR spectrum (Tylka et al. 1997), and the spectrum given by Moretti was used to generate X-rays and gamma rays from the CXB (Tylka et al. 1997).

The Geant4 parameters used in the simulations are given in Table 8.1. These parameters were previously verified against experimental data in the PSI experiment described in Chapter 7, for the case where secondary electrons produced by protons dominate the background. However, the simulations presented in this chapter typically used PENELOPE instead of the Space User's physics list, which were shown to generate almost identical background spectra in Chapter 6 and Chapter 7.

Setting	Value
Physics List	QGSP_BIC_HP_PEN
Default production cut length	1 μm
Minimum energy	0.1 keV
PIXE flag	True
Auger flag	True
Fluo flag	True
Scattering type	Multiple scattering

Table 8.1 Some of the Geant4 settings used for simulations in this chapter.

8.2 Event detection using total particle energy deposition thresholding

Figure 8.2 displays a sample image produced by the simple spherical shell model system using the previously described parameters for an integration time of 169 seconds. Both particle tracks and X-ray like events are present in this image, as expected.

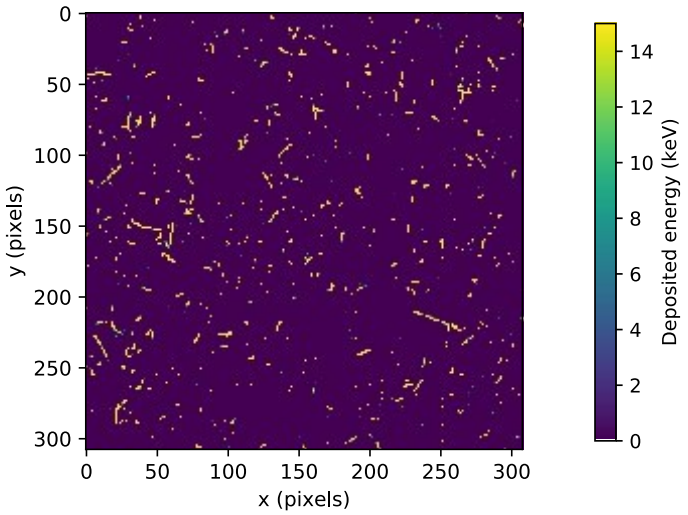

Figure 8.2 A raw image produced by the spherical shell model Geant4 simulations. This image represents 169 seconds of integration time. Colour thresholding was applied such that pixels containing more than 15 keV in deposited energy are displayed here as the same colour as those with 15 keV in deposited energy.

As discussed in Chapter 3, particle tracks do not directly induce X-ray-like background, as they can typically be removed using event detection. In this case, as the detector thickness is greater than 100 µm, summing the total track energies and removing events that fall outside the energy band is sufficient to remove all particle tracks from images. This is because under continuous slowing down approximations it is not possible for a proton or electron passing through the full detector to deposit less than 15 keV.

To account for the possibility of secondary particles hitting the same pixel as an incoming primary particle, or being produced in the detector, the pixel location for a particle was calculated from the original position the particle hit the detector. If the pixel location was identical to the pixel position of a particle that entered the detector earlier during the same event, the newer particle was deleted, and its energy deposition was added to the energy deposition of the earlier particle, which was usually its parent particle. The pixel width used for this was 130 µm, corresponding to the same expected pixel width at the ATHENA WFI.

The resulting image created using this energy thresholding is displayed in Figure 8.3.

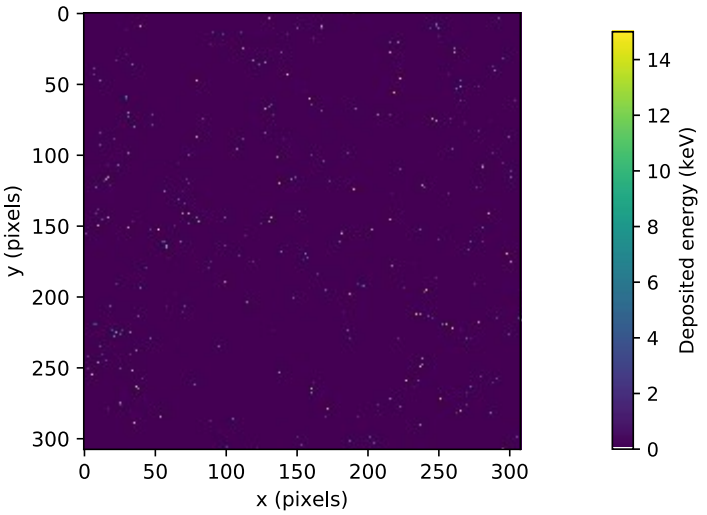

Figure 8.3 The resulting image produced when particles depositing more than 15 keV are removed. This energy thresholding technique provides a simple method of performing event detection on Geant4 simulation results.

As expected, particle tracks are no longer present in Figure 8.3. Figure 8.4 and Figure 8.5 show zoomed-in versions of Figure 8.2 and Figure 8.3, and further illustrate the ability of thresholding on the images to remove particle tracks produced in the simulation.

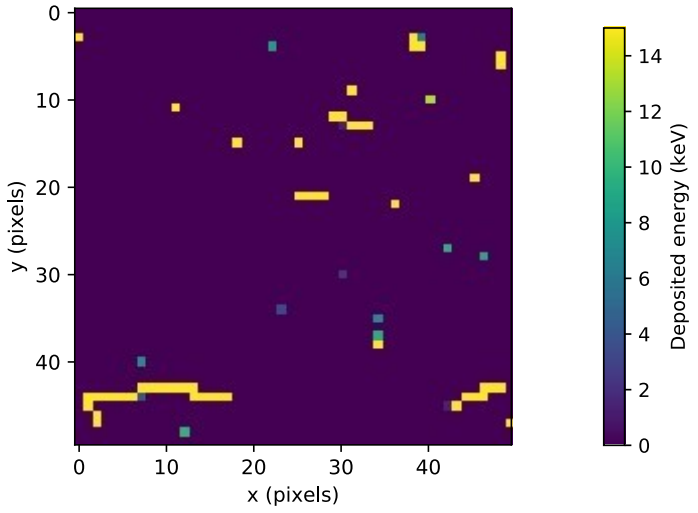

Figure 8.4 A small region of Figure 8.2, displaying raw energy deposition image data produced from Geant4 simulations.

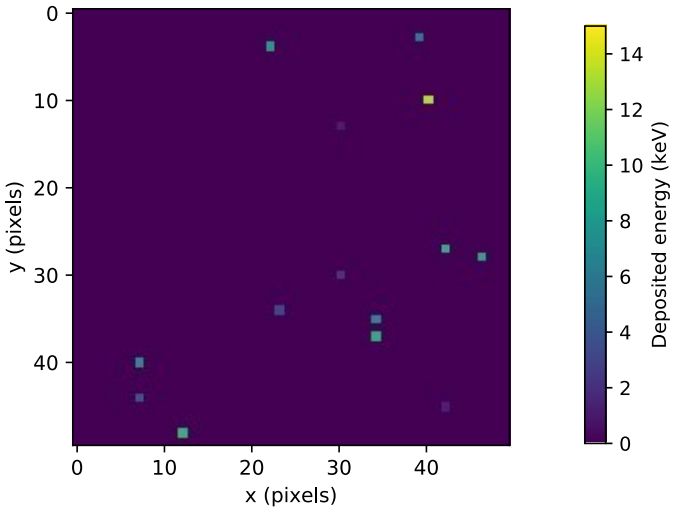

Figure 8.5 A small region of Figure 8.3. This image shows the same region as Figure 8.2, but with particle energy deposition thresholding applied to remove particle tracks.

While this method is more straightforward and less intensive than using an event detection algorithm, it does not account for pile-up. This can be seen in Figure 8.4 and Figure 8.5 where there are several instances of particles that are visible in Figure 8.5 that would typically be excluded by event detection algorithms as part of a particle track, due to being underneath or adjacent to another X-ray-like event or tracks. For these simulations, this deviation from actual event detected images should be negligible, as many space-based astronomy missions are designed to remove pile-up as much as possible. For instance, the ATHENA WFI has an integration time of < 5 ms (Meidinger et al. 2019), meaning that the effect of the pile-up of X-ray-like background should be negligible.

8.3 Simulation results

8.3.1 The total X-ray-like background spectrum

As has been discussed previously, the quality of scientific observations will be impacted by the background more significantly in regions of the spectrum where the background is most prominent. Figure 8.6 displays the spectrum of X-ray-like background produced by the spherical shell model simulation, split into components associated with a cosmic proton input spectrum, and CXB input spectrum.

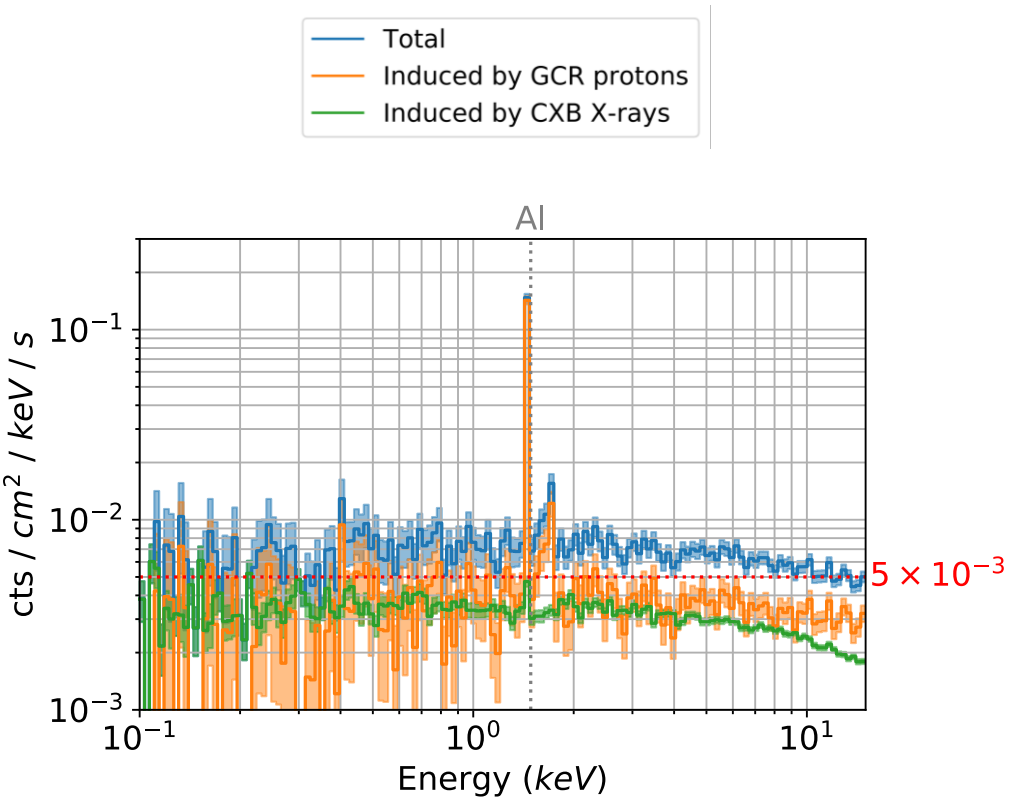

Figure 8.6 The X-ray-like background spectrum generated by cosmic protons and cosmic X-rays. The spectrum appears to have a nearly uniform distribution, except for the 1.48keV Al peak and a slight reduction at higher energies that may be due to a reduction in quantum efficiency. The red dotted line represents the target count rate for X-ray-like background of the ATHENA WFI, of $5 \times 10^{-3} cts / cm^2 / keV / s$.

According to Figure 8.6, the CXB induced background and GCR proton induced background appear to contribute approximately equally to the X-ray-like background across the energy deposition spectrum. This equivalent contribution contrasts with simulations performed on variants of the ATHENA WFI mass model (von Kienlin et al. 2018), where the CXB induced background is significantly lower than the GCR induced background. Simulations performed upon mass models of the ATHENA WFI, which will be presented in Chapter 11, indicate that differences in simulation geometry related to the presence of graded-Z shielding have a significant impact on the CXB while minimally impacting the GCR induced component, likely explaining the discrepancy here.

The GCR proton and CXB spectral components can be broken down further into particle components. Figure 8.7 and Figure 8.8 display the X-ray-like background associated with the GCR proton spectrum and CXB spectrum split into particle components, respectively. Here a soft photon or electron is defined as a particle that hit the detector with a kinetic energy of less than 15 keV, whereas a hard photon or electron is defined as a particle that hit the detector with a kinetic energy of greater than 15 keV.

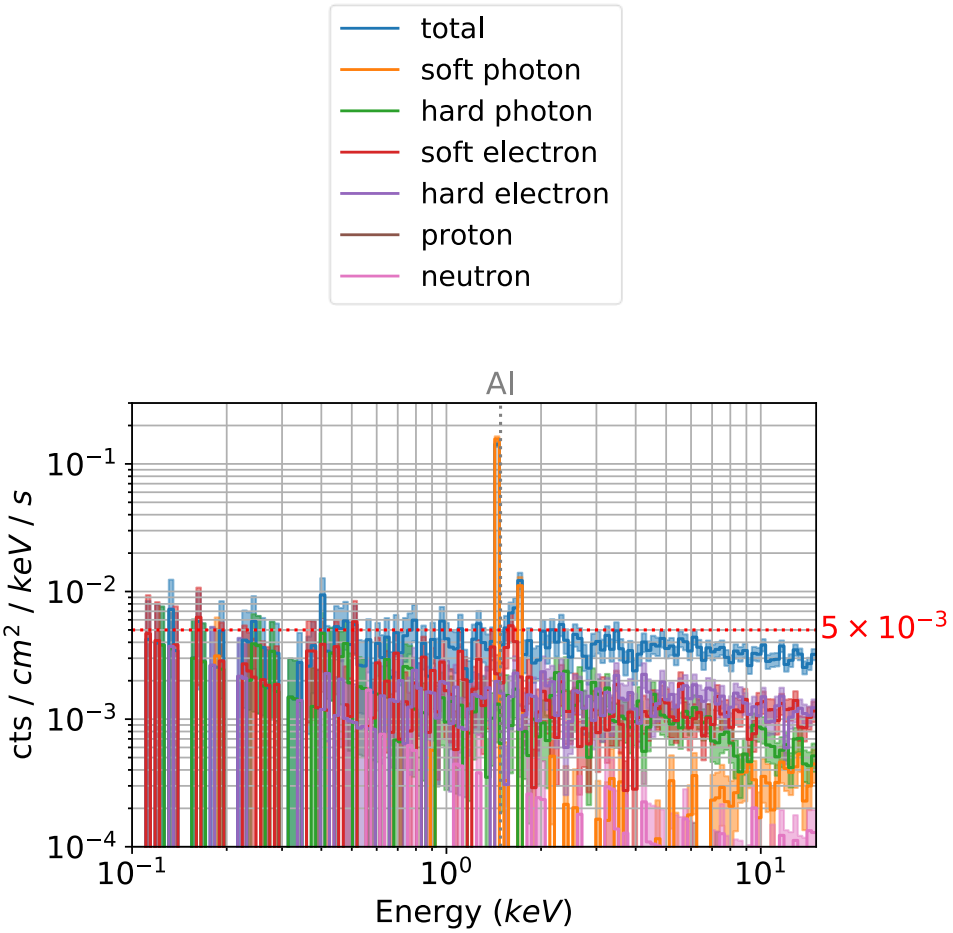

Figure 8.7 The same cosmic proton-induced background spectrum, as displayed in Figure 8.6, split into particle components. The dominant components appear to be the hard electron, soft electron, and hard photon components, although there is some non-insignificant soft photon contribution at approximately 10 keV and higher. The small soft photon fluorescence line at a slightly higher energy than the aluminium fluorescence line is likely the 1.74 keV silicon fluorescence line, which will not be present in real detector images due to differences in using event detection versus using the algorithm used here. The red dotted line represents the target count rate for X-ray-like background of the ATHENA WFI, of 5×10^{-3} *cts / cm² / keV / s.*

Particle Species	**0.1-15 keV mean flux (cts / cm2 / keV / s)**	**2-7 keV mean flux (cts / cm2 / keV / s)**	**Total Fluorescence Energy Counts (cts / cm2 / s)**
Total	$(4.3 \pm 0.1) \times 10^{-3}$	$(3.8 \pm 0.1) \times 10^{-3}$	N/A
Soft photons	Negligible	Negligible	$(6.8 \pm 0.3) \times 10^{-3}$
Hard photons	$(1.05 \pm 0.08) \times 10^{-3}$	$(1.22 \pm 0.07) \times 10^{-3}$	N/A
Soft electrons	$(1.13 \pm 0.08) \times 10^{-3}$	$(0.93 \pm 0.06) \times 10^{-3}$	Negligible
Hard electrons	$(1.05 \pm 0.06) \times 10^{-3}$	$(1.50 \pm 0.07) \times 10^{-3}$	N/A

Table 8.2 The mean fluxes of significant cosmic proton background components displayed in Figure 8.7 between several energy ranges.

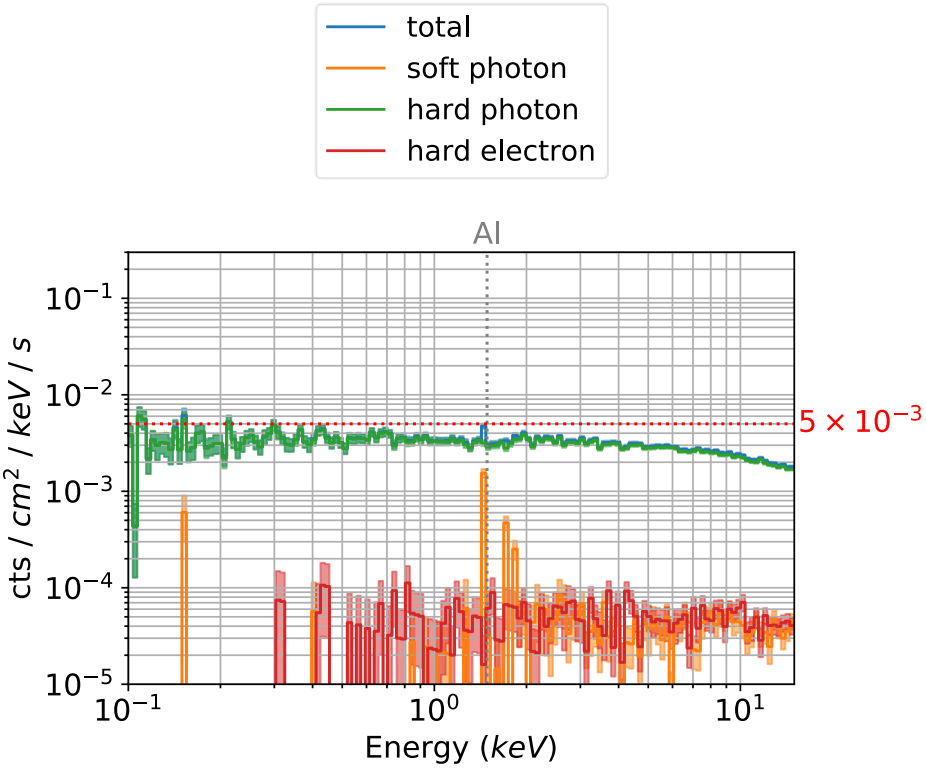

Figure 8.8 The cosmic X-ray induced background spectrum split into particle components. Here the background appears to have been almost entirely generated by hard photons through Compton scattering in the detector.

Particle Species	0.1-15 keV mean flux (cts / cm2 / keV / s)	2-7 keV mean flux (cts / cm2 / keV / s)	Total Fluorescence Counts (cts / cm2 / s)
Total	$(3.24 \pm 0.04) \times 10^{-3}$	$(3.14 \pm 0.03) \times 10^{-3}$	N/A

Table 8.3 The mean flux of CXB induced background between several energy ranges.

The CXB induced spectrum appears to be almost entirely composed of hard photons, indicating that the dominant mechanism causing CXB induced background is Compton scattering of CXB photons in the detector. This hard photon continuum appears to be approximately constant between 2 and 7 keV with a mean background of $(3.14 \pm 0.03) \times 10^{-3}$ cts / cm^2 / keV / s.

In contrast to the CXB induced spectrum, the GCR induced spectrum appears to be composed of numerous particle species, primarily hard photons, soft electrons and hard electrons. The only significant contribution to the spectrum from soft photons appears to be the Al fluorescence peak at 1.48 keV. As displayed in Table 8.2, the mean GCR induced background count rate between 2 keV

and 7 keV is $(1.22 \pm 0.07) \times 10^{-3}$ for the photon continuum and $(2.43 \pm 0.09) \times 10^{-3}$ for the electron continuum.

In addition to photons and electrons, the GCR spectral component also contains a smaller, but non-negligible neutron component. While this appears to be relatively small compared to the total GCR spectrum in this instance, it is possible that an increased mass surrounding the detector could increase the contribution of this component.

8.3.2 The kinetic energy spectrum of background inducing particles, and primary particles

In addition to studying the particle species impacting a detector, it is also instructive to study the kinetic energy distribution of background-inducing particles. Any shielding mechanism will only be able to attenuate or block particles within a specified energy range, meaning that to design effective shielding mechanisms, a knowledge of the kinetic energies of background-inducing particles is also required.

Chapter 3 discussed the fact that for some particle types the deposited energy within the detector does not necessarily represent the actual kinetic energy of particles impacting the detector. Processes such as backscattering for electrons, or Compton scattering for photons can cause less energy to be deposited in a detector than the total particle kinetic energy. It was also found in Chapter 7 that significant regions of the experimental spectrum were in fact dominated by fully-penetrating electrons that deposited only a small proportion of their energy. Therefore it is necessary to examine both the spectra of primaries that are inducing background, as well as the actual kinetic energy spectra of particles that are impacting the detector.

8.3.2.1 GCR proton simulations

Figure 8.9 displays the kinetic energy distribution of background-inducing particles impacting the detector in the GCR spherical shell model simulations split by the same particle classifications used in Section 8.3.1.

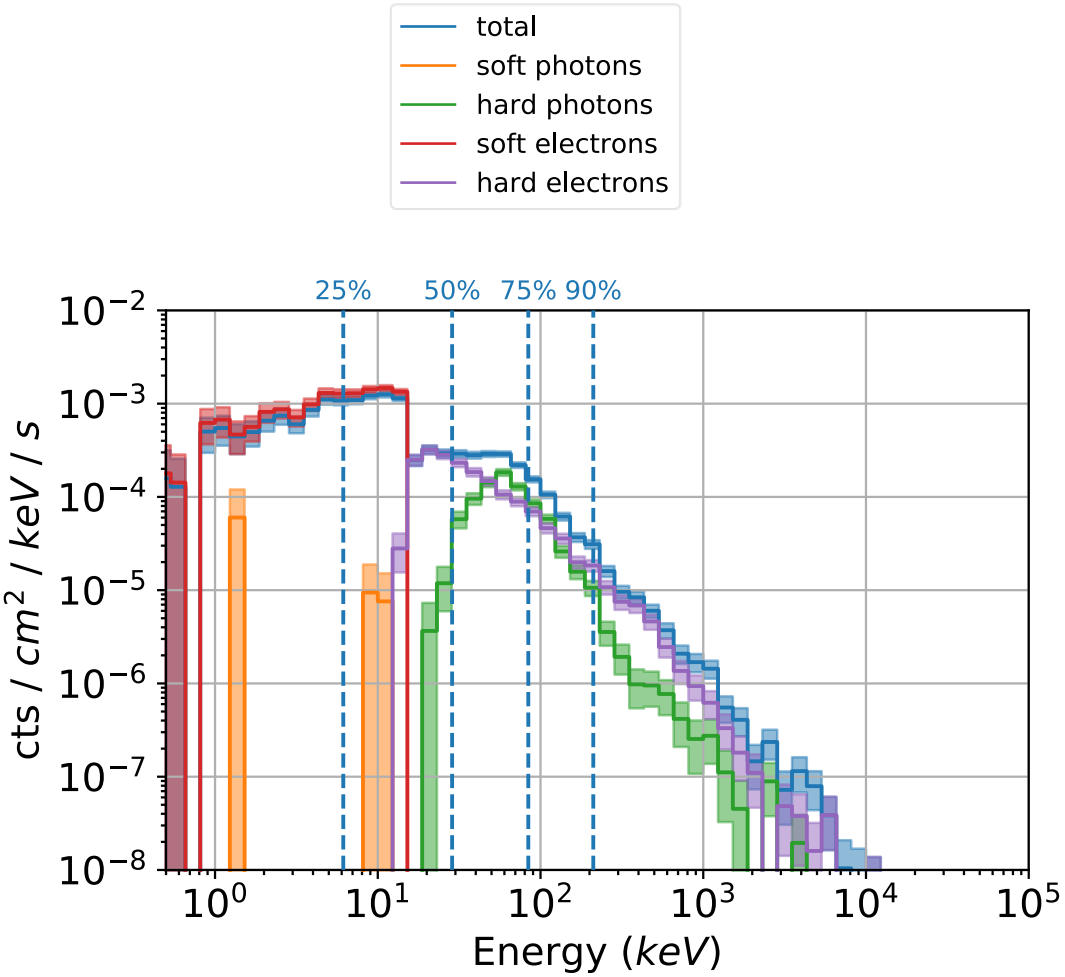

Figure 8.9 The kinetic energy spectrum of particles inducing X-ray-like background in the silicon detector.

Spectrum	25% percentile	50% percentile (median)	75% percentile	90% percentile
Total	6.14 keV	28.63 keV	84.14 keV	210.98 keV
Hard photon	55.24 keV	75.56 keV	114.44 keV	192.45 keV
Hard electron	32.37 keV	64.88 keV	151.64 keV	380.01 keV

Table 8.4 Percentiles for the kinetic energy of background inducing particles in cosmic proton simulations.

Figure 8.9 indicates that the background associated with hard photons peaks at approximately 70 keV before decreasing as approximately a power law. In contrast, the hard electron kinetic energy spectrum, which represents the electron backscattering spectrum, appears to decrease consistently with increasing energy.

To design shielding mechanisms, it is useful to plot the cumulative spectra or integral spectrum as opposed to just the energy spectrum. A cumulative spectrum allows for the effectiveness of a shielding mechanism to be analysed based on the maximum particle energy that a shield is capable of

blocking. For instance, if a shielding material is capable of blocking electrons of up to 10 keV in kinetic energy, then the fraction of total electrons of all energies that will be blocked by the shield can be read out from the plot of cumulative spectra.

Figure 8.10 displays the cumulative spectra for hard photons and hard electrons for the GCR simulations, normalised as a fraction of the total number of accepted hits for the particle classification.

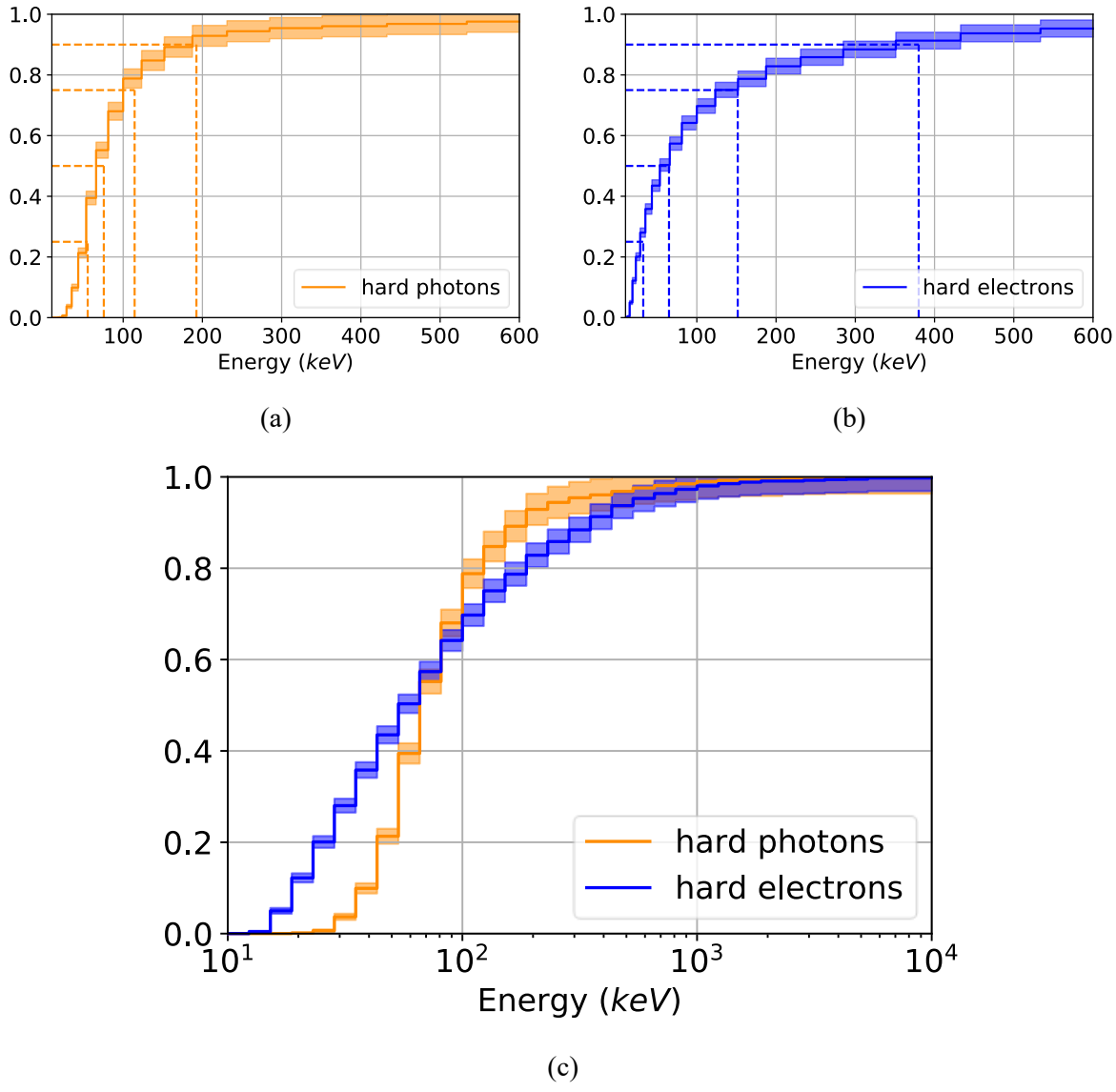

Figure 8.10 The cumulative spectrum for the kinetic energy of background inducing secondaries generated by cosmic protons. The cumulative spectrum allows the effectiveness of shielding to be assessed more easily by examination of the particle energies that a shielding mechanism is capable of blocking. Figure 8.10(a), Figure 8.10(b) display the same data as Figure 8.10(c), but plotted separately for clarity. The cumulative spectra are normalised here as a fraction of the total number of accepted hits for the particle classification.

Figure 8.10 indicates that in order to shield a detector from 90% of background inducing events created by cosmic proton-induced hard photons and electrons, shielding mechanisms would need to be capable of blocking photons of approximately 500 keV, and electrons of approximately 300 keV.

In addition to plotting the kinetic energy spectrum of background-inducing particles, it is also informative to plot the kinetic energy of the CXB or GCR primary particles that resulted in a background event.

Figure 8.11 displays the primary particle kinetic energy spectrum for background inducing hits in the cosmic proton simulations, and corresponding cumulative spectra.

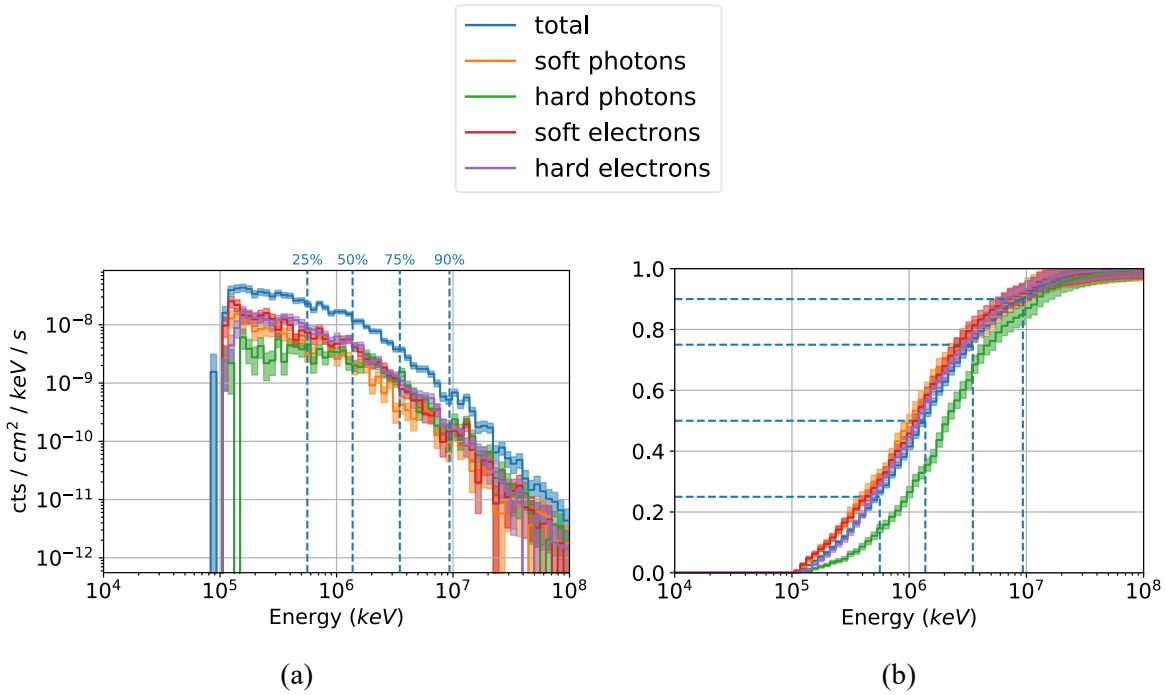

(a) (b)

Figure 8.11 The primary kinetic energy spectrum and corresponding cumulative energy spectrum for secondary radiation generated by cosmic protons. There appears to be a cutoff energy at approximately 100 MeV, which corresponds with the minimum energy of 104.4 MeV (calculated using stopping power data from NIST using Mathematica 12.0 (M. Berger et al. 2005; *Mathematica* 2019)*) required for a proton to penetrate aluminium of 4 cm, the thickness of the proton shield layer.*

Spectrum	25% percentile	Median / 50% percentile	75% percentile	90% percentile
Total	0.561 GeV	1.374 GeV	3.494 GeV	9.327 GeV
Soft photons	0.438 GeV	1.111 GeV	2.867 GeV	8.236 GeV
Hard photons	1.022 GeV	2.259 GeV	4.985 GeV	13.289 GeV
Soft electrons	0.468 GeV	1.205 GeV	2.796 GeV	7.317 GeV
Hard Electrons	0.525 GeV	1.266 GeV	3.262 GeV	7.444 GeV

Table 8.5 The percentiles for the kinetic energy of incoming protons that induce different X-ray-like background components. X-ray-like background induced by hard photons originates from higher energy protons than the other background components.

Figure 8.11 indicates that for all background-inducing particle components, there appears to be a minimum cut-off energy at approximately 10 MeV, which is the minimum energy required for a photon to penetrate 4 cm of aluminium, the thickness of the proton shield layer. Above the maximum

just after the cut off energy, the spectrum for all components except for the hard photon primary spectrum decreases with increasing primary kinetic energy.

The initial increase in hard photon spectrum with respect to increasing primary kinetic energy provides one explanation in addition to the low thickness of the detector for why the hard photon spectrum did not appear in the simulated spectra of the 200 MeV irradiation at PSI in Chapter 7. At an energy of 200 MeV, the primary spectrum of background inducing hard photons is significantly lower in Figure 8.11 than that of soft electrons or hard electrons, even though for the total hard photon background is comparable to the hard electron background.

This dominance of other background components over the hard photon component at energies around 200 MeV implies that the proton energy used at PSI was too low to test the production of hard photons in the space-based environment, and their effect on the X-ray-like background. Therefore, future experiments designed to test this should aim to use more energetic protons, perhaps at energies closer to the median energy of background generating protons in this simulation of 1.374 GeV, to test the physics of hard photon generation by protons.

Although this explains why there was no significant contribution to the background by hard photons in the 200 MeV experiment or simulations, it is unexpected that protons of higher kinetic energy might produce more hard photons despite having a lower stopping power as kinetic energy increases. One possible explanation might be that there is some threshold energy that protons require before being able to produce a background-inducing hard photon or intermediary particle. Because understanding the physics behind background generation is necessary to design background mitigation strategies, the physics underpinning hard photon production is further investigated in Chapter 9, where the chains of interactions leading to the creation of hard photons will be investigated.

8.3.2.2 CXB simulations

Figure 8.12 displays the kinetic energy spectra for background inducing particles (Figure 8.12(a)) and primaries (Figure 8.12(b)) in CXB simulations, for energy depositions within the 2 keV to 7 keV range.

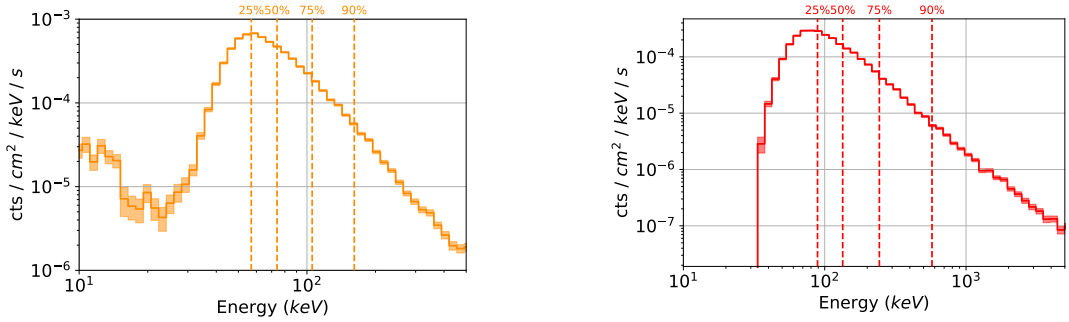

(a) (b)

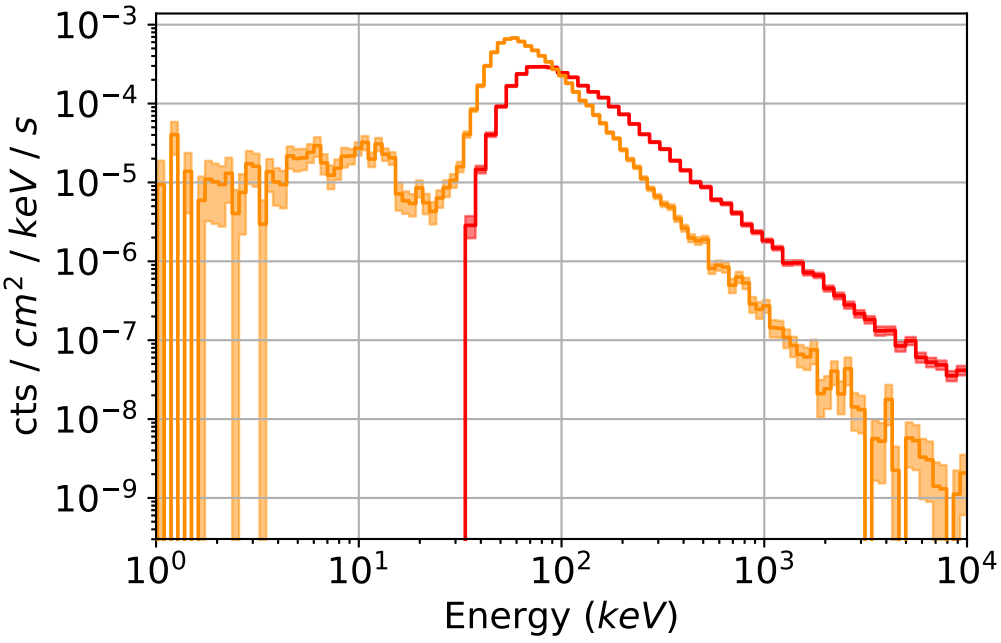

(c)

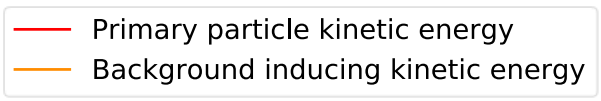

Figure 8.12 The CXB energy spectra for primary photons and for background inducing particles. Figure 8.12(a) and Figure 8.12(b) display the same data as Figure 8.12(c), but plotted separately for clarity. The spectra are similar but exhibit some key differences, implying that the CXB spectrum undergoes some Compton scattering while passing through spacecraft materials before reaching the detector. The maxima for the background inducing particle kinetic energy is lower than the primary particle kinetic energy, indicating that some photons are scattering through the aluminium proton shield and losing some energy before they impact the detector.

Spectrum	25% percentile	Median / 50% percentile	75% percentile	90% percentile
Background-inducing Particle Kinetic Energy	56.96 keV	73.92 keV	105.42 keV	161.32 keV
Primary Particle Kinetic Energy	88.95 keV	134.06 keV	243.60 keV	574.55 keV

Table 8.6 The percentiles for both the kinetic energy of particles that induce background and of the primary particles that initially hit the spherical shell model and cause at least one background hit.

The CXB primary spectrum in Figure 8.12 appears to represent approximately a power law, with a minimum cut-off energy between 30 keV and 40 keV, and a peak at approximately 80 keV. For comparison (Xcom 2010), 4 cm of Al is capable of attenuating a uniform distribution of 914 keV photons by 50%. 90% of primaries in this spectrum are of energies less than 574.55 keV, which means that to attenuate 90% of these particles by at least a factor of 50%, a further thickness of aluminium of 3.22 cm would be needed.

The CXB secondary spectrum given in Figure 8.12(a) appears similar to the primary spectrum in Figure 8.12(b). There is a peak in this spectrum at approximately 60 keV, a similar energy to the peak of the primary spectrum, and a similar magnitude of minimum cut off energy between approximately 30 keV to 40 keV. However, this cut off energy appears to be less sharp than the primary cut off energy. Other differing features include the separate peak and a steeper power-law tail at energies greater than the peak energy than in the primary spectrum.

These spectral features can be explained using the cross-section of Compton scattering of CXB photons within the detector. The minimum cut off energy between 30 keV and 40 keV represents the minimum energy required for a primary CXB photon to penetrate the proton shield and the increasing of Compton scattering cross-section with energy. However, as photon energy increases above approximately 50 keV, the Compton scattering cross-section peaks and then begins decreasing (Xcom 2010). This decreasing cross-section with photon energy beyond 50 keV might explain the decrease in CXB induced background from primary energies greater than 80 keV, as the decreasing Compton scattering cross-section counteracts the increasing probability of photons penetrating the proton shield.

The steeper tail in the CXB kinetic energy spectrum could be explained by Compton scattering of high energy photons within the proton shield, followed by a further Compton scattering event within the detector. The presence of scattering from the proton shield could also explain the smoothing around the minimum cut-off energy, as CXB photons that were of energies greater than the minimum

cut-off energy can be Compton scattered to energies below the cut-off energy as they pass through the proton shield.

Finally, the low energy peak between 1 keV and 15 keV are particles within the energy range generated from surfaces within line-of-sight of the detector. The quantity of these particles appears to be small relative to the quantity of Compton scattering photons in the detector, however they are sufficiently numerous as to appear on this spectrum.

8.3.3 The spatial distribution of background-inducing particle creation and detection locations

In addition to examining the spectral components of background, it is also instructive to examine the spatial distribution of both origin location and absorption location of background inducing components. Knowledge of background origin location, in particular, is necessary for informing shielding design, and the locations where shielding may need to be placed. In contrast, knowledge of absorption location may indicate that background varies across the pixels in a device, or at different depths in the device, which may inform how possible variations in device properties may impact the X-ray-like background.

Figure 8.13 displays the positions at which background hits the device, or what an actual event detected image might look like.

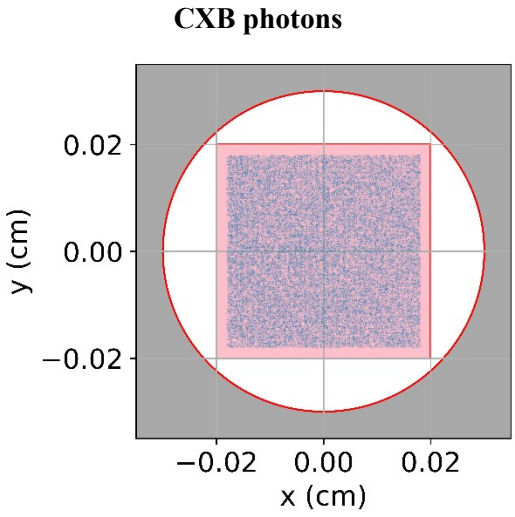

(a)

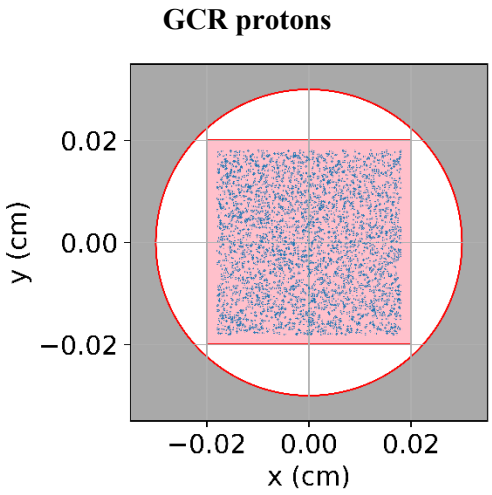

(b)

Figure 8.13 The positions at which particles impacted the device in simulations, with CXB hits in Figure 8.13(a), and cosmic protons induced background hits are plotted in Figure 8.13(b). It appears that there is no significant variation of background with image location, at least for the full energy range of 0.1 keV to 15 keV.

There appears to be no significant variation in the background across the image for either the CXB or cosmic proton components, indicating that in this situation it would not be necessary to calculate background for different regions separately. It should be noted however that in an actual mission the background might not always be entirely isotropic, due to the effect of the geometry of the solar system on cosmic rays or more complex spacecraft structures than a spherical shell.

In addition to plotting the positions at which particles induce background in the detector, it is useful to plot the positions at which background-inducing particles originate. Figure 8.14 and Figure 8.15 display the creation vertex positions of particle species flattened against different axes, for the CXB and cosmic proton spectra respectively.

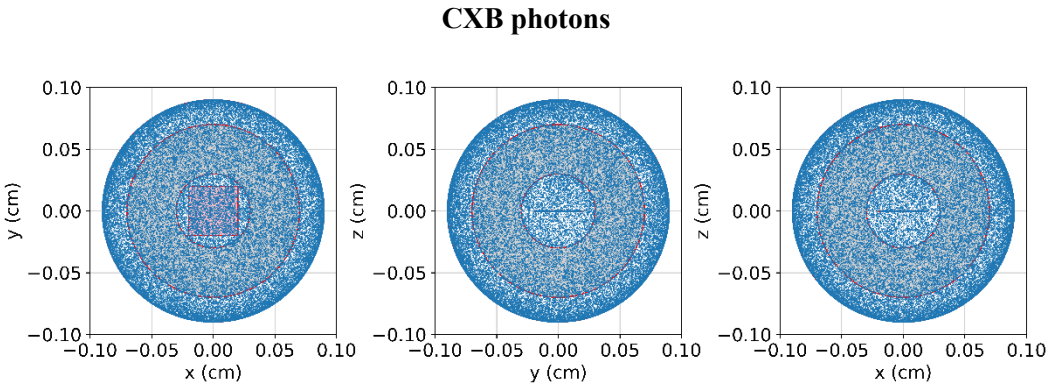

Figure 8.14 The creation vertex positions for the background induced in CXB simulations. The central square or line represents the position of the detector, and the grey circular region between the two red circles represents the aluminium proton shield shell. Almost all events are being induced directly by cosmic X-rays originating from the particle generation sphere surface.

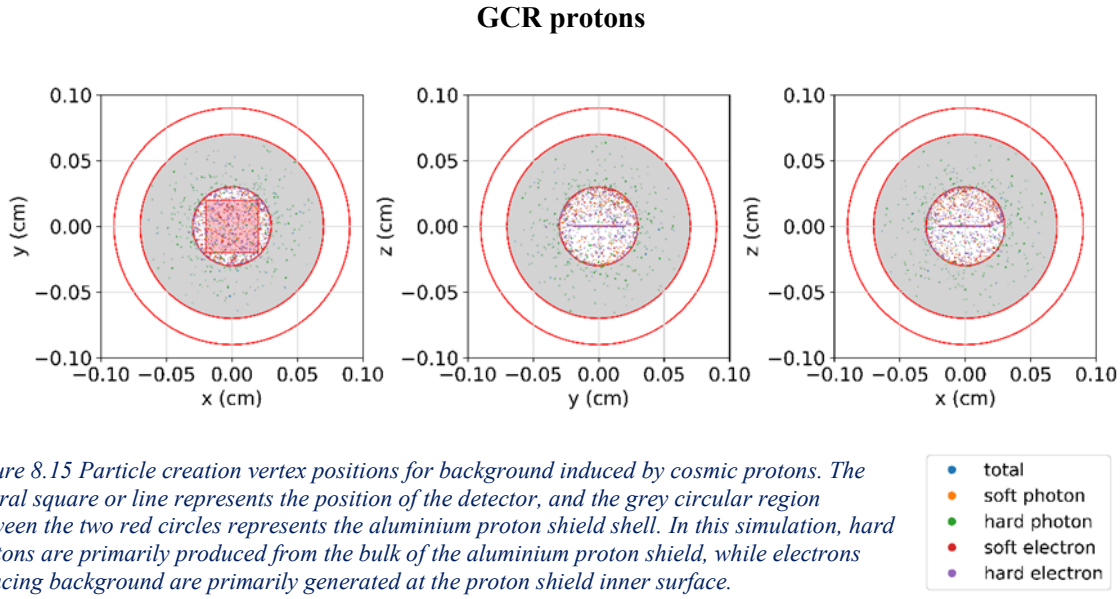

Figure 8.15 Particle creation vertex positions for background induced by cosmic protons. The central square or line represents the position of the detector, and the grey circular region between the two red circles represents the aluminium proton shield shell. In this simulation, hard photons are primarily produced from the bulk of the aluminium proton shield, while electrons inducing background are primarily generated at the proton shield inner surface.

Figure 8.14 indicates that photons inducing background in the CXB simulation appear to be themselves primarily CXB photons originating from the particle generation sphere, as was evidenced previously in Figure 8.12, and that these particles appear to be distributed approximately isotropically.

In contrast, Figure 8.15 appears to indicate that particles that induce background in the GCR cosmic proton case appear to primarily originate from both the bulk of the proton shield for hard photons and from the proton shield inner surface for other components.

The hard photon density is approximately isotropic, while the inner surface components exhibit a higher density above the detector than below, indicating that the BCB layer below the detector may be significantly attenuating device background. In contrast, the optical blocking filter appears to be too thin to attenuate background counts significantly relative to the BCB layer. Figure 8.16 displays a zoomed-in version of Figure 8.15 to further show this variation in background originating from above and below the detector.

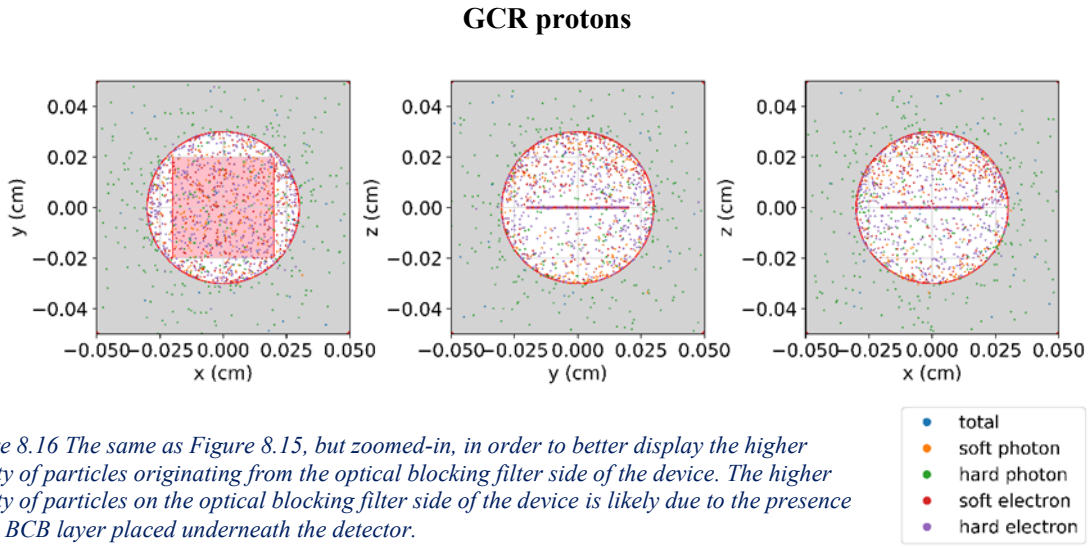

Figure 8.16 The same as Figure 8.15, but zoomed-in, in order to better display the higher density of particles originating from the optical blocking filter side of the device. The higher density of particles on the optical blocking filter side of the device is likely due to the presence of the BCB layer placed underneath the detector.

It can also be observed that almost all of the produced soft photons, soft electrons and hard electrons are produced from the Al spherical shell inner surface.

Hard photons appear to be the only component where a significant quantity of particles are produced from the Al spherical shell bulk. The distribution of bulk-produced hard photons exhibits higher concentrations closer to the Al spherical shell inner surface, and lowering concentrations with increased distance into the bulk of the Al spherical shell. In order to examine the origin location in further detail, it is necessary to plot the distribution of particle creation locations with respect to radial distance.

8.3.3.1 Radial distribution

In order to better display the distribution of particles that induce background, Figure 8.17 displays a histogram of all background events binned with respect to radial position $R = \sqrt{x^2 + y^2 + z^2}$.

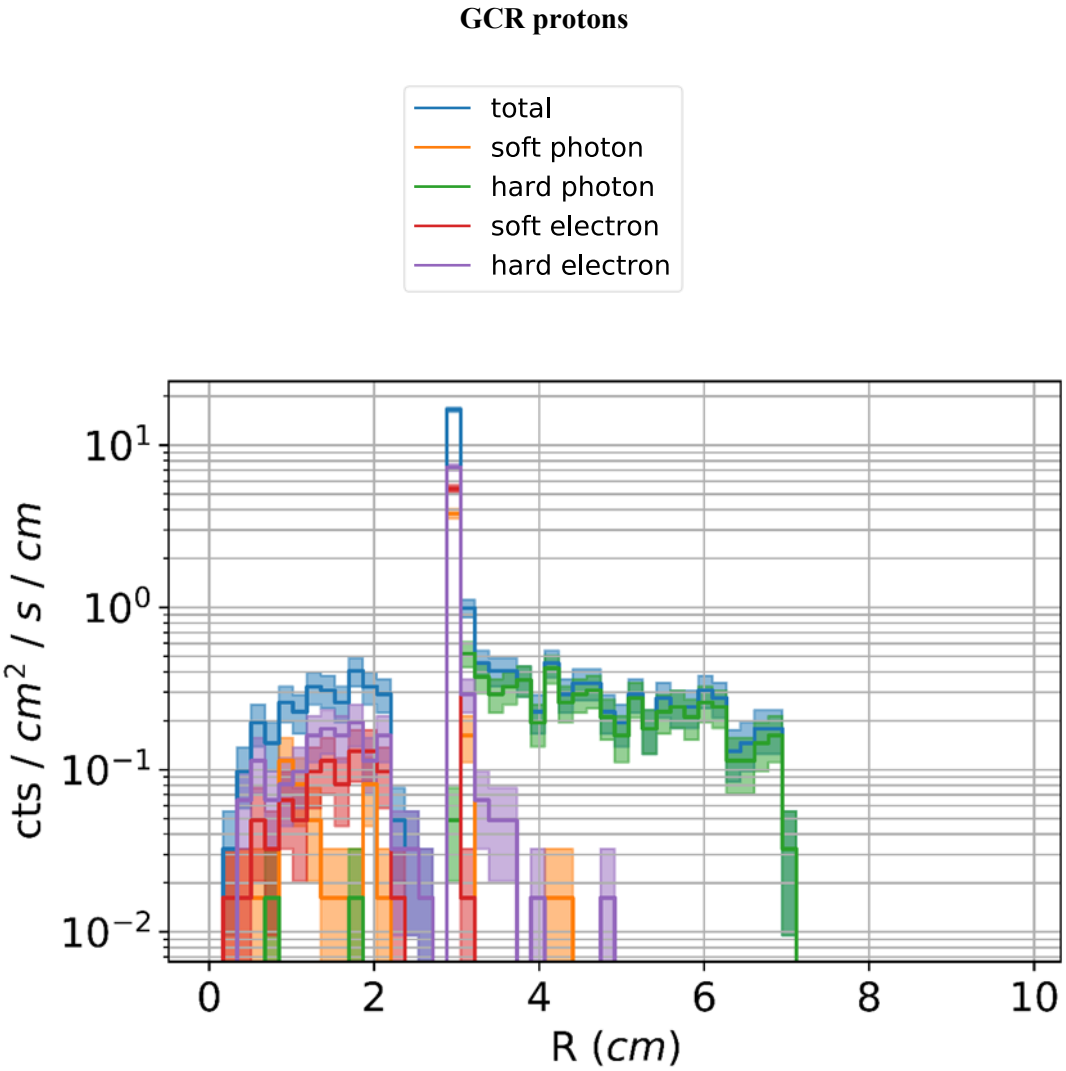

Figure 8.17 A histogram of the radial origin vertex position of particles that induce background. Soft photons, soft electrons and hard electrons that induce background appear to predominantly originate from the inner surface of the aluminium proton shield, while hard photon induced background appears to originate from the aluminium bulk, with an approximately exponentially decreasing generation probability with radial position. There is also some background associated with the on-chip layers at radial distances at 0.02 meters and below, although this background is small compared to background from the proton shield.

Figure 8.17 indicates that as stated previously, hard photons appear to originate from predominantly within the proton shield bulk in contrast to other components, which primarily originate from the inner surface of the proton shield. This is likely due to the fact that hard photons are significantly more penetrative than the other components, and are therefore able to penetrate further distances in aluminium. The hard photon radial density of origin locations appears to specifically decrease exponentially with increasing radial distance into the proton shield.

8.3.3.2 Angular distribution

In addition to plotting the radial distribution of particle creation vertex positions, the angular distribution of particle creation location can also be determined. While it is possible to do this by

converting the particle creation positions into spherical coordinates and then binning with respect to the angle from the detector normal, $\theta = \arccos\left(\frac{z}{R}\right)$, it is more useful to instead bin with respect to solid angle, $\cos\theta$. This is because an isotropic distribution in 3 dimensions is invariant with respect to the solid angle but not with respect to angle, due to the variation of a spherical area element with respect to polar angle θ. Figure 8.18 displays the differential flux with respect to solid angle for the cosmic proton-induced background between 0.1 keV and 15 keV while Figure 8.19 displays the differential background flux for the cosmic X-ray induced background. In each case, the differential flux was calculated by binning the normalised flux between different angles and dividing by $\sin\theta$, which approximates the difference in solid angle, $\delta\cos\theta$.

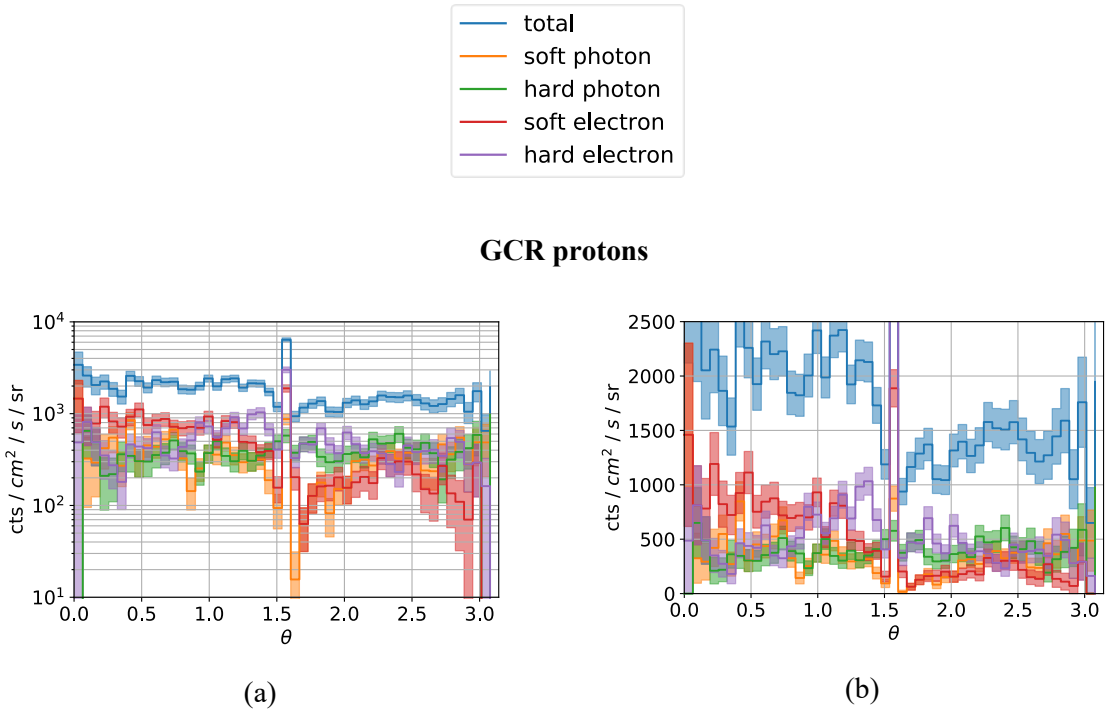

Figure 8.18 The angular distribution of particle creation locations with respect to the normal to the detector. For particles generated on the side of the detector shielded by the optical blocking filter, the particle differential flux appears approximately constant, whereas on the side shielded by the BCB layer, several components appear to vary in intensity, and the overall background appears to be reduced.

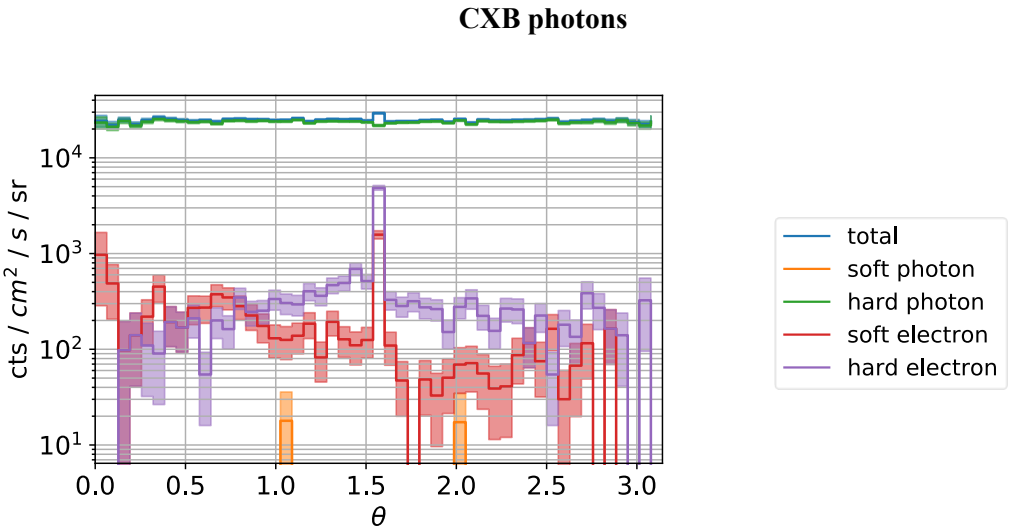

Figure 8.19 The angular distribution of background in cosmic X-ray background simulations. There appears to be no dependence on angle for the dominant hard photon component, which is as expected for a diffuse source of X-rays.

Figure 8.18a and Figure 8.18b indicate that there is significantly less background originating from surfaces below the detector as there are from above the detector, as was observed qualitatively in plots of the particle creation positions previously in figures Figure 8.15 and Figure 8.16. The hypothesis that this is due to the BCB layer attenuating low energy photons and electrons is further evidenced here by the fact that hard photons are the only component that maintains an approximately constant differential flux across most θ. This hypothesis makes sense intuitively as hard photons are expected to be mostly unaffected by the BCB.

In both the GCR proton and CXB cases, the soft electron and photon spectra appear to deviate significantly from isotropic sources below the detector. This deviation is likely due to the different thickness of BCB along particle trajectories at different angles, leading to more attenuation at angles further from the surface normal to the BCB. As this variation is relatively large, it may be possible to significantly reduce the background further by increasing BCB thickness so that even particles at a perpendicular angle must pass through a significant thickness of BCB and be attenuated accordingly.

8.3.4 The physics creation processes generating background inducing particles

In addition to looking at the origin location of particles as a function of particle type, it is also instructive to plot the creation process that generated a background-inducing particle as a function of position.

8.3.4.1 Creation processes as a function of radial position

Figure 8.20 and Figure 8.21 display histograms of background-inducing vertex radial positions for the CXB and GCR background components split by the creation process.

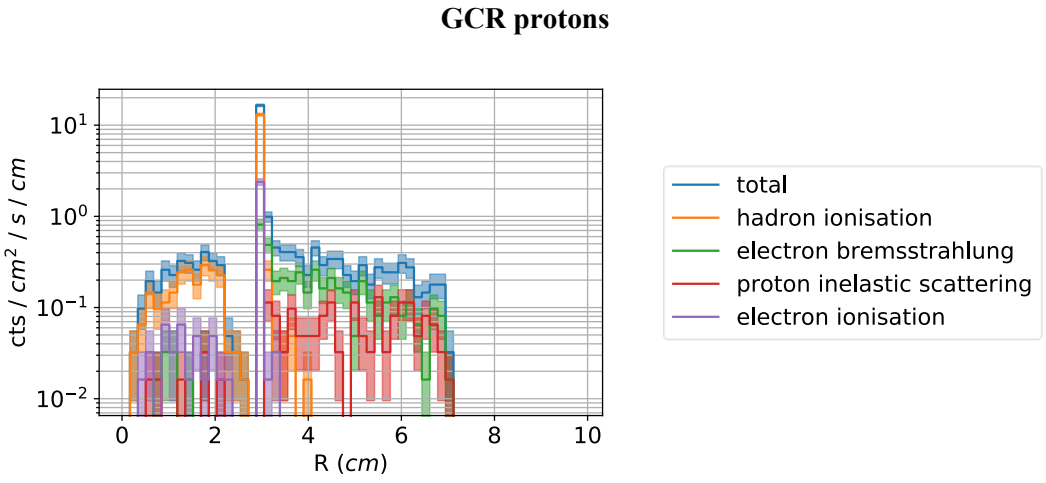

Figure 8.20 The radial creation location of background-inducing particles, split by creation process. Particles generated at the proton shield inner surface appear to be primarily generated by proton inelastic scattering or hadron ionisation, whereas particles generated further into the aluminium appear to be generated almost entirely by electron bremsstrahlung.

Creation Process	Fit Type	Fit Parameters
Proton inelastic scattering	Constant, c	$c = 15 \pm 3$ cts / cm² / s / cm
Electron bremsstrahlung	Exponential, $A\, e^{-\lambda R}$	$A = 160 \pm 51$ cts / cm² / s / cm $\lambda = 41 \pm 7$
All inner surface processes	N/A	0.1 – 15 keV: 3.66 ± 0.07 cts / cm² / s 2-7 keV: 1.23 ± 0.05 cts / cm² / s

Table 8.7 Fits to the creation processes as a function of radial creation position R.

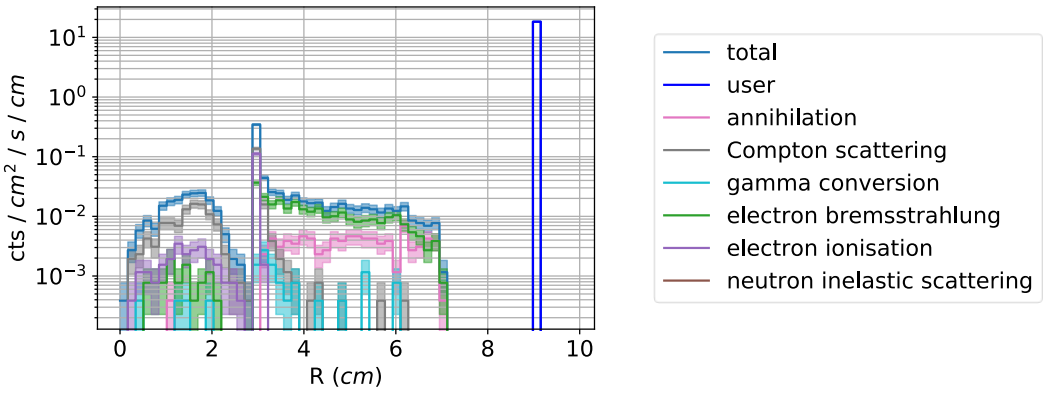

Figure 8.21 The radial creation location of background-inducing particles in the cosmic X-ray simulations. As expected, almost all these particles appear to originate from the particle generation surface at r=0.09 meters, indicating that these background events are created by the original cosmic X-rays Compton scattering in the detector.

Figure 8.21 indicates that as expected almost the entire cosmic X-ray induced spectrum appears to originate from primary cosmic X-rays that are Compton scattering in the detector, as was previously indicated in Sections 8.3.2.2 and 8.3.3. In Section 8.3.2.2 it was also shown that a significant number of incoming photons scatter in the Al proton shield at least once before scattering in the detector.

Figure 8.20, on the other hand, indicates that GCR-induced particles generated by all creation processes except for electron bremsstrahlung are almost entirely generated from the inner surface of the aluminium proton shield. These inner surface creation processes therefore likely represent the creation processes associated with the creation of soft photons, soft electrons and hard electrons.

Figure 8.22 displays the background spectrum in the GCR simulations split by both particle type, and the region of the simulation geometry that background-inducing particles were generated from.

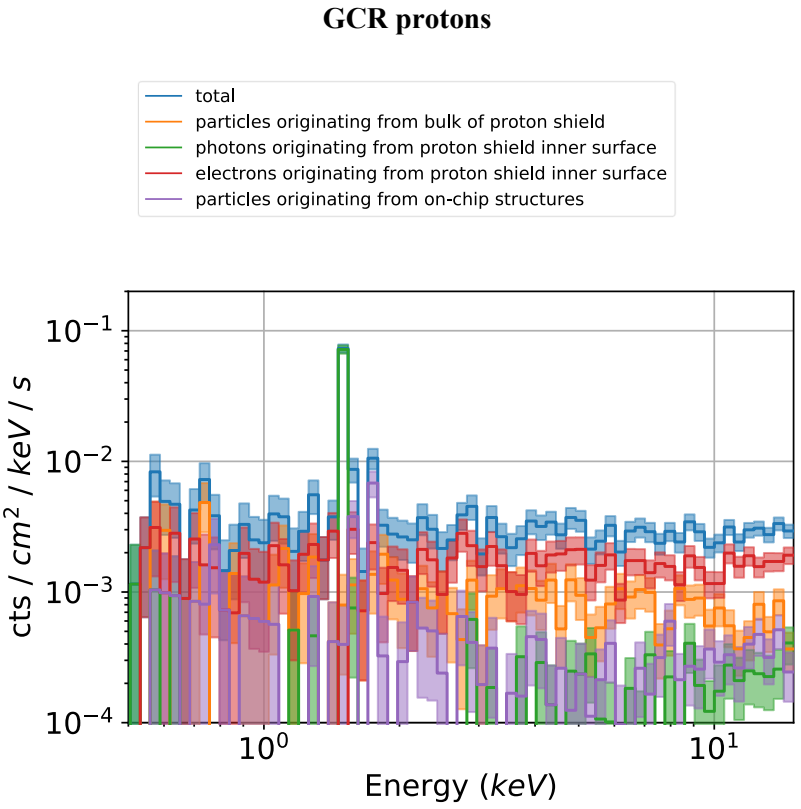

Figure 8.22 The spectrum generated by particles generated from different regions of the simulation geometry. The majority of the photon-induced spectrum originates from the proton shield bulk, while the majority of the electron-induced spectrum originates from the proton shield inner surface.

At radial positions beyond the inner surface, the electron backscattering creation process dominates, indicating that hard photons produced in the bulk Al are specifically being created as electron bremsstrahlung. The fact that these photons are specifically created by electrons indicates that these photons are not being created directly by incoming cosmic protons but are instead a result of knock-

on electrons scattering through the aluminium. The fact that there are several particle species involved in this chain of processes to creating a background event means that it will be challenging to determine which materials are optimal for a proton shield from the perspective of X-ray-like background.

8.3.4.2 Spectral composition

To examine the effect of different creation processes on the background spectrum, Figure 8.23 displays the background spectrum split into creation process components. Figure 8.23(a) and Figure 8.23(b) display the background from secondary photons and secondary electrons, respectively in GCR proton simulations.

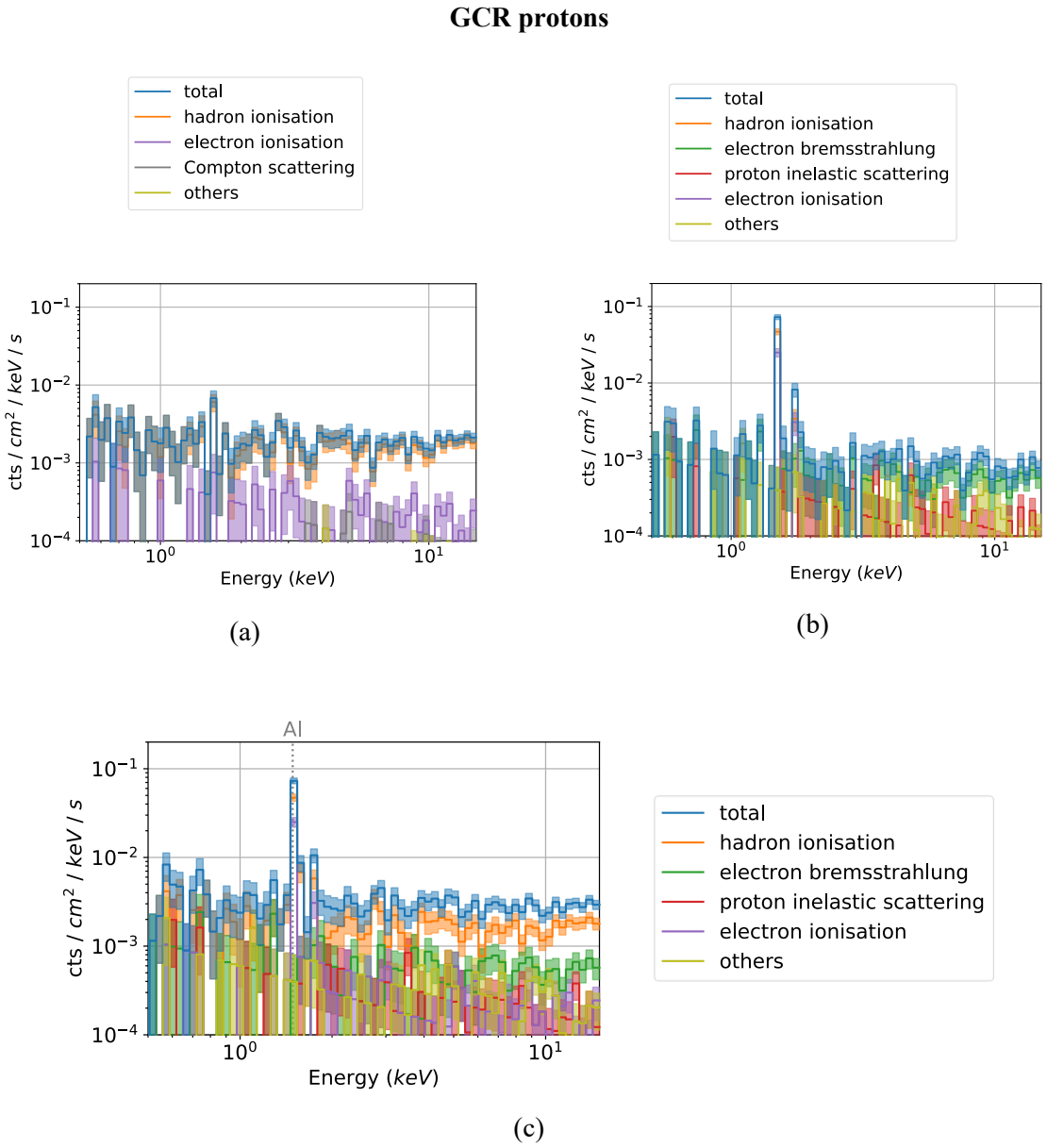

Figure 8.23 The background spectrum induced by cosmic protons, split by background inducing particle creation process. Figure 8.23(a) and Figure 8.23(b) display the background from secondary electrons and secondary photons, respectively, while Figure 8.23(c) displays the background from all particles split by creation process. The dominant creation processes appear to be hadron ionisation, followed by electron bremsstrahlung and then proton inelastic scattering.

Figure 8.23 indicates that the cosmic proton secondary electron background spectrum is dominated by electrons generated by hadron ionisation and that the secondary photon spectrum is primarily dominated by the electron bremsstrahlung and proton inelastic scattering creation processes. In each case, the spectra are approximately flat in the 0.1 keV – 15 keV background energy range.

In experiments described in Chapters 6 and 7, it was found that Geant4 was successfully able to replicate the spectra produced by hadron ionisation for hard electrons, and successful predictions of the variation of the spectra in both experiments when a magnetic field was applied gave evidence that Geant4 is simulating the soft electron continuum correctly. While there was an overestimation of X-

ray-like background between approximately 2 keV and 5 keV in the 200 MeV proton experiment, this may have either been related to Geant4's Compton scattering process, which did not influence the spectrum significantly in the simulations presented in Figure 8.23 or because of CCE effects in the experimental device used. There is therefore no reason in particular to believe currently that Geant4 is incorrectly simulating the electron physics that produced the spectrum in Figure 8.23(a).

Simulations of the 200 MeV irradiations in Chapter 7 also produced fluorescence lines created by hadron ionisation and electron ionisation that were in good agreement with experimental fluorescence lines, indicating that the predictions of fluorescence line intensity in spherical shell models given in this chapter are correct. However while the experiments in Chapters 6 and 7 give information about Geant4's accuracy at simulating electrons and soft photons, it is currently unknown whether the hard photon physics processes involved in the creation of the hard photon spectrum in Figure 8.23(b) are being correctly simulated, and further experiments may need to be performed at higher beamline energies or at photon beamlines to confirm their accuracy.

8.4 Conclusions

Simulations have been performed that indicate that the primary sources of background present in the space-based environment for a 450 μm thick detector, as predicted by Geant4, are soft electrons, backscattering electrons and hard photons. It was found that these components comprised approximately a third of the total continuum background each.

Analysis of the spherical shell model simulations successfully characterised many background features, including the primary energies that create different background components, the kinetic energies of particles that produce background and the origin location of background-inducing particles. In GCR proton simulations, background inducing soft electrons, soft photons and hard photons were found to originate diffusely from volumes surrounding the detector, and the majority of particles were found to originate from thin surfaces within line-of-sight of the detector. The exception to this was hard photons which were found to be created by electron bremsstrahlung and proton inelastic scattering, which were found to be primarily created within the bulk aluminium spherical shell surrounding the detector. In contrast, CXB photon simulations found that background was primarily generated by CXB photons themselves scattering in the detector, however some CXB photons Compton scattered in the proton shield before impacting the detector. This acted to slightly reduce the energy profile of photons that induced background.

It was found that all of the particle components were of sufficiently low energies that shielding a detector from them may be possible, providing that a shielding mechanism produces less background-inducing particles than it absorbs. Chapters 9, 10 and 11 will discuss possible mechanisms for

decreasing or removing background associated with each of these particle types, including the use of graded-Z shielding, and the use of magnetic diversion.

While these simulations have determined much of the structure and physics underpinning the creation of X-ray-like background for the specific case of a detector of 450 μm in thickness and an aluminium proton shield composed of 4 cm of aluminium, there remain several questions to be answered concerning how background varies with spacecraft structure and detector structure. To answer these questions, Chapter 9 will investigate the variation in the background with respect to these changes in geometry.

Chapter 9

The Effect of Spacecraft Geometry and Detector Design on Instrument Background

Now that the composition of X-ray-like background has been characterised for a basic spherical shell model, it is possible to investigate how varying features of the spherical shell model can alter the background. This chapter will investigate in particular how the spacecraft and detector design can influence X-ray-like background in a mission, using the context of a spherical shell model to investigate the physics of background generation.

9.1 The effect of device design on instrument background

The design of objects in spacecraft surrounding a detector is expected to be able to significantly alter the radiation incident upon a device. However, the spectrum of X-ray-like background radiation will induce in a device also depends on device characteristics such as the device thickness and the presence or absence of on-chip structures, as was indicated by the lowered background from underneath the device due the presence of an on-chip BCB in simulations in Chapter 8. This section will, therefore, investigate the impact of detector geometry on X-ray-like background and how a knowledge of device design can be used to inform background mitigation strategies.

9.1.1 Detector thickness

Detector thickness is one of the key parameters in determining how a detector will respond to radiation. An increasing detector thickness causes background induced by both soft photons and Compton scattering hard photons to increase, as the probability of an interaction occurring when a photon hits a detector increases with the amount of material the particle has to travel through. Therefore it is necessary to investigate the exact ways by which background varies with device thickness to assess how background might vary for devices with different thickness.

Additionally, it is necessary to investigate how the signal-to-noise ratio varies with device thickness. Device thicknesses are often increased to improve the number of signal photons received by a device,

and thereby improve the signal-to-noise ratio. However, increasing detector thickness may also increase the background present in a device and may cause a decrease in signal-to-noise ratio for the detection of low flux photons. Results presented in Section 9.1.1.6 will show that for thicknesses above several hundreds of μm, this is likely to be the case. As was discussed in Chapter 1, the signal-to-noise ratio can be given in terms of the flux of signal photons absorbed in the detector and the flux of X-ray-like background events, as described in Equation 1.5. Using the Beer-Lambert law equation 1.5 can be re-written as

$$\frac{S}{N} = \frac{\sqrt{t_I A}\left(F_S\left(1 - e^{-\lambda(E)t}\right)\right)}{\sqrt{F_S(1 - e^{-\lambda(E)t}) + B(E,t)}} \tag{9.1}$$

where t_I is the integration time, A is the detector area, F_S is the flux of signal photons hitting the detector, $\lambda(E)$ is the attenuation coefficient for photons of a given energy E, and $B(E,t)$ is the total background flux as a function of deposited energy E and detector thickness. Therefore the observation quality as a function of device thickness can be determined by a quality factor given by

$$QF = \frac{\frac{S}{N}}{\sqrt{t_I A}} = \frac{\left(F_S\left(1 - e^{-\lambda(E)t}\right)\right)}{\sqrt{F_S(1 - e^{-\lambda(E)t}) + B(E,t)}} \tag{9.2}$$

Where F_S is the flux of photons from a source of scientific interest, $\lambda(E)$ is the attenuation coefficient of the photons of interest in silicon as a function of photon energy, t is the thickness of the depletion region thickness in the detector, $B(E,t)$ is the background as a function of energy and thickness, t_I is the length of time of the observation, and A is the total pixel area of the detector. In this case, the constant F_S has been multiplied by $\left(1 - e^{-\lambda(E)t}\right)$ to reflect the quantum efficiency of the device it is impacted, where in Chapter 1 the quantum efficiency was contained within F_S.

To analyse the effect of varying detector thickness on X-ray-like background, it is worthwhile to establish a mathematical framework for the behaviour of background as device characteristics vary. Mathematically understanding the variation of background with respect to varying detector thickness often gives a more complete understanding of a system than can be found through Monte Carlo simulations of single geometries, and can allow for results to be based on a more rigorous theoretical framework.

The system displayed in Figure 9.1 was used to model the systems described in this chapter. The detector here was modelled as a cuboid block of silicon, which has a thickness t, and a face with approximately infinite sides.

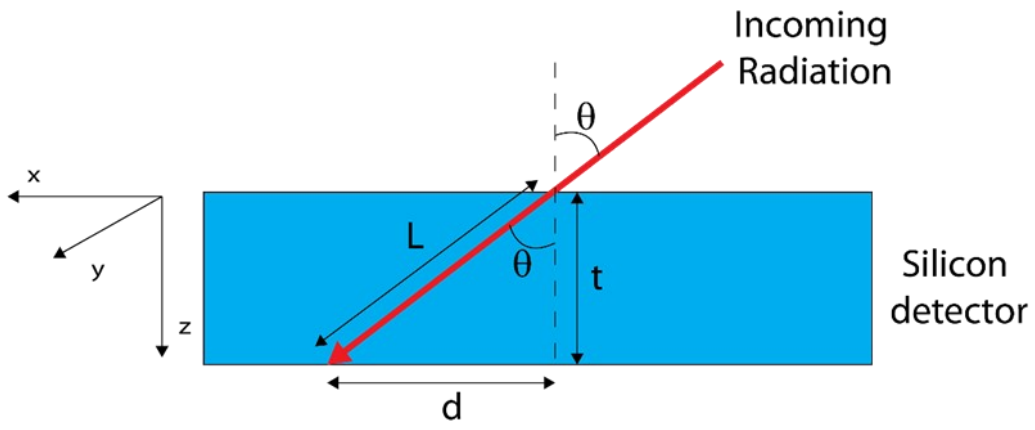

Figure 9.1 The detector geometry used for mathematics in this section.

The angle between the incoming particle and the normal to the detector is given by θ, while L and d are the distances the particle travels through the detector and along the face of the detector, respectively.

9.1.1.1 High energy Compton scattering photons

To characterise the background a device will receive from Compton scattering photons, a key parameter that must be determined is the mean probability of interaction, $\bar{P}$. $\bar{P}$ directly determines the mean number of background photon counts that a detector will receive, $\mathrm{B} = F_{Compt} \times \bar{P}$, where B is the mean number of background counts and F_{Compt} is the number of photons that impact the device which would Compton scatter to deposit a certain quantity of energy if the probability of interacting with the detector were guaranteed.

To specifically calculate the impact of high energy photons both originating from the CXB and interactions between GCR protons and spacecraft materials, several assumptions can be used to simplify the mathematics. The Klein-Nishina cross-section (Kamal 1969) for Compton scattering of high energy X-rays gives mass attenuation coefficients that correspond to half-value layers that are significantly larger than typical device thicknesses.

For example, 80 keV is a typical energy for hard photons that induce background in both GCR simulations and CXB simulations, as discussed in Chapter 8. An 80 keV photon energy corresponds to a half-value layer of 13.4 mm in silicon (Xcom 2010) which is significantly larger than typical device thicknesses, which often range between several μm and several hundred μm. The low attenuation coefficient for Compton scattering photons means that the assumption can be made that the photon flux present at a particular layer in the device is approximately constant, and that the absorbed flux of photons is approximately proportional to only the thickness of silicon they pass through.

Using this approximation, the mean probability for a hard photon inducing a background event can be calculated to be

$$\overline{\mathrm{P}} = 2\lambda_{\mathrm{Compt}} t \tag{9.3}$$

where λ_{Compt} is the attenuation coefficient of the device for a Compton scattering photon of a given energy. The derivation for this is given in Appendix D.1.

Equation 9.3 is equivalent to multiplying the mean path length of the photon through the detector (which is equal to $2t$) along the particle's direction of travel by λ_{Compt}. Equation 9.15 implies that the number of Compton scattering events received in a detector should scale linearly with detector thickness, which means that as expected Compton background events should become more significant for thicker detectors.

$\bar{P}$ can now be directly inserted into Equation 9.1 to give the total signal-to-noise ratio as

$$\frac{S}{N} = \frac{S}{\sqrt{S+B}} \tag{9.4}$$

$$= \sqrt{At_I}\left(\frac{F_S(1-e^{-\lambda t})}{\sqrt{F_S(1-e^{-\lambda t}) + 2F_{Compt}\lambda_{Compt} t}}\right) \tag{9.5}$$

And the quality factor as

$$QF = \frac{F_S(1-e^{-\lambda t})}{\sqrt{F_S(1-e^{-\lambda t}) + 2F_{Compt}\lambda_{Compt} t}} \tag{9.6}$$

This quality factor is displayed as solid lines for a range of incoming particle energies with respect to detector thickness t in Figure 9.2, where F_S and F_{Compt} are both set to 1. Dashed lines represent the quality factor in a situation where there is no X-ray-like background.

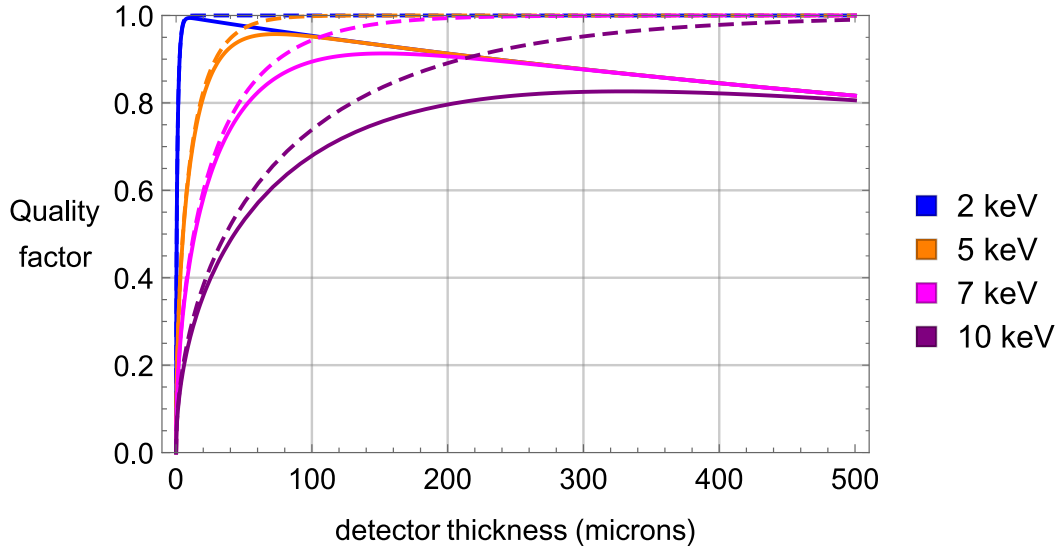

Figure 9.2 The quality factor as a function of thickness for the case of Compton dominated background (solid lines) as compared to the quality factor for incident observation photons where no background is present (dashed lines). In this case, all factors were set to 1 except for λ, which was set to the actual tabulated mass attenuation coefficient for photons in silicon, and λ_{Compt}, which was set to 0.001. Representative values for λ_{Compt} will be used in Section 9.1.1.6, after fitting is used to calculate λ_{Compt} from simulations.

Figure 9.2 indicates that the presence of Compton scattering photons significantly alters the quality factor profile as a function of t. With no Compton background, increasing detector thickness is always beneficial to the signal-to-noise ratio, albeit with diminishing returns as the quality factor approaches the maximum. With a dominant Compton background, however, the quality factor peaks before decreasing approximately linearly with increasing detector thickness. This means that despite quantum efficiency increasing with device thickness, if the Compton background is dominant relative to other background components, and comparable in intensity to the signal flux, increasing detector thickness may act to reduce the signal-to-noise ratio and reduce the scientific output of a mission.

To fully characterise the Compton background, however, λ_{Compt} needs to be determined for the particular energy range of interest as well as the particular spacecraft structure of the mission being examined. This shall be performed in Section 9.1.1.6, where λ_{Compt} is determined for the spherical shell model configuration.

9.1.1.2 Soft, fully absorbed photons

The mathematics required to model the background induced by Compton scattering relied upon the simplifying assumption that the attenuation length for a Compton scattering photon was low relative to detector thickness. For a photon that is fully absorbed in the depletion region by the photoelectric effect, this assumption becomes no longer valid, and the full analytical system must therefore be solved. This can be done mathematically, despite the presence of relatively complex mathematics. A distinction must also now be made between back-illuminated devices with no on-chip layers and

front-illuminated devices containing several on-chip layers, which may be capable of attenuating incident X-rays. Calculations for back-illuminated devices were performed first as part of this PhD work, and then calculations for front-illuminated devices could be built upon the initial calculations for the back-illuminated devices.

9.1.1.3 Soft photons impacting back-illuminated devices

Calculating the probability that a photon will be absorbed into a material is relatively straightforward if the photon's trajectory is at a normal to a device, which is approximately the case for signal X-rays entering the telescope through the optics. Off-axis background X-rays, however, hit the detector from numerous angles, and this angular distribution of X-rays adds additional complexity to the system, which must be taken into account in calculations.

By considering an isotropically distributed photon source irradiating a detector surface, with a probability of absorption exponentially decaying with distance into the surface, it is possible to derive the probability density function, $PDF_z(z)$, that a photon arriving at a known position but unknown direction will induce an X-ray-like background event;

$$PDF_z(z) = 2z\lambda^2 Ei(-\lambda z) + 2\lambda e^{-\lambda z} \tag{9.7}$$

The derivation for this is given in Appendix D.2. Here λ is the attenuation coefficient of the device for a particular photon of a given energy and $Ei(x) = \int_{-\infty}^{x} \frac{1}{t} e^t \, dt$ is known as the elliptic integral of x and is a function where values can be found from tabulated values.

To find the total probability that a photon will be absorbed within a detector, Equation 9.7 must be integrated between $z = 0$ and $z = t$, giving the total probability of absorption, P, as

$$P = 1 + e^{-\lambda t}(\lambda t - 1) + \lambda^2 t^2 Ei(-\lambda t) \tag{9.8}$$

Equation 9.8 is the same as the value of P for a photon impacting the device at a normal to the device surface, $P_\perp = 1 - e^{-\lambda t}$, plus an extra term, $\lambda t e^{-\lambda t} + \lambda^2 t^2 Ei(-\lambda t)$. As this extra term is always greater than or equal to 0, it can be seen that P is always greater than $P_\perp$. This can be observed in Figure 9.3, where absorption probabilities are plotted as a function of detector thickness for several different fluorescence line energies versus the value of $P_\perp$.

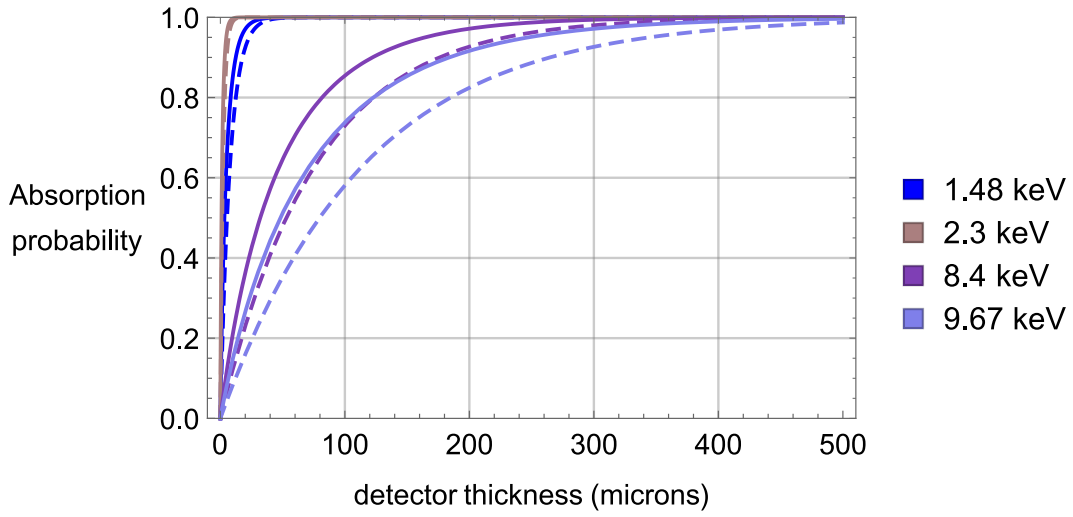

Figure 9.3 The absorption probability for several common fluorescence energies of Al, Mo and W, for cases where the particle impacts the device at a normal to the surface (dashed lines) and when incoming particles are distributed isotropically as described by Equation 9.34 (solid lines).

P can be then be used to give a signal-to-noise ratio for a soft photon dominated background of

$$\frac{S}{N} = \frac{S}{\sqrt{S+B}} \tag{9.9}$$

$$\frac{S}{N} = \sqrt{At_I}\left(\frac{F_S(1-e^{-\lambda t})}{\sqrt{(F_S+F_\gamma)(1-e^{-\lambda t}) + F_\gamma\left(\lambda t e^{-\lambda t} + \lambda^2 t^2 Ei(-\lambda t)\right)}}\right) \tag{9.10}$$

And a quality factor of

$$QF = \frac{F_S(1-e^{-\lambda t})}{\sqrt{(F_S+F_\gamma)(1-e^{-\lambda t}) + F_\gamma\left(\lambda t e^{-\lambda t} + \lambda^2 t^2 Ei(-\lambda t)\right)}} \tag{9.11}$$

where F_γ is the number of soft photons hitting the detector. As was done for the Compton case, QF is plotted in Figure 9.4 for a range of particle energy deposition energies, with F_S and F_γ set equal to 1.

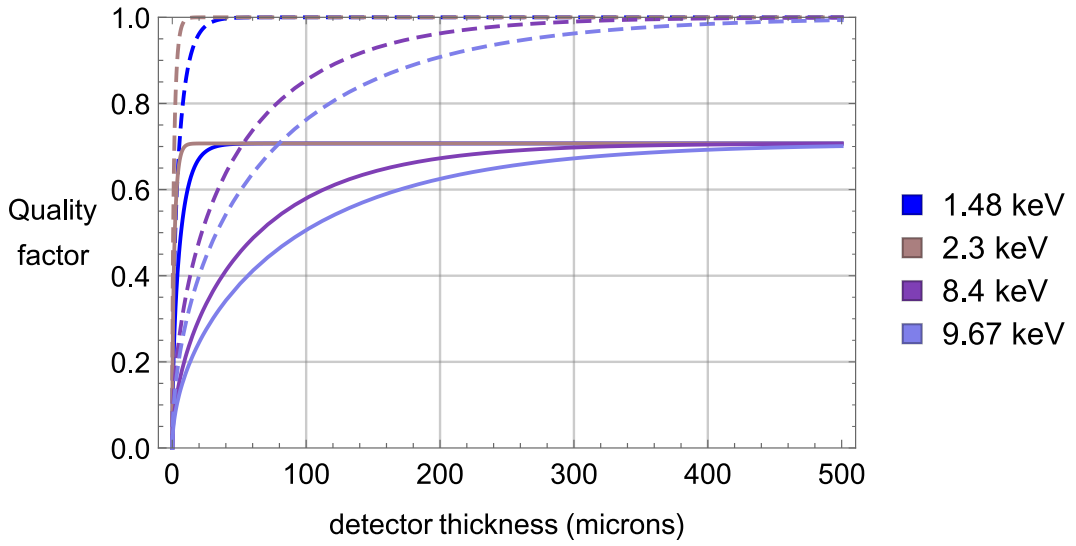

Figure 9.4 The quality factor for isotropic, background-inducing, soft photons (solid lines) as compared to the quality factor of perpendicularly impacting signal photons where no background is present (dashed lines). As soft photons in background are primarily composed of fluorescence photons, the plotted photon energies correspond to common fluorescence energies of aluminium, molybdenum and tungsten.

Figure 9.4 indicates that unlike the signal-to-noise ratio in the Compton scattering background dominated case, fully absorbed photons do not cause the signal-to-noise ratio to reduce with detector thickness. However, their presence does appear to reduce the overall signal-to-noise ratio by a significant level.

One parameter that can be used to quantify the reduction in signal-to-noise ratio due to soft photons is the quality factor in the limit where $t \to \infty$ and where $F_S = F_\gamma = 1$. This quality factor limit gives a measure of how the signal-to-noise ratio would reduce in a thick detector where the flux of soft photons is approximately equal to the flux from a scientific source.

Taking the limit as $t \to \infty$ causes $QF \to \frac{F_S}{\sqrt{F_S+F_\gamma}}$, which becomes $QF \to \frac{1}{\sqrt{2}} \approx 0.707$ when $F_S = F_\gamma = 1$, a significant reduction from the quality factor limit of 1 in the case where no background is present. This reduction of the signal-to-noise ratio means that for cases where the soft photon background is comparable to the signal flux, the signal-to-noise ratio may be significantly lower than would be expected if only the quantum efficiency of the device were taken into account.

9.1.1.4 Soft photons impacting front-illuminated and multi-layered devices

While this mathematics may be suitable for describing a back-illuminated device containing no on-chip filters or electronics, many devices are not designed with a clear, unobstructed line of sight to the sky. Often devices are front-illuminated or contain on-chip filter layers that may attenuate some photons before they reach a device.

Therefore, it is useful to generalise Equation 9.7 from Section 9.1.1.3 to multilayer devices. Fortunately, the expressions derived for this case are nearly identical to the single-layer system described in Section 9.1.1.3, and the geometry utilised in Figure 9.1 can be adapted into the geometry shown in Figure 9.5.

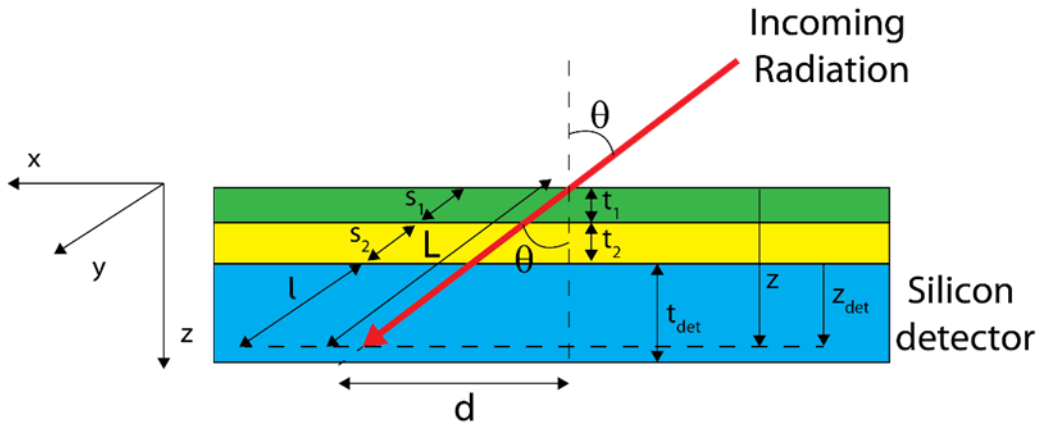

Figure 9.5 The geometry for the mathematics used in this section relating to multiple on-chip device layers, which may include structures like optical blocking filters or on-chip electronics. Here, $z = 0$ is defined to be the surface of the actual sensitive detector region.

Using similar methods to those used to derive the probability density functions in the case of a back-illuminated device, $PDF_{z_{det}}(z_{det})$ was determined to be

$$PDF_{z_{det}}(z_{det}) = 2\lambda' \left(e^{-\lambda_{det} z_{det} - \sum_{i=1}^{N} \lambda_i t_i} + \left(\lambda_{det} z_{det} + \sum_{i=1}^{N} \lambda_i t_i \right) Ei\left(-\lambda_{det} z_{det} - \sum_{i=1}^{N} \lambda_i t_i \right) \right) \tag{9.12}$$

where $\lambda' = \lambda_{det} + \frac{1}{z}\sum_{i=1}^{N}(\lambda_i - \lambda_{det})t_i$, λ_i is the attenuation coefficient for a photon in layer i and λ_{det} is the attenuation coefficient for the sensitive region of the detector. The derivation for this is given in Appendix D.3. Through integration from $z_{det} = 0$ to $z_{det} = t_{det}$, the total probability as a function of t can be determined. In this case, however, it is only possible to numerically integrate Equation 9.12, as it contains several non-integrable terms. Therefore the soft photon induced background for multilayer systems like this may need to be analysed using specific values for the thickness of layers and attenuation coefficients.

9.1.1.5 Fully absorbed and backscattered electrons

In contrast to the complexities involved with mathematical modelling of the Compton background or fully absorbed photon spectrum, the CSDA range for a 15 keV kinetic energy electron is only 3.0 µm in silicon (M. J. Berger et al. 2017). This range is sufficiently short that soft electron

induced background can be assumed to be approximately constant with respect to varying detector thickness above several μm. Background induced by hard backscattering electrons is also expected to not vary in intensity with respect to changing detector thickness as the simulations displayed in Chapter 7 indicated that backscattering electrons were found to only interact with the detector within the first few microns of the surface. Therefore, both soft electron and hard electron induced background which are not fully penetrating can be considered collectively as a constant background level F_e.

Therefore, the signal-to-noise ratio and quality factor in the electron dominated case can be described respectively as

$$\frac{S}{N} = \frac{S}{\sqrt{S+B}} \tag{9.13}$$

$$= \sqrt{At}\left(\frac{F_S(1-e^{-\lambda t})}{\sqrt{F_S(1-e^{-\lambda t})+F_e}}\right) \tag{9.14}$$

and

$$QF = \frac{F_S(1-e^{-\lambda t})}{\sqrt{F_S(1-e^{-\lambda t})+F_e}} \tag{9.15}$$

where F_e is the number of electrons hitting a device that deposit a certain quantity of energy. Figure 9.6 displays the QF for the electron dominated case, again with the fluxes F_S and F_B set to 1.

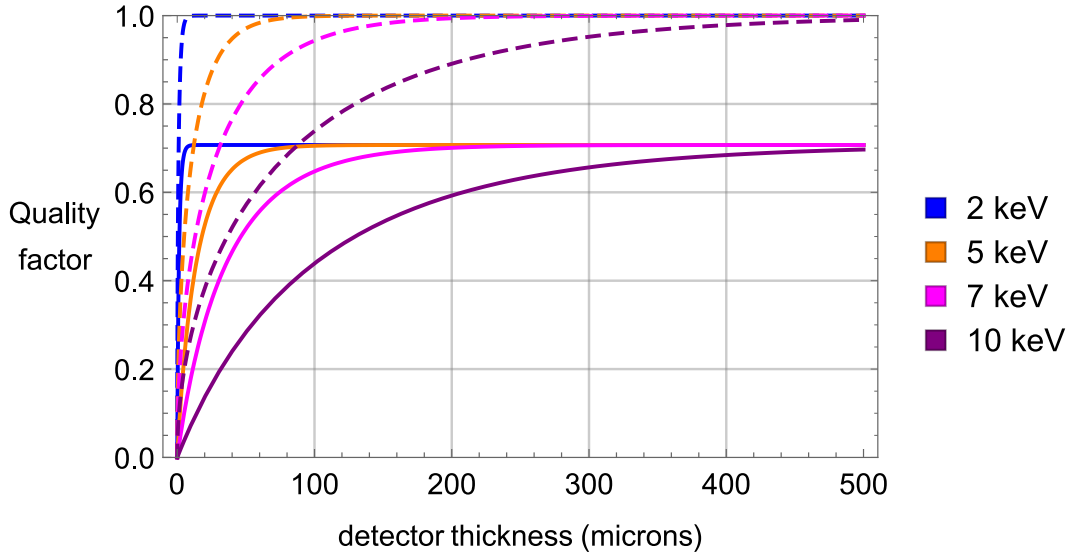

Figure 9.6 The quality factor where the background is dominated by electrons (solid lines) as compared to the quality factor for incident photons where no background is present. The background here is constant with respect to changing device thickness.

Despite being described by a different equation, Figure 9.6 appears very similar to Figure 9.4 describing the quality factor for fully absorbed photons. This is because similarly to the fully absorbed photon case, as $t \to \infty$, $QF \to \frac{F_S}{\sqrt{F_S+F_B}}$.

As in the fully absorbed photon case where the background flux is comparable to signal flux, the presence of the electron background acts to reduce the signal-to-noise ratio for all device thicknesses. This means that the signal-to-noise ratio is significantly lower than it would be in the case with no background.

While the electron-induced background is not expected to vary with detector thickness, Section 9.1.2 will investigate the effect of several configurations of aluminium optical blocking filters on the electron-induced background through Geant4 simulations. First, however, simulations with varying detector thicknesses were performed to test some of the mathematics described above and to acquire numerical values for modelling the full signal-to-noise ratio as a function of thickness using the equations derived in this section.

9.1.1.6 Simulations of the effect of varying device thickness on background

Simulations were set up in a similar format to those discussed in Chapter 8 and used the same analysis algorithms. As in Chapter 8, the proton shield was modelled as a 4 cm thick spherical shell of aluminium with a detector set to be a cuboid of silicon covered with a 90 nm aluminium optical blocking filter and a 5 μm sheet of BenzoCycloButene (BCB) on the opposite side, as shown in Figure 9.7. The detector volume was set to be 4 cm in width and length, but the thickness was set to vary for this set of simulations. As was discussed for simulations in Chapter 8, this general geometry was designed to emulate a simplified version of the expected design of the ATHENA WFI.

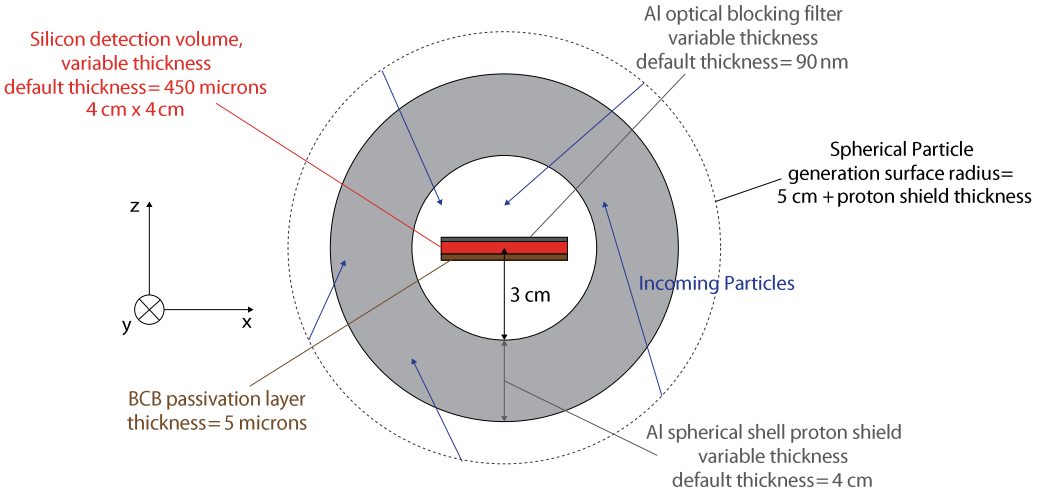

Figure 9.7 The geometry used for spherical shell model simulations in this chapter. Detector thickness, optical blocking filter thickness and proton shield thickness were all set to be variable, and simulations were performed varying each of these parameters for this chapter.

Multiple simulations were then run at detector thicknesses ranging from 15 µm to 450 µm in thickness for GCR proton and CXB input spectra.

Figure 9.8 displays the total X-ray-like background count rate between 2 keV and 7 keV plotted as a function of detector thickness, split into GCR proton and CXB induced components. Here it can be seen that the GCR proton induced and CXB induced components show different trends as detector thickness varies.

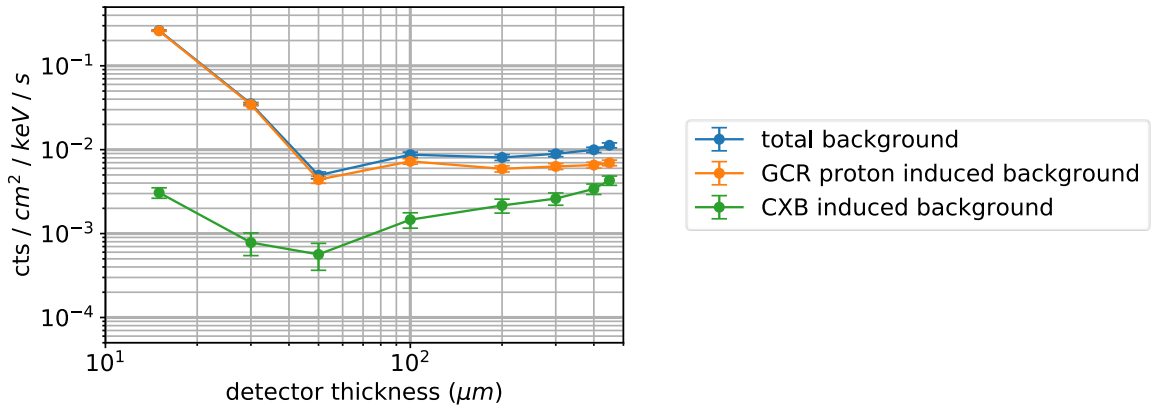

Figure 9.8 The variation in the mean background between 2 keV and 7 keV with respect to detector thickness. There is a significant initial drop in X-ray-like background from approximately 15 µm to 50 µm corresponding to minimally ionising particles disappearing from the spectra. Above 50 µm, the background increases approximately linearly, due to a linear increase in interactions between the detector and high energy Compton scattering photons.

The GCR proton induced X-ray like background component initially decreases dramatically as detector thickness increases, and then appears to approximately level off as device thickness exceeds approximately 100 µm in thickness. This is caused by the decrease in flux associated with counts due

to Minimally Ionising Particle (MIP) tracks, which become incapable of depositing energy in the detector energy range once the detector thickness exceeds approximately 50 μm as discussed in Chapter 3. Above 50 μm the GCR proton-induced spectrum then begins to increase linearly, corresponding to the expected increase in hard photon Compton scattering induced background with a constant electron component.

The CXB induced background also initially decreases between 15 μm and 50 μm and then begins to rise linearly at a larger rate of increase than the GCR induced background. The initial decrease in the background can be explained through the same mechanism as the decrease in GCR proton induced background, that the flux of CXB generated fully-penetrating particles such as knock-on electrons that are detected as X-ray-like events decrease with device thickness. The increasing background beyond 100 μm can also be explained by an increase in hard photon Compton scattering events as detector thickness increases.

Figure 9.9 shows the full spectra generated in simulations, where the MIP peak in the GCR proton simulations can be observed moving to the right of the spectrum and dropping in intensity with increasing detector thickness.

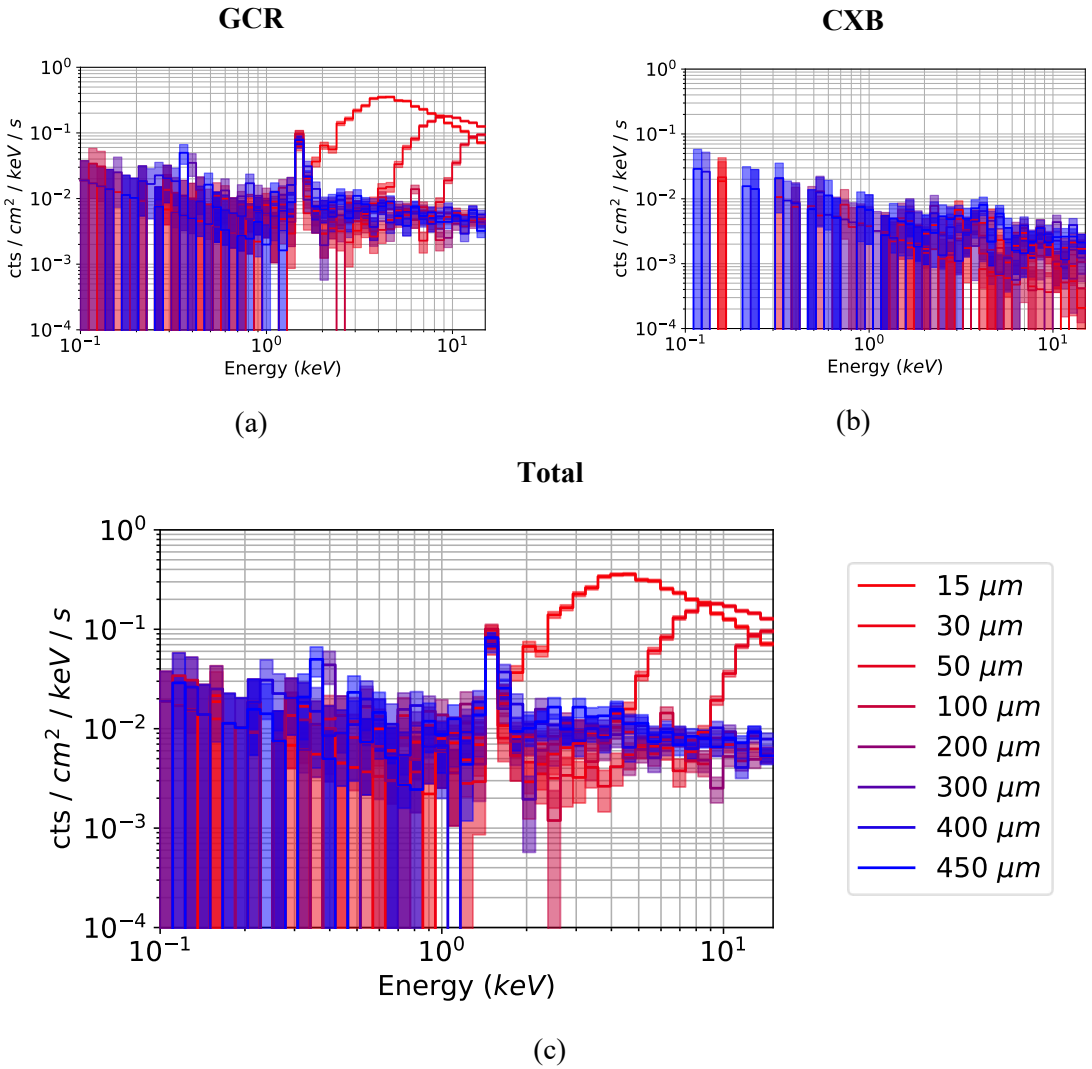

Figure 9.9 The background spectra for each simulated detector thickness for GCR protons, CXB photons and both GCR protons and CXB photons combined. As the detector thickness increases from 15 μm → 30 μm → 50 μm, the MIP peak above 1 keV can be seen to move to the right of the spectrum and decreases in intensity. However, the overall flat continuum of the spectrum appears to increase with further increases in detector thickness.

Figure 9.9 also shows that the increases in continuum spectra with increasing thickness appears to occur across the whole spectrum rather than just in a specific location.

Additionally, the count rates between 2 keV and 7 keV corresponding to GCR proton and CXB are further split by background-inducing particle type in Figure 9.10 and Figure 9.11. In both figures, the flux of charged particles initially decreases with increasing detector thickness, a trend that agrees with the interpretation that the low detector thickness background is dominated by MIPs.

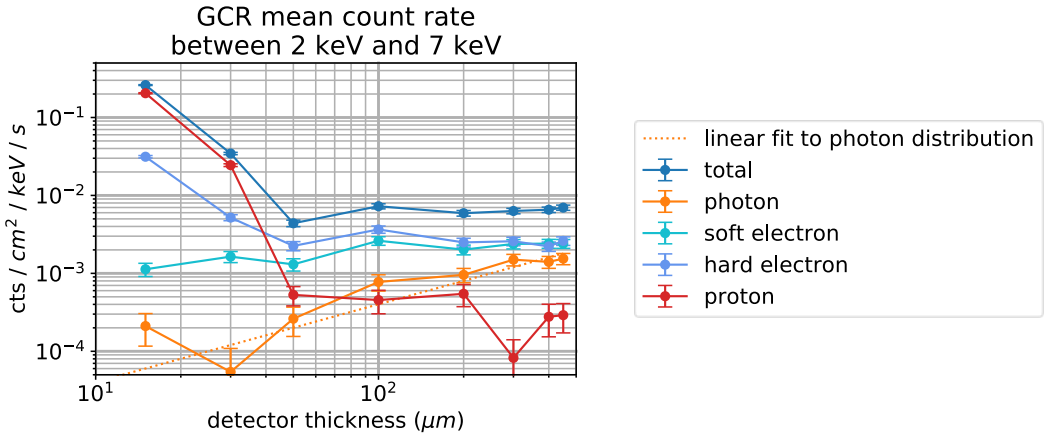

Figure 9.10 The GCR proton mean background count rate between 2 keV and 7 keV for varying detector thicknesses.

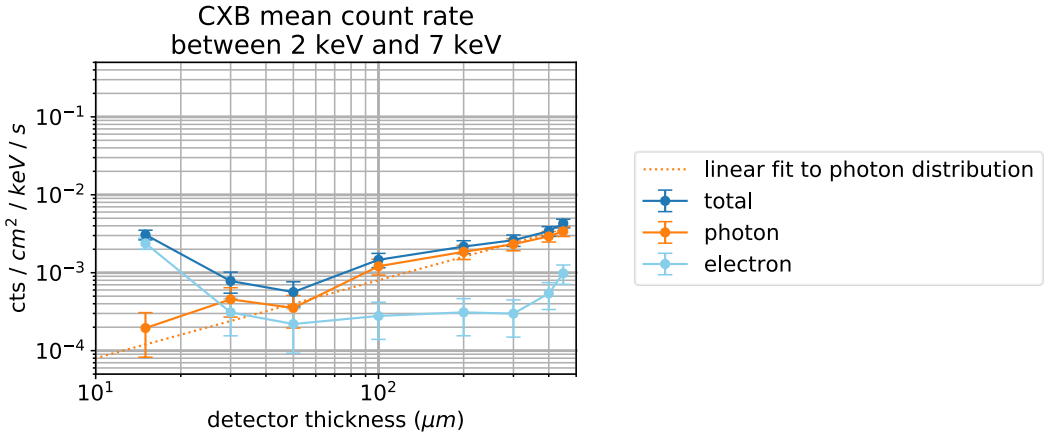

Figure 9.11 The CXB mean background count rate between 2 keV and 7 keV for varying detector thicknesses.

Figure 9.10 and Figure 9.11 also indicate that as expected, the linear increases in the background with increasing thicknesses above 50 μm are driven by increases in the photon spectra. Fits to this linear increase in spectra could be obtained, and are given in Table 9.1. These fits were used to calculate quality factors for both the full background and the GCR proton-induced background on its own, to represent the case where graded-Z shielding can remove the CXB entirely but not GCR proton-induced hard photons.

These quality factors were calculated using the equations for hard photon, and electron background that are derived in Appendix D and the simulated mean electron-induced background count rates determined in Chapter 8, and are plotted in Figure 9.12 and Figure 9.13 for an incoming flux of scientific photons of 5×10^{-3} cts / cm^2 / keV / s. It should be noted that the effects of minimally ionising particles at thicknesses below 50 μm were not included here.

Mean count rate between 2 keV and 7 keV	**Fit to $y = mx$** **$cts / cm^2 / keV / s / \mu m$**
GCR induced photon continuum	$m = (4.0 \pm 0.3) \times 10^{-6}$
CXB induced photon continuum	$m = (8.0 \pm 0.6) \times 10^{-6}$

Table 9.1 Fits to the mean background count rates between 2 keV and 7 keV. Both spectra had good fits to linear functions, in accordance with the mathematics described in earlier in this chapter and in Appendix D.

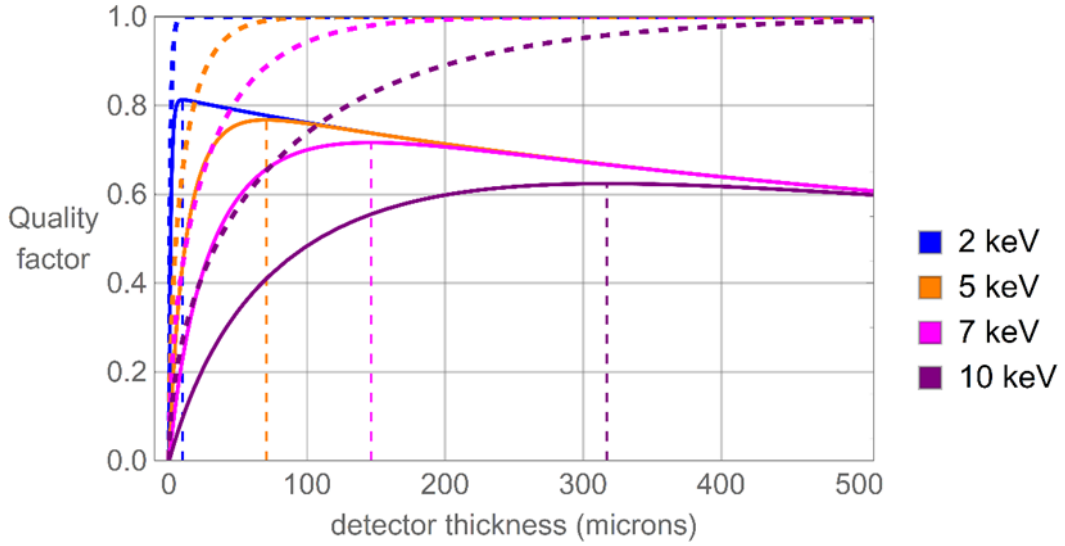

Figure 9.12 The quality factor at different energy depositions for the full background as calculated using the data in Figure 9.10 and Figure 9.11 (solid lines) as compared to the quality factor for incident photons where no background is present (dashed curves). The maximum points for the full background quality factor are indicated by the vertical dashed lines, giving the optimal device thickness for maximising the signal-to-noise ratio.

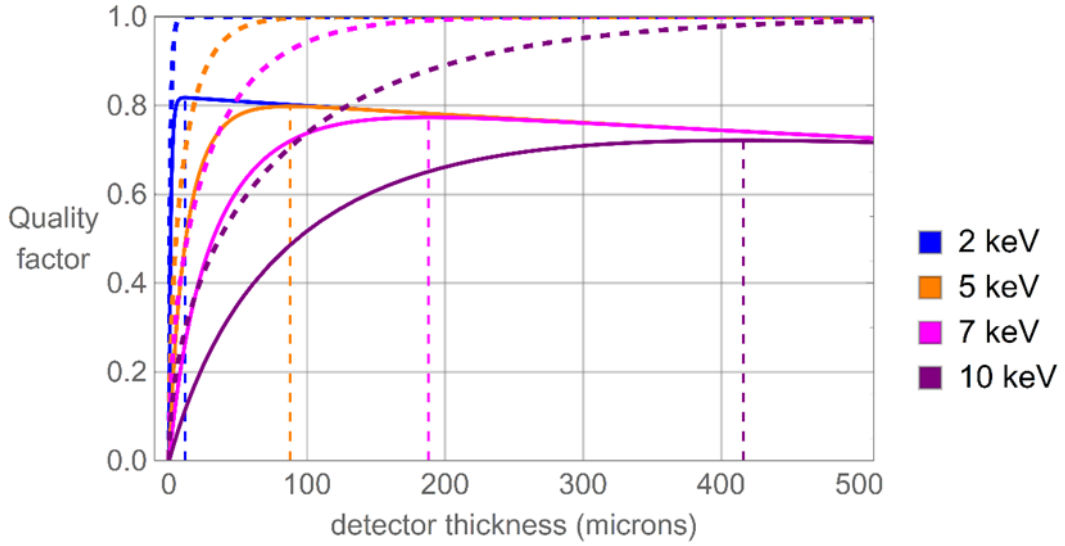

Figure 9.13 The quality factor for different energy depositions for the GCR proton only induced background as calculated using the data in Figure 9.10 and Figure 9.11 (solid lines) as compared to the quality factor for incident photons where no background is present (dashed curves). This might represent the case where the CXB has been removed by graded-Z shielding.

Figure 9.12 and Figure 9.13 both show peaks in signal-to-noise ratio at a detector thickness that increases with detection energy, followed by an approximately linear decrease in signal-to-noise ratio with increasing detector thickness. Figure 9.12 and Figure 9.13 appear similar to the plots of the Compton scattering quality factor in Section 9.1.1.1, where signal-to-noise ratio decreases approximately linearly with increasing detector thickness above some maximum value. This maximum value is situated at a thickness that increases with energy deposition.

The fact that signal-to-noise ratio peaks before linearly decreasing is an important finding, and one that may need to be taken into account in the design of devices for astronomical imaging of low flux sources. Device thickness is often increased to maximise quantum efficiency and thereby maximise the number of counts to increase the signal-to-noise ratio. However, the above analysis indicates that if the X-ray-like background is comparable to the scientific flux, then increasing the detector thickness may have a detrimental impact on the signal-to-noise ratio at thicknesses above the optimal thickness, despite an increasing quantum efficiency.

It was not possible to calculate the optimal detector thickness analytically; however, it was possible to calculate the optimal thickness as a function of energy using numerical methods in Mathematica (*Mathematica* 2019). To calculate the optimal detector thickness, the `Maximise` function was used to numerically determine the maximum value of the quality factor for a given particle kinetic energy. These calculated optimal thicknesses are displayed in Figure 9.14, where it can be seen that the optimal detector thicknesses as a function of energy fits to power-law distributions. Parameters for the power-law fits are given in Table 9.2.

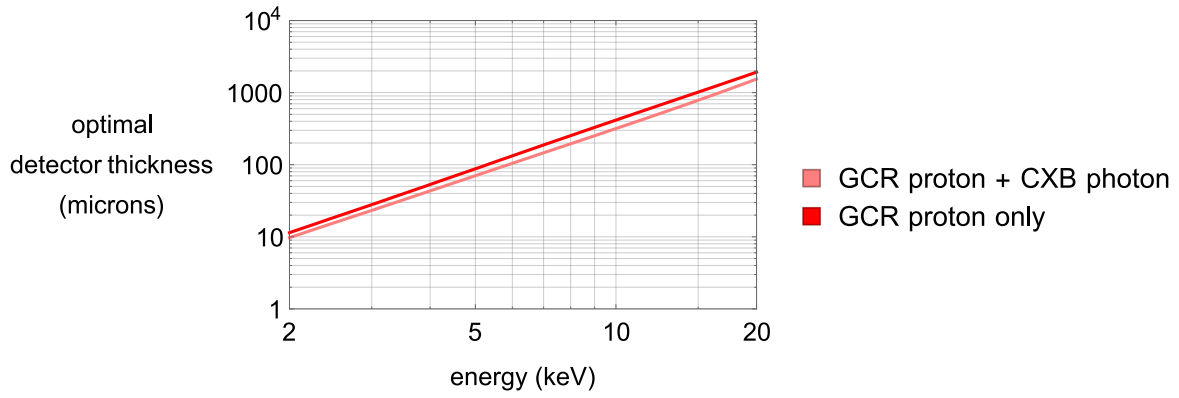

Figure 9.14 The optimal detector thickness for the maximisation of signal-to-noise ratio as a function of energy, as calculated by maximising Equation 9.2 with a linear continuum background as a function of thickness as calculated from the simulations, where parameters are given in Table 9.2.

Distribution	Fit to $y = Ax^{\gamma}$
GCR proton + CXB photon	$A = 1.974 \pm 0.009$ $\gamma = 2.207 \pm 0.002$
GCR proton only	$A = 2.539 \pm 0.009$ $\gamma = 2.214 \pm 0.001$

Table 9.2 Power law fit parameters for the optimal detector thickness distributions as a function of energy displayed in Figure 9.14, where energy (given here by x) is in units of keV, and detector thickness (given here by y) is in units of μm.

In both the GCR proton + CXB photon situation and GCR proton only situation the fit parameters are similar, although A and γ are slightly higher in the GCR proton case, leading to higher optimal thicknesses.

While the simulations performed in this section are likely representative of the general structure of background that a detector will experience, it should be noted that the exact background quantities will vary with radiation environment, spacecraft structure and detector design. Therefore, the distributions calculated above should be considered as representative rather than necessarily exact. The presence of optical blocking filters, in particular, has the potential to change the background induced by electrons, so simulations were also performed to examine the effect of optical blocking filters on X-ray-like background.

9.1.2 Optical blocking filters

Optical blocking filters are typically used to prevent straylight composed of optical photons from influencing detector images. Such filters are typically either placed directly on top of the detector (on-chip) or in the filter wheel above the detector and have a typical thickness on the order of tens of nanometers to hundreds of nanometers (Barbera et al. 2018). Several designs have been suggested for an optical blocking filter for the ATHENA WFI, including a 90 nm aluminium on-chip filter and 30 nm Al + 150 nm polyimide filter wheel filter (Meidinger et al. 2018).

On-chip filters have the secondary advantage that they may reduce background, as there is the possibility that they may either block some soft electrons from reaching the detector depletion region or prevent some hard electrons from scattering in the detector depletion region (Meidinger et al. 2016). However, as was discussed in previous work (Davis et al. 2018) there also exists the possibility that an on-chip filter might slow some high energy electrons such that they are either absorbed or backscatter within the detector energy range. Therefore, Geant4 simulations were performed to determine how different optical blocking filter configurations would affect the background.

9.1.2.1 Simulation design

The same spherical shell simulation design was used here as the simulations performed in Section 9.1.1.6 and displayed in Figure 9.7. However, for these simulations, optical blocking filter

thickness was varied instead of detector thickness from the default optical blocking filter thickness of 90 nm. Simulations were also performed where the optical blocking filter was removed to assess how the optical blocking filter influences background overall. An additional simulation was also performed using only a 'raised' optical blocking filter placed 2 cm above the detector surface to approximate an optical blocking filter placed in a filter wheel. For all of these simulations the optical blocking filter used was a 90 nm thick cuboid of aluminium.

9.1.2.2 Simulation results

The count rate between 2 keV and 7 keV for the on-chip optical blocking filter, no optical blocking filter, and raised optical blocking filter configurations are displayed in Figure 9.15.

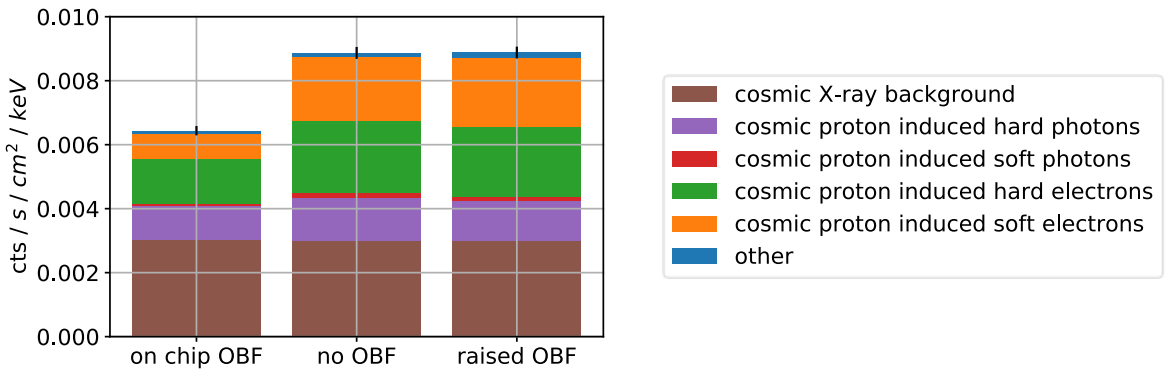

Figure 9.15 The components of the 2 keV to 7 keV mean background for each of the three cases. The on-chip optical blocking filter case exhibits the lowest mean background, primarily due to reductions in the cosmic proton induced electron components of background.

While there appears to be little significant difference in count rate between the no optical blocking filter and raised optical blocking filter cases shown in Figure 9.15, there is a relatively significant reduction of background in the on-chip optical blocking filter configuration. This reduction in X-ray-like background appears to primarily be caused by a reduction in cosmic proton induced electrons indicating that any reduction of high energy electrons into the detector energy range is not significant compared to the shielding of soft electrons. There also appears to be some decrease in count rate for cosmic proton-induced photons, although it is unclear whether this is significant compared to standard errors.

This reduction in soft electron and soft photon induced background is likely due to particles produced in the proton shield being absorbed or attenuated in the optical blocking filter, while particles produced in the optical blocking filter itself hit the same pixel as the initial primary particle that generated the particle because they are produced very close to the detector. Therefore event detection will remove particles produced in the optical blocking filter, while the optical blocking filter blocks some electrons and soft photons. This effect was seen previously in Chapter 8, where the 5 µm BCB

layer blocked a large number of background inducing particles hitting the bottom of the detector, and the geometry underpinning these situations is displayed in Figure 9.16.

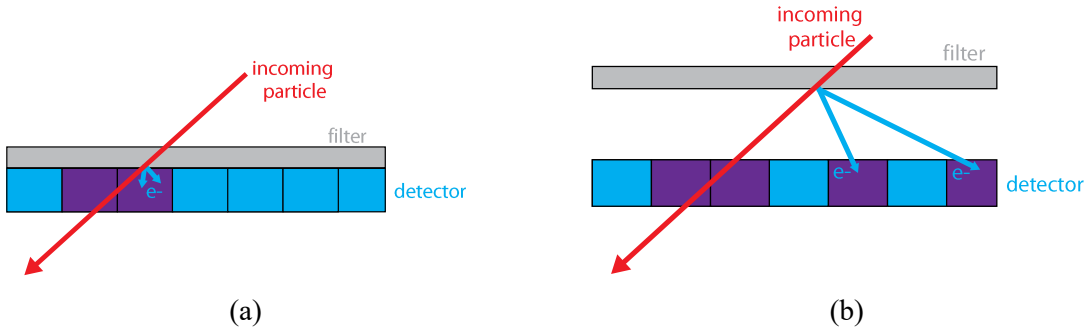

Figure 9.16 diagrams showing why the on-chip case (Figure 9.16(a)) might exhibit less background than in the case where the filter is raised some distance above the detector (Figure 9.16(b)). In the on-chip case, secondary particles produced from the filter usually impact the same pixel that the incoming particle hit, whereas in the raised filter case, secondary particles produced from the filter are more likely to hit other pixels than the incoming particle and are therefore more likely to appear as valid single pixel events.

Figure 9.17 displays the total background spectrum for each configuration. Here the reduction in X-ray-like background for the on-chip filter configuration can be further observed. It can be seen that the background continuum shape changes from a decreasing background with respect to energy to being approximately constant with respect to energy when the on-chip optical blocking filter is added. This change in spectral shape is consistent with simulations presented by Meidinger et al. (2016). The fluorescence line intensity can be also seen to drop in the optical blocking filter case relative to the other cases.

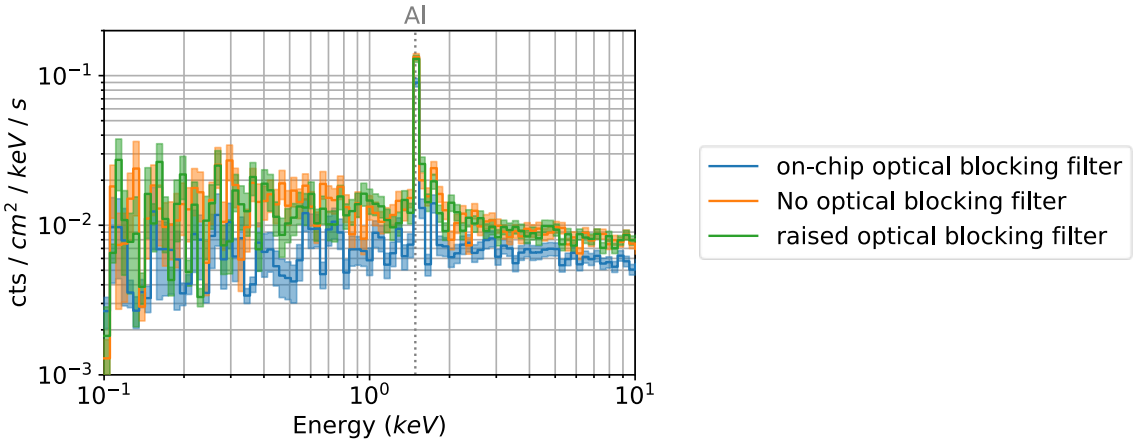

Figure 9.17 The X-ray-like background spectra for each of the three cases. The on-chip optical blocking filter background exhibits the lowest background. Additionally, it can be seen that the fluorescence line is also less intense in the on-chip optical blocking filter case.

9.1.2.3 Varying optical blocking filter thickness

As the presence of an on-chip optical blocking filter causes a reduction in X-ray-like background due to a lowered electron component, it is worthwhile to investigate how this reduction in background varies with optical blocking filter thickness.

To investigate this, additional GCR proton simulations were performed where the Al optical blocking filter volume was set to 45 nm, 120 nm, 150 nm and 180 nm. The GCR proton induced X-ray-like background spectra produced by each of these simulations, as well as the simulations both without an optical blocking filter and with a 90 nm filter are displayed in Figure 9.18.

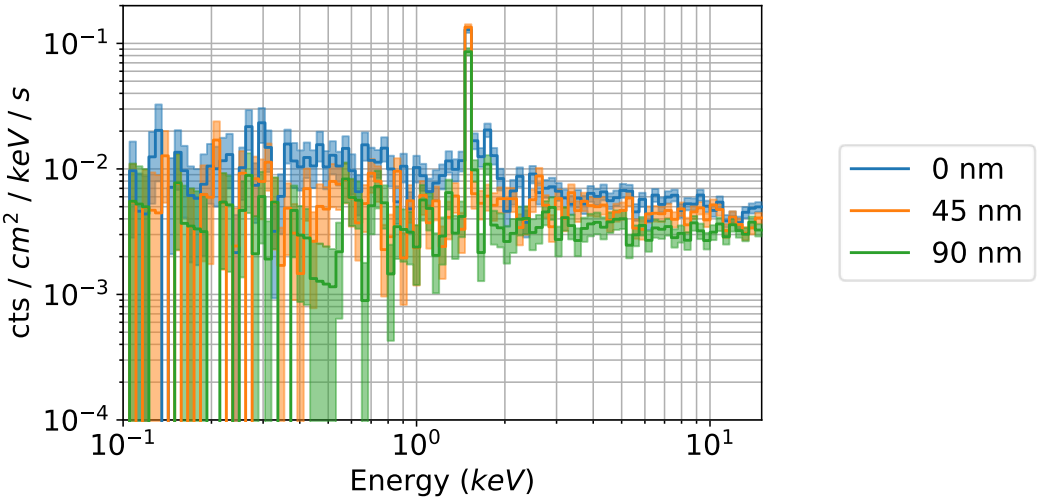

(a)

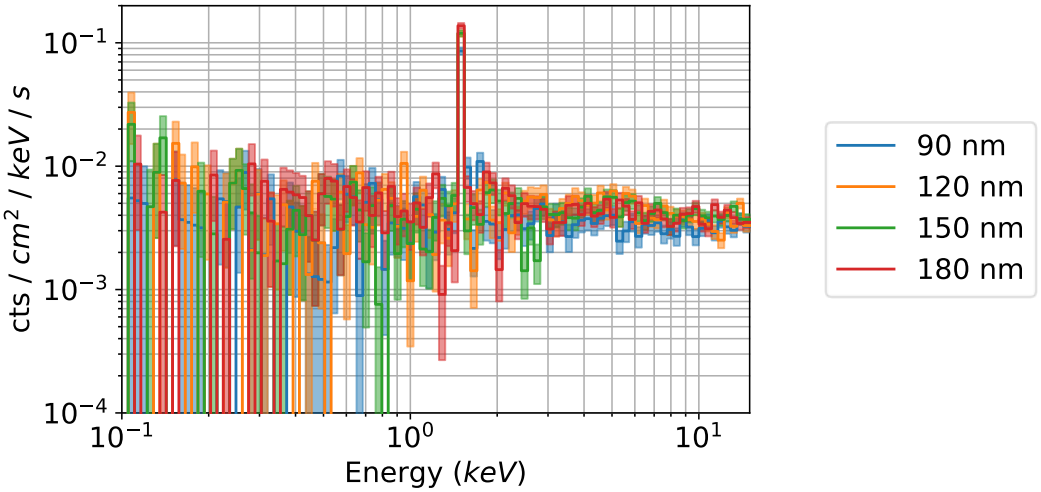

(b)

Figure 9.18 The GCR proton-induced X-ray-like background spectra for each of the different optical blocking filter thicknesses. Between 0 nm and 90 nm the X-ray-like background decreases, while between 90 nm and 120 nm the background increases. For 120 nm, 150 nm and 180 nm the background is approximately equal.

Figure 9.18(a) shows that for thicknesses up to 90 nm, the X-ray-like-background continuum spectrum decreases with increasing optical blocking filter thickness. However, Figure 9.18(b) indicates that for thicknesses above 90 nm, this trend ends and that the background increases for

thicknesses above 90 nm. These trends can also be seen in Figure 9.19, where the mean count rate between 2 keV and 7 keV is displayed as a function of optical blocking filter thickness.

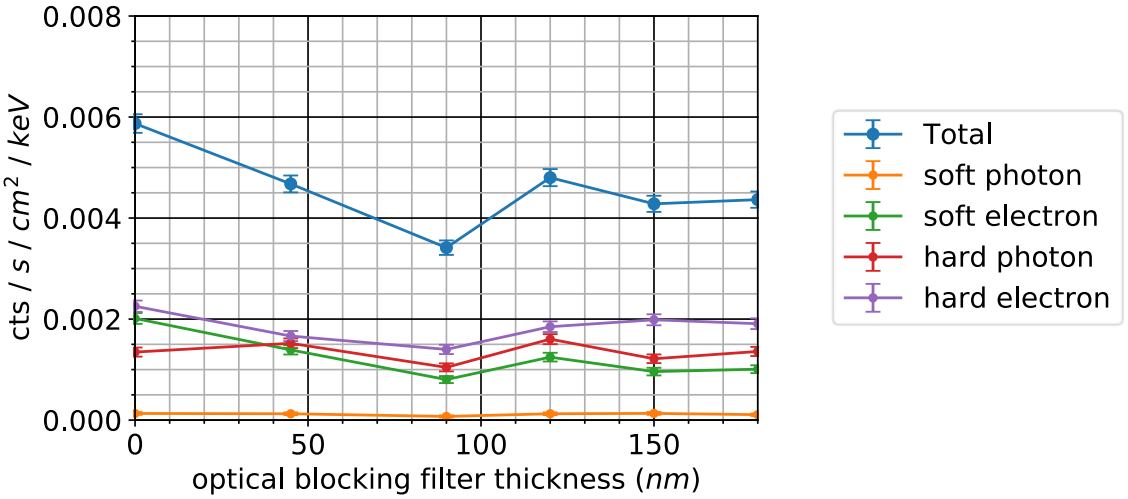

Figure 9.19 The mean GCR induced X-ray-like background between 2 keV and 7 keV plotted as a function of optical blocking filter thickness. The background is lowest in the 90 nm thick case.

Figure 9.19 shows that the 90 nm run produced the lowest mean count rate between 2 keV and 7 keV and that this count rate appears to be low due to electron count rates being at a minimum for this thickness. The hard photon spectrum also appears to be at a minimum in the 90 nm thickness simulations; however, this may be due to statistical errors, as it would not be expected that the hard photon count rate should be affected significantly by changing optical blocking filter thickness.

In conclusion, these simulations indicate that an on-chip optical blocking filter reduces the X-ray-like background generated by knock-on electrons. It also appears that a thickness of around 90 nm for an aluminium optical blocking filter gives the optimal background reduction, and a filter like this also appears to cause no background reduction if raised by several centimetres from the detector.

9.2 The effect of distant masses beyond the proton shield on background

While detector design such as the detector depletion region thickness and on-chip filters are important, as has been discussed previously, the surrounding spacecraft structure can significantly influence the X-ray-like background experienced by a detector.

In Chapter 8 it has been determined that even though a large number of particles originate from surfaces within line-of-sight of the detector, a significant number of particles originate from regions where there is an obstructed path from the particle vertex to the detector. This presents a potential issue for space missions in general where large masses are placed next to or near to a detector, as the presence of these may cause a large increase in background. In the case of the ATHENA WFI, the ATHENA X-ray Integral Field Unit (XIFU) (Barret et al. 2018; Lam Trong 2016), the second major

scientific instrument of ATHENA, presents a large mass of approximately 710 kg adjacent to the WFI, and could potentially induce a significant quantity of background in the WFI.

Different teams may develop external masses such as the ATHENA XIFU within the larger organisation of a mission, and it may therefore sometimes not be possible to easily request modifications to the design of a large mass instrument to reduce the background incident upon another detector. This means that shielding may be preferable to geometry changes for removing background created by the presence of other instruments.

As the background generated by large external masses may be induced by different particle components than those generated from within the proton shield, this may mean that a different format of shielding may be optimal for detectors situated near to large masses. The exact form of this shielding will depend upon the mechanisms by which external masses generate background, the physics of which will be investigated in this section.

9.2.1 Simulation design

To both determine the amount of extra background generated by distant masses, and to further investigate the physics underpinning hard photon background generation, the proton shield simulation in Section 9.1.1.6 was modified to include a removeable large external spherical shell mass of 600 kg of aluminium. This mass was placed adjacent to the proton shield spherical shell in the geometry displayed in Figure 9.20, and the input particle generation sphere was also expanded to include all masses within the simulation.

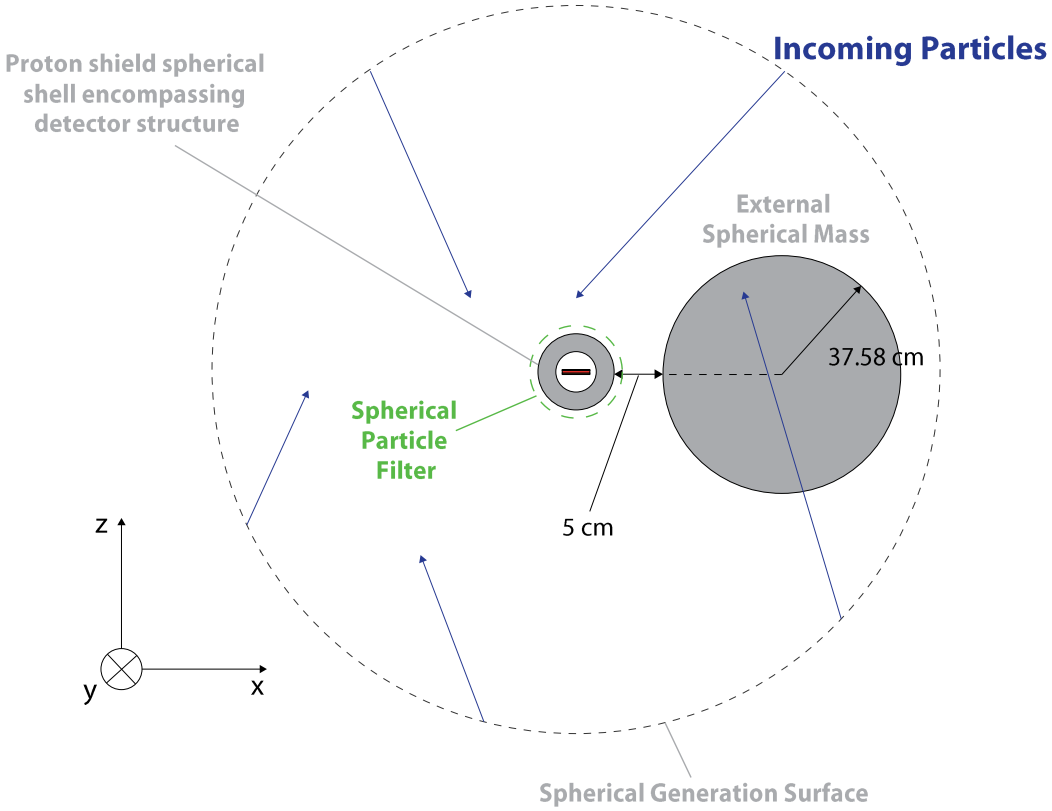

Figure 9.20 The geometry simulated in this section. A 600 kg sphere was placed 5 cm away from the spherical shell model used in previous simulations, and the particle generation sphere was expanded to include the full geometry. The external sphere was set so that it could easily be changed between vacuum or solid aluminium for different simulation runs. To investigate background generation physics, a spherical particle filter was also placed around the proton shield spherical shell, which was capable of being set such that only particles of a particular species would be allowed to pass through and thereby influence background.

In addition to these geometry changes, a thin spherical vacuum shell particle filter encompassing the proton shield spherical shell was also added. This filter was created through a modification of the G4VSensitiveDetector class, which was modified such that any particle tracks attempting to travel through the filter volume would be killed if they did not match a specified particle species that was set for that simulation. This filter layer meant that the background induced by different species of particles originating from the external sphere could be investigated in greater detail.

9.2.2 Simulation results

The mean count rates between 2 keV and 7 keV are displayed in Figure 9.21 and Figure 9.22 for each simulation where the external sphere was either removed or added, and for each particle filter. It should be noted that each configuration with different filters and the external mass switched on or off was a different simulation, so different bars with filters turned on do not necessarily add to give the same value as simulations with the filters turned off, due to statistical variation.

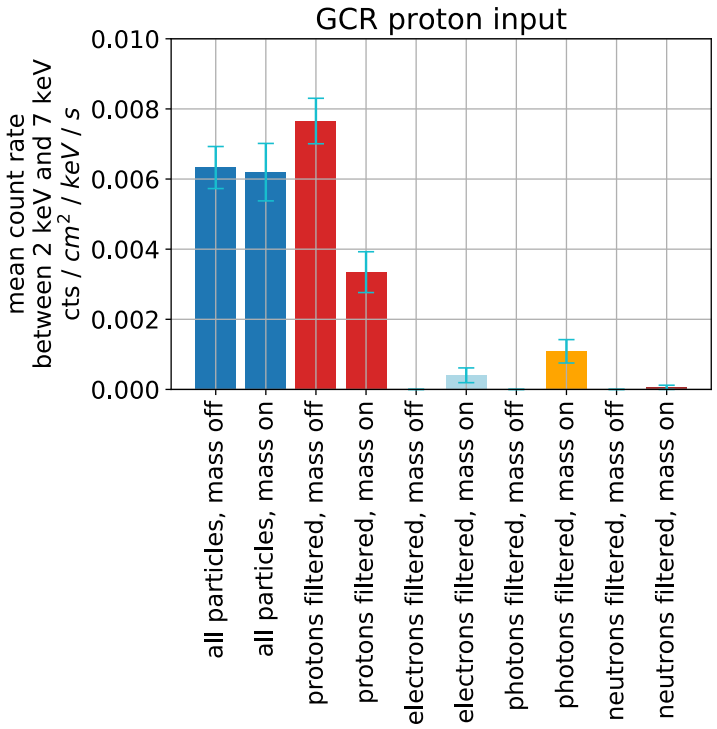

Figure 9.21 The mean count rate between 2 keV and 7 keV for GCR proton-induced background events, for different combinations of particles selected by the particle filter and with the additional spherical mass turned off and on. It should be noted that the fact each of these bars was produced by a separate simulation, which is why the mean count rate for protons only in the mass off case is higher than that of the 'all particles filtered' cases, due to statistical fluctuations. While it appears that the presence of the additional sphere does not alter the background more than can be explained by the error bars, it does appear that when the additional sphere is switched on, it does generate a significant number of electrons and photons which create background-inducing particles from the proton shield.

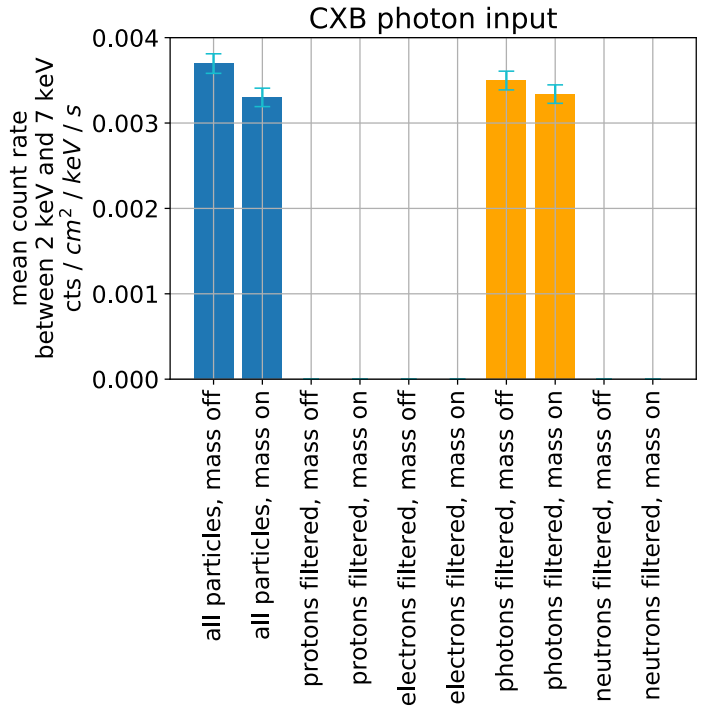

Figure 9.22 The mean count rate between 2 keV and 7 keV for CXB photon induced background events, for different combinations of particle filter and with the additional spherical mass turned off and on. While it appears that there is little difference in CXB induced background when the additional sphere is turned on, the vertex position plot which is shown in Figure 9.23(d) indicates that there should be some difference which may be within the error bars here.

Figure 9.21 and Figure 9.22 indicate that for this particular situation there is no significant variation in the total quantity of X-ray-like background events when the extra spherical mass is inserted into the simulation, at least within the statistical errors. It should be noted that this is likely the case for this specific simulation rather than a general case of adding extra masses to simulations, as later simulations in Section 9.3 will show that increases in proton shield thickness can cause significant increases in X-ray-like background.

Even though the presence of the extra spherical mass does not significantly alter the total X-ray-like background, it appears that the presence of the external sphere does modify the physics involved in background creation. This is because a significant quantity of X-ray-like background events are being created from photons, electrons and neutrons generated from the extra spherical mass.

This provides an insight into some of the physics causing the creation of X-ray-like background, in that a significant component of background is not created directly by cosmic protons, and is instead created by intermediate knock-on particles that were generated by cosmic protons. While it would be possible that some of the photons created in the additional sphere constitute parts of the hard photon spectrum in the detector, Figure 9.23(a) and Figure 9.23(b) indicate that this is not the case. No background-inducing particles were directly generated in the additional sphere in the simulation with no filter and the additional sphere turned on.

Figure 9.23 displays the vertex locations of background inducing events for the GCR and CXB simulations for both the additional mass being present and not present.

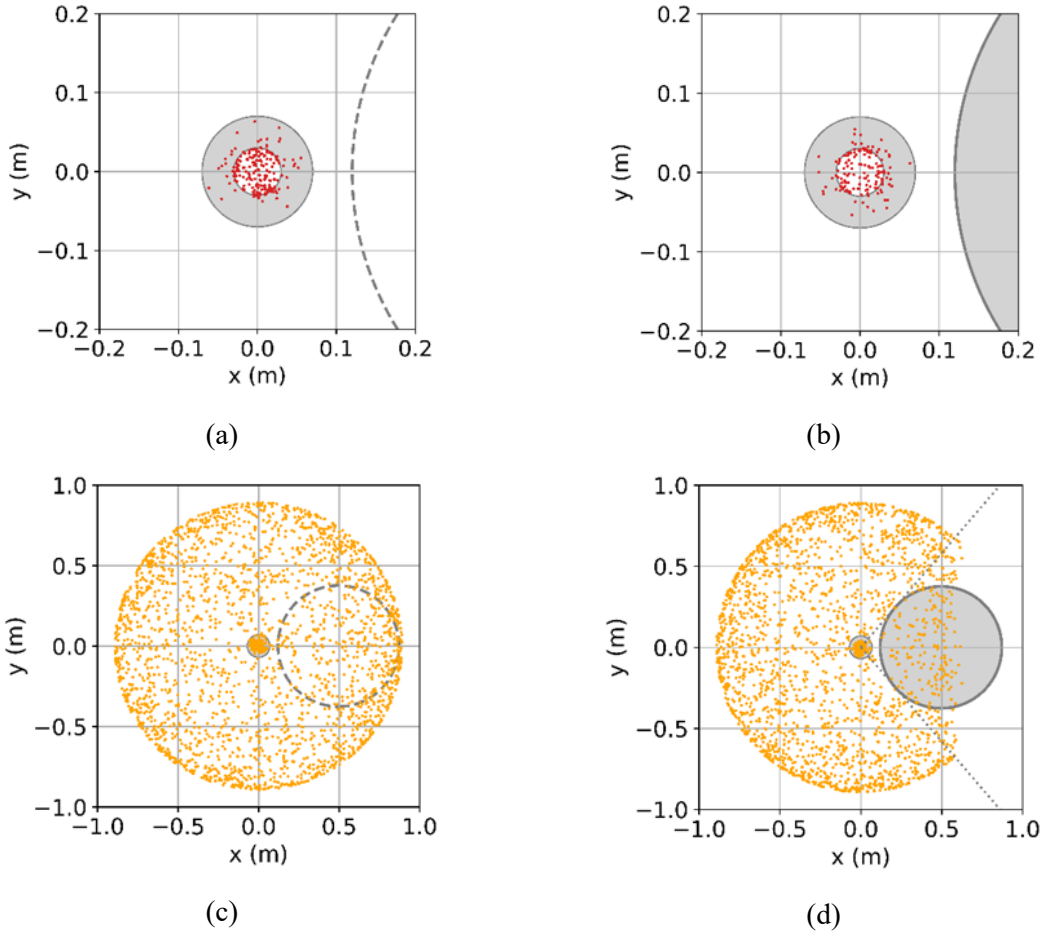

Figure 9.23 Vertex position plots for background-inducing particles in the simulations performed for this section. Figure 9.23(a) and Figure 9.23(b) show the vertex positions for GCR induced background, and indicate that no background-inducing particles originated directly from the additional sphere. Figure 9.23(c) and Figure 9.23(d) show vertex positions for the CXB induced background, and indicate that the additional sphere blocks out a certain solid angle of background inducing particles. Dotted lines have been drawn on Figure 9.23(d) to show the full solid angle that is encompassed by the additional sphere. Different distance scales were used for the two sets of plots for clarity.

Figure 9.23(c) and Figure 9.23(d) also show that the additional sphere alters the CXB-induced background by blocking out CXB from the solid angle that it encompasses. While Figure 9.22 previously indicated there was only a small drop in CXB induced background with the inclusion of the additional sphere it should be noted that the total solid angle encompassed by the additional sphere is only about 17% of the total solid angle.

9.3 The effect of varying proton shield thickness on background

As the simulations of the addition of an extra spherical mass in Section 9.2 show that many X-ray-like background events are generated from knock-on particles created in the additional sphere, the question arose of how additional mass from a thicker proton shield covering the entire detector solid angle might influence the background.

Determining how background varies with shielding thickness is particularly important for generally assessing how the addition of thick materials and surrounding instruments will affect the X-ray-like background in a detector. Full knowledge of how the proton shield thickness can influence background would also allow for the optimisation of proton shield thickness based on the requirement to both block soft protons while minimising the generated X-ray-like background.

Proton shields are designed to reduce the amount of radiation damage a detector will receive, and therefore increase the lifespan of a detector, by preventing soft protons and other high damaging ions and electrons from reaching the detector. Therefore, the thickness of a proton shield is typically designed with reducing the soft proton flux given spacecraft engineering constraints in mind, rather than the secondary side effect goal of reducing background. However, in cases where there is a range of acceptable thicknesses, it may be useful to choose a proton shield design that is optimised for background reduction given the constraints.

To investigate how proton shields can influence background, GCR proton simulations were performed utilising the same simulation design used in Section 9.1, but with a varying thickness of proton shield instead of optical blocking filter thickness or detector thickness. Here the inner radius was held constant at 4 cm, so extra material was only added to the outside of the proton shield, and the particle generation sphere and normalisation were adapted to accommodate this. The results for the integrated background count rate between 2 keV and 7 keV, and the spectra produced by these simulations are displayed in Figure 9.24 while the background spectra for each thickness are displayed in Figure 9.25, where the total background produced in each model is displayed as well as the contribution to the background from different particle components.

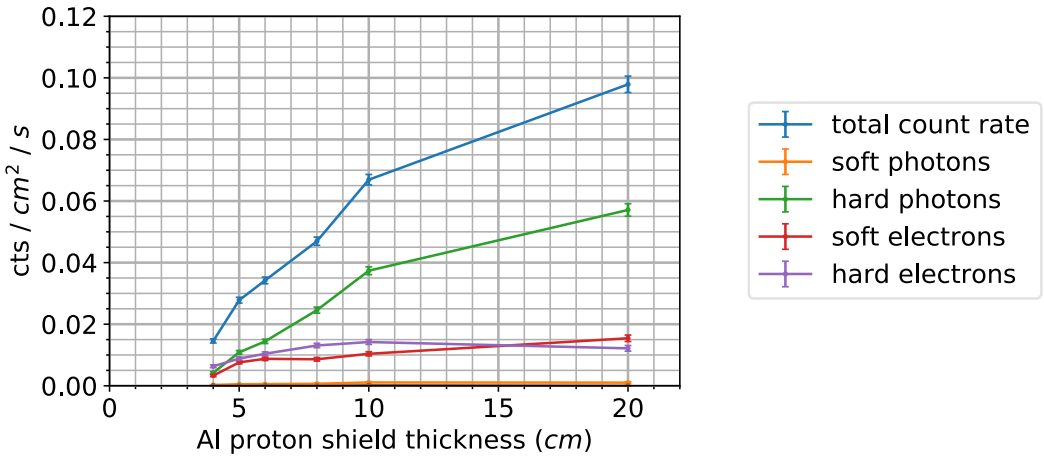

Figure 9.24 The X-ray-like background count rate between 2 keV and 7 keV for several spherical shell simulations with varying aluminium proton shield thicknesses.

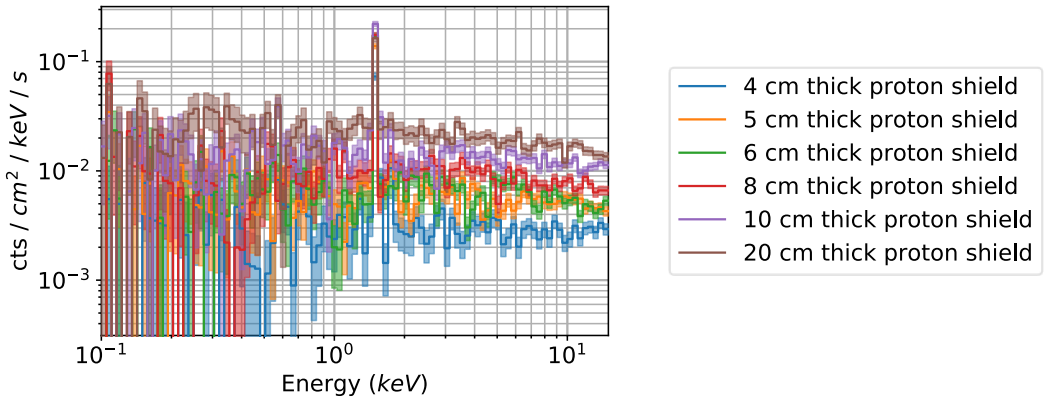

Figure 9.25 The GCR background spectra for each proton shield thickness. The background appears to raise across the full spectrum with increasing thickness.

Figure 9.24 indicates that the background increases approximately linearly for proton shield thicknesses between 4 cm to 10 cm and that the majority of this increase is driven by an increase in the quantity of hard s. At 20 cm, the background also appears to be significantly greater than the background at 10 cm, but less than would be predicted if the linear trend continued. A linear fit to the hard photon component between 4 cm and 10 cm is given in Table 9.3.

Fit details	***m*** **(cts/cm²/s/cm)**	***c*** **(cts/cm²/s)**
Hard photon component only, linear fit between 4 cm and 10 cm, $y = mx + c$	$(5.3 \pm 0.2) \times 10^{-3}$	$(-1.69 \pm 0.09) \times 10^{-4}$

Table 9.3 The parameters found for a linear fit to the X-ray-like background induced by hard photons in Figure 9.24 between 4 cm and 10 cm. x and y here correspond to the x-axis and y-axis of Figure 9.24.

While an increasing background induced by hard photons with increasing proton shield thickness is expected, it is not necessarily expected that the relationship is linear. Previously in Chapter 8 it was shown that the hard photon background degrades approximately exponentially with distance into the proton shield. This exponential decrease means that if the background were to simply be added on by the increase in photons originating from the new material, it would be expected that such background would increase as a function of one minus an exponential decay instead of a linear increase. Therefore something more complicated may be occurring than new background directly originating from the extra masses being added to the total X-ray-like background. Extra background is likely being produced from regions closer to the detector, which is increases with increasing proton shield thickness.

The ability of extra masses to increase the X-ray-like background originating from other spacecraft regions than the added region is displayed in Figure 9.26, where the fluorescence count rate is plotted as a function of proton shield thickness.

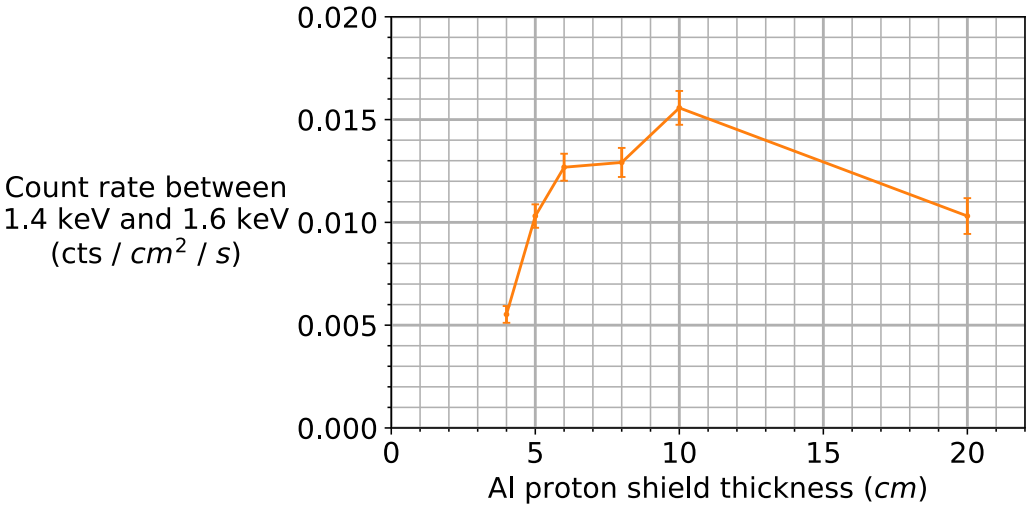

Figure 9.26 The count rate originating from soft photons between 1.4 keV and 1.6 keV in energy, which are dominated by fluorescence photons.

Figure 9.26 shows that the 1.49 keV aluminium fluorescence line increases in intensity as the aluminium proton shield increases in thickness until the 10 cm thickness simulation. In Chapter 8 it was found that almost all fluorescence originated from within the first few millimetres of the proton shield surface within line-of-sight of the detector, so this indicates that the presence of extra mass added to the outer surface of the proton shield is causing more particles to be produced from the proton shield inner surface.

The increase in intensity with proton shield thickness may be important for selecting locations that require graded-Z shielding as it means that surfaces within line-of-sight of the detector that are near large masses may generate more fluorescence. It also shows that a significant proportion of fluorescence photons are not being generated directly by the incoming protons, but by knock-on particles generated by the incoming protons. Therefore, it is likely that the linear increase in hard photons is also caused by an increase in the number of secondary particles inducing the production of further hard photons.

9.4 Investigating the increase in the background with increasing mass

The likelihood that the chain of processes causing the production of particles involves one or more intermediate steps involving highly penetrating electrons and photons could previously be seen in Section 9.2 and Section 9.3. Here it was found that a significant proportion of background inducing events were generated from GCR-induced electrons and photons in the XIFU sphere creating further secondaries inside the proton shield. The influence of highly penetrating intermediate particles could also be observed by further examination the data produced in the simulations of the 20 cm proton shield thickness.

To examine the full chain of events that led up to a particular X-ray-like background event from initial proton generation to interaction with the detector, a custom G4VUserInformation object was designed. Geant4 user information objects are general objects that can be assigned to every particle in a simulation and used to hold any information the user wishes to assign to the particle. The custom user information class for this simulation was designed such it would hold all useful information about a particle, including any useful information from the particle that generated it back to the original primary that began the event.

To store information from previous particles in the chain of processes, whenever a new particle was generated by a parent particle in the simulation, the entire user information object as well as the useful variables held within would be copied from the parent particle to the new particle. New information corresponding to physical parameters for the new particle was then appended to the copied user information object. When a hit was then later registered in the detector, the entire chain of particle species and particle energies could then be printed using saved information in the user information object of the particle that hit the detector.

It was found using this mechanism that in the 20 cm thick aluminium proton shield case, background inducing particles were generated by a large number of particle chains, as shown below in Figure 9.27.

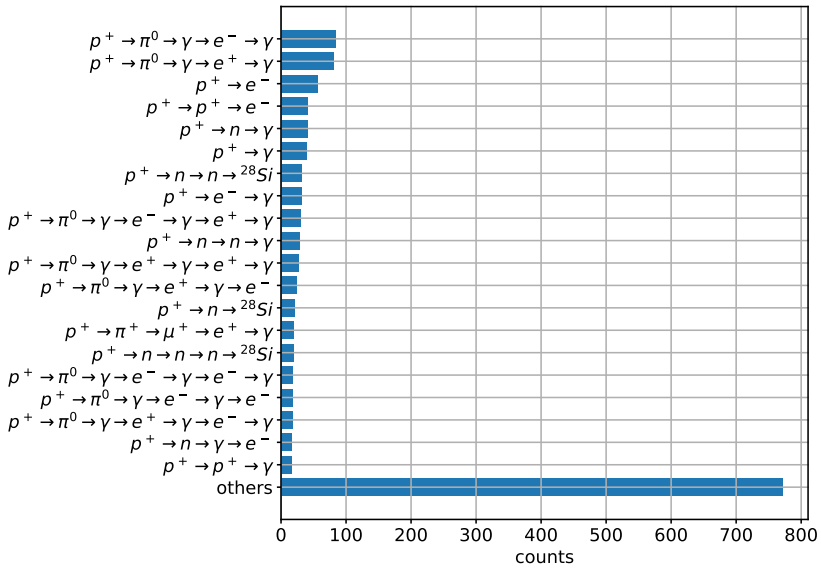

Figure 9.27 The quantity of particle interaction chains from the initial GCR proton primary up until the particle hit in the detector. The listed particle chains that are not in the 'others' category represent the 20 most numerous chains, so the fact that the others category represents significantly more particle hits than any individual particle chain indicates that there are a large number of particle chains that contribute significantly to X-ray-like background.

This particle chain information was combined with saved particle chain kinetic energy information to determine that 52.5% of particle chains contained at least one intermediate photon, 33.3% of particle chains contained at least one intermediate electron, and 32.3% of particle chains contained at least one intermediate neutron. The median energy for intermediate photons was 215 MeV, corresponding to a half-value layer of 9.4 cm in aluminium, for intermediate electrons the median kinetic energy was 86 MeV, corresponding to a CSDA range of 10.9 cm in aluminium, and for intermediate neutrons the median kinetic energy was 49.1 MeV.

As these particles can penetrate significant quantities of aluminium, it means that an intermediate particle could generate a hard photon capable of inducing X-ray-like background a significant distance from the point at which the intermediate particle was created. This adds a large amount of complexity to the relationship between additional masses in a spacecraft and the location of where additional background inducing particles are generated is complicated and likely difficult to model.

Figure 9.27 also indicates that it will likely be challenging to design shielding that can prevent each of these particle chains from occurring in the creation of hard photons, due to the large number of potential chains that can generate background. However, one method that may be able to attenuate the hard photon spectrum is graded-Z shielding, which is known to remove background generated by fluorescence lines and the CXB, but which may also be capable of removing hard photons. The effect of graded-Z shielding on both the CXB and GCR generated hard photon induced background will be investigated in Chapter 10.

9.5 Conclusions

Many detector and shielding configurations have been investigated in this chapter, and several significant results have been found.

Initially, analytical expressions were found to describe the variation of X-ray-like background with detector configuration and it was found that background induced by Compton scattering photons should be expected to increase linearly with increasing detector thickness. Expressions were also derived for the change in fluorescence line intensity for increasing detector thickness, and with the inclusion of on-chip layers, which differs from the quantum efficiency if background inducing particles hit the detector isotropically.

Next, the effect of device thickness and optical blocking filters on background and signal-to-noise ratio were investigated through spherical shell model simulations. As predicted, it was found that background increased approximately linearly with detector thickness beyond approximately 50 μm, and that this caused the signal-to-noise ratio for a signal flux of 5×10^{-3} cts / cm^2 / keV / s to be optimised at a detector thickness that is dependent on the source energy. This means that while

increasing detector thickness may increase quantum efficiency, it may not necessarily increase the signal-to-noise ratio in cases where the scientific flux is comparable to background flux, and may actually decrease the signal-to-noise ratio. It may, therefore, be necessary to limit the thickness of detectors in cases where a mission is designed to view low flux sources.

The simulations of varying aluminium optical blocking filter configurations also indicated that an on-chip filter is optimal for background minimisation, where the optimal thickness was found to be in the region of 90 nm.

Finally, simulations of varying proton shield thickness and the effect of an external spherical mass on the background were performed. Simulations of proton shield thickness found the background increased approximately linearly with proton shield thickness. Simulations of the external sphere, however, found no evidence in this specific situation and geometry that the inclusion of the extra spherical mass caused an increase in the background. It was found that the increases in mass correspond to an increase in particles generated from materials other than the added masses, including fluorescence from the proton shield inner surface. This was found to be because high energy intermediate particles are generated by the first proton interaction with the spherical shell model spacecraft, which are then capable of penetrating significant thicknesses of material and then produce further background inducing secondary particles from other shielding layers.

While detectors and surrounding spacecraft structures can be modified to reduce the background experienced by a detector, such changes must be considered within the context of other competing interests within the spacecraft design. In many cases, it may not be possible or ideal to modify existing designs such that background is minimised. However, a knowledge of the background that will be present for particular detector designs and spacecraft structure is crucial for designing bespoke shielding mechanisms for the removal of X-ray-like background in a particular mission. Some of these potential shielding mechanisms include graded-Z shielding or magnetic shielding, which will be discussed in the next chapter.

Chapter 10

Shielding Mechanisms

Now that previous chapters have established the particle structure of X-ray-like background, as well as how this can vary with the spacecraft geometry and detector design, it is possible to investigate mechanisms for shielding detectors from X-ray-like background. This chapter will investigate the ability of two shielding mechanisms, graded-Z shielding and active magnetic shielding, to prevent background-inducing particles from reaching X-ray detectors.

10.1 Graded-Z shielding

Graded-Z shielding (Fan et al. 1996; Atwell et al. 2013) is a shielding design that utilises the decrease in energy and intensity of fluorescence lines with atomic number to attenuate the cosmic X-ray background before it can reach the detector, as described in Chapter 3. It is also possible that graded-Z shielding may also be able to attenuate photons produced by GCR protons passing through shielding and also ensures that fluorescence lines do not significantly impact the spectrum. One possible design of graded-Z shielding is illustrated below in Figure 10.1.

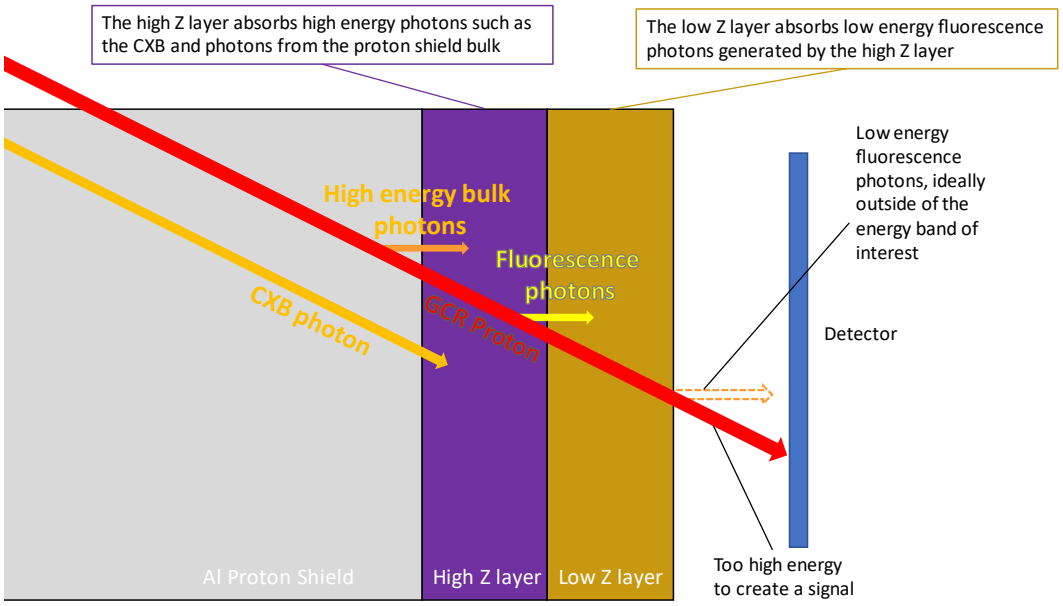

Figure 10.1 The design of graded-Z shielding that will be investigated in this chapter. Here the internal surface of a proton shield is coated with a high atomic number (high Z) layer and a low atomic number (low Z) layer to attenuate both high energy Compton scattering photons and low energy fluorescence photons.

Here, a CXB photon that is capable of passing through the proton shield is absorbed by the high-Z material, which has a higher attenuation coefficient than aluminium for photons in the typical energy range of the CXB. This high-Z layer will, however, likely generate a significant number of fluorescence photons within the energy range of the detector when cosmic protons pass through it. Therefore a low-Z layer is placed on the surface of the high-Z layer facing the detector which is sufficiently thick as to block fluorescence lines produced from either the aluminium proton shield or high-Z layer from reaching the detector. The low-Z layer may produce fluorescence lines of its own, but they will have a lower fluorescence yield and fluorescence energy (ideally of a lower fluorescence energy than the energy band of the detector) due to Moseley's Law (Moseley 1913). It is also possible that graded-Z shielding may be able to attenuate hard photons produced in spacecraft shielding before they can reach the detector, and this possibility will be examined in Section 10.1.3.

While graded-Z shielding has existed for some time as a concept, there is not a significant amount of published literature describing specific optimised designs for the removal of X-ray-like background from X-ray astronomical images, particularly for the removal of background induced by cosmic rays. Graded-Z shielding has, however, been used before in several missions to remove X-ray-like background, particularly in attempts to remove fluorescence lines and to attenuate the CXB, including in eRosita (Meidinger et al. 2010) and RHESSI (Smith et al. 2002). eRosita detects photons in a similar energy range to the intended energy range of the ATHENA WFI, of 0.3 keV – 10 keV (Predehl et al. 2014) as compared the ~0.2 keV to 15 keV (Meidinger et al. 2015) range for ATHENA WFI, and contained a 3 cm thick copper proton shield with three 1 mm graded-Z shielding layers in the configuration Al→B_4C→Be. The ATHENA WFI will also contain graded-Z shielding, most likely using a 3 cm thick proton shield of aluminium, a high-Z layer of molybdenum and a low-Z layer of Kapton.

Many of the challenges associated with designing graded-Z shielding are engineering difficulties, and are related to determining which materials are capable of being deposited onto each other while still being capable of surviving a spacecraft launch and the general environment of space. The engineering constraints of graded-Z shielding, as well as the engineering constraints imposed by other structures in the regions around the detector and baffle, can also make it challenging to cover every surface within line of sight of the detector with shielding materials. This may be either because the shielding cannot be attached to a particular surface or because it is too geometrically challenging to fit the shielding within the confines of existing spacecraft structures. Therefore it is instructive to investigate where fluorescence background primarily originates from on surfaces within line-of-sight of the detector, such that the placement of graded-Z shielding can be prioritised for such locations.

10.1.1 Determining the optimal locations for graded-Z shielding

To investigate the relationship between fluorescence intensity and position on surfaces within line-of-sight of the detector, a model can be set up as described in Figure 10.2.

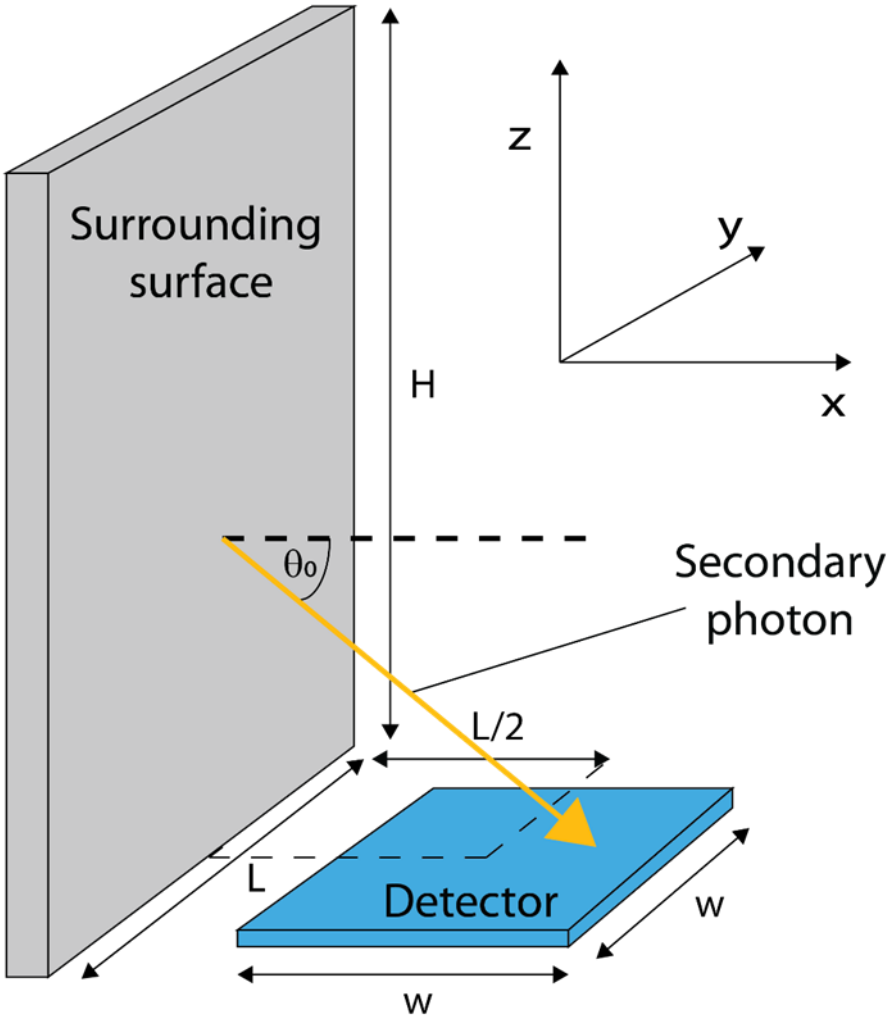

Figure 10.2 The geometry used in the mathematics for this section. A particle is generated on the grey vertical surface and has a probability of hitting the horizontal detector surface that depends on its initial location and can be determined using probability density functions. The origin of the coordinate system here, (0,0,0), is positioned at the center of the detector surface.

Here a particle is generated on the vertical surface at a point $\left(-\frac{L}{2}, y_0, z_0\right)$, where momentum is oriented at an angle to the normal θ_0, and with an azimuthal angle about the normal ϕ_0. This model can be used to effectively represent the situation of a square detector placed inside a cuboidal baffle, where the aim is to determine the probability of a fluorescence photon generated in the vertical surface hitting the detector as a function of z_0, or $PDF_{z_0}(z_0)$.

Using the geometry in Figure 10.2, and isotropic fluorescence emission, the joint probability density function for the emission location and location of the detector hit was found to be

$$PDF_{y_0,z_0,x,y} = \frac{z_0\left(x+\frac{L}{2}\right)}{\pi HL\left(\left(x+\frac{L}{2}\right)^2+(y-y_0)^2+z_0^2\right)^2} \tag{10.1}$$

The derivation for $PDF_{y_0,z_0,x,y}$ is given in Appendix E. To now find the full PDF_{z_0}, $PDF_{y_0,z_0,x,y}$ must now be integrated over the full ranges of y_0, x and y. This integration was performed using Mathematica (*Mathematica* 2019) with the constraints that z_0 and L are greater than 0 to give

$$PDF_{y_0,z_0} = \int_{y=-\frac{w}{2}}^{y=\frac{w}{2}}\int_{x=-\frac{w}{2}}^{x=\frac{w}{2}} PDF_{y_0,z_0,x,y}\,dx\,dy \tag{10.2}$$

$$\begin{aligned}=\frac{2z_0}{\pi HL}\Bigg(&\frac{\arctan\left(\frac{w-2y_0}{\sqrt{(L-w)^2+4z_0^2}}\right)+\arctan\left(\frac{w+2y_0}{\sqrt{(L-w)^2+4z_0^2}}\right)}{\sqrt{(L-w)^2+4z_0^2}}\\&-\frac{\arctan\left(\frac{w-2y_0}{\sqrt{(L+w)^2+4z_0^2}}\right)+\arctan\left(\frac{w+2y_0}{\sqrt{(L+w)^2+4z_0^2}}\right)}{\sqrt{(L+w)^2+4z_0^2}}\Bigg)\end{aligned} \tag{10.3}$$

Integrating across the full range of y_0 now gives

$$PDF_{z_0} = \int_{y_0=-\frac{L}{2}}^{y_0=\frac{L}{2}} PDF_{y_0,z_0}\,dy_0 \tag{10.4}$$

$$\begin{aligned}=\frac{z_0}{\pi HL}\Bigg(&\frac{(-L+w)\arctan\left(\frac{L-w}{\sqrt{(L-w)^2+4z_0^2}}\right)+(L+w)\arctan\left(\frac{L+w}{\sqrt{(L-w)^2+4z_0^2}}\right)}{\sqrt{(L-w)^2+4\,z_0^2}}\\&+\frac{(L-w)\arctan\left(\frac{L-w}{\sqrt{(L+w)^2+4z_0^2}}\right)+(-L-w)\arctan\left(\frac{L+w}{\sqrt{(L+w)^2+4z_0^2}}\right)}{\sqrt{(L+w)^2+4z_0^2}}\\&+\frac{1}{2}\left(\ln\left((L-w)^2+2z_0^2\right)-2\ln\left(L^2+w^2+2z_0^2\right)+\ln\left((L+w)^2+2z_0^2\right)\right)\Bigg)\end{aligned} \tag{10.5}$$

This can be expressed more simply as

$$k_{\pm} = \sqrt{(L \pm w)^2 + 4z_0^2} \tag{10.6}$$

$$d_{\pm} = L \pm w \tag{10.7}$$

$$\begin{aligned} PDF_{z_0} = \frac{z_0}{\pi HL}\Bigg(&\frac{1}{2}(\ln(d_-^2 + 2z_0^2) - 2\ln(L^2 + w^2 + 2z_0^2) + \ln(d_+^2 + 2z_0^2)) \\ &- \frac{d_-}{\mathrm{k}_-}\arctan\left(\frac{d_-}{k_-}\right) + \frac{d_+}{k_-}\arctan\left(\frac{d_+}{k_-}\right) + \frac{d_-}{k_+}\arctan\left(\frac{d_-}{k_+}\right) \\ &- \frac{d_+}{k_+}\arctan\left(\frac{d_+}{k_+}\right)\Bigg) \end{aligned} \tag{10.8}$$

or as

$$\begin{aligned} PDF_{z_0} = \frac{2z_0}{\pi HL}\Bigg(&\frac{1}{2}\left(\ln\left(d_-^2 + 2z_0^2\right) - 2\ln\left(L^2 + w^2 + 2z_0^2\right) + \ln\left(d_+^2 + 2z_0^2\right)\right) \\ &- \left[\left[\frac{d}{k}\arctan\left(\frac{d}{k}\right)\right]_{k=k_-}^{k=k_+}\right]_{d=d_-}^{d=d_+}\Bigg) \end{aligned} \tag{10.9}$$

This probability density function is proportional to the total intensity of fluorescence photons that hit the detector from a region of shielding. $PDF_{z_0}(z_0)$ can be directly used to determine the percentage of fluorescence photons that will be removed if graded-Z shielding is placed over a particle surface, based on the total probability density the shielding obstructs.

The method described above is very similar to the mathematics of 'view factors' (Howell 1982; Howell, Menguc, and Siegel 2015), a concept that is frequently used in calculations of radiative heat transfer between one surface and another.

While this means that it is possible to directly use view factors to determine the location of important areas to shield, this will only work in cases where a photon can be reasonably approximated as guaranteed to be absorbed within the detector. For situations where this isn't possible, such as for higher energy photons where quantum efficiency is low, Equation 10.1 must be multiplied by the interaction probability as a function of the angle at which the photon hits the detector before any integrations can be performed. Additionally, using the above probability density function method offers the advantage that the distribution of photon hits across the detector can be calculated by integrating Equation 10.1 across both y_0 and z_0 to give $PDF_{x,y}$.

To test the assumptions made in the derivation of Equation 10.1, simulations were performed using GCR proton input particles incident upon a cuboidal 4 cm thick proton shield with a 450 micron thick detector placed near the base of the internal cuboid. The geometry for this is displayed in Figure 10.3 and is the same geometry that will be used later for simulations of active magnetic shielding in Section 10.2.3.

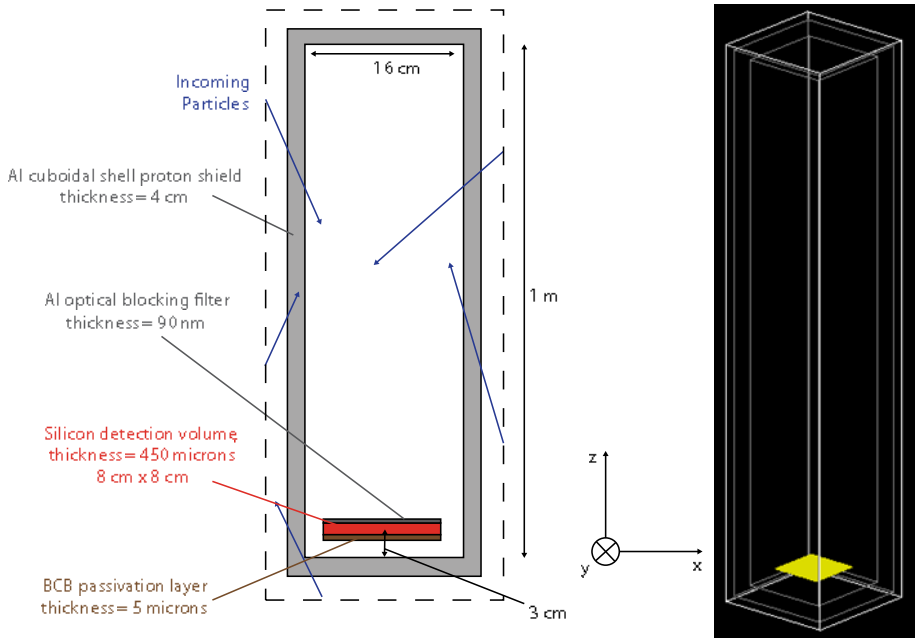

Figure 10.3 The Geant4 geometry used to determine and verify the accuracy of Equation 10.25 at determining the distribution of background-inducing fluorescence photons along surfaces in the geometry.

X-ray-like background events originating from fluorescence photons were separated from other forms of background. The secondary particle origin locations, also known as creation vertexes, along the walls of the cuboid were then binned and plotted as shown in Figure 10.4 alongside the probability density curve as calculated from Equation 10.9. Here the parameters used in Equation 10.9 were $H = 0.97$ m, $w = 0.08$ m and $L = 0.16$ m matching the geometry used. A normalisation factor also had to be applied to Equation 10.9 to match the total number of predicted counts, and this was found using standard least-squares fitting methods, although as this normalisation was only a factor that was multiplied by Equation 10.9 it only changed the magnitude not the shape of the curve.

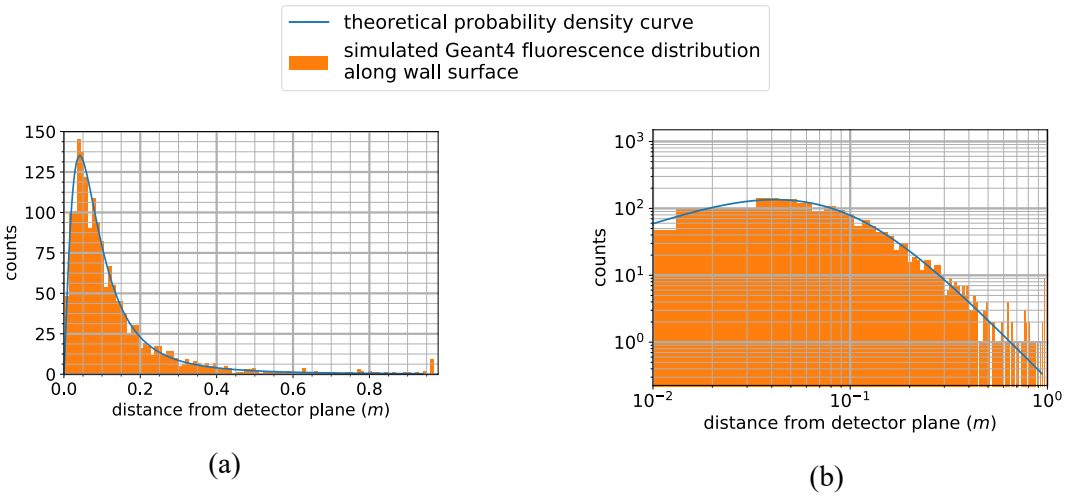

Figure 10.4 The binned creation vertex positions of fluorescence photons from the GCR proton Geant4 simulations compared to the theoretical probability density function from Equation 10.9. Figure (a) and (b) display the same data, but (a) is in linear space, while (b) is in log-log space. The theoretical curve appears to have good agreement with the simulated data.

Figure 10.4 displays a good fit between the theoretical curve predicted by Equation 10.9 and the Geant4 produced fluorescence photon intensity curve. This indicates that Equation 10.9 has significant predictive power and may potentially be used to accurately determine the most important regions of internal surfaces to shield without the necessity to simulate many configurations of shielding locations. Most photons, in this case, originate from within 20 cm of the detector surface, indicating that regions somewhat close to the detector are more important to shield than regions distant to the detector and that there are diminishing returns on adding shielding above that point.

This is also shown in Figure 10.5, which displays the cumulative density function corresponding to Equation 10.9 integrated, and shows that the median creation distance of a particle to the detector surface plane is at approximately 10 cm.

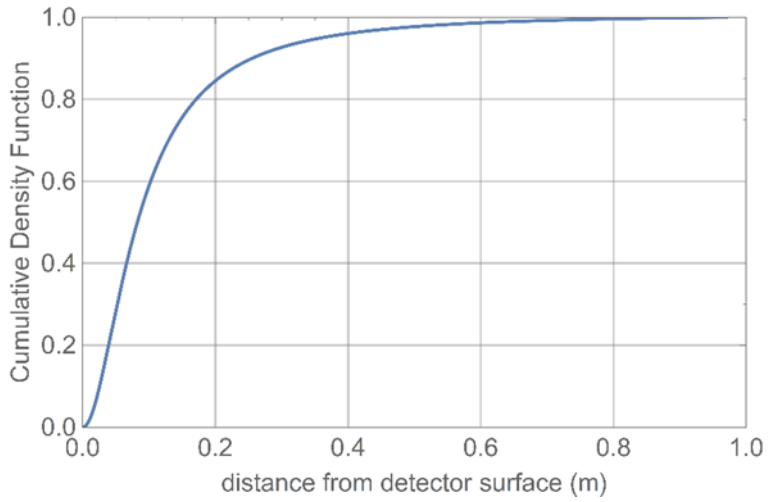

Figure 10.5 The cumulative density function for the probability distribution function in Equation 10.25 and the geometry displayed in Figure 10.3. The median, 25% percentile and 75% percentile are all within 20 cm from the detector surface plane in this situation.

A further simplification can also be made to Equation 10.9 for the special case when $L = w$, giving

$$PDF_{z_0} = \frac{2}{\pi H}\arctan\left(\frac{w}{z_0}\right) + \frac{z_0}{\pi H w}\left(\ln(z_0^2) - 2\ln(w^2 + z_0^2) + \ln(2w^2 + z_0^2) - \frac{2w\arctan\left(\frac{w}{\sqrt{w^2 + z_0^2}}\right)}{\sqrt{w^2 + z_0^2}}\right) \tag{10.10}$$

An additional useful special case is the case where $H \to \infty$. In many X-ray observatories, the baffle is significantly longer than the internal width of the baffle or width of the detector, meaning that the

baffle can be approximated as infinite in length. To calculate the probability density function as a function of z for this case, PDF_{z_0} first has to be re-normalised by the introduction of the normalisation constant $A(w,H)$, setting $A(w,H) \times \int_{z_0=0}^{z_0=\infty} PDF_{z_0} dz_0 = 1$ and calculating $A(w,H)$. $PDF_{z_0,H\to\infty}$ is then $PDF_{z_0,H\to\infty} = \lim_{H\to\infty} A(w,H) \times PDF_{z_0}$, giving

$$PDF_{z_0,H\to\infty} = \frac{4}{\pi w}\arctan\left(\frac{w}{z_0}\right) + \frac{2z_0}{\pi w^2}\left(\ln(2w^2 + z_0) + 2\ln\left(\frac{z_0}{w^2 + z_0^2}\right) - \frac{2w}{\sqrt{w^2 + z_0^2}}\arctan\left(\frac{w}{\sqrt{w^2 + z_0^2}}\right)\right) \quad (10.11)$$

Equation 10.11 is plotted in Figure 10.6 for $w = 0.1331$ m, while Figure 10.7 displays the corresponding cumulative density function plot, which is the integral of Equation 10.11 between $z_0 = 0$, and $z_0 = z_0$. Here distance from detector surface refers to z_0 in both plots.

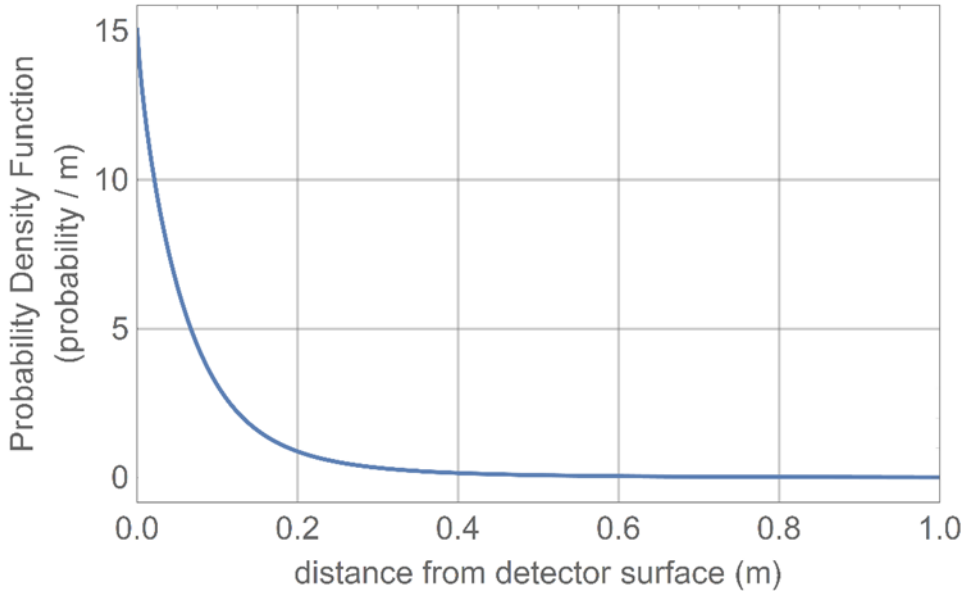

Figure 10.6 The probability density function for Equation 10.11 for $w = 0.1331$ m, the case where walls surrounding the chamber can be approximated as infinite in length.

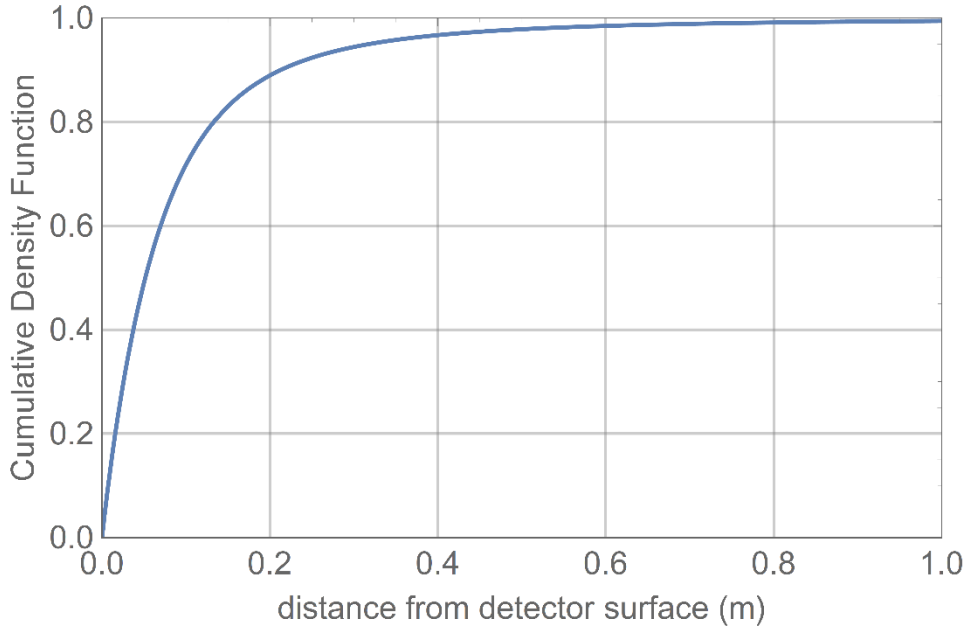

Figure 10.7 The cumulative density function calculated by integrating Equation 10.11 between $z_0 = 0$ and $z_0 = z_0$ and for $w = 0.1331$ m. The cumulative density function in this case implies that the majority of fluorescence counts will originate from within 0.2 m of the detector surface.

As well as plotting the one-dimensional probability density function across the emitting surface it is also possible to use Equation 10.3 to calculate the two-dimensional probability density function. Applying the same simplifications of $L = w$ and $H \to \infty$ along with normalising to 1 gives

$$PDF_{y_0,z_0,H\to\infty} = \frac{2}{w^2\pi}\left(\operatorname{arccot}\left(\frac{2z_0}{w-2y_0}\right) + \operatorname{arccot}\left(\frac{2z_0}{w+2y_0}\right) - \frac{z_0}{\sqrt{w^2+z_0^2}}\left(\arctan\left(\frac{w-2y_0}{2\sqrt{w^2+z_0^2}}\right) + \arctan\left(\frac{w+2y_0}{2\sqrt{w^2+z_0^2}}\right)\right)\right) \tag{10.12}$$

Equation 10.12 is plotted as a density contour plot in Figure 10.8 for $w = 0.1331$ m, showing the predicted spatial distribution of fluorescence across the fluorescence generating surface.

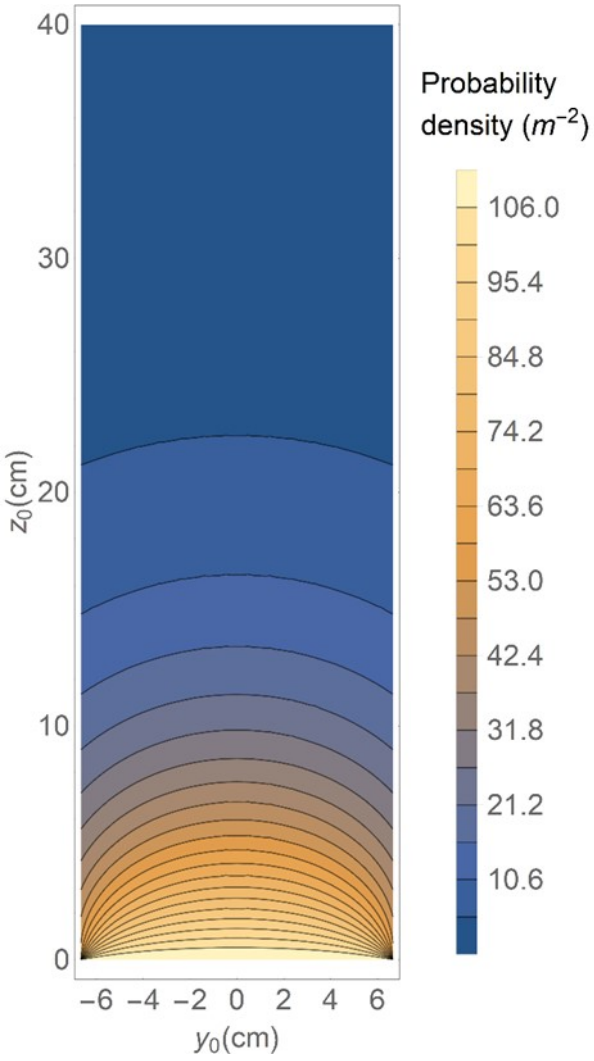

Figure 10.8 The 2D probability density function across the surface of the generation. Fluorescence intensity is strongest near $z_0 = 0$ and $y_0 = 0$.

Figure 10.8 predicts that fluorescence should peak at regions of the surface that are closer to the detector and closer to $y_0 = 0$. This means that shielding detectors from these regions should be prioritised, as shielding over these areas will reduce fluorescence most effectively.

10.1.2 The theoretical effectiveness of a graded-Z layer as a function of thickness

While this analysis provides an insight into the optimal locations to place shielding, the actual thickness of a graded-Z layer is also an important factor in determining its effectiveness. In some situations, it may be optimal to minimise the thickness of graded-Z shielding layers to take into account engineering considerations, while still maintaining the ability to effectively reduce fluorescence intensity. Therefore it is useful to calculate a representative quantity that can be used to estimate the necessary shielding layer thickness.

One quantity that could be used is the total probability that the graded-Z layer will absorb a photon of the relevant energy. While the common expression for the probability of a photon hitting the layer at a

normal could be used, of $1 - e^{-\lambda t}$ where λ is the attenuation coefficient of the layer and t is the thickness, it is unlikely that a photon will hit the layer at a normal to the layer surface as was discussed earlier in Section 9.1.1.1.

Therefore a better quantity to use may be the mean probability that a particle with an isotropically distributed momentum direction is absorbed in a shielding layer. The mathematics for calculating such an expression is identical to that shown in Section 9.1.1.1.2, where it was calculated that the probability that a diffusely distributed soft photon is absorbed into a detector when passing through it was given in Equation 9.8 as

$$P = 1 + e^{-\lambda t}(\lambda t - 1) + \lambda^2 t^2 Ei(-\lambda t) \tag{10.13}$$

where λ is the mass-energy absorption coefficient for the shielding layer, t is the detector thickness and $Ei(x) = \int_{-\infty}^{x} \frac{1}{t} e^t \, dt$ is the elliptic integral of x.

As examples, in the case of a room temperature molybdenum high Z layer shielding 100 keV photons, $\lambda = 8.27$ cm^{-1} (Xcom 2010), P can be found to equal 0.95 when $t = 2.60$ mm. In contrast, for a room temperature Be low-Z layer shielding the detector from a 1.48 keV photon fluorescence line from an aluminium proton shield, $\lambda = 1916.7$ cm^{-1} which means that P can be found to equal 0.95 when $t = 0.011$ mm.

While these numbers are useful for approximating the effectiveness of a graded-Z shielding layer, it should be noted that Equation 10.13 does not take into account the location of a detector relative to the graded-Z shielding. The detector location relative to the shielding will influence the thickness of shielding a photon will pass through before it reaches the detector, which may change the effectiveness of a graded-Z shielding layer.

10.1.3 Simulations of graded-Z shield configurations

In addition to determining the optimal location and thickness for graded-Z shield placement, it is also necessary to investigate the optimal material configurations that could be used to mitigate photon-induced X-ray-like background. While it is relatively clear how a particular material will affect the intensity of fluorescence lines as this is something that can be calculated using tabulated X-ray attenuation coefficients, it is less clear how the presence of graded-Z shielding can affect the background continuum.

Therefore simulations were performed across a range of graded-Z shielding configurations to assess the variation in continuum count rate with material configuration. The geometries used were similar to the spherical shell models simulated in Chapter 8 but with the modification that two additional inner spherical shell layers were placed on the internal surface of the existing 4 cm aluminium proton shield shell as shown in Figure 10.9. Each inner layer was 1 mm thick, where the innermost layer would

contain the low-Z candidate material, while the layer between the innermost layer and proton shield shell contained the high-Z candidate material. The mean count rates between 2 keV and 7 keV for the graded-Z shielding simulations are displayed in Figure 10.10 for both GCR proton and CXB input spectra.

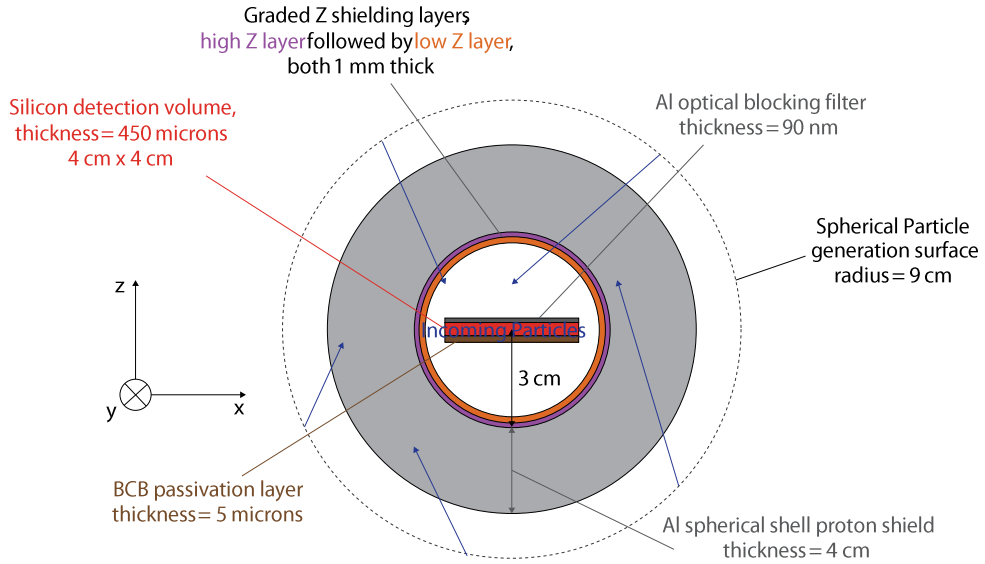

Figure 10.9 The simulation geometry used in this section. Two 1 mm thick inner graded-Z shielding layers were added to the simulation geometries described in previous chapters, with materials specified at simulation run time.

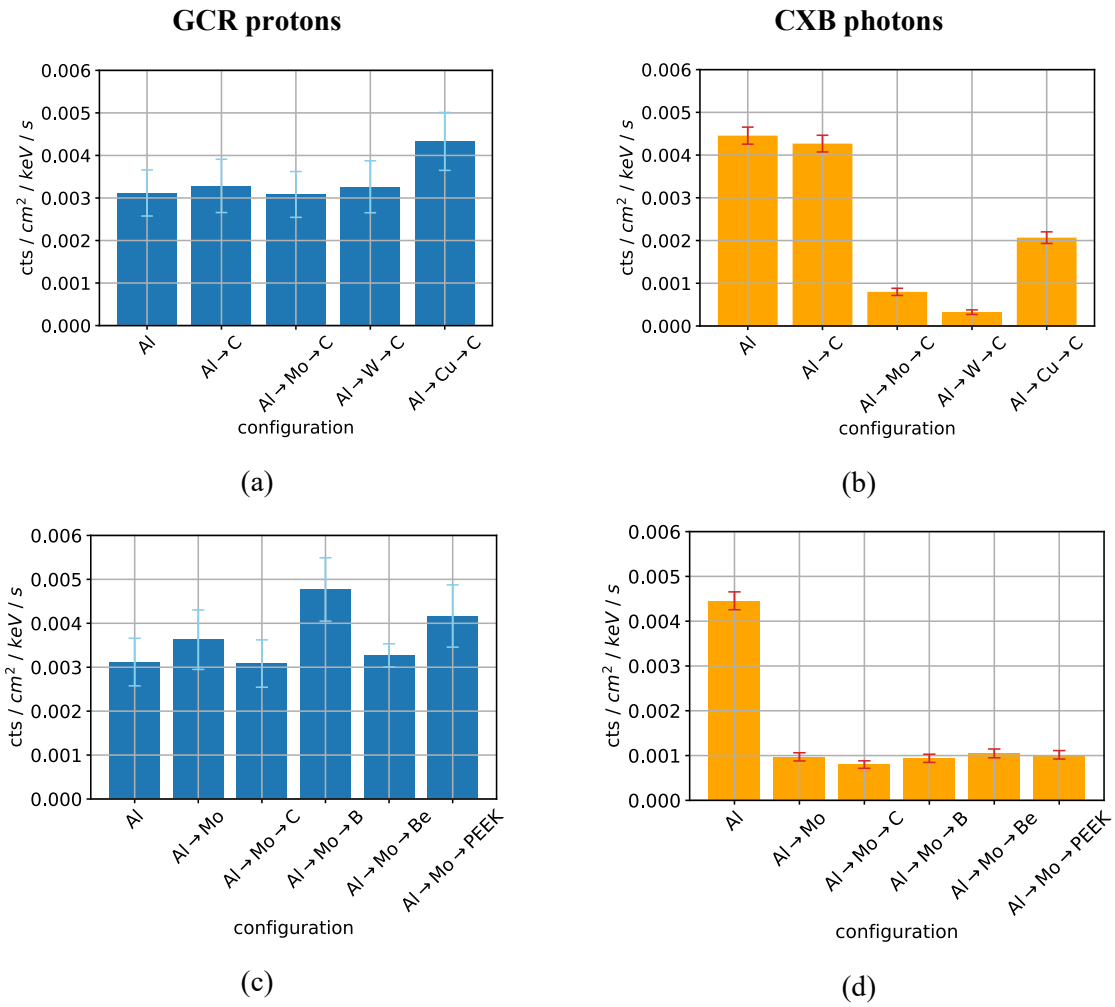

Figure 10.10 The mean count rate between 2 keV and 7 keV for multiple configurations of graded-Z shielding. Figure 10.10(a) and Figure 10.10(c) display configurations of varying high Z material and low Z material respectively for the GCR proton input spectrum, whereas figures Figure 10.10(b) and Figure 10.10(d) display configurations of varying high Z material and low Z material respectively for the CXB photon input spectrum.

The addition of the high Z layers appears to significantly reduce the CXB induced background for all the simulated low Z layer materials, as expected. In contrast, while it is the case that the GCR proton simulations exhibit high statistical errors here, there appears to be no evidence from these simulations that any graded-Z shielding configurations reduce the GCR proton induced background continuum mean count rate significantly versus the case with only the aluminium proton shield. This implies that while graded-Z shielding may be attenuating the hard photon spectrum produced by the aluminium proton shield, a significant quantity of hard photons may be being generated by the shielding layers such that the total flux of hard photons remains the same.

The spectra generated in the Al only, Al and Mo, and Al, Mo and C simulations are also displayed in Figure 10.11.

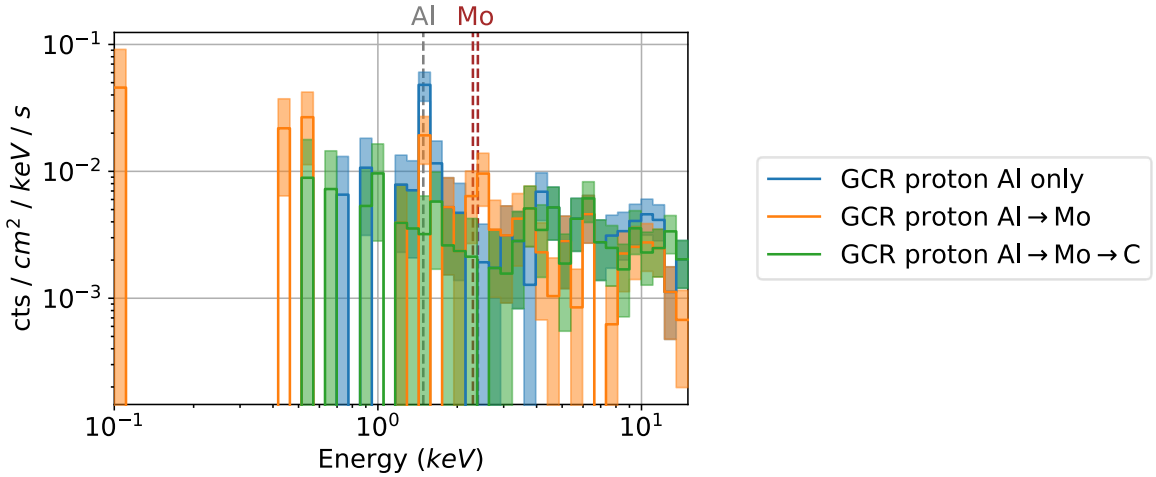

(a)

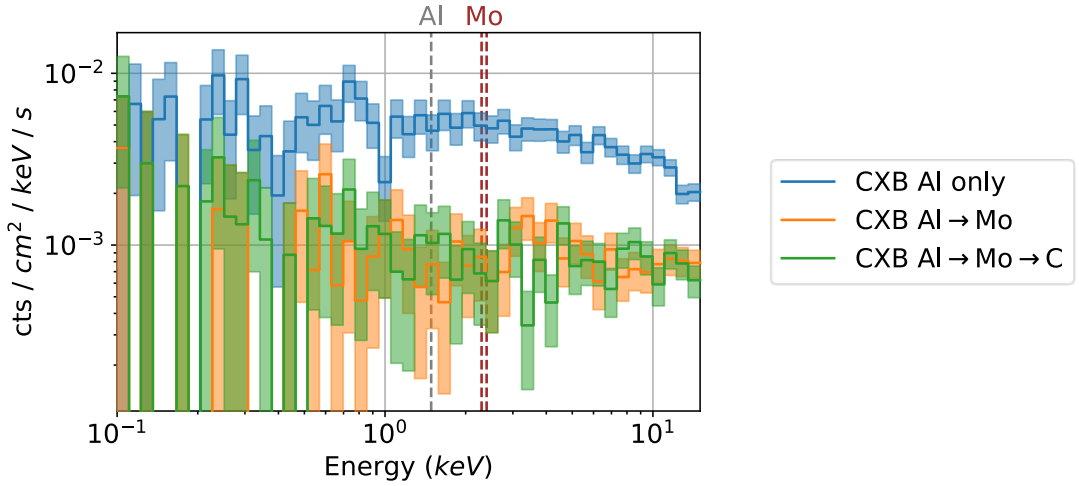

(b)

Figure 10.11 The energy deposition spectra produced by several graded-Z shielding combinations of the aluminium proton shield, 1 mm of molybdenum and 1 mm of carbon. Figure 10.11(a) displays the background induced by GCR protons, and Figure 10.11(b) displays the background induced by CXB photons.

Figure 10.11(b) indicates that the CXB induced spectrum not only decreases significantly with the introduction of the graded-Z shielding layers, but the spectrum also appears to flatten.

The above results indicate that the inclusion of graded-Z shielding layers simulated here are all effective at significantly reducing CXB induced background. To significantly reduce the GCR induced background however, it appears that these simulated graded-Z layers are not sufficient, and therefore other shielding mechanisms will need to be utilised. One such mechanism that may be capable of significantly reducing the GCR induced X-ray-like background is magnetic shielding, which can shield a detector by diverting knock-on electrons which would otherwise cause X-ray-like background, such that they miss the detector.

10.2 Shielding a detector from knock-on electrons using active magnetic shielding

As has been discussed previously in Chapter 2, particles in uniform magnetic fields follow magnetic field lines in a helical motion, where particles become more strongly confined to magnetic field lines if the magnetic field strength is increased. Through careful placement of magnets, magnetic field lines can be oriented in directions such that they can either confine charged particles along the magnetic field lines such that they hit other surfaces before hitting the detector, or divert charged particles such that they miss the detector.

There are two main classifications of magnetic shielding: active magnetic shielding, which refers to magnetic fields generated by electrical currents, and passive magnetic shielding, which refers to magnetic fields generated by permanent magnets.

The advantages of passive magnetic shielding in the space-based environment are that they require no electronics or power to operate, making them relatively straightforward to fit into existing spacecraft designs. They do exhibit the disadvantage for X-ray-like background purposes in particular however that such magnets typically need to be made from high-Z materials such as neodymium which may generate fluorescence lines if they are placed near to a detector with no graded-Z shielding.

Active magnetic shielding, on the other hand, can use wires made out of lower atomic number metals and can be made of aluminium at the cost of requiring more power due to a higher resistance than a more commonly used conductor like copper. Active magnetic shielding may also be simpler to model than permanent magnets as the magnetic field through a wire can be calculated using the Biot-Savart law. In contrast, permanent magnets may exhibit magnetic fields that are more complex. Active magnetic shielding also has the intrinsic advantage that the magnetic field strength can be controlled or turned off while in orbit, which may be useful for taking dark frames in some cases, or for some scientific purposes.

Magnetic diverters have been used for both background mitigation and radiation damage mitigation in many previous space missions (Spiga et al. 2008). ATHENA also plans to include a magnetic diversion mechanism for the diversion of soft protons and electrons approaching the detector from the baffle, a design which current simulations indicate will be very effective (Fioretti et al. 2018). The typical design for such diverters utilises a ring of permanent magnets surrounding the baffle between the optics and focal plane, which is placed at such a location with a sufficient magnetic strength as to divert electrons and protons away from the detector (Li et al. 2017).

Research has also been performed to investigate potential mechanisms for magnetic diversion of incoming cosmic rays themselves for both space astronomy missions in general as well as for human-manned missions (Westover et al. 2014), some of which are somewhat exotic designs such as the use of confined plasmas (Bamford et al. 2014). Designing a system that can do this is a significantly more

challenging task than deflecting electrons and soft protons, as cosmic rays capable of inducing background and causing radiation damage have significantly larger momenta/magnetic rigidities and approach the detector from all directions. This means that such a system would require a very strong magnetic field encompassing the spacecraft, which would likely need to be generated by strong superconducting magnets.

While magnetic diverters in previous missions have been effective at diverting incoming soft protons and electrons, the magnetic diverters that have been used in previous missions have only been used to divert soft protons and electrons that have been funnelled from outside the spacecraft through spacecraft optics and down the baffle. In contrast, there has been relatively little research published on the ability of magnets to divert knock-on electrons, which are produced from all surfaces surrounding a detector.

Designing a magnetic diverter that can deflect electrons approaching from the baffle is very different to designing a system that is capable of shielding a detector from knock-on electrons produced off-axis from surrounding surfaces to the detector, as protons and electrons travelling down the baffle are all approximately travelling in the same direction, and originate a long distance away from the detector. In contrast, knock-on electrons impact the detector from all directions and are produced significantly closer to the detector. This means that a magnetic shielding design for diverting knock-on electrons must be capable of simultaneously shielding the detector from electrons produced from any angle relative to the detector and at a multitude of emission directions. The magnetic field produced by such a design must also be sufficiently strong as to divert electrons before they can reach the detector.

While not directly applicable to magnetic shielding specifically, Steffan Hauf (2012) performed Geant4 simulations to assess the ability of electrostatic shielding to reduce the X-ray-like background in the ATHENA WFI. Hauf found that anodes and cathodes placed between graded-Z shielding layers reduced X-ray-like background by up to a factor of approximately 80%. Hauf also found that the most effective design of electrostatic shielding was to accelerate rather than decelerate electrons, making them too high energy to fall within the detector energy range.

Perinati et al. (2018) investigated the ability of permanent magnets placed near the ATHENA WFI to reduce the soft electron-induced background. They found that passive magnetic shielding indeed theoretically might be able to shield the detector from soft electrons. However, they also pointed out the concern that the magnetic field created might affect detector images or electronics, even though the influence of the magnetic field on electrons or holes in the detector or electronics would be expected to be small relative to the electric fields present.

The experiments in Chapters 6 and 7 used a Helmholtz coil magnetic field as a magnetic diversion mechanism. Moreover, in Chapter 6 it was found that the magnetic field produced by the Helmholtz coils successfully significantly reduced the number of electrons within the detector energy range impacting the detector. These experiments also provided an opportunity to test to see if the magnetic field of a magnetic diverter close to a detector might affect the electronics or outputted images of a detector, which generated a maximum mean magnetic field strength of approximately 0.52 mT at the detector surface plane.

The photon fluorescence lines in experiments at the STERIS beamline and PSI PIF in Chapter 6 did not change with magnetic field strength. While there was a slight shift in photon fluorescence line observed position in event detected data from the experiments with 200 MeV protons at the PSI PIF which correlated with magnetic field strength, this was found to be caused by the event detection algorithm applied generating a somewhat distorted spectrum at energies below approximately 2 keV in energy and unrelated to the presence of the magnetic field.

The electron spectrum and difference between electron spectra across different magnetic field strengths across the majority of the spectrum in PSI experiments was also consistent with simulated Geant4 spectra, as were the power-law distributions of the electron spectra in the STERIS beamline experiments. As was discussed in Chapter 6, experimental spectra in the STERIS beamline experiments did deviate significantly from simulation spectra, but this is believed to be due to incorrect dosimetry normalisation within the experiment.

Therefore overall no evidence was found that indicates the presence of the magnetic field altered the device internal physics, indicating that at least for the CCD97 that was used in these experiments, a magnetic shielding mechanism of several milliTesla in strength should not be expected to introduce systematic errors to photon observations.

10.2.1 The ability of a uniform magnetic field to reduce electron-induced background

Determining the trajectories of particles in magnetic fields is often complex, even for relatively simple magnetic fields, and it can be challenging to model particle trajectories in magnetic fields mathematically. However, many magnetic fields can be approximated as uniform in certain spatial regions, and the trajectory of particles in a uniform magnetic field is well-known mathematically. Therefore it is instructive to investigate how uniform magnetic fields may be applied in a spacecraft to remove knock-on electron-induced X-ray-like background.

Three possible ways that particles might be prevented from reaching a detector through the use of uniform fields are shown in Figure 10.12.

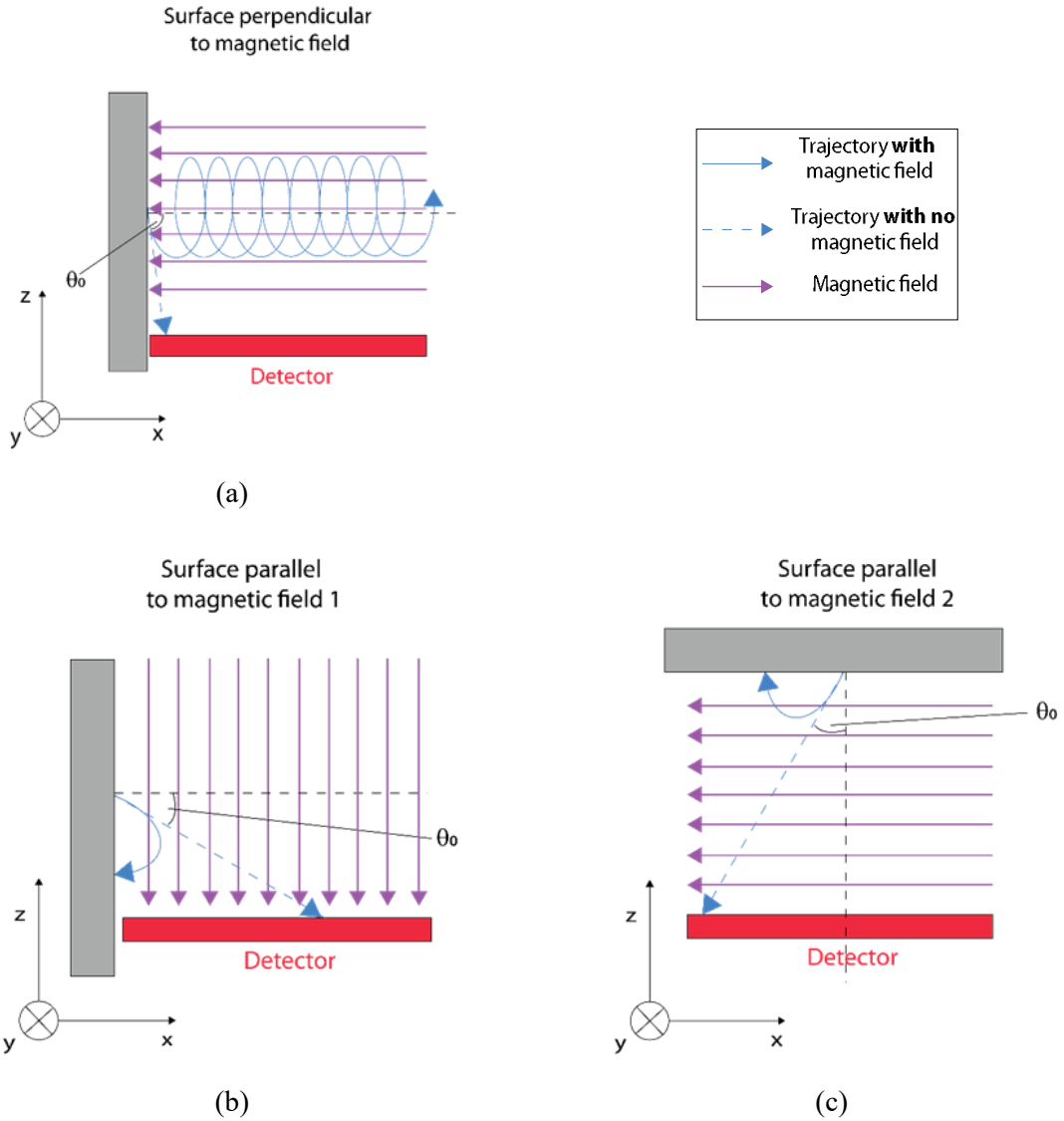

Figure 10.12 The different orientations of uniform magnetic fields that are capable of removing electron-induced background that will be investigated in this chapter.

Figure 10.12(a) displays a magnetic field that is parallel to a surface generating electrons but perpendicular to a detector. In this case, an electron is initially travelling towards the detector but passes through the magnetic field and becomes confined to it, travelling in a helical motion along the magnetic field lines without ever hitting the detector.

In contrast, in Figure 10.12(b), the uniform magnetic field is parallel to a surface where knock-on electrons are being generated. Electrons generated from the surface move around the magnetic field line in a circular motion, and if the magnetic field is sufficiently strong, the electron impacts the surface it originated from before it can travel far enough to impact the detector.

Figure 10.12(c) displays a similar geometry to Figure 10.12(a); however, the detector here is instead oriented perpendicularly to the magnetic field lines. In this case, if the electron gyroradius is sufficiently small, knock-on electrons again circle the magnetic field lines until they re-impact the

surface they emerged from without hitting the detector. While there are unlikely to be many surfaces parallel to the detector face in front of a detector, electrons produced from parallel surfaces behind the detector may induce background.

As each of these cases will likely occur in any magnetic shielding design in a complex spacecraft geometry, it is instructive to investigate mathematically how effectively a uniform magnetic field will shield a detector from electrons in each situation.

10.2.2 Assessing the effectiveness of uniform magnetic shielding mathematically

The maximum possible distance that a particle can travel from a surface perpendicularly to a uniform magnetic field is given by the diameter of its helical motion around the field line or twice the particle's gyroradius. However, for a given energy of a particle, the gyroradius is dependent upon the angle at which the particle is initially travelling relative to the magnetic field. This will be distributed using the same $\sin(2\theta)$ distribution that has been used previously in this thesis, if the magnetic field is parallel to the surface of emission.

For this reason, the maximum distance a particle will travel as a function of emission angle from the surface in a magnetic field will likely be significantly less than the maximum possible distance it could travel if the emission angle were optimised for travel distance. A particularly useful quantity that could be used to characterise the effectiveness of the magnetic field here would be the median maximum distance that a particle travels from the surface during its motion. The lower this value is, the more effectively a magnetic field could be said to be at shielding a detector from electrons of a particular energy.

The trajectory of a particle in a magnetic field was previously described in Chapter 2, where it was stated that for a uniform magnetic field oriented in the z-direction, the particle gyroradius is given by

$$r_g = \frac{\sqrt{\boldsymbol{p}_\perp^2}}{|q||\boldsymbol{B}|} \tag{10.14}$$

where $\boldsymbol{p}_\perp$ is the momentum of the particle perpendicular to the magnetic field, q is the charge of the particle, and $\boldsymbol{B}$ is the magnetic field, which has a component of B along positive x, z and x for the geometries shown in Figure 10.12(a), Figure 10.12(b) and Figure 10.12(c) respectively. Using this it is possible to calculate the maximum distance a particle will travel from the surface it originated from as a function of its original momentum direction, where for a positive gyrofrequency $\omega_g = \frac{v_\perp}{r_g}$, where $v_\perp$ is the velocity of the particle perpendicularly to the magnetic field, the minimum possible values for z in each case when ϕ_0 and θ_0 are varied are

$$z_{\perp,1,min} = -\frac{v}{\omega_g}(\sin(\phi_0) + 1)\sin(\theta_0) \tag{10.15}$$

$$z_{\parallel,1,min} = \frac{v}{\omega_g}\text{atan2}(\sin^2(\theta_0)\,(1+\cos^2(\phi_0)) - 1, -\cos(\phi_0)\sin(2\theta_0))\sin(\phi_0)\sin(\theta_0) \tag{10.16}$$

$$z_{\parallel,2,min} = -\frac{v}{\omega_g}\left(\sin(\phi_0)\sin(\theta_0) + \sqrt{1-\sin^2(\theta_0)\cos^2(\phi_0)}\right) \tag{10.17}$$

Where atan2(x, y) is the 2-argument arctangent, and v is the particle velocity. The derivation for these expressions is given in Appendix F.1.

These relations were used to calculate the median closest distance between the particle and the detector using Monte Carlo methods for each of the three geometries. Before this was done, it was necessary to derive analytical probability density functions for z_{min} such that Monte Carlo simulations are not necessarily needed for future calculations of the effectiveness of magnetic shielding. It was possible to do this for $z_{\perp,1,min}$ and $z_{\parallel,2,min}$, although the expression for $z_{\parallel,1,min}$ was too complex to solve for the probability density function analytically.

10.2.2.1 The probability density function for the perpendicular case

The probability density function for $z_{\perp,1,min}$, $PDF_{z_{\perp,1,min}}$, was determined using Equation 10.15 and some common expressions for magnetic fields to give

$$PDF_{z_{\perp,1,min}} = \frac{2\,sgn(\omega_g)\sqrt{-\omega_g z_{\perp,1,min}(2v + \omega_g z_{\perp,1,min})}(\omega_g z_{\perp,1,min} - v)}{3\pi v^2 z_{\perp,1,min}} \tag{10.18}$$

Where the limits for $z_{\perp,1,min}$ are $-\frac{2v}{\omega_g} < z_{\perp,1,min} \leq 0$ for positive ω_g. The full derivation of this is given in Appendix F.2.

This function is plotted in Figure 10.13 and Figure 10.14 alongside probability density functions that were predicted by a Monte Carlo simulation that was performed using Equation 10.15. Here the speed v was calculated as a function of kinetic energy E_k using the relativistic Equation $v = \frac{c\sqrt{E_k(E_k+2m_0c^2)}}{E_k+m_0c^2}$, where c is the speed of light and m_0 is set to the rest mass of an electron. The agreement between Equation 10.18 and the Monte Carlo simulated probability density functions indicates that the mathematics performed here is correct.

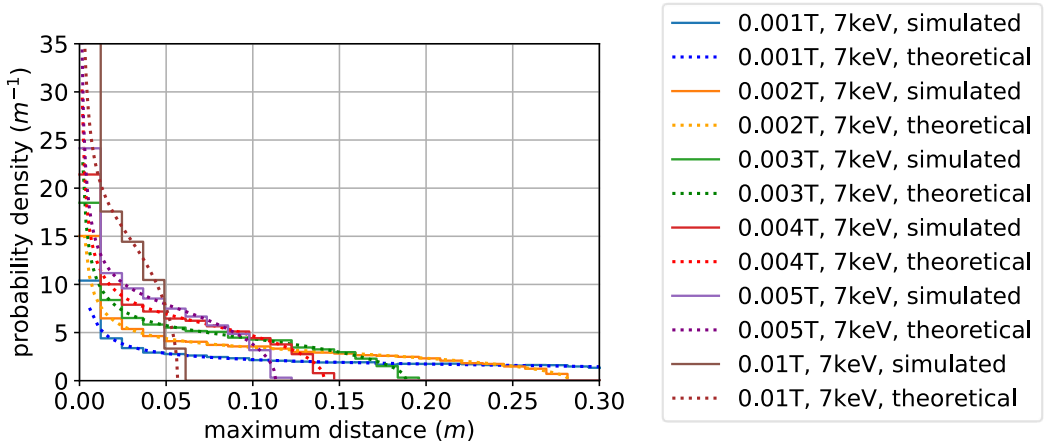

Figure 10.13 Theoretical and simulated probability density functions given by $PDF_{z_{\perp,1,min}}$ as a function of the magnitude of the maximum distance $z_{\perp,1,min}$ for multiple magnetic fields for the perpendicular case. The simulated and theoretical curves agree well for all parameters.

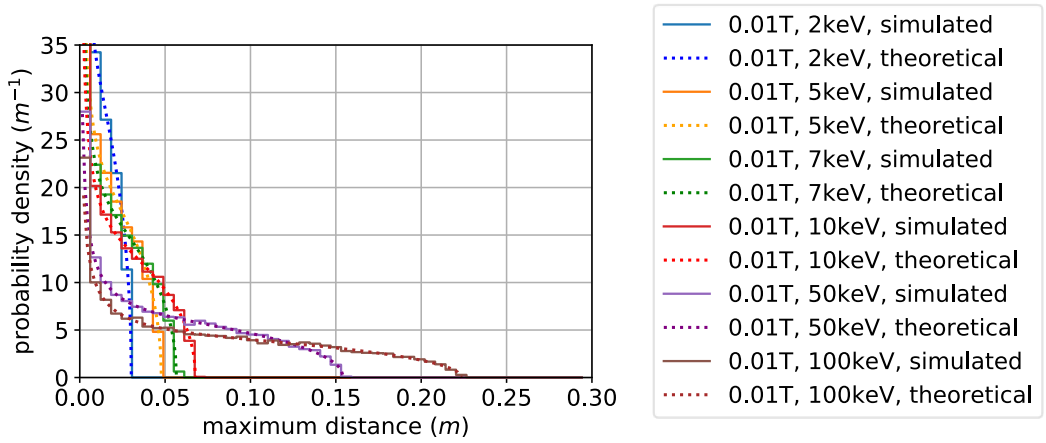

Figure 10.14 Theoretical and simulated probability density curves given by $PDF_{z_{\perp,1,min}}$ as a function of the magnitude of the maximum distance $z_{\perp,1,min}$ for multiple particle energies for the perpendicular case. The simulated and theoretical curves agree well for all parameters.

Figure 10.13 and Figure 10.14 indicate that there is a low probability in the perpendicular case of a particle reaching near its maximum possible distance of twice its gyroradius, as the probability density function is infinite at 0 m, but quickly decreases and in some cases flattens out as it approaches the maximum possible distance.

10.2.2.2 The probability density function for the first parallel case

While it was not possible to analytically calculate the probability density function for the first case of the magnetic field being parallel to the generation surface, it was possible to perform similar Monte Carlo simulations of the maximum vertical distance that particles reached as were performed in Section 10.2.2.1. The results for these simulations are displayed in Figure 10.15 and Figure 10.16.

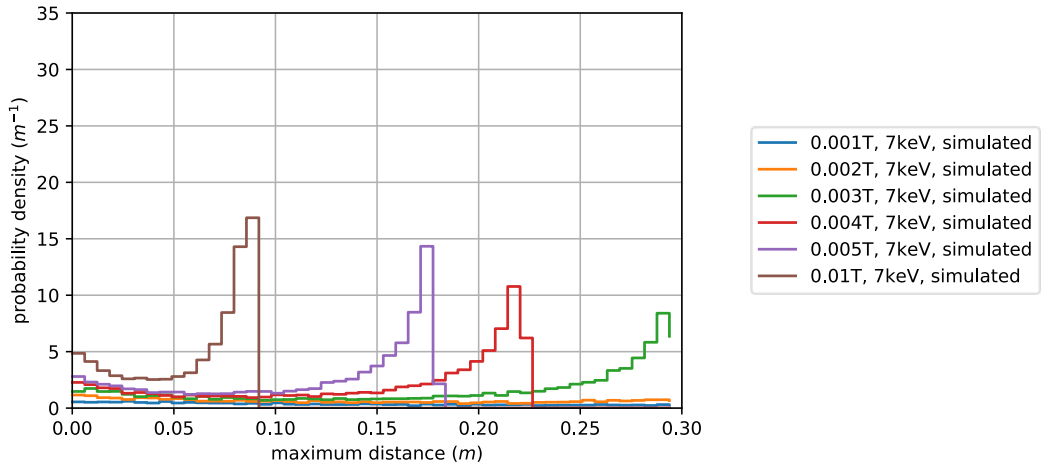

Figure 10.15 Simulated probability density functions for varying magnetic field strengths in the first parallel geometry. The probability density functions were generated by applying Monte Carlo methods to Equation 10.16.

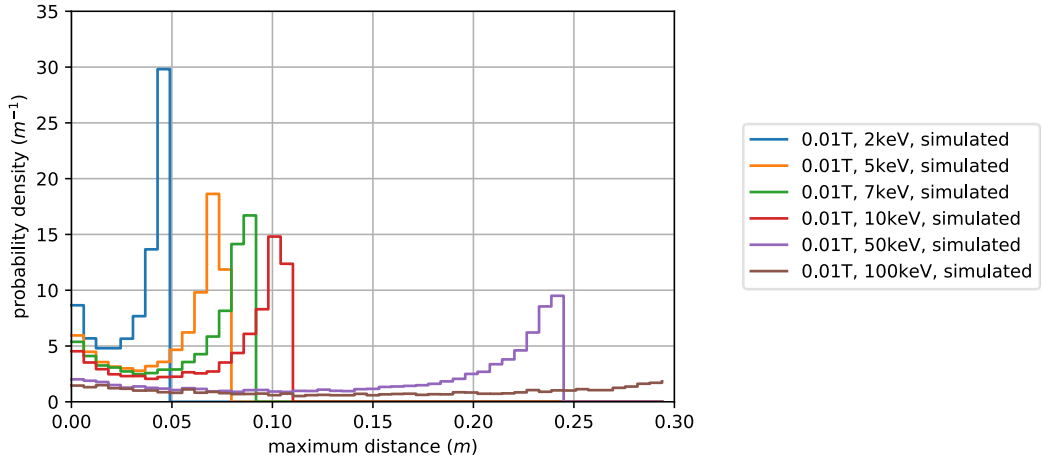

Figure 10.16 Simulated probability density functions for varying particle energies in the first parallel geometry. The probability density functions were generated by applying Monte Carlo methods to Equation 10.16.

Figure 10.15 and Figure 10.16 indicate that unlike in the perpendicular case where the majority of particles achieved a maximum vertical distance of significantly less than the maximum possible distance, in this case, the majority of particles reach distances that are close to the maximum reachable distance. This feature may make it more difficult to shield a detector from particles originating from geometries like this, as it means a magnetic field will need to be sufficiently strong as to lower the maximum possible vertical distance as much as possible. This is in contrast to the perpendicular case where it may be possible to rely on the statistics of particle generation to ensure that few particles reach the maximum possible vertical distance in a weaker magnetic field.

10.2.2.3 The probability density function for the second parallel case

For the second parallel case, the probability distribution function of $z_{\parallel,2,min}$ is found to be

$$PDF_{z_{\parallel,2,min}} = \frac{|\omega_g|}{\pi v}\sqrt{4 - \frac{\omega_g^2 z_{\parallel,2,min}^2}{v^2}} \tag{10.19}$$

Where the limits are $-\frac{2v}{\omega_g} \leq z_{\parallel,2,min} \leq 0$. The derivation of this function is given in Appendix F.3.

The same probability density plots as were produced for the perpendicular case in Section 10.2.2.1 and Section 10.2.2.2 can also be produced for this parallel case using both Equation 10.19 and Monte Carlo modelling of Equation 10.17, the results of which are shown in Figure 10.17 and Figure 10.18.

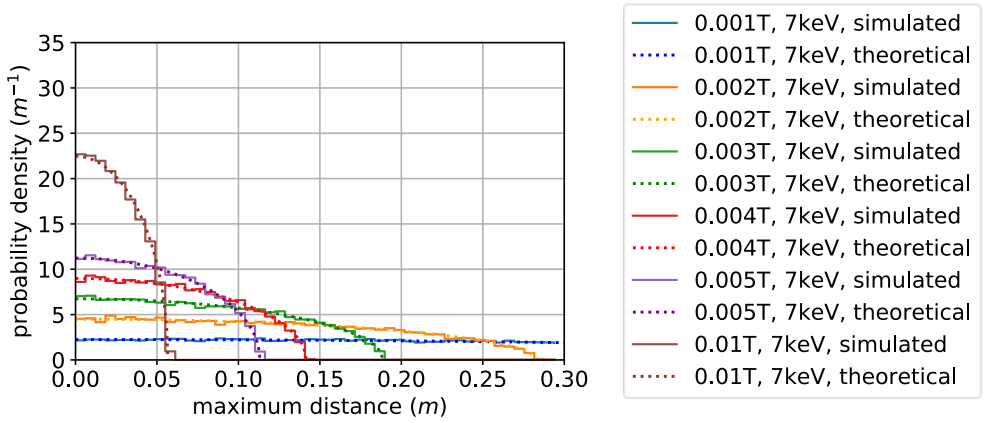

Figure 10.17 Monte Carlo simulations giving the probability density function, $PDF_{z_{\parallel,2,min}}$, of the magnitude of the maximum distance $z_{\parallel,2,min}$ for the second parallel surface-magnetic field case for varying magnetic field strength. The theoretical curves were calculated using Equation 10.19.

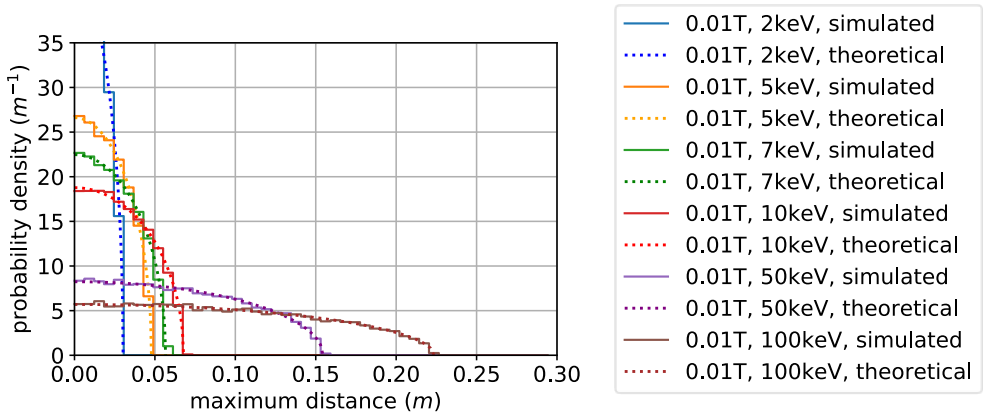

Figure 10.18 Monte Carlo simulations giving the probability density function, $PDF_{z_{\parallel,2,min}}$, of the magnitude of the maximum distance $z_{\parallel,2,min}$ for the second parallel surface-magnetic field case for varying electron kinetic energy. The theoretical curves were calculated using Equation 10.19.

Figure 10.17 and Figure 10.18 both show good agreement between the simulated and theoretical probabilities and again show that the probability of a particle reaching a distance decreases with distance.

10.2.2.4 The mean and median for each case

In addition to plotting the full probability density function for different magnetic field strengths and particle kinetic energies, it is also instructive to examine the variation in the median distance. While the mean for the perpendicular case in Equation 10.18, and the second parallel case in Equation 10.19 can be calculated to be

$$\overline{z_{\perp,1,min}} = \int_{z_{\perp,1,min}=-\frac{2v}{\omega_g}}^{z_{\perp,1,min}=0} z_{\perp,1,min} \times PDF_{z_{\perp,1,min}} dz_{\perp,1,min} = \frac{2}{3}\frac{v}{\omega_g} \approx 0.667\, r_g \tag{10.20}$$

$$\overline{z_{\parallel,2,min}} = \int_{z_{\parallel,2,min}=-\frac{2v}{\omega_g}}^{z_{\parallel,2,min}=0} z_{\parallel,2,min} \times PDF_{z_{\parallel,2,min}} dz_{\parallel,2,min} = \frac{8}{3\pi}\frac{v}{\omega_g} \approx 0.849\, r_g \tag{10.21}$$

respectively, where r_g is the particle gyroradius, it was not possible to analytically calculate the median for either case. The median could, however, be calculated using Monte Carlo methods.

The median allows for a more accurate indicator than the mean of how effectively a magnetic field is removing the background, as in this case, it indicates the distance which only 50% of particles will reach and indicates how strong a magnetic field needs to be to prevent particles originating at a given height from reaching the detector. The median maximum vertical distance, or alternatively the median values of $|z|$, for the perpendicular and second parallel geometries as a function of magnetic field strength are displayed in Figure 10.19 and Figure 10.20, respectively, for several electron energies.

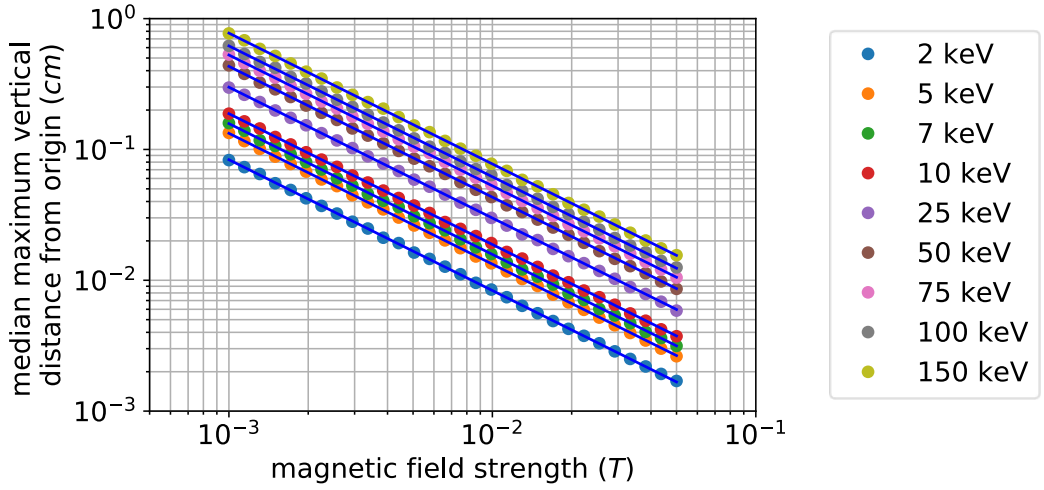

Figure 10.19 The median of the maximum vertical distances reached by particles in the perpendicular field to generation surface case. The straight lines on the plot represent fits of the function $d = \frac{A}{B}$, where B is the magnetic field strength, which fit the data well.

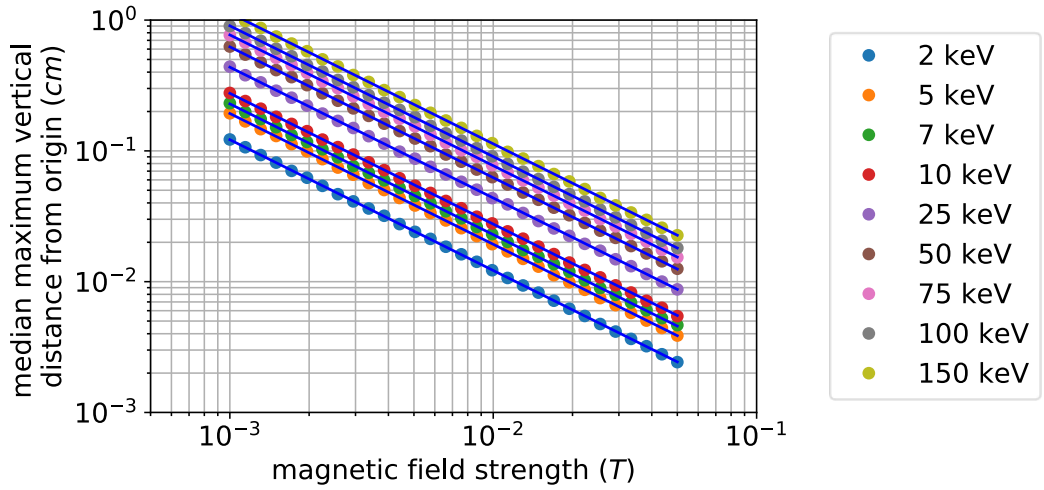

Figure 10.20 The median maximum vertical distance reached by particles in the second parallel field to generation surface case. The straight lines on the plot again represent fits of the function $d = \frac{A}{B}$, where B is the magnetic field strength, which fit the data well.

Each curve in Figure 10.19 and Figure 10.20 could be fitted with a high degree of accuracy to the function $d = \frac{A}{B}$, where d is the median maximum distance, and A is a fitted constant, which is invariant with respect to magnetic field strength B. It was also found that A fits a power-law distribution as a function of energy for both geometries, as shown in Figure 10.21 and Figure 10.22 for the perpendicular case and second parallel case, respectively.

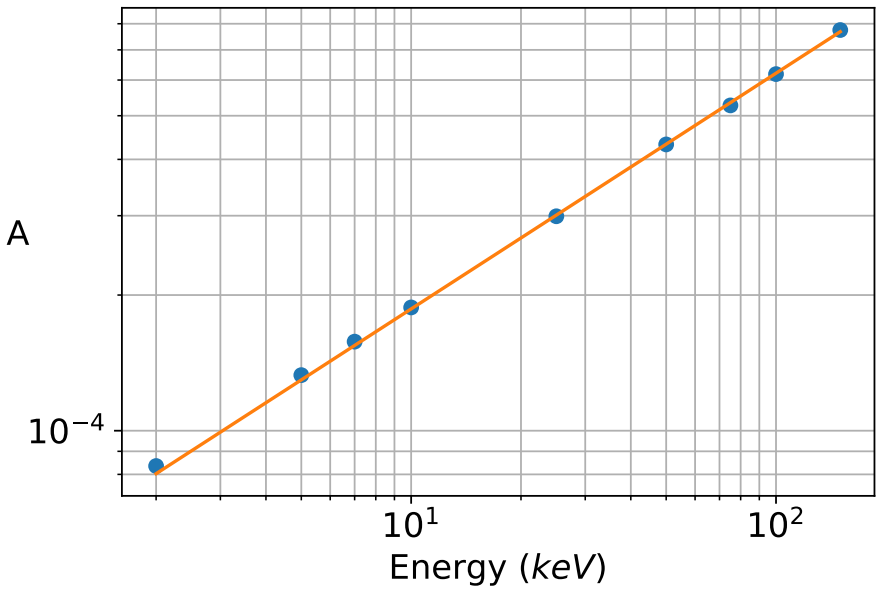

Figure 10.21 The fitted variable A in $d = \frac{A}{B}$ which was obtained from the curves in Figure 10.19, plotted as a function of incoming particle energy. The resulting distribution fits a power law.

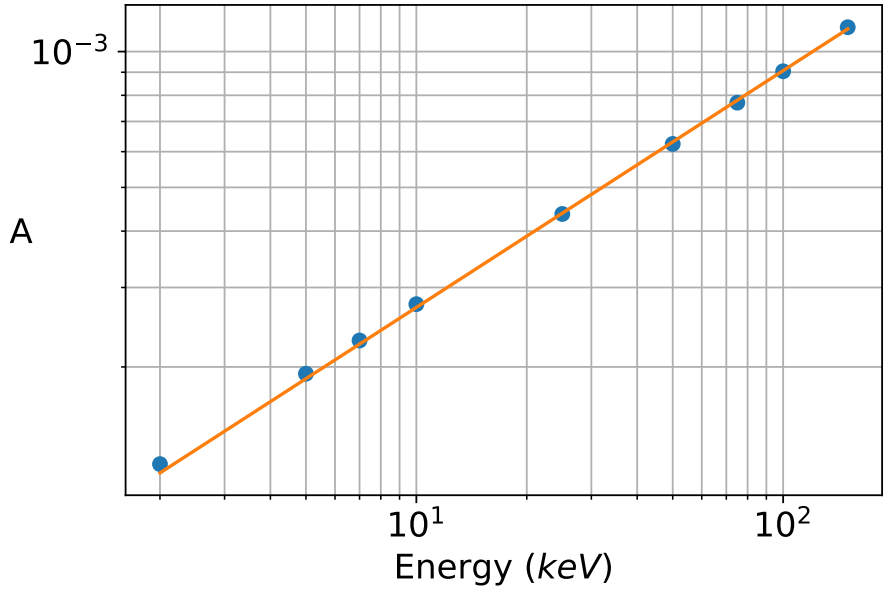

Figure 10.22 The power-law fit to A in the perpendicular magnetic field surface case obtained from the curves in Figure 10.20.

The distributions in Figure 10.21 and Figure 10.22 were fitted to $A = \alpha E^{\lambda}$ where the resulting fit parameters are given in Table 10.1.

Geometry	**Fit to $d = \frac{\alpha E^{\lambda}}{B}$**
Perpendicular case	$\alpha = (8.1 \pm 0.2) \times 10^{-5}$ $\lambda = -0.525 \pm 0.005$
Parallel case 2	$\alpha = (5.6 \pm 0.1) \times 10^{-5}$ $\lambda = -0.524 \pm 0.004$

Table 10.1 The fitting parameters for the median as a function of particle energy and magnetic field strength for each geometry. E is the particle kinetic energy in units of keV, B is in units of Tesla, while d is the median vertical distance from the origin location in units of meters.

The resulting function for the median maximum vertical distance a particle can travel from its origin surface in both the perpendicular and the second parallel case can be described by

$$d = \frac{\alpha E^{\lambda}}{B} \tag{10.22}$$

This equation provides a possible quick method of assessing the effectiveness of a uniform magnetic shielding mechanism with a magnetic field strength B at preventing electrons of a particular energy E from impacting a detector a given distance away.

10.2.3 Simulations of a Helmholtz coil for active magnetic shielding of X-ray-like background from knock-on electrons

While the above calculations are useful for making approximate calculations about the effectiveness of a magnetic field at shielding a detector from a particular electron energy, full Geant4 simulations are needed to fully quantitatively assess how effectively magnetic fields can reduce X-ray-like background. Real magnetic fields are also often significantly more complex than uniform magnetic fields, and only possible to simulate rather than analyse analytically.

To determine the exact effectiveness of an active magnetic shielding configuration, simulations were run using Geant4 with a Helmholtz coil configuration similar to those performed earlier for the experiments described in Chapters 6 and 7. The geometry used in the active magnetic shielding simulations is displayed in Figure 10.23.

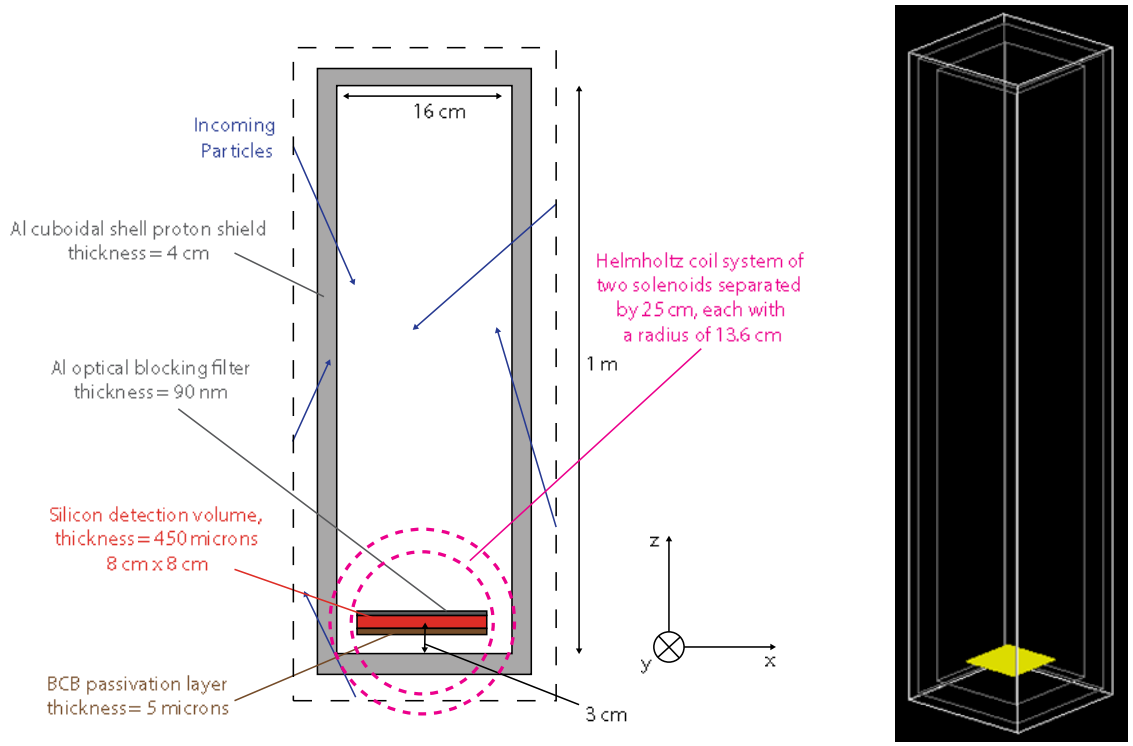

Figure 10.23 The geometry used for simulations in this section. A cuboidal geometry was used with a 4 cm Al proton shield thickness, as a structure that might approximate the geometry surrounding a detector more accurately than a spherical shell model.

The proton shield structure used in these simulations was cuboidal, in contrast to most of the simulations described in Chapters 8 and 9, where spherical shell proton shields were used. The reason why a spherical shell proton shield structure was not used in these simulations is that the effectiveness of magnetic shielding would be expected to be heavily dependent on the origin location of knock-on electrons. A cuboidal proton shield structure was therefore chosen to approximate better the actual structure that might surround a detector at the cost of simulation speed due to the increased volume of

the simulation. As knock-on electrons are primarily produced by cosmic protons, the simulations were only run using the GCR proton input spectrum.

10.2.3.1 Simulation results

The trajectories of particles produced by a Helmholtz magnetic field structure and a uniform magnetic field are significantly different, as a Helmholtz magnetic field structure decreases in strength with increasing distance from the solenoids. The Geant4 trajectories of 5 keV electrons generated from a Lambertian surface in a Helmholtz magnetic field structure are displayed in Figure 10.24. Here the same magnetic field was utilised as in the STERIS beamline and PSI PIF beamline simulations in Chapters 5 and 6, with a simulated current of 2 A passing through the ‘wires’, albeit with a radius of 13.6 cm as opposed to 6.8 cm in the experiments. The Helmholtz coils were placed such that they were separated by 25 cm on each side of the detector. It should be noted that the magnetic field strength could be increased significantly around the detector in this case if the coils were moved closer together inside the proton shield here.

It can be seen in Figure 10.24 that a region with a significantly lower density of electrons is generated around the detector, indicating that a Helmholtz coil magnetic field is indeed effective at shielding the detector from particles.

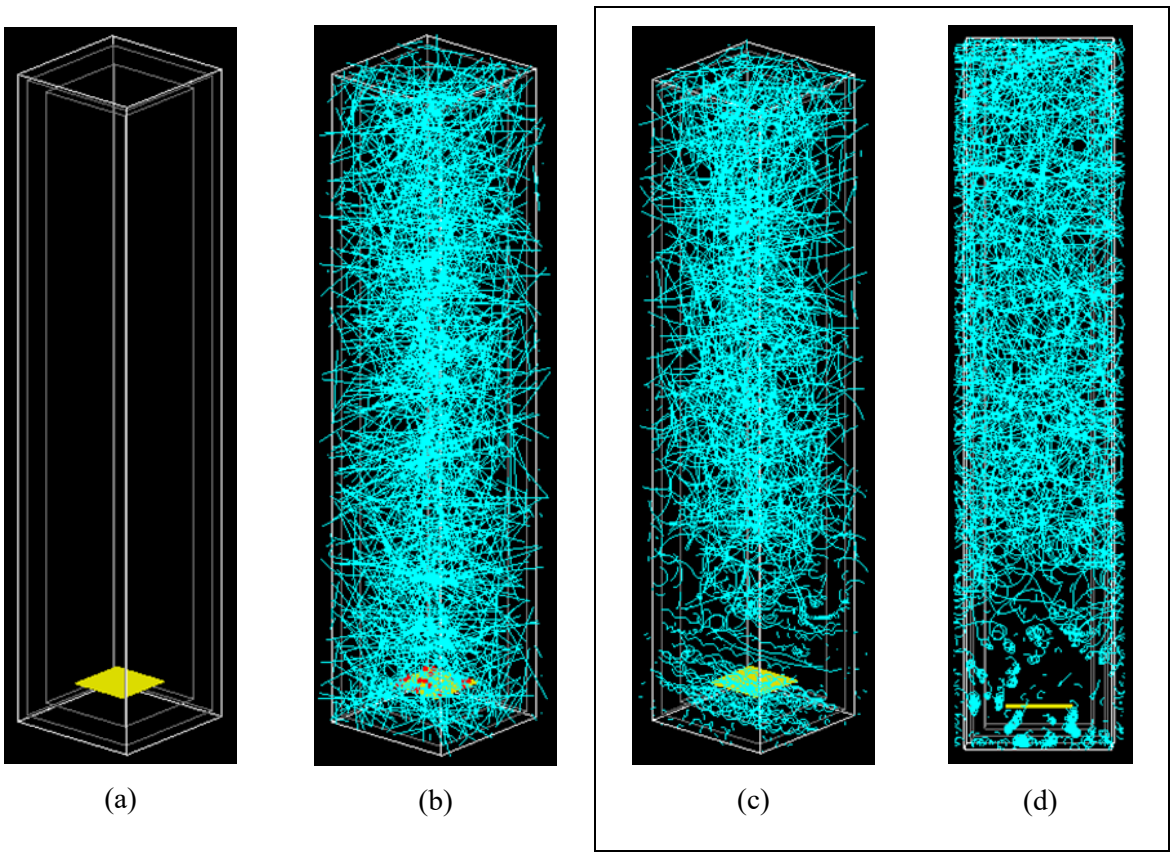

Figure 10.24 The trajectories of electrons with 5 keV in kinetic energy travelling through the geometry and magnetic field used in the simulations in this section, when distributed by Lambert's cosine law on the surface of the cuboidal world volume. Figure 10.24(a) shows the empty geometry, Figure 10.24(b) shows the trajectories when the magnetic field is not present, and Figure 10.24(c) and Figure 10.24(d) show the trajectories when the Helmholtz coil magnetic field is turned on from two different viewpoints. The location of the detector is shown as a yellow square. It can be seen in Figure 10.24(c) and Figure 10.24(d) that close to the detector, where the Helmholtz coil central position is located, electrons are significantly confined such that they follow helical motions around magnetic field lines.

For these images, the proton shield structure was set to vacuum such that the electrons would pass through unimpeded, whereas in the full simulations the proton shield was set to be solid aluminium.

In the STERIS beamline and PSI PIF experiments, the maximum current through the solenoids used was 2 A; however, this was only used as the maximum to prevent the epoxy insulation surrounding coil wires from becoming damaged due to high temperatures created by Ohmic heating. For solenoids to be used on a spacecraft, it would not be expensive to use wires that could withstand significantly higher temperatures and currents than the coils used in the experiments described in this thesis, as the coils that were used here were inexpensive coils that were initially designed for educational purposes.

Cooling mechanisms could also be implemented to keep the wires from overheating, which would also have the effect of lowering the resistance in the wires, reducing the amount of power that would be required to keep the coils operating at a particular current. Cooling mechanisms are commonly implemented for many applications in spacecraft, and the ATHENA XIFU will even include a Detector Cooling System (DCS). The DCS is sufficiently effective at cooling that it is capable of reducing temperatures to several tens of milliKelvin (Prouvé et al. 2018).

The power requirements for a Helmholtz coil of the design described in this section are given in Table 10.2 for room temperature, where the wire area was set to be approximately 0.0024 mm^2, as was the case for the Teltron solenoids used in Chapters 6 and 7. In addition to the power requirements for copper wire solenoids, the power requirements for aluminium wire solenoids are also given. The lower atomic number makes aluminium potentially viable as an alternative to copper with fewer fluorescence lines and lower mass, at the expense of having higher resistivity.

Current (A)	Power requirement at room temperature for copper wire solenoids	Power requirement at room temperature for aluminium wire solenoids	Magnetic field strength at central point of coils
2	0.192 kW	0.294 kW	4.7 mT
4	0.768 kW	1.175 kW	9.4 mT
6	1.728 kW	2.643 kW	14.2 mT
8	3.072 kW	4.698 kW	18.9 mT
10	4.800 kW	7.341 kW	23.6 mT

Table 10.2 The power requirements for the Helmholtz coil magnetic field configuration of the Helmholtz coil configuration used in these simulations, consisting of a total of 1280 turns of wire with a radius of 13.6 cm, at room temperature. The power requirement can however be significantly reduced using cooling mechanisms, and the room temperature values for power consumption here are only given as examples for comparison.

While the power requirements given in Table 10.2 are relatively large, it is foreseen that through cooling mechanisms, and through optimisation by increasing the solenoid wire area or decreasing solenoid radius, the power requirements given here could be significantly reduced. The required current could also be reduced through a reduction in separation between solenoids, which would significantly increase the central magnetic field strength for a given current. This design could also be replicated using permanent magnets, which would remove the power requirements for the system entirely.

The results for the full simulations using GCR protons as the input spectrum are displayed in Figure 10.25, where the mean count rate between 2 keV and 7 keV is plotted as a function of the current through the coils. The current was taken as the same current that would pass through the solenoids used in the experiments described in Chapters 5 and 6, albeit with a doubled solenoid radius. The mean count rate appears to significantly reduce as the current is increased, indicating that the configuration is effective as a magnetic shield.

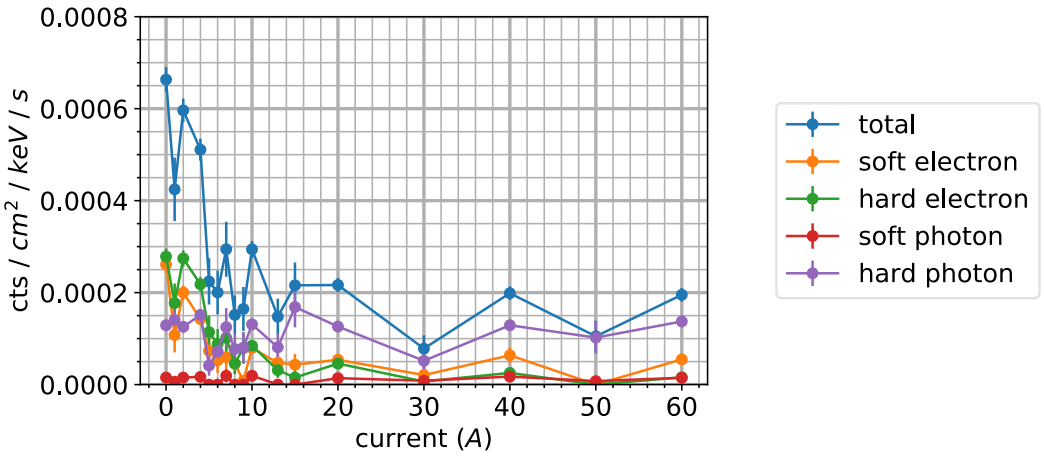

Figure 10.25 The mean count rate between 2 keV and 7 keV for different currents corresponding to the Helmholtz coil magnetic field current. The count rate appears to decrease significantly with increasing current above 4 A. Different simulation runs were performed with a different quantity of incoming particles, which is why some runs have significantly better statistics than others in this plot.

The reduction in count rate appears to be significant for both soft electrons and hard electrons, even though the median kinetic energy for background-inducing hard electrons is significantly higher than the median kinetic energy for soft electrons, as was shown in Chapter 8.

This may be explained from a qualitative perspective by the analysis described in Section 10.2.2 which showed that in the magnetic field perpendicular to generation surface case (which is the most similar case to the geometry given here), the median distance a particle will travel from its generation surface in a magnetic field is small relative to the maximum possible distance it can possibly travel.

An alternate explanation may also be that the angle at which backscattering electrons are most likely to deposit within the detector energy range is such that a relatively weak magnetic field is capable of preventing electrons from generating an X-ray-like event. This explanation might be evidenced by some of the experimental and simulation results given in Chapter 7.

In Chapter 7 it was found that a wide region of produced spectra were composed of high energy, fully-penetrating electrons. This region of the spectrum did not vary significantly with changes in magnetic field strength during the 200 MeV experiment or in the simulations for that experiment, and was primarily composed of particles that were in the region of ~100 keV in kinetic energy, which is similar to common energies of backscattering electrons that were determined in Chapter 8. This indicates that in that experiment the Helmholtz coil magnetic field was not strong enough to divert fully-penetrating particles away from the detector.

However the results given in Figure 10.25 indicate that in a simulation much more similar to the actual space-based environment, the Helmholtz coils are very effective at removing X-ray-like background due to backscattering electrons. This indicates that the removal of background here may

be in some way related to the specifics of the backscattering angular cross-section, and angle of incidence for backscattering electrons impacting the detector.

In addition to investigating the mean count rate across 2 keV – 7 keV as a function of current, it is instructive to determine how the spectrum changes with Helmholtz coil current. The spectrum for several currents is plotted in Figure 10.26 below, where it appears that the presence of the magnetic field appears to flatly reduce the continuum spectrum without significantly altering the shape of the spectrum.

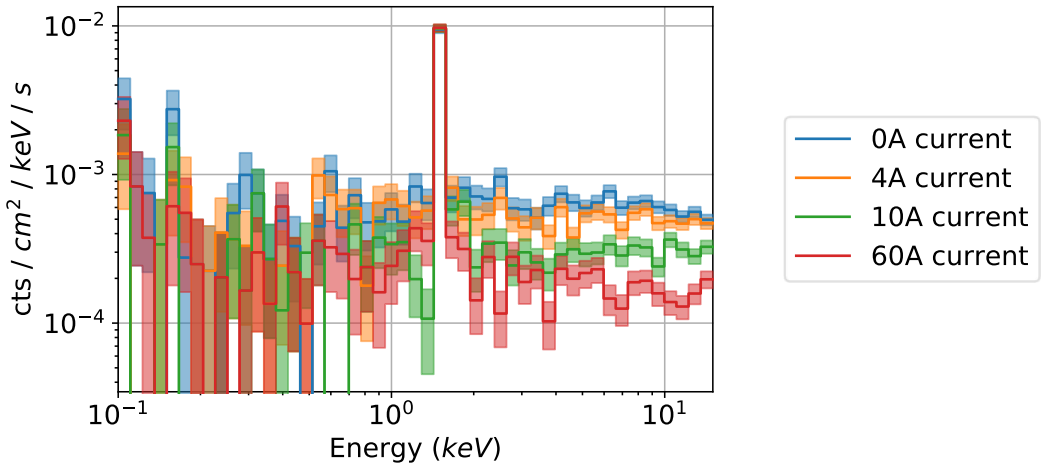

Figure 10.26 The energy deposition spectra for several different currents corresponding to different magnetic fields.

The spatial distribution of X-ray-like events across the detector for the 0 A and 10 A cases are also displayed in Figure 10.27, where the distribution appears to be approximately spatially uniform. This means that the introduction of a Helmholtz magnetic field would not appear to introduce systematic errors associated with background sampling across images.

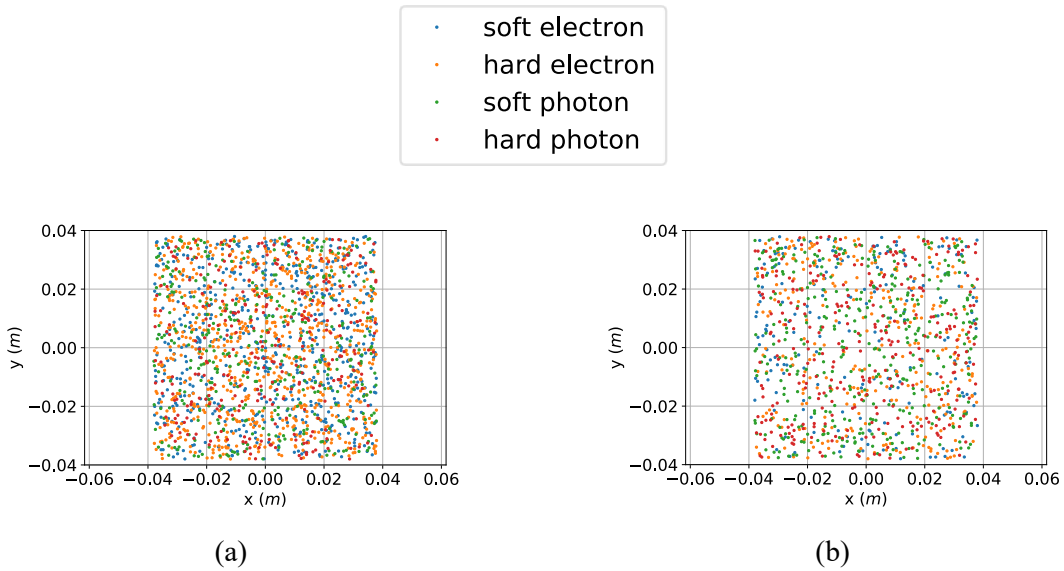

Figure 10.27 The spatial distribution of X-Ray-like events on the detector for both the no magnetic field case, Figure 10.27(a), and the 10 A Helmholtz current case, Figure 10.27(b). In each case, the spatial distribution is uniform.

It is also instructive to investigate the spatial distribution of particle vertex positions, particularly the distribution of X-ray-like background inducing origin locations along the baffle axis, which is displayed in Figure 10.28.

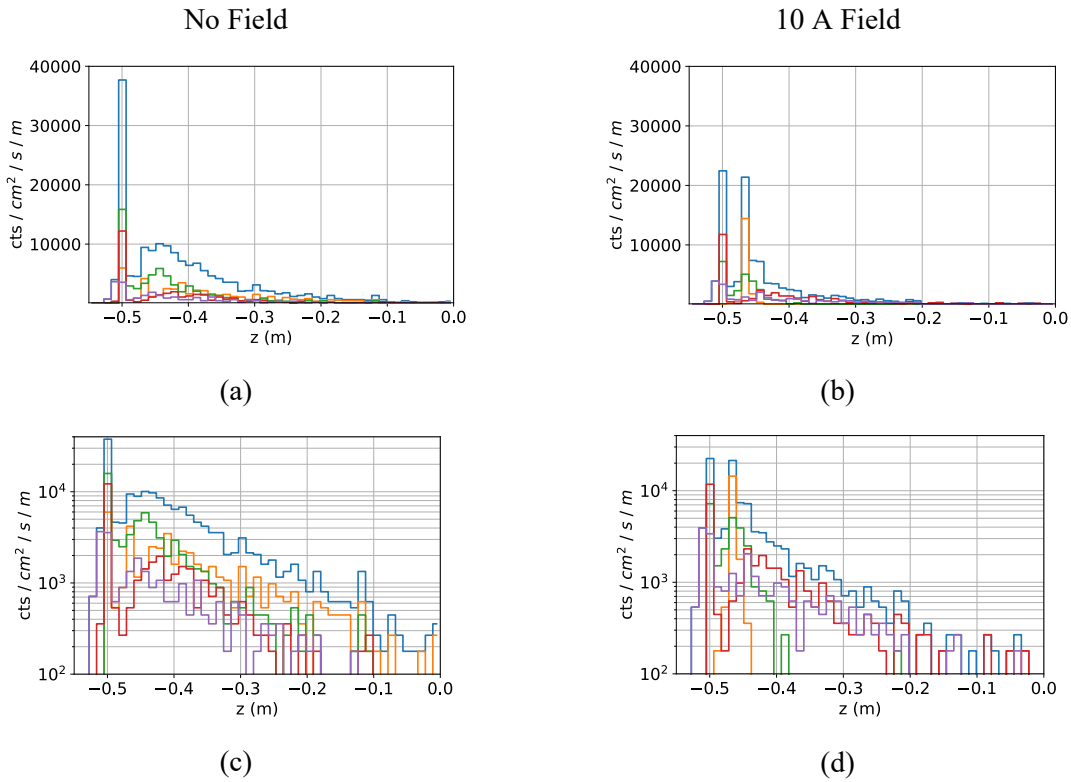

Figure 10.28 The distribution of X-ray-like background counts as a function of their vertex position along the baffle axis. Figure 10.28(c) and Figure 10.28(d) are identical to Figure 10.28(a) and Figure 10.28(b) respectively, except their axes have been scaled logarithmically.

Figure 10.28 indicates that as expected, the magnetic field decreases the number of electrons originating from more distant surfaces to the detector more effectively than from surfaces closer to the detector. In particular, it can be seen that a significant proportion of background counts in Figure 10.28(b) and Figure 10.28(d) originate from the surface behind the detector, which is only 3 cm away from the detector itself. Some of these are hard electron counts, meaning the effectiveness of the Helmholtz magnetic shielding may be further improved by suspending the detector a larger distance away from the back surface of the baffle, or by adding more material underneath the detector to block knock-on electrons.

It can also be seen that a significant number of soft electron background counts in Figure 10.28(b) and Figure 10.28(d) originate from the detector volume itself at -0.47 m, which are not present in the plots for no magnetic field. This implies that these counts are produced from the detector itself and are spiralling backwards in the magnetic field back into the detector. As these particles will likely hit the detector in locations near to the pixel from which they were produced by some high energy particle, it

is likely that self-anticoincidence methods (Burrows et al. 2019; Bulbul et al. 2020) could be used to remove these electrons from background images. This would increase the effectiveness of the magnetic shielding even further.

Overall the Helmholtz magnetic field design appears to be very effective at removing electron-induced X-ray-like background from images. The effectiveness of this magnetic shielding could be optimised from this simple design in several ways, including by for instance increasing the distance between the detector and surfaces within line of sight of the detector faces and increasing the thickness of on-chip layers. It is also possible that more complex magnetic fields may produce further increases in effectiveness. These might be achieved by the addition of more solenoids to the geometry.

It may also be possible to replicate the field of the solenoids here using permanent magnets, perhaps by using single large magnets for each solenoid that have a surface current such that they replicate the effect of a coil of wires. Alternatively, it may be possible to replicate a solenoid field using a ring of magnets for each solenoid similar to that used by magnetic diverters in current missions. While passive magnetic shielding like this would remove the power requirements of generating such a magnetic field, the magnets may need to be graded-Z shielded to ensure that fluorescence from high atomic number materials in the magnets does not influence the detector background.

Additionally, combining magnetic shielding with a graded-Z shielding configuration that is capable of attenuating hard photons produced by GCR protons and self-anticoincidence algorithms means that it may be possible to significantly reduce the GCR proton-induced background, as well as background induced by the CXB, GCR electron and GCR alpha-induced background. However, further research into hard photon generation and graded-Z shielding is necessary before this might be achieved.

10.3 Conclusions

The ability of graded-Z shielding and magnetic shielding methods to mitigate X-ray-like background induced by electrons and hard photons was investigated in this chapter.

Calculations were performed to determine the locations at which X-ray-like background inducing photons originated. An equation giving the intensity of background-inducing photons as a function of generation position was determined that can be used for calculations for optimal graded-Z shielding locations. This equation was verified against Geant4 simulations of a baffle-like proton shield structure around a detector.

Simulations were also performed for multiple graded-Z shield material configurations surrounding a detector in a spherical shell model configuration. It was found that none of the graded-Z shielding

configurations tested appeared to have a significant impact on the cosmic proton-induced hard photon Compton background, although they did reduce the CXB induced background significantly.

Calculations were also performed to analyse the effect of a uniform magnetic field on the electron-induced background. Probability density functions were found for two possible orientations of magnetic fields and generation surfaces. It was found that for both of these situations that the diffuse statistical distribution of electron momenta means that the magnetic field was significantly more effective at protecting a theoretical detector from electrons than would be suggested by looking at the maximum possible distance an electron can travel in a magnetic field due to its gyroradius alone. The calculations were backed up by Monte Carlo simulations which were also used to find a relationship between the median vertical distance in the direction of the detector reached by a particle from its origin location d, the magnetic field B and the particle kinetic energy E of the form $d = \frac{\alpha E^{\lambda}}{B}$.

Finally, Geant4 simulations were performed using a Helmholtz coil magnetic field with a cuboidal proton shield structure. The simulations found that the magnetic field was very effective at reducing the background induced by both low energy soft electrons and high energy hard electrons. This indicates that a Helmholtz coil magnetic field is likely to be an effective active magnetic shielding design for shielding a detector from all knock-on electrons, providing that the power requirements of the configuration can be kept sufficiently low, perhaps through cooling mechanisms.

Now that the effectiveness of the shielding methods investigated in this chapter has been established from a general perspective, it is worthwhile to investigate how these shielding methods function on a full simulated mass model of a spacecraft. The next chapter will therefore investigate X-ray-like background in the full ATHENA WFI mass model, and the effect of graded-Z shielding on this background.

Chapter 11

Modelling the Background of the ATHENA WFI

While spherical shell models are useful for assessing the general structure and physics that should be present in the environment around a space-based detector, the actual spacecraft structure surrounding a particular detector is significantly more complex than a spherical shell. To study some of the major differences between background in an actual mass model versus these simplified spherical shell models presented in this chapter, simulations were performed based on several GDML mass models that were produced during the design of the structures surrounding the ATHENA WFI.

The GDML models were developed by members of the ATHENA background working group to determine the X-ray-like background that would be experienced by the ATHENA WFI when surrounded by different material configurations. The simulations were initially run and analysed specifically to determine what background levels the ATHENA WFI would experience, but also act as a useful comparison between the expected background for a real detector and the spherical shell model simulations that have been performed for this thesis.

Figure 11.1 shows a visualisation of one of the geometries simulated in this chapter. Each of the geometries simulated in this chapter are of the general form shown in Figure 11.1, with minor variations made to some of the dimensions, materials and placement of shielding within the geometries.

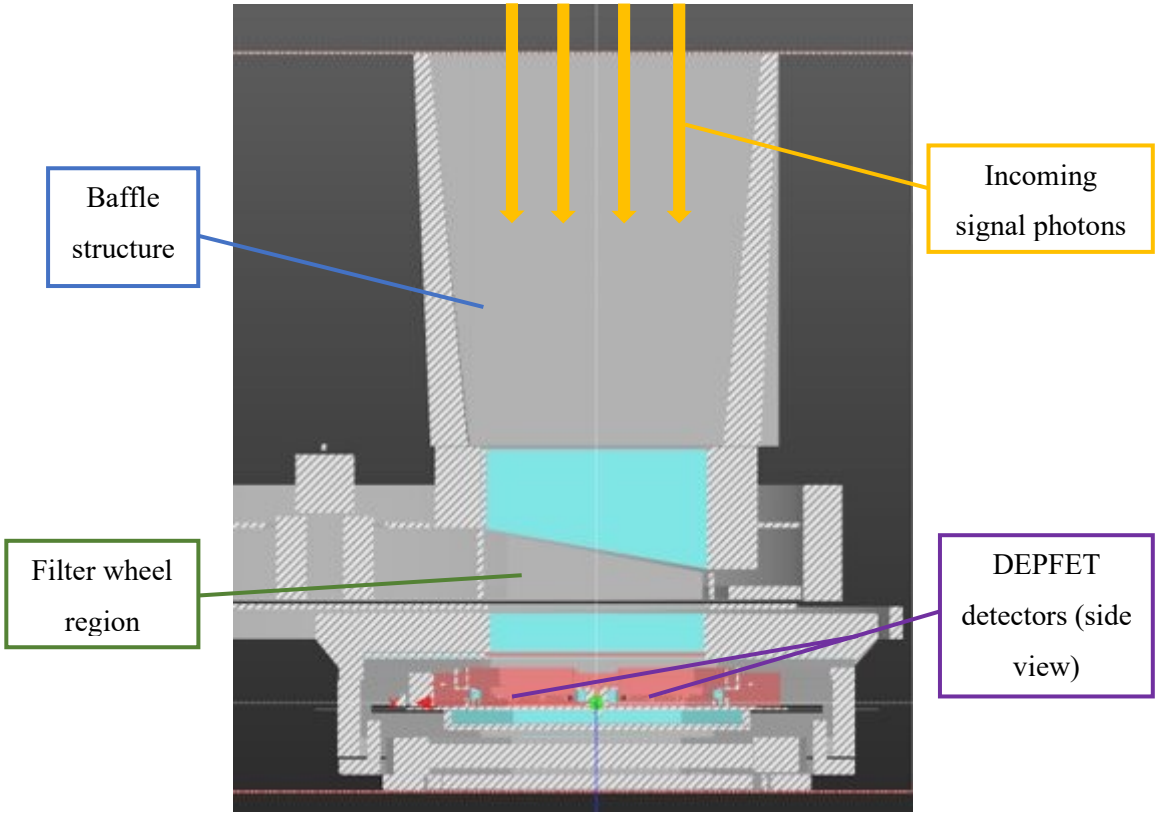

Figure 11.1 One of the geometries used for simulation of the ATHENA WFI in this chapter, image created by Oliver Hetherington. This model corresponds to index 3 in Table 11.1 later in this chapter. Light blue regions here represent placements of PEEK as a graded-Z shielding layer, and red regions represent molybdenum. All the variants described in this chapter only exhibit minor geometric and material variations on the model shown in this figure.

As can be seen from Figure 11.1, only the features directly surrounding the ATHENA WFI are simulated in this chapter. No external features such as the XIFU mass, magnetic diverter or anything outside of the science instruments module are simulated. As has been discussed earlier in Chapter 9, it is not believed that any of these structures will cause a significant increase in background, due to their distance from the ATHENA WFI. However, as usual it always remains a possibility that some unsimulated structure present in the real spacecraft could in principle cause a significant increase in background, and the results of these simulations should always be considered within this context.

11.1 The X-ray-like background spectrum and background spectral components

Figure 11.2 displays the background spectrum produced by simulations using incident cosmic protons as primary particles impacting version E00023277_00 of the ATHENA WFI mass model, while Figure 11.3 and Figure 11.4 show the GCR proton and CXB spectral components in further detail. Here the total background spectrum was constructed from the addition of the secondary photon and secondary electron components rather than all background-inducing components to remove some features that would not be present in the physical device spectrum. While this does mean components associated with particles such as neutrons are not accounted for here, other simulations performed by

the ATHENA WFI background working group indicate that these components do not significantly affect the background (von Kienlin et al. 2018).

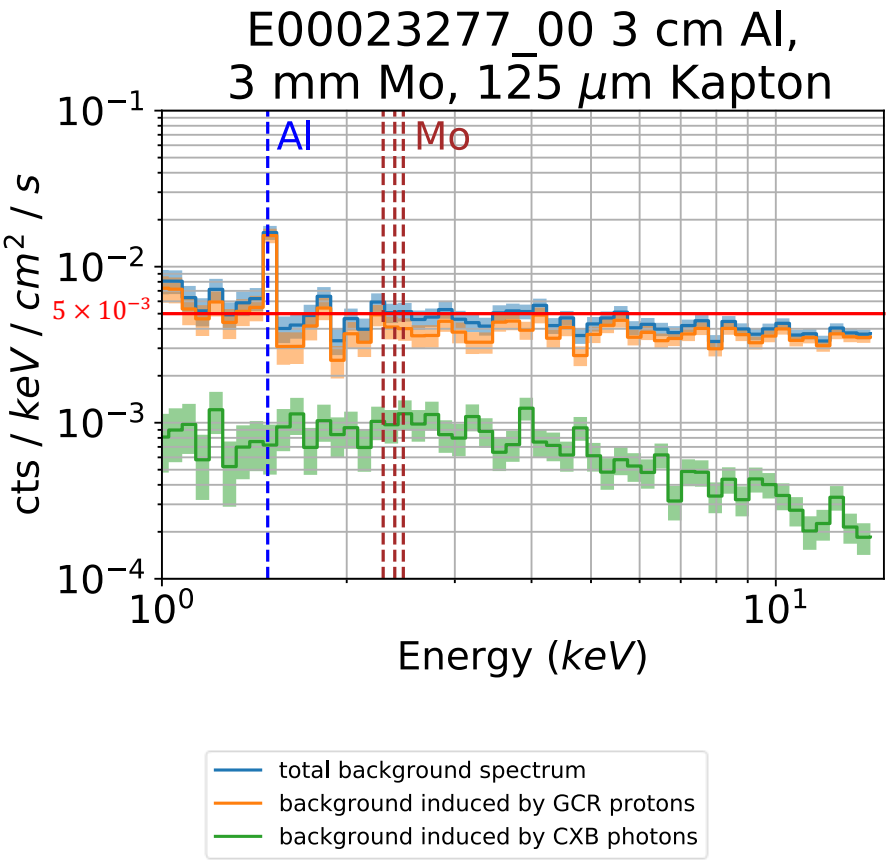

Figure 11.2 The spectrum produced by cosmic protons impacting the ATHENA WFI mass model. The spectrum appears to exhibit a similar structure and order of magnitude to simulations performed on the spherical shell model used above. The red dotted line represents the target count rate for X-ray-like background of the ATHENA WFI, of $5 \times 10^{-3} cts / cm^2 / keV / s$.

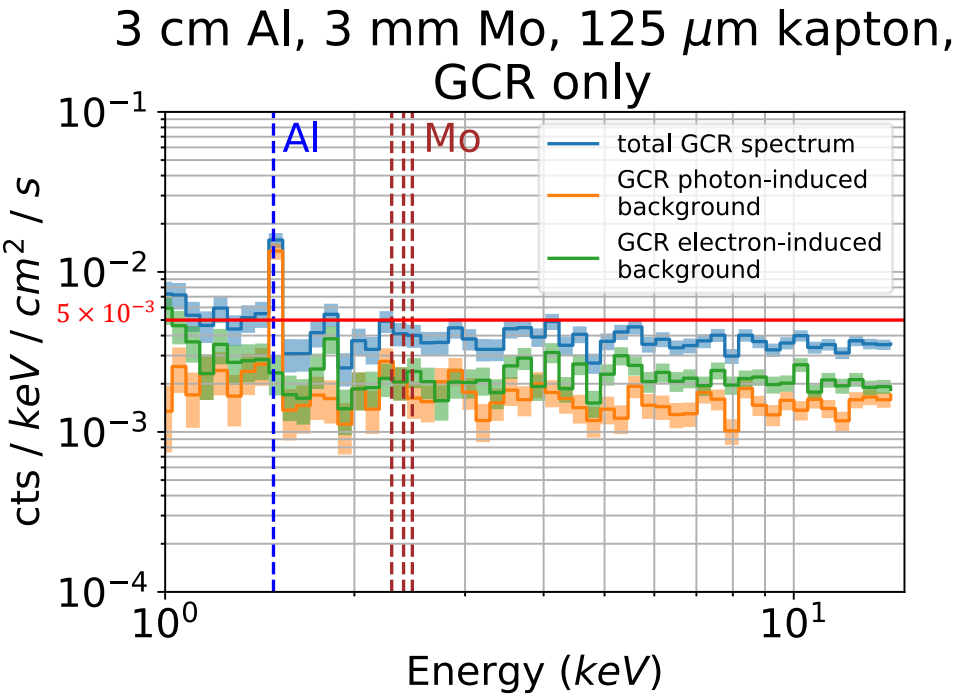

Figure 11.3 The spectrum produced by galactic cosmic ray protons impacting the ATHENA WFI mass model. The spectrum appears to be comprised almost equivalently of both secondary photon induced background, and secondary electron induced background. The red dotted line represents the target count rate for X-ray-like background of the ATHENA WFI, of $5 \times 10^{-3} cts / cm^2 / keV / s$.

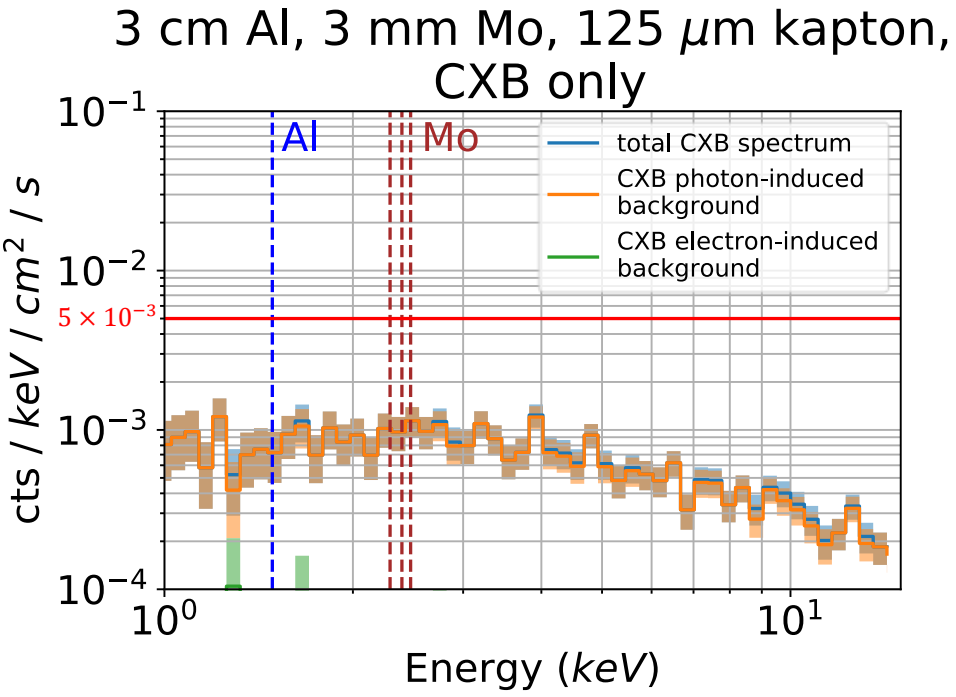

Figure 11.4 The spectrum produced by the cosmic X-ray background impacting the ATHENA WFI mass model. The spectrum appears to be dominated by background induced by photons. The red dotted line represents the target count rate for X-ray-like background of the ATHENA WFI, of $5 \times 10^{-3} cts / cm^2 / keV / s$.

Figure 11.2 indicates that the mean GCR proton-induced X-ray-like background across the spectrum is indeed similar to the mean background in the spherical shell model case (shown previously in Figure 8.6 and Figure 8.7 in Section 8.3.1), albeit with a significantly lower CXB induced background. This is likely caused by the presence of graded-Z shielding placed on surfaces surrounding the detector.

Figure 11.3 also shows that as was the case in the spherical shell model simulations, the GCR proton spectrum is also composed of almost equivalently of secondary electrons and secondary photons. The fact that the X-ray-like background from this model is similar to that from the spherical model simulations indicates that spherical shell models have the potential to produce similar results to more complex spacecraft design structures for GCR proton induced background.

To further examine the graded-Z shielding, and its effectiveness at reducing the CXB-induced background, it is instructive to plot the creation vertex locations of background-inducing particles.

11.2 CXB simulations

Figure 11.5 displays the creation vertex locations for particles that induce background for the CXB mass model simulation. It should be noted that Figure 11.5 is heavily zoomed out relative to the general geometry shown in Figure 11.1 to show the particle generation sphere, which is significantly larger than the ATHENA WFI geometry.

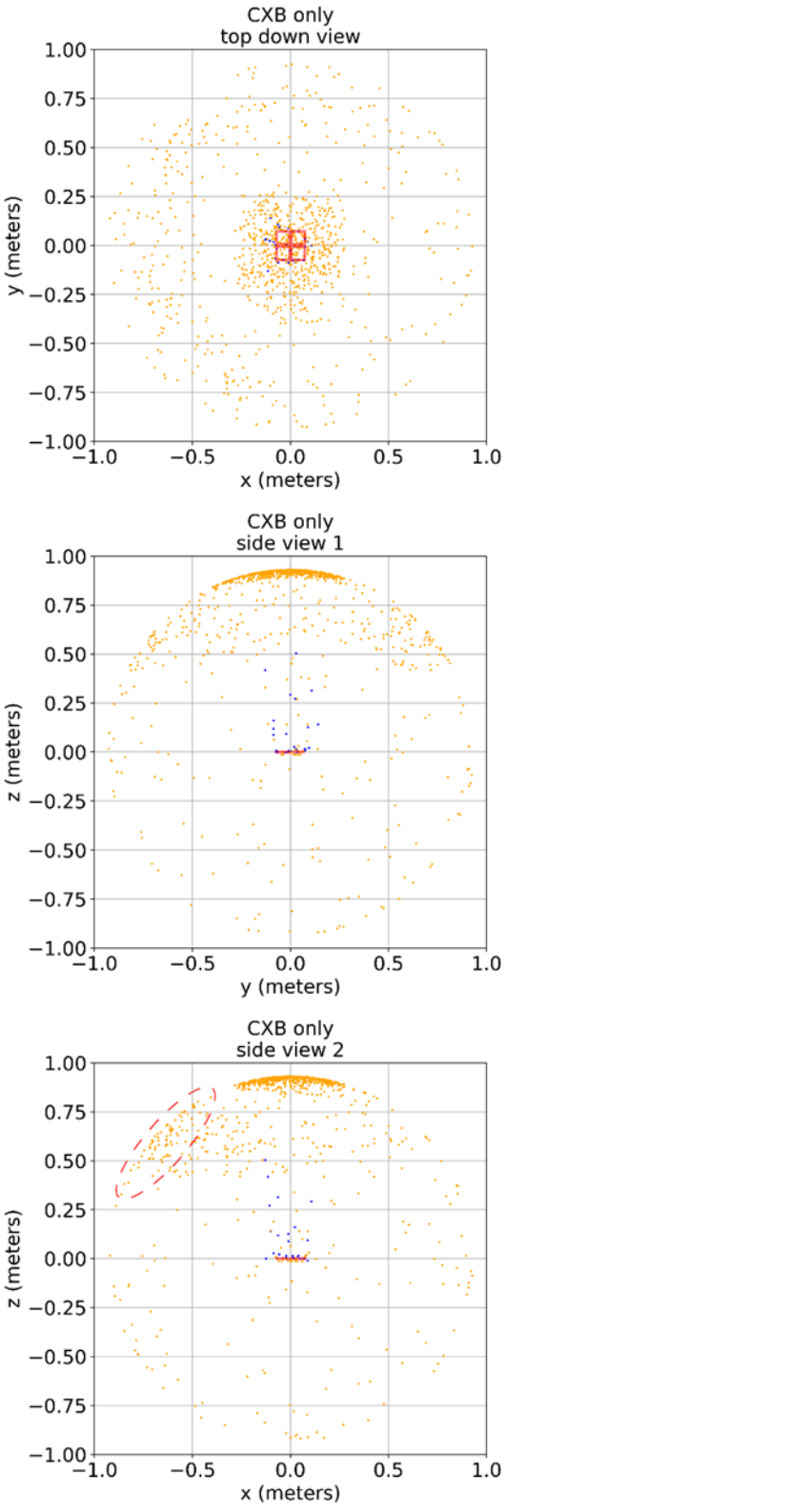

Figure 11.5 The creation vertex locations of particles that induce background in the CXB mass model simulations. Background inducing CXB photons primarily originate from areas within direct line-of-sight of the detector along the baffle, although there appear to be some regions to the left and right along the x and y-axis from the regions outside of direct line-of-sight that have a higher density of creation vertices than surrounding regions, which are labelled with the red dashed ellipse.

Figure 11.5 indicates that unlike in the spherical model case, the flux of background-inducing CXB photons is not isotropic and that the majority of background-inducing CXB photons appear to originate from directly within line-of-sight of the detector.

Additionally, there appears to be a large number of photons originating from a location anticlockwise to the dominant peak of CXB photons directly above the device. To show this peak in greater detail, Figure 11.6 displays the differential flux as a function of angle to the device surface normal, θ.

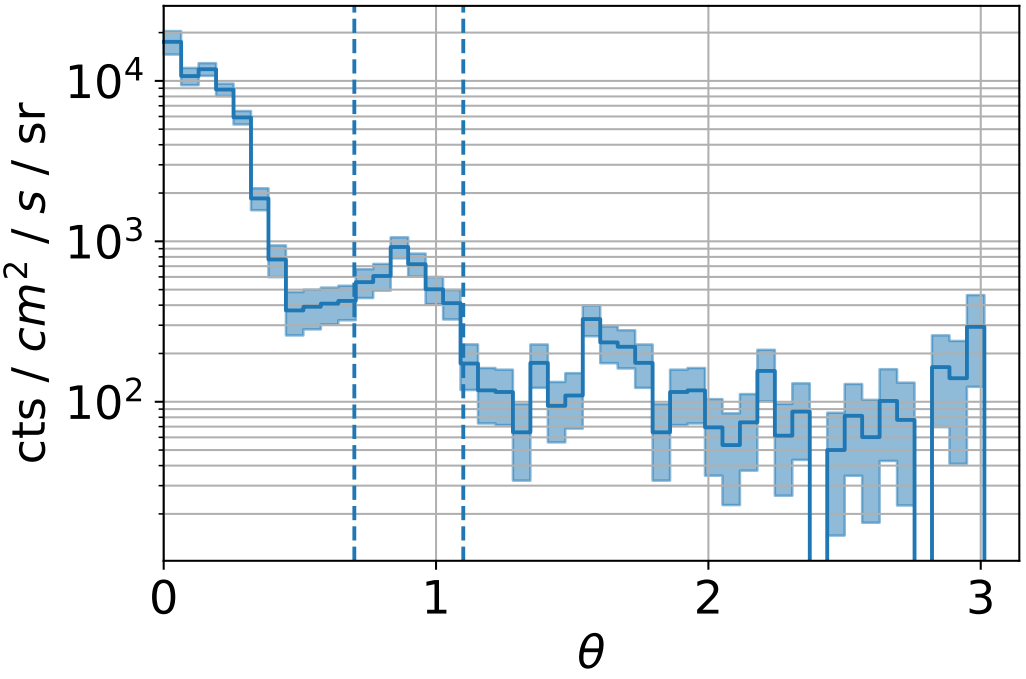

Figure 11.6 A normalised histogram of the differential flux with respect to solid angle of CXB photon vertex locations, where θ is the angle relative to the detector surface normal. There appear to be two main peaks, a peak at θ = 0 radians, and a peak between approximately θ = 0.7 radians and θ = 1.1 radians, where vertical dashed lines have been plotted as a guide.

The smaller peak in CXB photons can be seen from Figure 11.6 to be between approximately θ = 0.7 radians and θ = 1.1 radians. As shall be shown in Figure 11.8 later, this angular range corresponds to a solid angle encompassing a region of the spacecraft structure that has a thinner quantity of aluminium and is one of the only surfaces within line-of-sight of the detector containing no graded-Z shielding.

The existence of this smaller peak in conjunction with the graded-Z shielding simulations performed in Chapter 9 indicates that the graded-Z shielding used here is significantly attenuating the CXB.

11.3 GCR proton simulations

As well as viewing the origin location of background-inducing particles originating from the CXB, it is also instructive to view the origin location of background-inducing particles produced by cosmic protons. Figure 11.7 displays the particle creation vertex locations for particles that induce

background in the cosmic proton simulations, in a similar way to the particle creation vertex plots displayed in Figure 8.14, Figure 8.15 and Figure 8.16, but for two versions of the full mass model, which were variants of a model named E00023277_00.

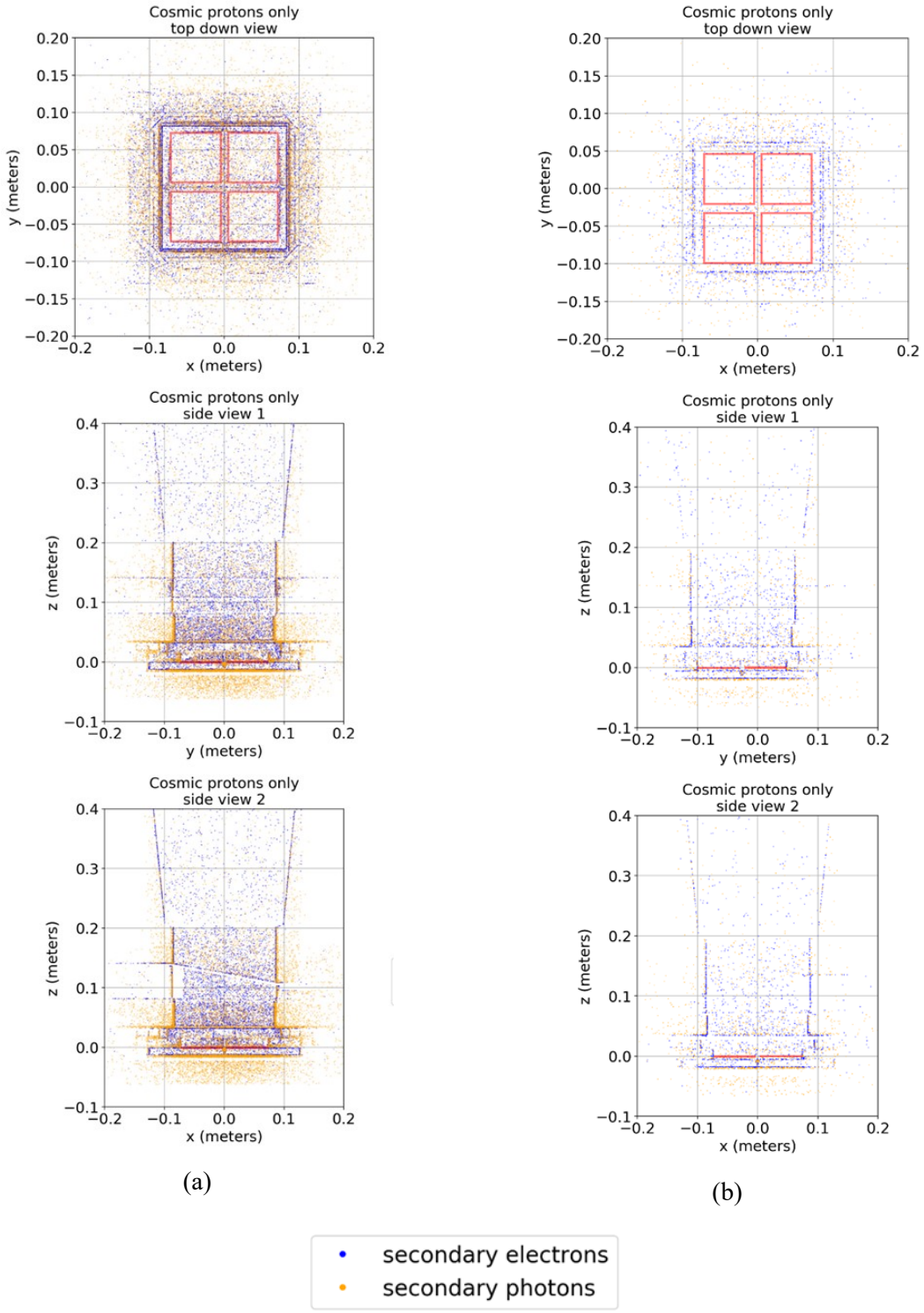

Figure 11.7 The particle creation positions for each background inducing event in two variants of the ATHENA WFI mass model simulations, for the cosmic proton input spectrum for GCR protons. Both sets of figures show simulations different variants of version E00023277_00. Figure 11.7(a) corresponds to 4 cm of Al, followed by 3 mm of Mo and then 1 mm of PEEK, while Figure 11.7(b) corresponds to the 3 cm of Al, followed by 3 mm of Mo and then 125 μm of kapton model used earlier. The spacecraft structure can be observed as well as the distribution of both background-inducing photons and background-inducing electrons. Electrons appear to be almost entirely generated from inner surfaces, and photons appear to be generated both from surfaces and from deeper into materials, as expected. While it may appear that Figure 11.7(b) has a lower flux of particles, it is actually because the Figure 11.7(b) simulation was run for significantly less than time than the simulation in Figure 11.7(a).

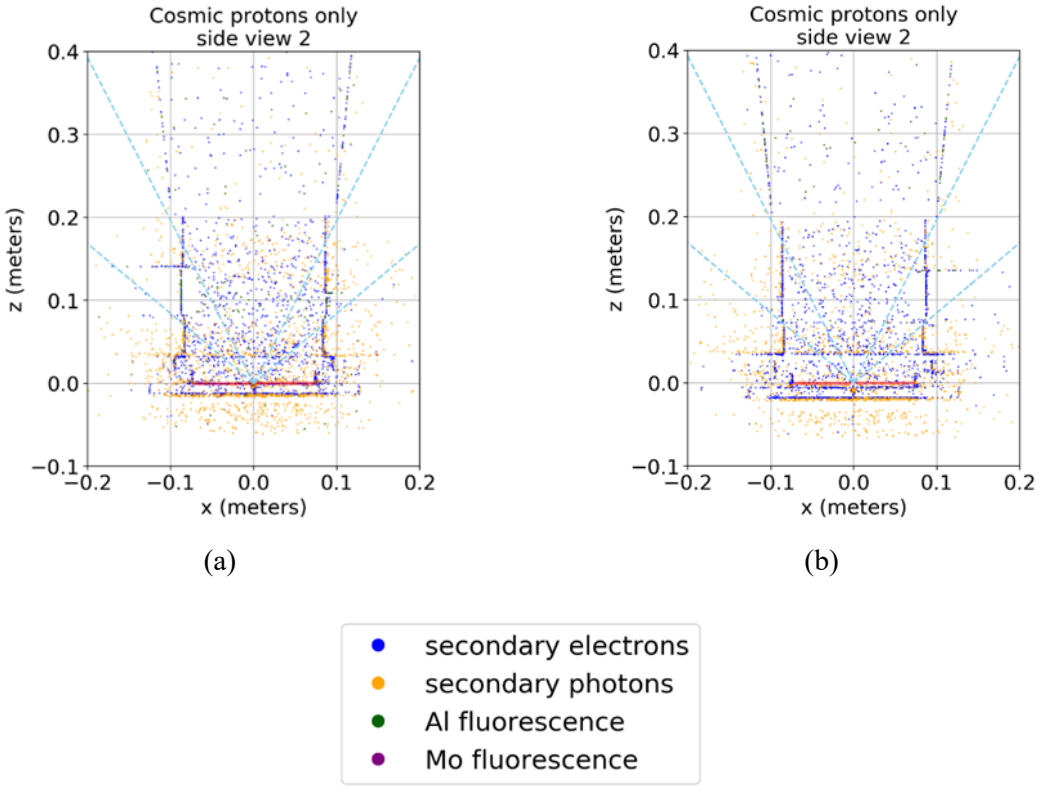

Figure 11.8 The plot of GCR components as displayed in Figure 11.7, but with lines representing angles to the normal of $\theta = 0.7$ radians and $\theta = 1.1$ radians. Both sets of figures show simulations different variants of version E00023277_00. Figure 11.8(a) corresponds to 4 cm of Al, followed by 3 mm of Mo and then 1 mm of PEEK, while Figure 11.8(b) corresponds to the same 3 cm of Al, followed by 3 mm of Mo and then 125 μm of kapton model used earlier. Figure 11.8(b) also contains graded-Z shielding around the regions where CXB photons were previously penetrating to hit the detector. The region where less material and no graded-Z shielding is present in the simulation in Figure 11.8(a) approximately corresponds with the same angles from which excess CXB photons are also originating, indicating that the reduced CXB induced background may be explained by the graded-Z shielding placed on materials surrounding the detector.

Figure 11.8 displays similar characteristics to that displayed previously in spherical shell model simulations throughout Section 8.3.3, where photons appear to originate from surfaces in both the bulk of the spacecraft structure and from inner surfaces.

One region of interest is the region between approximately $z = 0.75$ m and $z = 0.15$ m, where there are significantly fewer photons inducing background than from other regions of the mass model. In this region there is less bulk aluminium than at other regions in the model, meaning that beyond the relatively thin surface of aluminium there is only vacuum, from which high energy photons cannot be produced.

The effect of this region being covered by graded-Z shielding, which correspond to the filter wheel structure, can be seen in Figure 11.9, where the background spectrum corresponding to the mass model where the filter wheel is uncovered is compared to the newer mass model where the filter wheel region is covered by kapton. The fluorescence line count rate drops in this case by a factor of $53\% \pm 6\%$, indicating that leaving a given surface unshielded could lead to a large rise in the number of fluorescence photons received.

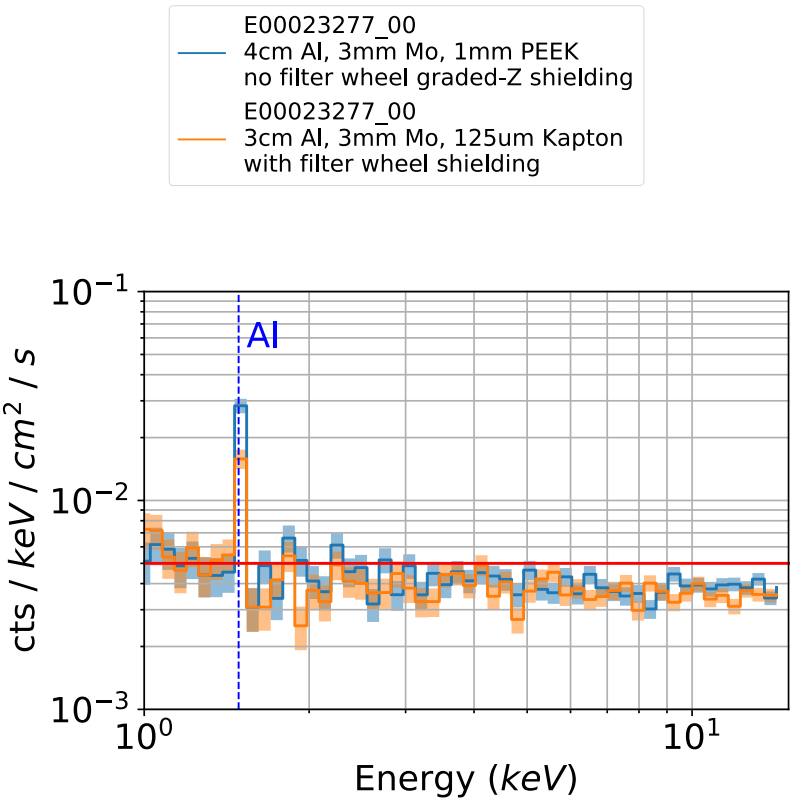

Figure 11.9 Comparing the spectrum produced by two different mass model configurations. The only difference between the two configurations that appears to exceed standard errors is a $53\% \pm 6\%$ *drop in fluorescence in the mass model configuration with kapton, which is likely due to the increased coverage of graded-Z shielding around the filter wheel structure. The solid red line represents the target count rate for X-ray-like background of the ATHENA WFI, of* $5 \times 10^{-3} cts / cm^2 / keV / s$.

11.4 Variations in the background with mass model design

Several different variants on the mass models displayed above were also run as part of the analysis to determine the effect of varying spacecraft structure on the mean X-ray-like background. The results of these simulations and analysis are displayed in Figure 11.10, displaying total count rates and the background spectra for each configuration.

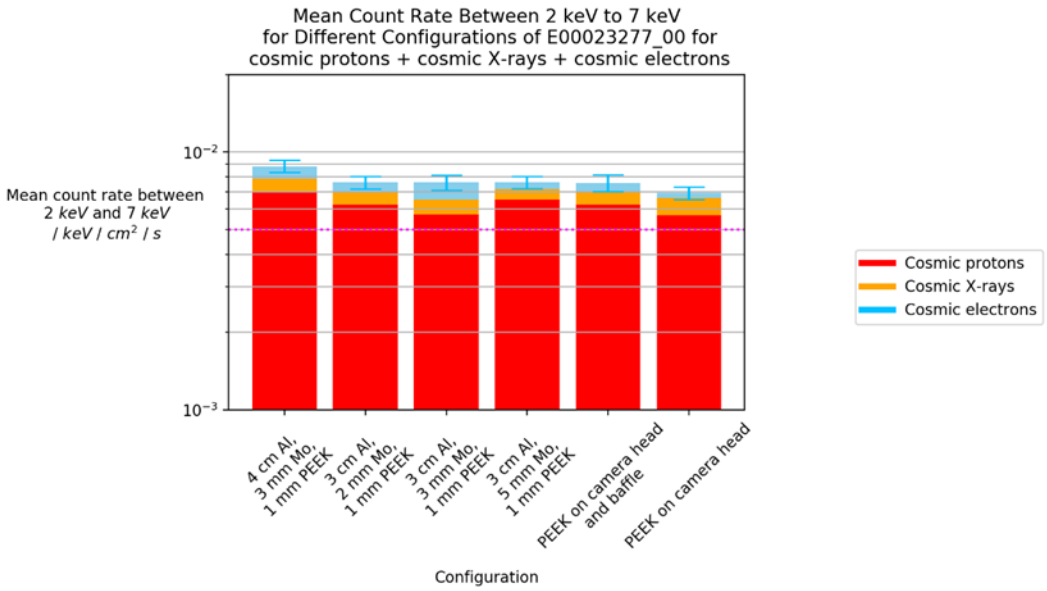

Figure 11.10 The mean count rate produced by different configurations of the ATHENA WFI mass model. There appears to be no significant differences between the mean count rates for different mass models that cannot be explained by the standard error. The effect of cosmic alpha particles was also simulated, but the statistics acquired were not sufficiently significant to be included in this plot.

Each configuration appears to exhibit only minor differences in spectra and mean count rate. There does appear to be a slight relative difference increase in count rate for the configuration with 4 cm of Al, but this increase is sufficiently small that it may be within standard error.

Figure 11.11 displays the X-ray-like background spectra for each of these configurations, which are indexed in Table 11.1.

Configuration	Index
4 cm Al, 3 mm Mo, 1 mm PEEK	1
3 cm Al, 2 mm Mo, 1 mm PEEK	2
3 cm Al, 3 mm Mo, 1 mm PEEK	3
3 cm Al, 5 mm Mo, 1 mm PEEK	4
3 cm Al, 3 mm Mo, 1 mm PEEK with additional PEEK on camera head and baffle	5
3 cm Al, 3 mm Mo, 1 mm PEEK with additional PEEK on camera head only	6

Table 11.1 The mass model configurations used in Figure 11.11.

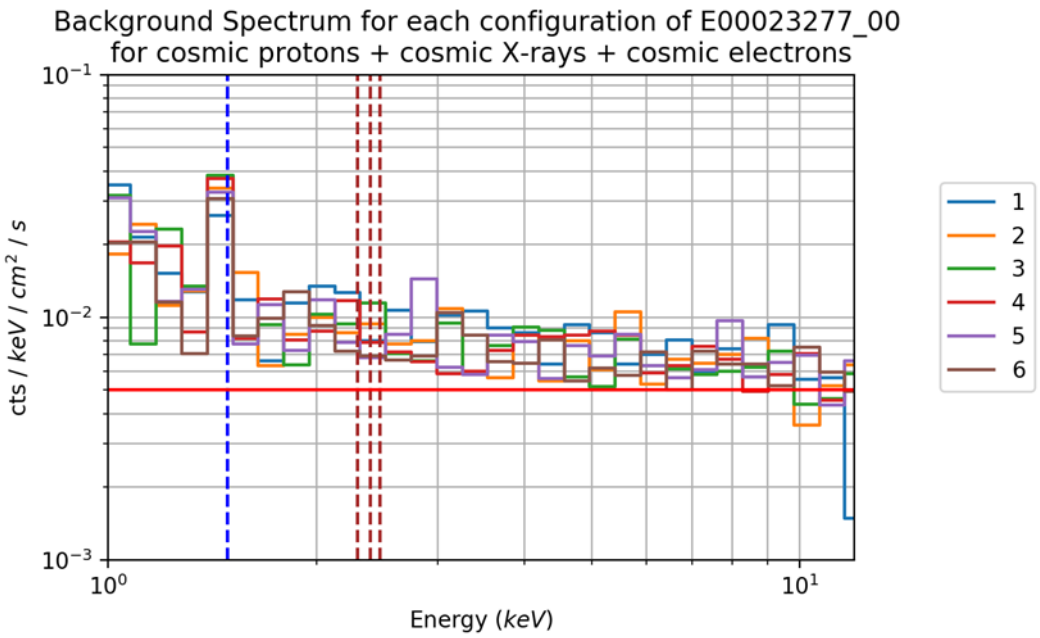

Figure 11.11 The X-ray-like background spectrum produced by each mass model configuration. The spectrum produced by each model in Table 11.1 appears to exhibit the same characteristics and do not seem to deviate significantly from each other. The solid red line represents the target count rate for X-ray-like background of the ATHENA WFI, of $5 \times 10^{-3} cts / cm^2 / keV / s$.

Figure 11.11 shows few variations in spectrum with mass model configuration that exceed statistical errors.

Figure 11.10 and Figure 11.11 indicate that the thickness of the graded-Z shielding layers has little impact on background count rates, although changes in proton shield thickness may increase the background count rate as indicated by the spherical shell model simulations in Chapter 9.

11.5 Conclusions

While the geometry of the real ATHENA WFI mass model differs significantly from the spherical shell model simulations presented earlier in this thesis, the overall background appears to have a very similar structure and mean count rate. Plots of the creation vertex of background-inducing particles also appeared very similar in background structure and location to creation vertex plots from spherical shell model simulations displayed in Chapter 8, indicating that background is being produced by the same overall mechanisms as in the spherical shell models. This means that spherical shell models do indeed seem to be reasonable geometries to use for the examination of the general physics of background generation and shielding.

Analysis of the origin location of background inducing particles also indicated that significant amounts of fluorescence and CXB photons can pass through gaps in graded-Z shielding. Covering an exposed region of shielding within the mass model caused a nearly 50% reduction in fluorescence line

intensity, indicating that in missions where graded-Z shielding is being used, care must be taken to ensure there are no uncovered regions in shielding where fluorescence might leak through.

Finally simulations performed on variants of the mass model using slightly different geometries. It was found that an increase in proton shield thickness from 3 cm to 4 cm caused an increase in background, as was also shown in spherical shell simulations in Chapter 9. However, it was found that there was no significant variation in GCR proton induced spectrum with changes in graded-Z shielding layer thickness. This was not unexpected, as simulations in Chapter 10 examining graded-Z shielding using spherical shell models also found this to be case, it does mean that more graded-Z materials may need to be tested or more creative strategies designed to shield detectors from hard photons produced in the proton shield bulk.

Chapter 12

Conclusions

Three research areas were explored in this thesis: the validation of the use of Geant4 for simulations of X-ray-like background in space, the particle composition of X-ray-like background within the space-based environment, and two shielding mechanisms for reducing X-ray-like background. This chapter summarises some of the key results that were found and some of the ways in which this research could and will be expanded upon in the future.

12.1 Summary of experimental Geant4 validation work for simulations of the space-based environment (Chapters 6 and 7)

Two major experiments were performed at the STERIS beamline in Harwell, Oxfordshire, and at the Proton Irradiation Facility (PIF) at the Paul Scherrer Institut (PSI), Switzerland, with incoming proton energies of 6 MeV and 200 MeV respectively. These experiments were designed to approximate the situation of a cosmic ray passing through spacecraft shielding and generating secondary particles that then cause X-ray-like background. The experimental results were compared with corresponding Geant4 simulations to determine how accurately Geant4 could replicate the experimental results. The following bullet points summarise key results from this work:

- The ability of Geant4 to simulate the generation and detection of high energy, fully-penetrating knock-on electrons was validated. As this validates many of Geant4's electromagnetic physics processes, this is also evidence that Geant4's simulation of fully-penetrating protons is accurate.
- The ability of Geant4 to simulate the generation and detection of fully absorbed and backscattering knock-on electrons originating from different materials was partially validated using magnetic fields.
- Geant4 was found to be accurate at simulating the generation and detection of fully absorbed and backscattering electrons depositing above 5 keV originating from aluminium, however, below 5 keV the number of electrons produced by approximately a factor of 2. This discrepancy may have been caused by unsimulated aspects of the CCD97 detector used.

- The knock-on electron spectrum was found to vary little with generation material in either experiment.
- The thicknesses of PEEK and beryllium tested in the 200 MeV beamline experiment were found to be sufficient to remove the 2.3 keV molybdenum fluorescence line from spectra, as expected.

The discoveries made in this experiment have contributed to knowledge of the successes and limitations of current versions of Geant4 and some of its physics lists. The validation of Geant4's ability to simulate fully-penetrating electrons is a particularly useful finding, which means that simulations of spectra generated by fully-penetrating particles such as Minimally Ionising Particle (MIP) protons can be trusted.

The discovery that simulations overpredicted the X-ray-like background between 2 keV and 4 keV in 200 MeV proton irradiations of aluminium may also be an important finding. There are several possible explanations for why this may have been the case, including the possibility that Geant4 significantly overestimated the number of fully-depositing electrons generated in general, or that the the unsimulated aspects of the CCD97 may reduce the X-ray-like background induced by electrons. Depending on the cause of the issue, corrections may need to be made to future Geant4 simulations of the CCD97, or potentially to Geant4 physics lists in order to solve the issue and ensure that Geant4 is accurate for use in the X-ray-like background context, especially because this issue could mean that background induced by electrons could be significantly overestimated.

Experiments are currently being designed at the Center for Electronic Imaging at the Open University to repeat the 200 MeV proton irradiation experiment presented in this thesis, but with a significantly thicker detector. This experiment will aim to examine in further detail the overestimation of electrons seen in the experiments presented here and may also be able to validate Geant4's treatment of Compton scattering photons produced by incoming proton primaries.

12.2 Summary of characterisation of X-ray-like background within the space-based environment using Geant4 spherical shell simulations and the ATHENA WFI mass model (Chapters 8 and 9)

Geant4 simulation work presented in this thesis successfully characterised the particle composition of X-ray-like background for a 4 cm thick proton shield spherical shell spacecraft model with a 450 μm thick detector, and for spherical shell models with a variety of different proton shield, optical blocking filter and detector thicknesses. The following bullet points summarise some of the key results from this work:

- For the baseline 4 cm thick proton shield model, with a 450 μm thick detector, a 5 μm thick BCB layer and a 90 nm thick optical blocking filter layer, the contribution of cosmic protons and CXB to X-ray-like background were found to be approximately equal.
- For the baseline spherical shell model, the cosmic proton background continuum was found to originate almost entirely from soft electrons, hard electrons and hard photons. Each of these particle types contributed approximately a third of the continuum.
- The energies and spatial distribution of each background component were characterised. The angular distribution for hard photons and soft photons were found to be approximately isotropic.
- Each background component generated by incoming cosmic protons except hard photons were found to originate from within several millimetres of the inner surface of the proton shield.
- X-ray-like background generated by incoming CXB photons was found to be primarily directly caused by CXB photons Compton scattering in the detector.
- The presence of an external massive spherical shell was not found to alter the X-ray-like background significantly for the cases modelled.
- Increasing the proton shield thickness caused each background component to increase in intensity. This was found to likely be related to the fact that generation of background-inducing particles often includes an intermediate particle.
- The presence of both the optical blocking filter layer and BCB passivation layer were found to reduce X-ray-like background significantly. Out of the simulations performed, the simulation with a 90 nm optical blocking filter layer exhibited the least X-ray-like background.
- Mathematical expressions were derived for the expected X-ray-like background as a function of detector thickness for several types of background component. These expressions were used in conjunction with simulations to determine the expected signal-to-noise ratio as a function of detector thickness, and it was found that signal-to-noise ratio peaks at a thickness that is dependent on the photon energy of interest.

The characterisation of X-ray-like background presented in this thesis provides insights into the key particle types and particle energies that detectors will need to be shielded from in future X-ray astronomy missions. The characterisation of the cosmic proton induced hard photon background may be particularly important, as this background currently has no shielding mechanism that can mitigate it. Designing shielding mechanisms for the hard photon background in future missions will likely be difficult due to the complexity of processes involved in their creation, in particular the presence of intermediate particles discovered in this work. However, it is hoped that the work presented in this

thesis might represent a first step towards characterising the hard photon background that will need to be shielded.

On-chip layers were, however, shown to be an effective method for mitigating X-ray-like background produced by electrons in general. It may therefore be the case that on-chip layers could be used in future space missions to remove background even if they are not necessarily needed for other purposes such as blocking straylight.

The discovery that signal-to-noise ratio appears to peak and then decrease with detector thickness is also an important finding. Without the consideration of background, it might be assumed that increasing detector thickness increases the signal-to-noise ratio because the quantum efficiency improves, increasing the signal. However, the work presented in this thesis shows that for cases where the signal flux is comparable to background, the signal-to-noise ratio may decrease significantly with detector thickness beyond a certain optimal thickness due to the background and associated noise increasing in intensity faster than the signal. This indicates that the influence of X-ray-like background may need to be taken into account in the initial detector design, as the use of a thick detector has the potential to significantly reduce the quality of science during a mission investigating low flux sources.

12.3 Summary of graded-Z shielding and magnetic shielding research and simulations (Chapters 10 and 11)

Graded-Z shielding and magnetic shielding were both investigated through mathematical methods and Geant4 simulations as shielding mechanisms for the mitigation of X-ray-like background in this thesis, and both were found to be effective at removing background in specific configurations. The following bullet points summarise some of the key results from this work:

- Mathematical methods were developed to characterise the effectiveness of graded-Z shielding, which better reflect the effectiveness of graded-Z shielding than the exponential Beer-Lambert law.
- Mathematical methods were developed to predict the locations where fluorescence background is most probable to originate from. It was found that for fully absorbed photons this was very similar to the mathematics of ‘view factors’ in thermal physics. Geant4 simulations were used to confirm that the mathematical methods developed could very accurately model the spatial distribution of where on spacecraft surfaces aluminium fluorescence lines generated by cosmic protons originate from.
- Simulations of graded-Z shielding found that low Z shielding layers were effective at attenuating fluorescence lines and that high Z layers were effective at attenuating the CXB.

However, graded-Z shielding was found to have no significant effect on the cosmic proton induced hard photon background.

- Mathematical methods were developed in order to assess the general effectiveness of uniform magnetic fields at preventing electrons from reaching a detector. These methods were combined with non-Geant4 Monte Carlo simulations to show that magnetic fields are significantly more effective than the gyroradius of a particle in a magnetic field would suggest.
- Several simple equations were produced that are capable of accurately characterising the effectiveness of a uniform magnetic field at shielding a detector from electrons produced diffusely from surfaces.
- Geant4 simulations of cosmic protons impacting a cuboidal spacecraft structure found that the magnetic field produced by a Helmholtz coil structure is able to significantly reduce, and for reasonably strong magnetic fields almost entirely remove the X-ray-like background due to both soft electrons and hard electrons.
- Simulations run on multiple different configurations of the ATHENA WFI mass model were used to characterise the background in a more realistic context than a spherical shell model, although spherical shell models were found to be similar qualitatively to the actual mass model in terms of the mechanisms and physics causing background.
- Simulations of the ATHENA mass model configurations found that small gaps in graded-Z shielding can cause large increases in fluorescence.
- Simulations of the ATHENA mass model also found that graded-Z shielding configurations did not significantly impact the background continuum due to cosmic protons, as was previously found in spherical shell model simulations.

The discovery that graded-Z shielding did not significantly influence the cosmic proton induced hard photon background, while unfortunate, is an important null result and indicates that other shielding mechanisms may need to be designed to mitigate the hard photon background. It also indicates that there is no detrimental impact of graded-Z shielding on background, and that there may be a large amount of freedom for choosing a graded-Z shielding configuration to remove fluorescence lines and to reduce CXB-induced background without accidentally increasing the GCR-induced background. Graded-Z shielding was found in simulations to remove almost all of the CXB-induced background, which illustrates the importance of including graded-Z shielding in an X-ray mission spacecraft design in general.

Work was also performed to determine the generation location of fluorescence photons. The discovery that fluorescence can be modelled as originating isotropically from surfaces surrounding a detector means it may be possible to calculate the effectiveness of shielding at reducing fluorescence

using mathematical or simple computational methods. This could be significantly quicker than using Geant4 simulations, which are sometimes very time-consuming to perform, particularly for incoming cosmic protons.

Magnetic field simulations and analysis found that magnetostatic fields should be an effective mechanism for shielding a detector from knock-on electron induced background. Simulations of a Helmholtz coil-like magnetic field, which might be generated either from solenoids or from permanent magnets, found the X-ray-like background from both soft electrons and hard electrons was either significantly reduced or entirely removed. As electrons cause between a half and two-thirds of X-ray-like background generated by cosmic protons (as found in Chapter 8), magnetic shielding therefore has the potential to remove up to a majority of the X-ray-like background in space astronomy missions. The main flaw with magnetic shielding was found to be that cooling mechanisms might be required if active shielding is used so that power requirements can be minimised.

Finally, simulations performed on the full ATHENA WFI mass model found that small gaps in graded-Z shielding are capable of significantly increasing fluorescence, and that care must be taking when designing graded-Z shielding to ensure that all relevant surfaces are covered with shielding to prevent fluorescence leakage.

The combination of graded-Z shielding and magnetic shielding together could therefore be used to remove both CXB induced background, and up to the majority of the cosmic proton induced background as well as cosmic proton induced fluorescence lines. As graded-Z shielding is currently being used aboard missions such as eRosita, and is planned to be used aboard ATHENA, a significant amount of research is already being done into possible graded-Z shielding configurations. It is anticipated that graded-Z shielding will be used aboard many space missions in the future.

However, magnetic shielding of specifically knock-on electrons is relatively new, and more research will be needed before it can be used in space missions. While magnetic diversion mechanisms have been used in the past to protect detectors from soft protons and electrons passing through spacecraft optics, as discussed in Chapter 10, this is quite a different task to shielding a detector isotropically from knock-on electrons.

Now that the work performed here has confirmed the theoretical viability of a Helmholtz coil structure for the diversion of knock-on electrons, more detailed engineering designs for such a structure could be investigated. As part of this, designs for possible cooling mechanisms or permanent magnet configurations will have to be developed to further increase the Technology Readiness Level (TRL) of magnetic shielding as a concept. It will also be of key interest to further investigate whether or not magnetic shielding might influence detector physics at all, although the irradiations presented in Chapter 6 and Chapter 7 found no evidence that presence of the magnetic field was altering the

functioning of the CCD97 used. Other possible shielding configurations should also be investigated as magnetic shielding candidates, and it is anticipated that there could be many possible candidate configurations that would successfully reduce X-ray-like background.

Appendix

A. The physics of magnetic fields

The physics of magnetic fields discussed here are described in many textbooks including "Introduction to Plasma Physics and Controlled Fusion" (Chen 1984) for instance.

All particle motion in a magnetic field can be described by the commonly known Lorentz force law, given by

$$\boldsymbol{F} = q\,\boldsymbol{v} \times \boldsymbol{B} \tag{A.1}$$

Where $\boldsymbol{F}$ is the force acting on a particle, q is the particle's charge, $\boldsymbol{v}$ is the velocity of the particle and $\boldsymbol{B}$ is the magnetic field the particle is moving through. The Lorentz force law applies in both special relativity as well as classically, as long as $\boldsymbol{F}$ is defined as $\boldsymbol{F} = \frac{d\boldsymbol{p}}{dt}$, where $\boldsymbol{p}$ is the particle's momentum. The first fact that can be derived about magnetic fields is the conservation of kinetic energy of the particle. This can be shown using the scalar product of the particle momentum with the Lorentz force law,

$$\boldsymbol{p} \cdot \frac{d\boldsymbol{p}}{dt} = q\,\boldsymbol{p} \cdot (\boldsymbol{v} \times \boldsymbol{B}) \tag{A.2}$$

The left-hand side can be simplified using $\frac{d|\boldsymbol{p}|^2}{dt} = \boldsymbol{p} \cdot \frac{d\boldsymbol{p}}{dt}$, where the right-hand side simply reduces to zero, since $\boldsymbol{p}$ is always parallel to $\boldsymbol{v}$, and because $\boldsymbol{v} \times \boldsymbol{B}$ is always perpendicular to $\boldsymbol{v}$. Therefore,

$$\frac{d|\boldsymbol{p}|^2}{dt} = 0 \tag{A.3}$$

This means that a magnetic field is incapable of changing the magnitude of a charged particle's momentum, and in turn is also incapable of changing the magnitude of a particle's velocity, or its kinetic energy. This fact is particularly useful in discussions in Chapter 10 of the effect of magnetic fields on radiation flux, as it means that magnetic fields are not capable of directly altering the energy spectrum of charged radiation, only the path in which individual particles travel.

A useful feature that can be derived from the conservation of kinetic energy in a magnetic field is that the relativistic gamma factor, $\gamma = \frac{1}{\sqrt{1-\frac{v^2}{c^2}}}$, remains constant throughout the motion, meaning that the relativistic kinematics for a particle in a magnetic field are exactly the same as the classical kinematics, as long as the classical mass m is redefined as $m = \gamma m_0$.

Analytically determining the effect of a magnetic field on particle trajectories more specifically can be very complex. However, while a complete solution to the Lorentz force law for a particular particle in a varying magnetic field requires a full solution to the differential equation created by Equation A.1, a general first-order solution can be obtained through approximating the magnetic field to vary slowly and be approximately uniform with regards to the period of the particle's oscillation in the magnetic field.

Setting $\boldsymbol{B}$ to be a constant means that the Lorentz force law can be separated into two equations in terms of the forces parallel and perpendicular to the magnetic field,

$$\boldsymbol{F}_{||} = 0 \tag{A.4}$$

$$\boldsymbol{F}_{\perp} = \begin{bmatrix} F_1 \\ F_2 \end{bmatrix} = q|\boldsymbol{B}| \begin{bmatrix} 0 & -1 \\ 1 & 0 \end{bmatrix} \begin{bmatrix} v_1 \\ v_2 \end{bmatrix} \tag{A.5}$$

Here, the subscripts 1 and 2 will be set to denote components that are perpendicular to the magnetic field, so v_1 and v_2 are the two components of velocity which are perpendicular to the magnetic field. Equation A.4 means that the component of velocity parallel to the magnetic field lines is conserved throughout the motion and that the magnitude of velocity perpendicular to the magnetic field must also be conserved in order to preserve the conservation of kinetic energy that was derived previously.

Equation A.5 is a coupled, ordinary differential Equation, and after some calculus and algebra can be solved to give the equation

$$\boldsymbol{v}_{\perp} = \begin{bmatrix} \cos(\omega_g t) & -\sin(\omega_g t) \\ \sin(\omega_g t) & \cos(\omega_g t) \end{bmatrix} \begin{bmatrix} v_1 \\ v_2 \end{bmatrix}_{t=0} \tag{A.6}$$

Here, $\omega_g = \frac{q|\boldsymbol{B}|}{m}$, and is known as the particle gyrofrequency. This equation is the general equation for a circular motion about a point at an angular frequency of ω_g. To find the point the particle rotates about, as well as the radius of circular motion, $\boldsymbol{v}_{\perp}$ can be integrated with respect to time to give

$$\boldsymbol{x}_{\perp} = \frac{1}{\omega_g} \begin{bmatrix} \sin(\omega_g t) & \cos(\omega_g t) - 1 \\ -(\cos(\omega_g t) - 1) & \sin(\omega_g t) \end{bmatrix} \boldsymbol{v}_{\perp,t=0} + \boldsymbol{x}_{\perp,t=0} \tag{A.7}$$

The central point of this motion is known as the 'guiding centre' and can be found by taking the mean position of $\boldsymbol{x}_\perp$ across one full rotation of the system, i.e. integrating $\boldsymbol{x}_\perp$ with respect to $\phi = \omega_g t$ between $\phi = 0$ and $\phi = 2\pi$. This integral results in a guiding centre of

$$\boldsymbol{x_c} = \frac{1}{\omega_g}\begin{bmatrix} 0 & -1 \\ 1 & 0 \end{bmatrix}\boldsymbol{v}_{t=0} + \boldsymbol{x}_{\perp,t=0} \tag{A.8}$$

Finally, the radius of circular motion about the guiding centre, or 'gyroradius' can be found by taking the distance between any point on the circular trajectory, and the guiding centre. In this case, the distance can be found as the magnitude of $\boldsymbol{x_c} - \boldsymbol{x}_{t=0}$, which gives the gyroradius as

$$r_g = \frac{|\boldsymbol{v}_{t=0}|}{\omega_g} = \frac{m|\boldsymbol{v}_\perp|}{|q||\boldsymbol{B}|} = \frac{|\boldsymbol{p}_\perp|}{|q||\boldsymbol{B}|} \tag{A.9}$$

The gyroradius r_g is particularly useful as a length scale comparison; as a measure of showing how effectively a magnetic field will divert a charged particle from its original path. In fact, the mathematical measure of curvature for a trajectory in any magnetic field is actually defined as $\kappa = \frac{1}{r_g}$. A smaller r_g represents a more tightly confined motion around the particle's guiding centre, and therefore can be viewed as a measure of the effectiveness of a magnetic field at confining a particle to motion along its magnetic field lines.

Equation A.9 can also be expressed as a function of the kinetic energy perpendicular to the magnetic field, as

$$r_g = \frac{1}{|q||\boldsymbol{B}|c}\sqrt{(E_k + m_0c^2)^2 - (m_0c^2)^2} \tag{A.10}$$

Here, c is the speed of light, E_k is the particle kinetic energy associated with momentum components perpendicular to the magnetic field, and m_0 is the particle rest mass. For non-relativistic particles, the simpler classical mechanics approximation may be used:

$$r_g = \frac{\sqrt{2mE_k}}{|q||\boldsymbol{B}|} \tag{A.11}$$

B. Mathematics for Monte Carlo methods in the space-based environment

B.1 Probability density functions

Some of the following common rules for probability density functions that are used in this thesis are given here. These relations as well as others can be found in "Modern Mathematical Statistics with Applications" (Devore and Berk 2012).

The probability density function $PDF_x(x)$ for a random variable x is defined as

$$P(a < x < b) = \int_a^b PDF_x(x)\,dx \tag{B.1}$$

Where x is the random variable in question, $P(a < x < b)$ denotes the probability that x is between a and b. In this thesis, the variable in the subscript of the PDF denotes the form and structure of the probability density function as a functional, while the variable in the brackets denotes the variable to be inserted into the equation. In this thesis probability density functions are sometimes be shortened such that $PDF_x(x) \rightarrow PDF_x$ for the sake of brevity.

A joint probability density function is the probability density function for more than one random variables, and is given by the product of the probability density functions for each variable. The probability of each variable taking a value with a specified range of limits is then given by the integral of the joint probability density function across each limit and variable. For example, the joint probability density function for x and y might be given as $PDF_{x,y}(x,y) = PDF_x(x) \times PDF_y(y)$, which has a joint probability of $a < x < b$ and $c < y < d$ of

$$\begin{aligned} P\big((a < x < b) \wedge (c < y < d)\big) &= \int_a^b \int_c^d PDF_x(x) \times PDF_y(y) dxdy \\ &= \int_a^b \int_c^d PDF_{x,y}(x,y) dxdy \end{aligned} \tag{B.2}$$

Probability density functions can also be multiplied by constants or added to other probability density functions in the same way that regular probabilities can be.

If a random variable is dependent on another random variable, the probability density function for the dependent variable can be calculated by performing a change of variables on the integral in the right hand side of Equation B.1. For example, for $y = f(x)$,

$$\int PDF_x(x)\,dx = \int PDF_x\big(f^{-1}(y)\big)\left|\frac{df^{-1}(y)}{dy}\right| dy = \int PDF_y(y)\,dy \tag{B.3}$$

Equation B.3 can be generalised for joint probability density functions to

$$PDF_{\boldsymbol{z}}\left(\boldsymbol{z} = f(\boldsymbol{x})\right) = PDF_{\boldsymbol{x}}\left(f^{-1}(\boldsymbol{z})\right) \times J_{\boldsymbol{z}}\left(f^{-1}(\boldsymbol{z})\right) \tag{B.4}$$

Where $\boldsymbol{z}$ is a vector of dependent variables, $\boldsymbol{x}$ is a vector of independent variables, and J represent the Jacobian, such that $J_{\boldsymbol{z}}(\boldsymbol{x})$ for example would represent the Jacobian of **x** with respect to **z**.

These relations can be used to calculate the probability density functions for functions of two or more variables, some of which are given in equations B.5 to B.8 below.

$$PDF_z(z = x + y) = \int_{-\infty}^{\infty} PDF_x(x) PDF_y(z - x)\, dx \tag{B.5}$$

$$PDF_z(z = x - y) = \int_{-\infty}^{\infty} PDF_x(x) PDF_y(x - z)\, dx \tag{B.6}$$

$$PDF_z(z = x \times y) = \int_{-\infty}^{\infty} PDF_x(x) PDF_y\left(\frac{z}{x}\right) \frac{1}{|x|}\, dx \tag{B.7}$$

$$PDF_z\left(z = \frac{y}{x}\right) = \int_{-\infty}^{\infty} PDF_x(x) PDF_y(zx)|x|\ dx \tag{B.8}$$

B.2 Deriving Lambert's cosine law for incident radiation in space

To simulate the radiation environment impacting a spacecraft through Monte Carlo methods, incoming radiation must first be generated on a surface surrounding the spacecraft and given a direction and orientation. The law determining the probabilistic direction at which radiation is emitted from a surface follows what is known either as Lambert's Cosine Law (Lambert 1760), or equivalently as Knudsen's Law (Feres and Yablonsky 2004) when discussing thermal physics.

Both Galactic Cosmic Rays and the Cosmic X-ray Background enter the solar system from all angles, representing an isotropic distribution. This means that the quantity of radiation impacting a surface can be modelled as proportional to the area of the surface from which it is generated. It also means that that the distribution of both cosmic rays and X-rays impacting a spacecraft can be modelled as originating from a 'diffuse radiator', or 'Lambertian radiator'.

A Lambertian radiator is a surface that emits particles or X-rays such that the radiance of the surface is independent of viewing angle towards the surface. It can be mathematically determined that this corresponds to a probability of a primary particle being emitted from a position on the surface at an angle from the normal to the surface of θ is proportional to $\sin(2\theta)$ as shown by Zhao et al. (2013). This can be equivalently derived by considering the diagram displayed in Figure B.1.

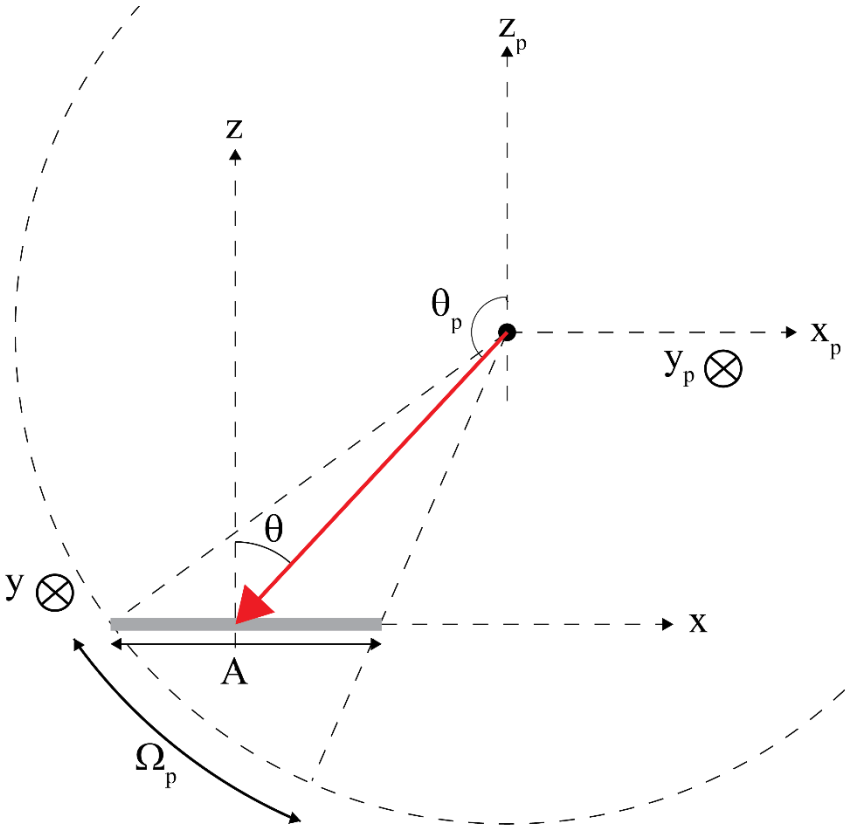

Figure B.1 A diagram displaying the geometric configuration for Lambert's/Knudsen's law

For a particle to impact area A, the combined probability of two events must be considered: the probability of a particle being generated at position P, and the probability that the momentum of the particle is oriented such that the particle's trajectory will eventually pass through the area A. The former will be described first.

The probability that a particle will be generated at position P is uniformly distributed across space, such that

$$PDF_{x,y,z}(x,y,z)dx\,dy\,dz = N\,dx\,dy\,dz \tag{B.9}$$

Equation B.9 can be converted into spherical coordinates through the transformation $\mathrm{x} = \mathrm{r}\sin(\theta)\cos(\phi), \mathrm{y} = \mathrm{r}\sin(\theta)\sin(\phi), z = r\cos(\theta)$ and $dx\,dy\,dz = r^2\sin(\theta)dr\,d\theta\,d\phi$, giving

$$PDF_{r,\theta,\phi}(r,\theta,\phi)drd\theta d\phi = Nr^2\sin(\theta)\,drd\theta d\phi \tag{B.10}$$

This means that the probability of a particle being emitted from a spherical shell volume increases with sphere radius and varies with $\sin(\theta)$.

Next, the probability that the particle is emitted in such a direction that it passes through an area, A, needs to be determined. One way to do this is to translate the coordinate system such that the origin is now placed on top of the point $P = (x, y, z)$, the point where the particle was generated.

Symmetry means that the probability of the particle being emitted into any given solid angle about the origin in this new coordinate system should be uniform,

$$PDF_{\theta_p,\phi_p}(\theta_\mathrm{p},\phi_\mathrm{p})d\Omega_\mathrm{p} = N_p d\Omega_\mathrm{p} \tag{B.11}$$

or

$$PDF_{\theta_p,\phi_p}(\theta_\mathrm{p},\phi_\mathrm{p})d\theta_\mathrm{p}d\phi_\mathrm{p} = N_p \sin(\theta_p)\, d\theta_\mathrm{p}d\phi_\mathrm{p} \tag{B.12}$$

Where N_p is a constant. To calculate the solid angle in these coordinates encompassing surface A, the coordinate system expressed in Equation B.12 needs to be converted to the Cartesian coordinate system (x_p, y_p, z_p). To do this requires the use of the Jacobian

$$|J| = \begin{vmatrix} \frac{\partial\theta_p}{\partial x_p} & \frac{\partial\phi_p}{\partial x_p} \\ \frac{\partial\theta_p}{\partial y_p} & \frac{\partial\phi_p}{\partial y_p} \end{vmatrix} = \begin{vmatrix} \frac{x_p\, z_p}{\sqrt{\mathrm{x_p^2+y_p^2}}\left(\mathrm{x_p^2+y_p^2+z_p^2}\right)} & -\frac{y_p}{x_p^2+y_p^2} \\ \frac{y_p\, z_p}{\sqrt{\mathrm{x_p^2+y_p^2}}\left(\mathrm{x_p^2+y_p^2+z_p^2}\right)} & \frac{x_p}{x_p^2+y_p^2} \end{vmatrix} \tag{B.13}$$

$$= \frac{|z_p|}{\sqrt{x_p^2+y_p^2}\left(x_p^2+y_p^2+z_p^2\right)}$$

Here z_p can be treated as a constant, as the surface A is entirely situated at $z = 0$, or $z_p = -z$. The full probability distribution for landing within the boundaries of $dA = dx\, dy = dx_p dy_p$ can then be expressed as

$$PDF_{x_p,y_p}(x_p,y_p) = |J| \times \mathrm{PDF}_{\theta_\mathrm{p},\phi_\mathrm{p}}(\theta_p,\phi_p) \tag{B.14}$$

$$= \frac{|z_p|}{\sqrt{x_p^2+y_p^2}\left(x_p^2+y_p^2+z_p^2\right)} \times N_p \sin(\theta_p) \tag{B.15}$$

$$= N_p \frac{|z_p|}{\sqrt{x_p^2+y_p^2}\left(x_p^2+y_p^2+z_p^2\right)} \sin(\arccos(z_p/r_p)) \tag{B.16}$$

$$= N_p \frac{|z_p|}{\sqrt{x_p^2+y_p^2}\left(x_p^2+y_p^2+z_p^2\right)} \times \frac{\sqrt{x_p^2+y_p^2}}{\sqrt{x_p^2+y_p^2+z_p^2}} \tag{B.17}$$

$$= \frac{N_p}{r^2}\cos(\theta_p) \tag{B.18}$$

This expression means that the flux present at a given small area originating from a source at point P decreases with both r^2, and varies with $\cos(\theta_p)$. θ_p in this case can be interpreted as the same as the angle to the normal θ, as geometrically from Figure B.1 it can be seen that $\theta_p = \pi - \theta$, and

$\cos(\pi - \theta) = -\cos(\theta)$, which can be multiplied by -1 for the replacement of $\cos(\theta_p)$ in Equation B.18 with no loss of generality, as probability needs to be positive. Therefore,

$$PDF_{x,y}(x,y)dxdy = \frac{N_p}{r^2}\cos(\theta)\,dxdy \tag{B.19}$$

To obtain the overall probability that a given particle will be produced at a position P and then pass through area dA, the PDFs described in equations B.10 and B.19 have to be multiplied together as

$$PDF_{x,y,r,\theta,\phi}(x,y,r,\theta,\phi) = \frac{N_p}{r^2}\cos(\theta)dxdy \times Nr^2\sin(\theta)drd\theta d\phi \tag{B.20}$$

$$= N_p N\cos(\theta)\sin(\theta)\,dxdydrd\theta d\phi \tag{B.21}$$

$$= N_p N\sin(2\theta)\,dxdydrd\theta d\phi \tag{B.22}$$

Or equivalently,

$$PDF_{x,y,r,\theta,\phi}(x,y,r,\theta,\phi)dx\,dy\,dr\,d\Omega = N_p N\cos(\theta)\,dx\,dy\,dr\,d\Omega \tag{B.23}$$

To determine $PDF_{x,y,\theta}(x,y,\theta)$, $PDF_{x,y,r,\theta,\phi}(x,y,r,\theta,\phi)$, could be integrated across r and ϕ while keeping θ constant. However, it is simpler to utilise the normalisation of Equation B.22 to calculate $PDF_{x,y,\theta}(x,y,\theta)$. This normalisation can be performed by recognising that when integrating Equation B.22 across ϕ and r, the $\sin(2\theta)$ can be removed from the integrals. This means that $PDF_{x,y,\theta}(x,y,\theta)$ will be proportional to $\sin(2\theta)$, and that $\int\int\int\int N_p N\,dx\,dy\,dr\,d\phi$ can be set as equal to a single normalisation constant n. Solving $\int_0^{\frac{\pi}{2}} n\,sin(2\theta)\,d\theta = 1$ gives a value of $n = 1$, meaning that the full probability density for finding a particle's momentum having an angle θ relative to the normal to the surface is simply

$$PDF_\theta(\theta) = \sin(2\theta) \tag{B.24}$$

B.3 Mathematically distributing isotropic incoming radiation trajectories

Determining the angular distribution of particles requires generating a set of random variables determining the position of a particle on a surface, and the momentum direction of the particle, represent four random variables in total.

To distribute particle positions, a suitable surface must be chosen such that it encloses all relevant objects within the simulation volume, and that each area element of the surface is exposed to a full unobscured view of the edges of the simulation world. Particles must then be generated upon the surface such that the probability of a particle landing on a particular region of area A is only dependent on A itself. In other words, the probability of landing in a region $dA = dx\,dy$ is a constant.

For a spherical surface, this can therefore be expressed by a probability density function of

$$PDF_{x,y}(x,y)dx\,dy = \frac{1}{A}dx\,dy \tag{B.25}$$

where

$$dx\,dy = R^2\sin(\theta_p)d\theta_p\,d\phi_p \tag{B.26}$$

meaning that

$$PDF_{\theta_p,\phi_p}(\theta_p,\phi_p)d\theta_p\,d\phi_p = \frac{1}{A}R^2\sin(\theta_p) \tag{B.27}$$

$$= \frac{1}{4\pi}\sin(\theta_p)d\theta_p\,d\phi_p \tag{B.28}$$

And that

$$PDF_{\theta_p}(\theta_p)d\theta_p = \frac{1}{2}\sin(\theta_p)d\theta_p \tag{B.29}$$

$$PDF_{\phi_p}(\phi_p)d\phi_p = \frac{1}{2\pi}d\phi_p \tag{B.30}$$

Here generating ϕ_p is relatively straightforward as it only requires uniformly generating a value of ϕ_p from 0 to 2π.

Generating a value of θ_p is more complicated, as it requires generating a value of θ_p that is distributed by $\frac{1}{2}\sin(\theta_p)$ between $\theta_p = 0$ and $\theta_p = \pi$. It is possible to generate θ_p using the sampling method described in Section 5.3.2.

Integrating both $PDF_{\theta_p}(\theta_p)$ and a uniform distribution $PDF_u(u) = 1$ between θ_p and u respectively gives

$$\int_0^{\theta_p}\frac{1}{2}\sin(\theta_p)\,d\theta_p = \int_0^u du \tag{B.31}$$

$$\frac{1}{2}(1-\cos(\theta_p)) = u \tag{B.32}$$

$$\cos(\theta_p) = 1-2u \tag{B.33}$$

$$\theta_p = \arccos(1-2u) \tag{B.34}$$

This means that θ_p can be generated by first creating a uniform random distribution between 0 and 1, and then substituting the generated values into Equation B.34 to get the correctly distributed values of θ_p.

To distribute particle momentum directions, particle momenta can be distributed by Lambert's cosine law above using either of the two methods described above. To distribute momenta using the second method,

$$\int_0^{\theta} \sin(2\theta)\, d\theta = \int_0^{u} du \tag{B.35}$$

$$\frac{1}{2}(1 - \cos(2\theta)) = u \tag{B.36}$$

$$\cos(2\theta) = 1 - 2u \tag{B.37}$$

$$\theta = \frac{1}{2}\arccos(1 - 2u) \tag{B.38}$$

And ϕ, in this case, is again a uniform distribution between 0 and 2π.

C. Additional figures from analysis of 200 MeV proton experiment and simulations

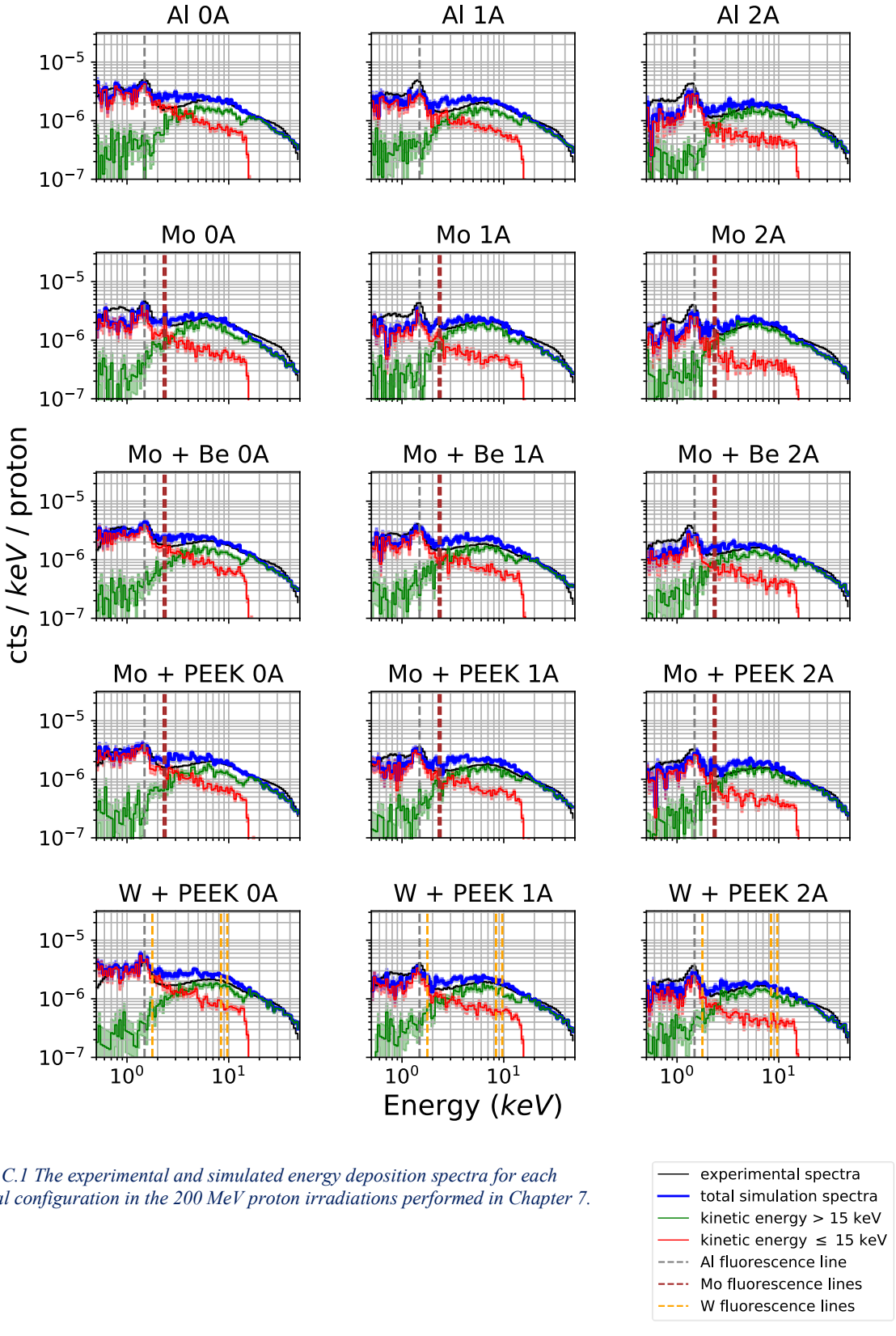

Figure C.1 The experimental and simulated energy deposition spectra for each material configuration in the 200 MeV proton irradiations performed in Chapter 7.

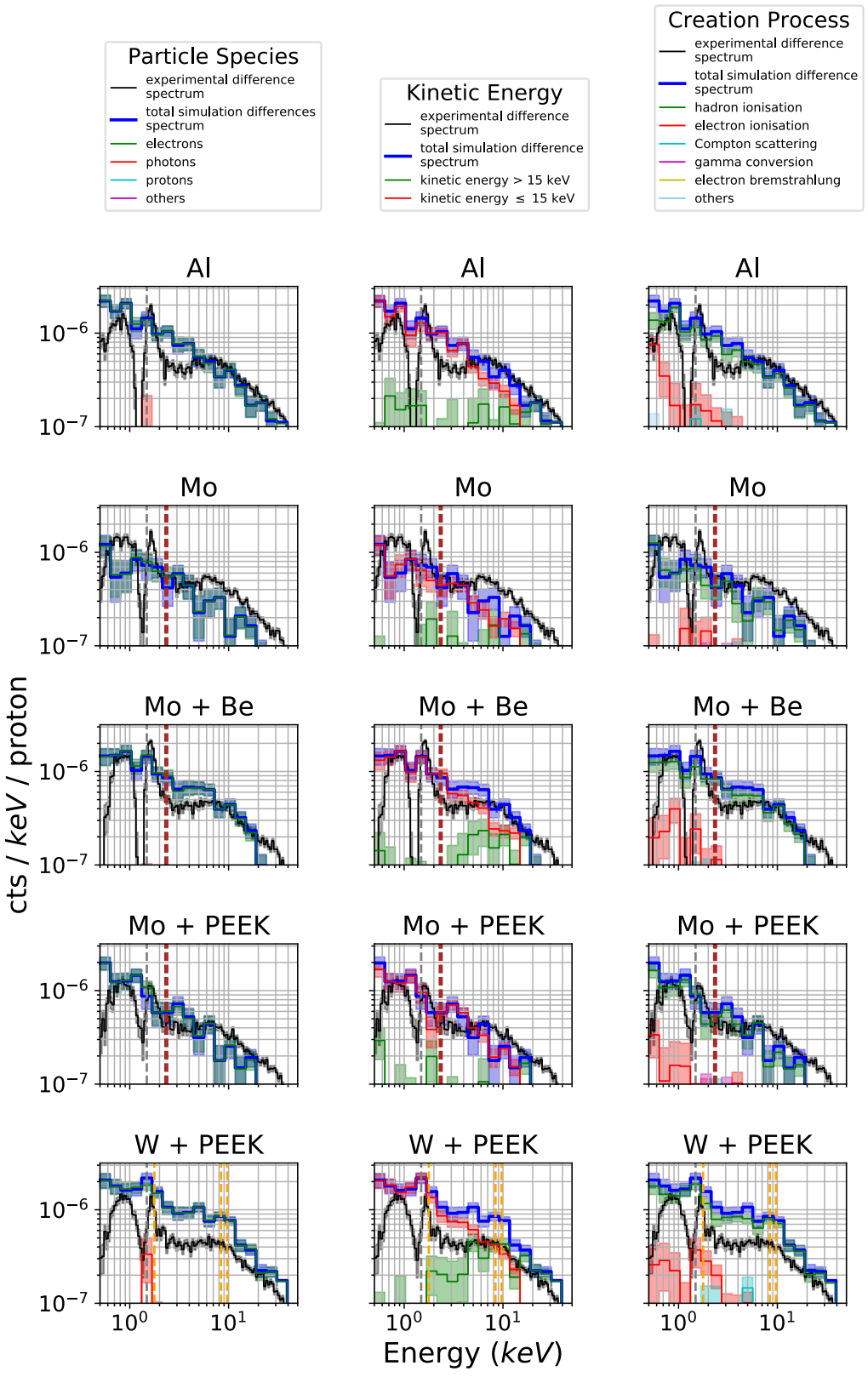

Figure C.2 The experimental and simulated magnetic difference spectra for each material configuration in the 200 MeV proton irradiation described in Chapter 7, split by either particle species, Geant4 creation process or particle kinetic energy. The accuracy of Geant4 at simulating the irradiation appears to depend significantly on the irradiated material configuration. It is also believed that the event detection process introduced significant normalisation errors into some of the spectra specifically, and this is believed to be why the W + PEEK simulated magnetic difference spectrum differs from experiment significantly.

D. Deriving the background event probability and quality factors for isotropically distributed particles impacting a device

D.1 Compton scattering photons

The system displayed in Figure D. was used to model the systems described in this appendix section. The detector here was modelled as a cuboid block of silicon, which has a thickness t, and a face with approximately infinite sides.

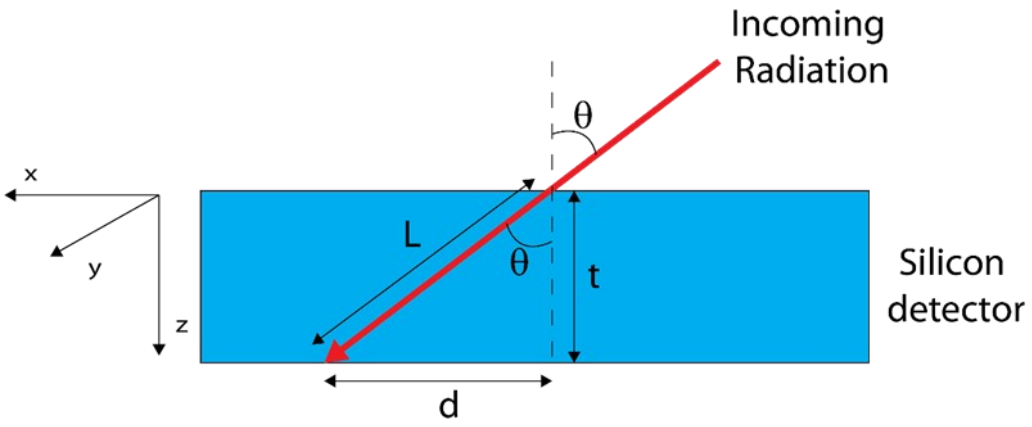

Figure D.1 The detector geometry used for mathematics in this appendix section.

The angle between the incoming particle and the normal to the detector is given by θ, while L and d are the distances the particle travels through the detector and along the face of the detector, respectively.

The probability of a photon passing through a device generating a Compton scattering event can be approximated as

$$P = 1 - e^{-\lambda_{\text{Compt}} l} \approx \lambda_{\text{Compt}} l \tag{D.1}$$

where λ_{Compt} is the attenuation coefficient for a photon of that can deposit a given energy in the detector, which is only able to Compton scatter in the detector. If λ_{Compt} is small, which is true to a first-order Taylor expansion, where l is the thickness of material along the axis of the incident particle. This relation is true when $\lambda_{Compt} l \ll 1$ or when $l \ll \frac{1}{\lambda_{Compt}}$.

Combining Equation D.1 with the probability density function for a diffuse photon distribution on the surface of the detector, allows for the intensity of Compton scattering background as a function of detector thickness to be calculated. The initial angular impact distribution of a diffusely distributed photon is given by Lambert's cosine law, as stated in Appendix B.2,

$$P(\theta \leq \Theta < \theta + d\theta) = PDF_{\theta}(\theta)d\theta \tag{D.2}$$

$$= 2\cos(\theta)\sin(\theta)\,d\theta \tag{D.3}$$

$$= \sin(2\theta)\,d\theta \tag{D.4}$$

To calculate the probability distribution for the quantity of Compton scattering events that take place, a change of variables is needed to convert Equation D.4 into the probability distribution for the path length as the particle passes through the detector. Before this can be done, path length needs to be expressed as a function of the incident angle of the photon into the material, and the detector thickness. It can be seen from the geometry displayed in Figure D.1 that $l = \frac{t}{\cos(\theta)} = t\sec(\theta)$, and that $\theta = \arccos\left(\frac{t}{l}\right)$. Therefore,

$$\frac{d\theta}{dl} = \frac{t}{l\sqrt{l^2 - t^2}} \tag{D.5}$$

Applying the change of variables $\theta \rightarrow l$ to Equation D.4, the probability distribution for l can be described by

$$P(l \leq L < l + dl) = PDF_l(l)\,dl \tag{D.6}$$

$$= \sin\left(2\arccos\left(\frac{t}{l}\right)\right)\left|\frac{d\theta}{dl}\right| dl \tag{D.7}$$

$$= \sin\left(2\arccos\left(\frac{t}{l}\right)\right)\frac{t}{l\sqrt{l^2 - t^2}}\,dl \tag{D.8}$$

$$= \frac{2t}{l^2}\sqrt{l^2 - t^2}\,\frac{t}{l\sqrt{l^2 - t^2}}\,dl \tag{D.9}$$

$$= \frac{2t^2}{l^3}\,dl \tag{D.10}$$

Therefore, the mean probability $\bar{P} = \lambda_{\text{Compt}}\bar{l}$ that a particle will be absorbed in the detector can be determined by multiplying PDF_l by λl and integrating over the entire domain of l, which in this case is (t, ∞),

$$\overline{\mathrm{P}} = \lambda_{\text{Compt}}\bar{l} = \lambda_{\text{Compt}}\int_{l=t}^{l=\infty} l \times \frac{2t^2}{l^3}\,dl \tag{D.11}$$

$$= \lambda_{\text{Compt}}\int_{l=t}^{l=\infty} \frac{2t^2}{l^2}\,dl \tag{D.12}$$

$$= 2\lambda_{\text{Compt}}t \tag{D.13}$$

This is equivalent to multiplying the mean path length of the photon through the detector along the particle's direction of travel by λ_{Compt}. Equation D.13 implies that the number of Compton scattering events received in a detector should scale linearly with detector thickness, which means that as expected Compton background events should become more significant for thicker detectors.

P can now be directly inserted into Equation 9.1 described in Chapter 9 to give the total signal-to-noise ratio as

$$\frac{S}{N} = \frac{S}{\sqrt{S+B}} \tag{D.14}$$

$$= \sqrt{At_I}\left(\frac{F_S(1-e^{-\lambda t})}{\sqrt{F_S(1-e^{-\lambda t}) + 2F_{Compt}\lambda_{Compt}t}}\right) \tag{D.15}$$

And the quality factor as

$$QF = \frac{F_S(1-e^{-\lambda t})}{\sqrt{F_S(1-e^{-\lambda t}) + 2F_{Compt}\lambda_{Compt}t}} \tag{D.16}$$

D.2 Soft photons impacting back-illuminated devices

This appendix section also uses the geometry shown in Figure D.1 , given in Appendix D.1. The absorption probability for a photon travelling through silicon of thickness l along the incoming photon's direction of travel can be given as

$$P = 1 - e^{-\lambda l} \tag{D.17}$$

where λ is the mass attenuation coefficient for a photon of a given energy in the detector. This means that the probability density function for the photon to be absorbed at a distance l is

$$PDF_l(l) = \frac{dP}{dl} = \lambda e^{-\lambda l} \tag{D.18}$$

Therefore multiplying by $PDF_\theta(\theta) = \sin(2\theta)$ gives $PDF_{l,\theta}(l,\theta)$ as

$$PDF_{l,\theta}(l,\theta) = \left(\lambda e^{-\lambda l}\right) \times (\sin(2\theta)) = \lambda \sin(2\theta)\, e^{-\lambda l} \tag{D.19}$$

to find the total probability density function with respect to z, a coordinate transformation needs to be performed to convert $PDF_{l,\theta}(l,\theta)$ into a function of z and then an integration must be performed across the entire domain of the other variables within the resulting probability density function. The simplest way of doing this is to convert $PDF_{l,\theta}(l,\theta)$ into $PDF_{l,z}(l,z)$ and integrate between the minimum and maximum values of l, which are $l = z$ and $l = \infty$ respectively. The Jacobian for this transformation can be found using $\theta = \arccos\left(\frac{z}{l}\right)$ as well as the trivial relation $l = l$ to be

$$|J| = \begin{vmatrix} \frac{\partial l}{\partial l} & \frac{\partial l}{\partial z} \\ \frac{\partial \theta}{\partial l} & \frac{\partial \theta}{\partial z} \end{vmatrix} \tag{D.20}$$

$$= \begin{vmatrix} 1 & 0 \\ \frac{z}{l\sqrt{l^2 - z^2}} & \frac{1}{\sqrt{l^2 - z^2}} \end{vmatrix} \tag{D.21}$$

$$= \frac{1}{\sqrt{l^2 - z^2}} \tag{D.22}$$

Equivalently, this can be found by just taking the Jacobian as $\left|\frac{\partial \theta}{\partial z}\right|$. Therefore,

$$PDF_{l,z}(l, z) = \frac{1}{\sqrt{l^2 - z^2}} \lambda \sin(2\theta)\, e^{-\lambda l} \tag{D.23}$$

$$= \frac{\lambda}{\sqrt{l^2 - z^2}} \frac{2z\sqrt{l^2 - z^2}}{l^2} e^{-\lambda l} \tag{D.24}$$

$$= \frac{2\lambda z}{l^2} e^{-\lambda l} \tag{D.25}$$

$PDF_{l,z}(l, z)$ can now be integrated between $l = z$ and $l = \infty$ to give

$$PDF_z(z) = \int_z^{\infty} \frac{2\lambda z}{l^2} e^{-\lambda l} dl \tag{D.26}$$

$$= 2\lambda z \left[-\lambda Ei(-\lambda l) - \frac{1}{z} e^{-\lambda z} \right]_{l=z}^{l=\infty} \tag{D.27}$$

$$= 2z\lambda^2 Ei(-\lambda z) + 2\lambda e^{-\lambda z} \tag{D.28}$$

Where $Ei(x) = \int_{-\infty}^{x} \frac{1}{t} e^t\, dt$ is known as the elliptic integral of x and is a function where values can be found from tabulated values.

To find the total probability that a photon will be absorbed within a detector, Equation D.28 must be integrated between $z = 0$ and $z = t$, giving

$$P = \int_{z=0}^{z=t} PDF_z(z) dz \tag{D.29}$$

$$= \int_{z=0}^{z=t} \left(2z\lambda^2 Ei(-\lambda z) + 2\lambda e^{-\lambda z} \right) dz \tag{D.30}$$

$$= \left[e^{-\lambda z}(\lambda z - 1) + \lambda^2 z^2 Ei(-\lambda z) \right]_{z=0}^{z=t} \tag{D.31}$$

$$= 1 + e^{-\lambda t}(\lambda t - 1) + \lambda^2 t^2 Ei(-\lambda t) \tag{D.32}$$

To determine the signal-to-noise ratio, P can be substituted into Equation 9.1 given in Chapter 9 to give a signal-to-noise ratio for a soft photon dominated background of

$$\frac{S}{N} = \frac{S}{\sqrt{S + B}} \tag{D.33}$$

$$= \sqrt{At}\left(\frac{F_S\left(1-e^{-\lambda t}\right)}{\sqrt{F_S(1-e^{-\lambda t})+F_\gamma\left(1+e^{-\lambda t}(\lambda t-1)+\lambda^2 t^2 Ei(-\lambda t)\right)}}\right) \quad \text{(D.34)}$$

$$= \sqrt{At}\left(\frac{F_S(1-e^{-\lambda t})}{\sqrt{(F_S+F_\gamma)(1-e^{-\lambda t})+F_\gamma\left(\lambda t e^{-\lambda t}+\lambda^2 t^2 Ei(-\lambda t)\right)}}\right) \quad \text{(D.35)}$$

And a quality factor of

$$QF = \frac{F_S(1-e^{-\lambda t})}{\sqrt{(F_S+F_\gamma)(1-e^{-\lambda t})+F_\gamma\left(\lambda t e^{-\lambda t}+\lambda^2 t^2 Ei(-\lambda t)\right)}} \quad \text{(D.36)}$$

D.3 Soft photons impacting front illuminated and multi-layered devices

The geometry used in this appendix section is shown in Figure D.2.

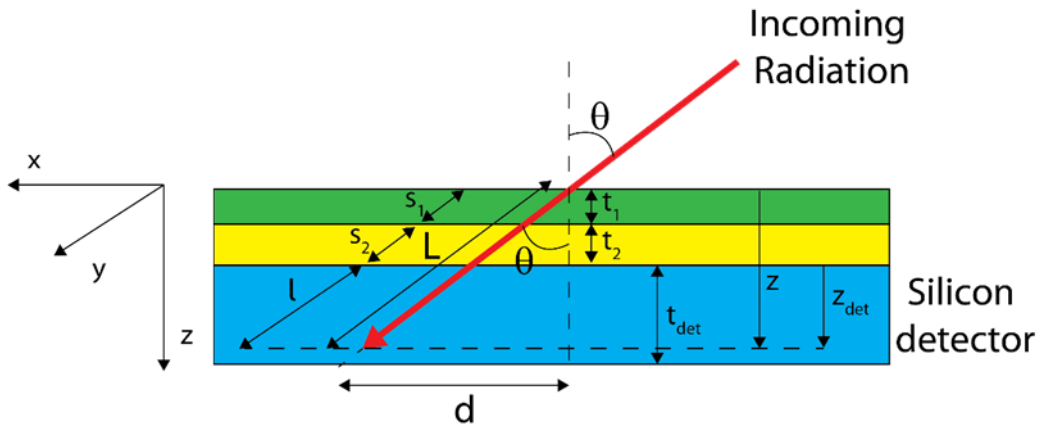

Figure D.2 The geometry for the mathematics used in this section relating to multiple on-chip device layers, which may include structures like optical blocking filters or on-chip electronics. Here, $z = 0$ is defined to be the surface of the actual sensitive detector region.

For a multilayer device, the probability that a particle is absorbed somewhere within the device or the front layers up until the position z in the device, assuming that z is within the silicon bulk is

$$P = 1 - e^{-\sum_{i=1}^{N}\lambda_i s_i} e^{-\lambda_{det} l} \quad \text{(D.37)}$$

$$= 1 - e^{-\sum_{i=1}^{N}\lambda_i s_i - \lambda_{det} l} \quad \text{(D.38)}$$

$$= 1 - e^{-\sum_{i=1}^{N}\lambda_i s_i - \lambda_{det}\left(L-\sum_{i=1}^{N} s_i\right)} \quad \text{(D.39)}$$

$$= 1 - e^{-\lambda_{det} L - \sum_{i=1}^{N}(\lambda_i - \lambda_{det}) s_i} \quad \text{(D.40)}$$

Here λ_i is the mass attenuation coefficient in layer i. Since $s_i = \frac{t_i}{\cos(\theta)}$ and $\cos(\theta) = \frac{z}{L}$, s_i can be expressed as $s_i = \frac{t_i L}{z}$. Therefore,

$$P = 1 - e^{-\lambda_{det}L - \sum_{i=1}^{N}(\lambda_i - \lambda_{det})\frac{t_i L}{z}} \tag{D.41}$$

$$= 1 - e^{-\left(\lambda_{det} + \frac{1}{z}\sum_{i=1}^{N}(\lambda_i - \lambda_{det})t_i\right)L} \tag{D.42}$$

$$= 1 - e^{-\lambda' L} \tag{D.43}$$

Where $\lambda' = \lambda_{det} + \frac{1}{z}\sum_{i=1}^{N}(\lambda_i - \lambda_{det})t_i$, and

$$PDF_L(L) = \frac{\partial P}{\partial L} = \lambda' e^{-\lambda' L} \tag{D.44}$$

Here λ_i is the attenuation coefficient for a particular i, s_i is the distance a particle travels through layer i, λ_{det} is the attenuation coefficient of the silicon bulk and L is the length the particle travels through the whole detector. It can be seen that Equation D.44 is identical to Equation D.18, except that $\lambda \rightarrow \lambda'$. As none of the steps up to the derivation of $PDF_z(z)$ require an integral with respect to z, $PDF_z(z)$ can be determined using a transformation of Equation D.18 in the bulk silicon case from $\lambda \rightarrow \lambda'$. Therefore,

$$PDF_z(z) = 2z\lambda'^2 Ei(-\lambda' z) + 2\lambda' e^{-\lambda' z} \tag{D.45}$$

Another useful way to express Equation D.45 is in terms of the distance into the bulk silicon itself, $z_{det} = z - \sum_{i=1}^{N} t_i$. This means that $\lambda' z = \lambda_{det} z + \sum_{i=1}^{N}(\lambda_i - \lambda_{det})t_i$ becomes $\lambda' z = \lambda_{det} z_{det} + \sum_{i=1}^{N} \lambda_i t_i$. $PDF_{z_{det}}(z_{det})$ can be expressed with the same structure as PDF_z because the change of variables of Equation D.45 for $z \rightarrow z_{det}$ has a Jacobian of $\left|\frac{\partial z}{\partial z_{det}}\right| = 1$. Therefore

$$PDF_{z_{det}}(z_{det}) = 2\lambda' \left(e^{-\lambda_{det} z_{det} - \sum_{i=1}^{N} \lambda_i t_i} + \left(\lambda_{det} z_{det} + \sum_{i=1}^{N} \lambda_i t_i\right) Ei\left(-\lambda_{det} z_{det} - \sum_{i=1}^{N} \lambda_i t_i\right)\right) \tag{D.46}$$

E. Determining probability density functions for the emission locations of soft photon-induced X-ray-like background events

To investigate the relationship between fluorescence intensity and position on surfaces within line-of-sight of the detector, a model can be set up as described in Figure E.1 .

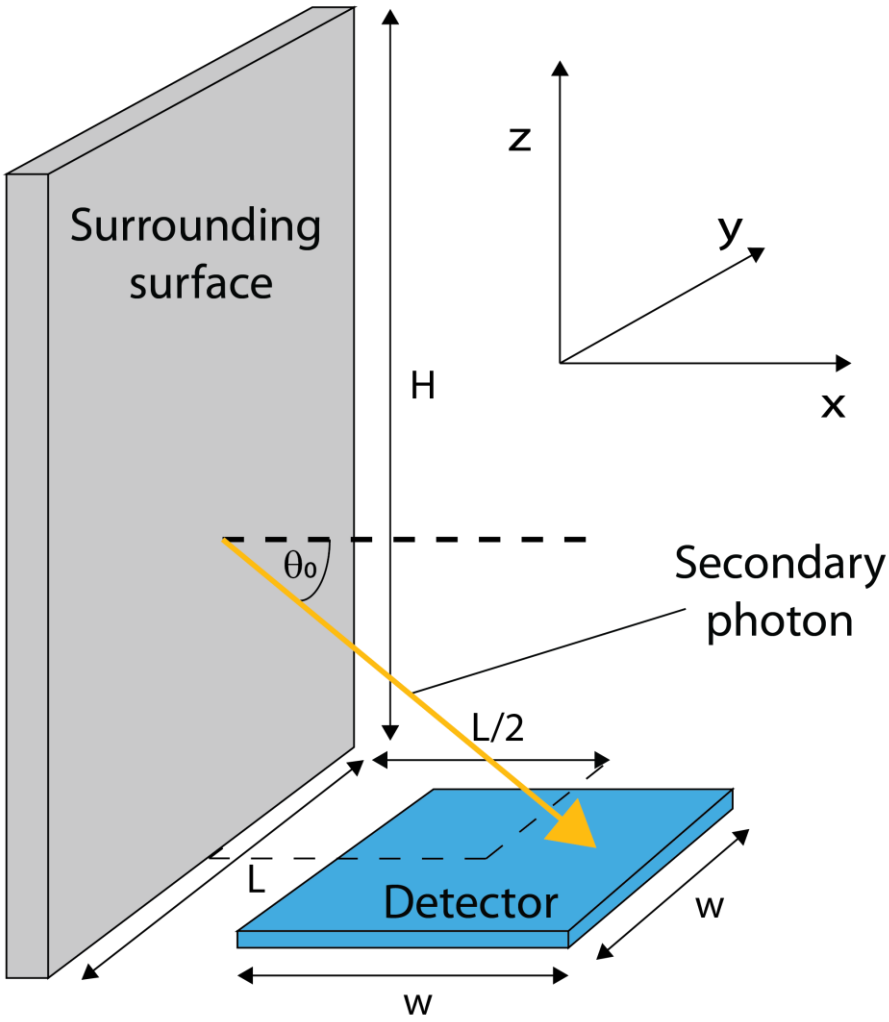

Figure E.1 The geometry used in the mathematics for this section. A particle is generated on the grey vertical surface and has a probability of hitting the horizontal detector surface that depends on its initial location and can be determined using probability density functions. The origin of the coordinate system here, (0,0,0), is positioned at the center of the detector surface.

Here a particle is generated on the vertical surface at a point $\left(-\frac{L}{2}, y_0, z_0\right)$, where momentum is oriented at an angle to the normal θ_0, and with an azimuthal angle about the normal ϕ_0. This model can be used to effectively represent the situation of a square detector placed inside a cuboidal baffle, where the aim is to determine the probability of a fluorescence photon generated in the vertical surface hitting the detector as a function of z_0, or $PDF_{z_0}(z_0)$.

The photon's position is probabilistically uniformly distributed across the vertical surface, and its momentum is given by a Lambertian cosine distribution, which gives a joint probability distribution function for y_0, z_0, θ_0 and ϕ_0 as

$$PDF_{y_0,z_0,\theta_0,\phi_0} = \frac{1}{2\pi HL}\sin(2\theta_0) \tag{E.1}$$

Where $-\frac{L}{2} < y_0 < \frac{L}{2}$, $0 < z_0 < H$, $0 \leq \theta_0 < \frac{\pi}{2}$ and $0 \leq \phi_0 < 2\pi$. To find the probability distribution for the event of the fluorescence photon hitting the detector, it is necessary first to calculate the position where the particle will impact the detector as a function of its initial position and momentum. The position of impact can be calculated by first considering the general trajectory of the particle over time, which is given by

$$\begin{bmatrix} x \\ y \\ z \end{bmatrix} = |v|t \begin{bmatrix} \cos(\theta_0) \\ \sin(\theta_0)\sin(\phi_0) \\ \sin(\theta_0)\cos(\phi_0) \end{bmatrix} + \begin{bmatrix} -\frac{L}{2} \\ y_0 \\ z_0 \end{bmatrix} \tag{E.2}$$

This can be solved for $z = 0$ to give

$$|v|t = -\frac{z_0}{\sin(\theta_0)\cos(\phi_0)} \tag{E.3}$$

Substituting this into the equations for x and y in Equation E.2 gives

$$x = -z_0\cot(\theta_0)\sec(\phi_0) - \frac{L}{2} \tag{E.4}$$

and

$$y = -z_0\tan(\phi_0) + y_0 \tag{E.5}$$

which also gives

$$\phi_0 = \arctan\left(\frac{y_0 - y}{z_0}\right) + n\pi \tag{E.6}$$

and

$$\theta_0 = -\operatorname{arccot}\left(\frac{x + \frac{L}{2}}{z_0\sec(\phi_0)}\right) = (-1)^{n+1}\operatorname{arccot}\left(\frac{x + \frac{L}{2}}{\sqrt{(y - y_0)^2 + z_0^2}}\right) \tag{E.7}$$

For $z_0 > 0$, where n is any integer. Equation E.7 can also be used to calculate that

$$\sin(2\theta_0) = \frac{(-1)^{n+1}\left(2\left(x + \frac{L}{2}\right)\sqrt{(y - y_0)^2 + z_0^2}\right)}{\left(x + \frac{L}{2}\right)^2 + (y - y_0)^2 + z_0^2} \tag{E.8}$$

To find the probability density function $PDF_{x,y}$ it is necessary to find the Jacobian for $\theta_0, \phi_0 \rightarrow x, y$, which is given by

$$\left|J_{\theta_0,\phi_0\to x,y}\right| = \begin{vmatrix} \frac{\partial\theta_0}{\partial x} & \frac{\partial\theta_0}{\partial y} \\ \frac{\partial\phi_0}{\partial x} & \frac{\partial\phi_0}{\partial y} \end{vmatrix} \tag{E.9}$$

$$= \begin{vmatrix} -\frac{(-1)^{n+1}\sqrt{(y_0-y)^2+z_0^2}}{\left(x+\frac{L}{2}\right)^2+(y-y_0)^2+z_0^2} & \frac{(-1)^{n+1}\left(x+\frac{L}{2}\right)(y-y_0)}{\sqrt{(y-y_0)^2+z_0^2}\left(\left(x+\frac{L}{2}\right)^2+(y-y_0)^2+z_0^2\right)} \\ 0 & -\frac{z_0}{(y-y_0)^2+z_0^2} \end{vmatrix} \tag{E.10}$$

$$= \left|(-1)^{n+1}\frac{z_0}{\sqrt{(y-y_0)^2+z_0^2}\times\left(\left(x+\frac{L}{2}\right)^2+(y-y_0)^2+z_0^2\right)}\right| \tag{E.11}$$

$$= \frac{z_0}{\sqrt{(y-y_0)^2+z_0^2}\times\left(\left(x+\frac{L}{2}\right)^2+(y-y_0)^2+z_0^2\right)} \tag{E.12}$$

The probability density function for y_0, z_0, x, y can now be found to be

$$PDF_{y_0,z_0,x,y} = PDF_{y_0,z_0,\theta_0,\phi_0}\times\left|J_{\theta_0,\phi_0\to x,y}\right| \tag{E.13}$$

$$= \frac{1}{2\pi HL}\sin(2\theta_0)\times\left|J_{\theta_0,\phi_0\to x,y}\right| \tag{E.14}$$

$$= \frac{1}{2\pi HL}\frac{(-1)^{n+1}\left(2\left(x+\frac{L}{2}\right)\sqrt{(y-y_0)^2+z_0^2}\right)}{\left(x+\frac{L}{2}\right)^2+(y-y_0)^2+z_0^2} \times\frac{z_0}{\sqrt{(y-y_0)^2+z_0^2}\times\left(\left(x+\frac{L}{2}\right)^2+(y-y_0)^2+z_0^2\right)} \tag{E.15}$$

$$= \frac{z_0(-1)^{n+1}\left(x+\frac{L}{2}\right)}{\pi HL\left(\left(x+\frac{L}{2}\right)^2+(y-y_0)^2+z_0^2\right)^2} \tag{E.16}$$

n can be determined here from the observation using the geometry of the system that to reach $z = 0$, ϕ_0 must be between π and $\frac{3\pi}{2}$. For Equation E.6 to always produce a value of $\pi < \phi_0 < \frac{3\pi}{2}$ for any value of y, y_0 or z_0, n must be equal to 1. Therefore Equation E.16 reduces to

$$PDF_{y_0,z_0,x,y} = \frac{z_0\left(x+\frac{L}{2}\right)}{\pi HL\left(\left(x+\frac{L}{2}\right)^2+(y-y_0)^2+z_0^2\right)^2} \tag{E.17}$$

To now find the full PDF_{z_0}, $PDF_{y_0,z_0,x,y}$ must now be integrated over the full ranges of y_0, x and y. This integration was performed using Mathematica (*Mathematica* 2019) with the constraints that z_0 and L are greater than 0 to give

$$PDF_{y_0,z_0} = \int_{y=-\frac{w}{2}}^{y=\frac{w}{2}}\int_{x=-\frac{w}{2}}^{x=\frac{w}{2}} PDF_{y_0,z_0,x,y}\,dx\,dy \tag{E.18}$$

$$= \frac{2z_0}{\pi HL}\left(\frac{\arctan\left(\frac{w-2y_0}{\sqrt{(L-w)^2+4z_0^2}}\right)+\arctan\left(\frac{w+2y_0}{\sqrt{(L-w)^2+4z_0^2}}\right)}{\sqrt{(L-w)^2+4z_0^2}}\right. \tag{E.19}$$
$$\left. -\frac{\arctan\left(\frac{w-2y_0}{\sqrt{(L+w)^2+4z_0^2}}\right)+\arctan\left(\frac{w+2y_0}{\sqrt{(L+w)^2+4z_0^2}}\right)}{\sqrt{(L+w)^2+4z_0^2}}\right)$$

Integrating across the full range of y_0 now gives

$$PDF_{z_0} = \int_{y_0=-\frac{L}{2}}^{y_0=\frac{L}{2}} PDF_{y_0,z_0}\,dy_0 \tag{E.20}$$

$$= \frac{z_0}{\pi HL}\left(\frac{(-L+w)\arctan\left(\frac{L-w}{\sqrt{(L-w)^2+4z_0^2}}\right)+(L+w)\arctan\left(\frac{L+w}{\sqrt{(L-w)^2+4z_0^2}}\right)}{\sqrt{(L-w)^2+4\,z_0^2}}\right.$$
$$+\frac{(L-w)\arctan\left(\frac{L-w}{\sqrt{(L+w)^2+4z_0^2}}\right)+(-L-w)\arctan\left(\frac{L+w}{\sqrt{(L+w)^2+4z_0^2}}\right)}{\sqrt{(L+w)^2+4z_0^2}} \tag{E.21}$$
$$\left.+\frac{1}{2}(\ln((L-w)^2+2z_0^2)-2\ln(L^2+w^2+2z_0^2)+\ln((L+w)^2+2z_0^2))\right)$$

This can be expressed more simply as

$$k_{\pm} = \sqrt{(L \pm w)^2 + 4z_0^2} \tag{E.22}$$

$$d_{\pm} = L \pm w \tag{E.23}$$

$$\begin{aligned} PDF_{z_0} = \frac{z_0}{\pi HL}\Bigg(&\frac{1}{2}(\ln(d_-^2 + 2z_0^2) - 2\ln(L^2 + w^2 + 2z_0^2) + \ln(d_+^2 + 2z_0^2)) \\ &- \frac{d_-}{\mathrm{k}_-}\arctan\left(\frac{d_-}{k_-}\right) + \frac{d_+}{k_-}\arctan\left(\frac{d_+}{k_-}\right) + \frac{d_-}{k_+}\arctan\left(\frac{d_-}{k_+}\right) \\ &- \frac{d_+}{k_+}\arctan\left(\frac{d_+}{k_+}\right)\Bigg) \end{aligned} \tag{E.24}$$

or as

$$\begin{aligned} PDF_{z_0} = \frac{2z_0}{\pi HL}\Bigg(&\frac{1}{2}\left(\ln\left(d_-^2 + 2z_0^2\right) - 2\ln\left(L^2 + w^2 + 2z_0^2\right) + \ln\left(d_+^2 + 2z_0^2\right)\right) \\ &- \left[\left[\frac{d}{k}\arctan\left(\frac{d}{k}\right)\right]_{k=k_-}^{k=k_+}\right]_{d=d_-}^{d=d_+}\Bigg) \end{aligned} \tag{E.25}$$

F. Derivations of minimum vertical positions for particles generated from surfaces in uniform magnetic shielding fields

The geometries displayed in Figure F.1 are used for the calculations in the F appendices.

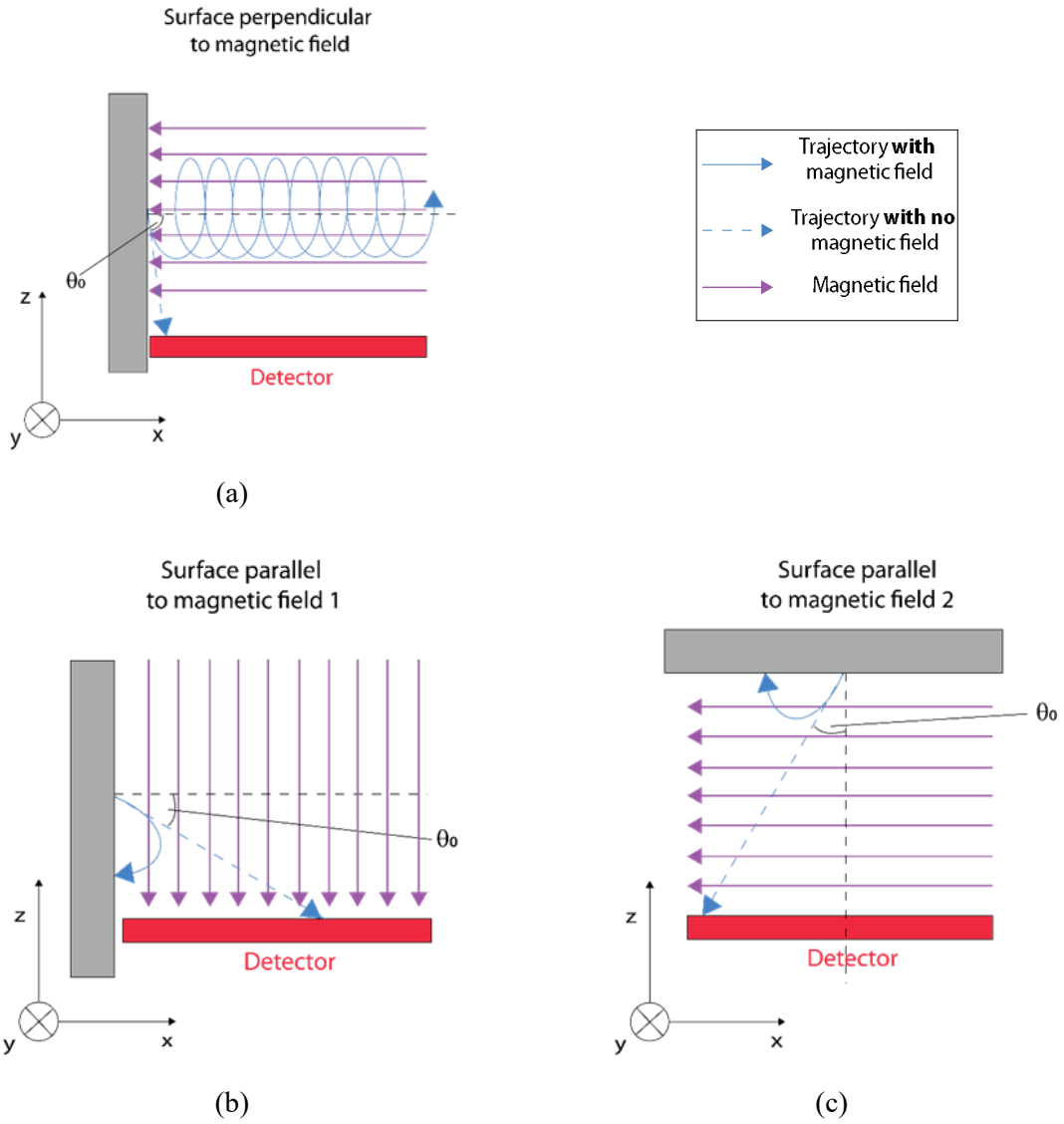

Figure F.1 The different orientations of uniform magnetic fields that are capable of removing electron-induced background that will be investigated in this chapter.

F.1 Deriving the minimum vertical position of a particle emitted from a surface in a uniform magnetic field

As was described in Chapter 2, for a uniform magnetic field oriented in the z-direction, the commonly used parameter, particle gyroradius, is given by

$$r_g = \frac{\sqrt{\boldsymbol{p}_\perp^2}}{|q||\boldsymbol{B}|} \tag{F.1}$$

where $\boldsymbol{p}_\perp$ is the momentum of the particle perpendicular to the magnetic field, q is the charge of the particle, and $\boldsymbol{B}$ is the magnetic field, which has a component of B along positive x, z and x for the geometries shown in Figure F.1(a), Figure F.1(b) and Figure F.1(c) respectively. Using this it is possible to calculate the maximum distance a particle will travel from the surface it originated from as a function of its original momentum direction, where the particle velocity as a function of time can be given by

$$\boldsymbol{v}_\perp = \begin{bmatrix} \cos\left(\frac{v_{\perp,0}t}{r_g}\right) & \sin\left(\frac{v_{\perp,0}t}{r_g}\right) \\ -\sin\left(\frac{v_{\perp,0}t}{r_g}\right) & \cos\left(\frac{v_{\perp,0}t}{r_g}\right) \end{bmatrix} \boldsymbol{v}_{\perp,\mathbf{0}} \tag{F.2}$$

Where $\boldsymbol{v}_\perp$ is the velocity perpendicular to the magnetic field, $\boldsymbol{v}_{\perp,\mathbf{0}}$ is the initial velocity perpendicular to the magnetic field, $v_{\perp,0}$ is the magnitude of the initial perpendicular velocity, and t is time. Equation F.2 can be integrated with respect to time to give

$$\boldsymbol{r}_\perp = \int_0^t \boldsymbol{v}_\perp \, dt = \frac{r_g}{v_{\perp,0}} \begin{bmatrix} \sin\left(\frac{v_{\perp,0}t}{r_g}\right) & 1-\cos\left(\frac{v_{\perp,0}t}{r_g}\right) \\ -\left(1-\cos\left(\frac{v_{\perp,0}t}{r_g}\right)\right) & \sin\left(\frac{v_{\perp,0}t}{r_g}\right) \end{bmatrix} \boldsymbol{v}_{\perp,\mathbf{0}} + \boldsymbol{r}_{\perp,\mathbf{0}} \tag{F.3}$$

where $\boldsymbol{r}_\perp$ is the component of the position of the particle perpendicular to the magnetic field. This expression can be generalised for each of the three cases to

$$\boldsymbol{r} = \int_0^t \boldsymbol{v} \, dt = \frac{1}{\omega_g} \underline{\underline{\boldsymbol{M}}} \boldsymbol{v}_\mathbf{0} + \boldsymbol{r}_\mathbf{0} \tag{F.4}$$

Where $\underline{\underline{\boldsymbol{M}}}$ for each of the three cases is

$$\underline{\underline{\boldsymbol{M}}}_{\perp,\mathbf{1}} = \underline{\underline{\boldsymbol{M}}}_{\parallel,\mathbf{2}} = \begin{bmatrix} \omega_g t & 0 & 0 \\ 0 & \sin(\omega_g t) & 1-\cos(\omega_g t) \\ 0 & -(1-\cos(\omega_g t)) & \sin(\omega_g t) \end{bmatrix} \tag{F.5}$$

$$\underline{\underline{\boldsymbol{M}}}_{\parallel,\mathbf{1}} = \begin{bmatrix} \sin(\omega_g t) & 1-\cos(\omega_g t) & 0 \\ -(1-\cos(\omega_g t)) & \sin(\omega_g t) & 0 \\ 0 & 0 & \omega_g t \end{bmatrix} \tag{F.6}$$

where $\omega_g = \frac{qB}{\gamma m_0}$ is the gyrofrequency of the system, γ is the Lorentz factor for the particle and m_0 is the rest mass of the particle, and the labels ($\perp$,1), ($\parallel$,1) and ($\parallel$,2) refer to the geometries given in Figure F.1(a), Figure F.1(b) and Figure F.1(c) respectively.

The initial velocity of the particle in each case can be described using

$$\boldsymbol{v}_{\perp,\mathbf{1}} = \boldsymbol{v}_{\parallel,\mathbf{1}} = \begin{bmatrix} v\cos(\theta_0) \\ v\sin(\theta_0)\sin(\phi_0) \\ v\sin(\theta_0)\cos(\phi_0) \end{bmatrix} \tag{F.7}$$

$$\boldsymbol{v}_{\parallel,\mathbf{2}} = \begin{bmatrix} v\sin(\theta_0)\cos(\phi_0) \\ v\sin(\theta_0)\sin(\phi_0) \\ -v\cos(\theta_0) \end{bmatrix} \tag{F.8}$$

where θ_0 is the angle the particle is produced at relative to the normal to the particle generation surface, and ϕ_0 is the azimuthal angle of emission around the normal to the generation surface. Setting $\boldsymbol{r_0} = \mathbf{0}$ and substituting $\boldsymbol{v}_{\perp,\mathbf{1}}, \boldsymbol{v}_{\parallel,\mathbf{1}}$ and $\boldsymbol{v}_{\parallel,\mathbf{2}}$ into Equation F.4, the value of z as a function of t in each case are found to be

$$z_{\perp,1} = \frac{2v}{\omega_g}\sin(\theta_0)\sin\left(\frac{1}{2}\omega_g t\right)\cos\left(\phi_0 - \frac{1}{2}\omega_g t\right) \tag{F.9}$$

$$z_{\parallel,1} = vt\cos(\phi_0)\sin(\theta_0) \tag{F.10}$$

$$z_{\parallel,2} = \frac{-v}{\omega_g}\left(\cos(\theta_0)\sin(\omega_g t) + \left(1 - \cos(\omega_g t)\right)\sin(\phi_0)\sin(\theta_0)\right) \tag{F.11}$$

$z_{\perp,1}$ and $z_{\parallel,2}$ must now be minimised with respect to t, while $z_{\parallel,1}$ must be solved for the case where $x_{\parallel,1} = 0$, where $x_{\parallel,1}$ is

$$x_{\parallel,1} = \frac{v}{\omega_g}\left(\cos(\theta_0)\sin(\omega_g t) + \left(1 - \cos(\omega_g t)\right)\sin(\phi_0)\sin(\theta_0)\right) \tag{F.12}$$

Minimising $z_\perp$ and $z_{\parallel,2}$ with respect to t gives

$$z_{\perp,1,min} = -\frac{v}{\omega_g}(\sin(\phi_0) \pm 1)\sin(\theta_0) \tag{F.13}$$

$$z_{\parallel,2,min} = -\frac{v}{\omega_g}\left(\sin(\phi_0)\sin(\theta_0) \pm \sqrt{1 - \sin^2(\theta_0)\cos^2(\phi_0)}\right) \tag{F.14}$$

While solving $x_{\parallel,1} = 0$ for t and inserting into Equation F.10 gives

$$z_{\parallel,1,min} = \frac{v}{\omega_g}(\mathrm{atan2}((\sin^2(\phi_0) + 1)\sin^2(\theta_0) - 1, -\sin(2\theta_0)\cos(\phi_0)) + 2\pi C)\sin(\phi_0)\sin(\theta_0) \tag{F.15}$$

Where C is an integer.

Therefore, for a positive ω_g the minimum possible values for z in each case when ϕ_0 and θ_0 are varied are

$$z_{\perp,1,min} = -\frac{v}{\omega_g}(\sin(\phi_0) + 1)\sin(\theta_0) \tag{F.16}$$

$$z_{\parallel,1,min} = \frac{v}{\omega_g}\operatorname{atan2}(\sin^2(\theta_0)\,(1 + \cos^2(\phi_0)) - 1, -\cos(\phi_0)\sin(2\theta_0))\sin(\phi_0)\sin(\theta_0) \tag{F.17}$$

$$z_{\parallel,2,min} = -\frac{v}{\omega_g}\left(\sin(\phi_0)\sin(\theta_0) + \sqrt{1 - \sin^2(\theta_0)\cos^2(\phi_0)}\right) \tag{F.18}$$

F.2 The probability distribution for the perpendicular case

It is possible to calculate the probability density function for $z_{\perp,1,min}$ in Equation F.16, Appendix F.1, using several substitutions and the methods described in Appendix B.1 . The substitution $\alpha = -\frac{v}{\omega_g}\sin(\theta_0)$, $\beta = (\sin(\phi_0) + 1)$ can be used, meaning that $\theta_0 = \arcsin\left(\frac{-\omega_g \alpha}{v}\right)$ and that $\sin(2\theta_0) = -\frac{2\alpha\omega_g}{v}\sqrt{1 - \left(\frac{\alpha\omega_g}{v}\right)^2}$. ϕ_0 has two possible values, either $\phi_0 = 2\pi n + \arcsin(\beta - 1)$ or $\phi_0 = 2\pi n + \pi - \arcsin(\beta - 1)$ where n is any integer. As $PDF_{\theta_0,\phi_0} = \frac{1}{2\pi}\sin(2\theta_0)$ is invariant with respect to ϕ_0, and the derivatives of each value for ϕ_0 with respect to β only differ by a factor of -1, the single value of $\phi_0 = 2\pi n + \arcsin(\beta - 1)$ can be used for calculations with the caveat that the overall probability distribution must be multiplied by a factor of 2 to account for both solutions. The Jacobian is then

$$J = \begin{vmatrix} \frac{\omega_g}{\sqrt{v^2 - \alpha^2\omega_g^2}} & 0 \\ 0 & \frac{1}{\sqrt{1 - (1-\beta)^2}} \end{vmatrix} = \frac{|\omega_g|}{\sqrt{v^2 - \alpha^2\omega_g^2}\sqrt{1 - (1-\beta)^2}} \tag{F.19}$$

Therefore the probability density function of α and β is

$$PDF_{\alpha,\beta} = \frac{2 \times |\omega_g| \sin(2\theta_0)}{2\pi\sqrt{v^2 - \alpha^2\omega_g^2}\sqrt{1 - (1-\beta)^2}} \tag{F.20}$$

$$= \frac{|\omega_g| \times \frac{2\alpha\omega_g}{v}\sqrt{1 - \left(\frac{\alpha\omega_g}{v}\right)^2}}{\pi\sqrt{v^2 - \alpha^2\omega_g^2}\sqrt{1 - (1-\beta)^2}} \tag{F.21}$$

$$= \frac{2\,sgn(\omega_g)|\omega_g|^2\alpha}{\pi v^2\sqrt{1 - (1-\beta)^2}} \tag{F.22}$$

The limits of these variables are $-\frac{v}{\omega_g} < \alpha \leq 0$ for positive ω_g, $0 \leq \alpha < -\frac{v}{\omega_g}$ for positive ω_g, and $0 \leq \beta \leq 2$. Now the final step that must be taken is perform the substitution $\alpha = \frac{z_{\perp,1,min}}{\beta}$ and integrate

over β in order to find the probability density function for $z_{\perp,1,min}$. This integration has to be performed while utilising the limit that $-\frac{v}{\omega_g} < \alpha \leq 0$, meaning that $-\frac{v}{\omega_g} < \frac{z_{\perp,1,min}}{\beta} \leq 0$ or that $\beta > -\frac{\omega_g z_{\perp,1,min}}{v}$, Performing this substitution and integration gives

$$PDF_{z_{\perp,1,min}} = \int_{\beta=0}^{\beta=2} \frac{2\, sgn(\omega_g)|\omega_g|^2 \left(\frac{z_{\perp,1,min}}{\beta}\right)}{\pi v^2 \sqrt{1-(1-\beta)^2}} \times \left|\frac{1}{\beta}\right| \delta\left(-\frac{\omega_g z_{\perp,1,min}}{v} < \beta\right) d\beta \tag{F.23}$$

$$= \int_{\beta=-\frac{\omega_g z_{\perp,1,min}}{v}}^{\beta=2} \frac{2\, sgn(\omega_g)|\omega_g|^2 z_{\perp,1,min}}{\pi v^2 \beta^2 \sqrt{1-(1-\beta)^2}} d\beta \tag{F.24}$$

$$= \frac{2\, sgn(\omega_g)\sqrt{-\omega_g z_{\perp,1,min}(2v+\omega_g z_{\perp,1,min})}(\omega_g z_{\perp,1,min} - v)}{3\pi v^2 z_{\perp,1,min}} \tag{F.25}$$

Where the limits for $z_{\perp,1,min}$ are $-\frac{2v}{\omega_g} < z_{\perp,1,min} \leq 0$ for positive ω_g.

F.3 The probability distribution for the second parallel case

For the second parallel case, several more steps must be taken than in the perpendicular case to find the probability distribution of $z_{\parallel,2,min}$. The first step is to perform the substitution $S_\theta = \sin(\theta_0)$ and $S_\phi = \sin(\phi_0)$ which can be used to convert Equation F.18 in Appendix F.1 into

$$z_{\parallel,2,min} = -\frac{v}{\omega_g}\left(S_\phi S_\theta + \sqrt{1 - S_\theta^2(1-S_\phi^2)}\right) \tag{F.26}$$

Where the joint probability distribution for S_ϕ and S_θ can be calculated using $PDF_{\theta,\phi} = \frac{\sin(2\theta)}{2\pi}$ to be

$$PDF_{S_\theta,S_\phi} = \frac{2S_\theta}{\pi\sqrt{1-S_\phi^2}} \tag{F.27}$$

Where $0 < S_\theta \leq 1$ and $-1 \leq S_\phi \leq 1$. A change of variables now needs to be performed on Equation F.27 where S_ϕ can be replaced with x and S_θ. Rearranging Equation F.26 gives

$$S_\phi = \frac{v^2(1-S_\theta^2) - \omega_g^2 z_{\parallel,2,min}^2}{2\omega_g S_\theta v z_{\parallel,2,min}} \tag{F.28}$$

and

$$\frac{\partial S_\phi}{\partial z_{\parallel,2,min}} = \frac{v^2(S_\theta^2-1) - \omega_g^2 z_{\parallel,2,min}^2}{2\omega_g S_\theta v z_{\parallel,2,min}^2} \tag{F.29}$$

The limits of $-1 \leq S_\phi \leq 1$ also need to be taken into account, and substituting Equation F.28 into these limits gives $-1 \leq \frac{v^2(1-S_\theta^2)-\omega_g^2 z_{\parallel,2,min}^2}{2\omega_g S_\theta v z_{\parallel,2,min}} \leq 1$, which for $\omega_g > 0$ reduces to $-1 - \frac{\omega_g z_{\parallel,2,min}}{v} \leq S_\theta < 1$ for $-\frac{2v}{\omega_g} \leq z_{\parallel,2,min} \leq -\frac{v}{\omega_g}$ and $1 + \frac{\omega_g z_{\parallel,2,min}}{v} \leq S_\theta < 1$ for $1 < -\frac{v}{\omega_g} < z_{\parallel,2,min} \leq 0$ after some

calculation. Substituting Equation F.28 into PDF_{S_θ,S_ϕ} and multiplying by $\left|\frac{\partial S_\phi}{\partial z_{\parallel,2,min}}\right|$ with the constraints that $z_{\parallel,2,min} < 0$ gives the full joint probability density function for $z_{\parallel,2,min}$ and S_θ as

$$PDF_{z_{\parallel,2,min},S_\theta} = \frac{2S_\theta\left(v^2\left(1-S_\theta^2\right)+\omega_g^2 z_{\parallel,2,min}^2\right)}{-\pi z_{\parallel,2,min}\sqrt{-\prod_{n=-1,1,m=-1,1}(v(n+mS_\theta)+\omega_g z_{\parallel,2,min})}} \tag{F.30}$$

where $\Pi_{n=-1,1,m=-1,1}$ represents a product over the values of n and m. To obtain the single variable probability distribution function for $z_{\parallel,2,min}$, $PDF_{z_{\parallel,2,min},S_\theta}$ must now be integrated across the full range of S_θ for both the limits $-1-\frac{\omega_g z_{\parallel,2,min}}{v} \le S_\theta < 1$ for $-\frac{2v}{\omega_g} \le z_{\parallel,2,min} \le -\frac{v}{\omega_g}$ and $1+\frac{\omega_g z_{\parallel,2,min}}{v} \le S_\theta < 1$ for $1 < -\frac{v}{\omega_g} < z_{\parallel,2,min} \le 0$. Fortunately, each of these integrals produces the same result of

$$\begin{aligned} PDF_{z_{\parallel,2,min}} &= \int_{S_\theta=1+\frac{\omega_g z_{\parallel,2,min}}{v}}^{S_\theta=1} PDF_{z_{\parallel,2,min},S_\theta} dS_\theta \\ &= \int_{S_\theta=-1-\frac{\omega_g z_{\parallel,2,min}}{v}}^{S_\theta=1} PDF_{z_{\parallel,2,min},S_\theta} dS_\theta \end{aligned} \tag{F.31}$$

$$= \frac{|\omega_g|}{\pi v}\sqrt{4-\frac{\omega_g^2 z_{\parallel,2,min}^2}{v^2}} \tag{F.32}$$

Where the limits are $-\frac{2v}{\omega_g} \le z_{\parallel,2,min} \le 0$.

Bibliography

Ackermann, M., M. Ajello, A. Allafort, L. Baldini, J. Ballet, G. Barbiellini, M. G. Baring, et al. 2013. "Detection of the Characteristic Pion-Decay Signature in Supernova Remnants." *Science* 339 (6121): 807–11. https://doi.org/10.1126/science.1231160.

Adriani, O., Y. Akaike, K. Asano, Y. Asaoka, M. G. Bagliesi, G. Bigongiari, W. R. Binns, et al. 2017. "Energy Spectrum of Cosmic-Ray Electron and Positron from 10 GeV to 3 TeV Observed with the Calorimetric Electron Telescope on the International Space Station." *Physical Review Letters* 119 (18): 181101. https://doi.org/10.1103/PhysRevLett.119.181101.

Agostinelli, S., J. Allison, K. Amako, J. Apostolakis, H. Araujo, P. Arce, M. Asai, et al. 2003. "GEANT4 - A Simulation Toolkit." *Nuclear Instruments and Methods in Physics Research, Section A: Accelerators, Spectrometers, Detectors and Associated Equipment* 506 (3): 250–303. https://doi.org/10.1016/S0168-9002(03)01368-8.

Aguilar, M., D. Aisa, B. Alpat, A. Alvino, G. Ambrosi, K. Andeen, L. Arruda, et al. 2015. "Precision Measurement of the Proton Flux in Primary Cosmic Rays from Rigidity 1 GV to 1.8 TV with the Alpha Magnetic Spectrometer on the International Space Station." *Physical Review Letters* 114 (17): 34. https://doi.org/10.1103/PhysRevLett.114.171103.

Aird, James, Andrea Comastri, Marcella Brusa, Nico Cappelluti, Alberto Moretti, Eros Vanzella, Marta Volonteri, et al. 2013. "The Hot and Energetic Universe: The Formation and Growth of the Earliest Supermassive Black Holes." *ArXiv* 1306.2325: 8.

Antiochos, S. K., C. R. DeVore, and J. A. Klimchuk. 1999. "A Model for Solar Coronal Mass Ejections." *The Astrophysical Journal* 510 (1): 485–93. https://doi.org/10.1086/306563.

Apostolakis, John. n.d. "Magnetic Field." Geant4 Beginners Course. Accessed September 23, 2020. https://doi.org/10.5.

Assa'd, Ahmad M. D., and Mohamed M. El-Gomati. 1998. "Backscattering Coefficients for Low Energy Electrons." *Scanning Microscopy* 12 (1): 185.

Atwell, William, Kristina Rojdev, S. K. Aghara, and Sirikul Sriprisan. 2013. "Mitigating the Effects of the Space Radiation Environment: A Novel Approach of Using Graded-Z Materials." *AIAA SPACE 2013 Conference and Exposition*, 1–12. https://doi.org/10.2514/6.2013-5385.

Bähr, Alexander, Stefan Aschauer, Bettina Bergbauer, Peter H. Lechner, Petra Majewski, Norbert

Meidinger, Sabine M. Ott, et al. 2014. “Development of DEPFET Active Pixel Sensors to Improve the Spectroscopic Response for High Time Resolution Applications.” In *Space Telescopes and Instrumentation 2014: Ultraviolet to Gamma Ray*, 9144:914411. https://doi.org/10.1117/12.2055411.

Bakr, S., D. D. Cohen, R. Siegele, S. Incerti, V. Ivanchenko, A. Mantero, A. Rosenfeld, and S. Guatelli. 2018. “Latest Geant4 Developments for PIXE Applications.” *Nuclear Instruments and Methods in Physics Research, Section B: Beam Interactions with Materials and Atoms* 436: 285–91. https://doi.org/10.1016/j.nimb.2018.10.004.

Bamford, R. A., B. Kellett, J. Bradford, T. N. Todd, M. G. Benton, R. Stafford-Allen, E. P. Alves, et al. 2014. “An Exploration of the Effectiveness of Artificial Mini-Magnetospheres as a Potential Solar Storm Shelter for Long Term Human Space Missions.” *Acta Astronautica* 105 (2): 385–94. https://doi.org/10.1016/j.actaastro.2014.10.012.

Barbera, Marco, Giancarlo Parodi, Antonino Buttacavoli, Alfonso Collura, Kurt Dittrich, Fabio D’Anca, Salvatore Ferruggia Bonura, et al. 2018. “Structural Modelling and Mechanical Tests Supporting the Design of the ATHENA X-IFU Thermal Filters and WFI Optical Blocking Filter.” In , 153. https://doi.org/10.1117/12.2314451.

Barcons, X., K. Nandra, D. Barret, J. W. Den Herder, A. C. Fabian, L. Piro, and M. G. Watson. 2015. “Athena: The X-Ray Observatory to Study the Hot and Energetic Universe.” *Journal of Physics: Conference Series* 610 (1). https://doi.org/10.1088/1742-6596/610/1/012008.

Barret, Didier, Jan-Willem den Herder, Thien Lam Trong, Luigi Piro, Massimo Cappi, Juhani Houvelin, Richard Kelley, et al. 2018. “The ATHENA X-Ray Integral Field Unit (X-IFU).” In *Space Telescopes and Instrumentation 2018: Ultraviolet to Gamma Ray*, edited by Jan-Willem A. den Herder, Kazuhiro Nakazawa, and Shouleh Nikzad, 10699:51. SPIE. https://doi.org/10.1117/12.2312409.

Barret, Didier, Thien Lam Trong, Jan-Willem den Herder, Luigi Piro, Xavier Barcons, Juhani Huovelin, Richard Kelley, et al. 2016. “The Athena X-Ray Integral Field Unit (X-IFU).” In *Space Telescopes and Instrumentation 2016: Ultraviolet to Gamma Ray*, edited by Jan-Willem A. den Herder, Tadayuki Takahashi, and Marshall Bautz, 9905:99052F. International Society for Optics and Photonics. https://doi.org/10.1117/12.2232432.

Basaglia, Tullio, Min Cheol Han, Gabriela Hoff, Chan Hyeong Kim, Sung Hun Kim, Maria Grazia Pia, and Paolo Saracco. 2015. “Investigation of Geant4 Simulation of Electron Backscattering.” *IEEE Transactions on Nuclear Science* 62 (4): 1805–12. https://doi.org/10.1109/TNS.2015.2442292.

Batič, Matej, Gabriela Hoff, Maria Grazia Pia, Paolo Saracco, and Georg Weidenspointner. 2013. "Validation of Geant4 Simulation of Electron Energy Deposition." *IEEE Transactions on Nuclear Science* 60 (4): 2934–57. https://doi.org/10.1109/TNS.2013.2272404.

Berger, M.J., J.S. Coursey, M.A. Zucker, and J Chang. 2017. "Stopping-Power & Range Tables for Electrons, Protons, and Helium Ions." *Nistir* 4999: 1–17. https://doi.org/10.18434/T4NC7P.

Berger, MJ, JS Coursey, MA Zucker, and J Chang. 2005. "NIST Standard Reference Database 124: Stopping-Power and Range Tables for Electrons, Protons, and Helium Ions."

Beutier, T., E. Delage, M. Wouts, … O Serres - Proceedings of the, Undefined 2003, O. Serres, and P. F. Peyrard. 2003. "Fastrad New Tool for Radiation Prediction." In *Proceedings of the 7th European Conference on Radiation and Its Effects on Components and Systems, 2003*, RADECS 200:181–83. Noordwijk, The Netherlands: IEEE.

Bolst, David, Giuseppe A.P. Cirrone, Giacomo Cuttone, Gunter Folger, Sebastien Incerti, Vladimir Ivanchenko, Tatsumi Koi, et al. 2017. "Validation of Geant4 Fragmentation for Heavy Ion Therapy." *Nuclear Instruments and Methods in Physics Research, Section A: Accelerators, Spectrometers, Detectors and Associated Equipment* 869 (October): 68–75. https://doi.org/10.1016/j.nima.2017.06.046.

Boscherini, M., O. Adriani, M. Bongi, L. Bonechi, G. Castellini, R. D'Alessandro, A. Gabbanini, et al. 2003. "Radiation Damage of Electronic Components in Space Environment." In *Nuclear Instruments and Methods in Physics Research, Section A: Accelerators, Spectrometers, Detectors and Associated Equipment*, 514:112–16. North-Holland. https://doi.org/10.1016/j.nima.2003.08.091.

Brown, Robert G. 2007. "Classical Electrodynamics, Part II," 357.

Bulbul, Esra, Ralph Kraft, Paul Nulsen, Michael Freyberg, Eric D. Miller, Catherine Grant, Mark W. Bautz, et al. 2020. "Characterization of the Particle-Induced Background of XMM-Newton EPIC-Pn: Short- and Long-Term Variability." *The Astrophysical Journal* 891 (1): 13. https://doi.org/10.3847/1538-4357/ab698a.

Burrows, David N., Steve Allen, Marshall Bautz, Esra Bulbul, Tanmoy Chattopadhyay, Julia Erdley, Abraham D. Falcone, et al. 2019. "US Contributions to the Athena Wide Field Imager." In *UV, X-Ray, and Gamma-Ray Space Instrumentation for Astronomy XXI*, edited by Oswald H. Siegmund, 11118:34. SPIE. https://doi.org/10.1117/12.2528532.

Burt, Joe, and Bob Smith. 2012. "Deep Space Climate Observatory: The DSCOVR Mission." In *IEEE Aerospace Conference Proceedings*, 1–13. https://doi.org/10.1109/AERO.2012.6187025.

Cane, H. V., G. Wibberenz, I. G. Richardson, and T. T. Von Rosenvinge. 1999. "Cosmic Ray Modulation and the Solar Magnetic Field." *Geophysical Research Letters* 26 (5): 565–68. https://doi.org/10.1029/1999GL900032.

"CCD97-00 Back Illuminated 2-Phase IMO Series Electron Multiplying CCD Sensor Datasheet." n.d. *E2v Technologies*, no. 3.

Chen, Francis F. 1984. *Introduction to Plasma Physics and Controlled Fusion*. *Introduction to Plasma Physics and Controlled Fusion*. Springer US. https://doi.org/10.1007/978-1-4757-5595-4.

Christon, S. P., T. E. Eastman, T. Doke, L. A. Frank, G. Gloeckler, H. Kojima, S. Kokubun, et al. 1998. "Magnetospheric Plasma Regimes Identified Using Geotail Measurements: 2. Statistics, Spatial Distribution, and Geomagnetic Dependence." *Journal of Geophysical Research: Space Physics* 103 (A10): 23521–42. https://doi.org/10.1029/98ja01914.

Corti, C, V Bindi, C Consolandi, and K Whitman. 2016. "SOLAR MODULATION OF THE LOCAL INTERSTELLAR SPECTRUM WITH VOYAGER 1 , AMS-02, PAMELA , AND BESS." *The Astrophysical Journal* 829 (1): 8. https://doi.org/10.3847/0004-637x/829/1/8.

Davis, C. S.W., D. Hall, J. Keelan, J. O'Farrell, M. Leese, and A. Holland. 2018. "Mitigation Strategies against Radiation-Induced Background for Space Astronomy Missions." In *Journal of Instrumentation*, 13:C01015. IOP Publishing. https://doi.org/10.1088/1748-0221/13/01/C01015.

Devore, Jay L., and Kenneth N. Berk. 2012. *Modern Mathematical Statistics with Applications*. Springer Texts in Statistics. New York, NY: Springer New York. https://doi.org/10.1007/978-1-4614-0391-3.

Diebold, Sebastian, Chris Tenzer, Emanuele Perinati, Andrea Santangelo, Michael Freyberg, Peter Friedrich, and Josef Jochum. 2015. "Soft Proton Scattering Efficiency Measurements on X-Ray Mirror Shells." *Experimental Astronomy* 39 (2): 343–65. https://doi.org/10.1007/s10686-015-9451-4.

Ding, Xuehao. 2018. "Reducing the ATHENA WFI Background." 2018. http://cs229.stanford.edu/proj2018/report/216.pdf.

Dondero, Paolo, and A Mantero. 2017. "A 'Space Dedicated' GEANT4 Physics List from the AREMBES Project." 12th Geant4 Space Users Workshop. 2017. https://indico.esa.int/event/160/contributions/1136/.

Dondero, Paolo, Alfonso Mantero, Vladimir Ivanchencko, Simone Lotti, Teresa Mineo, and Valentina Fioretti. 2018. "Electron Backscattering Simulation in Geant4." *Nuclear Instruments and*

Methods in Physics Research, Section B: Beam Interactions with Materials and Atoms 425: 18–25. https://doi.org/10.1016/j.nimb.2018.03.037.

Doyle, Dominic, Göran Pilbratt, and Jan Tauber. 2009. "The Herschel and Planck Space Telescopes." *Proceedings of the IEEE* 97 (8): 1403–11. https://doi.org/10.1109/JPROC.2009.2017106.

Eastman, T. E., S. P. Christon, T. Doke, L. A. Frank, G. Gloeckler, H. Kojima, S. Kokubun, et al. 1998. "Magnetospheric Plasma Regimes Identified Using Geotail Measurements: 1. Regime Identification and Distant Tail Variability." *Journal of Geophysical Research: Space Physics* 103 (A10): 23503–20. https://doi.org/10.1029/98ja01915.

Elkington, S. R., M. K. Hudson, A. A. Chan, S. R. Elkington, M. K. Hudson, and A. A. Chan. 2001. "Enhanced Radial Diffusion of Outer Zone Electrons in an Asymmetric Geomagnetic Field." *AGUSM* 2001: SM32C-04.

Eraerds, Tanja, Valeria Antonelli, Chris Davis, David Hall, Oliver Hetherington, Andrew Holland, Jonathan Keelan, et al. 2020. "Enhanced Simulations on the ATHENA/WFI Instrumental Background." In *Space Telescopes and Instrumentation 2020: Ultraviolet to Gamma Ray*, edited by Jan-Willem A. den Herder, Kazuhiro Nakazawa, and Shouleh Nikzad, 11444:49. SPIE. https://doi.org/10.1117/12.2560932.

Evans, Steven W. 2003. "Natural Environment near the Sun/Earth-Moon L2 Libration Point." NASA Report. 2003. http://snap.lbl.gov/pub/bscw.cgi/S4b738c42/d84104/SNAP-TECH-03009.pdf.

Fabian, A. C., and X. Barcons. 1992. "The Origin of the X-Ray Background." *Annu. Rev. Astron. Astrophys* 30 (1): 429–56. https://doi.org/10.1146/annurev.aa.30.090192.002241.

Fairfield, D. H. 1992. "On the Structure of the Distant Magnetotail: ISEE 3." *Journal of Geophysical Research* 97 (A2): 1403. https://doi.org/10.1029/91ja02388.

Fan, Wesley C., Clifton R. Drumm, Stanley B. Roeske, and Gary J. Scrivner. 1996. "Shielding Considerations for Satellite Microelectronics." *IEEE Transactions on Nuclear Science* 43 (6 PART 1): 2790–96. https://doi.org/10.1109/23.556868.

Farquhar, Robert W., and David W. Dunham. 1990. "Use of Libration-Point Orbits for Space Observatories." *International Astronomical Union Colloquium* 123 (January): 391–95. https://doi.org/10.1017/s0252921100077332.

"FASTRAD Software for Space Radiation Analysis." n.d. Accessed September 24, 2020. https://www.fastrad.net/.

Fedder, J. A., and J. G. Lyon. 1995. "The Earth's Magnetosphere Is 165 RE Long: Self-Consistent Currents, Convection, Magnetospheric Structure, and Processes for Northward Interplanetary

Magnetic Field." *Journal of Geophysical Research: Space Physics* 100 (A3): 3623–35. https://doi.org/10.1029/94ja02633.

Feres, R., and G. Yablonsky. 2004. "Knudsen's Cosine Law and Random Billiards." *Chemical Engineering Science* 59 (7): 1541–56. https://doi.org/10.1016/j.ces.2004.01.016.

Fioretti, Valentina, Andrea Bulgarelli, Silvano Molendi, Simone Lotti, Claudio Macculi, Marco Barbera, Teresa Mineo, et al. 2018. "Magnetic Shielding of Soft Protons in Future X-Ray Telescopes: The Case of the ATHENA Wide Field Imager." *The Astrophysical Journal* 867 (1): 9. https://doi.org/10.3847/1538-4357/aade99.

Fioretti, Valentina, Teresa Mineo, Andrea Bulgarelli, Paolo Dondero, Vladimir Ivanchenko, Fan Lei, Simone Lotti, Claudio Macculi, and Alfonso Mantero. 2017. "Geant4 Simulations of Soft Proton Scattering in X-Ray Optics: A Tentative Validation Using Laboratory Measurements." *Experimental Astronomy* 44 (3): 413–35. https://doi.org/10.1007/s10686-017-9559-9.

Fortescue, P, G Swinerd, and J Stark. 2011. *Spacecraft Systems Engineering*.

Freyberg, Michael J., Ulrich G. Briel, Konrad Dennerl, Frank Haberl, Gisela D. Hartner, Elmar Pfeffermann, Eckhard Kendziorra, Marcus G. F. Kirsch, and David H. Lumb. 2004. "EPIC Pn-CCD Detector Aboard XMM-Newton: Status of the Background Calibration." In *X-Ray and Gamma-Ray Instrumentation for Astronomy XIII*, 5165:112. SPIE. https://doi.org/10.1117/12.506277.

"Geant4 User Documentation." n.d. Accessed September 11, 2020. https://geant4.web.cern.ch/support/user_documentation.

Gombosi, Tamas I., Bart van der Holst, Ward B. Manchester, and Igor V. Sokolov. 2018. "Extended MHD Modeling of the Steady Solar Corona and the Solar Wind." *Living Reviews in Solar Physics*. Springer. https://doi.org/10.1007/s41116-018-0014-4.

Gonzalez-Riestra, R., and P.M. Rodriguez-Pascual. 2014. "The Behaviour of the XMM-Newton Background: From the Beginning of the Mission until May 2014." *XMM-SOC-GEN-TN-0014*.

Gruber, D. E., J. L. Matteson, L. E. Peterson, and G. V. Jung. 1999. "The Spectrum of Diffuse Cosmic Hard X-Rays Measured with HEAO 1." *The Astrophysical Journal* 520 (1): 124–29. https://doi.org/10.1086/307450.

Hall, David, Andrew Holland, and Martin Turner. 2008. "Simulating and Reproducing Instrument Background for X-Ray CCD Spectrometers in Space." In *High Energy, Optical, and Infrared Detectors for Astronomy III*, 7021:70211Y. https://doi.org/10.1117/12.790711.

Hall, David J., and Andrew Holland. 2010. "Space Radiation Environment Effects on X-Ray CCD

Background." *Nuclear Instruments and Methods in Physics Research, Section A: Accelerators, Spectrometers, Detectors and Associated Equipment* 612 (2): 320–27. https://doi.org/10.1016/j.nima.2009.10.057.

Hall, David J., Jonathan Keelan, Chris Davis, Oliver Hetherington, Mark Leese, and Andrew D. Holland. 2018. "Predicting the Particle-Induced Background for Future x-Ray Astronomy Missions: The Importance of Experimental Validation for GEANT4 Simulations." In *High Energy, Optical, and Infrared Detectors for Astronomy VIII*, edited by Andrew D. Holland and James Beletic, 10709:124. SPIE. https://doi.org/10.1117/12.2500298.

Hall, David James. 2010. "Exploring the Impact of Detection Physics in X-Ray CCD Imagers and Spectrometers." The Open University.

Hathaway, David H. 2015. "The Solar Cycle." *Living Reviews in Solar Physics* 12 (1): 1–87. https://doi.org/10.1007/lrsp-2015-4.

Hauf, Steffan. 2012. "Studies on the Background of the Wide Field Imager Aboard the IXO and ATHENA X-Ray Telescopes." Technische Universitat Darmstadt.

Hauf, Steffen. 2009. "Simulations on the SIMBOL-X Detector Background." Technische Universitat Darmstadt.

"Helmholtz Pair of Coils D 1000644 Instruction Sheet." 2015. 3B Scientific Physics. 2015. https://www.3bscientific.co.uk/product-manual/1000644_EN.pdf.

Herbst, K, A Kopp, and B Heber. 2013. "Influence of the Terrestrial Magnetic Field Geometry on the Cutoff Rigidity of Cosmic Ray Particles" 31: 1637–43. https://doi.org/10.5194/angeo-31-1637-2013.

Hess, Victor. 1912. "Über Beobachtungen Der Durchdringenden Strahlung Bei Sieben Freiballonfahrten." *Physikalische Zeitschrift 13*, 1084–91.

Heynderickx, D., B. Quaghebeur, J. Wera, E. J. Daly, and H. D. R. Evans. 2005. "New Radiation Environment and Effects Models in the European Space Agency's Space Environment Information System (SPENVIS)." In *Space Weather*, 2:26–29. John Wiley & Sons, Ltd. https://doi.org/10.1029/2004SW000073.

Horne, Richard B., Richard M. Thorne, Yuri Y. Shprits, Nigel P. Meredith, Sarah A. Glauert, Andy J. Smith, Shrikanth G. Kanekal, et al. 2005. "Wave Acceleration of Electrons in the Van Allen Radiation Belts." *Nature* 437 (7056): 227–30. https://doi.org/10.1038/nature03939.

Howell, John R., M. Pinar Menguc, and Robert Siegel. 2015. *Thermal Radiation Heat Transfer*. https://doi.org/10.1201/b18835.

Howell, John R. 1982. *A Catalog of Configuration Factors*. *University of Austin, Texas*. McGraw-Hill.

"Https://Eosweb.Larc.Nasa.Gov/Project/Misr/Gallery/South_atlantic_anomaly." n.d. https://eosweb.larc.nasa.gov/project/misr/gallery/south_atlantic_anomaly.

"Https://Www.Swpc.Noaa.Gov/Products/Geospace-Magnetosphere-Movies." n.d. https://www.swpc.noaa.gov/products/geospace-magnetosphere-movies.

"Introduction to Geant4." 2010. 2010. http://citeseerx.ist.psu.edu/viewdoc/download?doi=10.1.1.464.7495&rep=rep1&type=pdf.

Janesick, James, Tom Elliott, Richard Bredthauer, Charles Chandler, and Barry Burke. 1988. "Fano-Noise-Limited CCDs." In *X-Ray Instrumentation in Astronomy II*, edited by Leon Golub, 0982:70. SPIE. https://doi.org/10.1117/12.948704.

Janesick, James R. 2001. *Scientific Charge-Coupled Devices*. SPIE Press.

Janesick, James R., Tom Elliott, Stewart Collins, Morley M. Blouke, and Jack Freeman. 1987. *Scientific Charge-Coupled Devices*. *Optical Engineering*. Vol. 26. SPIE Press. https://doi.org/10.1117/12.7974139.

Jansen, F, D Lumb, B Altieri, J Clavel, M Ehle, C Erd, C Gabriel, et al. 2001. "XMM-Newton Observatory. I. The Spacecraft and Operations." *Astronomy and Astrophysics*. https://doi.org/10.1051/0004-6361:20000036.

Kalos, Malvin H., and Paula A. Whitlock. 1986. *Monte Carlo Methods*. J. Wiley & Sons.

Kamal, A. 1969. "Passage of Charged Particles Through Matter. In: Nuclear Physics." *Nuclear Physics A* 123 (4): 328–55. https://doi.org/10.1007/978-3-642-38655-8.

Kienlin, Andreas von, Tanja Eraerds, Esra Bulbul, Valentine Fioretti, Fabio Gastaldello, Catherine E. Grant, David Hall, et al. 2018. "Evaluation of the Athena/WFI Instrumental Background." In *Space Telescopes and Instrumentation 2018: Ultraviolet to Gamma Ray*, edited by Jan-Willem A. den Herder, Kazuhiro Nakazawa, and Shouleh Nikzad, 10699:53. SPIE. https://doi.org/10.1117/12.2311987.

Kim, Sung Hun, Maria Grazia Pia, Tullio Basaglia, Min Cheol Han, Gabriela Hoff, Chan Hyeong Kim, and Paolo Saracco. 2015. "Validation Test of Geant4 Simulation of Electron Backscattering." *IEEE Transactions on Nuclear Science* 62 (2): 451–79. https://doi.org/10.1109/TNS.2015.2401055.

Kivelson, MG, MG Kivelson, and CT Russell. 1995. *Introduction to Space Physics*.

Kokubun, Susumu, Tatsundo Yamamoto, Mario H. Acuña, Kanji Hayashi, Kazuo Shiokawa, and Hideaki Kawano. 1994. “The GEOTAIL Magnetic Field Experiment.” *Journal of Geomagnetism and Geoelectricity* 46 (1): 7–21. https://doi.org/10.5636/jgg.46.7.

Koldobskiy, Sergey A., Gennady A. Kovaltsov, and Ilya G. Usoskin. 2018. “A Solar Cycle of Cosmic Ray Fluxes for 2006–2014: Comparison between PAMELA and Neutron Monitors.” *Journal of Geophysical Research: Space Physics* 123 (6): 4479–87. https://doi.org/10.1029/2018JA025516.

Koon, Wang Sang, Martin W Lo, Jerrold E Marsden, and Shane D Ross. 2000. “Dynamical Systems, the Three-Body Problem and Space Mission Design.” In *Equadiff 99*, 1167–81. World Scientific Publishing Company. https://doi.org/10.1142/9789812792617_0222.

Kuntz, K D, and S L Snowden. 2008. “The EPIC-MOS Particle-Induced Background Spectra.” *Astronomy and Astrophysics* 478 (2): 575–96. https://doi.org/10.1051/0004-6361:20077912.

Kurczynski, P., R. H. Pehl, E. L. Hull, D. Palmer, M. J. Harris, H. Seifert, B. J. Teegarden, et al. 1999. “Long-Term Radiation Damage to a Spaceborne Germanium Spectrometer.” *Nuclear Instruments and Methods in Physics Research, Section A: Accelerators, Spectrometers, Detectors and Associated Equipment* 431 (1): 141–47. https://doi.org/10.1016/S0168-9002(99)00283-1.

Lam Trong, Thien. 2016. “X-IFU Technical Challenge.” In *Space Telescopes and Instrumentation 2016: Ultraviolet to Gamma Ray*, 9905:99052G. https://doi.org/10.1117/12.2233634.

Lambert, Johann. 1760. “Photometrie.”

Lepping, R. P., L. F. Burlaga, B. T. Tsurutani, K. W. Ogilvie, A. J. Lazarus, D. S. Evans, and L. W. Klein. 1991. “The Interaction of a Very Large Interplanetary Magnetic Cloud with the Magnetosphere and with Cosmic Rays.” *Journal of Geophysical Research* 96 (A6): 9425. https://doi.org/10.1029/91ja00670.

Li, Liansheng, Chunyu Wang, Loulou Deng, Fuchang Zuo, Zhiwu Mei, and Zhengxin Lv. 2017. “Design and Simulation of a Magnetic Diverter Structure for the X-Ray Detecting System.” In *Astrophysics and Space Science Proceedings*, 47:543–53. Springer Netherlands. https://doi.org/10.1007/978-3-319-19309-0_54.

Lotti, Simone, Claudio Macculi, Matteo D’Andrea, Valentina Fioretti, Paolo Dondero, Alfonso Mantero, Gabriele Minervini, Luigi Piro, and Andrea Argan. 2018. “Estimates for the Background of the ATHENA X-IFU Instrument: The Cosmic Rays Contribution.” In *Space Telescopes and Instrumentation 2018: Ultraviolet to Gamma Ray*, edited by Jan-Willem A. den Herder, Kazuhiro Nakazawa, and Shouleh Nikzad, 10699:61. SPIE. https://doi.org/10.1117/12.2313236.

Lumb, D H, R S Warwick, M Page, and A De Luca. 2002. “X-Ray Background Measurements with XMM-Newton EPIC.” *Astronomy and Astrophysics* 389 (1): 93–105. https://doi.org/10.1051/0004-6361:20020531.

Lutz, G., R. H. Richter, and L. Strüder. 2001. “Novel Pixel Detectors for X-Ray Astronomy and Other Applications.” *Nuclear Instruments and Methods in Physics Research, Section A: Accelerators, Spectrometers, Detectors and Associated Equipment* 461 (1–3): 393–404. https://doi.org/10.1016/S0168-9002(00)01258-4.

Maezawa, K., and T. Hori. 1998. “The Distant Magnetotail: Its Structure, IMF Dependence, and Thermal Properties.” In *Geophysical Monograph Series*, 105:1–9. Blackwell Publishing Ltd. https://doi.org/10.1029/GM105p0001.

Mann, I. R., L. G. Ozeke, K. R. Murphy, S. G. Claudepierre, D. L. Turner, D. N. Baker, I. J. Rae, et al. 2016. “Explaining the Dynamics of the Ultra-Relativistic Third Van Allen Radiation Belt.” *Nature Physics* 12 (10): 978–83. https://doi.org/10.1038/nphys3799.

Mathematica. 2019. Champaign, Illinois: Wolfram Research, Inc.

Mauk, Barry. 1996. “Introduction to Geomagnetically Trapped Radiation.” *Eos, Transactions American Geophysical Union* 77 (21): 199. https://doi.org/10.1029/96eo00138.

McEvoy’s Handbook of Photovoltaics. 2018. Elsevier. https://doi.org/10.1016/c2015-0-01840-8.

McNamara, P. W. 2006. “LISA Pathfinder.” In *AIP Conference Proceedings*, 873:49–58. AIP. https://doi.org/10.1063/1.2405021.

Meidinger, Norbert, Sebastian Albrecht, Michael Bonholzer, Johannes Müller-Seidlitz, Kirpal Nandra, Sabine Ott, Markus Plattner, and Wolfgang Treberspurg. 2019. “Status of the Wide Field Imager Instrument for Athena.” In *UV, X-Ray, and Gamma-Ray Space Instrumentation for Astronomy XXI*, edited by Oswald H. Siegmund, 11118:33. SPIE. https://doi.org/10.1117/12.2528109.

Meidinger, Norbert, Robert Andritschke, Stefanie Ebermayer, Johannes Elbs, Olaf H ¨ Alker, Robert Hartmann, Sven Herrmann, et al. 2010. “Development of the Focal Plane PNCCD Camera System for the X-Ray Space Telescope EROSITA.” https://doi.org/10.1016/j.nima.2010.03.126.

Meidinger, Norbert, Josef Eder, Tanja Eraerds, Kirpal Nandra, Daniel Pietschner, Markus Plattner, Arne Rau, and Rafael Strecker. 2016. “The Wide Field Imager Instrument for Athena.” Edited by Jan-Willem A. den Herder, Tadayuki Takahashi, and Marshall Bautz. *Space Telescopes and Instrumentation 2016: Ultraviolet to Gamma Ray* 48 (3): 99052A. https://doi.org/10.1117/12.2231604.

———. 2018. “The Wide Field Imager Instrument for Athena.” Edited by Jan-Willem A. den Herder, Tadayuki Takahashi, and Marshall Bautz. *Contributions of the Astronomical Observatory Skalnate Pleso* 48 (3): 498–505. https://doi.org/10.1117/12.2231604.

Meidinger, Norbert, Josef Eder, Maria Fürmetz, Kirpal Nandra, Daniel Pietschner, Markus Plattner, Arne Rau, et al. 2015. “Development of the Wide Field Imager for Athena.” *UV, X-Ray, and Gamma-Ray Space Instrumentation for Astronomy XIX* 9601: 96010H. https://doi.org/10.1117/12.2187012.

Minow, Joseph I., William C. Blackwell, and Anne M. Diekmann. 2004. “Plasma Environment and Models for L2.” In *42nd AIAA Aerospace Sciences Meeting and Exhibit*, 1079. https://doi.org/10.2514/6.2004-1079.

Moody, Ian ;, Marc ; Watkins, Ray ; Bell, Matthew ; Soman, Jonathan Keelan, Andrew Holland, Ian ; Moody, Marc ; Watkins, Ray ; Bell, and Matthew ; Soman. 2017. “CCD QE in the Soft X-Ray Range.” *E2v Technical Note*.

Moore, Thomas E. 1991. “Origins of Magnetospheric Plasma.” *Reviews of Geophysics* 29 (S2): 1039–48. https://doi.org/10.1002/rog.1991.29.s2.1039.

Moretti, A., C. Pagani, G. Cusumano, S. Campana, M. Perri, A. Abbey, M. Ajello, et al. 2009. “A New Measurement of the Cosmic X-Ray Background.” *Astronomy and Astrophysics* 1126 (2): 501–9. https://doi.org/10.1063/1.3149419.

Moretti, A, S Vattakunnel, P Tozzi, R Salvaterra, P Severgnini, D Fugazza, F Haardt, and R Gilli. 2012. “Spectrum of the Unresolved Cosmic X-Ray Background: What Is Unresolved 50 Years after Its Discovery.” *Astronomy and Astrophysics* 548: 87. https://doi.org/10.1051/0004-6361/201219921.

Moseley, H.G.J. 1913. “ XCIII. The High-Frequency Spectra of the Elements .” *The London, Edinburgh, and Dublin Philosophical Magazine and Journal of Science* 26 (156): 1024–34. https://doi.org/10.1080/14786441308635052.

Nandra, K, X Barcons, J W den Herder, M Watson, D Barret, A Fabian, L Piro, and others. 2014. “ATHENA the Advanced Telescope for High Energy Astrophysics. A Mission Addressing the Hot and Energetic Universe Science Theme.” *Mission Proposal Submitted to ESA on Behalf of the Athena Team (April 2014), Http://Www. the-Athena-x-Ray-Observatory. Eu*.

Nandra, Kirpal. 2012. “The Advanced Telescope for High-Energy Astrophysics.” *ESA*, 1–36.

Ness, Jan-Uwe, A.N. Parmar, and L.A. Valencic. 2014. “XMM- Newton Publication Statistics : XMM- Newton Publication Statistics.” *Astronomische Nachrichten* 335 (2): 210–20.

https://doi.org/10.1002/asna.v335.2.

Odstrcil, D. 2003. “Modeling 3-D Solar Wind Structure.” *Advances in Space Research* 32 (4): 497–506. https://doi.org/10.1016/S0273-1177(03)00332-6.

Ott, S., A. Bähr, T. Brand, T. Dauser, N. Meidinger, M. Plattner, and W. Stechele. 2016. “New Evaluation Concept of the Athena WFI Camera System by Emulation of X-Ray DEPFET Detectors.” *Journal of Instrumentation* 11 (1): C01028. https://doi.org/10.1088/1748-0221/11/01/C01028.

Pandola, L., C. Andenna, and B. Caccia. 2015. “Validation of the Geant4 Simulation of Bremsstrahlung from Thick Targets below 3 MeV.” *Nuclear Instruments and Methods in Physics Research, Section B: Beam Interactions with Materials and Atoms* 350 (May): 41–48. https://doi.org/10.1016/j.nimb.2015.03.033.

“Paul Scherrer Institut (PSI).” n.d. https://www.psi.ch/en/pif.

Pavón-Carrasco, F. Javier, and Angelo De Santis. 2016. “The South Atlantic Anomaly: The Key for a Possible Geomagnetic Reversal.” *Frontiers in Earth Science* 4 (April). https://doi.org/10.3389/feart.2016.00040.

Perinati, Emanuele, Marco Barbera, Sebastian Diebold, Alejandro Guzman, Andrea Santangelo, and Chris Tenzer. 2017. “Preliminary Assessment of the ATHENA/WFI Non-X-Ray Background.” *Experimental Astronomy* 44 (3): 387–99. https://doi.org/10.1007/s10686-017-9541-6.

Perinati, Emanuele, Daniele Spiga, Andrea Santangelo, and Chris Tenzer. 2018. “A Magnetic Electron Repeller to Improve the ATHENA/WFI Background Level.” In *Space Telescopes and Instrumentation 2018: Ultraviolet to Gamma Ray*, edited by Jan-Willem A. den Herder, Kazuhiro Nakazawa, and Shouleh Nikzad, 10699:152. SPIE. https://doi.org/10.1117/12.2312699.

Perinati, Emanuele, Chris Tenzer, Andrea Santangelo, Konrad Dennerl, Michael Freyberg, and Peter Predehl. 2012. “The Radiation Environment in L-2 Orbit: Implications on the Non-X-Ray Background of the EROSITA Pn-CCD Cameras.” *Experimental Astronomy* 33 (1): 39–53. https://doi.org/10.1007/s10686-011-9269-7.

Perko, J. S., and L. A. Fisk. 1983. “Solar Modulation of Galactic Cosmic Rays: 5. Time-Dependent Modulation.” *Journal of Geophysical Research: Space Physics* 88 (A11): 9033–36. https://doi.org/10.1029/JA088iA11p09033.

Pianetta, Piero. 1986. “3.2 Low-Energy Electron Ranges in Matter.” In *X-Ray Data Booklet*.

Pilbratt, Goran L. 2003. “Herschel Space Observatory Mission Overview.” In *IR Space Telescopes*

and Instruments, edited by John C. Mather, 4850:586. SPIE. https://doi.org/10.1117/12.461767.

Pourrouquet, Pierre, Jean Charles Thomas, Pierre Francois Peyrard, Robert Ecoffet, and Guy Rolland. 2011. "FASTRAD 3.2: Radiation Shielding Tool with a New Monte Carlo Module." In *IEEE Radiation Effects Data Workshop*. Las Vegas, NV, USA: IEEE. https://doi.org/10.1109/REDW.2010.6062530.

Predehl, Peter, Robert Andritschke, Werner Becker, Walter Bornemann, Heinrich Bräuninger, Hermann Brunner, Thomas Boller, et al. 2014. "EROSITA on SRG." In *Space Telescopes and Instrumentation 2014: Ultraviolet to Gamma Ray*, edited by Tadayuki Takahashi, Jan-Willem A. den Herder, and Mark Bautz, 9144:91441T. SPIE. https://doi.org/10.1117/12.2055426.

Prouvé, T., J. M. Duval, I. Charles, N. Y. Yamasaki, K. Mitsuda, T. Nakagawa, K. Shinozaki, et al. 2018. "ATHENA X-IFU 300 K-50 mK Cryochain Demonstrator Cryostat." *Cryogenics* 89 (January): 85–94. https://doi.org/10.1016/j.cryogenics.2017.11.009.

Ralchenko et al., Y. n.d. "NIST Atomic Spectra Database." National Institute of Standards and Technology.

Ratcliffe, J. A., and Thomas E. Holzer. 1973. "An Introduction to the Ionosphere and Magnetosphere." *American Journal of Physics* 41 (5): 761–62. https://doi.org/10.1119/1.1987378.

Rau, A., N. Meidinger, K. Nandra, M. Porro, D. Barret, A. Santangelo, C. Schmid, et al. 2013. "The Hot and Energetic Universe: The Wide Field Imager (WFI) for Athena+." *ArXiv Preprint ArXiv:1308.6785* 1308: 6785.

Reames, Donald V. 2013. "The Two Sources of Solar Energetic Particles." *Space Science Reviews*. Springer. https://doi.org/10.1007/s11214-013-9958-9.

Reeves, G. D., H. E. Spence, M. G. Henderson, S. K. Morley, R. H.W. Friedel, H. O. Funsten, D. N. Baker, et al. 2013. "Electron Acceleration in the Heart of the Van Allen Radiation Belts." *Science* 341 (6149): 991–94. https://doi.org/10.1126/science.1237743.

Rossi, Alessandro. 2008. "Resonant Dynamics of Medium Earth Orbits: Space Debris Issues." *Celestial Mechanics and Dynamical Astronomy* 100 (4): 267–86. https://doi.org/10.1007/s10569-008-9121-1.

Rothwell, P., and J. Quenby. 1958. "Cosmic Rays in the Earth's Magnetic Field." *Il Nuovo Cimento* 8 (2 Supplement): 249–56. https://doi.org/10.1007/BF02962532.

Russell, C T. 1993. "Planetary Magnetospheres." *Reports on Progress in Physics*. IOP Publishing. https://doi.org/10.1088/0034-4885/56/6/001.

Schartel, Norbert, Maria Santos-Lleo, Arvind Parmar, and Jean Clavel. 2010. “10 Years of : Commemorating XMM-Newton’s First Decade.” *ESA Bulletin*, no. 141 (February): 2–9. https://doi.org/http://dx.doi.org/10.5930/issn.0376-4265.

Schwadron, N. A., L. Townsend, K. Kozarev, M. A. Dayeh, F. Cucinotta, M. Desai, M. Golightly, et al. 2010. “Earth-Moon-Mars Radiation Environment Module Framework.” *Space Weather* 8 (1). https://doi.org/10.1029/2009SW000523.

Shen, V. K., D. W. Siderius, W. P. Krekelberg, and H. W. Hatch. 2018. “NIST Standard Reference Simulation Website - National Institute of Standards and Technology.” *NIST Standard Reference Database Number 173*.

Simpson, James, John Lane, Christopher Immer, and Robert Youngquist. 2001. “Simple Analytic Expressions for the Magnetic Field of a Circular Current Loop.” *Recon*, no. February 2001: 1–3.

Smith, D. M., R. P. Lin, P. Turin, D. W. Curtis, J. H. Primbsch, R. D. Campbell, R. Abiad, et al. 2002. “The RHESSI Spectrometer.” *Solar Physics* 210 (1–2): 33–60. https://doi.org/10.1023/A:1022400716414.

Soman, Matthew Richard. 2014. “High-Resolution Detectors for Soft X-Ray Spectroscopy.” The Open University. https://doi.org/10.21954/ou.ro.0000a424.

Spiga, D., V. Fioretti, A. Bulgarelli, E. Dell’Orto, L. Foschini, G. Malaguti, G. Pareschi, G. Tagliaferri, and A. Tiengo. 2008. “A Magnetic Diverter for Charged Particle Background Rejection in the SIMBOL-X Telescope.” *Space Telescopes and Instrumentation 2008: Ultraviolet to Gamma Ray* 7011 (Lc): 70112Y. https://doi.org/10.1117/12.789917.

Sternglass, E. J. 1957. “Theory of Secondary Electron Emission by High-Speed Ions.” *Physical Review* 108 (1): 1–12. https://doi.org/10.1103/PhysRev.108.1.

Stone, E.C., A.M. Frandsen, R.A. Mewaldt, E.R. Christian, D. Margolies, J.F. Ormes, and F. Snow. 1998. “The Advanced Composition Explorer.” *Space Science Reviews* 86 (1/4): 1–22. https://doi.org/10.1023/A:1005082526237.

Strüder, L., U. Briel, K. Dennerl, R. Hartmann, E. Kendziorra, N. Meidinger, E. Pfeffermann, et al. 2001. “The European Photon Imaging Camera on XMM-Newton: The Pn-CCD Camera.” *Astronomy and Astrophysics* 365 (1): L18--L26. https://doi.org/10.1051/0004-6361:20000066.

Svestka, Zarek. 1976. *Solar Flares*. Springer Netherlands. https://doi.org/10.1007/978-94-010-1459-5.

Swinerd, Graham. 2009. *How Spacecraft Fly*. Springer New York. https://doi.org/10.1007/978-0-387-76572-3.

Tóth, Gábor, Bart van der Holst, Igor V. Sokolov, Darren L. De Zeeuw, Tamas I. Gombosi, Fang

Fang, Ward B. Manchester, et al. 2012. “Adaptive Numerical Algorithms in Space Weather Modeling.” *Journal of Computational Physics* 231 (3): 870–903. https://doi.org/10.1016/j.jcp.2011.02.006.

Turner, M. J.L., A. Abbey, M. Arnaud, M. Balasini, M. Barbera, E. Belsole, P. J. Bennie, et al. 2001. “The European Photon Imaging Camera on XMM-Newton: The MOS Cameras.” *Astronomy and Astrophysics* 365 (1): L27–35. https://doi.org/10.1051/0004-6361:20000087.

Tutt, James H., Andrew D. Holland, Neil J. Murray, David J. Hall, Richard D. Harriss, Andrew Clarke, and Anthony M. Evagora. 2012. “The Noise Performance of Electron-Multiplying Charge-Coupled Devices at Soft x-Ray Energy Values.” *IEEE Transactions on Electron Devices* 59 (8): 2192–98. https://doi.org/10.1109/TED.2012.2200488.

Tutt, James H, Andrew D Holland, David J Hall, Richard D Harriss, and Neil J Murray. 2012. “The Noise Performance of Electron-Multiplying Charge-Coupled Devices at X-Ray Energies.” *IEEE Transactions on Electron Devices* 59 (1): 167–75. https://doi.org/10.1109/TED.2011.2172611.

Tutt, James Henry. 2012. “Development of CCD and EM-CCD Technology for High Resolution X-Ray Spectrometry Development of CCD and EM-CCD Technology for High Resolution X-Ray Spectrometry.” https://doi.org/10.21954/ou.ro.0000f0aa.

Tylka, A.J., J.H. Adams, Paul R. P.R. Paul R. Boberg, Buddy Brownstein, W.F. William F. Dietrich, E.O. Erwin O. E.O. Erwin O. Flueckiger, E.L. Edward L. Petersen, et al. 1997. “CREME96: A Revision of the Cosmic Ray Effects on Micro-Electronics Code.” *IEEE Transactions on Nuclear Science* 44 (6 part 1): 2150–60. https://doi.org/10.1109/23.659030.

Washimi, H., G. P. Zank, Q. Hu, T. Tanaka, and K. Munakata. 2015. “MHD Modeling of the Outer Heliospheric Structures around the Heliopause.” *Astrophysical Journal* 809 (1). https://doi.org/10.1088/0004-637X/809/1/16.

Weiland, J L, N Odegard, R S Hill, E Wollack, G Hinshaw, M R Greason, N Jarosik, et al. 2011. “Seven-Year Wilkinson Microwave Anisotropy Probe (WMAP*) Observations: Planets and Celestial Calibration Sources.” *Astrophysical Journal, Supplement Series* 192 (2): 19. https://doi.org/10.1088/0067-0049/192/2/19.

Weinberg, S. 1995. *The Quantum Theory of Fields*. Cambridge university press.

Westover, Shayne, Rainer Meinke, Shaun Nerolich, Scott Washburn, Roberto Battiston, William Burger, Dallas Kasaboski, and Francis Davies. 2014. “Magnet Architectures and Active Radiation Shielding Study (MAARSS) Final Report for NASA Innovative Advanced Concepts Phase II.”

Xcom, NIST. 2010. “Photon Cross Sections Database.” *Gaithersburg: National Institute of Standards and Technology. Http://Www. Nist. Gov/Physlab/Data/Xcom*.

“XMM-Newton Users Handbook.” 2019. 2019. https://xmm-tools.cosmos.esa.int/external/xmm_user_support/documentation/uhb/.

Young, Hugh D. 1992. *University Physics*. Addison-Wesley.

Zhao, Xiao Yun, Huan Yu Wang, Feng Wu, Xiang Cheng Meng, Yu Qian Ma, Hong Lu, Hui Wang, et al. 2013. “A Geometric Factor Calculation Method Based on the Isotropic Flux Assumption.” *Chinese Physics C* 37 (12): 126201. https://doi.org/10.1088/1674-1137/37/12/126201.